Inversion of Time Domain Electromagnetic Data for the Detection of Unexploded Ordnance

by

Leonard Rodriguez Pasion

B.Sc., Simon Fraser University, 1996
M.Sc., University of British Columbia, 1999

A THESIS SUBMITTED IN PARTIAL FULFILLMENT OF
THE REQUIREMENTS FOR THE DEGREE OF

DOCTOR OF PHILOSOPHY

in

THE FACULTY OF GRADUATE STUDIES

(Geophysics)

THE UNIVERSITY OF BRITISH COLUMBIA

August 2007

© Leonard Rodriguez Pasion, 2007

Inversion of Time Domain Electromagnetic Data for the Detection of Unexploded Ordnance

by

Leonard Rodriguez Pasion

B.Sc., Simon Fraser University, 1996
M.Sc., University of British Columbia, 1999

A THESIS SUBMITTED IN PARTIAL FULFILLMENT OF
THE REQUIREMENTS FOR THE DEGREE OF

DOCTOR OF PHILOSOPHY

in

THE FACULTY OF GRADUATE STUDIES

(Geophysics)

THE UNIVERSITY OF BRITISH COLUMBIA

August 2007

© Leonard Rodriguez Pasion, 2007

Abstract

Unexploded Ordnance (UXO) discrimination is achieved by extracting parameters from geophysical data that reflect characteristics of the target that generated the measured signal. Model-based parameters are estimated through data inversion, where the optimal parameters are those that produce acceptable agreement between observed and predicted data and satisfy any prior information we have of the target. These parameters are then used as inputs to statistical classification methods to determine the likelihood that the target is, or is not, a UXO. The task of accurately recovering model parameters is more difficult when sensor data are contaminated with geological noise originating from magnetic soils. In regions of highly magnetic soil, magnetometry and electromagnetic sensors often detect large anomalies that are of geologic, rather than of metallic origin. In this thesis I investigate different methods of recovering the dipole polarization tensor from time domain electromagnetic (TEM) data. The different data inversion methods are characterized by the amount of a priori information used. Different a priori information considered include target location and depth estimated from other data sets, and knowledge of the different types of UXO that can be expected at the site. In the first part of this thesis, I assume that the influence of background geology can be removed through a data pre-processing procedures such that the UXO can be assumed to sit in free space. In the second part of this thesis we take a closer look at the influence of viscous remnant magnetization on electromagnetic data. Several software and hardware based approaches are proposed for improving detection and discrimination of UXO in geologically magnetic areas.

Table of Contents

Abstract ii

Table of Contents iii

List of Tables ix

List of Figures xi

Acknowledgements xxiv

Dedication xxvi

1 Introduction 1

2 An Approximate Forward Model For TEM Data 15

2.1 Introduction 15

2.2 Developing an Approximate Forward Model 16

2.2.1 Response of a Spherical Body 16

2.2.2 Approximating the Magnetic Polarizability Dyadic for an Axi-Symmetric Body 21

2.2.3 Parameterizing $L(t)$ 23

2.2.4 The Approximate Forward Model 28

2.3 Some Characteristics of the Dipole Model 35

2.3.1 The Relationship Between a Horizontal Loop Tx and the Transverse and Axial 35

2.3.2 The Similarity Between Rod and Plate Responses 38

2.4 Conclusion 45

3 Inversion of Time Domain Electromagnetic Data 46
3.1 Formulation of the Inverse Problem 46
3.1.1 Inversion Methodology 46
3.2 Defining the Objective Function 50
3.2.1 Defining the Data Covariance Matrix 50
3.2.2 Forming the Data Vector $\mathbf{d}^{obs}$ 57
3.2.3 Defining the Forward Model $\mathcal{F}[\mathbf{m}]$ 60
3.3 Estimating Dipole Parameters Using a Local Search Algorithm 61
3.4 Analysis for Interpreting Local Search Parameter Estimates 66
3.4.1 Parameter variance for the unconstrained case 67
3.4.2 Calculating the Parameter Covariance Matrix when there are constrained parameters 68
3.5 Unconstrained inversion of TEM data over a 105 mm Projectile 69
3.5.1 Application of a Local Search Algorithm 71
3.5.2 Application of a Global Search Algorithm 75
3.6 A Comparison of Two and Three Polarization Inversions 79
3.6.1 Fitting Cued interrogation style Geonics EM63 TEM data from a 3.5 inch Rocket 80
3.6.2 Fitting TEM data from an array of Geonics EM61 Mark 2 sensors 82
3.6.3 Summary 88
3.7 Conclusion 90

4 Joint and Cooperative Inversion of Time Domain Electromagnetic Data 92
4.1 Introduction 92
4.2 Dipole modelling of TEM and Magnetics Data 99
4.2.1 Magnetic Forward Modelling 99
4.2.2 Time Domain EM Forward Modelling 100
4.3 Cooperative Inversion of TEM and Magnetics Data 101
4.3.1 Inversion of Magnetics Data 101
4.3.2 Inversion of TEM Data with Location Constraint 102
4.3.3 Estimation of Shape and Size from Magnetics Data 103

4.4 Joint Inversion of TEM and Magnetics Data 104
4.5 Field Data Example 107
4.6 Conclusion 112

5 Application of a Simple Library Method for Identifying UXO 116
5.1 Introduction 116
5.2 Method 117
5.3 Results and Analysis 118
5.3.1 Development of a Target Library From Test Stand Data 118
5.3.2 Application of the Library method to data collected at the Sky Research Ashland Test Plot Data 121
5.4 Fitting both dipole and soil parameters simultaneously 129
5.5 Application to Field Data from Camp Lejeune, North Carolina 130
5.6 Conclusion 135

6 Establishing Data Quality Requirements for Inversion Using Simulations 137
6.1 Factors affecting data quality 138
6.1.1 Signal to Noise Ratio 139
6.1.2 Errors due to inaccurate sensor positioning 142
6.2 Survey Design Parameters that Affect Detection 146
6.2.1 Receiver Loop Size 146
6.2.2 Target depth and orientation 147
6.2.3 Determining a maximum line spacing for detection 148
6.3 Data Requirements for Discrimination 153
6.3.1 Monte Carlo analysis 154
6.3.2 Results 163
6.3.3 Utilizing simulation results 163
6.4 Conclusion 166

7 Detection of UXO in Magnetic Environments 169
7.1 Magnetic Properties of Soils 171

7.2 Viscous Remanent Magnetization of a Collection of Single Domain Grains 172
7.3 The Magnetic Susceptibility of a Collection of Single Domain Grains 174
7.4 Modelling the Electromagnetic Response of Viscous Remanent Soil 178
7.4.1 The Electromagnetic Response of a 1-D Layered Earth 178
7.4.2 The Effect of Magnetic Susceptibility on the Electromagnetic Response . . 181
7.4.3 Comparing the Electromagnetic Response of a Steel Object and Viscous Remanent Magnetic Soils 186
7.5 Application to ITEP Landmine Test Lanes 187
7.6 Conclusion 190

8 Processing of Electromagnetic Data Acquired in Magnetic Settings 191
8.1 The Electromagnetic Response of a Viscous Remnant Magnetic Halfspace 192
8.2 The Effect of Height Variations on the Sensor Response 196
8.3 The Additivity of Background and Target Responses 202
8.4 Estimating the response of the background geology 204
8.5 Testing EMI Processing Methods using simulated TEM Data 207
8.5.1 Simulated Noise 209
8.5.2 Baseline noise 210
8.5.3 Sensor Position Uncertainty 210
8.5.4 Simulating the Magnetic Background Signal 211
8.5.5 Examples of Simulated Data Sets 212
8.6 Picking Targets in highly magnetic soils 214
8.7 The accuracy of filtering when estimating the background response 224
8.8 The effect of VRM noise on recovered model parameters 227
8.9 Processing of data collected on Kaho'olawe Island, Hawaii 232
8.9.1 Geonics EM63 TEM data 233
8.9.2 Geophex GEM3 Frequency Domain Electromagnetic Data 240
8.10 Improving detection and identification by using horizontal components of the secondary field 247
8.10.1 Application to Synthetic Data 248
8.10.2 Inversion Results 250

8.10.3 Summary 250
8.11 Conclusion 251

9 Conclusions 253

I Appendices 257

A Comparison of the Dipole Model and Data collected at the USACE ERDC 258
A.1 TEM Data Collection at the U.S. Army Engineer Research and Development Center (ERDC) Unexploded Ordnance (UXO) Test Site 259
A.1.1 Plan Measurements 259
A.1.2 Decay Measurements 262
A.1.3 Analysis 262

B A Differential EMI Approach for Detecting UXO in Magnetic Geology 279
B.1 Introduction 279
B.2 The TEM Response of VRM soils and Metallic Objects 280
B.3 Soil Compensation Processing Applied to Variable Transmitter Waveform TEM Data 282
B.3.1 Instrumentation 282
B.3.2 Soil Model Fitting 285
B.3.3 Differential Analysis 286
B.3.4 Kaho'olawe Island Navy QA Grid Data 287
B.3.5 Waimea Geophysical Proveout at the Former Waikaloa Maneuver Area . . 301
B.4 Conclusion 305

C The Effect of Transmitter waveform on the TEM Response 311
C.1 Effect of Tx pulse length 311
C.2 Effect of Tx Pulse Ramp off 313
C.3 Effect of Tx Pulse time constant 314
C.4 Effect of Previous pulses 316
C.5 Response due to the EM63 and EM61 pulse 319

C.6 Summary 320

D The magnetization decay for different waveforms 321

D.1 The Magnetization decay $M(t)$ for Finite width pulse 321

D.2 The $\partial M/\partial t$ response for a finite width pulse 323

D.3 The $\partial M/\partial t$ response for a ramp-on response 324

Bibliography 327

List of Tables

3.1 Comparison of recovered model parameters from the local analysis and parameters derived from the Neighbourhood Algorithm (NA-Bayes) (Sambridge, 1999a,b). . . 72

3.2 Comparison of NA-Bayes and local analysis. 74

3.3 Comparison of two different starting models. 74

3.4 Comparison of NA-Bayes and local analysis. 74

3.5 Comparison of three and two polarization inversions of data collected over the SCAR in Figure 3.21. 85

3.6 Comparison of two and three-polarization inversions of data collected over the OE scrap in Figure 3.23. 86

3.7 Comparison of 2 and 3 polarization inversions of data collected over a buried 37 mm projectile. 88

4.1 Comparison of the recovered model parameters for: (B) a Stokes mortar at a depth of 60 cm, (C) a Stokes mortar at a depth of 100 cm, unconstrained location, and (D) a Stokes mortar at a depth of 100 cm, with location constrained to ± 5 cm of the real location. Row (A) lists the correct parameters. 95

5.1 Description of UXO in our target library. 119

5.2 Blind test results when inverting dynamically acquired data. 126

5.3 Blind test results when inverting static data. 127

5.4 Blind test results when inverting static data. 132

6.1 Summary of average absolute deviations for $k_1 = 5$ and $k_2 = 1$ results of Figure 6.17 162

6.2 Summary of average absolute deviations for $k_1 = 10$ and $k_2 = 1$ results of Figure 6.17 162

7.1 Frequency dependent susceptibilities and ground reference heights (GRH) for a pair of landmine test lanes in Oberjettenberg, Germany and Benkovac, Croatia. The column titled $\Delta\chi$ contains the difference in susceptibility measured by the Bartington MS2D meter. 171

7.2 Susceptibility measurements ($\times 10^{-5}$ S.I.) at the Seagull Site. 177

8.1 Comparing recovered parameters for data in Figure 8.26. 229

8.2 Ground truth for Grids 2D and 2E. 232

8.3 Inversion Results for a Stokes Mortar buried in a background of magnetic soils. . . 251

List of Figures

1.1 Some typical UXO. 1

1.2 The basic steps to detecting and discriminating UXO. 2

1.3 An example of magnetometer systems and magnetometer data. 4

1.4 Examples of some scrap targets excavated during a UXO remediation project at the Former Camp Croft Army Training Facility Spartanburg, South Carolina. 5

1.5 A pop can excavated during cleanup activities with the Montana Army National Guard at Limestone Hills in Helena, Montana. 6

1.6 Examples of electromagnetic sensors. 7

1.7 Examples of electromagnetic induction sensor data 8

1.8 Ground penetrating radar. (a) Photo of a 250 MHz Noggin Smart Cart manufactured by Sensors and Software. (b) A cross-section of data collected at Camp Lejeune. The hyperbolas in the left circle indicate a single target, while the data in the right circle show a the presence of multiple scatterers. 9

1.9 Example of detecting UXO in a magnetic setting. 13

2.1 Geonics EM63 data collected over a 155 mm projectile at the USACE-ERDC test-stand in Vicksburg, MS. The transition from a single peak at early times to a double peak at later times is characteristic of a horizontal, rod-like target. 16

2.2 Geonics EM63 data collected over a BDU-28 submunition at the USACE-ERDC teststand in Vicksburg, MS. 17

2.3 Fitting the time decay of a sphere using $L(t)$. 18

2.4 First solution ($s = 1$) to the sphere transcendental equation (Equation 2.4). 19

2.5 A comparison of some different parameterizations for a sphere. 24

2.6 Fitting the time decay of a sphere using Equation 2.15. 25

2.7 Fitting the time decay of a sphere using $L(t)$. 27
2.8 The behaviour of parameter β for various size spheres with varying permeability μ. 28
2.9 Relating the aspect ratio of a steel target with the ratio k_1/k_2 29
2.10 Relating the aspect ratio of a steel target with the ratio β_1/β_2 30
2.11 The field (unprimed) co-ordinate system for a buried target. The unit vectors $\hat{\mathbf{x}}$, $\hat{\mathbf{y}}$, and $\hat{\mathbf{z}}$ define the field co-ordinate system, and $\hat{\mathbf{x}}'$, $\hat{\mathbf{y}}'$, and $\hat{\mathbf{z}}'$ define the body-fixed co-ordinate system. 31
2.12 The strength of the induced transverse and axial dipoles for a horizontal, rod-like target 36
2.13 Synthetically generated EM63 data for a horizontal 105 mm projectile at a depth of 1 m. 37
2.14 Excitation of a vertical UXO. Relative contributions of the axial (red) and transverse (blue) polarizations are indicated in (a). Excitation of the transverse component occurs when the transmitter loop is positioned away from the target, such that the primary field has a horizontal component. The total induced dipole moment is plotted in (b). 39
2.15 Excitation of a UXO oriented with a 45 degree dip. Relative contributions of the axial (red) and transverse (blue) polarizations are indicated in (a). The total induced dipole moment is plotted in (b). 40
2.16 Synthetically generated EM63 data for a vertical 105 mm projectile at a depth of 1 m. 41
2.17 Plate and rod geometry for examples in Figures 2.18 to 2.19. 42
2.18 Comparison of the response for (a) a plate-like target whose normal is horizontal and (b) a vertical rod-like target. 43
2.19 Comparison of the rod and plate data. The right panel shows that the difference between the plate and rod data is of the same order as the standard deviation of the EM63 noise ($\sigma = 2.07$ mV). 44
2.20 Profiles of the data in Figure 2.18. The data profile along $y = 0$ m over either the plate (panel (c)) or rod (panel (c)) is the same. The data profile along $x = 0$ m is wider over the plate (panels (b)) than the rod (panel (d)). 44

3.1 Geonics EM63 error simulation results at a location directly above a vertical 81 mm mortar. 53
3.2 Geonics EM63 error simulation results for a vertical 81 mm mortar. 54
3.3 Spatial dependence of percent error over 81 mm mortar buried at a depth of 30 cm. 55
3.4 Calculated and theoretical noise floor for Geonics EM63 data collected on Grid 1914. 56
3.5 Gridded image of time channel 5 of Geonics EM63 data collected on the 2114 Grid. 57
3.6 Comparison of Geonics EM63 data noise in two areas of Grid 2114 at FLBGR. . . 58
3.7 Filtered EM61 Sky Array data acquired over Grid K15. 59
3.8 Examples of data masking applied to anomalies from grid L14. 60
3.9 An example of determining if an anomaly should be inverted as two separate targets. 62
3.10 Data collection setup for the example of Section 3.5. 70
3.11 Inversion of data collected over a 105 mm projectile: Comparison of four soundings. 72
3.12 Inversion of data collected over a 105 mm projectile: Comparison of 5 of the 26 time channels. 73
3.13 1D marginals for position and orientation obtained using the Neighbourhood Algorithm. 76
3.14 1-D Marginal distributions for the dipole polarization decay parameters. 77
3.15 2-D Marginals calculated using the Neighbourhood Algorithm. Confidence regions of 60 (green contour), 90 (blue contour), and 99 (red contour) percent are indicated. 77
3.16 1-D Marginal distributions for the dipole polarization decay parameters. 78
3.17 "Cued interrogation" style data collection at Marine Corps Base Camp Lejeune in North Carolina. 80
3.18 A data fit result when inverting for a three polarization dipole model from Geonics EM63 data collected over a 3.5 inch rocket. Both figures are screen outputs from UXOLab. 81
3.19 Comparison of recovered axial ($L_1(t)$) and transverse ($L_2(t)$) polarizations when inverting data over a 3.5 inch rocket. 82
3.20 Photo of the Sky Research EM61 MK2 array at the Former Lowry Bombing and Gunnery Range (FLBGR). 83

3.21 A SCAR without a nose and tail buried horizontally at a depth of 60 cm in the FLBGR UXO test plot. 83
3.22 Data fit for the first time channel of the Sky Research Geonics EM61 Mark 2 Array collected over the SCAR of Figure 3.21. 84
3.23 Photo of a piece of OE scrap from a 100 lb bomb buried at a depth of 30 cm. . . . 86
3.24 Data fit for the first time channel of the Sky Research Geonics EM61 Mark 2 Array collected over the OE scrap in Figure3.23. 87
3.25 Data fit for the first time channel of the Sky Research Geonics EM61 Mark 2 Array collected over a vertical 37 mm projectile buried at a depth of one foot. 89

4.1 Photo and decay constants of a particular Stokes Mortar and the TEM response at 1.105 ms measured parallel to the length of the Stokes Mortar for two depths of burial. 94
4.2 Inversion of TEM data for a Stokes mortar at a depth of 60 cm. The signal-to-noise ratio is large, allowing for accurate parameter recovery without constraints placed on the location. 97
4.3 Comparison of the data fit for a Stokes mortar at a depth of 100 cm. 97
4.4 Spheroid dimensions that can produce the same dipole as a 105 mm shell at 45 degrees inclination to the Earth's field. 98
4.5 Results from the magnetics inversion step of the cooperative inversion. The black dots in (a) indicate sensor locations at which data are collected. 102
4.6 Results from the TEM inversion step of the cooperative inversion. 103
4.7 Using orientation information for constraining the recovered spheroid shape. . . . 105
4.8 Parameters recovered by joint inversion. The recovered value for γ_1 falls on the constraint of 40. 108
4.9 Magnetics and TEM data collected over the Yuma Proving Ground Calibration Grid. Picked targets are plotted as white circles. 110
4.10 Magnetic data fit and recovered magnetics dipole parameters when inverting the 105 mm M456 Heat target. 111
4.11 TEM data fit and recovered dipole parameters when inverting the 105 mm M456 heat TEM data. 113
4.12 Recovered k and β values when inverting spheres buried in the calibration grid. . . 114

4.13 Recovered k and β parameters when inverting TEM data anomalies from 155mm, 105mm, 60mm, 40mm, and M75 targets in the calibration grid. 115

5.1 Comparison of k_1 and k_2 parameters derived from ERDC test stand data. 120

5.2 Axial ($L_1(t)$) and transverse ($L_2(t)$) polarization curves for targets within our library. 121

5.3 Dynamic and static data acquisition modes using the Geonics EM63. 122

5.4 Comparison of signal noise ratio for data anomalies acquired statically and dynamically over ten targets in the Sky Research Inc. test plot. 123

5.5 Application of the library method to dynamically collected data measured over an ATC M230 2.75 inch rocket (surface plot). 124

5.6 Application of the library method to dynamically collected data measured over an ATC M230 2.75 inch rocket (comparison of measured decay curves. 125

5.7 Fitting results when applying the library matching to a metal scrap not included in the library. The normalized misfit is higher than when fitting targets within the library. 128

5.8 Application of the library method to cell 68 containing a 2.75 inch rocket. Even though the anomaly was correctly identified, the feature in the data at late time result in an atypically large misfit. 129

5.9 Data misfit when applying the library method to data statically collected over an ATC MK118. The algorithm incorrectly classified this target. 131

5.10 Data misfit for a sounding taken directly over an ATC MK118. The estimated soil noise is of approximately the same order as the data, possibly causing the difficulty in correctly identifying the target. 132

5.11 First channel of Geonics EM63 data collected on the Grid A1 at the Marine Corps Base Camp Lejeune in North Carolina. 133

5.12 Photos of adapters at the Camp Lejeune site. 134

5.13 Receiver Operator Characteristic curve for the fingerprinting method applied to Grid A1. 134

6.1 Comparison of different signal to noise ratios for a channel of EM61-MK2 data. . 140

6.2 A line profile comparison of different signal to noise ratios for a channel of EM61-MK2 data. 141
6.3 (a) Data examples. (b) Comparison of signal strength to background noise. Signal 3 is not included since its amplitude is much larger than the Signals 1 and 2, and the noise. 143
6.4 Comparisons of different signal to noise ratios for a channel of EM61-MK2 data. The different color profiles represent the North-South lines. 144
6.5 Effect of position errors on an anomaly. 145
6.6 Images and profiles of the measured response for each coil configuration for a vertically oriented object at 0.5 m depth. 149
6.7 Images and profiles of the measured response for each coil configuration for a vertically oriented object at 1.0 m depth. 150
6.8 Width of an anomaly as a function of orientation. 151
6.9 The width of an anomaly as a function of depth. 151
6.10 The anomaly radius for an (a) horizontal and (b) vertical target as a function of depth for different signal to noise ratios. 152
6.11 The anomaly radius for an (a) horizontal and (b) vertical target as a function of depth for different signal to noise ratios. 152
6.12 Location of target was chosen to be within a square with sides equal to the line spacing as indicated by the grey box. The line and station spacing is indicated by dX and dY, respectively. The orange rectangle represents the orientation relative to the line direction of the EM61-MK2's 1 m x 0.5 m receiver/transmitter. 155
6.13 Influence of line spacing, station spacing, target depth and signal to noise ratio on success rate for inversion. 158
6.14 The primary field shape beneath a 1m x 1m transmitter loop. 159
6.15 An example of ambiguities in the recovered model parameters. In this example $k_1/k_2 = 5$. 159
6.16 An example of ambiguities in the recovered model parameters. In this example $k_1/k_2 = 2$. 160

6.17 Example of the spread in k_1 and k_2 parameters for two different targets ($k_1 = 5, k_2 = 1$, blue dots; and $k_1 = 10, k_2 = 1$, red dots). As position errors and station spacing increases, the absolute deviation of the k_1 and k_2 parameters also increase. 161

6.18 A plot of the relationship between the Figure of Merit, ξ, and the square root of the sum of squares of the average relative deviations for a target with $k_1 = 5$ and $k_2 = 1$. 164

6.19 A plot of the relationship between the Figure of Merit, ξ, and the square root of the sum of squares of the average relative deviations for a target with $k_1 = 5$ and $k_2 = 1$. Only simulations with a line spacing of 0.5 m are plotted. 165

6.20 A plot of the relationship between the Figure of Merit, ξ, and the square root of the sum of squares of the average relative deviation for all targets simulated in this analysis. For the simulations in this plot there were no sensor positioning errors. . 167

7.1 Seeded UXO test grid located on Kaho'olawe Island, Hawaii. 169

7.2 Geonics EM63 data acquired on Kaho'olawe island, Hawaii. 170

7.3 GEM data acquired on Kaho'olawe island, Hawaii. 170

7.4 Comparison of the Log-Uniform (or Frohlich) distribution and the Cole-Cole distribution. 176

7.5 Frequency dependent susceptibility models for sample 7468-2734AP-6". 178

7.6 Susceptibility analysis of a soil pit in Grid 2E at Kaho'olawe. 179

7.7 Forward modelled electromagnetic responses for half-spaces with magnetic viscosity and conductivities of σ =0.01, 0.1 and 1.0 S/m. 182

7.8 Forward modelled frequency domain electromagnetic responses to a step-off transmitter current for a half-spaces with magnetic viscosity and a conductivity of σ =0.1 S/m. 184

7.9 Forward modelled time domain electromagnetic responses to a step-off transmitter current for half-spaces with magnetic viscosity and a conductivity of σ =0.1 S/m. . 185

7.10 Comparing the frequency domain responses of a steel spheroid and a complex susceptibility half-space 186

7.11 Forward modelled time domain electromagnetic responses of a steel spheroid and a complex susceptibility half-space. 187

7.12 Forward modelled time domain electromagnetic responses for half-space models with susceptibility models based on soil susceptibility measurements of Oberjettenberg and Benkovac landmine test lanes. 189
7.13 Comparison of the Benkovac and Oberjettenberg soil responses as a function of sensor height. 189

8.1 Comparison of Bartington MS2B susceptibility measurements with electromagnetic sensor data. Data collected on the Kaho'olawe Grid 2E are presented. 195
8.2 Comparison of Bartington MS2D susceptibility measurements with the inphase component of GEM3 data. The MS2D measures the phasor sum of the complex susceptibility at $f = 0.98$ kHz. 196
8.3 Relationship between height and signal strength 197
8.4 Photo of FLBGR Geophysical proveout 198
8.5 Detrending results of measured elevation data from the FLBGR geophysical proveout 198
8.6 Height simulation example based on measured elevation data from the FLBGR geophysical proveout 199
8.7 Effect of height errors on sensor data acquired over VRM soils. 200
8.8 Tilt test carried out on Kaho'olawe Island using a Geonics EM61 Mark 2. 201
8.9 Height test carried out on Kaho'olawe Island using a Geonics EM61 Mark 2. . . . 202
8.10 Studying the effect of a conductive or magnetic background halfspace on the dipole polarization tensor of a sphere using the formulation of Das (2006). 203
8.11 Processing EMI data in a magnetic setting. 206
8.12 Example of recovered values for different targets. Parameters were estimated through inversions of Geonics EM63 data that were acquired on the USACE ERDC test stand in Vicksburg, MS. 208
8.13 Baseline noise for magnetic soil simulations 211
8.14 Example of geologic background response spatial variation. 212
8.15 Data simulated for a 40 mm buried at a depth of 50 cm. 213
8.16 Soil fitting results for data simulated for a 40 mm projectile in a background geology whose mean response in the first time channel is 20 mV. 215

8.17 Target Picking results for a 40 mm projectile and 60 mm mortar buried in a magnetic background. 217
8.18 Soil fitting results for synthetically generated 40 mm projectile data. 218
8.19 Soil fitting results for synthetically generated 60 mm mortar. 219
8.20 Soil target histograms for a ATC 40 mm projectile buried at a depth of 25 cm. The long wavelength background response is 20 mV. 220
8.21 The pdf and cumulative distribution for a 40 mm buried at a depth of 25 cm in a magnetic background that has a response of 20 mV in the first time channel. 221
8.22 Soil target histograms for a ATC 40 mm projectile buried at a depth of (a) 25 cm and (b) 50 cm. The long wavelength background response is 20 mV. The pdf for the soil and target nearly overlap when the 40 mm is 50 cm deep. 222
8.23 Accuracy of estimating target anomalies by filtering 225
8.24 Histograms summarizing the accuracy of estimating target anomalies by filtering . 226
8.27 Inverting data in magnetic geology: polarization magnitude and depth comparison . 229
8.28 Distribution of recovered axial polarization decay parameters γ_1 and β_1. 230
8.29 Inverting data in magnetic geology: recovered polarizations 231
8.30 The first and tenth time channel of Geonics EM63 data collected over Grid 2D and 2E on Kaho'olawe Island, Hawaii. 234
8.31 The soil model amplitude A and misfit ϕ for Geonics EM63 data collected on Kaho'olawe. 235
8.32 Values of misfits when fitting Geonics EM63 soundings in Grids 2D and 2E with a soil model. 236
8.33 Estimated probability density function and cumulative density function for the soil misfit of the Kaho'olawe EM63 data. 237
8.34 Target picking results when using the P_{FA}. Sounding locations are indicated by gray dots. Gray circles indicate emplaced non-UXO items such as frag, while gray squares indicate emplaced UXO items. 238
8.35 Target picking results when choosing anomalies whose $P_{FA} < 0.005$. Target picks where there is only a single sounding has a misfit falling below the threshold are removed from the list. 239

8.36 A photo of Alex Oren from Geophex Ltd. collecting data at the Kaho'olawe UXO test site. Data were collected with cart mounted version of the GEM-3. A 1 m circular transmitter loop was used for the demonstration. 240
8.37 Geophex GEM3 data collected over grid 2E at Kaho'olawe. 241
8.38 The calculated log of the misfit from fitting the model of equation 8.31 to the GEM3 data. The three separate survey events are clearly seen. 242
8.39 Histograms of the 3 surveys that make up the Grid 2E dataset. 243
8.40 Probability density functions and cumulative density functions for the soil misfit of the three surveys of Grid 2E. 244
8.41 Target picking results when using P_{FA} for detection. The positions of the GEM3 sensor are indicated by grey points. 244
8.42 Results from median filtering data from Figure 8.38. 245
8.43 Target picking using the median filtered version of the log of the soil misfit ϕ. A target is defined when a log (ϕ) anomaly has three pixels greater than one. 246
8.44 Field TEM data collected by the Zonge NanoTEM. The magnetic materials at the right hand portion of the survey are less evident in the horizontal component. . . . 247
8.45 Photo and Decay Constants for a Stokes mortar. 248
8.46 Geonics EM63 TEM data collected on Kaho'olawe island. Overlaid on the data are modelled responses of two layer models. 249
8.47 First time channel of synthetic data. 250

A.1 $4m \times 4m$ area on which a series of EM63 surveys were taken over different targets at several depths and orientations. 263
A.3 (a) Measurement of a 60 mm and 81 mm in jig. (b) Measurement of Scrap 5 and a Steel Disk. Unfilled symbols (e.g. 'o') indicate negative data that has its absolute value plotted. Predicted response is obtained by fitting the measurement with Equation A.1. 264
A.4 (a) Photograph of setup used to measure response of smaller scrap targets. (b) Voltage decay measurements for scrap targets 1 to 4. (c) Voltage decay measurements for scrap targets 5 to 8. Unfilled symbols (e.g. 'o') indicate negative data that has its absolute value plotted. 265

A.5 Measured response of scrap targets 1 to 8 along a line. Panel (a) and (b) plot the response along a line for the first time channel ($t = 0.18msec$). Panel(c) and (d) plot the response along a line for the tenth time channel ($t = 0.72msec$). Each target is located at station $0cm$. 266

A.6 Arrangement of EM63 and target for obtaining decay functions. 269

A.7 $L_1(t)$ and $L_2(t)$ decay functions for different targets. 270

A.8 Measured voltage curves for a 81 mm Mortar without fins at different heights from the sensor. Unfilled symbols (e.g. '□') indicate negative data that have absolute value plotted. These curves were inverted to obtain $L_1(t)$ and $L_2(t)$. Clearly, the decay nature of the signal changes when the mortar is brought close to the sensor. The resulting $L_1(t)$ and $L_2(t)$ curves are used to predict the decay at intermediate angles in Figure A.9. 271

A.9 Predicting the measured voltage decay curves for an 81 mm mortar without fins at different orientations θ. Unfilled symbols (e.g., '□') indicate negative data that have absolute value plotted. The $L_1(t)$ and $L_2(t)$ decay curves recovered from measurements with Z=60 cm and Z=52 cm (Figure A.8), respectively, are used to predict the voltage curves in the top two panels. The $L_1(t)$ and $L_2(t)$ decay curves recovered from measurements with Z=102 cm and Z=95 cm, respectively, are used to predict the voltage curves in the bottom two panels. The prediction of the measured curves is more successful when the target is farther away from the sensors. 272

A.10 Predicting the measured voltage decay curve for Scrap 5 using the dipole model. . 273

A.11 Geonics EM63 data acquired over a vertical 60 mm mortar 273

A.12 Geonics EM63 data acquired over a horizontal 60 mm mortar 274

A.13 Geonics EM63 data acquired over a 60 mm mortar 274

A.14 Geonics EM63 data acquired over a vertical 81 mm mortar 275

A.15 Geonics EM63 data acquired over a horizontal 81 mm mortar 276

A.16 Geonics EM63 data acquired over an 81 mm mortar with a dip of 43 degrees. . . . 276

A.17 Geonics EM63 data acquired over a vertical Stokes mortar 277

A.18 Geonics EM63 data acquired over a horizontal Stokes mortar 277

A.19 Geonics EM63 data acquired over a Stokes mortar with a dip of 54 degrees 278

B.2 Transmitter waveforms for the four Geonics EM61MKII chips. 283

B.3 The effect of different waveforms on different time constant targets. The grey area represents the measurement range of the standard EM61Mk2 TEM sensor. 284

B.4 Photographs of the detailed grid of planks established to investigate coil orientation within Grid 2E. 287

B.5 Targets measured in plank survey. (a) Photo of the steel nut placed on the surface. (b) Photo of the 90 mm projectile placed on the surface. 288

B.6 The first channel of TEM data interpolated to common locations. The steel nut and 90 mm projectile locations are indicated by the '□' and '△' symbols, respectively. 288

B.7 Misfit comparison. 289

B.8 Decay comparisons. 290

B.9 Line 2 misfit comparison. 291

B.10 Line 5 signal/misfit comparison. 292

B.11 Comparison of 4ms chip raw data and the 4ms data predicted from the 10 ms chip data. The bolt and UXO are not present for this data. 294

B.12 Comparison of 2ms chip raw data and the 2ms data predicted from the 10 ms chip data. The bolt and UXO are not present for this data. 295

B.13 Comparison of 4ms chip raw data and the 4ms data predicted from the 10 ms chip data. The bolt and UXO are present for this data. 296

B.14 Comparison of 2ms chip raw data and the 2ms data predicted from the 10 ms chip data. The bolt and UXO are present for this data. 297

B.15 Comparison of 4ms chip raw data and the 4ms data predicted from the 10 ms chip data. The bolt and UXO are not present for this data. 298

B.16 Comparison of 4ms chip raw data and the 4ms data predicted from the 10 ms chip data. The bolt and UXO are present for this data. 299

B.17 Decay comparisons. 299

B.18 Comparison of misfits when applying the differential. 300

B.19 Comparison of background soil signal strengths at Kaho'olawe and Waimea. 301

B.20 Waimea raw data 10 ms. White circles indicate emplaced items. 302

B.21 Waimea raw data 4 ms. White circles indicate emplaced items. 303
B.22 Waimea raw data 2 ms. White circles indicate emplaced items. 304
B.23 Waimea detrending example on the 10 ms chip data. 304
B.24 Detrended Waimea data from the 10 ms chip. 305
B.25 Detrended Waimea data from the 4 ms chip. 306
B.26 Detrended Waimea data from the 2 ms chip. 307
B.27 Waimea Soil Histogram for the 10 ms chip data. 307
B.28 Waimea Soil Histogram for the 4 ms chip data. 308
B.29 Waimea Soil Histogram for the 2 ms chip data. 308
B.30 (a) Raw 10 ms chip data for the first time channel. (b) Data greater than twice the standard deviation of the background noise. (c) The soil misfit calculated for the data above the background noise. 309
B.31 (b) Raw 4 ms chip data for the first time channel. (b) Data greater than twice the standard deviation of the background noise. (c) The soil misfit calculated for the data above the background noise. 309
B.32 (a) Raw 2 ms chip data for the first time channel. (b) Data greater than twice the standard deviation of the background noise. (c) The soil misfit calculated for the data above the background noise. 310
B.33 Decay comparisons. 310

C.1 Examples of TEM transmitter waveforms (a) A step-off waveform (b) A single rectangular pulse (c) A typical exponential on/ramp off transmitter pulse commonly used in TEM sensors that measure in the off-time. T_a is the length of the exponential increase in transmitter current and T_b is the length of the linear turn-off ramp. . 312
C.2 Effect of pulse length on the time decay function $L(t)$ 313
C.3 Response due to a linear ramp-off 315
C.4 Examples of how the step-off response affected by the exponential time constant τ. 316
C.5 Effect of a pair of bipolar pulses on a step-off response. 317
C.7 Effect of a single Geonics EM63 and EM61 pulse on a step off response. 319

D.1 Waveforms 321

Acknowledgements

First and foremost, I would like to thank my long-time supervisor Doug Oldenburg for taking me on as a graduate student. I can not imagine a better supervisor: always encouraging, understanding, and a really nice guy. He cared about my work, and my well-being as a graduate student.

My supervisory committee of Doug Oldenburg, Elizabeth Hearn, and Felix Hermann, and my examination committee of Michael Freidlander, Scott Dunbar, and Mark Everett took time off of their summer to read this thesis. Their numerous suggestions improved the manuscript.

I would like to thank Stephen Billings, who has been both a good pal and research partner during my time at UBC - always good for a laugh and some insight into different UXO research problems. His drive and foresight has led to the development of a research program at UBC and Sky Research Inc. that has given me the opportunity to continue working in the field of UXO detection while staying in Vancouver.

The work in this thesis was funded, in part, by the Army Research Office, the Strategic Environmental Research and Development Program (SERDP), and the United States Army Corps of Engineers (USACE) Engineer Research and Develop Center (ERDC). The USACE-ERDC Geotechnical Lab in Vicksburg, MS have been tremendous supporters of my work, not only financially, but also by giving me the opportunity to participate in a number of data collection field projects. I would like to thank Dwain Butler and Don Yule for the many years of support. I would also like to thank Jose Llopis, Janet Simms, Ryan North, and Troy Broston with whom I have spent time in the field collecting data for this thesis.

To say I had a long tenure as a graduate student, is clearly an understatement. The lone benefit of staying in graduate school for so long was the opportunity to meet some great people. I can't list all the UBC folk but they include Sean Walker, Kevin Kingdon, Gwenn Flowers (who gave me a place to stay when I was living out of my office!), Stephane Rondenay and Camille Li, Jane Shkolnik and Kristy Roloff (the astronomers), Phil Hammer, Barry Zelt, Megan Sheffer, Nicolas

Lhomme, Christina Trotter, Dave Hildes, Kris Innanen, ... the list could just keep going and going. These people were my skiing pals, drinking pals, or pals to hang out with in the coffee room. I should note that the many hours I spent socializing in the coffee room delayed the completion of my thesis, but made coming to work much more enjoyable.

The pressure to produce research that isn't irrelevant or to prepare a presentation that won't be a reputation sinker, can be a bit stressful (especially when making minimum wage). For some unknown reason, any grad school related bitterness would be (at least temporarily) forgotten by simply hanging out with some of my old friends from Powell River. They are remarkable people - a combination of funny and crazy - and, quite simply, really good guys. Although I wouldn't run into them often, my old friends - Jeff Lawlor, Jim Tait, Tom Marcaccini, Don Gordon, Rob Bryce, Colin Koszman and Chris Matheson - helped me complete this thesis.

My mom, dad and sisters provided continuous encouragement and support during my graduate student time. My mom was my greatest cheerleader. One of my greatest regrets is being unable to finish my thesis soon enough so she could see its completion.

Finally, I thank Candice Wingerter. Candice was with me at every step during my graduate student years. Her support extends far beyond my thesis work, and what she has meant to me can not be put into words.

Dedication

My dad always told me that success can only be achieved through hard work and sacrifice. I have come to realize that my dad's sacrifices and hard work through the years made it possible for me to go to university and complete a doctoral degree. As a small token of thanks, I dedicate all the work that went into completing this thesis to my dad.

Chapter 1

Introduction

An explosive ordnance is a munition that is either launched or fired with the intent of detonation at a specified target. An unexploded ordnance (UXO) is an explosive ordnance that, because of a malfunction, remains undetonated 1.1. As a result, the ordnance can be found at the ground surface, partially buried, or buried at a depth of up to 8 m beneath the surface. UXO are found in post-conflict areas and military training areas. Post-conflict areas contaminated with UXO have led to numerous casualties and economic difficulties (Landmine Action, 2002). Within these post-conflict areas, poorly marked or abandoned firing ranges present a particular threat to safety due to higher concentrations of UXO (Moyes, 2005). Military training within the United States of America has led to approximately 10 million acres of UXO-contaminated land with an estimated cleanup cost exceeding the tens of billions of dollars (Defense Science Board, 2003). The remediation of UXO-contaminated land has been made a high priority by the United States Department of Defense in

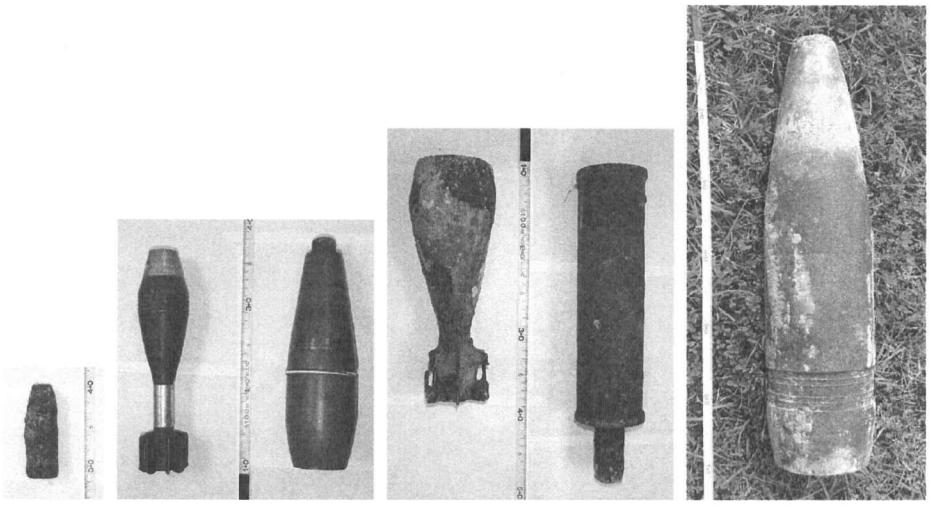

Figure 1.1: Some typical UXO.

order to either maintain safe usage for continuing military operations or to permit land transfer to the private sector (MacDonald et al., 2004). Approximately 200 million dollars per year is spent by the United States of America Department of Defense on the UXO cleanup problem (Defense Science Board, 2003).

The remediation of UXO contaminated sites can be described as a three step process: (1) detection, (2) discrimination, and (3) excavation (Figure 1.2). In the context of the UXO remediation

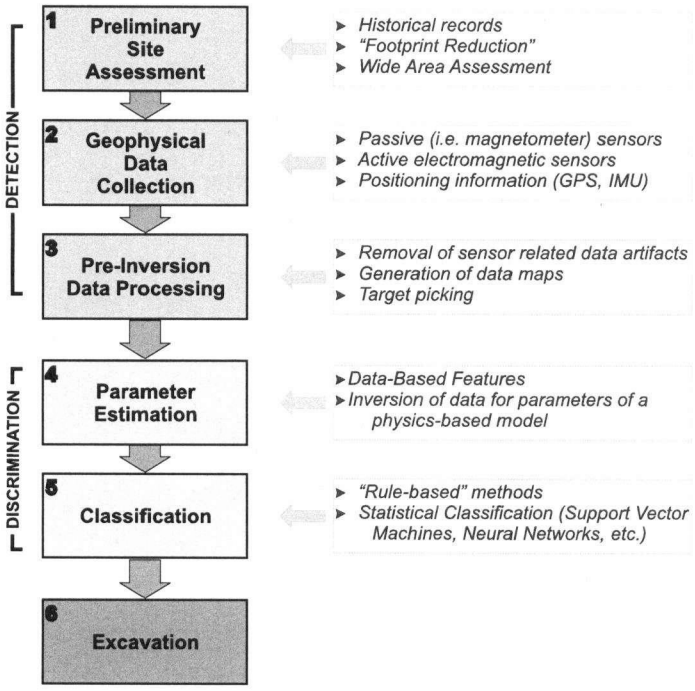

Figure 1.2: The basic steps to detecting and discriminating UXO.

problem, detection is the process of determining the location of subsurface metallic targets that are potentially UXO. Since many UXO contaminated sites can be in the order of thousands of acres, a preliminary site assessment is generally carried out to delineate boundaries of UXO contamination such that ground based geophysical detection surveys can be more efficiently fielded. This process of "Footprint Reduction" is achieved through the examination historical records and airborne surveys. Synthetic aperture radar (SAR), light detection and ranging (LiDAR), and high resolution ortho-photography are remote sensing technologies capable of detecting surface ordnance indicators such as craters, tire tracks, or metal debris. Aircraft equipped with geophysical sensors can provide a coarse level of subsurface detection. In particular, low-flying (i.e., within a few meters

of the ground) helicopters equipped with magnetometers successfully detect large caches of buried ordnance or very large single targets (Nelson et al., 2005).

While airborne systems can delineate regions of high UXO contamination (such as bombing targets), ground based geophysical surveys are required to detect isolated, smaller and deeper targets. Magnetic and electromagnetic surveys are the standard geophysical techniques used for UXO remediation. Electromagnetics and magnetometry have proven to be successful in detecting UXO in recent UXO remediation projects and UXO technology demonstrations. Magnetometry is a passive detection system. The high magnetic susceptibility of a ferrous target causes distortions to the Earth's field which are measured by a magnetometer (Figure 1.3). In general, the magnetometer is far enough away from the target such that the secondary field can be approximated well by a dipole. Magnetometry is a valuable geophysical tool for UXO detection due to the ease of data acquisition and its ability to detect relatively deep targets. However, magnetic data can have large false alarm rates due to geological noise, and there is an inherent non-uniqueness when trying to determine the orientation, size and shape of a target (Billings, 2004).

Electromagnetic induction (EMI) sensors detect a buried target by illuminating the subsurface with a time varying primary field. If the buried target is conductive, eddy currents will be induced in the target, and subsequently decay. These currents produce a secondary magnetic field which is then sensed by a receiver coil. In contrast to magnetometry, electromagnetic induction surveys are relatively immune to geologic noise and are more diagnostic for target shape and size but have a reduced depth of investigation.

"Mag and Flag" is the traditional method of UXO detection. This technique uses analog, handheld metal detectors to sweep UXO-contaminated land. The term "Mag" is used because the traditional metal detectors for this purpose were magnetometers. Locations where the detector has signalled the presence of a metallic item are flagged for excavation. Therefore "Mag and Flag" is strictly a detection technique, and has no ability to discriminate between UXO and non-UXO items. Several factors make "Mag and Flag" an inefficient technique for UXO remediation. Detection performance is limited by the ability of the operator. Human factors, such as fatigue, heat, motivation and hunger, can negatively impact the quality of collected data and the ability to recognize the presence of buried targets. There is also limited quality control of the "Mag and Flag" procedure since a data maps of the survey area are not produced and, therefore, it is not possible to confidently

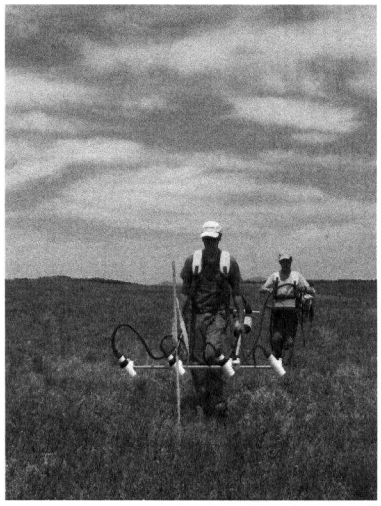

(a) An array of magnetometers being used to collect data at Chevellier Ranch, Montana.

(b) A magnetometer array mounted on a helicopter. Helicopter magnetometer surveys for UXO detection are flown as close to 1 m above the surface and at a speed of approximately 80 km/hour.

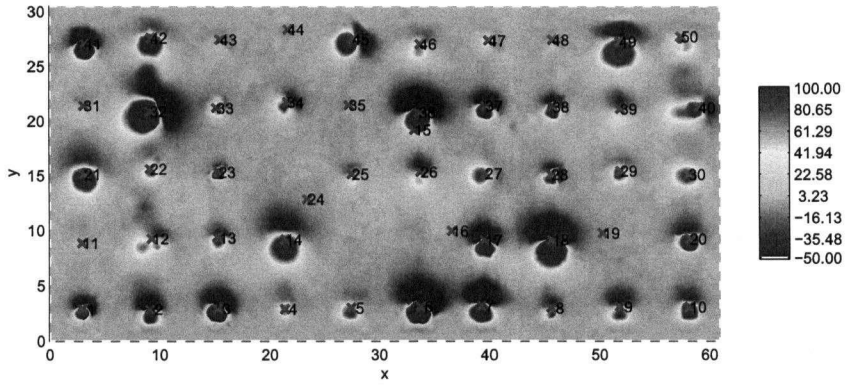

(c) Magnetometer data collected over the Former Lowry Bombing range test plot. Distances are in meters, and the units of the measurement are nano-Teslas. These data were collected by a magnetometer array with a sensor spacing of 0.30 m. The image was created by using minimum curvature gridding.

Figure 1.3: Examples of magnetometer systems and magnetometer data.

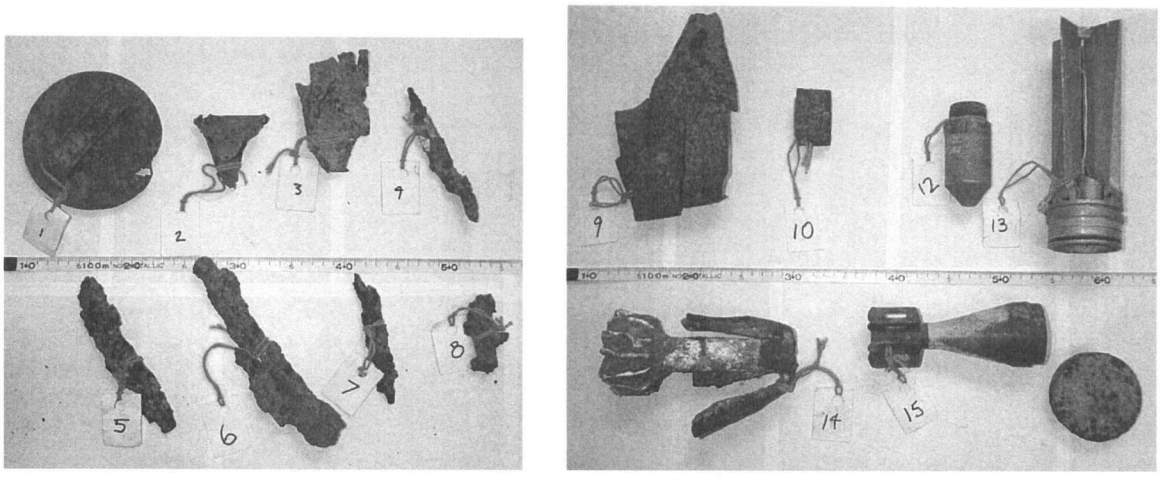

Figure 1.4: Examples of some scrap targets excavated during a UXO remediation project at the Former Camp Croft Army Training Facility Spartanburg, South Carolina.

assess the UXO contamination at site. Secondly, UXO contaminated areas are, generally, also contaminated with large amounts of metallic non-UXO items such as fragments of exploded ordnance (Figure 1.4) or debris from troop activities (Figure 1.5). In many areas the ratio of metallic non-UXO items to UXO can exceed 100:1. The largest cost of UXO remediation is excavation, due to the potential explosive or chemical hazard that each excavation presents (Defense Science Board, 2003). Practical and cost-effective strategies for remediation require both detection and algorithms for discriminating between UXO and non-UXO. The need for improved detection and discrimination has led to an increased emphasis in the use of digital geophysics and data processing.

Figure 1.6 contains photos of some electromagnetic induction detectors currently being used for UXO detection. There are two types of electromagnetic sensors: time domain (or pulse induction) electromagnetic (TEM) detectors and frequency domain (or continuous wave) electromagnetic (FEM) detectors. Time domain sensors operate by illuminating the subsurface with a finite pulse primary field. Once the primary field has been terminated, a receiver measures the time decay of the secondary field (Figure 1.7(a) and (b)). The rate of decay is a function of the material properties and shape of the buried target. Frequency domain methods incorporate a transmitter that produces a continuous, periodic (for example, sinusoidal) primary field. A receiver continuously measures the secondary field, with the amplitude and phase of the received signal providing target information (Figure 1.7(c) and (d)).

Ground penetrating radar (GPR) is a high frequency electromagnetic geophysical technique that

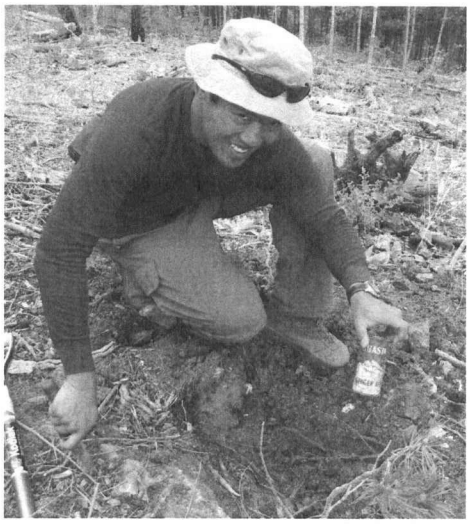

Figure 1.5: A pop can excavated during cleanup activities with the Montana Army National Guard at Limestone Hills in Helena, Montana.

has been considered for UXO detection (Figure 1.8). GPR is an electromagnetic detection technique that operates at higher frequencies than EMI sensors, and therefore its physics is governed by the EM wave equation. A polarized pulse propagates into the subsurface. The pulse subsequently reflects off of discontinuities in electromagnetic properties and returns to the surface. The time delay and amplitude of the reflected pulse is measured at the surface. GPR has the ability to accurately determine depth and location of targets, and to delineate multiple targets. GPR's high sensitivity to soils and subsurface structure degrades its performance in production settings, limiting its use. Research has yet to produce a GPR system (detection and processing) suitable for reliable UXO detection and discrimination. However, GPR's strengths has led to research for incorporating GPR into multisensor systems, in particular for the very near-surface detection requirements of landmine detection (for example the United States Army Handheld Standoff Mine Detection System (HSTAMIDS)).

Once a geophysical data survey is completed, a number of processing steps are applied to the data such that accurate maps of the survey data are created. Generating accurate maps of the survey involves the careful integration of sensor position information (for example Global Positioning Systems (GPS) and Inertial Measurement Units (IMU)) with sensor measurements, and removal of sensor related data artifacts such as instrument drift and spikes. These data maps provide a record of the spatial coverage of the survey. If the signal due to background geology is insignificant, or it can

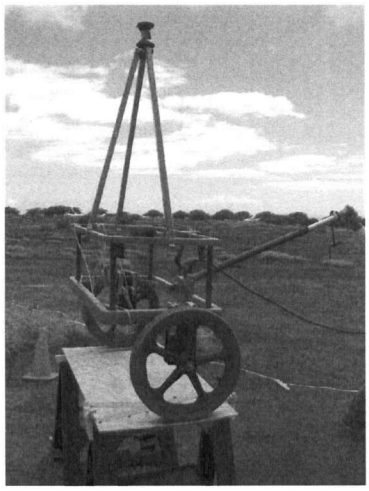

(a) The Geonics EM61 Mark II TEM Sensor being calibrated at Kaho'olawe Island, Hawaii, U.S.

(b) The Geonics EM63 Mark TEM Sensor collecting data at the Yuma Proving Grounds, Nevada, U.S.

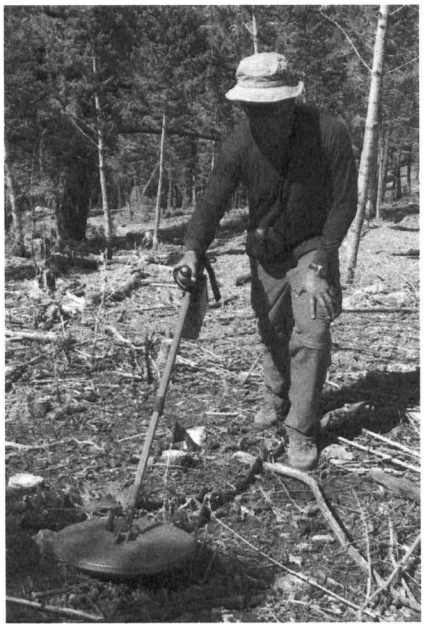

(c) The Minelabs F14A TEM Sensor being used during target validation work at Limestone Hills, Montana, U.S.

(d) The Geophex GEM-3 FEM Sensor collecting data at Chevallier Ranch, Montana, U.S.

Figure 1.6: Photos of some electromagnetic induction detectors currently being used for UXO detection.

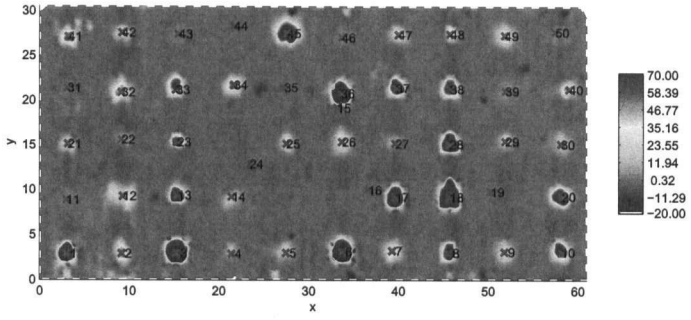

(a) First time channel (0.18 ms) of Geonics EM63 Data

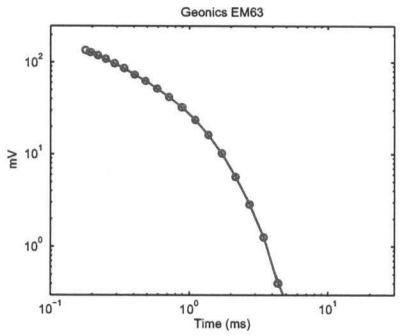

(b) Time decay of a SCAR measured by the Geonics EM63.

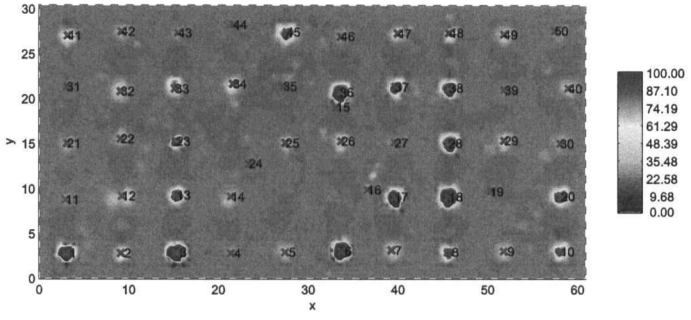

(c) Geophex GEM-3 data. The imaginary component of the data at 2490 Hz is plotted.

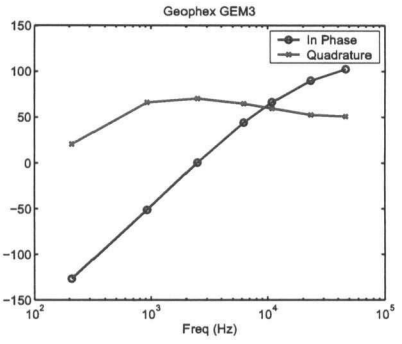

(d) Frequency sounding measured by the Geophex GEM-3 sensor positioned over a SCAR.

Figure 1.7: Examples of electromagnetic induction sensor data. These data were acquired over the Former Lowry Bombing and Gunnery Range test plot. The soundings in (b) and (d) were measured over a Sub-Caliber Aircraft Rocket (SCAR) Body.

(a) GPR instrument

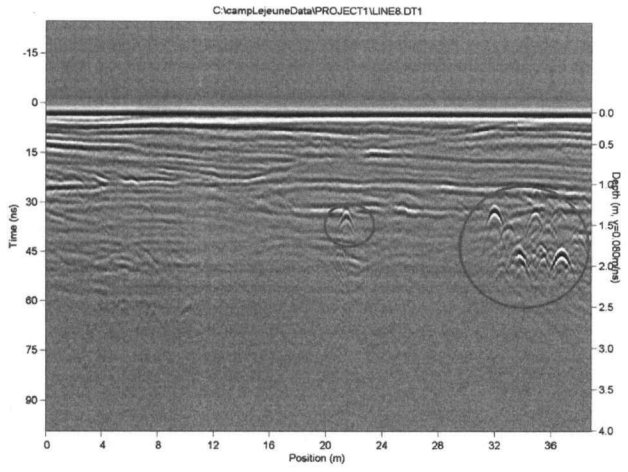

(b) Data from

Figure 1.8: Ground penetrating radar. (a) Photo of a 250 MHz Noggin Smart Cart manufactured by Sensors and Software. (b) A cross-section of data collected at Camp Lejeune. The hyperbolas in the left circle indicate a single target, while the data in the right circle show a the presence of multiple scatterers.

be removed through filtering, the processed data are then used to generate target lists. These target lists identify anomalies within the data map that the interpreter believes are potentially from UXO. In general, an initial target list is generated automatically by identifying anomalies whose maximum amplitude or energy exceeds a threshold level chosen by the interpreter. The threshold level is generally chosen with the objective of maximizing the detection of buried ordnance expected at a site without including anomalies from sensor noise or smaller items (such as fragments from exploded ordnance). Target picking is often refined by visual inspection.

Discrimination is the process of determining, for each anomaly in the target list, the likelihood of it being a UXO. The objective is to minimize the number of false positives and, therefore, unnecessary excavations. UXO discrimination is achieved by extracting parameters from geophysical data that reflect characteristics of the target that generated the measured signal. These parameters come in two forms: (1) data-based parameters that are directly inferred from the data, such as amplitude and energy and (2) model-based parameters that are variables of a mathematical forward model (such as the dipole model) that can reproduce the data. Data and model based parameters can then be used as input to statistical classification methods (such as support vector machines and

neural networks) to determine the likelihood that the target is a UXO. The parameters are related to the physical properties of an object are and we refer to them as physics-based forward models. Model-based parameters are recovered from inversion of the geophysical data. The optimal parameter set minimizes a data misfit function (such as a least squares measure) and satisfies any prior information we have of the target.

The choice of forward modeling method has a large impact on inversion, and therefore discrimination, performance. The ideal forward model can accurately reproduce the data with a minimum number of parameters, while being computationally efficient. The response of a compact metallic target to a electromagnetic field can be computed through solutions of Maxwell's equations. Numerical solutions of Maxwell's equations, under continual development, are promising (e.g. Haber et al. (2000); Carin (2000); Hiptmair (1998); Shubitidze et al. (2002a)); however, the computational time requirements for obtaining a solution still make them impractical for use as part of a rigorous inversion procedure. The dipolar nature of the electromagnetic responses of compact metallic objects measured with sensor/target geometries typical for UXO surveys (Casey and Baertlein, 1999; Grimm et al., 1997) has lead to a number of techniques for estimating the elements of the magnetic polarization tensor that define the induced dipole strength. These dipole model based techniques have shown great promise for discrimination (Bell et al., 2001b; Zhang et al., 2003; Pasion and Oldenburg, 2001a). The magnetic polarization tensor's components are functions of the size, shape, and material properties of the buried target of interest and therefore provide a model vector from which the target characteristics can be inferred. Target identification is then achieved by including the recovered model parameters as part of feature vectors that are input into statistical classification algorithms (Billings, 2004; Collins et al., 2001; Beran, 2005).

The success of dipole model based discrimination algorithms depends on the accuracy of the dipole model, and ability of the data to constrain the inversion for the dipole parameters. Inversion algorithms that incorporate inaccurate models will have biased parameter estimates, even when using noise free data. In the case of dipole models, non-dipole components in the data will bias the estimates. When plotting a target's recovered parameters from inaccurate models in feature space, the parameter bias results in a greater spread in the target's parameter cluster. More complex models have the ability to model more subtle features within the data. However, parameter estimate variance can increase with model complexity, and, therefore, data fidelity must be able to support their use.

If data are unable to constrain parameters, a priori information must be included in the inversion. In many cases sensor data are unable to constrain the inversion such that the true polarization tensor can not be recovered (Pasion et al., 2004; Bell, 2005). Poor data quality, due to a low signal to noise ratio or survey design (for example, poor spatial coverage and inadequate illumination of both axial and transverse excitations), make the use of parameter estimation difficult. In such cases, a priori information can be introduced when searching model, or feature, space. Examples of a priori information include target location estimates from processing previously acquired data sets (for example, magnetics (Zhang et al., 2003; Pasion et al., 2003) or ground penetrating radar (Shamatava et al., 2004)), and restricting the model type to be rod-like targets. A further restriction in model space would be to assign higher probabilities to encountering different targets. A simple implementation of this concept is to develop a list of candidate UXO likely to be encountered during a survey, then to determine, for each member of the library, the likelihood of generating the anomaly.

The task of discriminating UXO from non-UXO items is more difficult when sensor data is contaminated with geological noise originating from magnetic soils. The magnetic properties of soils are mainly due to the presence of iron. The magnetic character of the soil is dominated by the presence of ferrimagnetic minerals such as maghaemite (αFe_2O_4) and magnetite (Fe_3O_4). Maghaemite is considered the most important of the minerals within archaeological remote sensing circles (for example Scollar et al. (1990)). Magnetite is the most magnetic of the iron oxides, and is the most important mineral when considering the effects of magnetic soils on EM measurements. Hydrated iron oxides such as muscovite, dolomite, lepidocrocite, and geothite are weakly paramagnetic, and are less important in the context of UXO detection.

Electromagnetic sensors are sensitive to the presence of magnetite and especially when the soils have magnetic viscosity. Electromagnetic sensors illuminate the subsurface with a time or frequency varying primary field. Suppose that we apply a magnetic field H to an area containing magnetic soil. The magnetization vector of the soils will try to adjust to align itself with the exciting field. At the instant the magnetic field is applied there is an immediate change in magnetization and, possibly, an additional time dependent change in magnetization. This time dependent phenomenon is referred to as magnetic viscosity or magnetic after-effect. A time constant τ is used to characterize the time for the magnetization vector to rotate from its minimum energy orientation prior to application of the field, to its new orientation. For a sample of magnetic grains which has a large

range of relaxation times that are distributed uniformly over their spectrum, the magnetic moment of the soil sample will decay logarithmically. The time derivative of the decaying magnetic field produced by the decaying magnetization decays as t^{-1}. This t^{-1} decay have been observed in archaeological prospecting (Colani and Aitken, 1966), TEM surveys carried out over laeteritic soils for mineral exploration (Buselli, 1982), and also in TEM surveys carried out on Kaho'olawe Island, Hawaii (Ware, 2001).

Figure 1.9 contains an example of the effect that magnetic soil can have when detecting UXO using time domain electromagnetic sensor data. A study consisting of electromagnetic data collection and soil sampling was completed on the island of Kaho'olawe, Hawaii (Li et al., 2005, 2006). The presence of viscous remnant magnetic soils due to the weathered basalt parent material produces a background response that is comparable to that of a UXO in free space. In addition, movement of the sensor produce anomalies of the same spatial wavelength of UXO.

Thesis Outline

Pasion (1999) suggested that a buried target's dipole polarization tensor could be extracted from multi-channel time domain electromagnetic data, and the decay characteristics of the polarization tensor could be diagnostic of the targets size and shape. In this thesis I further develop the dipole modelling and inversion methodologies described in Pasion (1999) for application to real-world UXO remediation projects. During this research we focussed on developing practical strategies for interpreting TEM data for improved target detection and discrimination. As a result, every attempt was made to include results using real sensor data from both test stands and from field surveys.

Chapter 2 (*"An Approximate Forward Model For TEM Data"*) reviews parameterizations of the time dependent dipole polarization tensor for modelling the time domain electromagnetic response of axi-symmetric targets. Analysis of TEM data collected during a visit to the Engineer Research Development Center in Vicksburg, MS, USA are used to assess the validity of this model.

Chapters 3 to 5 considers different techniques for inverting TEM data for parameters of the approximate dipole model. These approaches are distinguished by the amount of a priori information that we consider during the parameter estimation. We first invert data with no prior information in Chapter 3 (*"Inversion of Time Domain Electromagnetic Data"*). In Chapter 4 (*" Joint and Cooper-*

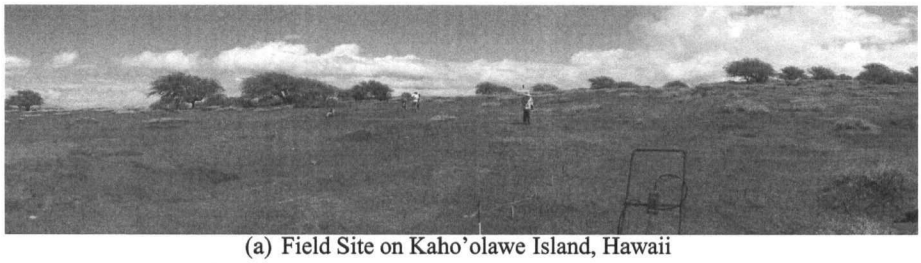

(a) Field Site on Kaho'olawe Island, Hawaii

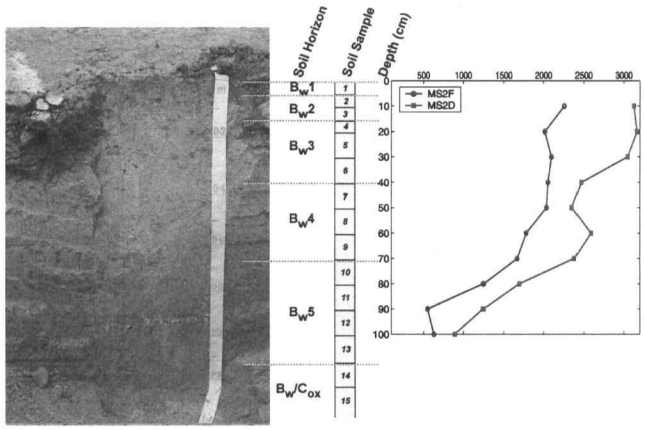

(b) A soil pit dug at approximately the center of the site. The plot to the right indicate the magnetic susceptibility measured by two different susceptibility meters (at two different frequencies of measurement).

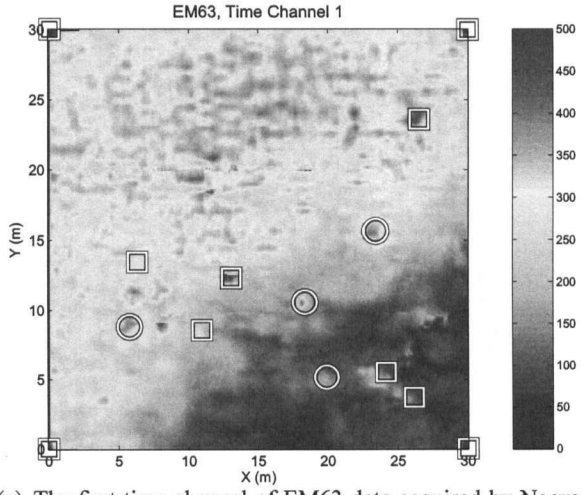

(c) The first time channel of EM63 data acquired by Naeva Geophysics over a seeded test plot. The circles represent locations of UXO and the squares mark location of other metallic scrap.

Figure 1.9: Example of detecting UXO in a magnetic setting.

ative Inversion of Time Domain Electromagnetic Data"), we invert data with positional information being provided through the processing of previously acquired magnetics data. In Chapter 5 (*"Application of a Simple Library Method for Identifying UXO"*), we consider a scenario where we have a library of possible UXO. We then determine which library member is most likely to have produced the anomaly.

The success of inversion techniques is largely dependent on data quality. That is, the inversion of data that have a lower signal to noise ratio, poorer spatial coverage, or less accurate sensor positioning information will be less likely to provide accurate parameter estimations. Indeed, if the data quality is low enough, we should not attempt an inversion for dipole parameters. Chapter 6 (*"Establishing data quality requirements for inversion and discrimination using simulations"*) considers the data quality requirements for inverting TEM data. Simulations of a single time channel of Geonics EM61 Mark 2 TEM data are inverted, and relationships between the spread of the cluster classes and data quality are established.

The effects of magnetic soils on UXO detection and discrimination are considered in Chapters 7 to 8. Chapter 7 (*"Detection of UXO in Magnetic Environments"*) studies why magnetic soils can produce such a significant response in electromagnetic sensors. Field examples from the island of Kaho'olawe, Hawaii, U.S.A. and landmine test lanes in Oberjettenberg, Germany and Benkovac, Croatia are used to demonstrate this effect. Chapter 8 (*"Processing of Electromagnetic data in Magnetic Geology"*) investigates different methods of processing data collected in magnetic environments. The processing techniques of this chapter exploit the different spatial, temporal, and spectral differences of viscous remnant magnetic soil and compact metallic responses. Appendix B (*"A Differential Electromagnetics Approach for detecting UXO in Magnetic Geology"*) describes application of the soil fitting procedures of Chapter 8 to multiple transmitter pulse lengths. The method of illuminating the subsurface with transmitter pulse lengths suggested by Candy (1996) is tested using data from a specially designed Geonics EM61 Mark 2 TEM sensor.

A conclusion chapter summarizes the work in this thesis and its contributions to UXO remediation technology.

Chapter 2

An Approximate Forward Model For Time Domain Electromagnetic Data

2.1 Introduction

Time domain electromagnetic metal detectors are one of the primary geophysical survey instruments used in UXO detection. Figures 2.1 and 2.2 show examples of TEM data measured by a Geonics EM63 TEM sensor on the USACE-ERDC UXO test stand in Vicksburg, MS. Figure 2.1 contains data collected over a horizontal 155 mm M4831A1 projectile where the Geonics EM63 transmitter loop was 1 m above the ordnance. This particular 155 mm projectile is 870 mm long and weighs 47 kg. Figure 2.2 contains data collected over a horizontal BDU-28 submunition at a depth of 24.5 cm from the Geonics EM63 transmitter loop. The BDU-28 weighs 785 gm, and has a length of 95 mm and diameter of 70 mm. In both Figures 2.1 and 2.2, subfigure (a) contains plan view images of the data (in mV) for 4 of the 26 time channels that are measured by the Geonics EM63. Data were collected at points indicated by the white dots in the upper left plot (i.e., the plot for time channel 1). The images were created by using minimum curvature gridding to interpolate between these collection points. Subfigure (b) plots the 26 measured time decays at the four locations indicated by the symbols plotted in the images of (a).

In order to invert measured TEM data for the physical parameters of the target, it is necessary to have a forward model to describe the TEM response for a buried metallic object. Numerical solutions of Maxwell's equations, under continual development, are promising (e.g. Haber et al. (2000); Carin (2000); Hiptmair (1998); Shubitidze et al. (2002a)); however, the computational time requirements for obtaining a solution still make them impractical for use as part of a rigorous inversion procedure. Our approach, therefore, is to use an approximate forward modelling that can adequately reproduce the measured electromagnetic anomaly in a minimal amount of time. The

challenge of this approach is to develop the simplest model (i.e. a model with a minimum number of parameters) while still being to accurately reproduce the features of TEM data.

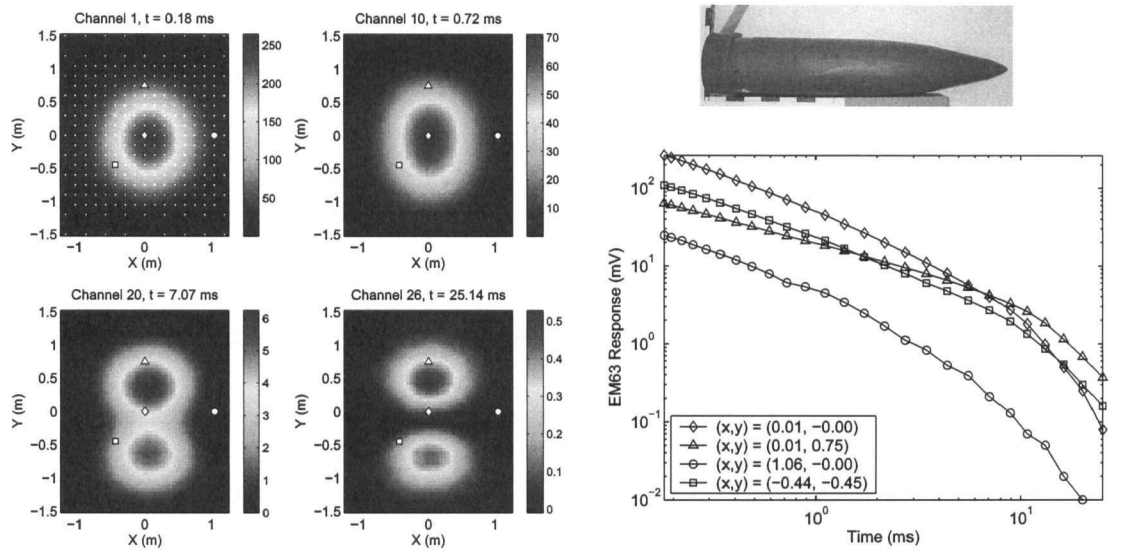

(a) Plan view of data.

(b) Soundings for stations indicated by white symbols.

Figure 2.1: Geonics EM63 data collected over a 155 mm projectile at the USACE-ERDC teststand in Vicksburg, MS. The transition from a single peak at early times to a double peak at later times is characteristic of a horizontal, rod-like target.

2.2 Developing an Approximate Forward Model

The development of the approximate forward modelling is presented in four steps. We begin with the response of a sphere, so that the magnetic polarization dyadic $\overline{\overline{\mathbf{M}}}$ is introduced. This dyadic is then altered so that it is applicable to an axi-symmetric body. This generates the "two-dipole" model mathematically. Next, we introduce a parameterization for the time decays of each of the two dipoles, and finally, we combine everything to generate our approximate forward modelling.

2.2.1 Response of a Spherical Body

Consider a permeable and conducting sphere of radius a illuminated by a uniform primary field $\mathbf{B}^P$. At a time $t = 0$ the primary field is terminated, and eddy currents are induced in the sphere; they subsequently decay because of the finite conductivity of the sphere. The secondary field $\mathbf{B}^S$

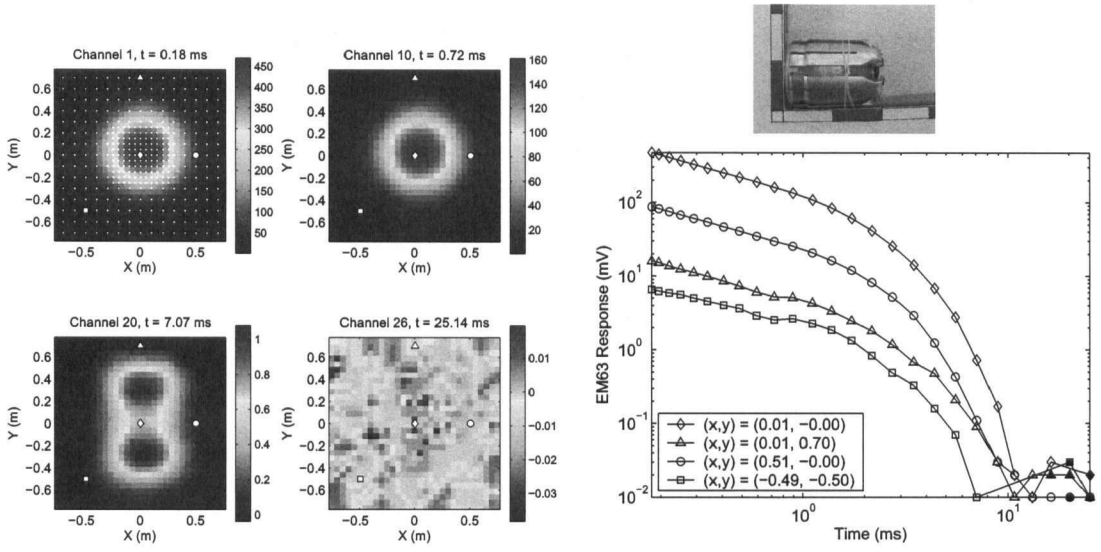

(a) Plan view of data. By $t = 25.14$ ms the signal due to the BDU 28 is smaller than the sensor noise.

(b) Soundings for stations indicated by white symbols.

Figure 2.2: Geonics EM63 data collected over a BDU-28 submunition at the USACE-ERDC test-stand in Vicksburg, MS.

generated by the decaying currents is dipolar:

$$\mathbf{B}^S(t) = \frac{\mu_o}{4\pi r^3}\,\vec{\mathbf{m}}(t)\cdot\left(3\hat{\mathbf{r}}\hat{\mathbf{r}} - \bar{\bar{\mathbf{I}}}\right) \tag{2.1}$$

where μ_o is the magnetic permeability of free space, $\vec{\mathbf{m}}(t)$ is the dipole moment induced at the center of the sphere at time t, r is the distance between the observation point and the sphere center, $\hat{\mathbf{r}}$ is the unit vector pointing from the sphere center to the observation point P, and $\bar{\bar{\mathbf{I}}}$ is the identity dyadic. The dipole moment is

$$\vec{\mathbf{m}}(t) = \frac{2\pi}{\mu_o}\,\mathbf{B^P}\,L^{\mathbf{B}}(t) \tag{2.2}$$

where

$$L^{\mathbf{B}}(t) = 6a^3\mu_r\sum_{s=1}^{\infty}\frac{\exp\left(-t/\tau\right)}{q_s^2 + (\mu_r - 1)(\mu_r + 2)} \tag{2.3}$$

where $\tau = \sigma\mu a^2/q_s^2$ and $\mu_r = \mu/\mu_o$ is the relative permeability (Kaufman and Keller, 1985). In general, the magnetic permeability of highly permeable materials is a function of many parameters, including the strength of the incident magnetic field, temperature, and magnetic history. The many different types of steel produced have a wide range of magnetic permeabilities. In addition, the

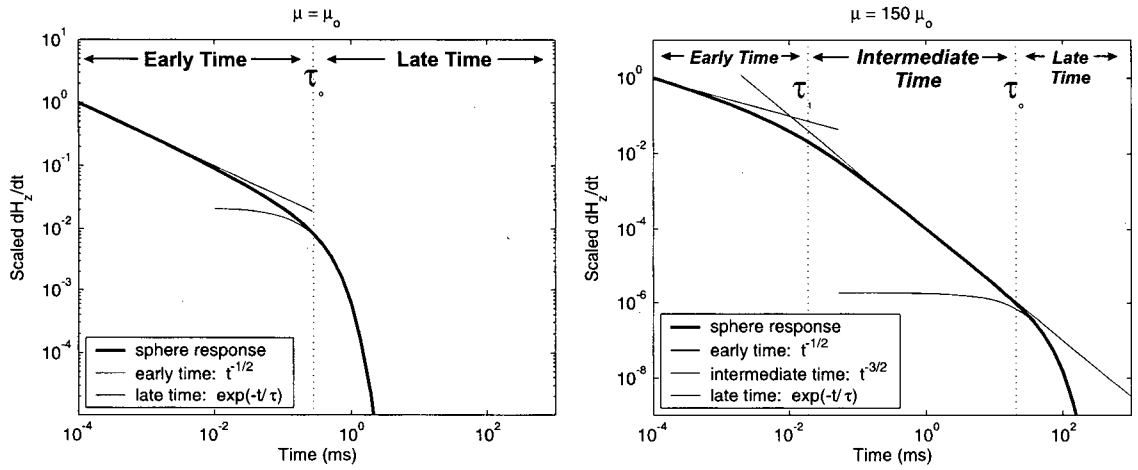

(a) Non-Permeable Sphere (b) Permeable Sphere

Figure 2.3: (a) The time decay behaviour of the magnetic flux density $\mathbf{B}$. (b) The time decay behaviour of the time derivative of the magnetic field $\partial\mathbf{B}/\partial t$. Both $\mathbf{B}$-field and $\partial\mathbf{B}/\partial t$ responses are normalized such that at $t = 0.0001ms$ the response is unity.

physical condition (for example, level of corrosion) of a target could affect the effective magnetic permeability. However, calculated TEM responses assuming a constant permeability of $\mu_r = 150$ for steel and $\mu_r = 1$ for aluminum compared well with laboratory TEM measurements of steel and aluminum targets (Pasion, 1999). Therefore we feel that equations 2.1 to 2.3 are suitable for the analysis that follows here. The values q_s are roots to the transcendental equation

$$\tan q_s = \frac{(\mu_r - 1)\, q_s}{q_s^2 + (\mu_r - 1)}. \tag{2.4}$$

Figure 2.3 shows the $\partial\mathbf{B}/\partial t$ response for both a magnetically permeable (e.g., steel) and nonpermeable (e.g., aluminum) sphere with a radius of 2.5 cm and a conductivity of 3.54 $\times 10^6$ S/m. The magnetic sphere has a permeability of $\mu_r = 150$. At early time both permeable and non-permeable spheres have a characteristic decay of $t^{-1/2}$. At late time the sphere response is exponential. The largest time constant τ in the summation of equation (2.3) determines the onset of the late time exponential behaviour, and is referred to as the fundamental time constant:

$$\tau_o = \frac{\sigma \mu_r \mu_o a^2}{q_1^2}, \tag{2.5}$$

where q_1 is determined by solving the transcendental equation 2.4 with $s = 1$. Figure 2.4 plots values of q_1 as a function of the sphere permeability. The fundamental time constant for a non-

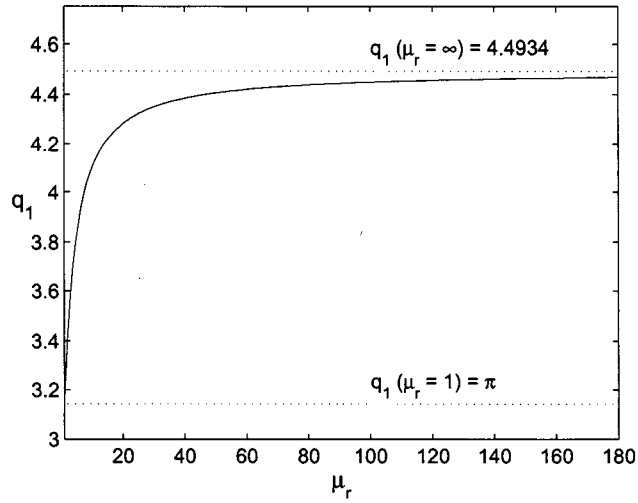

Figure 2.4: First solution ($s = 1$) of the sphere transcendental equation (Equation 2.4) as a function of magnetic permeability.

permeable sphere is

$$\tau_o\left(\mu_r = 1\right) = \frac{\sigma\mu_o a^2}{\pi^2}. \tag{2.6}$$

The value of q_1 approaches 4.4934 as μ_r approaches infinity. Therefore for highly permeable spheres

$$\tau_o\left(\mu_r = \infty\right) = \frac{\sigma\mu_o a^2}{\left(4.4934\right)^2}. \tag{2.7}$$

The blue lines in Figure 2.3 represent fits to the function $\exp(-t/\tau_o)$, where $\tau_o = 0.29$ ms for the non-permeable sphere and $\tau_o = 20.6$ ms for the permeable sphere.

For permeable spheres there exists an intermediate time stage during which the response decays as $t^{-3/2}$. An additional time constant τ_1 for permeable spheres defines the transition from the $t^{-1/2}$ early time decay to the $t^{-3/2}$ intermediate decay:

$$\tau_1 = \tau_o\left(\frac{q_1}{\mu_r}\right)^2 \tag{2.8}$$

(Bell et al., 2001a; Smith et al., 2004). Weichman (2004) refers to τ_1 as the *magnetic crossover time*. Weichman (2004) derives the expressions for τ_o and τ_1 for general compact permeable and

conductive targets. Steel targets will typically have magnetic permeabilities greater than 100 and, therefore have magnetic crossover times that are approximately four orders of magnitude less than their fundamental time constant, i.e., $\tau_1/\tau_o = O\left(10^{-4}\right)$. For the example of Figure 2.3, $\tau_1 = 0.0185$. Since typical time domain systems begin measurement after 0.1 ms, this early time regime will be rarely seen in most cases (for examples see EM63 data soundings of Figures 2.1 and 2.2).

Equation (2.1) reveals that the secondary **B**-field of a sphere in a uniform primary field is equivalent to the **B**-field of a single magnetic dipole located at the center of the sphere and oriented parallel to the primary field. For convenience, we write the relationship between the induced dipole and the primary field as $\vec{\mathbf{m}} = \bar{\bar{\mathbf{M}}} \cdot \mathbf{B^P}$, where $\bar{\bar{\mathbf{M}}}$ is the magnetic polarizability dyadic. For a sphere,

$$\bar{\bar{\mathbf{M}}} = \frac{2\pi}{\mu_o} L^{\mathbf{B}}(t)\, \bar{\bar{\mathbf{I}}} = \frac{2\pi}{\mu_o} \begin{bmatrix} L^{\mathbf{B}}(t) & 0 & 0 \\ 0 & L^{\mathbf{B}}(t) & 0 \\ 0 & 0 & L^{\mathbf{B}}(t) \end{bmatrix}. \tag{2.9}$$

Baum (1999) details the characteristics of the magnetic polarizability dyadic and notes that the triple degeneracy of the magnetic polarizability dyadic reflects the symmetry of the sphere.

The sphere solution possesses several characteristics that we retain in the formulation of our approximate solution for an axi-symmetric target. Firstly, the secondary field resulting from the induced currents generated in a sphere, illuminated by a uniform, step-off primary field, is dipolar at all points outside the sphere. We will also represent the secondary field for more general shapes as a dipolar field (see equation 2.1). A dipolar field approximation is reasonable for any observation point far enough away from any localized current distribution (Jackson, 1975), and it has been reported that for observation points greater than one to two times the target length, a dipolar field assumption is adequate (Casey and Baertlein, 1999; Grimm et al., 1997). Indeed, higher-order multipoles induced in a target will decay at early times (Grimm et al., 1997).

Secondly, the induced dipole moment in the center of a sphere is given by the dyadic product $\bar{\bar{\mathbf{M}}} \cdot \mathbf{B}^P$. This form indicates that the induced dipole is proportional to the projection of the primary field along the direction of the induced dipole. The components of $\bar{\bar{\mathbf{M}}}$ scale the strengths of the dipoles. The magnetic polarizability dyadic, in the case of the sphere, contains the function $L^{\mathbf{B}}(t)$ that contains all the information about the time decay of the sphere and it depends upon the material properties, shape, and size of the target. Our hypothesis is that more general metallic shapes can also

be approximately modelled with an induced dipole equal to the dyadic product $\bar{\bar{\mathbf{M}}} \cdot \mathbf{B}^P$. However, choosing the right functional form of $\bar{\bar{\mathbf{M}}}$ will be crucial.

2.2.2 Approximating the Magnetic Polarizability Dyadic for an Axi-Symmetric Body

Analytic expressions for $\bar{\bar{\mathbf{M}}}$ for the time domain response of a permeable and conducting nonspherical axi-symmetric body are not available. Therefore, we base our form of $\bar{\bar{\mathbf{M}}}$ on the magnetostatic polarizability for a spheroid. Recall that, for the time domain response of a sphere, the structure of $\bar{\bar{\mathbf{M}}}$ is identical to the structure of the magnetostatic polarizability dyadic of a sphere. The analytic solution for the magnetostatic response of a magnetic prolate spheroid is equivalent to the field of a magnetic dipole induced at the spheroid center (Das et al., 1990):

$$\begin{aligned}\vec{\mathbf{m}}^{spheroid} &= \vec{\mathbf{m}}_1 + \vec{\mathbf{m}}_2 \\ &= k_1 \left[\left(\hat{\mathbf{z}}' \cdot \mathbf{B}^p \right) \hat{\mathbf{z}}' \right] + k_2 \left[\left(\hat{\mathbf{y}}' \cdot \mathbf{B}^p \right) \hat{\mathbf{y}}' + \left(\hat{\mathbf{x}}' \cdot \mathbf{B}^p \right) \hat{\mathbf{x}}' \right] = \begin{bmatrix} k_2 & 0 & 0 \\ 0 & k_2 & 0 \\ 0 & 0 & k_1 \end{bmatrix} \cdot \mathbf{B}^p,\end{aligned} \tag{2.10}$$

where k_1 and k_2 are the polarizability constants, which are functions of the conductivity, permeability, shape, and size. Equation 2.10 reveals that the total induced dipole can be written as the sum of two orthogonal dipoles $\vec{\mathbf{m}}_1$ and $\vec{\mathbf{m}}_2$. The first dipole moment $\vec{\mathbf{m}}_1$ is parallel to the major axis of the spheroid, and its strength is proportional to the product of the primary field along that direction and the polarizability k_1. The second dipole moment is perpendicular to the major axis, and its magnitude is proportional to the component of the primary field along that direction and the polarizability k_2. A consequence of k_1 and k_2 being functions of the spheroid's shape and size is that the orientation of the effective dipole will not be solely determined by the direction of the primary field, as is the case for a sphere. In addition, the orientation of $\vec{\mathbf{m}}^{spheroid}$ will be influenced by the aspect ratio of the spheroid.

The polarization dyadic in Equation 2.10 suggests a magnetic polarization dyadic for the TEM

problem of the form

$$\bar{\bar{\mathbf{M}}} = \begin{bmatrix} L_2(t) & 0 & 0 \\ 0 & L_2(t) & 0 \\ 0 & 0 & L_1(t) \end{bmatrix}, \tag{2.11}$$

where we have simply replaced k_1 and k_2 in Equation 2.10 with the dipole decay functions $L_1(t)$ and $L_2(t)$. The resultant induced dipole moment for this definition of the magnetic polarization dyadic is then

$$\begin{aligned} \vec{\mathbf{m}}(t) &= \vec{\mathbf{m}}_1(t) + \vec{\mathbf{m}}_2(t) \\ &= L_1(t)\left[\left(\hat{\mathbf{z}}' \cdot \mathbf{B}^p\right)\hat{\mathbf{z}}'\right] + L_2(t)\left[\left(\hat{\mathbf{y}}' \cdot \mathbf{B}^p\right)\hat{\mathbf{y}}' + \left(\hat{\mathbf{x}}' \cdot \mathbf{B}^p\right)\hat{\mathbf{x}}'\right]. \end{aligned} \tag{2.12}$$

For modelling frequency domain data, we can simply replace the time dependent functions with the frequency dependent functions $L_1(\omega)$ and $L_2(\omega)$.

The approximate forward model represents the TEM response of an axi-symmetric target with two orthogonal dipoles. The first dipole is parallel to the symmetry axis of the target, and the second dipole is perpendicular to the symmetry axis. These dipoles decay independently according to the decay laws $L_1(t)$ and $L_2(t)$, respectively. The dipole strengths are proportional the projection of the primary field onto the respective dipole directions.

The dipole model produces TEM responses that are consistent with those observed field measurements of UXO. As Figures 2.1 and 2.2 demonstrate, the shape anomaly of the measured response for compact targets can change with time. This observed field behavior can be duplicated by letting the axial and transverse dipoles decay independently of each other. By assigning a different decay characteristic (governed by its decay parameters) to each dipole, the relative contribution by each dipole to the secondary field can vary with time. The data examples of Figures 2.1 and 2.2 are for horizontal ordnance. The anomaly changes from a single peak at earlier times to a double peaked anomaly at late times. The early time single peak is due to both axial transverse mode contributing. At later times the transverse mode decayed away, leaving the axial excitation being the dominate mode. The horizontally oriented axial mode produces a characteristic double peaked anomaly.

2.2.3 Parameterizing $L(t)$

The time decay for a conductive body of arbitrary size and shape in an insulating medium illuminated by a step-off primary field is determined by the sum of exponentials (Kaufman, 1994). Carin et al. (2001) described the time domain impulse response of an axi-symmetric target as an infinite sum of exponentials,

$$L_1(t) = m_1(0)\,\delta(t) + \frac{\partial}{\partial t}\sum_k u(t)\, m_{1k} \exp(-\omega_{1k} t) \tag{2.13}$$

$$L_2(t) = m_2(0)\,\delta(t) + \frac{\partial}{\partial t}\sum_k u(t)\, m_{2k} \exp(-\omega_{2k} t) \tag{2.14}$$

where $m_z(0)$ and $m_p(0)$ represent the dipole contributions of ferrous targets. While it is possible to model the TEM response with a number of exponents (Snyder et al., 1999), the inverse problem to determine the weights and time constants is potentially difficult (Istratov and Vyvenko, 1999). Therefore, our approach is to parameterize $L(t)$ with a simple empirical function defined by a minimum number of parameters, while still being to replicate all the features of the TEM decay.

Since the time decay for a sphere is determined by the sum of exponentials, and is a subset of the class of axi-symmetric targets, the form for $L(t)$ should, at least, be able to duplicate the time decay features observed for the sphere. Several parametric forms for $L(t)$ have been considered (Bell et al., 2001a; Smith et al., 2004; Pasion, 1999; Benavides and Everett, 2006). An example of a simple parameterization that can replicate the early, intermediate and late time stages of the permeable sphere decay is

$$L(t) = \frac{k}{\alpha t^{1/2} + t^{\beta}} \exp(-t/\gamma), \tag{2.15}$$

where $\beta > 1/2$. At early times, $L(t) = (k/\alpha)\, t^{-1/2}$ (see Figure 2.5). At intermediate times the decay will have a power law behavior of $kt^{-\beta}$. The transition between early and intermediate times (i.e. the magnetic crossover time) occurs at

$$\tau_1 = \alpha^{\frac{1}{(\beta - 1/2)}}. \tag{2.16}$$

At late time the decay will be exponential with a time constant of γ. For the case of a sphere, $\beta = 3/2$, and the magnetic crossover time is $\tau_1 = \alpha$. Figure 2.6 compares the fit of equation 2.15

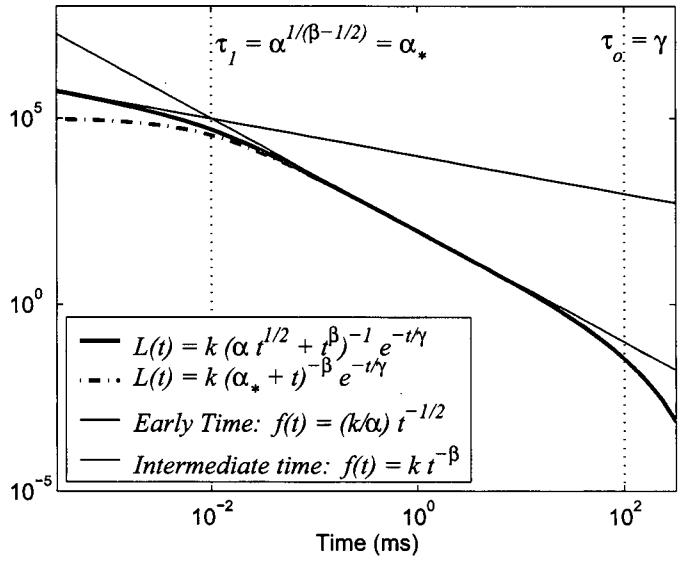

Figure 2.5: Some examples of parameterizations that model the three decay stages observed for a sphere.

to modelled sphere data.

The three stages observed for the sphere response was been observed in measured polarization decays of UXO targets (Pasion, 1999). The decays were recorded from 0.01 ms to 100 ms with a Geonics PROTEM47 time domain sensor using a 40 m square transmitter loop. We observed that when there was a transition from early to intermediate time stages, the magnetic crossover time τ_1 was less than 0.1 ms. The fundamental time constants τ_o were less than 100 ms, and had a median of approximately 10 ms. In this paper we analyze data from a Geonics EM63 time domain sensor. The Geonics EM63 measures the time domain response from 0.18 ms to 25 ms, and therefore we only have to model a power law decay followed by the late stage exponential decay. Therefore, we can set $\alpha = 0$ without affecting our ability to fit the data, and arrive at the expression

$$L(t) = kt^{-\beta} \exp(-t/\gamma). \tag{2.17}$$

This form for the $\partial \mathbf{B}/\partial t$ decay law was suggested to us in a personal communication from J.D. McNeill.

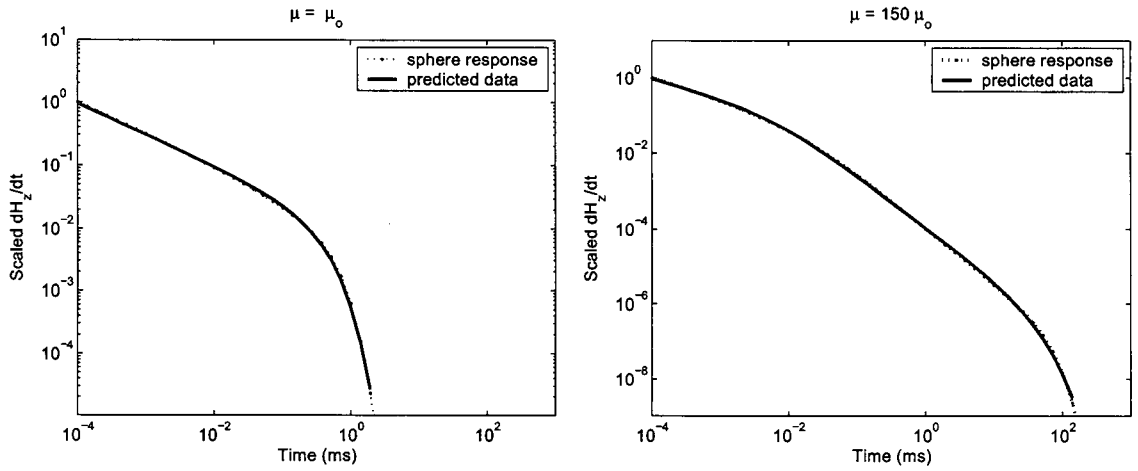

(a) TEM response of a non-permeable sphere

(b) TEM response of a permeable sphere

Figure 2.6: Time domain responses for a magnetically (a) non-permeable and (b) permeable sphere. The solid lines are responses evaluated from Equation (2.15). The agreement supports the validity of (2.15) as a representation of the time domain responses.

Pasion (1999) suggested a form of the decay law for the **B**-field is

$$L(t) = k\ (t+\alpha)^{-\beta} \exp(-t/\gamma)\,. \tag{2.18}$$

The parameter k controls the magnitude of the modelled response. The three parameters α, β, and γ, control the duration and characteristics of the three different stages of the time decay curve. The duration of the relatively flat early time stage is proportional to the parameter α. The linear decrease of response observed during the intermediate time stage is determined by $t^{-\beta}$. The exponential decay characterizing the late time stage is controlled by the parameter γ. Figures 2.7(a) and (c) demonstrate the ability to reproduce the secondary **B**-field for a non-permeable and permeable sphere, respectively.

The time derivative $\partial\mathbf{B}/\partial t$, measured directly with most TEM receivers, can also be modelled with Equation 2.18. Figure 2.7(b) and (d) plot the $\partial\mathbf{B}/\partial t$ curves for a non-permeable and permeable sphere, respectively. The early time behaviour for the nonpermeable sphere follows a $t^{-1/2}$ decay, and these curves are different from those of **B** in Figures 2.7(a) and (c). Nevertheless, the curves are still represented by early time turn-overs, and power-law and exponential decays that can be accommodated by Equation 2.18. The suitability is demonstrated by the fit between the laboratory

measured response and a predicted response obtained by evaluating Equation 2.18.

Pasion (1999) demonstrated how the decay parameters in 2.18 are related to the size and shape of the target. Figure 2.8 suggests that the value of β obtained for a sphere may be diagnostic in determining whether the sphere is permeable or non-permeable. For a steel sphere ($\mu_r = 150$), we see, for spheres with radii between 5 to 15 cm, that β falls between 1.11 and 1.35, while for a non-permeable sphere ($\mu_r = 1$), β has a value of approximately 0.5, which corresponds to the early time $t^{-1/2}$ behavior that Kaufman (1994) predicted for a non-permeable sphere.

The recovered k values for targets ranging from a steel plate to a steel rod are shown in Figure 2.9(a), and the calculated k-ratios are shown in Figure 2.9(b). For a steel plate, the k-ratio $k_1/k_2 < 1$. For a steel bar the k-ratio $k_1/k_2 > 1$. The recovered k values for aluminum targets are shown in Figure 2.9(c). The opposite orientation effect was observed for an aluminum rod, that is $k_1/k_2 < 1$ (Figure 2.9(d)).

In addition to the relative strength of the dipoles being shape dependent, the slope of the time decay response during the intermediate time stage is dependent upon the target shape. This effect was seen in steel targets only. The steepness of the response during the intermediate time stage is reflected in the parameter β. The recovered β values for targets ranging from a steel plate to a steel rod are shown in Figure 2.10(a), and β values for aluminum targets are shown in Figure 2.10(c). A dipole that decays at a greater rate will have a larger β. The rate of decay of the $\partial B/\partial t$ response is greater when the plane of a steel plate is perpendicular to the primary field (axial excitation), than when the plane of a steel plate is parallel to the primary field (transverse excitation). Thus, for a steel plate, $\beta_1/\beta_2 > 1$. In the case of a rod, the $\partial B/\partial t$ response decays faster (and thus β is larger) when the main axis of the rod is perpendicular to the primary field (transverse excitation). In the case of a steel rod $\beta_1/\beta_2 < 1$ (Figure 2.10(b)).

For aluminum targets the response shape looks essentially the same for each of the targets. The $\partial B/\partial t$ response exhibits a power law decay of $t^{-1/2}$ and is exponential at later times. The decay curves for aluminum targets are essentially the same regardless of target shape, and therefore there is no relationship between the β-ratio and the aspect ratio (Figure 2.10(d)).

Additional tests by Beran (2005) confirmed the relationships between the parameters in 2.18 and the target size and shape by using data synthetically generated with the Method of Auxiliary Sources (MAS) code (Shubitidze et al., 2002a) code. In the following section, we generically denote

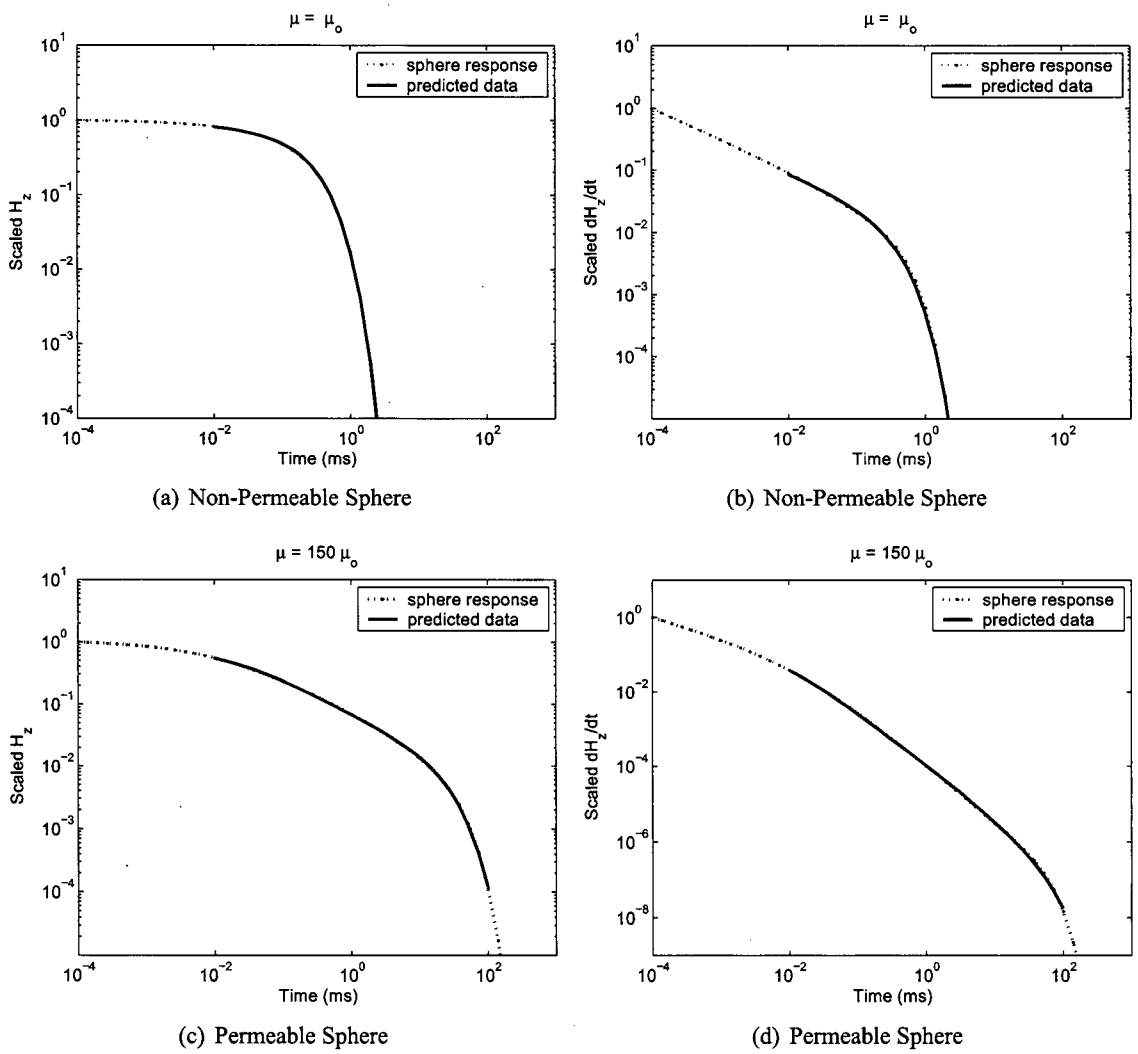

Figure 2.7: The time decay behaviour of the magnetic flux density $\mathbf{B}$ is plotted for (a) a non-permeable and (c) a permeable sphere. The time decay behaviour of the time derivative of the magnetic field $\partial\mathbf{B}/\partial t$ is plotted in (b) and (d) for a non-permeable and permeable sphere, respectively. The responses are normalized to be equal to one at 10^{-4} ms. The solid lines are responses evaluated from eq. (2.18) between 0.01 ms and 100 ms, which is generally the time range of interest for TEM UXO sensor. The agreement supports the validity of (2.18) for modelling the time domain response.

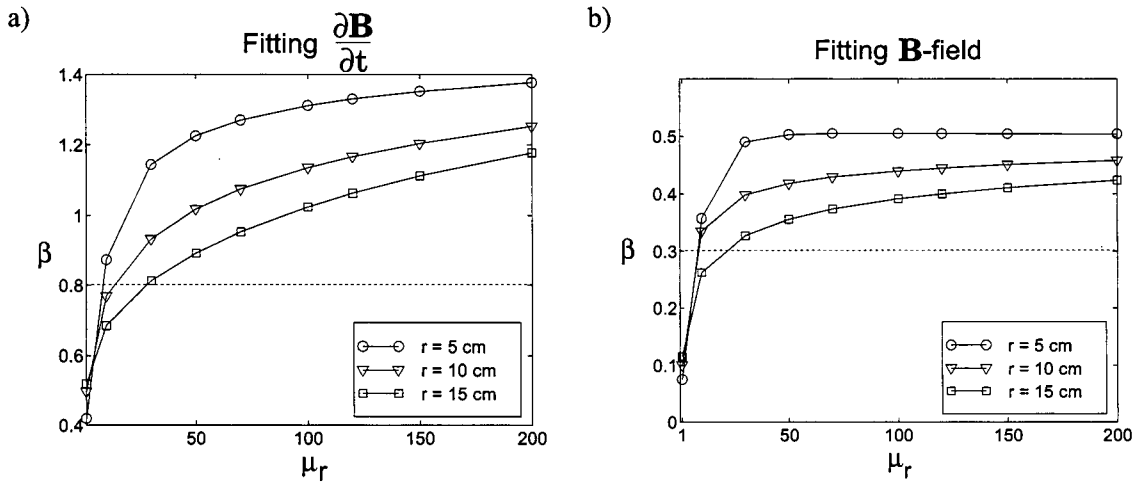

Figure 2.8: The behaviour of parameter β for various size spheres (radius = 5, 10, and 15 cm) with varying permeability μ. Panel (a) contains results of recovering β by fitting the $\partial \mathbf{B}/\partial t$ data. Panel (b) contains results of recovering β by fitting the $\mathbf{B}$-field.

the TEM response as $\boldsymbol{\xi}(\mathbf{r}, t)$ where $\boldsymbol{\xi}$ can be the magnetic field or its time derivative. The time dependent decay of $\boldsymbol{\xi}$ is given by Equation 2.18.

2.2.4 The Approximate Forward Model

With the above background, we can write an approximate expression for the secondary field response of an axi-symmetric target. First, let us switch from the body-fixed (primed) coordinate system to a space-fixed coordinate system, which is more amenable to the definitions of target and sensor location of a typical field survey (Figure 2.11). A vector $\mathbf{v}'$ in the body-fixed coordinate system is related to a vector $\mathbf{v}$ in the space-fixed coordinate system via the Euler rotation tensor $\mathbf{A}(\phi, \theta, \psi)$ by (Arfken, 1985)

$$\mathbf{v}' = \mathbf{A}\,\mathbf{v}, \tag{2.19}$$

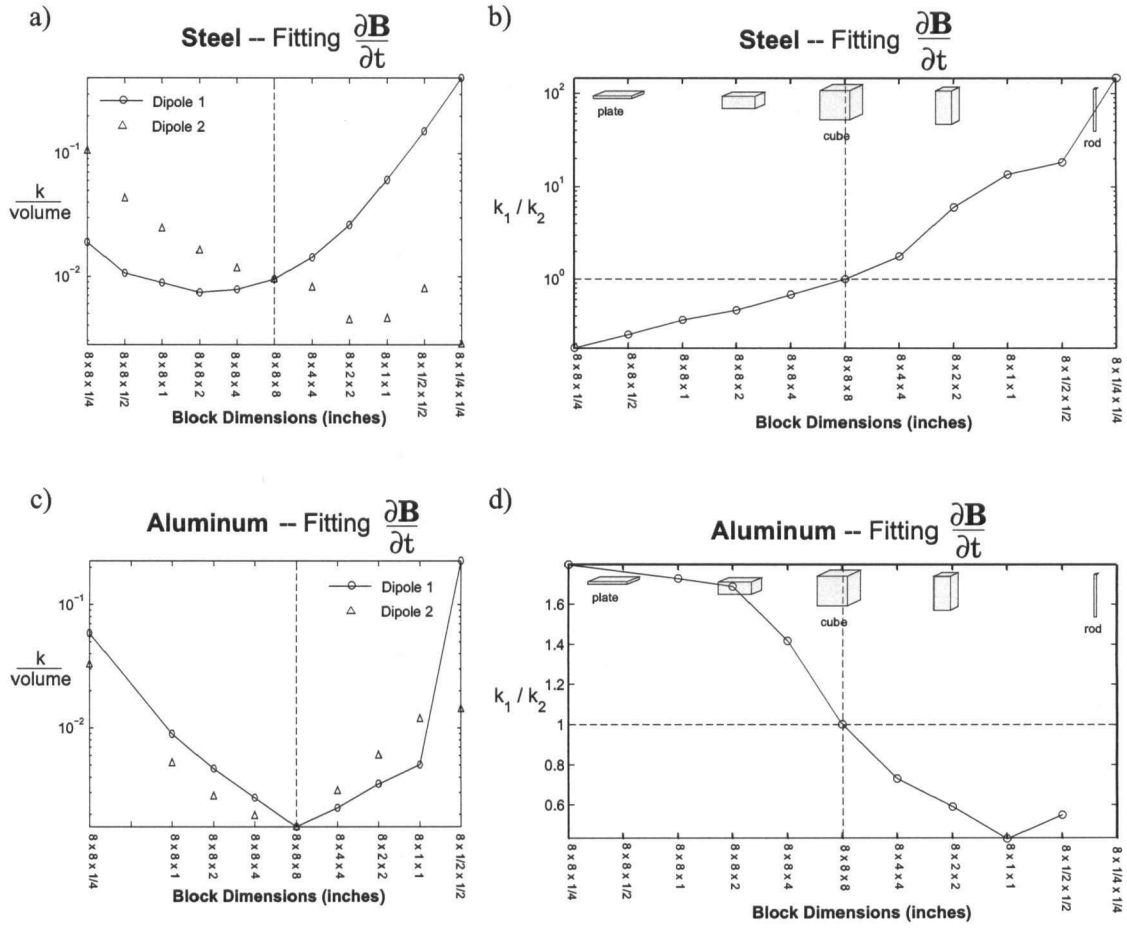

Figure 2.9: Relating the aspect ratio of a steel target with the ratio k_1/k_2. Plot (a) contains the recovered k parameter from fitting the measured $\partial \mathbf{B}/\partial t$ response of steel axi-symmetric targets. Plot (b) illustrates the relationship between the k_1/k_2 ratio derived from $\partial \mathbf{B}/\partial t$ data and the shape of a steel target. Plot (c) contains the recovered k parameter from fitting the measured $\partial \mathbf{B}/\partial t$ response of aluminum axi-symmetric targets. Plot (d) illustrates the relationship between the k_1/k_2 ratio and the shape of an aluminum target.

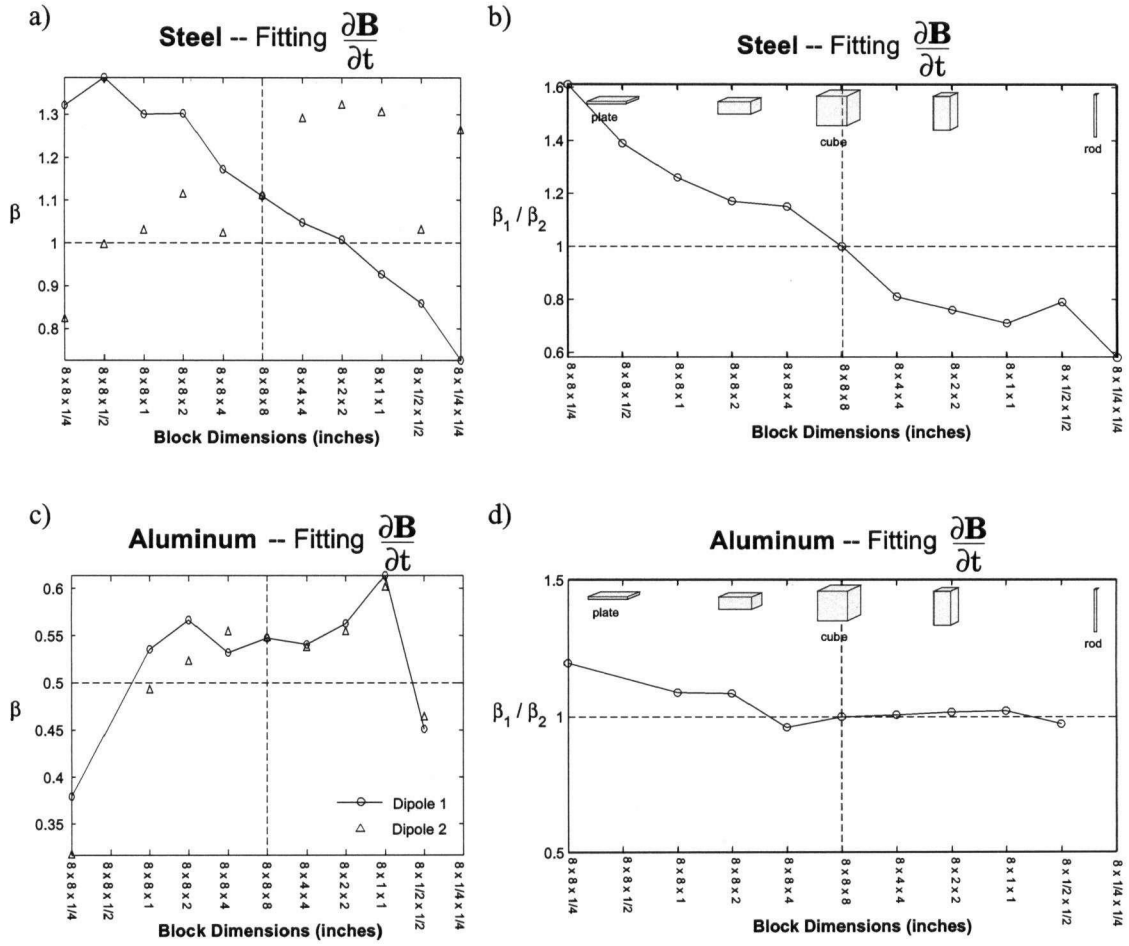

Figure 2.10: Relating the aspect ratio of a steel target with the ratio β_1/β_2. Plot (a) contains the recovered β parameter from fitting the measured $\partial\mathbf{B}/\partial t$ response of steel axi-symmetric targets. Plot (b) illustrates the relationship between the β_1/β_2 ratio derived from $\partial\mathbf{B}/\partial t$ data and the shape of a steel target. Plot (c) contains the recovered β parameter from fitting the measured $\partial\mathbf{B}/\partial t$ response of aluminum axi-symmetric targets. Plot (d) illustrates the relationship between the β_1/β_2 ratio and the shape of an aluminum target.

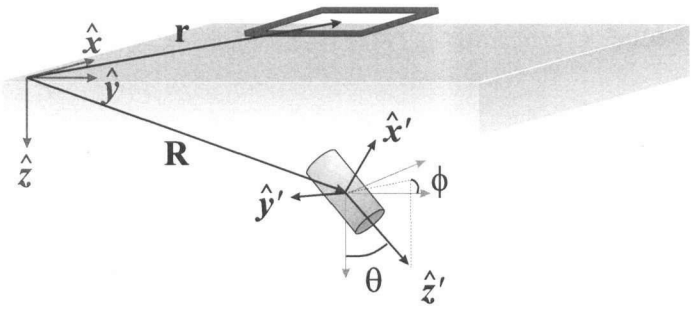

Figure 2.11: The field (unprimed) co-ordinate system for a buried target. The unit vectors $\hat{\mathbf{x}}$, $\hat{\mathbf{y}}$, and $\hat{\mathbf{z}}$ define the field co-ordinate system, and $\hat{\mathbf{x}}'$, $\hat{\mathbf{y}}'$, and $\hat{\mathbf{z}}'$ define the body-fixed co-ordinate system.

where we adopt the "x-convention" rotation matrix:

$$\mathbf{A} = \begin{bmatrix} \cos\psi\cos\theta\cos\phi - \sin\psi\sin\phi & \cos\psi\cos\theta\sin\phi + \sin\psi\cos\phi & -\cos\psi\sin\theta \\ -\sin\psi\cos\theta\cos\phi - \cos\psi\sin\phi & -\sin\psi\cos\theta\sin\phi + \cos\psi\cos\phi & \sin\psi\sin\theta \\ \sin\theta\cos\phi & \sin\theta\sin\phi & \cos\theta \end{bmatrix}, \tag{2.20}$$

where θ is the angle between the symmetry axis of the target ($\hat{\mathbf{z}}'$ in Figure 2.11) and the vertical axis in the space-fixed coordinate system ($\hat{\mathbf{z}}$ in Figure 2.11), and ϕ is the angle between the projection of $\hat{\mathbf{z}}'$ onto the horizontal plane and $\hat{\mathbf{x}}$. The angle ψ represent a rotation about the body-fixed $\hat{\mathbf{z}}'$ axis.

The approximate forward modelling is written by substituting the definition of the induced dipole of Equation 2.12 into the expression for a dipole field (Equation 2.1), and carrying out the dyadic product. Let us consider a target whose center is located at $\mathbf{R}$ in the space-fixed coordinate system. The secondary response $\boldsymbol{\xi}(\mathbf{r}, t)$, measured at a receiver/transmitter location $\mathbf{r}$ and at a time t after the termination of the primary field, is then the sum of the responses of the three orthogonal dipoles:

$$\boldsymbol{\xi}(\mathbf{r}, t) = \boldsymbol{\xi}_1(\mathbf{r}, t) + \boldsymbol{\xi}_2(\mathbf{r}, t) + \boldsymbol{\xi}_3(\mathbf{r}, t), \tag{2.21}$$

where

$$\boldsymbol{\xi}_i(\mathbf{r}, t) = \frac{\mu_o}{4\pi}\left(3\left[\vec{\mathbf{m}}_i(t)\cdot(\mathbf{r}-\mathbf{R})\right]\frac{(\mathbf{r}-\mathbf{R})}{|\mathbf{r}-\mathbf{R}|^5} - \frac{\vec{\mathbf{m}}_i(t)}{|\mathbf{r}-\mathbf{R}|^3}\right) \tag{2.22}$$

and

$$\vec{\mathbf{m}}_1(t) = L_1(t)\left(\hat{\mathbf{z}}' \cdot \mathbf{B}^p\right)\hat{\mathbf{z}}', \tag{2.23}$$

$$\vec{\mathbf{m}}_2(t) = L_2(t)\left(\hat{\mathbf{y}}' \cdot \mathbf{B}^p\right)\hat{\mathbf{y}}', \tag{2.24}$$

$$\vec{\mathbf{m}}_3(t) = L_3(t)\left(\hat{\mathbf{x}}' \cdot \mathbf{B}^p\right)\hat{\mathbf{x}}'. \tag{2.25}$$

The unit vectors are given by Equation 2.20.

If we assume axial symmetry, the rotation about $\hat{\mathbf{z}}'$ can be set to $\psi = 0$ and the Euler rotation tensor can be written:

$$\mathbf{A} = \begin{bmatrix} \cos\theta\cos\phi & \cos\theta\sin\phi & -\sin\theta \\ -\sin\phi & \cos\phi & 0 \\ \sin\theta\cos\phi & \sin\theta\sin\phi & \cos\theta \end{bmatrix} \tag{2.26}$$

The secondary response $\boldsymbol{\xi}(\mathbf{r}, t)$, is then the sum of the responses of two orthogonal dipoles:

$$\boldsymbol{\xi}(\mathbf{r}, t) = \boldsymbol{\xi}_1(\mathbf{r}, t) + \boldsymbol{\xi}_2(\mathbf{r}, t), \tag{2.27}$$

where

$$\vec{\mathbf{m}}_1(t) = L_1(t)\left(\hat{\mathbf{z}}' \cdot \mathbf{B}^p\right)\hat{\mathbf{z}}', \tag{2.28}$$

$$\vec{\mathbf{m}}_2(t) = L_2(t)\left[\left(\hat{\mathbf{x}}' \cdot \mathbf{B}^{\mathbf{P}}\right)\hat{\mathbf{x}}' + \left(\hat{\mathbf{y}}' \cdot \mathbf{B}^{\mathbf{P}}\right)\hat{\mathbf{y}}'\right], \tag{2.29}$$

are the dipole parallel and perpendicular to the axis of symmetry. The unit vectors are given by Equation 2.26.

In this thesis, I use three representations of the polarization tensor elements $L_i(t)$:

1. Instantaneous Amplitude: For this representation, we do not parameterize $L_i(t)$. Instead, the amplitude at each measured time t_j is a model parameter

$$L_i(t_j) = L_i^j. \tag{2.30}$$

For N inverted time channels, the i^{th} polarization decay is described by a parameter vector

$\mathbf{p}_i$ of length N

$$\mathbf{p}_i = \left[L_i^1,\, L_i^2,\, \cdots L_i^N\right]. \tag{2.31}$$

2. Pasion (1999): As was discussed in Section 2.2.3, the parameterized form of the decay law suggested by Pasion (1999) is

$$L_i(t) = k_i\ (t + \alpha_i)^{-\beta_i} \exp(-t/\gamma_i). \tag{2.32}$$

The parameter vector for this representation is

$$\mathbf{p}_i = [k_i,\, \alpha_i,\, \beta_i,\, \gamma_i] \tag{2.33}$$

3. McNeill: As was suggested by J.D. McNeill (Personal Communication):

$$L_i(t) = k_i\, t^{-\beta_i} \exp(-t/\gamma_i) \tag{2.34}$$

The parameter vector for the McNeill representation is

$$\mathbf{p}_i = [k_i,\, \beta_i,\, \gamma_i]. \tag{2.35}$$

In summary, the approximate response of a buried metallic object can be model as three orthogonal dipoles (Equation 2.21) or, for the case of axi-symmetric targets, two orthogonal dipoles (Equation 2.27). When two polarizations model the response, the representative model vector is

$$\mathbf{m} = [X,\, Y,\, Z,\, \phi,\, \theta,\, \mathbf{p}_1,\, \mathbf{p}_2], \tag{2.36}$$

where X and Y denote the surface projection of the centroid of the body, and Z is the depth of the object below the surface. The orientation of the target is described by the angles θ and ϕ. The remaining parameters describe the decay characteristics of the two dipoles: $\mathbf{p}_1$ describe the dipole parallel to the axis of symmetry ($\vec{\mathbf{m}}_1$), and $\mathbf{p}_2$ describe the dipole perpendicular to the axis of symmetry ($\vec{\mathbf{m}}_2$).

When three polarizations are required to model the response, the model vector is

$$\mathbf{m} = [X,\, Y,\, Z,\, \phi,\, \theta,\, \psi,\, \mathbf{p}_1,\, \mathbf{p}_2,\, \mathbf{p}_3]\,, \tag{2.37}$$

where an additional angle ψ is required to describe the rotation about the $\hat{\mathbf{z}}$ axis, and three sets of decay parameters ($\mathbf{p}_1$, $\mathbf{p}_2$, and $\mathbf{p}_3$) describe the decay of the three polarizations. Thus, the inversion for the model $\mathbf{m}$ will immediately give estimates of target location and orientation. Information on the shape, size, and material parameters of the target may later be inferred from the remaining parameters.

2.3 Some Characteristics of the Dipole Model

2.3.1 The Relationship Between a Horizontal Loop Tx and the Transverse and Axial

In the next chapter different data inversion strategies for determining the polarizations are considered. The ability to resolve the different polarization components is directly related to the ability of the transmitter loop to illuminate both polarizations. The optimal sensor for this purpose would generate a primary field that illuminates the target at a number of angles. This can be accomplished through multiple transmitter loops. Although such instrumentation are under development (for example, Gasperikova et al., 2006), most sensors use a horizontal loop transmitter. Due to symmetry, the primary field will be vertical directly beneath the center of the loop, with the horizontal component of the primary field increasing when moving away from directly beneath the loop. Illumination of the target from multiple angles is achieved by spatially scanning a region above the target. Away from the transmitter loop the signal-to-noise ratio of the signal will decrease significantly, thereby limiting the ability to illuminate the target.

Figure 2.12 demonstrates how the axial, transverse, and total dipole moment changes as a function of target position and orientation relative to a 1 m x 1 m square, horizontal loop transmitter. The length and direction of the induced dipoles in Figure 2.12 (as well as Figures 2.14 and 2.15) were calculated using the polarizations for a 105 mm projectile. Directly over a horizontal target ($x = 0.0$ m), only the transverse component ($L_2(t)$ and $\vec{\mathbf{m}}_2(t)$ in Equation 2.29) contribute to the measured signal. For this case, the transverse dipole (represented by the blue arrow in Figure 2.12(a), 3rd drawing from the top) is parallel to the induced dipole (represented the red arrow in Figure 2.12(b), 3rd drawing from the top). The axial component of the dipole is excited when the transmitter is positioned away from the target. The axial and transverse dipole contribute additively to the response. Figure 2.13 shows the amount of signal due to each polarization at the first time channel of EM63 data for a horizontal 105 mm projectile at a depth of 1 m. The polarization values used to calculate the response were estimated using data from the USACE-ERDC test stand in Vicksburg, MS. The polarizations at the first time channel are $L_1(t = 0.18ms) = 134.3$ and $L_2(t = 0.18ms) = 78.1$ for the axial and transverse components, respectively.

Figure 2.13(a) shows, in plan view, the forward modelled data with its contributions from the

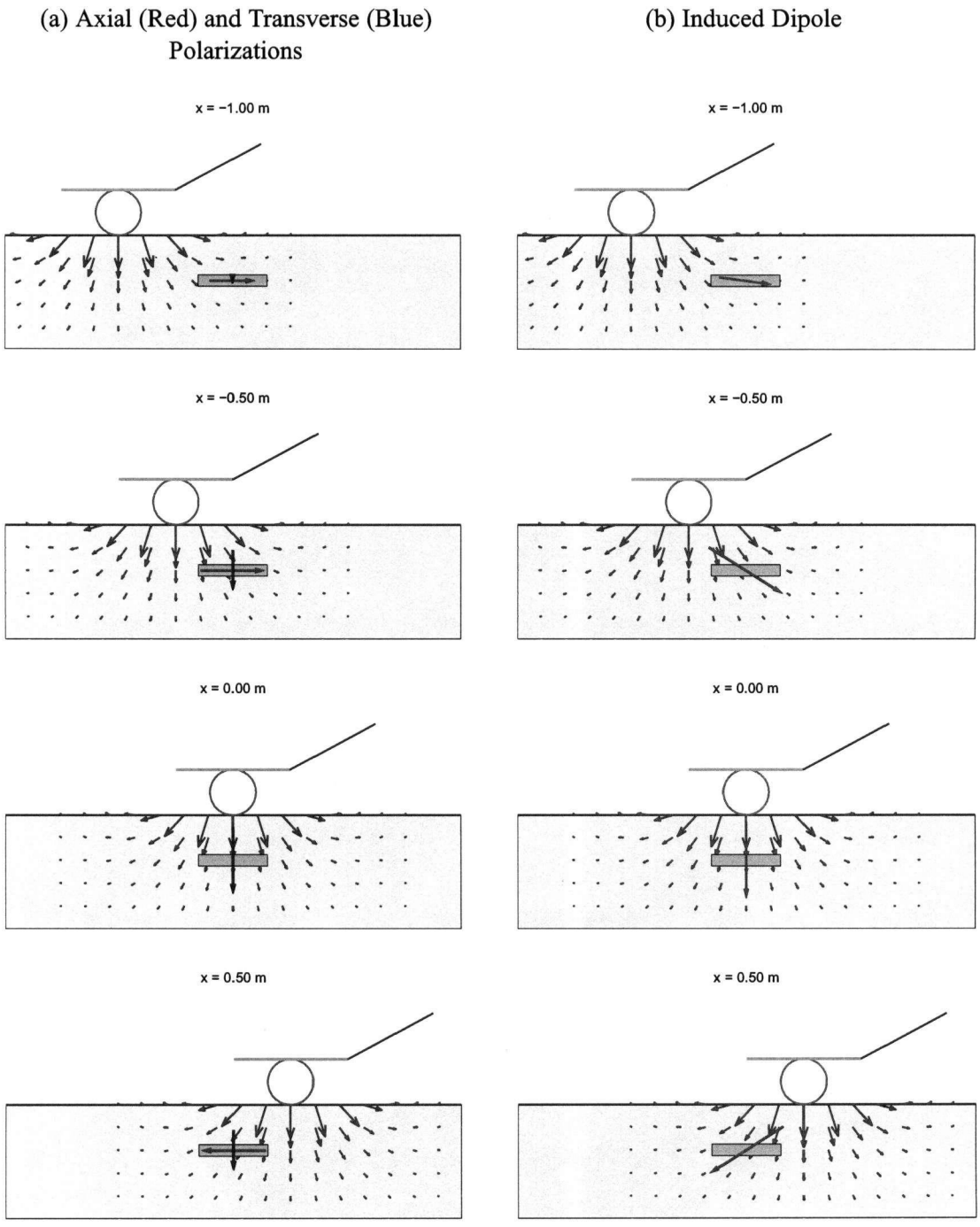

Figure 2.12: The strength of the induced transverse and axial dipoles for a horizontal, rod-like target. The relative strength of the polarization values are $L_1/L_2 = 1.72$.

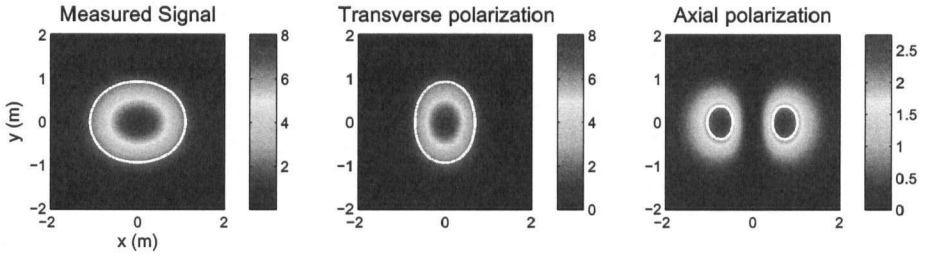

(a) Plan view of data at the first time channel ($t = 0.18$ ms)

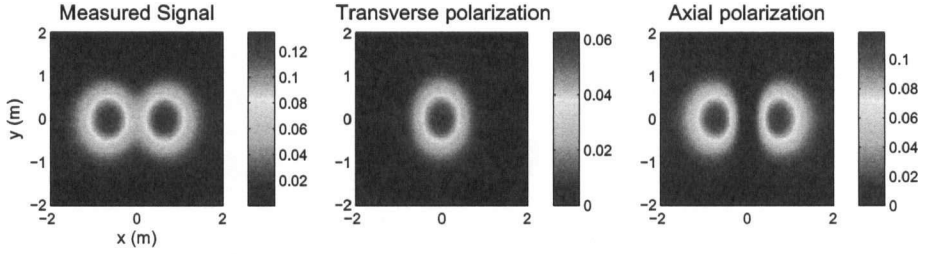

(b) Plan view of data at time channel 20 ($t = 7.1$ ms)

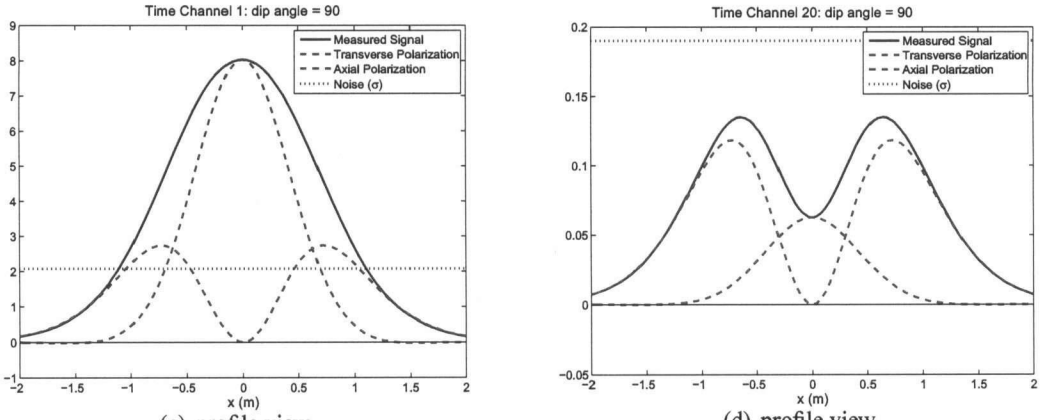

(c) profile view

(d) profile view

Figure 2.13: Synthetically generated EM63 data for a horizontal 105 mm projectile at a depth of 1 m. The polarizations at the first time channel are $L_1\,(t = 0.18ms) = 134.3$ and $L_2\,(t = 0.18ms) = 78.1$ for the axial and transverse components, respectively. The white contour line in (a) represents the estimated standard deviation for noise, from a EM63 survey carried out at the Sky Research UXO Test Site. There is no white contour line in (b) because, for $t = 7.1$ ms the signal is smaller than the estimated standard deviation of the noise. (c) and (d) compare the relative contributions of the axial and transverse polarizations to the measured signal along a line $y = 0$ m.

transverse and axial polarizations for the first time channel. The white contour drawn at 2.07 mV represents the estimated standard deviation for noise. The noise statistic estimate was obtained using data from an EM63 survey carried out on the Sky Research UXO Test Site. Along a line $x = 0$, the projection of the primary field along the axial direction ($\hat{\mathbf{z}} \cdot \mathbf{B}^P$) is zero, and thus the only contribution to the signal is due to the transverse component. The contribution of axial component makes the anomaly longer along the length of the target.

For many ordnance, the transverse component will have a smaller time constant than the axial component. In that case, the late time data will be dominated by the axial component. At later time (Figure 2.13(b)) the ratio between the axial and transverse components strength is larger ($L_1/L_2(t = 0.18ms) = 1.72$, compared to $L_1/L_2(t = 7.07ms) = 5.81/0.61 = 9.52$). Therefore, the contribution of the axial component is greater at later times, and we observe the characteristic double-peak anomaly of a horizontal target (as shown in Figures 2.1 and 2.2). Figure 2.13(c) compares the transverse and axial polarizations along a profile taken at $y = 0$ m.

The least favorable orientation for resolving both polarizations with a horizontal loop transmitter is for a vertical target (Figure 2.14). The relationship between the polarization excitations and the transmitter position is the reverse of the horizontal case. The contribution of the transverse excitation to the measured secondary field will be smaller than for the previously considered horizontal target, because the axial polarization will generally be larger than the transverse polarization, and the only way to excite the transverse component is with the cart away from the target, where the signal to noise ratio can be small. Figure 2.16 compares the contributions of the transverse and axial polarizations to the signal from a vertical 105 mm projectile whose center is located at a depth of 1 m below the surface. The transmitter loop is assumed to be 0.4 m above the ground. Indeed, for a deep enough and small enough target, the signal due to the transverse polarization can be less than the noise level of the instrument. For such a case, the ability to identify the target through a data inversion for polarization parameters will be more difficult (Pasion et al., 2004).

2.3.2 The Similarity Between Rod and Plate Responses

In Section 2.3.1 we observed how the response of a target is dependent on the transmitter, receiver, and target geometry. In particular, the response of a rod-like target can be similar to the response of a plate-like target that is rotated 90 degrees (Figure 2.17). This ambiguity leads to a local minimum

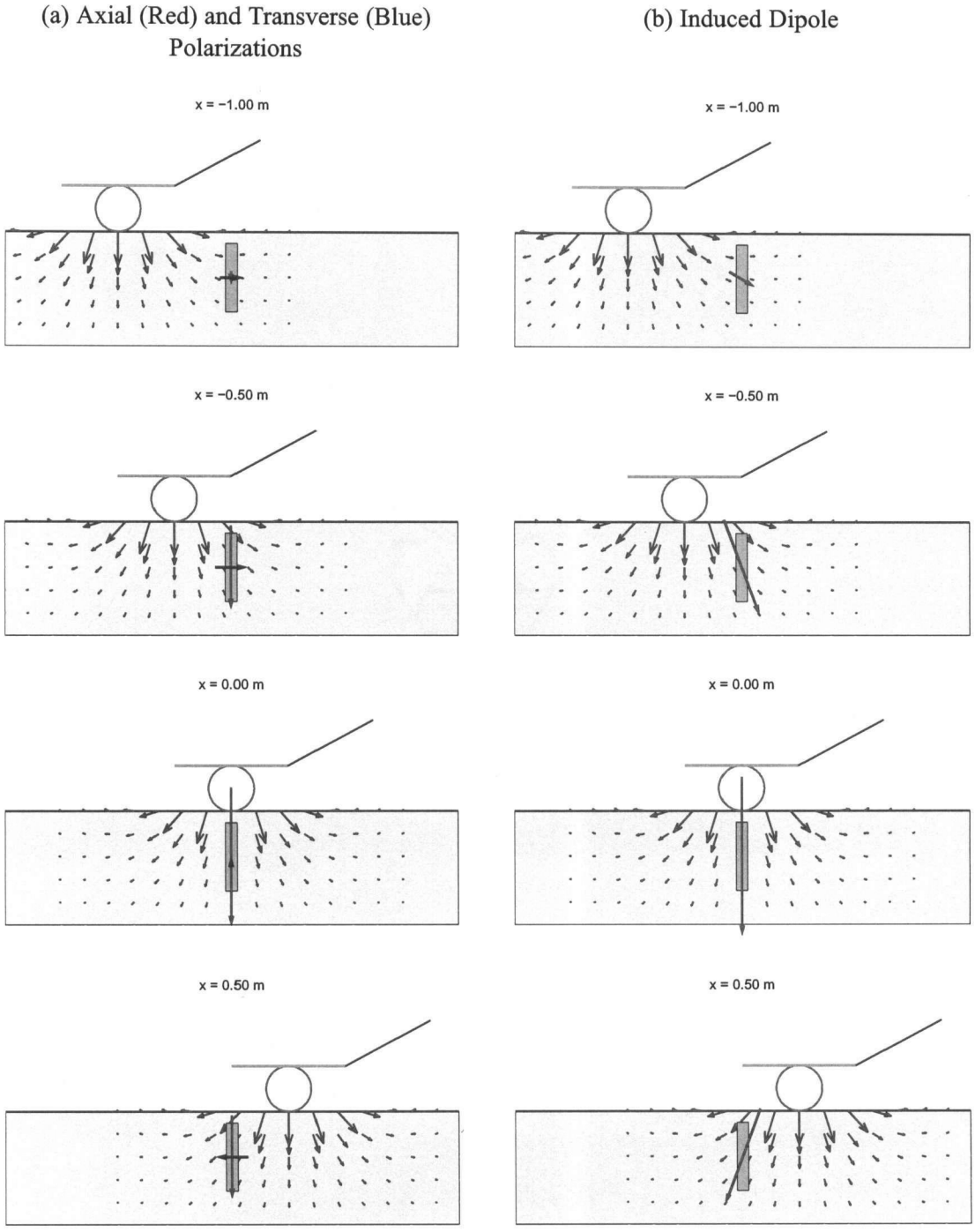

Figure 2.14: Excitation of a vertical UXO. Relative contributions of the axial (red) and transverse (blue) polarizations are indicated in (a). Excitation of the transverse component occurs when the transmitter loop is positioned away from the target, such that the primary field has a horizontal component. The total induced dipole moment is plotted in (b).

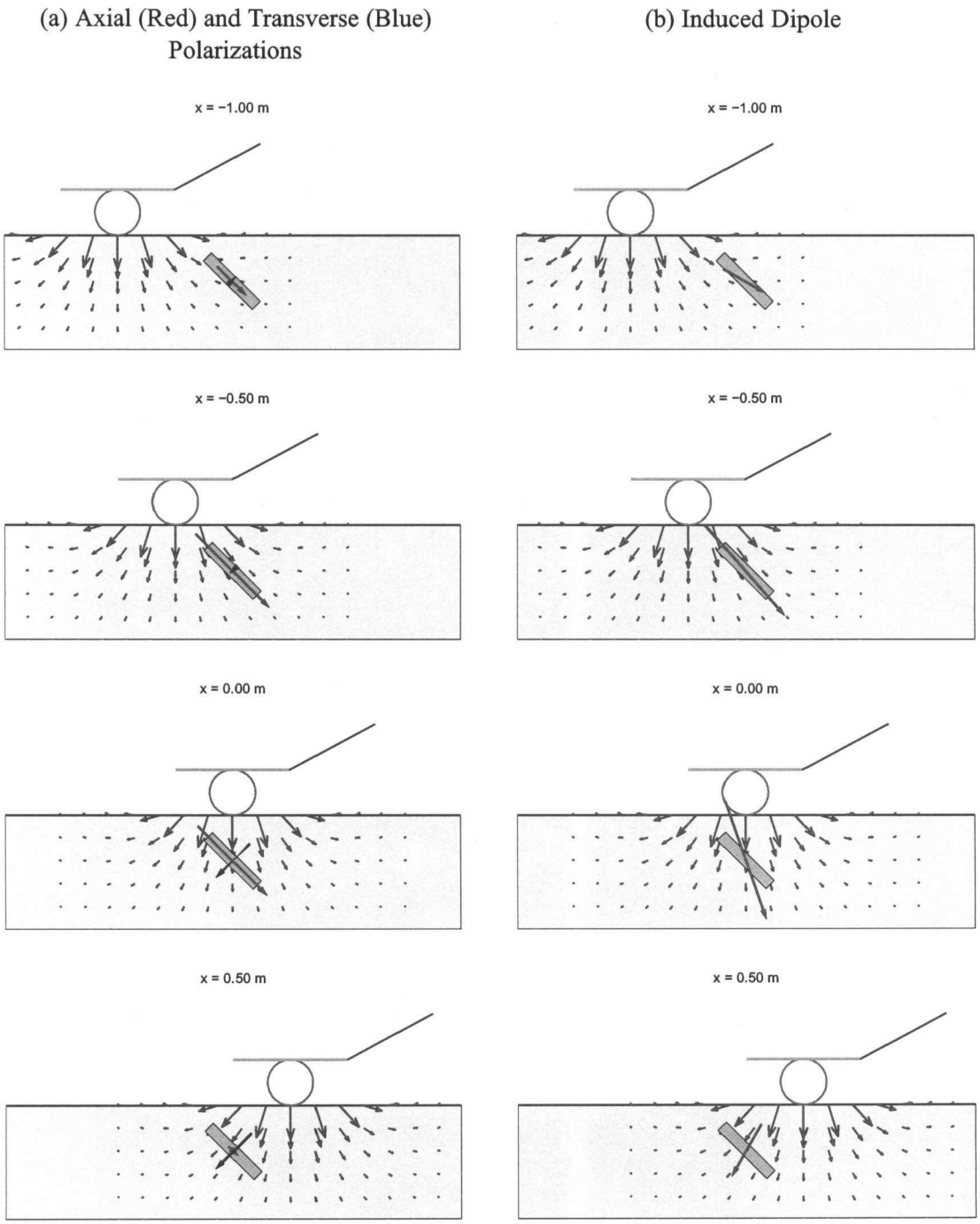

Figure 2.15: Excitation of a UXO oriented with a 45 degree dip. Relative contributions of the axial (red) and transverse (blue) polarizations are indicated in (a). The total induced dipole moment is plotted in (b).

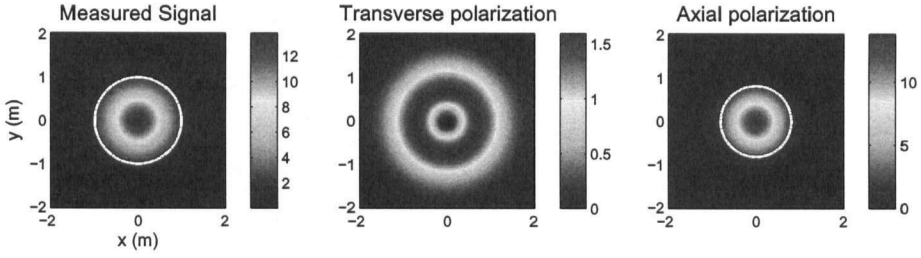

(a) Plan view of data at time channel 20 ($t = 0.18ms$).

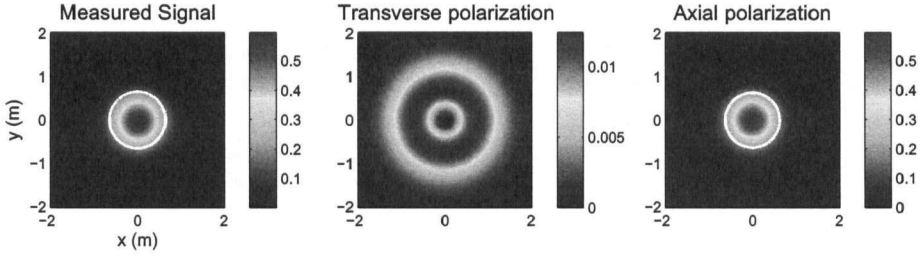

(b) Plan view of data at time channel 20 ($t = 7.1ms$).

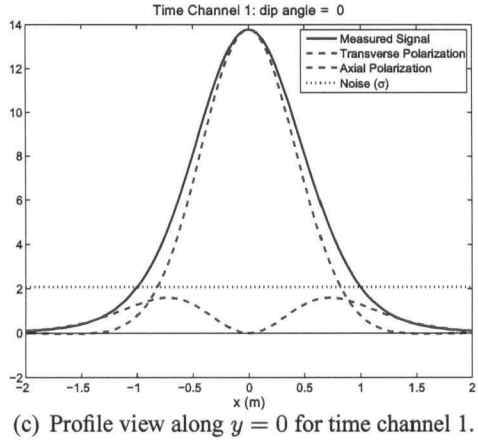

(c) Profile view along $y = 0$ for time channel 1.

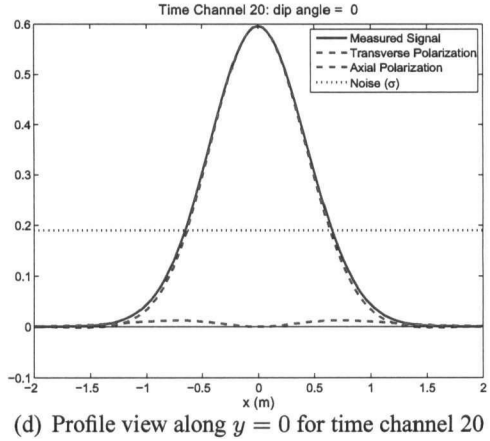

(d) Profile view along $y = 0$ for time channel 20

Figure 2.16: Synthetically generated EM63 data for a vertical 105 mm projectile at a depth of 1 m. The polarizations at the first time channel are $L_1(t = 0.18ms) = 134.3$ and $L_2(t = 0.18ms) = 78.1$ for the axial and transverse components, respectively. The white contour line in (a) represents the estimated standard deviation for noise, from a EM63 survey carried out at the Sky Research UXO Test Site.

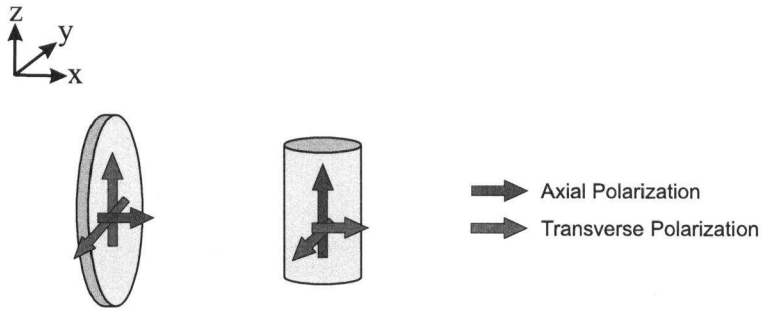

Figure 2.17: Plate and rod geometry for examples in Figures 2.18 to 2.19.

at the plate solution when minimizing noisy data from a rod (Pasion et al., 2004).

To explain why this local minimum might occur, let us consider the first time channel data from a 105 mm projectile ($L_1(t_1) = 134.3$ and $L_2(t_1) = 78.1$). Let us consider a plate-like target whose polarization parameters at the first time channel is the reverse of the 105 mm projectile, i.e., $L_1(t_1) = 78.1$ and $L_2(t_1) = 134.3$.

The response of the plate and rod oriented as illustrated in Figure 2.17 are compared in Figure 2.18. We consider the first time channel of data. The top panels of Figures 2.18(a) and (b) indicate that the response of the two different targets are very similar. A plot of the difference between the two responses is in Figure 2.19. The response of the rod or plate is identical directly above the target, since the primary field is vertical when the sensor is positioned directly above the target and $L_1^{rod} = L_2^{plate}$. Differences in the rod and plate response occur away from directly above the target when horizontal components of the primary field illuminate the target. The signal to noise decreases as the sensor moves away from the target, and at some distance from the target data from a rod will be indistinguishable from the data from a plate-like target.

Figure 2.20 compares the plate and rod response over data profiles at $y = 0$ and $x = 0$. Along a line $y = 0$ the response of the plate will be identical to the response of the rod. As symmetry suggests, the response of the rod along $x = 0$ is identical to the rod response along $y = 0$. The plate response along $x = 0$ is different, since there is no contribution from its axial component, since the axial component is perpendicular to the primary field along this line. The difference between the rod and plate response along this line is due to a dipole whose strength is proportional to $\left(\hat{\mathbf{y}} \cdot \mathbf{B}^P\right) L_2^{plate}$.

The above comparison of rod and plate responses is an example of how inadequate signal to

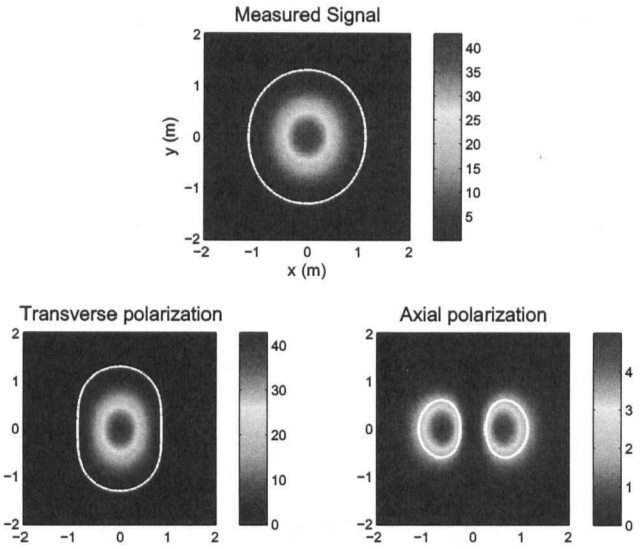

(a) A plate-like target ($L_1(t_1) = 78.1$ and $L_2(t_1) = 134.3$)

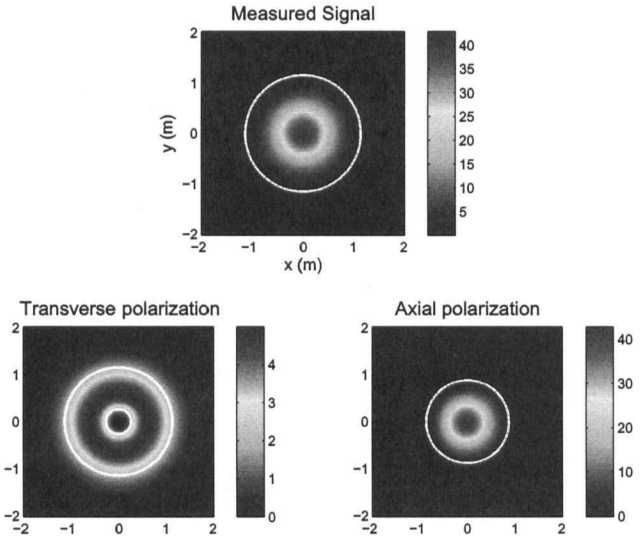

(b) ($L_1(t_1) = 134.3$ and $L_2(t_1) = 78.1$)

Figure 2.18: Comparison of the response for (a) a plate-like target whose normal is horizontal and (b) a vertical rod-like target. Since the primary field is predominantly vertical, the response of the plate-like target is mainly due to the polarization induced in the plane of the plate (i.e., the transverse polarization) and the response of the rod is mainly due to the polarization along the rod (i.e. axial polarization). The white contour line indicates the noise level of the EM63 at the first time channel.

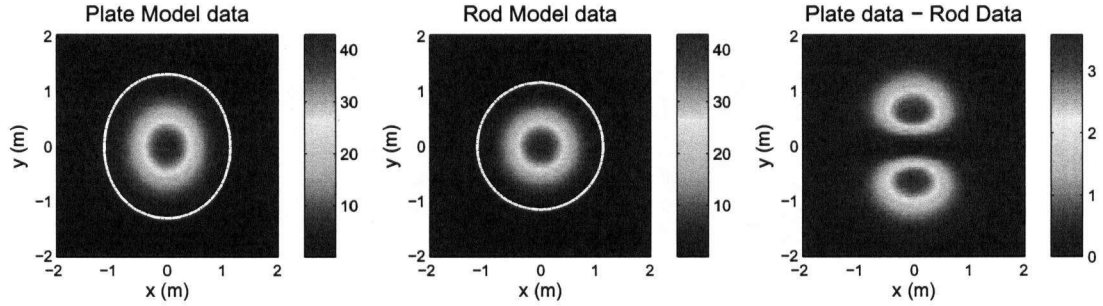

Figure 2.19: Comparison of the rod and plate data. The right panel shows that the difference between the plate and rod data is of the same order as the standard deviation of the EM63 noise ($\sigma = 2.07$ mV).

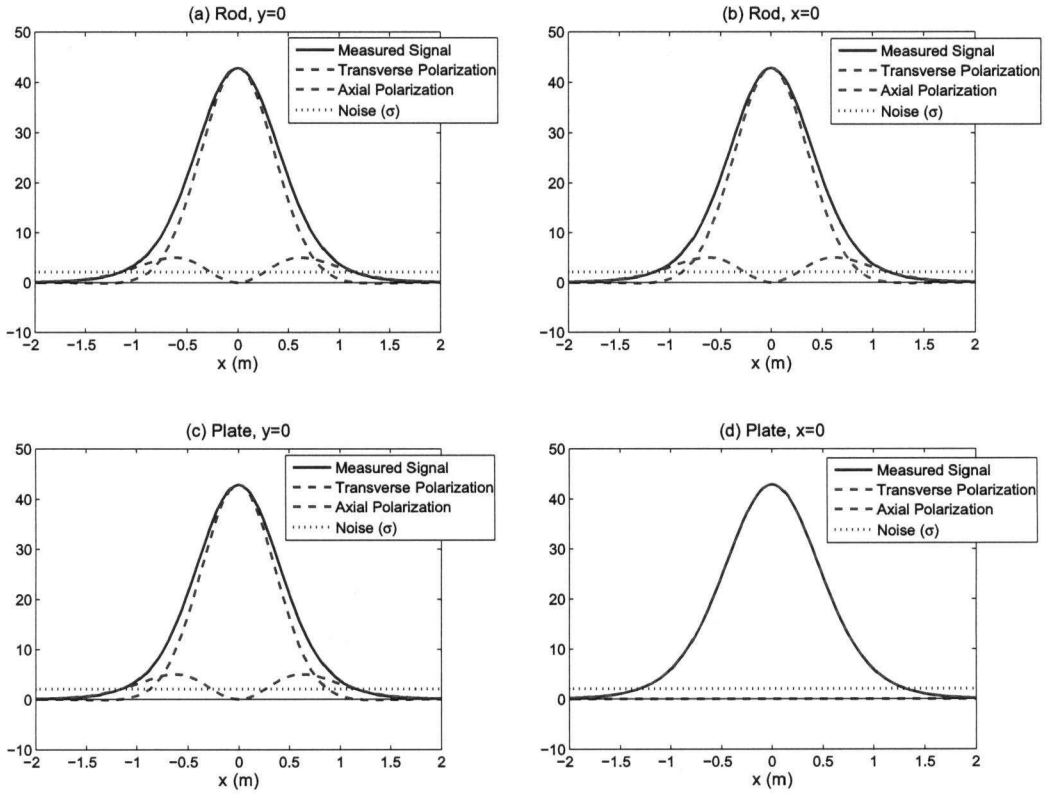

Figure 2.20: Profiles of the data in Figure 2.18. The data profile along $y = 0$ m over either the plate (panel (c)) or rod (panel (c)) is the same. The data profile along $x = 0$ m is wider over the plate (panels (b)) than the rod (panel (d)).

noise and spatial coverage of the data will lead to ambiguities in the measured data, and thus an inability to robustly recover model parameters through inversion.

2.4 Conclusion

Our general approach to the processing of EM data is to invert data for model parameters that are representative of the physical characteristics of the target. The parameters can subsequently be used as inputs to classification algorithms. A critical component of this process is the selection of the forward model. An ideal forward model is one that: (1) can accurately reproduce sensor data, (2) whose parameters are representative of the physical characteristics of the target, (3) is simple (i.e., has a minimum number of parameters) and (4) can compute the sensor data in a minimal amount of time.

In this chapter, we presented a dipole model for representing the secondary response of a compact metallic target. The development of the model originates from the analytic solutions of sphere responses, and is extended through an analogy with the magnetostatic dipole response of a spheroid. We showed that the dipole model is capable of accurately modelling data for sensor/target geometries typically found in UXO surveys. A parameterization for the temporal response of the dipole polarization elements was chosen such that the three decay stages of a sphere can be modelled. These parameters are representative of the physical characteristics, i.e., shape and material properties, of the target. The chapter concludes with an investigation into some of the ambiguities of the dipole parameters with certain target shape and orientation combinations.

Chapter 3

Inversion of Time Domain Electromagnetic Data

The previous chapter described an approximate forward modelling procedure for the time domain electromagnetic response of a compact, conductive (and possibly permeable), axi-symmetric target. We also showed that the values of the decay parameters are a function of the shape and size of the target. Therefore, accurate determination of the decay parameters by inverting the sensor data will produce a feature vector that can be used to aid discrimination.

The inverse problem is a two part procedure: parameter estimation and inference. Parameter estimation describes the procedure to determine appropriate model parameter vectors by combining prior information about the model vector and the ability of the model vector to predict the data collected in a TEM survey. Inference establishes the reliability of our recovered parameter estimates. This chapter begins by outlining the basic equations and techniques of both parameter estimation and inference. The chapter concludes with different examples of inverting for polarization tensor components from Geonics EM63 TEM sensor data.

3.1 Formulation of the Inverse Problem

3.1.1 Inversion Methodology

In this thesis, the Bayesian framework is used to formulate the inverse problem. The Bayesian framework was been previously described numerous times (for examples see Tarantola, 1987; Ulrych et al., 2001; Menke, 1989). Therefore a brief overview of the Bayesian framework is presented here. The solution to the inverse problem is the combination of the information known about the model parameters $\mathbf{m}$ prior to the experiment and the ability of our physical forward model F to reproduce the experimental data. The prior information is represented as the probability distribu-

tion $p(\mathbf{m})$. The ability of the model to reproduce the experimental data $\mathbf{d}_{obs}$ is described in the conditional probability density of the experimental data $p(\mathbf{d}_{obs}|\mathbf{m})$. The prior and the conditional probability density (also called the likelihood function) of the experimental data are combined via Bayes theorem to form the a posteriori conditional probability density $p(\mathbf{m}|\mathbf{d}_{obs})$ of the model:

$$p(\mathbf{m}|\mathbf{d}_{obs}) = \frac{p(\mathbf{m})\, p(\mathbf{d}_{obs}|\mathbf{m})}{p(\mathbf{d}_{obs})} \tag{3.1}$$

where $p(\mathbf{d}_{obs})$ is the marginal probability density of the experimental data. Equation (3.1) shows how the prior and the experiment data are combined, and therefore is a mathematical expression of the inversion philosophy. That is, if we can regard the prior $p(\mathbf{m})$ as the probability density assigned to $\mathbf{m}$ prior to experiment, then the a posteriori conditional probability density $p(\mathbf{m}|\mathbf{d}_{obs})$ is the probability density we ascribe to $\mathbf{m}$ after collecting the data. The a posteriori conditional probability density encapsulates all the information we have on the model parameters and the model that maximizes it is usually regarded as the solution to the inverse problem.

Characterizing Data Statistics

The likelihood function $p(\mathbf{d}_{obs}|\mathbf{m})$ gives an indication of the misfit between predicted and observed data, and therefore depends on both the measurement errors and modelling errors. For this work we will assume that the errors follow a Gaussian distribution:

$$p(\mathbf{d}_{obs}|\mathbf{m}) = \sqrt{\frac{(2\pi)^{-N}}{\det V_d}} \exp\left[-\frac{1}{2}\left(\mathbf{d}_{obs} - F[\mathbf{m}]\right)^T V_d^{-1}\left(\mathbf{d}_{obs} - F[\mathbf{m}]\right)\right] \tag{3.2}$$

where F is the forward modelling operator and V_d is the covariance matrix of the data errors. This assumption is motivated by the ease in which the resulting inverse problem can be formulated and by the central limit theorem's assertion that as the number of error sources approach infinity, the distribution of errors approaches the normal distribution (provided the the distribution of error sources have finite variance). We recognize that real field data have errors unaccounted for in the forward modelling operator (for example inaccurate sensor positioning, "spikes" in the data and sensor drift) that can lead to non-Gaussian error distributions. Incorrect characterization of the data statistics can bias the values of the recovered parameters and also invalidate the parameter variance analysis (Billings et al., 2003).

Representing the Prior Information

We can incorporate information about the model parameters through the specification of the prior $p(\mathbf{m})$. Discussed below are two variants which are important for our work.

Case I: Bounds on the parameters are known. Here we are provided with the maximum and minimum values that a parameter can achieve. Consider an individual parameter m_j. If the only a priori information we have of m_j are the lower and upper bounds m_j^L and m_j^U, then a probability density function that is uniform on the interval $\left[m_j^L, m_j^U\right]$ is used. The prior is then

$$p_b(m_j) = \begin{cases} const. & \text{if } m_j^L \leq m_j \leq m_j^U, \\ 0 & \text{otherwise.} \end{cases} \tag{3.3}$$

The joint probability for all of the parameters is

$$p(\mathbf{m}) = \prod_{j=1}^{n_p} p_b(m_j). \tag{3.4}$$

The posterior probability density function (pdf) is thus equal to zero outside the supplied bounds.

Case II: Prior pdf's are available For some parameters we may have more information. For instance, marginal pdf's can be obtained from the magnetics inversion. Billings et al. (2004) showed that location estimates from magnetics data were well approximated by a Gaussian distribution. For these parameters we characterize the functionals by the exponential

$$p_g(m_j) = c\exp\left(-f\left(m_j - \bar{m_j}\right)\right), \tag{3.5}$$

where the Gaussian prior of m_j is centered on a prior model $\bar{m_j}$ with a standard deviation σ_j, such that

$$f(m_j - m_j) = \frac{1}{2\sigma_j^2}\left(m_j - \bar{m_j}\right)^2.$$

The joint pdf is again obtained by multiplying the individual pdfs as in equation (3.4).

Summarizing the Posterior Information

The a posteriori conditional probability density defines the distribution of models posterior to the collection of the data. A distribution is commonly characterized by its moments. Therefore, the posterior mean model for the i^{th} parameter m_i is calculated by computing the first-order moment of the posterior

$$\langle m_i \rangle = \int_{\mathcal{M}} m_i \; p\left(\mathbf{m}|\mathbf{d}\right) d\mathbf{m}. \tag{3.6}$$

If the posterior is Gaussian or "bell shaped", then the mean would be equal to the maximum $p\left(\mathbf{m}|\mathbf{d}\right)$ model. The covariance matrix is the second-order moment of the estimate calculated about its mean:

$$[\mathbf{V_m}]_{ij} = \int_{\mathcal{M}} m_i m_j p\left(\mathbf{m} \mid \mathbf{d}\right) d\,\mathbf{m} - \langle m_i \rangle \langle m_j \rangle . \tag{3.7}$$

The diagonals of $\mathbf{V_m}$ are the posterior variances of the model parameters, and the off diagonal elements give information on the trade-off between model parameters. Of course, the concepts of mean and covariance matrix are most useful if $p\left(\mathbf{m}|\mathbf{d}\right)$ has a single peak. If there are multiple peaks in the a posteriori pdf then the marginal pdf is more useful property. The marginal distribution for a parameter is the pdf irrespective of the remaining parameters. The marginal distribution is calculated by

$$M\left(m_i\right) = \int \ldots \int p\left(\mathbf{m} \mid \mathbf{d}\right) \prod_{\substack{k=1 \\ k \neq i}}^{n_p} dm_k \tag{3.8}$$

where there are n_p parameters.

If we seek a single model, then it is natural to choose the model which is most likely to occur. We estimate a value of $\mathbf{m}$ that maximizes the log of the a posteriori conditional probability density

$$\mathbf{m}^* = \arg\max_{\mathbf{m}} \{\log\left(p\left(\mathbf{m}|\mathbf{d}_{obs}\right)\right)\}. \tag{3.9}$$

The solution to the inverse problem can then be cast as the optimization problem

$$\begin{aligned} &\text{minimize} \quad \phi\left(\mathbf{m}\right) = \sum_j \frac{1}{2\sigma_j^2}\left(m_j - \bar{m}_j\right)^2 + \frac{1}{2}\|V_d^{-1/2}\left(\mathbf{d}^{obs} - \mathcal{F}\left(\mathbf{m}\right)\right)\|^2 \\ &\text{subject to} \quad m_i^L \leq m_i \leq m_i^U \end{aligned} \tag{3.10}$$

where j represents the index of parameters whose Gaussian pdf's are known, and i represents model parameters which have upper and lower bounds. We note that if we have no prior information about the parameters, then the maximum likelihood solution is that which maximizes $p\left(\mathbf{d}_{obs}|\mathbf{m}\right)$, that is,

$$\text{minimize} \quad \phi\left(\mathbf{m}\right) = \frac{1}{2}\|V_d^{-1/2}\left(\mathbf{d}^{obs} - \mathcal{F}\left(\mathbf{m}\right)\right)\|^2. \tag{3.11}$$

3.2 Defining the Objective Function

Previously, I noted that the solution to the inverse problem could be cast as an optimization problem. If we assume only uniform priors, our problem is then to minimize a data misfit function subject to box constraints:

$$\phi\left(\mathbf{m}\right) = \frac{1}{2}\|V_d^{-1/2}\left(\mathbf{d}^{obs} - \mathcal{F}\left(\mathbf{m}\right)\right)\|^2 \quad \text{subject to} \quad m_i^L \leq m_i \leq m_i^U, \tag{3.12}$$

where i represents model parameters which have upper and lower bounds. Finding a model that minimizes equation (3.12) involves defining a data covariance V_d, the data vector $\mathbf{d}^{obs}$ and the forward model $\mathcal{F}\left(\mathbf{m}\right)$. In this section we define these different components of the objective function.

3.2.1 Defining the Data Covariance Matrix

The relation between a datum d_j and the model $\mathbf{m}$ can be expressed as

$$d_j = \mathcal{F}_j\left(\mathbf{m}\right) + e_j, \quad \text{where } j = 1, 2, 3, \ldots N, \tag{3.13}$$

where $\mathcal{F}_j$ is the forward mapping, e_j is the error on the j^{th} datum, and there are N data.

The source of data errors can generally be categorized as either modeling errors, natural, or cultural errors. Modeling errors include any discrepancy between the approximate forward mapping and an exact forward model. There are, essentially, two sources of modelling error. The first is any inaccuracy in the functional form of the forward mapping. When inverting for the dipole polarization, higher order multi-poles act as correlated noise that has the potential to bias the recovered parameters. The second source of modeling errors are due to uncertainties in the modeling parameters that are not included in the model vector $\mathbf{m}$. Uncertainties in sensor positioning and ori-

entation fall under this category. The data uncertainty resulting from these errors is approximately proportional to the signal strength.

The remaining error types are baseline errors. These are random errors that are present in sensor data even when the sensor is not in the presence of any conducting material. Efferso et al. (1999) examined the effect of AM and VLF transmitters on TEM measurements. They observed, for their particular TEM instrument, a standard deviation for the voltage signal that exhibited a $1/t$ proportionality when AM transmitter noise is log-gated and stacked. Munkholm and Auken (1996) showed that log-gated and stacked white noise maps onto the TEM response as errors with a standard deviation exhibiting a $1/\sqrt{t}$ decay.

Error estimates appear in the inverse problem through the data covariance matrix. For ease of notation we can rewrite the objective function as

$$\begin{aligned}\Phi(\mathbf{m}) &= \frac{1}{2}\|\mathbf{V_d}^{-1/2}\left(\mathbf{d}^{obs} - \mathcal{F}(\mathbf{m})\right)\|^2 \\ &= \frac{1}{2}\mathbf{R}(\mathbf{m})^T\mathbf{R}(\mathbf{m}) \\ &= \frac{1}{2}\sum_{i=1}^{N} r_i(\mathbf{m})^2\end{aligned} \tag{3.14}$$

where

$$\mathbf{R} = \mathbf{V_d}^{-1/2}\left(\mathbf{d}^{obs} - \mathcal{F}(\mathbf{m})\right) \tag{3.15}$$

is the residual vector and $r_i(\mathbf{m})$ is the i^{th} component of the function $\mathbf{R}$. The data covariance matrix $\mathbf{V_d}^{-1/2}$ adjusts the relative contribution of each r_i to the objective function, and therefore controls how closely each datum is fit by the predicted data. The data covariance matrix plays a very important and practical role in the minimization of the data misfit objective function as it provides us with a way to deal with the large dynamic range (typically several orders of magnitude) of TEM data. We assume independently distributed Gaussian errors, and use the following data covariance matrix:

$$\left[\mathbf{V_d}^{-1/2}\right]_{ij} = \begin{cases} 0 & \text{if } i \neq j, \\ \dfrac{1}{\delta_i + \epsilon_i} & \text{if } i = j \end{cases}, \tag{3.16}$$

where δ_i is a percentage of the i^{th} datum

$$\delta_i = \%\text{ error} \times \left[\mathbf{d}^{obs}\right]_i, \tag{3.17}$$

and ϵ_i is a base level error that is present in the i^{th} datum in the absence of a target.

Defining the percent error component δ_i

Simulations can show that Gaussian errors in the position and orientation can produce non-Gaussian, position dependent data errors. Figure 3.1 contains simulated data for the first time channel of the Geonics EM63 instrument acquired directly above a vertical 81 mm mortar at a depth of 30 cm. Directly above the target, the value of the first time channel of data is 529.86 mV. Figures 3.1(a) plots the histogram, and best fit Gaussian distribution, for voltages when there is a 2 cm error in the reported sensor height. The distribution is skewed due to the nonlinear spatial decay of the signal as a function of height above the target. The distributions for a sensor location error of 2 cm (Figure 3.1(b)) and orientation error of 2 degrees (Figure 3.1(c)) are one-sided due to the geometry of the problem. Above a vertical target, the maximum value occurs when the transmitter loop is horizontal, and directly above the target. When modelling data assuming the error from Figures 3.1(a), (b), and (c), we see that the most significant contributor to the error is the height. Figure 3.2 contains a result when repeating the simulations, but moving the observation to $(x, y, z) = (0.5, 0.5, 0.3)$ m. Away from the vertical anomaly, the sensor location (x, y) and orientation error have the same level of data uncertainty as the height.

The above example suggest that the uncertainty of the data is location and model dependent. When simulating data collected over a vertical 81 mm mortar at a depth of 30 cm, we found small position errors (2 cm standard deviation) and orientation errors (2 degree standard deviation in pitch, roll, and yaw) result in a nearly Gaussian error that is approximately 15 percent of the data value (Figure 3.3). The spatial variability of the percent error is not very significant. We note that there are situations when filtering of the position and orientation data can be applied to reduce the amount of data uncertainty. For example, if we know that the sensor motion is smooth, a simple low-pass filtering can be applied the position and orientation data.

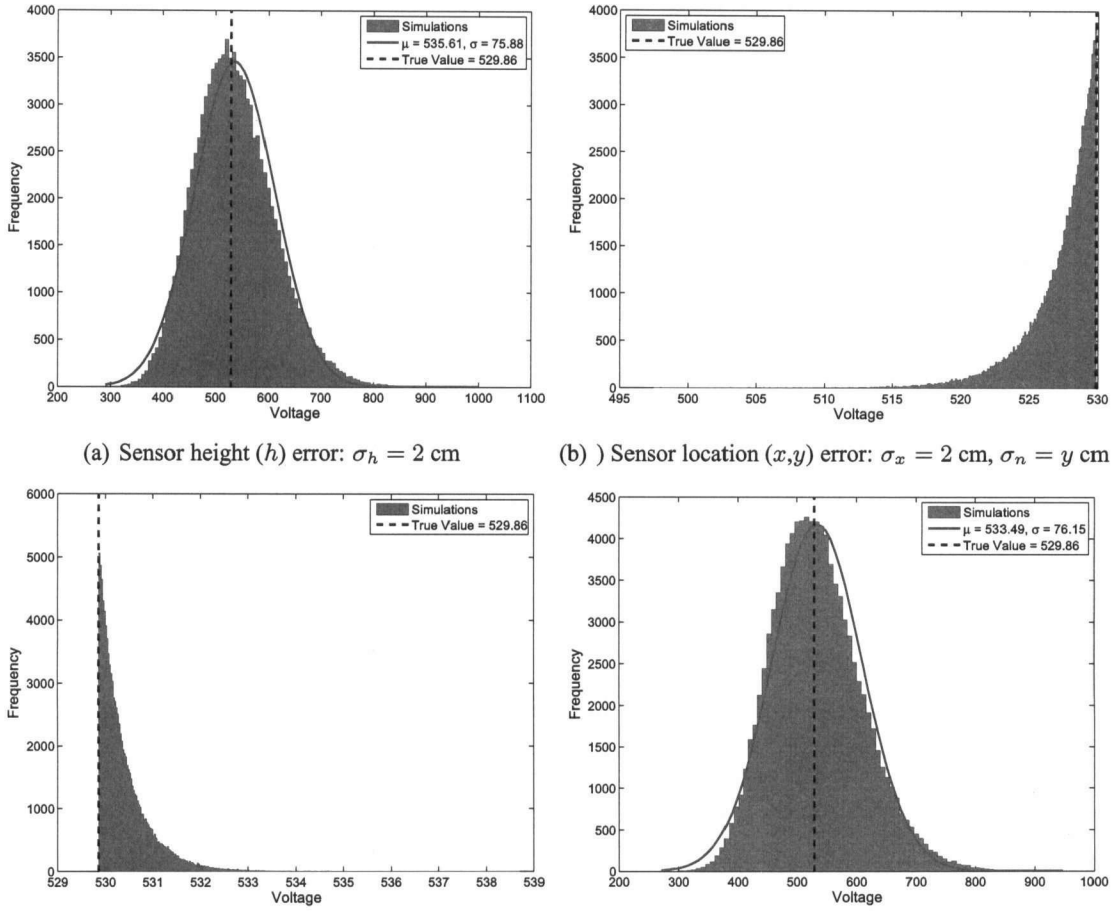

(a) Sensor height (h) error: $\sigma_h = 2$ cm

(b)) Sensor location (x,y) error: $\sigma_x = 2$ cm, $\sigma_n = y$ cm

(c) Sensor orientation error: $\sigma_{pitch} = \sigma_{roll} = \sigma_{azimuth} = 2$ degrees.

(d) All errors from (a),(b), and (c) combined

Figure 3.1: Error simulation results. Geonics EM63 first time channel data from a vertical 81 mm target is simulated. The sensor is positioned at (x,y,z) = (0,0,0.3) m, and the 81 mm mortar is located at (0,0,-0.3) m. When there are no errors in sensor positioning and orientation, the signal is 529.86 mV. Histograms (a) to (c) summarize contributions to the data spread from errors in the sensor height, location and orientation errors. Plot (d) shows the result when all errors are included. Directly over a target, the height variation contributes most to the signal errors.

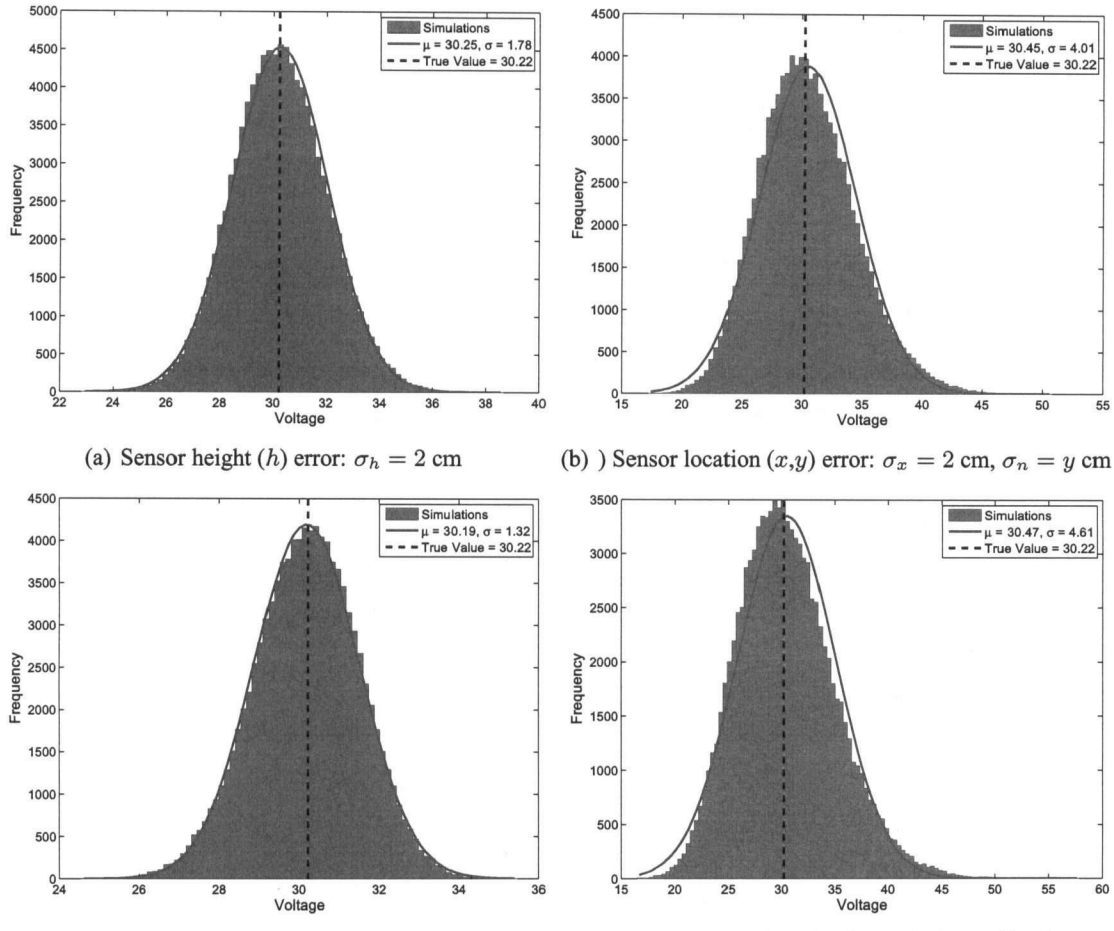

(a) Sensor height (h) error: $\sigma_h = 2$ cm

(b)) Sensor location (x,y) error: $\sigma_x = 2$ cm, $\sigma_n = y$ cm

(c) Sensor orientation error: $\sigma_{pitch} = \sigma_{roll} = \sigma_{azimuth} = 2$ degrees.

(d) All errors from (a),(b), and (c) combined

Figure 3.2: Error simulation results. Geonics EM63 first time channel data from a vertical 81 mm target is simulated. The sensor is positioned at (x,y,z) = (0.5,0.5,0.3) m, and the 81 mm mortar is located at (0,0,-0.3) m. When there are no errors in sensor positioning and orientation, the 30.22 mV. Panels (a) to (c) summarize contributions to the data spread from errors in the sensor height, location and orientation errors. Plot (d) shows the result when all errors are included. The errors are nearly normal.

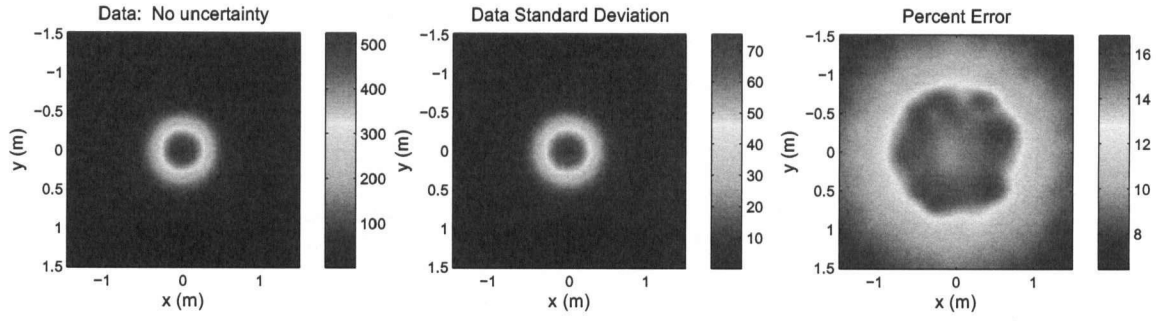

(a) Percent error over a vertical 81 mm mortar.

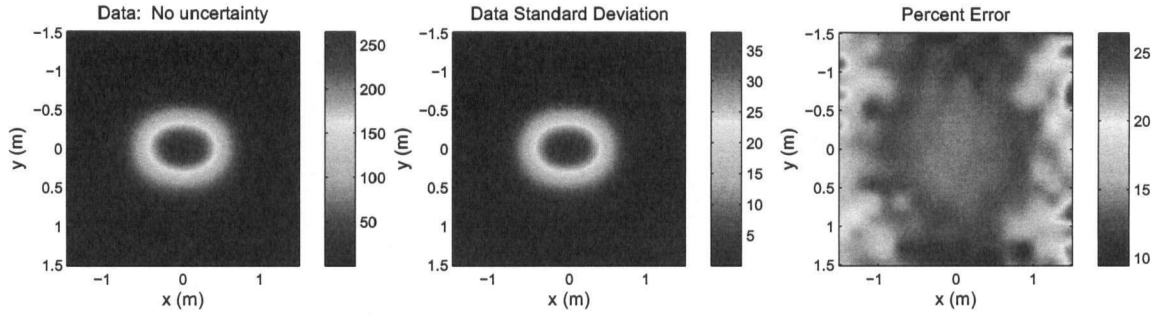

(b) Percent error over a horizontal 81 mm mortar.

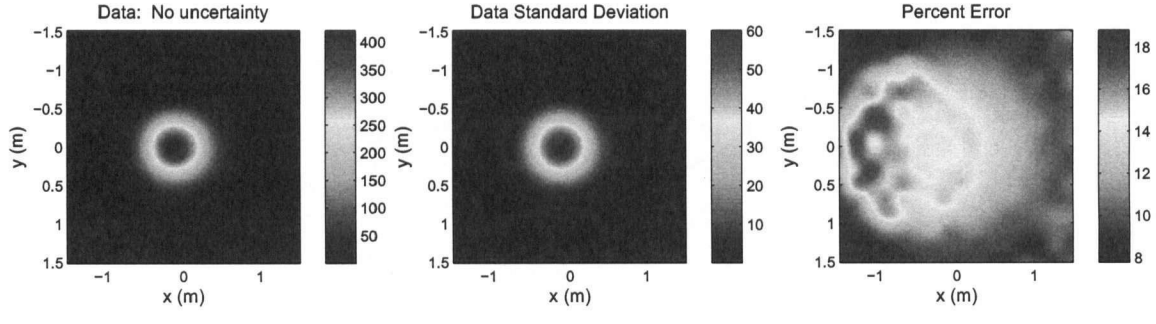

(c) Percent error over a 81 mm mortar with a 45 degree dip.

Figure 3.3: Spatial dependence of percent error over 81 mm mortar buried at a depth of 30 cm. Sensor height and location uncertainties are Gaussian with a standard deviation of 2 cm. Sensor orientation have Gaussian Errors of 2 degrees. This example shows that the error introduced through position and orientation uncertainty is dependent on the relative position of the sensor and target.

Defining the baseline error component ϵ_i

One strategy for determining the base line error is to select a section of data within a grid that has no targets, and calculate the data statistics for each time channel within that grid. A single value represents the baseline error for the entire grid . Figure 3.4 shows a calculated noise floor for Former Lowry Bombing and Gunnery Range (FLBGR) Grid 1914 and the theoretical $1/\sqrt{t}$ decay due to Gaussian input noise. The estimated noise floor (black line in Figure 3.4) was obtained by

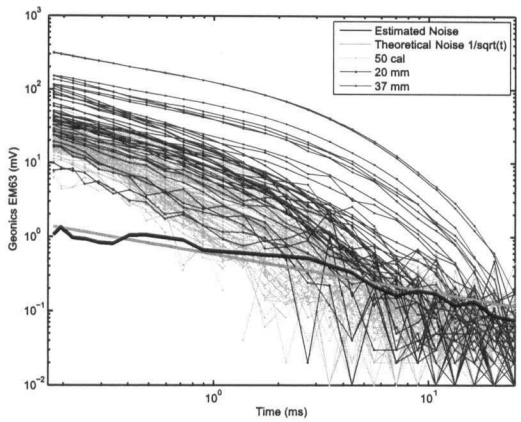

Figure 3.4: Calculated and theoretical noise floor for Geonics EM63 data collected on Grid 1914. Data over validated 50 calibre bullets, and 20 mm and 37 mm projectiles are also plotted.

selecting soundings where no targets are present, and fitting a Gaussian model for each of the 26 time channels. A $1/t$ function was fit to the estimated noise to obtain the green line in Figure 3.4.

We have found that noise characteristics often change with survey event. For example, Figure 3.5 plots the fifth time channel of data for FLBGR Grid 2114. The northerly portion of Grid 2114, from approximately 88 to 105 m, is less noisy than the southerly portion of the data. Also, a geologic artifact runs diagonally to the southeast corner to the grid. Figure 3.6 demonstrates how the noise estimate will change as a function of where the data is sampled. At the time of writing this chapter, our research group had already developed and implemented into the software package UXOLab a method of estimating a spatially varying background noise.

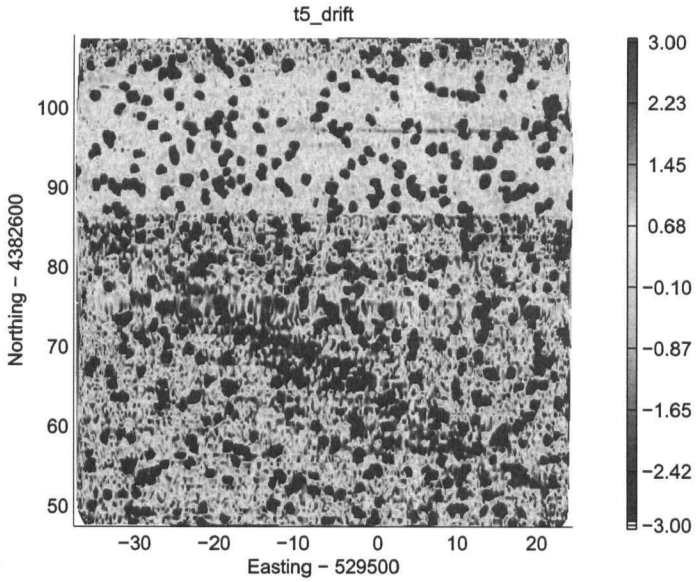

Figure 3.5: Gridded image of time channel 5 of Geonics EM63 data collected on the 2114 Grid.

3.2.2 Forming the Data Vector $\mathbf{d}^{obs}$

Anomalies are inverted for parameters of an approximate forward model that approximates the response of a single target in free space. Sensor drift, background geology, and nearby targets are non-random errors in the data that bias the estimated polarization parameters. Detrending the data and masking the individual anomalies help to reduce these effects.

Detrending Data

It is common practice to apply a low pass filter to data to reduce instrument drift, dc offsets, and geologic responses from the data. We study the effectiveness of filtering the background response in Chapter 8. Median filters are commonly applied along lines of data. Figure 3.7 contains EM61 Mark 2 data acquired on FLBGR Grid K15. The data were filtered using an approximately 20 m window. In this case the window was too large to reject the geologic feature that looks like an upside-down horseshoe. Once the geologic feature was observed, the data were reinverted using a 7 m long filter which was more effective.

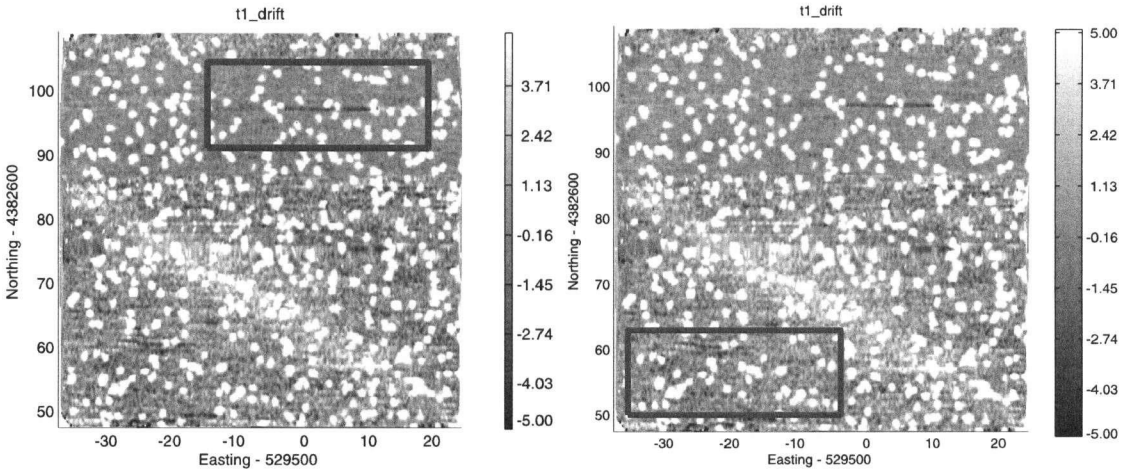

(a) Mask of less noisy area of grid 2114

(b) Mask of noisier area of grid 2114

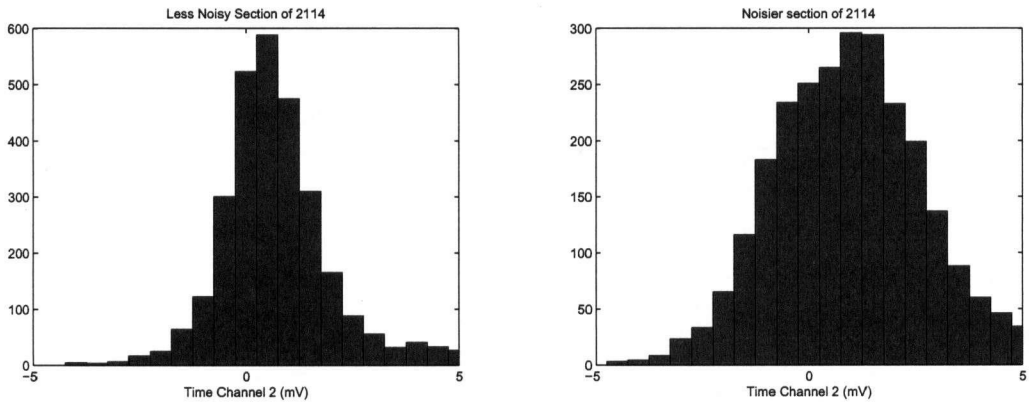

(c) Time channel 2 data histogram for masked area in (a)

(d) Time channel 2 data histogram for masked area in (b)

Figure 3.6: Comparison of Geonics EM63 data noise in two areas of Grid 2114 at FLBGR. Data from the first time channel are displayed. Masks indicating less noisy and more noisy areas of the grid are shown as red rectangles in (a) and (b), respectively. Although these masked areas include targets, it is clear that the width of the noisy distribution is higher in the (d).

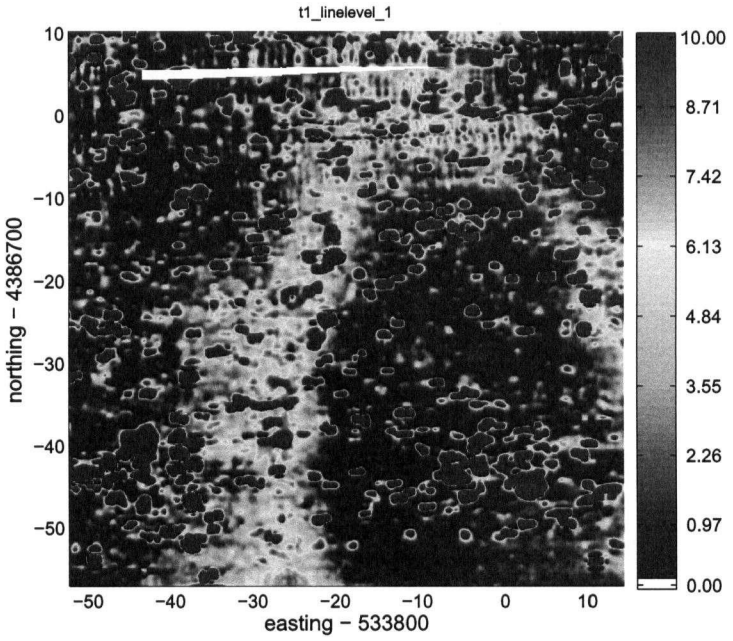

Figure 3.7: Filtered EM61 Sky Array data acquired over Grid K15. A median filter with a 20 m filtering window was unable to remove the geologic anomaly.

Defining the Data to be Inverted 1: Spatial coverage Once data anomalies are to be inverted, a mask is defined that represents the spatial limits of the data to be inverted. The masking procedure helps ensure that signal from adjacent anomalies does not affect inversion results. In addition, from a practical standpoint, inverting the minimum number of data reduces the computational time.

When processing data from the FLBGR, we defined a default circular mask with 2 m radius and centered on the selected target location (for example, Figure 3.8(a) anomaly 72). An automated correction to remove overlaps is then performed (for example, Figure 3.8(a) anomaly 159 and 66). The anomaly mask must be manually redrawn in cases where the automated mask contains signal energy from an adjacent target. As an example, consider anomaly 257 in Figure 3.8(b). To the NE of the target, there is a smaller anomaly that is not included in the inversion target list. Therefore, the mask overlap removal does not exclude the small anomaly. As a result, the data processor manually redrew that mask to exclude the small anomaly. Re-drawing masks represents a significant amount of the effort during the quality control process.

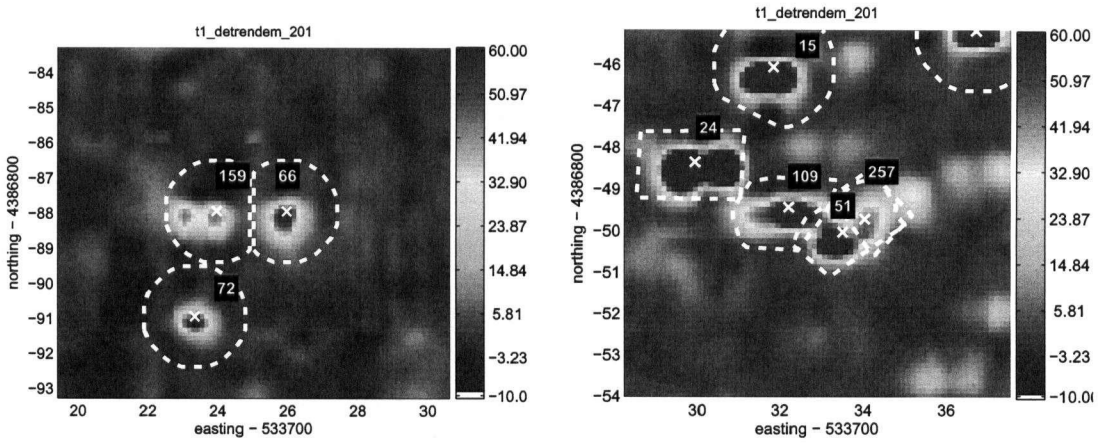

(a) Default masking for well separated targets.

(b) Manually defined masks for closely spaced targets

Figure 3.8: Examples of data masking applied to anomalies from grid L14. Data were collected using the Sky Research Inc. Geonics EM61 array.

Defining the Data to be Inverted 2: Time Channels Figure 3.4 compares anomalies from 50 calibre bullets, 20 mm, and 37 mm targets to the base-level noise of the survey. For these targets it is clear that at later times the signal from the target will sit within the base level noise of the instrument. Inverting these late time channels is of little help in constraining the dipole parameters. We generally set a minimum signal to noise ratio for a time channel to be included in the inversion.

3.2.3 Defining the Forward Model $\mathcal{F}[\mathrm{m}]$

Determining if a double-peaked anomaly should be inverted as a single target or a pair of targets Visual examination of spatial anomaly pattern can be misleading for determining the number of objects. A horizontal target with a dominant axial polarization (as is the case with rod-like UXO) can lead to an anomaly with a pair of peaks. The peak separation is a function of the target depth and transmitter loop size. When processing anomalies, we are faced with deciding if the anomaly is best fit with a single target, or with a pair of targets. For the case of a pair of targets we segmented the anomaly into two separate anomalies, and inverted each masked portion of the anomaly with a single dipole model.

A visual comparison of the two results determined which model should be used. Figure 3.9 demonstrates this process using anomalies 257 and 51 from Figure 3.8(b). After inverting 51 and 257 individually, the anomaly was inverted as a single target. For this anomaly, it was decided that

a single target was the best interpretation. Although, the misfit and correlation coefficient helped to make this decision, the data processor largely makes the decision through experience of looking at many different anomalies.

Determining if a single target should be inverted for 2 or 3 unique polarizations A 3 x 3 magnetic polarizability tensor characterizes the induced dipole of a metal target. In the principal reference frame, it has three orthogonal polarizations and degenerates to two polarizations for a rationally symmetric or body-of-revolution (BOR) target that is widely assumed in EMI processing. A target that can be characterized by 3 unique polarization tensor components does not have a symmetry axis, and is not likely intact UXO. In Section 3.6 we demonstrate how inversion of a low signal-to-noise ratio anomaly from an axi-symmetric target can result in two transverse components that are not equal. Obviously, this result is undesirable as three distinct polarizations are an indicator of non-UXO targets.

Determining the parameterization for the polarization decay There are a number of different techniques for parameterization of the temporal behavior of the polarization tensor. One common approach is to solve for the polarization value at each time channel. Other approaches involve parameterizing each polarization, such that the information contained in each polarization can be summarized by only a few parameters (instead of measuring the polarization at each of the 26 time channels of the EM63, the polarization is summarized by 3 or 4 parameters). These parameterizations are generally inspired by the different decay regimes observed in compact targets. At very early times, the decay of the voltage will follow a $t^{-1/2}$ decay, followed by a steeper power law decay ($t^{-3/2}$ for a sphere). At the late stage of the response decays exponentially. Depending on the locations of the TEM sensor time gates and the noise levels of the data, the early and late time stages may not be seen in sensor data, and therefore model parameters describing these features will be poorly constrained upon inversion.

3.3 Estimating Dipole Parameters Using a Local Search Algorithm

Production-setting UXO data processing often requires investigating several thousands of anomalies at a single site. The full characterization of the probability distribution for models and the evaluation

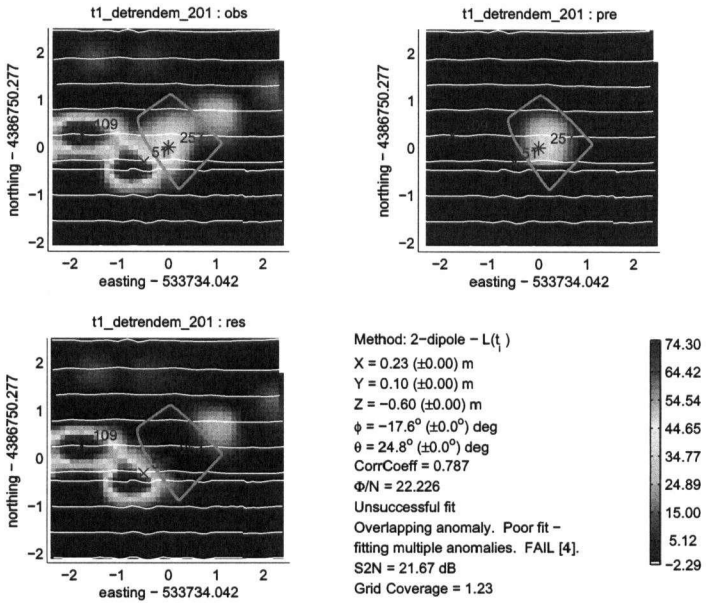

(a) Default inversion of Anomaly 257.

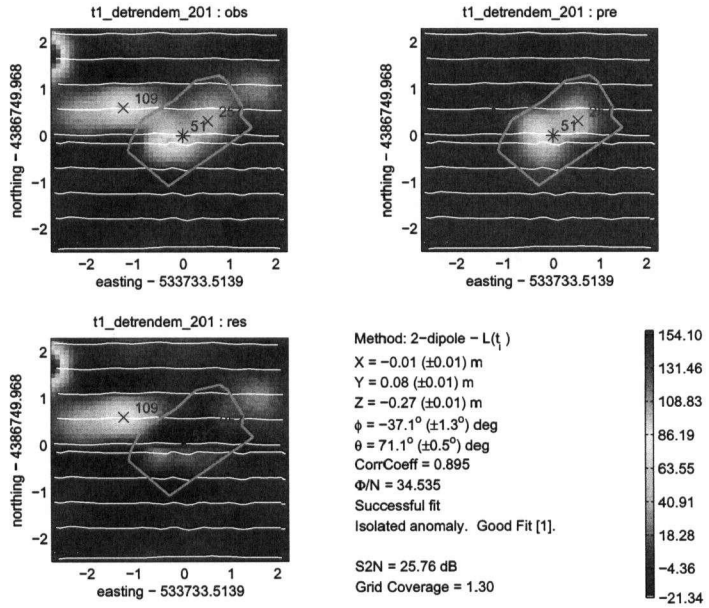

(b) Inversion of Anomaly 51 when 257 is included

Figure 3.9: An example of determining if an anomaly should be inverted as two separate targets. Anomalies 51 and 257 were initially inverted as two separate targets. (a) shows the result when inverting 257. (b) shows the result when the two anomalies are inverted as a single target.

of the Bayesian integrals for the mean, covariance and marginals (i.e., equations 3.6 to 3.8) requires sampling many points in model space and numerous forward-model evaluations. The global methods required for this task are instructive for understanding the structure of the inverse problem and does not have problems with local minima. However, computation time required for the numerous forward model evaluations does not make global methods feasible for processing the numerous anomalies to be investigated in a production setting. Therefore, we use local methods to calculate the maximum a posteriori estimate $\mathbf{m}_*$, via equation (3.9). In this thesis, we consider uniform priors such that the inverse problem is to determine $\mathbf{m}_*$ by minimizing a data misfit objective function where model parameters are subject to box constraints.

Pasion (1999) used a Newton's method code to solve an unconstrained minimization problem for determining dipole parameters. The basic Newton method formulation involves making an initial guess of the model parameters, then repeatedly improving on this guess until the data predicted by our guess matches as closely as possible to the actual observed data. The basic steps of an unconstrained minimization algorithm are:

1. **Choose a starting model** $\mathbf{m}_o$

2. **Compute a search direction** $\delta\mathbf{m}$. The search direction indicates the direction in which to perturb the current guess. The search direction is chosen to be the Newton step that minimizes the local quadratic model about the current iterate $\mathbf{m}_k$.

3. **Compute a step length** λ. The step length indicates how much the current guess should be perturbed in order to decrease the objective function. Because the local quadratic model about the current iterate is only approximate, the minimum of the model will not necessarily reduce the actual objective function. A positive scalar λ is chosen such that $\phi(\mathbf{m}_k + \lambda\delta\mathbf{m}) < \phi(\mathbf{m}_k)$. The step length λ is found by a line search.

4. **Update estimate of model**. Set $\mathbf{m}_{k+1} = \mathbf{m}_k + \lambda\delta\mathbf{m}$.

5. **Test for convergence**. If the updated guess $\mathbf{m}_{k+1}$ is adequate, then the algorithm is terminated. Otherwise, return to step 2.

Typical stopping criteria include the gradient of the objective function being zero and the algorithm having "stalled" i.e., successive iterations produce only small relative changes in the model. Prac-

tical convergence criteria for numerical optimization are well established (for example, Dennis and Schnabel, 1983).

The effectiveness of local search algorithms improves when the model parameters are well scaled (for example, see Dennis and Schnabel, 1983; Gill et al., 1981). The goal of scaling is to ensure that each parameter is of equal importance during the optimization. The dipole model parameters can vary by several orders of magnitude, and thus scaling can be an important part of the optimization problem. We use a diagonal matrix $\mathbf{W_m}$ to linearly transform the model parameters. The values of the diagonal are chosen to be the inverse of a vector of typical values, i.e.

$$[\mathbf{W_m}]_{ii} = \frac{1}{m_i^{typ}}, \tag{3.18}$$

where m_i^{typ} are typical values of the model vector $\mathbf{m}$. A new model vector $\tilde{\mathbf{m}} = \mathbf{W_m m}$ is defined. If the typical values of the model (m_i^{typ}) are chosen carefully, the elements of the transformed model vector $\tilde{\mathbf{m}}$ will, approximately, be of the same order.

In this thesis we will be enforcing constraints on the parameters. Therefore, for the examples in this thesis, we use the function Matlab functions `lsqnonlin` and `fmincon` (Mathworks, 2002). The function `lsqnonlin` is an implementation of the interior-reflective Newton method described in Coleman and Li (1994, 1996), and can be used to solve box-constrained least squares minimization.

The function `fmincon` is used in cases where linear constraints are applied to the model. The function `fmincon` solves the following problem

$$\text{minimize} \quad \phi(\mathbf{m}) \tag{3.19}$$

$$\text{subject to} \quad c_{eq}(\mathbf{m}) = 0 \tag{3.20}$$

$$c(\mathbf{m}) \leq 0 \tag{3.21}$$

$$\mathbf{A}_{eq}\mathbf{m} = \mathbf{b} \tag{3.22}$$

$$\mathbf{A}\mathbf{m} \leq \mathbf{b} \tag{3.23}$$

$$m_i^L \leq m_i \leq m_i^U, \tag{3.24}$$

where (3.20) and (3.21) apply non-linear inequality and equality constraints, respectively. Linear equality constraints are defined by (3.22). Non-linear constraints and linear equality constraints are not used in this thesis. Linear inequality constraints are included by defining the matrix $\mathbf{A}$ and vector $\mathbf{b}$ in (3.23).

We use linear constraints in a number of ways. When inverting for the instantaneous amplitude model (Equation (2.30)) we use a linear constraint to ensure that the polarization is monotonically decreasing. To demonstrate how this requirement is implemented, consider the two-polarization instantaneous amplitude model. If the axial and transverse polarization curves $L_1(t)$ and $L_2(t)$ are defined at three times ($t = t_1$, t_2, and t_3), the model vector is

$$\mathbf{m} = [X, Y, Z, \theta, \phi, L_1(t_1), L_1(t_2), L_1(t_3), L_2(t_1), L_2(t_2), L_2(t_3)]. \tag{3.25}$$

Monotonically decreasing estimated polarizations (i.e., $L_1(t_1) > L_1(t_2) > L_1(t_3)$ and $L_2(t_1) > L_2(t_2) > L_2(t_3)$) are enforced by using (3.23) with

$$\mathbf{A} = \begin{bmatrix} 0 & 0 & 0 & 0 & 0 & -1 & 1 & 0 & 0 & 0 & 0 \\ 0 & 0 & 0 & 0 & 0 & 0 & -1 & 1 & 0 & 0 & 0 \\ 0 & 0 & 0 & 0 & 0 & 0 & 0 & 0 & -1 & 1 & 0 \\ 0 & 0 & 0 & 0 & 0 & 0 & 0 & 0 & 0 & -1 & 1 \end{bmatrix} \tag{3.26}$$

and $\mathbf{b}$ is an eleven element column vector of zeros.

Linear constraints are also used when we want to determine the best rod-like model that fits the data. In cases where the data quality is very low, this strategy may be of interest. Pasion et al. (2004) showed that when inverting a two-polarization model (Equation 2.27) there is local minimum resulting in anomalies from rod-like targets being fit by plate-like target that are rotated by 90 degrees. Therefore, for the two-polarization inversions, we sometimes bias inversion results towards an axi-symmetric rod-like target by inverting for a model where the axial polarization is larger than the transverse polarization (i.e., $L_1(t_1) > L_2(t_1)$, $L_1(t_2) > L_2(t_2)$, and $L_1(t_3) > L_2(t_3)$). The

appropriate constraint is then

$$\mathbf{A} = \begin{bmatrix} 0 & 0 & 0 & 0 & 0 & -1 & 0 & 0 & 1 & 0 & 0 \\ 0 & 0 & 0 & 0 & 0 & 0 & -1 & 0 & 0 & 1 & 0 \\ 0 & 0 & 0 & 0 & 0 & 0 & 0 & -1 & 0 & 0 & 1 \end{bmatrix} \tag{3.27}$$

with b again an eleven element column vector of zeros. If box constraints are the only constraints required, the function `lsqnonlin`, rather than `fmincon`, is used to solve the least-squares problem. The function `lsqnonlin` is preferred because it is designed specifically for the least-squares problem, and therefore can take advantage of the specific structure of the least-squares objective function (see Dennis and Schnabel, 1983, Chapter 10 for a discussion of the least-squares objective function structure).

Local optimization algorithms do not guarantee convergence to a global minimum. With local optimization algorithms at best we can hope that our model will lie close to the model that globally minimizes our objective function. We recognize that, with a poor choice of starting parameters, the algorithm might get trapped in a local minimum. We address the problem of local minima by choosing multiple starting models. We define a number of depths and orientations. For each combination of depth and orientation, we perform a linear inverse problem to calculate the polarization tensor at the first time channel by fixing the depth and orientation. Some number of combinations of orientation and depth with the smallest misfits are then chosen for inversion. We then select from all of the solutions, the one which has the smallest value of $\Phi(\mathbf{m})$.

3.4 Analysis for Interpreting Local Search Parameter Estimates

Once the model parameters $\mathbf{m}_*$ which minimizes the objective function $\Phi(\mathbf{m})$ have been obtained, we must still examine the reliability and precision of the estimated parameters. Measurements are random and data are noisy. Thus it is not sufficient to obtain a set of model parameter estimates $\mathbf{m}_*$ and claim that these parameters are the best estimates of the unknown parameters $\mathbf{m}_+$. The parameters that may best describe one measurement may indeed be different than the parameters obtained from a second measurement on the same sample UXO.

3.4.1 Parameter variance for the unconstrained case

For an unconstrained problem, the gradient of the objective function is zero at a minimum, i.e.,

$$\nabla\Phi\left(\mathbf{m}_*, \mathbf{d}^*_{obs}\right) = 0. \tag{3.28}$$

The objective function $\Phi(\mathbf{m})$ is written as $\Phi\left(\mathbf{m}_*, \mathbf{d}^*_{obs}\right)$ to explicitly state the dependence of the objective function on the observed data. If the observed data were slightly perturbed, the location of the minimum would also be slightly perturbed. The gradient at this shifted minimum would then be zero:

$$\nabla\Phi\left(\mathbf{m}_* + \delta\mathbf{m}_*, \mathbf{d}^*_{obs} + \delta\mathbf{d}^*_{obs}\right) = 0. \tag{3.29}$$

The gradient can then be expanded as a Taylor Series about the solution such that

$$\begin{aligned}\nabla\Phi\left(\mathbf{m}_* + \delta\mathbf{m}_*, \mathbf{d}^*_{obs} + \delta\mathbf{d}^*_{obs}\right) = \nabla\Phi\left(\mathbf{m}_*, \mathbf{d}^*_{obs}\right) + \\ \nabla^2\Phi\left(\mathbf{m}_*, \mathbf{d}^*_{obs}\right)\delta\mathbf{m}_* + \left[\frac{\partial}{\partial\mathbf{d}_{obs}}\nabla\Phi\left(\mathbf{m}_*, \mathbf{d}^*_{obs}\right)\right]\delta\mathbf{d}_{obs} + H.O.T.\end{aligned} \tag{3.30}$$

where $H.O.T.$ represent the higher-order terms. When the objective function $\Phi(\mathbf{m})$ is the sum of squares, the gradient of $\Phi(\mathbf{m})$ is

$$\nabla\Phi\left(\mathbf{m}_*\right) \approx \mathbf{J}^T\left(\mathcal{F}\left[\mathbf{m}\right] - \mathbf{d}_{obs}\right), \tag{3.31}$$

where the Jacobian $\mathbf{J}$ is defined as

$$\mathbf{J}_{ij}\left(\mathbf{m}\right) = \frac{\partial r_i}{\partial \mathbf{m}_j}, \tag{3.32}$$

and $i = 1, \ldots, N$ indexes the data, and $j = 1, \ldots, M$ indexes the model parameters. The variable r_i was introduced in equation 3.14. Therefore the derivative of $\nabla\Phi$ with respect to $\mathbf{d}_{obs}$ is simply the Jacobian matrix $\mathbf{J}^{*T}$. Using equation 3.29 in equation 3.30 and retaining only first-order terms, we get

$$\delta\mathbf{m}_* \approx \mathbf{H}^{*-1}\mathbf{J}^{*T}\delta\mathbf{d}_{obs} \tag{3.33}$$

where $\mathbf{H}^*$ is the Hessian matrix evaluated at the minimum of Φ (i.e., $\mathbf{H}^* = \nabla^2\Phi\left(\mathbf{m}_*\right)$).

The model covariance matrix $\mathbf{V_m}$ is defined as the expected value of $\delta\mathbf{m}^*\delta\mathbf{m}^{*T}$

$$\mathbf{V_m} \equiv E\left(\delta\mathbf{m}^*\delta\mathbf{m}^{*T}\right). \tag{3.34}$$

Substitution of equation 3.33 gives

$$\mathbf{V_m} \equiv E\left(\mathbf{H}^{*-1}\mathbf{J}^{*T}\delta\mathbf{d}_{obs}\delta\mathbf{d}_{obs}^T\mathbf{J}^*\mathbf{H}^{*-1}\right) \tag{3.35}$$

The Hessian and Jacobian in the above expressions are evaluated at $\mathbf{m} = \mathbf{m}_*$, and are therefore constants. As a result they can be taken outside of the expectation value expression, and

$$\mathbf{V_m} = \mathbf{H}^{*-1}\mathbf{J}^{*T}\mathbf{V_d}\mathbf{J}^*\mathbf{H}^{*-1}, \tag{3.36}$$

where

$$\mathbf{V_d} = E\left(\delta\mathbf{d}_{obs}\delta\mathbf{d}_{obs}^T\right) \tag{3.37}$$

is the covariance matrix of the data. In the case when the observations all have normally distributed and uncorrelated errors, the data covariance matrix reduces to a diagonal matrix.

3.4.2 Calculating the Parameter Covariance Matrix when there are constrained parameters

Upper and lower constraints are often applied when inverting certain parameters. These "box" constraints represent minimum and maximum extents of a uniform a priori distribution of the parameters. When a parameter equals a constraint (i.e., the constraint is active), its variance is not estimated. The variances of the remaining parameters are calculated in a manner similar to the previous section, with Lagrange multipliers being introduced to account for the constrained parameters.

Let the vector $\mathbf{g}(\mathbf{m})$ represent all the equality constraints, including those inequality constraints active at the final model. The Lagrangian is given by

$$\mathcal{L}(\mathbf{m}, \lambda) = \Phi(\mathbf{m}) - \sum_i \lambda_i g_i(\mathbf{m}), \tag{3.38}$$

where $\lambda = [\lambda_1, ..., \lambda_k]^T$ is the vector of Lagrange coefficients. Setting the gradient of the Lagrangian to zero gives

$$\nabla\Phi(\mathbf{m}) = \nabla g(\mathbf{m}) \cdot \lambda. \tag{3.39}$$

This equation must be satisfied at $\mathbf{m} = \mathbf{m}^*$. By carrying out the sensitivity analysis demonstrated in the unconstrained case, it is straightforward to show that the covariance matrix for the constrained optimization problem is

$$\mathbf{V}_m = \mathbf{P}\,\mathbf{A}^{-1}\,\mathbf{J}^T\,\mathbf{V}_d\,\mathbf{J}\,\mathbf{A}^{-1}\,\mathbf{P}^T, \tag{3.40}$$

where

$$\mathbf{A} \equiv \mathbf{H}^* - \sum_i \lambda_i \frac{\partial^2 g_i}{\partial \mathbf{m} \partial \mathbf{m}}, \tag{3.41}$$

and

$$\mathbf{P} = \mathbf{I} - \mathbf{A}^{-1}\left(\frac{\partial \mathbf{g}}{\partial \mathbf{m}}\right)^T \left[\frac{\partial \mathbf{g}}{\partial \mathbf{m}}\mathbf{A}^{-1}\left(\frac{\partial \mathbf{g}}{\partial \mathbf{m}}\right)^T\right]^{-1} \frac{\partial \mathbf{g}}{\partial \mathbf{m}} \tag{3.42}$$

is a projection matrix, where

$$\left[\frac{\partial \mathbf{g}}{\partial \mathbf{m}}\right]_{ij} = \frac{\partial g_i}{\partial m_j}. \tag{3.43}$$

For linear constraints $\mathbf{A} = \mathbf{H}$, and the model covariance matrix is then

$$\mathbf{V}_m = \mathbf{P}\,\mathbf{H}^{*-1}\,\mathbf{J}^T\,\mathbf{V}_d\,\mathbf{J}\,\mathbf{H}^{*-1}\,\mathbf{P}^T. \tag{3.44}$$

3.5 Unconstrained inversion of TEM data over a 105 mm Projectile

We now invert a TEM field data set acquired at the ERDC UXO test site in Vicksburg, Mississippi (Figure 3.10). The Geonics EM63 instrument used for the survey is a multi-time channel time domain unit consisting of a 1 m × 1 m square transmitter coil and a single coaxial horizontal circular receiver loop mounted on a two-wheel trailer. Measured voltages are averaged over 26 geometrically spaced time gates, spanning the range 0.18 ms to 25.14 ms.

A 105 mm projectile is placed in the ground with its center at 2.0 m East, 1.83 m North and at a depth of 0.44 m from the surface. The projectile was placed horizontal ($\theta = 90°$), with its tip pointing to the North ($\phi = 0°$). Once the target was placed in the ground, it was not covered in soil. The survey consisted of a 2 m × 2 m grid centered on the target, containing 5 lines running

(a) The Geonics EM63 MKI. The bottom 1 m x 1m loop is the transmitter loop, and the white 50 cm diameter circular loop is the receiver.

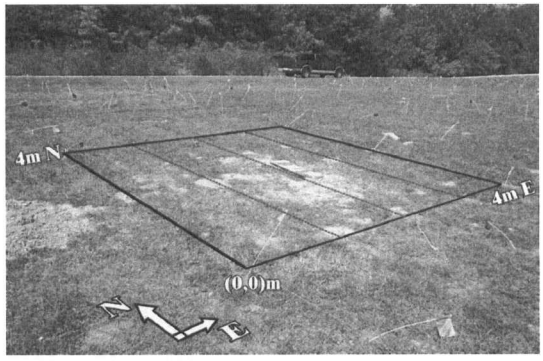

(b) Location of measurement. Data were taken on 0.5 m lines, with 10 cm station separation.

(c) Buried 105 mm projectile. For this measurement soil was not replaced in the hole. A small piece of plywood was placed over the hole to prevent the Geonics EM63 from falling in.

Figure 3.10: Data collection setup for the example of Section 3.5.

North-South separated at 50 cm line spacing, with stations located at 5 cm intervals along each line. A measured signal of less than 1 mV is assumed to be indistinguishable from the noise. The resulting data set contains 1882 total data points.

3.5.1 Application of a Local Search Algorithm

The inversion is carried out with the data assigned a standard deviation of five percent and a base level error of $\epsilon = 1$ mV. The first stage of the time decay evident in Figure 2.5 is not observed in the time window recorded by the EM63. Therefore, we invert these data by using parameterizing the polarization decays with Equation 2.34, i.e., $L_i(t) = k_i t^{-\beta_i} \exp(t/\gamma_i)$, where $i = 1, 2$ for the axial and transverse polarizations, respectively. The observed and predicted data are compared in Figures 3.11 and 3.12. We remind the reader that only the measured data, and not the values of the image obtained from interpolating the measured data, are included in the objective function. Figure 3.12 shows a plan view comparison for five of the 26 time channels. At early times the anomaly has a single peak located approximately above the UXO center. This peak splits into two distinct peaks at late time. The recovered model predicts data that reflects this behavior. Figure 3.11 compares the decay curve measured at four stations on the survey.

The recovered location and orientation parameters are listed in Table 3.1. The recovered easting of 2.04 m differs from the true value of 2.00 m by 4 cm. The recovered northing of 1.78 m differs from the true value of 1.83 cm by 6 cm, thus placing the inducing dipole closer to the projectile tail. These errors are of the same magnitude as can be expected in spotting the station location in the field survey. In addition, the buried 105 mm projectile has a copper rotating band near the tail of the projectile. It has been suggested that the presence of the rotating band will shift the location of the induced dipole from the target center towards the tail (Miller, 2000). The recovered burial depth of 0.45 m is 1 cm deeper than the expected depth of 0.44 m. The orientation parameters θ and ϕ are well recovered.

The recovered decay parameters are listed in Table 3.1 and the diagnostics applied to these parameters are listed in Table 3.2. In Pasion (1999), the average of the β parameters, $\bar{\beta} = (\beta_1 + \beta_2)/2$, was shown to be diagnostic of the magnetic permeability. The value of $\bar{\beta} = 0.89 (> 0.8)$ indicates that the target is likely to be magnetically permeable. The ratios $k_1/k_2 = 2.69 (> 1)$ and $\beta_1/\beta_2 = 0.67 (< 1)$ indicate, for a magnetically permeable target, that the TEM response is likely

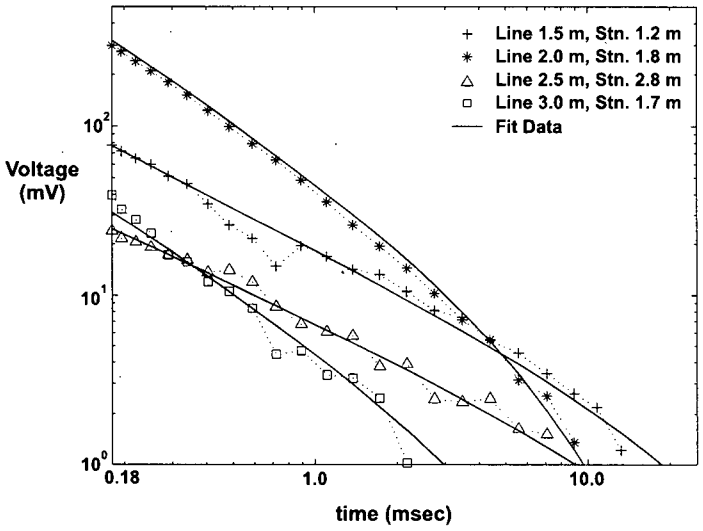

Figure 3.11: The observed and predicted decay curves for four stations in the 105 mm projectile UXO field data set inversion. The predicted decay of the vertical component of the measured voltages are represented by the solid lines, and the symbols represent the Geonics EM63 field measurements.

Parameter	Known values	Local Analysis		NA-Bayes Analysis		
		Recovered Parameters	Standard Deviation	Recovered Parameters	Mean	Standard Deviation
Northing x (m)	1.83	1.78	0.001	1.78	1.78	0.004
Easting y(m)	2.00	2.05	0.001	2.04	2.04	0.02
Depth z (m)	0.44	0.45	0.001	0.47	0.47	0.01
ϕ (degrees)	0	9.71	0.29	9.4	9.5	1.5
θ (degrees)	90	85.0	0.19	84.2	84.3	0.8
k_1	(69.6)	74.2	0.75	76.7	76.7	1.5
β_1	(0.64)	0.71	0.016	0.72	0.72	0.02
γ_1	(20.4)	22.7	2.6	26.7	26.6	0.6
k_2	(20.1)	27.6	0.56	29.4	29.1	1.0
β_2	(1.08)	1.06	0.024	1.08	1.08	0.01
γ_2	(7.59)	5.73	0.63	6.74	6.8	1.0

Table 3.1: Comparison of recovered model parameters from the local analysis and parameters derived from the Neighbourhood Algorithm (NA-Bayes) (Sambridge, 1999a,b).

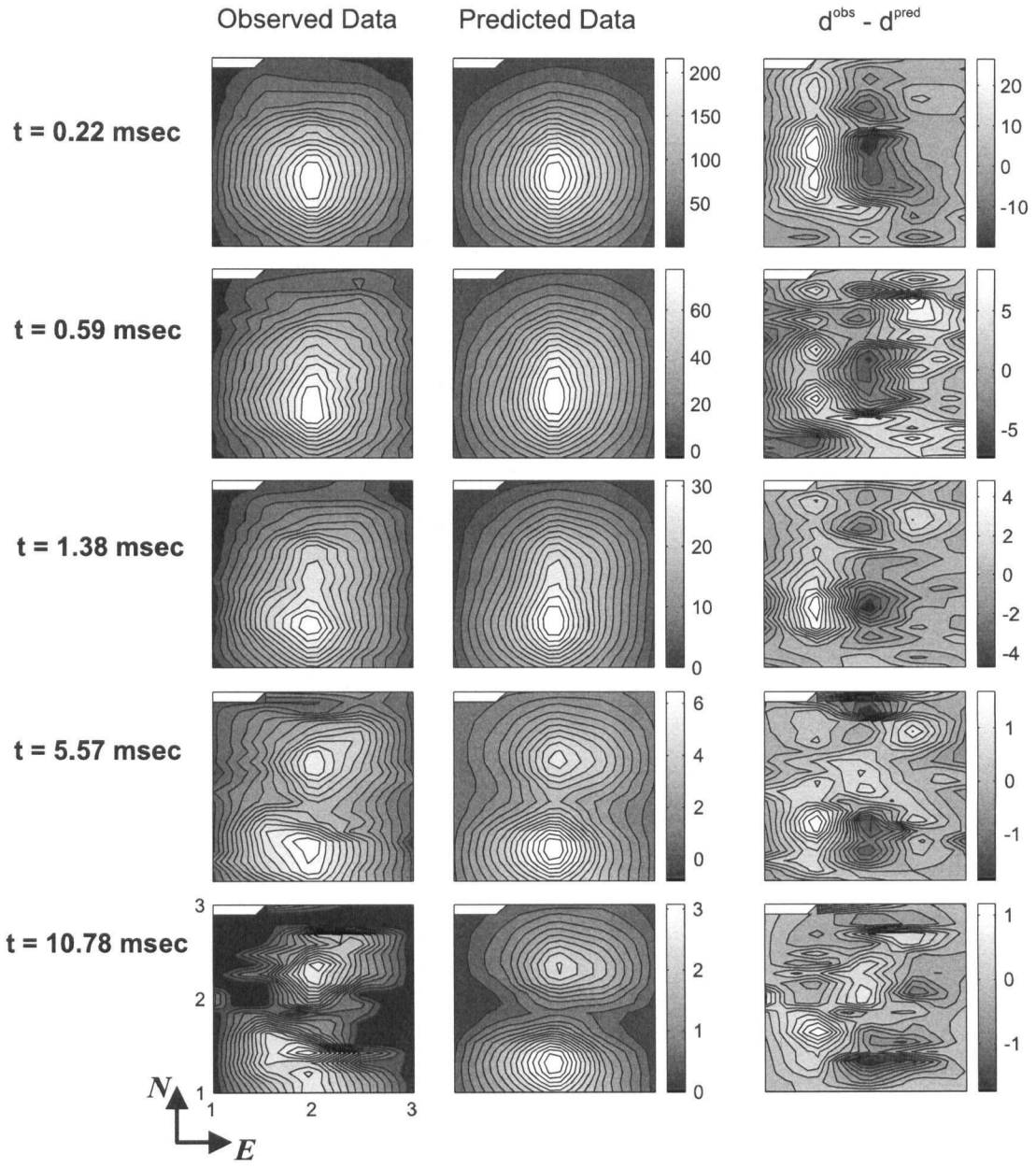

Figure 3.12: Plan view plots of the observed and predicted data for 5 of the 26 time channels in the 105 mm projectile UXO field data set inversion. The predicted data provide a reasonable match to the TEM response measured by the Geonics EM63.

to be from a rod-like target.

	Local Analysis Recovered Parameters	NA-Bayes Recovered Parameters	NA-Bayes Standard Deviation
$(\beta_1 + \beta_2)/2$	0.89	0.90	.05
k_1/k_2	2.69	2.64	0.2
β_1/β_2	0.67	0.67	0.1

Table 3.2: Comparison of NA-Bayes and local analysis.

When inverting data, multiple starting models can improve the chances that the optimization algorithm will find the global, rather than a local, minimum of the objective function. Table 3.3 contains an example of recovered parameter results when using a very good starting model, and a very poor starting model. Application of our standard diagnostics are calculated and compared in Table 3.4. The model recovered by the poor starting model is characteristic of a plate-like target,

		Good Starting Model			Poor Starting Model		
Parameter	Known values	$\mathbf{m}_o$	Recovered Parameters	σ	$\mathbf{m}_o$	Recovered Parameters	σ
Northing x (m)	1.83	2.0	1.78	0.001	3.0	1.79	0.001
Easting y (m)	2.00	2.0	2.05	0.001	3.0	2.09	0.001
Depth z (m)	0.44	0.52	0.45	0.001	1.57	0.31	0.003
phi (degrees)	0	-45	9.71	0.29	0	-101.7	0.58
theta (degrees)	90	45	85.0	0.19	0	14.5	0.19
k_1	(69.6)	88.9	74.2	0.75	1	11.1	0.87
β_1	(0.64)	0.8	0.71	0.016	1	0.87	0.096
γ_1	(20.4)	4.7	22.7	2.6	1	1.72	0.027
k_2	(20.1)	22.2	27.6	0.56	1	27.28	0.33
β_2	(1.08)	1.15	1.06	0.024	1	0.98	0.013
γ_2	(7.59)	3.13	5.73	0.63	1	75.44	25.80

Table 3.3: Comparison of two different starting models.

	Good Starting Model	Poor Starting Model
$\bar{\beta} = (\beta_1 + \beta_2)/2$	0.89	0.92
k_1/k_2	2.69	0.41
β_1/β_2	0.67	0.89

Table 3.4: Comparison of NA-Bayes and local analysis.

that is closer to the surface than the true target location, and is rotated 90 degrees from the true

orientation. The existence of this type of local minimum was noted in Chapter 2 and in simulations of single channel EM61 MK2 data (Pasion et al., 2004).

3.5.2 Application of a Global Search Algorithm

The local minimum encountered in the previous example motivates the use of a global optimization algorithm. We use the Neighborhood Algorithm (Sambridge, 1999a,b) to sample model space and evaluate the Bayesian integrals for the mean, covariance and marginal probabilities for the 105 mm projectile example. The Neighbourhood Algorithm uses a geometric approach for searching model space. For a suite of sampling points, nearest neighbour regions, or Voronoi cells, are constructed that partition model space. A pair of tuning parameters then control the numbers of cells to resample, and how many samples to generate within these cells. The success of this method relies on the ability to sample carefully in the regions of good fit. Monte Carlo integration uses the sample to numerically evaluate the integrals for the mean, covariance and marginal probabilities (Equations 3.6, 3.7, and 3.8, respectively).

Figure 3.13 contains plots of the 1-D marginal distributions for the location and orientation. The 1-D marginals for the dipole polarization decay parameters are plotted in Figure 3.14. Two-D marginal distributions for parameter pairs (x, y), (k_1, k_2), and (β_1, β_2) are plotted in Figure 3.15. Confidence regions of 60, 90, and 99 percent are indicated by contours. These plots indicate that we have greater than 99 percent confidence that the target is rod-like (i.e., $k_1/k_2 > 1$ and $\beta_1/\beta_2 < 1$). The marginal distributions of the diagnostic parameters are plotted in Figure 3.16, again confirming the rod-like interpretation.

Tables 3.1 and 3.2 compare the results of the Neighbourhood algorithm with the local methods. The results are comparable to the local method when the better starting model was used. The linearized estimates of the standard deviations are generally smaller than those obtained through the NA Bayes analysis.

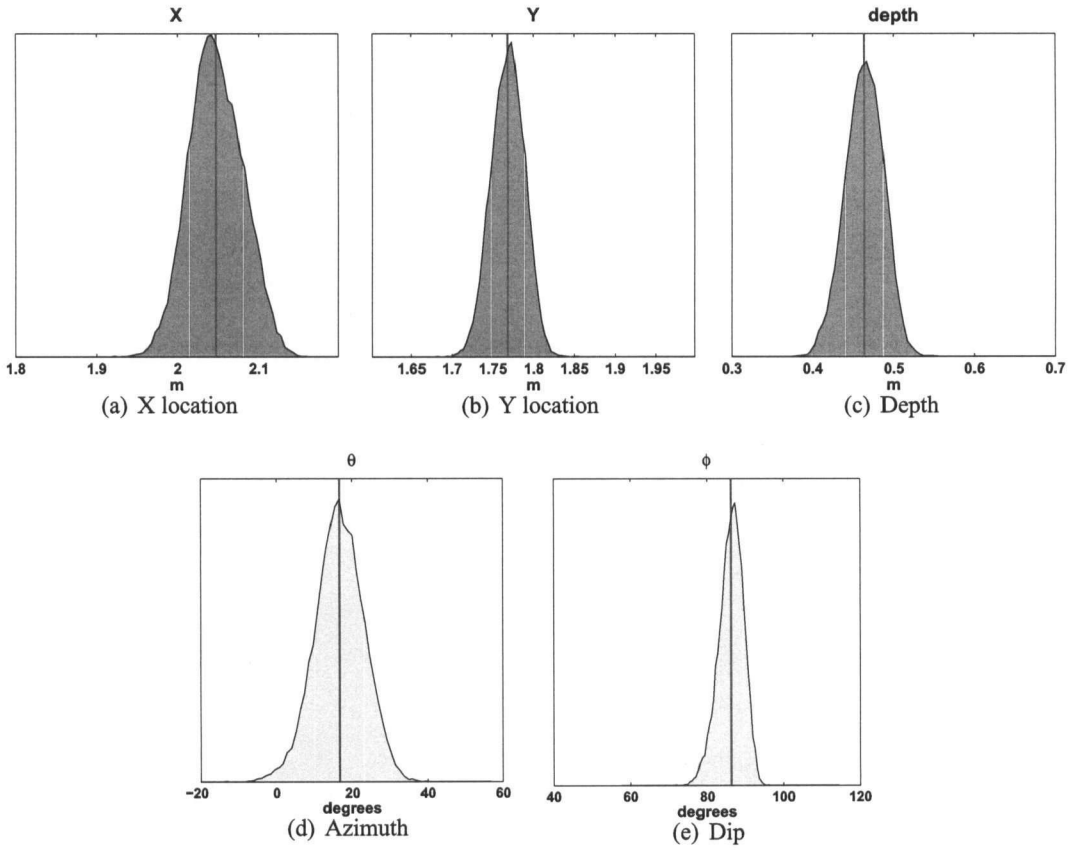

(a) X location (b) Y location (c) Depth

(d) Azimuth (e) Dip

Figure 3.13: 1D marginals for position and orientation obtained using the Neighbourhood Algorithm.

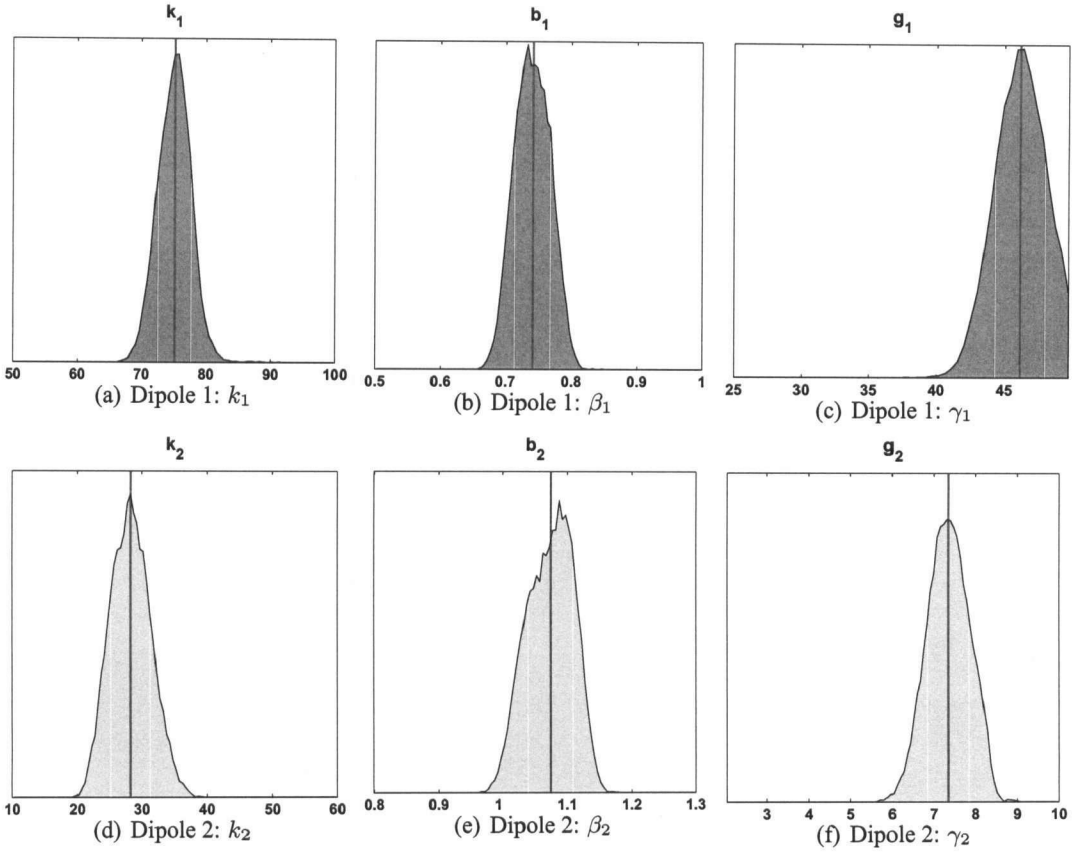

(a) Dipole 1: k_1 (b) Dipole 1: β_1 (c) Dipole 1: γ_1

(d) Dipole 2: k_2 (e) Dipole 2: β_2 (f) Dipole 2: γ_2

Figure 3.14: 1-D Marginal distributions for the dipole polarization decay parameters.

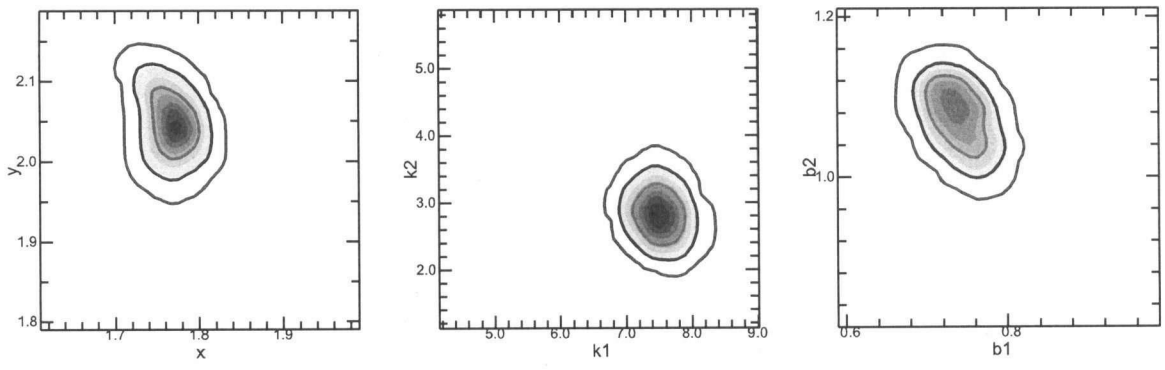

Figure 3.15: 2-D Marginals calculated using the Neighbourhood Algorithm. Confidence regions of 60 (green contour), 90 (blue contour), and 99 (red contour) percent are indicated.

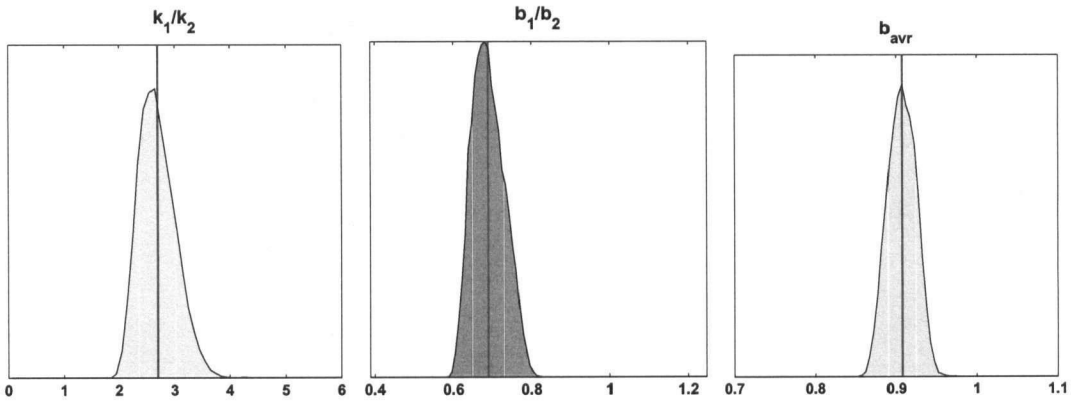

(a) k_1/k_2 (b) β_1/β_2 (c) $(\beta_1 + \beta_2)/2$

Figure 3.16: 1-D Marginal distributions for the dipole polarization decay parameters.

3.6 A Comparison of Two and Three Polarization Inversions

In Chapter 2 we presented two variations of the dipole model: the two-polarization model and the three-polarization model. The two polarization model contains two unique elements of the dipole polarization tensor, and is suitable for axi-symmetric targets such as most UXO. The three polarization model contains three unique elements of the dipole polarization tensor and thus models non-axial symmetric targets, such as some scrap, better (that is, with a lower data misfit) than the two polarization model. The discrimination of non-axially symmetric targets becomes dependent on the choice of model. When using the three-polarization model, a non-axial symmetric target is characterized by three unique polarization tensors (i.e., $L_x \neq L_y \neq L_z$). When using a two-polarization model, large data misfits may indicate that the target is not axially symmetric.

In the buried 105 mm projectile example of Section 3.5, we inverted for the model parameters of the two-polarization model. This choice of model was arbitrary. When inverting field data as part of a real-world ordnance cleanup project what model should we choose? Although it is desirable to have a model that can fit data as well as possible, variances in recovered model parameters increase with model complexity. In particular, if we are inverting data over a UXO we do not want to have a situation where the data quality is not high enough to resolve the three components of the three-polarization model well. Such a situation may lead to a false-negative characterization of the target. There are several standard techniques for model selection. These include Akaike Information Criterion (AIC), Schwarz Criterion (also known as the Bayesian Information Criterion (BIC)), Minimum Description Length (MDL), and Likelihood ratio tests (LRT). These techniques, although established through different means, essentially reward models that fit data while penalizing model complexity.

In this section we compare fitting TEM data with three-polarization elements (L_x, L_y, and L_z) of the tensor or two unique elements ($L_x = L_y$ and L_z), which represents an axial-symmetric target. In principle, if the data collected over an axially symmetric, rod-like target are of high enough quality, an inversion that attempts to recover three-polarizations should recover two of the polarization elements as being equal. In this section I invert data from a number of different targets, both UXO and non-UXO, for both the two and three-polarization models. I compare data misfits, the recovered parameters and their variances for both the two and three-polarization models.

3.6.1 Fitting Cued interrogation style Geonics EM63 TEM data from a 3.5 inch Rocket

In the summer of 2006, geophysical data were collected at the Marine Corps Base Camp Lejeune in North Carolina. "Cued interrogation" style data were collected with the Geonics EM63 (Figure 3.17). Figure 3.18 shows an example of inverting Geonics EM63 data collected over a horizon-

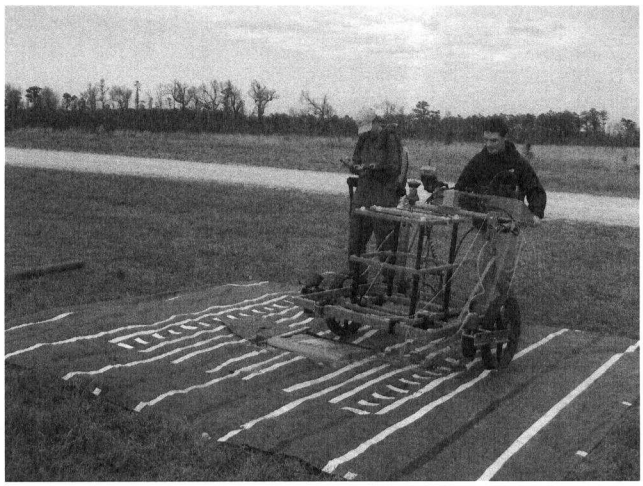

Figure 3.17: "Cued interrogation" style data collection at Marine Corps Base Camp Lejeune in North Carolina.

tal 3.5 inch rocket without fins. The rocket was placed in a shallow pit in the ground, and an EM63 sensor traversed the area at a slow, controlled pace to maximize the S/N of the measured anomaly. The inversion results in Figure 3.18 are for three-polarizations parameterized by Equation 2.30. The data were also inverted using two and three-polarization models that were parameterized using equations 2.30, 2.32, and 2.34. The resulting polarization curves are plotted in Figure 3.19. Inversion of the data, regardless of the number of polarizations and the parameterization of the polarizations, reveal a single, dominant, axial polarization. For the three-polarization models, the transverse polarizations are equal (i.e., $L_x = L_y$) and less than the axial polarization, thereby suggesting an axi-symmetric target. The transverse polarizations for both the two and three-polarization models are similar. The inversion results are what we hope to expect for any inverted anomaly.

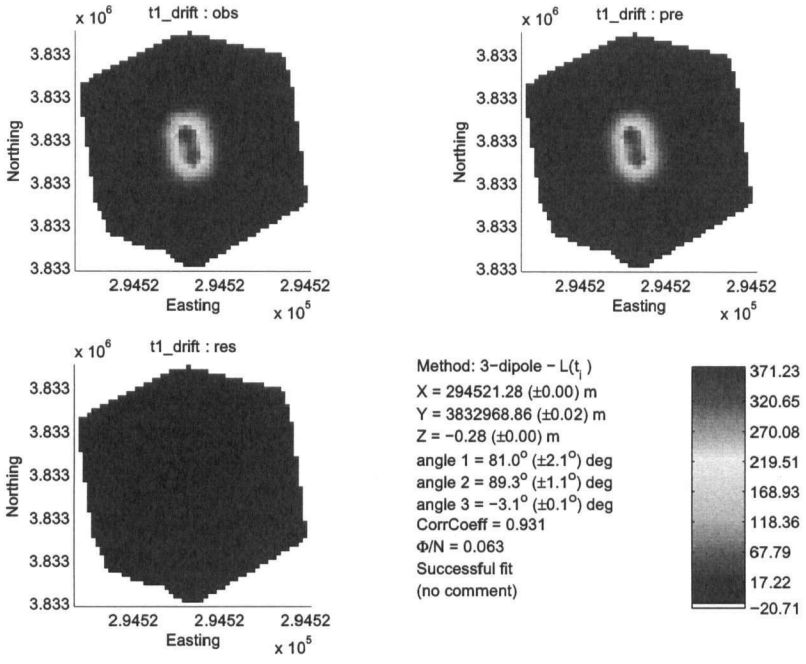

(a) The first time channel of data is plotted.

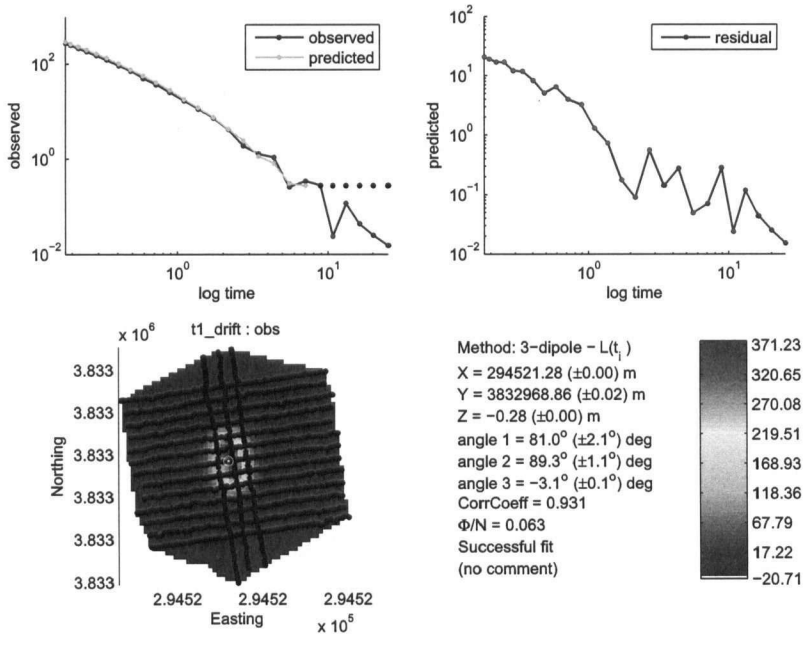

(b) The fit to a sounding directly over the target. The black dots in the upper left panel indicate uninverted channels due to low signal to noise ratios.

Figure 3.18: A data fit result when inverting for a three polarization dipole model from Geonics EM63 data collected over a 3.5 inch rocket. Both figures are screen outputs from UXOLab.

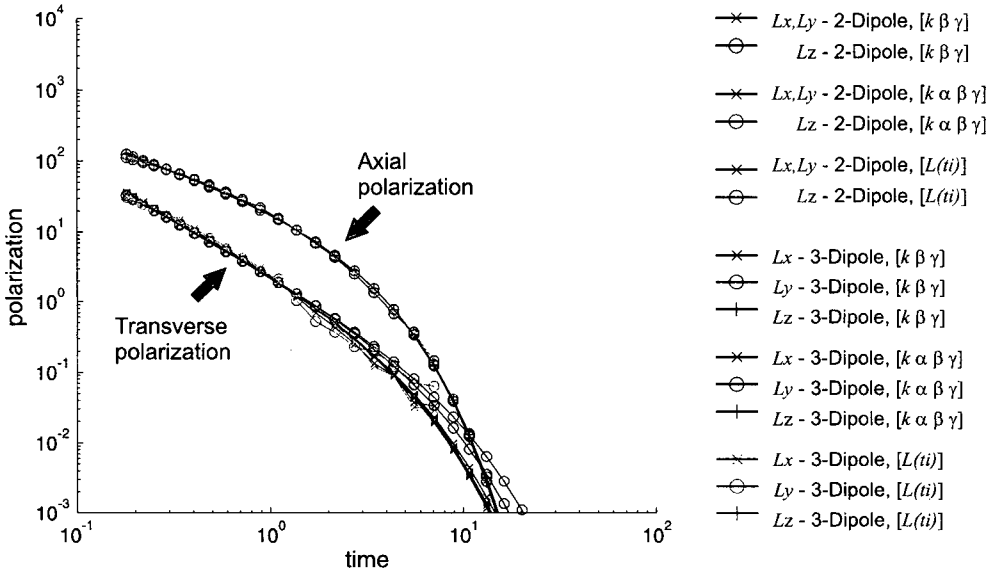

Figure 3.19: Comparison of recovered axial ($L_1(t)$) and transverse ($L_2(t)$) polarizations when inverting data over a 3.5 inch rocket.

3.6.2 Fitting TEM data from an array of Geonics EM61 Mark 2 sensors

Data were collected by the Sky Research, Inc 5 sensor EM61 array at the Former Lowry Bombing and Gunnery Range (FLBGR) test plot (Figure 3.20). These data were subsequently inverted using both a two-polarization and three-polarization model. Since the Geonics EM61 Mark 2 only has four time channels, we will not parameterize the polarization decay and, instead, use the instantaneous amplitude (Equation 2.30). In the next three examples we will look at the data fits of (1) a horizontal Sub-Caliber Aircraft Rocket (SCAR), (2) OE scrap which is not axisymmetric, and (3) a vertical 37 mm projectile.

Data Fit over a Sub-Caliber Aircraft Rocket (SCAR) Body

The first example will be for the body section (i.e., no fins or nose) of a SCAR buried a depth of 60 cm and oriented horizontally (Figure 3.21). The SCAR is oriented in an optimal way for resolving both the axial and transverse polarizations (see arguments in Chapter 2).

First time channel data fits for the SCAR are found in Figure 3.22(a) (three-polarization model) and Figure 3.22(b) (two-polarization model). The fit to the data is quantified by the correlation coefficient (CorrCoeff) and a normalized misfit Φ/N, where Φ is the weighted least-squares objective

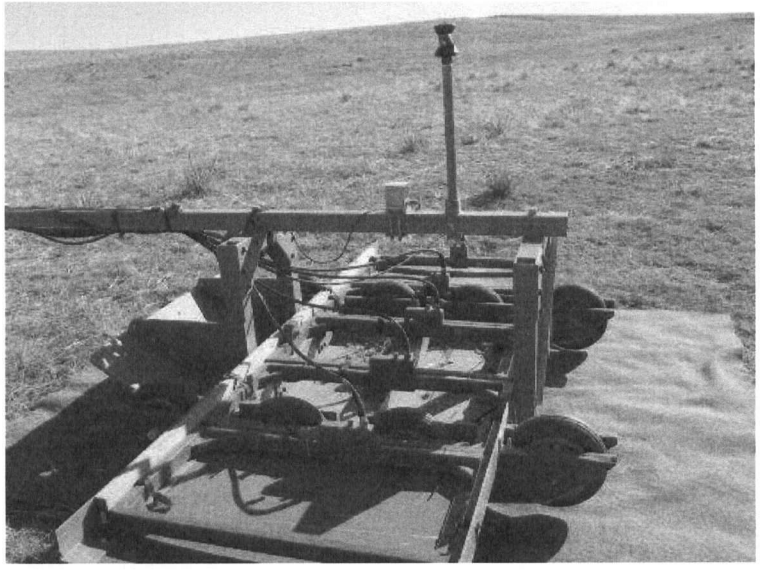

Figure 3.20: Photo of the Sky Research EM61 MK2 array at the Former Lowry Bombing and Gunnery Range (FLBGR).

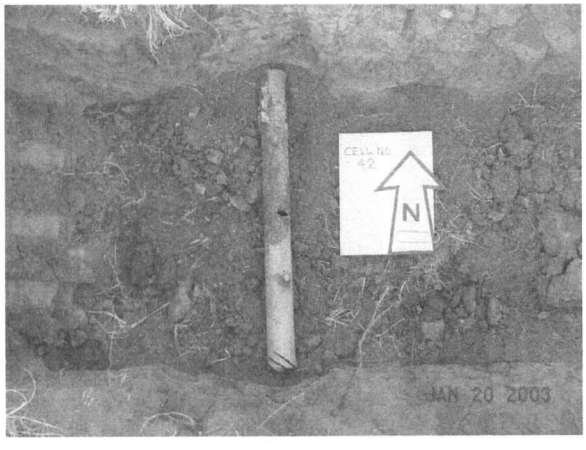

Figure 3.21: A SCAR without a nose and tail buried horizontally at a depth of 60 cm in the FLBGR UXO test plot.

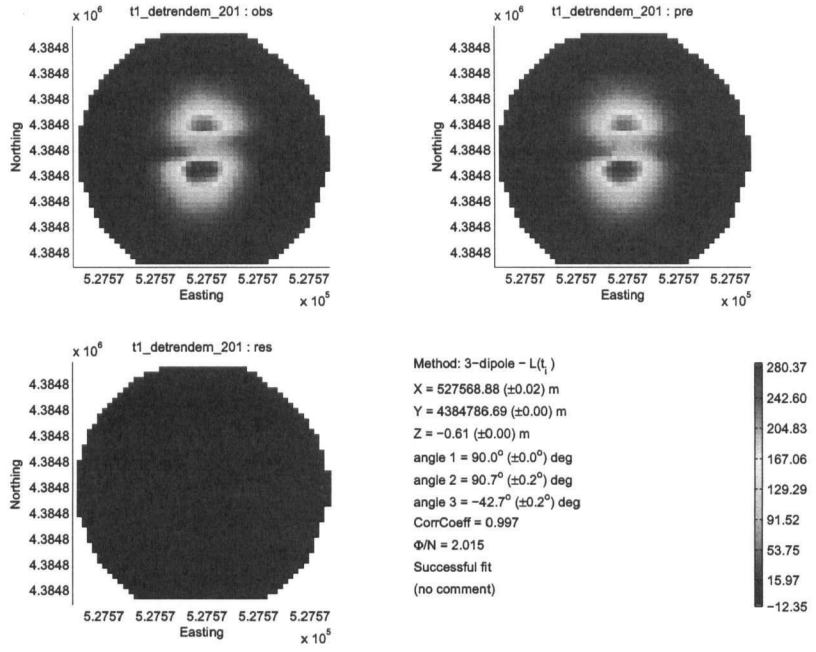

(a) Three-polarization model fit

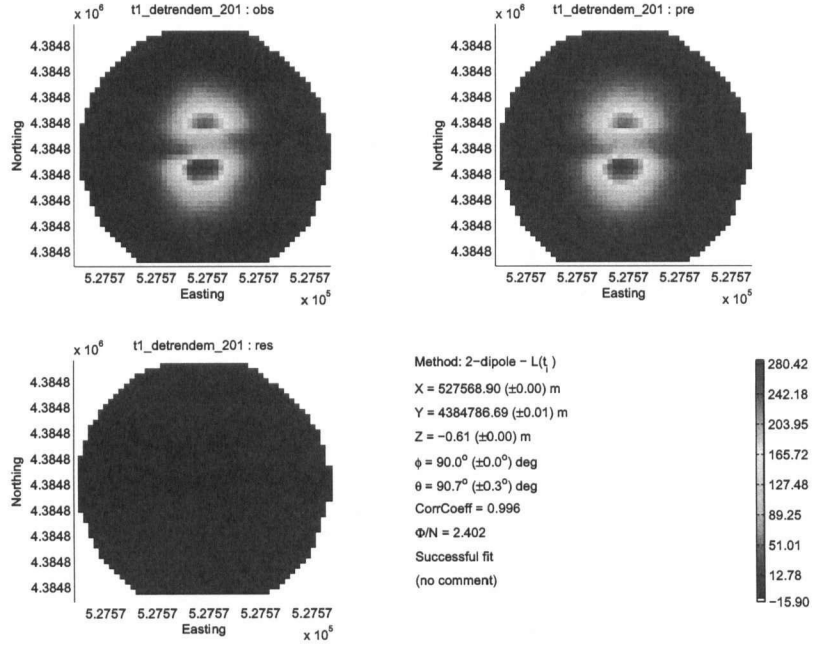

(b) Two-polarization model fit

Figure 3.22: Data fit for the first time channel of the Sky Research Geonics EM61 Mark 2 Array collected over the SCAR of Figure 3.21.

function and N is the number of data. Both inversions recover the location and depth parameters accurately, and the quality of fit is approximately the same. Table 3.5 summarizes the recovered two-polarization and three-polarization model parameters and their variance. The recovered axial

	Two-polarizations		Three-polarizations		
	$L_x = L_y$	L_z	L_x	L_y	L_z
t_1	56.1±0.6	243.9±3.8	51.3±3.5	61.6±4.7	246.6±1.5
t_2	35.6±0.5	192.0±2.7	32.4±17.8	39.3±13.3	194.2±0.5
t_3	18.7±0.3	139.4±2.0	17.3±1.2	20.3±0.7	140.8±0.5
t_4	7.4±0.4	88.7±1.1	6.5±0.7	8.3±0.1	89.8±0.2

Table 3.5: Comparison of three and two polarization inversions of data collected over the SCAR in Figure 3.21.

and transverse polarizations and their variances are nearly the same for both the three and two polarization models. For this example, we can conclude that the data quality was high enough to support successful parameter estimation using either model type.

Data fit over OE Scrap

The next example is OE scrap (23 lbs) from a 100 lb bomb buried at a foot (Figure 3.23). The scrap

Figure 3.23: Photo of a piece of OE scrap from a 100 lb bomb buried at a depth of 30 cm.

is clearly not axially symmetric, and thus we would expect the three-polarization model to have a better fit than the two-polarization model. Figures 3.24(a) and (b) verify the improved fit when including an additional polarization.

Table 3.6 lists the recovered model parameters and their respective variances. When using the

	Two polarizations		Three polarizations		
	$L_x = L_y$	L_z	L_x	L_y	L_z
t_1	982.9±70.7	992.8±150.2	757.0±3.9	602.8±0.3	910.3±0.8
t_2	531.8±29.2	671.2±86.0	510.8±0.2	320.0±0.2	506.5±0.3
t_3	185.2±4.2	329.0±11.5	251.2±0.7	107.5±0.2	185.4±1.2
t_4	31.2±2.1	96.4±13.2	73.43±0.08	16.9±0.1	34.7±0.1

Table 3.6: Comparison of two and three-polarization inversions of data collected over the OE scrap in Figure 3.23.

two-polarization model, the variances (or model uncertainties) are much greater, suggesting that we should "trust" the model recovered by the two-polarization inversion less than the model recovered by the three-polarization model, even though the fit appears to be adequate.

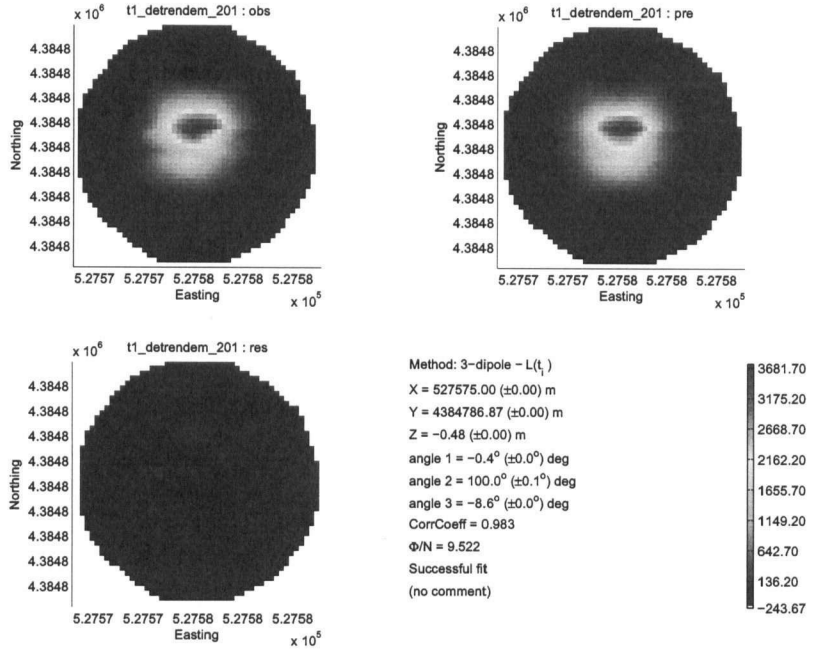

(a) three-polarization model fit

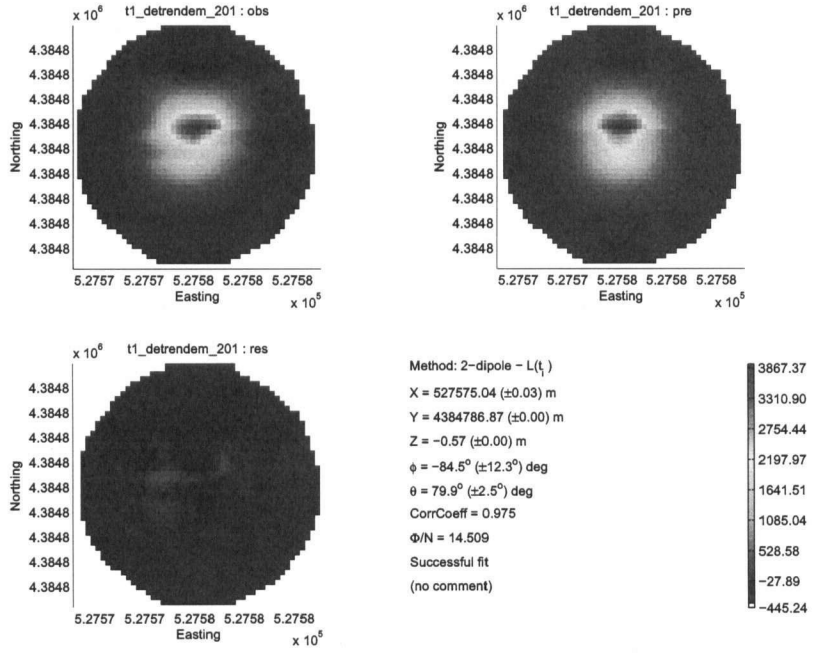

(b) two-polarization model fit

Figure 3.24: Data fit for the first time channel of the Sky Research Geonics EM61 Mark 2 Array collected over the OE scrap in Figure3.23.

Data Fit over a Vertical 37 mm Projectile

The final example is over data measured above a vertical 37 mm projectile buried at depth of one foot. From the arguments in Chapter 2, the projectile is positioned in the least advantageous orientation to resolve the transverse components. The quality of data fits are nearly the same (Figures 3.25(a) and (b)). For the first two time channels, the recovered data parameters are nearly the same. However, for the final two time channels, the axial polarizations recovered by the three-polarization model indicate a non axially symmetric target. The data are unable to accurately constrain these parameters due to the lower signal to noise ratio for these later time channels.

	2-polarizations		3-polarizations		
	$L_x = L_y$	L_z	L_x	L_y	L_z
t_1	19.3±1.7	33.4±0.4	18.45±0.04	19.44±0.06	44.7±0.6
t_2	12.6±0.8	24.5±0.9	11.2±0.3	12.67±0.07	32.8±0.7
t_3	9.1±0.5	14.6±0.7	5.96±0.02	12.2±0.2	19.0±0.1
t_4	4.2±0.2	8.1±0.5	2.71±0.02	5.19±0.03	10.69±0.05

Table 3.7: Comparison of 2 and 3 polarization inversions of data collected over a buried 37 mm projectile.

3.6.3 Summary

The results from this section were presented to illustrate the differences when inverting two or three unique polarizations. Three Geonics EM61 anomalies were inverted in this section:

1. **SCAR rocket body:** An anomaly from a rod-like target with sufficient data quality such that three-polarization inversion correctly recovered a pair of transverse polarization tensors that are similar.

2. **OE Scrap:** An anomaly from a piece of scrap without axial symmetry with sufficient data quality such that the inversion with three polarizations produce a lower misfit and lower model variances than the inversion with only two polarizations.

3. **37 mm projectile:** An anomaly from a rod-like target without sufficient data quality to correctly recover unique transverse polarization components when inverting for three-polarization tensors.

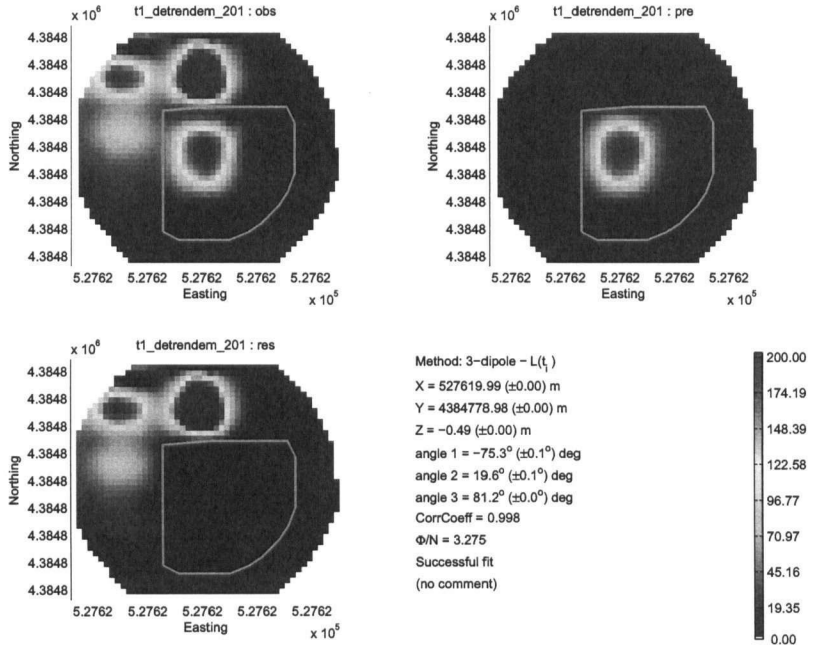

(a) Three-polarization model fit

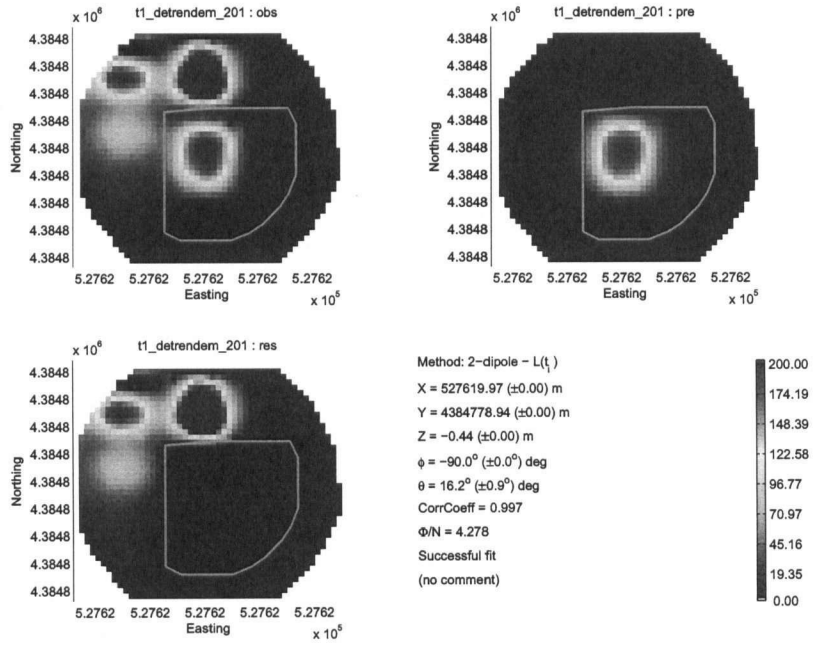

(b) Two-polarization model fit

Figure 3.25: Data fit for the first time channel of the Sky Research Geonics EM61 Mark 2 Array collected over a vertical 37 mm projectile buried at a depth of one foot.

In the case of the 37 mm projectile, the recovered three polarization model did not reflect the axi-symmetric character of the target. For this anomaly, it may be a better strategy to invert for the simpler two-polarization dipole model.

Some work has to be completed which characterizes the data quality required in order for all three polarizations to be constrained. In addition, a model selection criteria that provide a systematic way of incorporating misfit, variance and model selection criteria should be included in processing. In previous applications of processing EM63 and EM61 data (Billings, 2007) on live site data, we have used a simple and conservative approach to decide if either two or three distinct polarizations should be used. Both a two and three-polarization model was inverted, and the data misfit was recorded. If the data misfit of the three polarization inversion was less than 0.85 times the misfit of the two polarization inversion, we use the three polarization model.

3.7 Conclusion

This chapter described our basic methodology for estimating polarization tensor parameters from sensor data. The objective of inversion is to characterize the a posteriori distribution of models. The global methods used to fully characterize the probability density function and evaluate the Bayesian integrals require numerous evaluations of the forward model, and are impractical for processing numerous anomalies. Therefore, our objectives is to use local methods to calculate the maximum a posteriori estimate. Linearized analysis of the misfit provides estimates for the model parameter variances. We have found that linearized estimates underestimates the results from the global analysis. Prior to inversion, several important pre-processing steps are required. These include estimating the noise of the data set, selecting anomalies, and developing a suite of starting models. Data acquired over a 105 mm projectile was used to demonstrate the inversion procedure. Both local and global methods were used with similar results. Application of the local method using a poor starting point demonstrated the importance of using a suite of starting models to avoid the problem of local minima.

The chapter concludes with a comparison of two and three polarization inversion results. An example using EM61 Mark 2 data showed that, when using a three polarization model, the ability to correctly recover unique transverse polarization components when inverting an anomaly from

a rod-like is limited by data quality. A model selection criteria that provide a systematic way of incorporating misfit, variance and model selection criteria should be included in processing.

Chapter 4

Joint and Cooperative Inversion of Time Domain Electromagnetic Data

Magnetics and electromagnetic surveys are the primary techniques used for UXO remediation projects. Magnetometry is a valuable geophysical tool for UXO detection because of the ease of data acquisition and its ability to detect relatively deep targets. However, magnetics data can have large false alarm rates due to geological noise, and there is an inherent non-uniqueness when trying to determine the orientation, size and shape of a target. Electromagnetic surveys, on the other hand, are relatively immune to geologic noise and are more diagnostic for target shape and size but have a reduced depth of investigation. In this section we aim to improve discrimination ability by developing an interpretation method that takes advantage of the strengths of both techniques. We consider two different approaches to the problem: (1) Interpreting the data sets cooperatively, and (2) interpreting the data sets jointly. For cooperative inversion, information from the inversion of one type of data is used as a constraint for inverting another. In joint inversion, target model parameters common to the forward solution of both types of data are identified and the model parameters from all the survey data are recovered simultaneously. We compare the confidence with which we can discriminate UXO from non-UXO targets when applying these different approaches to results from individual inversions. In this section we focus on the details of the joint and cooperative inversion methodologies.

4.1 Introduction

Electromagnetic and magnetic surveys are the standard geophysical techniques used for UXO remediation. Electromagnetic detection of a buried target is accomplished by illuminating the subsurface with a time varying primary field. If the buried target is conductive, eddy currents will be induced

in the target, and subsequently decay. These currents produce a secondary magnetic field which is then sensed by a receiver coil at the surface. Magnetometry is a passive detection system. The high magnetic susceptibility of a ferrous target causes distortions to the Earth's field which are measured by a magnetometer. Electromagnetics and magnetometry have proven to be successful in detecting UXO in recent UXO remediation projects and UXO technology demonstrations.

The dipolar nature of the electromagnetic responses of compact metallic objects measured with sensor/target geometries typical for UXO surveys has lead to a number of techniques for estimating the elements of the magnetic polarization tensor that define the induced dipole moment. The magnetic polarization tensor's components are functions of the size, shape, location, orientation and material properties of the buried target of interest and therefore provide a model vector from which the target characteristics can be inferred. The accuracy with which the polarization tensor can be recovered depends on the noise levels of the induction sensor, the amount of geologic noise in the inverted data, and accurate accounting of survey parameters such as sensor orientation and location.

As an illustration of the difficulty of UXO discrimination in conditions of lower signal-to-noise and poor spatial coverage, consider the recovery of the polarization tensor components from a pair of synthetic data sets generated from a Stokes mortar. Figure 4.1(a) is a photo of a Stokes mortar and the measured dipole decay parameters of the mortar are listed in Figure 4.1(b). The dipole polarization decay parameters were calculated from data collected in at the USACE ERDC UXO test site (Appendix A). The TEM response is computed for a Stokes mortar buried at depths of 60 cm and 100 cm and oriented 30 degrees from horizontal. The TEM responses at 1.105 ms measured on a line parallel to the strike of the mortar are compared in Figure 4.1c.

We assume that the TEM sensor has a noise floor of 0.5 mV. When the mortar is buried at a depth of 60 cm, the large signal-to-noise ratio results in an accurate recovery of the dipole parameters (Table 4.1), and an accurate prediction of the observed data (Figures 4.2(a) and 4.2(b)). The signal from a mortar buried at 100 cm is much weaker and, as Figure 4.3c demonstrates, a significant portion of the data lies within the noise level of the sensor. Inversion of these data result in recovered model parameters that accurately reproduce the data (Figure 4.3(a middle panels and Figure 4.3(b) green line) but are not the parameters of the Stokes mortar (Table 4.1). Location and orientation were not correctly recovered. With the data located on the right side of the survey obscured by the sensor noise, the inversion attempted to place the location of the target at the center of the data peak.

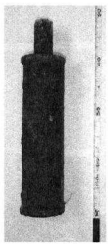

(a) Photo of a Stokes Mortar

k_1	43.9
α_1	0.02
β_1	0.73
γ_1	9.1
k_2	4.9
α_2	0.001
β_2	1.09
γ_2	10.8

(b) Polarization tensor parameters used for forward modelling

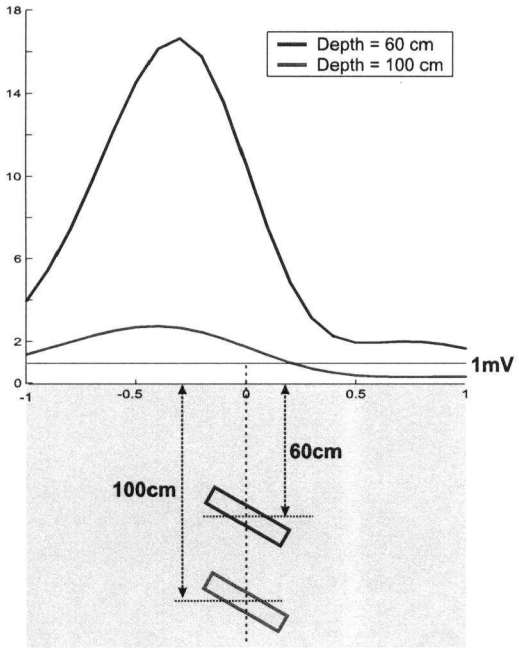

(c) Dipole response (in mV) at 1.105 ms of a Stokes Mortar located at depths of 60 and 100 cm.

Figure 4.1: Photo and decay constants of a particular Stokes Mortar and the TEM response at 1.105 ms measured parallel to the length of the Stokes Mortar for two depths of burial.

	Location X,Y (m)	**Depth (m)**	**Azimuth (degrees)**	**Dip (degrees)**	k_1	k_2	k_1/k_2	Interpretation
A	(0,0)	1.0	90.0	60.0	43.9	4.9	8.96	rod-like
B	(-0.01,0.00)	0.60	90.0	59.9	43.28	4.91	8.81	rod-like
C	**(-0.38,0.05)**	**0.86**	**-16.7**	**62.7**	**7.86**	**11.57**	**0.68**	**plate-like**
D	(0.01,0.00)	0.99	89.3	62.3	39.77	6.08	6.54	rod-like

Table 4.1: Comparison of the recovered model parameters for: (B) a Stokes mortar at a depth of 60 cm, (C) a Stokes mortar at a depth of 100 cm, unconstrained location, and (D) a Stokes mortar at a depth of 100 cm, with location constrained to ± 5 cm of the real location. Row (A) lists the correct parameters.

The non-uniqueness demonstrated in this unsuccessful inversion can be reduced by accurate knowledge of the target location. If we constrain the data to within ± 5 cm of the real target location the recovered parameters and location of the target are successfully obtained (Figure 4.3(a)).

The magnetostatic secondary field response of typical UXO can also be well approximated with a dipole. The magnetostatic polarization tensor for the dipole induced in a magnetic spheroid is well known (McFee, 1989) and enables one to forward model the magnetic dipole response of a spheroid of arbitrary size, shape, orientation, and location. However, inverting magnetics data directly for the size, shape, and orientation of the best fitting spheroid is not possible due to inherent non-uniqueness (Billings et al., 2002). That is, for a spheroid at a particular orientation there exists an infinite number of spheroids that could produce the same dipole moment (Figure 4.4). Ordnance discrimination using magnetostatic data has been achieved by recognizing that intact ordnance tend to become demagnetized after impact while shrapnel tend to have a significant component of remnant magnetization. A level of discrimination is achieved by classifying targets as scrap when the direction of magnetization deviates from the direction of the Earth's field by a large amount (Billings et al., 2002; Nelson et al., 1998; Lathrop et al., 1999). Billings et al. (2002) demonstrated identification ability when the different ordnance types expected in the survey area are known. A ranking scheme was developed by assuming that a particular target type is more likely when it requires less remnant magnetization to fit the measured dipole moment.

To summarize, it is not possible to get unambiguous shape information from magnetometer data alone, and TEM data can have difficulty in generalizing this information when data are incomplete and/or noisy. This motivates the research to combine information from these two surveys.

It has been recognized that the performance of EM interpretation algorithms improve when lo-

cation information from magnetics is used as a constraint. Cooperative inversion has been applied to interpret magnetometry data and single time channel TEM data (for example Nelson and McDonald (1999)) as well as magnetometry data and multi-frequency EM data (for example Collins et al. (2001)).

The objective of this research is to improve our ability to discriminate between UXO and non-UXO items by developing interpretation methods which take advantage of the strengths and overcome some shortcomings of both techniques. In this section we consider interpreting magnetics and electromagnetics data sets jointly and cooperatively. In both cases the ability of the magnetics method to accurately determine an items location is used to stabilize the inversion of TEM data, and the ability of TEM to determine the orientation of a buried target is used to reduce magnetics' implicit non-uniqueness such that the target shape and size can be inferred from the magnetics' data. Examples will be given for multiple time channel time domain electromagnetics and magnetics data sets.

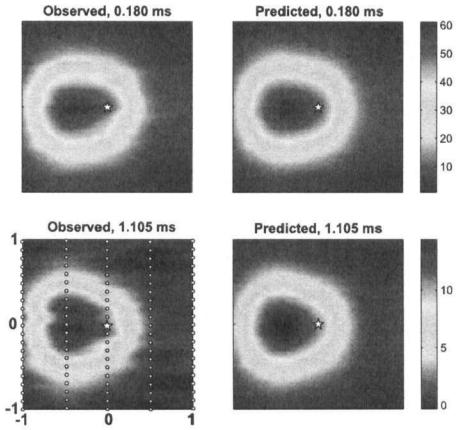

(a) Synthetically generated "observed" data (left) and predicted (right) data from parameters recovered from an inversion.

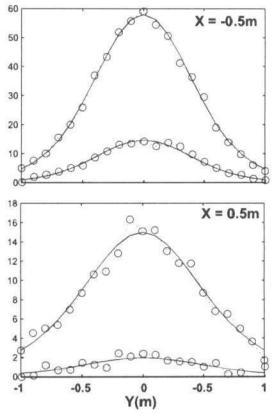

(b) Observed data at t = 0.180 ms and t = 1.105 ms, and along lines x = -0.5 m and x = 0.5 m.

Figure 4.2: Inversion of TEM data for a Stokes mortar at a depth of 60 cm. The signal-to-noise ratio is large, allowing for accurate parameter recovery without constraints placed on the location.

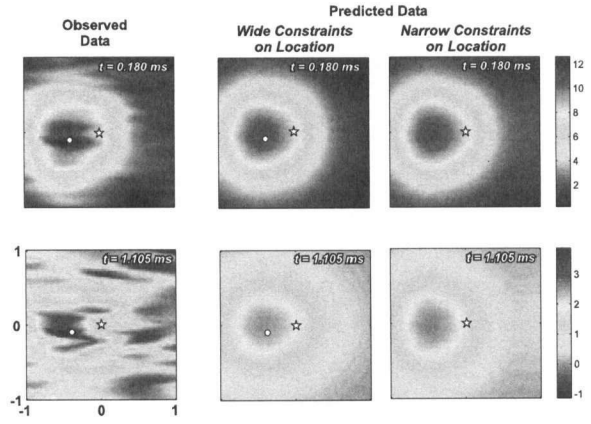

(a) Comparison of observed data and data predicted from the recovered polarization tensor. Location of the Stokes mortar is indicated by a star. When the location is unconstrained the inversion recovers a location, indicated by the circle, coincident with the peak of the signal (middle panels).

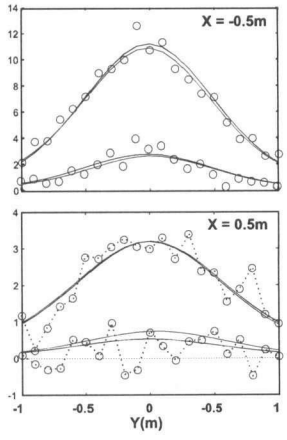

(b) Observed data at t = 0.180 ms and t = 1.105 ms, and along lines x = -0.5 m and x = 0.5 m. The green lines represent predicted data for an inversion with location unconstrained. Blue lines represent data predicted for an inversion with location constrained.

Figure 4.3: Comparison of the data fit for a Stokes mortar at a depth of 100 cm. Without constraints on the target location, it is possible to recover parameters unrepresentative of the target yet able to reproduce the observed data.

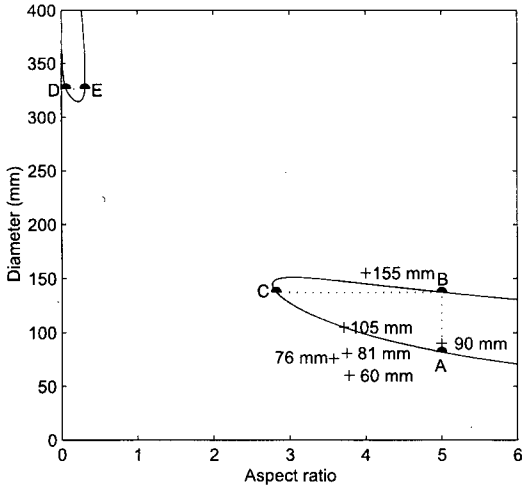

(a) Spheroid dimensions that can produce the same induced dipole.

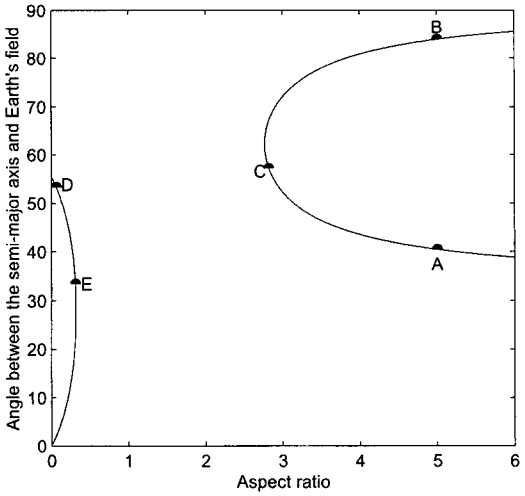

(b) Spheroid aspect ratio and angle from the Earth's field that can produce the same induced dipole. Constraining the angle at which the ordnance of the target lies will reduce the ambiguity of the spheroid solution.

	Diameter (mm)	Aspect Ratio	Angle (degrees)
A	82	5	40.5
B	138	5	84.0
C	138	2.82	57.2
D	327	0.06	53.4
E	327	0.31	33.4

(c) Spheroid dimensions, and their angles relative to the Earth's field, that produce the same dipole moment as a 105 mm projectile at 45° inclination.

Figure 4.4: Spheroid dimensions that can produce the same dipole as a 105 mm shell at 45 degrees inclination to the Earth's field.

4.2 Dipole modelling of TEM and Magnetics Data

In order to invert measured TEM and magnetics data for the physical parameters of the target, it is necessary to have forward models to describe the TEM and magnetic response for a buried metallic object. We restrict our forward model to axi-symmetric metallic targets, since this geometric subset adequately describes all UXO and much of the buried metallic scrap encountered in a remediation survey. We also assume negligible contribution of the host medium to the measured signal.

4.2.1 Magnetic Forward Modelling

Spheroids have been used to approximate the magnetostatic response of ordnance by several authors (Butler et al., 1998; McFee, 1989; Altshuler, 1996). The magnetic field induced in a spheroid by the Earth's field can be decomposed into a multipole expansion. The dipole term of the field is

$$\mathbf{b}^S = \frac{\mu_o}{4\pi r^3}\vec{\mathbf{m}} \cdot \left(3\hat{\mathbf{r}}\hat{\mathbf{r}} - \bar{\bar{\mathbf{I}}}\right), \tag{4.1}$$

where $\hat{\mathbf{r}}$ is the unit vector from the field measurement point and the spheroid center, $\bar{\bar{\mathbf{I}}}$, and $\vec{\mathbf{m}}$ is the induced dipole moment. The quadrapole term of the multipole expansion is zero due to the symmetry of the spheroid. The next non-zero term is the octopole moment which, for distances from the target that exceed a few body lengths, is negligible. Therefore, for many of the geometries encountered in UXO surveys, the response of a spheroid is accurately modelled by the dipole moment. The induced dipole moment can be written as

$$\vec{\mathbf{m}}_{Mag} = \frac{V}{\mu_o}\mathbf{A}^T\mathbf{F}^{Mag}\,\mathbf{A}\cdot\mathbf{b}^p_{Mag}, \tag{4.2}$$

where V is the spheroid volume, $\mathbf{A}$ is the Euler rotation tensor, $\mathbf{b}^p_{Mag}$ is the Earth's field, and $\mathbf{F}^{Mag}$ is the magnetostatic polarization tensor. The spheroid shape information is contained in the magnetostatic polarization tensor. We refer the reader to McFee (1989) for the functional relationship between the magnetostatic polarization tensor and the aspect ratio e and spheroid diameter a .

4.2.2 Time Domain EM Forward Modelling

In the time domain electromagnetic induction method a time-varying magnetic field is used to illuminate a conducting target. This primary field induces surface currents on the target which then generate a secondary magnetic field that can be sensed above ground. With time, the surface currents diffuse inward or decay due to Ohmic dissipation of eddy currents, and the observed secondary field consequently decays. The rate of decay, and the spatial behaviour of the secondary field, are determined by the target's conductivity, magnetic permeability, shape, and size.

The electromagnetic response of the target will be primarily dipolar (Casey and Baertlein, 1999; Grimm et al., 1997) for the target/sensor geometries of UXO surveys. The induced dipole has the same form as the magnetostatic dipole of equation (4.2)

$$\vec{\mathbf{m}}_{EM}(t) = \frac{V}{\mu_o}\mathbf{A}^T\mathbf{F}^{EM}(t)\ \mathbf{A}\cdot\mathbf{b}^P_{EM}, \tag{4.3}$$

where $\mathbf{A}$ is the Euler rotation tensor, $\mathbf{b}^p_{EM}$ is the primary field generated by the sensor transmitter loop, and $\mathbf{F}^{EM}$ is the electromagnetic polarization tensor. The target's shape, size, and material properties (i.e., conductivity and magnetic susceptibility) are contained in $\mathbf{F}^{EM}$. The primary field in the TEM case ($\mathbf{b}^P_{EM}$) will vary with transmitter/receiver location. In a typical survey, TEM soundings will be acquired at a number of different locations at the surface and the target will have been illuminated from several angles. As a result, the inherent ambiguity of the magnetic method is avoided. The polarization tensor $\mathbf{F}^{EM}(t)$ for an axi-symmetric target has the form

$$\mathbf{F}^{EM}(t)\begin{bmatrix} L_2(t) & 0 & 0 \\ 0 & L_2(t) & 0 \\ 0 & 0 & L_1(t). \end{bmatrix} \tag{4.4}$$

The analytic expressions for the time domain response are restricted to a metallic sphere, and even an expression for a permeable and conducting non-spherical axi-symmetric body is not available. Our approach, therefore, is to use an approximate forward model that can adequately reproduce the measured electromagnetic anomaly with minimal computational effort. In Pasion and Oldenburg

(2001a) the following form for polarization tensor elements was suggested:

$$L_i = k_i \left(t + \alpha_i\right)^{-\beta_i} \exp\left(-t/\gamma_i\right). \tag{4.5}$$

The validity of this reduced modelling was verified through a series of empirical tests (Pasion and Oldenburg, 2001b).

4.3 Cooperative Inversion of TEM and Magnetics Data

We formulate the cooperative inversion of TEM and magnetics as a three part procedure. Firstly the magnetic data are inverted to yield the best-fit magnetic dipole $\vec{\mathbf{m}}_{Mag}$. The recovered location of the dipole and the variance on the location are used as a priori information in the inversion of the TEM data. This results in an improved recovery of parameter values from which to perform TEM discrimination. In addition, the orientation of the item is obtained. This is the information required to obtain shape/size information from the magnetic data.

We demonstrate the cooperative inversion procedure using the Stokes mortar example of Figure 4.3. The mortar is located at a depth of 100 cm ($Z = 1.00$ m) and located at the center of the survey ($(X, Y) = (0, 0)$ cm). Synthetic Geonics EM63 TEM data were generated. The time channels range from 0.180 ms to 25 ms. Two noise components were added to the forward modelled response to make the TEM synthetic data set more realistic. First, a 5% random Gaussian noise was added. Second, the sensor noise floor was emulated by adding an additional Gaussian noise with a standard deviation of 0.5 mV. Synthetic magnetic data were generated by representing the Stokes mortar with a spheroid with an eccentricity of $e = 4.5$ and radius $a = 0.046$ m (volume $0.0018m^3$). A normal error with standard deviation of 2cm was added to the station location of the magnetic measurements. For both the TEM and magnetics data, stations were separated at 10 cm on lines separated by 50 cm.

4.3.1 Inversion of Magnetics Data

The first step of the cooperative inversion is to determine the dipole moment $\vec{\mathbf{m}}^{mag} = (\vec{m}_x, \vec{m}_y, \vec{m}_z)$ that produces the best fit to the observed magnetic data, and the location $\mathbf{R} = (X, Y, Z)$ of the best-

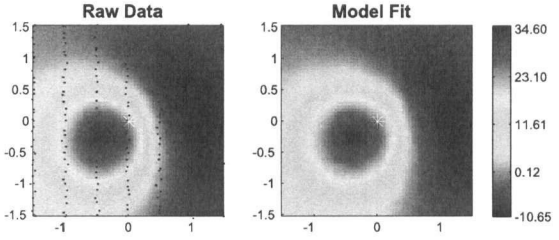

(a) Comparison of Observed Data and Predicted data for the Magnetics inversion

Parameter	Recovered
X (m)	0.01 ± 0.004
Y (m)	-0.01 ± 0.004
Z (m)	1.00 ± 0.005
Moment (Am^2)	0.5879 ± 0.0058
Azimuth (degrees)	86.3 ± 0.5
Dip (degrees)	-38.5 ± 0.4
Angle from Earth's field (degrees)	48.4 ± 0.3

(b) Recovered magnetic Dipole and Location

Figure 4.5: Results from the magnetics inversion step of the cooperative inversion. The black dots in (a) indicate sensor locations at which data are collected.

fit dipole. We define a model vector

$$\mathbf{m} = [X, Y, Z, \vec{m}_x, \vec{m}_y, \vec{m}_z, b]\,, \tag{4.6}$$

where the parameter b is a dc offset that is included to account for regional shifts in the data set. The parameters are recovered by solving equation 3.11. Variance estimates of the parameters are obtained by local error analysis (Pasion, 1999). Figure 4.5(a) compares the observed synthetic data and response predicted by the recovered parameters. The recovered parameters are listed in Figure 4.5(b).

4.3.2 Inversion of TEM Data with Location Constraint

The second step is to use the location information from the magnetics inversion to help stabilize the TEM inversion. The inversion methodology outlined in the previous step is applied to TEM data collected over the same target. The objective of this step is to obtain the following 13 model parameter vector

$$\vec{\mathbf{m}}_{EM} = [X, Y, Z, \phi, \theta, k_1, \alpha_1, \beta_1, \gamma_1, k_2, \alpha_2, \beta_2, \gamma_2]\,, \tag{4.7}$$

where the location (X, Y, Z) is constrained by the recovered magnetics location. We define a uniform prior centered on the recovered magnetics location and with a width equal to twice the estimated standard deviation. The TEM dipole parameters are constrained to be positive and have upper

bounds that are large enough to allow for the largest target expected in a typical survey. Figure 4.6 summarizes the cooperative inversion result. Figure 4.6(a) compares the data fit, and the table in Figure 4.6(b) compares the recovered and expected parameters. The location and orientation have

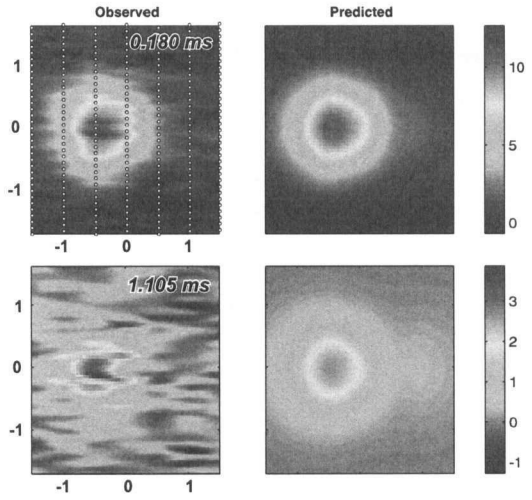

(a) Comparison of Observed Data and Predicted data for the TEM inversion

Parameter	Expected	Recovered
X (m)	0.00	0.01 ± 0.00
Y (m)	0.00	-0.01 ± 0.00
Z (m)	1.00	0.98 ± 0.00
Azimuth	90	89.7 ± 0.9
Dip	60	63.2 ± 0.7
k_1	43.9	41.76 ± 1.54
α_1	0.02	0.02 ± 0.04
β_1	0.73	0.78 ± 0.08
γ_1	9.1	40.0 (constraint)
k_2	4.9	6.40 ± 1.49
α_2	0.001	0.01 ± 0.1
β_2	1.09	0.96 ± 0.34
γ_2	10.8	8.89 ± 21.37

(b) Recovered magnetic Dipole and Location

Figure 4.6: Results from the TEM inversion step of the cooperative inversion.

been accurately recovered. The γ parameters are poorly recovered because they are constrained by the late time response which, for this example, is contaminated by the noise. The k parameters are accurately recovered and their values would be appropriate for characterizing the target.

4.3.3 Estimation of Shape and Size from Magnetics Data

The relationship between the size and shape of the best fit spheroid that can produce the observed dipole moment has been previously established (Billings et al., 2002). The functional relationship of the ordnance orientation and the induced dipole moment is

$$\vec{\mathbf{m}} = \begin{bmatrix} m^{\perp} \\ m^{\parallel} \end{bmatrix} = \frac{B_o \pi e a^3}{6\mu_o} \begin{bmatrix} (F_2 - F_1)\cos\theta \sin\theta \\ F_2 \cos^2\theta + F_1 \sin^2\theta \end{bmatrix} \tag{4.8}$$

where we choose a coordinate with axes parallel and perpendicular to the Earth's field (Billings et al., 2002). Without any additional information there are two known components of the dipole (we obtained dipole magnitude and angle from Earth's field from the magnetics inversion, thereby

allowing us to calculate $\vec{\mathbf{m}}^{\perp}$ and $\vec{\mathbf{m}}^{\parallel}$). We need to find three unknown parameters of the spheroid (a, e, θ). We need a constraint on the orientation in order to uniquely determine the demagnetization factors F_2 and F_1, and therefore the aspect ratio and size of the best fit spheroid.

When the orientation is obtained from the TEM inversion (azimuth 89.7^o and dip = 63.2^o) the recovered spheroid is 80 mm in diameter and has an aspect ratio of 5.5 (i.e., length = 44 cm, volume = 0.0015 m^3). The spheroid used to forward model the data (i.e., diameter = 90 mm, aspect ratio = 4.5, volume = 0.0018 m^3) is slightly longer and skinnier than the recovered spheroid but has approximately the same volume. Figure 4.7(a) shows some of the possible spheroids that can generate the magnetic dipole, and how knowledge of the orientation enables us to select a single spheroid. The solid line represents a suite of possible spheroids and the dotted line represents the ordnance orientation (relative to the Earth's field) recovered from the TEM inversion. The above method for determining the dimensions of the object will generally work well in the absence of any remanent magnetization. When remanence is present a modified method of identification using magnetics is to: (1) generate a list of possible ordnance, (2) determine the range of dipole moments that can be induced in each ordnance by varying the relative angle of the ordnance with the Earth's field, and (3) find which target requires the least amount of additional magnetization to reproduce the magnetic dipole recovered in the magnetics inversion. Figure 4.7(b) shows the possible induced dipole moments for a number of ordnance. Each ordnance item sweeps out an arc as its orientation is varied. The recovered dipole moment is plotted as a black star. Without knowledge of the orientation of each ordnance, the ordnance items can be ranked according to distance the recovered moment to the ordnance respective arcs. Knowledge of the ordnance orientation reduces each arc to a single point (indicated by a symbol on each arc), thereby refining our discrimination ability.

4.4 Joint Inversion of TEM and Magnetics Data

In both TEM and magnetostatic forward modelling, the response is approximated by the dipole produced by a spheroid. Ideally the joint inversion procedure would be to recover the location, orientation, and spheroid properties that can best reproduce the TEM and magnetostatic dipoles. The model vector in this ideal case would be

$$\mathbf{m} = [X, Y, Z, \phi, \theta, a, e, \mu, \sigma, \mathbf{m}^{REM}], \tag{4.9}$$

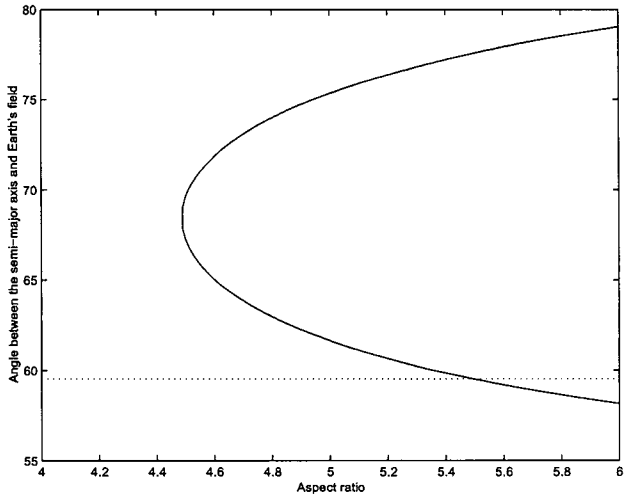

(a) Constraining spheroid size and shape with the orientation from the TEM inversion.

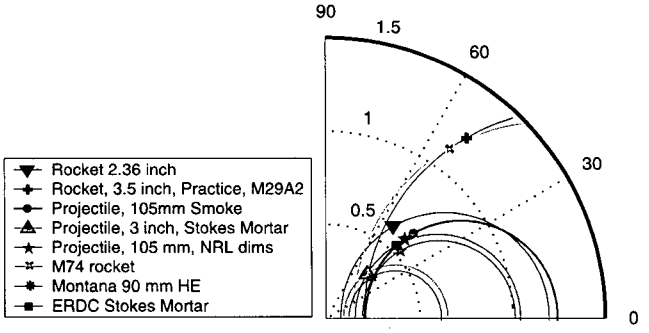

(b) Comparing the possible dipole moments oriented between 0 and 90 degrees from a collection of ordnance.

Figure 4.7: Using orientation information for constraining the recovered spheroid shape.

where (X, Y, Z) is the location, ϕ and θ represent the orientation, and $\mathbf{m}^{REM}$ is the remanent magnetization of the target. The spheroid is characterized by a semi-major axis a, an eccentricity e, the magnetic permeability μ, and the conductivity σ. However, the TEM forward model does not allow the model parameters to be written as explicit functions of the spheroid dimensions and material properties. Therefore the only parameters common to both the TEM and magnetostatic forward modelling will be the location and orientation. Consequently, the model parameter vector which we seek to recover in the joint inversion procedure is

$$\mathbf{m} = [X,\ Y,\ Z,\ \phi,\ \theta,\ F_1,\ F_2,\ k_1,\ \alpha_1,\ \beta_1,\ \gamma_1, k_2,\ \alpha_2,\ \beta_2,\ \gamma_2] \tag{4.10}$$

We invert for the magnetostatic polarization tensor components F_1 and F_2 (or equivalently the demagnetization factors) instead of the spheroid eccentricity and size, because the objective function is a much simpler function of F_1 and F_2 than the spheroid dimensions a and e.

The magnetics and electromagnetic surveys are independent geophysical experiments. The application of Bayes theorem for independent probability density functions gives

$$p\left(\mathbf{m}|\mathbf{d}_{obs}^{Mag}, \mathbf{d}_{obs}^{EM}\right) = \frac{p\left(\mathbf{m}\right) p\left(\mathbf{d}_{obs}^{Mag}|\mathbf{m}\right) p\left(\mathbf{d}_{obs}^{EM}|\mathbf{m}\right)}{p\left(\mathbf{d}_{obs}\right)}, \tag{4.11}$$

where we have defined a new observed data vector as $\mathbf{d}_{obs} = \left(\mathbf{d}_{obs}^{Mag}, \mathbf{d}_{obs}^{EM}\right)^T$. We again choose to maximize the log of the a posteriori probability density

$$\mathbf{m}^* = \arg\max_{\mathbf{m}}\{\log\left(p\left(\mathbf{m}|\mathbf{d}_{obs}^{Mag}, \mathbf{d}_{obs}^{EM}\right)\right)\} \tag{4.12}$$

$$= \arg\max_{\mathbf{m}}\{\log\left(p\left(\mathbf{m}\right)\right) + \log\left(p\left(\mathbf{d}_{obs}^{Mag}|\mathbf{m}\right)\right) + \log\left(p\left(\mathbf{d}_{obs}^{EM}|\mathbf{m}\right)\right)\}. \tag{4.13}$$

When assuming normally distributed errors in the data, the maximization of equation (4.13) is equivalent to minimizing the following objective function:

$$\Phi\left(\mathbf{m}\right) = \alpha\|V_d^{mag\,-1/2}\left(\mathcal{F}^{Mag}\left[\mathbf{m}\right] - \mathbf{d}_{obs}^{mag}\right)\|^2 + \left(1-\alpha\right)\|V_d^{tem\,-1/2}\left(\mathcal{F}^{Tem}\left[\mathbf{m}\right] - \mathbf{d}_{obs}^{Tem}\right)\|^2 \tag{4.14}$$

$$= \alpha\ \Phi^{Mag}\left(\mathbf{m}\right) + \left(1-\alpha\right)\Phi^{EM}\left(\mathbf{m}\right), \tag{4.15}$$

subject to constraints. The parameter α is introduced since we often only have knowledge of the relative difference in errors and not the absolute errors of each data set. The parameter α controls the relative degree to which we fit the misfit of the magnetics data and the TEM. If we know the value of the data errors for both data sets and can use an accurate value for the data covariance matrices then the expected value for the least squares data misfit is equal to the number of data. The value of α that would make the magnetics and TEM objective functions equal at solution would be

$$\alpha = \frac{N^{EM}}{N^{EM} + N^{Mag}}. \tag{4.16}$$

In general, it is not possible to accurately specify the variance of the data and modelling errors of the sensor data. Here, we estimate the value of the magnetics and TEM data misfit at the solution by inverting the data sets individually and using the final misfits as estimates. The value of α is then estimated as

$$\alpha = \frac{\Phi^{EM}\left(\mathbf{m}_*^{em}\right)}{\Phi^{EM}\left(\mathbf{m}_*^{em}\right) + \Phi^{Mag}\left(\mathbf{m}_*^{mag}\right)}. \tag{4.17}$$

where $\mathbf{m}_*^{em}$ and $\mathbf{m}_*^{mag}$ are the models recovered from inversion of TEM and magnetics data sets individually. We recognize that there will be situations where we may have poor estimates for the target misfit of the objective functions and a more rigorous exploration of the weighting parameter α is required.

The parameters recovered from application of this joint inversion methodology to the synthetic data set are listed in Figure 4.8. As was the case in the cooperative inversion, the low signal-to-noise in the late time channels does not allow for reliable recovery of the γ parameters.

4.5 Field Data Example

We demonstrate the cooperative inversion methodology on magnetics and TEM data collected over the calibration grid at the Yuma Proving Grounds UXO Standardized Test Site. Magnetics data were collected using a G-Tek Ltd. TM4 magnetometer array. The array consists of four Geometrics G-822 cesium vapour magnetometer and was configured with a sensor separation of 25 cm and position of 30 cm above the ground. TEM data were collected using a Geonics EM63 sensor. The Geonics EM63 measured the time decay of the targets at 26 time channels. The first and last time

m_i	**Expected**	**Recovered**
X (m)	0.00	0.0
Y (m)	0.00	0.0
Z (m)	1.00	1.0
Azimuth	90	90.0
Dip	60	61.6

(a) Location and Orientation

m_i	**Expected**	**Recovered**
F_1	21667	22435
F_2	3065	3356

(b) Magnetostatic polarization tensor components multiplied by volume.

m_i	**Expected**	**Recovered**
k_1	43.9	40.60
α_1	0.02	0.02
β_1	0.73	0.78
γ_1	9.1	40.0 (constraint)
k_2	4.9	6.44
α_2	0.001	0.01
β_2	1.09	0.97
γ_2	10.8	8.33

(c) TEM Dipole parameters

Figure 4.8: Parameters recovered by joint inversion. The recovered value for γ_1 falls on the constraint of 40.

channels are centered at 0.18 ms and 25 ms, respectively. Lines of EM63 data were collected at a spacing of 0.5 m. Any position and orientation difficulties associated with cart pulled sensors operating on rough terrain were negligible due to the level and smooth ground surface.

An image of the median filtered magnetics data is shown in Figure 4.9(a). An image of the first channel (t = 0.18 ms) of lag corrected and median filtered TEM data is shown in Figure 4.9(b). A comparison of Figures 4.9(a) and (b) reveals that the TEM data were less sensitive to the magnetic geologic material than the magnetics data. In particular, the large magnetic anomaly in the lower-right section of the anomaly did not produce a response in the TEM data. The relative insensitivity of the TEM data to the geology motivated us to perform target picking on the TEM data set. A target list was automatically generated by setting a threshold on the first channel TEM data. The final picks are overlayed on the magnetics and TEM images.

The cooperative inversion procedure involves inverting the magnetics data for the location of the target, and using the location information to constrain the inversion of the TEM data. Cooperative inversion was carried out for targets whose magnetics data contained sufficient signal strength and low enough geologic noise to enable accurate determination of the target's magnetic dipole moment. We review the steps of this procedure using data from a 105 mm M456 Heat projectile. The 105 mm is buried at (X,Y)=(12 m, 2 m) at a depth of 0.8 m with long axis horizontal. The data fit and recovered dipole moment parameters from inverting the magnetics data are shown in Figure 4.10.

Figure 4.11 shows the recovered dipole parameters and data fit, for the time channel centered at 7.07 ms, when inverting the TEM data both with and without using the estimate of the depth from the magnetics inversion as a constraint. Each location constraint is provided as a value x with a standard deviation ϵ. The parameter p in the constrained inversion is required to lie in the range $x - \epsilon \leq p \leq x + \epsilon$. In both cases the recovered model is able to accurately reproduce the observed data. Both inversions correctly predicted a horizontal target (the recovered dip reported in Figure 4.11 is measured from the vertical axis) and the horizontal location of the model is the same. However, the depth of the object from the unconstrained inversion differs from that of the constrained inversion. This example highlights the inability of TEM data alone to constrain the depth of the target. There is a trade-off between the depth of the dipole and the k parameters; the co-operative inversion recovered a dipole ($k_1 = 32.2$, $k_2 = 12.9$) at approximately the correct depth (depth = 0.79 m), while the unconstrained inversion places a stronger dipole ($k_1 = 47.2$,

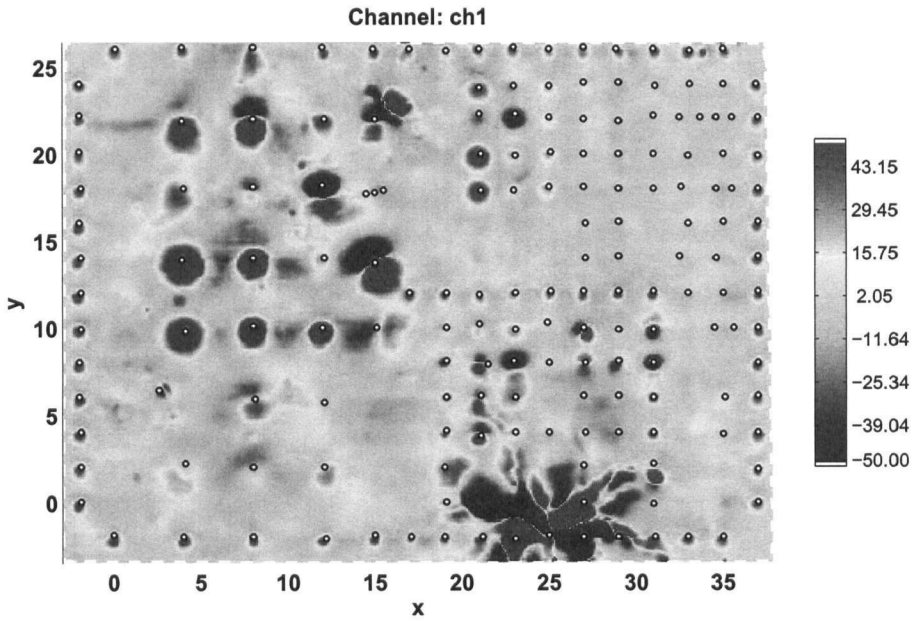

(a) Magnetics data.

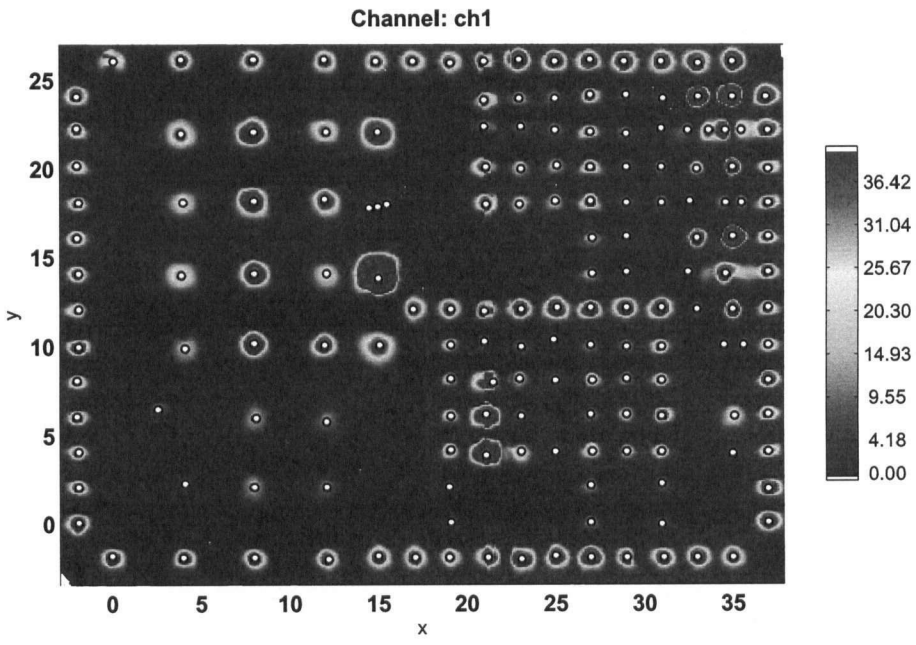

(b) First channel of Geonics EM63 data.

Figure 4.9: Magnetics and TEM data collected over the Yuma Proving Ground Calibration Grid. Picked targets are plotted as white circles.

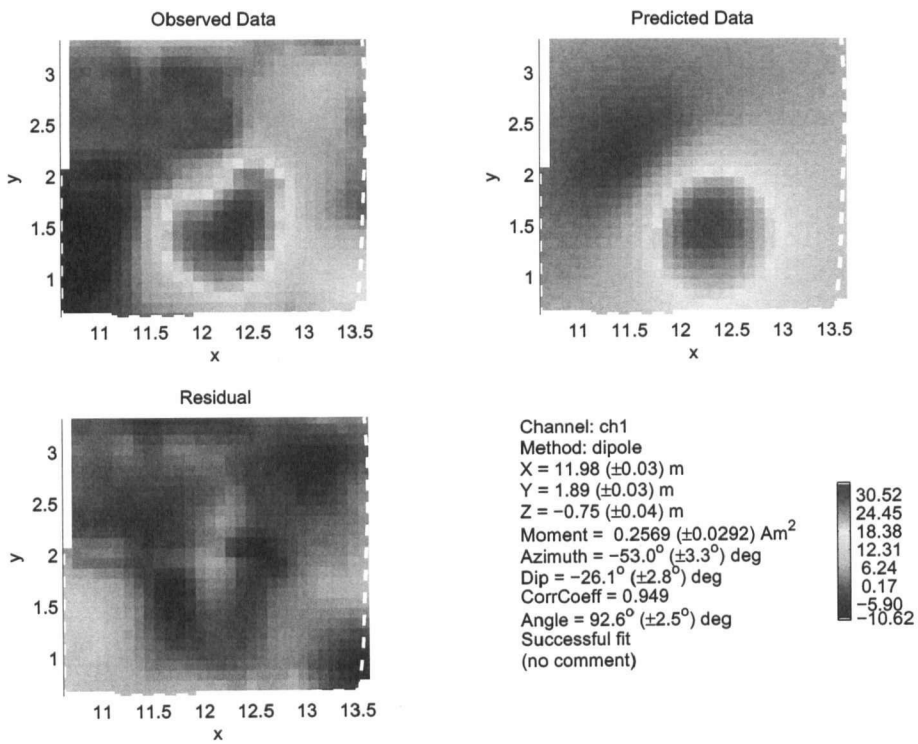

Figure 4.10: Magnetic data fit and recovered magnetics dipole parameters when inverting the 105 mm M456 Heat target.

$k_2 = 23.4$) deeper (depth = 0.96 m). The change in k values has the potential to alter one of our primary diagnostics: if the ratio $k_1/k_2 > 1$ then the object is interpreted as rod-like. Here we obtain 2.5 and 2.03 respectively for the constrained and unconstrained inversion. Remaining polarization tensor parameters (α, β, and γ) control the decay of the induced dipole and are similar for both inversions. In the constrained inversion the final value of the parameter is sometimes equal to one of the bounds. When this occurs we no longer have a good way to estimate uncertainties and we output the uncertainty as n/a.

By using the location information from the magnetics inversion we more accurately recover the TEM dipole polarization tensor parameters of the target. As an example, we can consider the inversion results for the steel spheres that are used to make the edges of the calibration grid. When we invert these spheres and plot them on a parameter plot we expect the points to be tightly clustered since all the spheres in the grid are similar in size and material properties. Figure 4.12(a) shows that by cooperatively inverting the data the recovered k parameters cluster much more tightly on a k_1 vs. k_2 parameter plot than when the TEM data are inverted without the magnetic data. Improvement in clustering of the β parameters is not achieved by the cooperative inversion (Figure 4.12(b)).

Figure 4.13 contains parameter plots including 5 of the target types (155mm, 105mm, 60mm, 40mm, and M75) in the calibration grid. The small number of anomalies for each target type make it difficult to draw a definite conclusion on the ability of cooperative inversion to more tightly cluster the parameters. Regardless of the few target anomalies, there appears to be marginal improvement of the clustering in the k_1 vs. k_2 parameter plot when the TEM is co-operatively inverted. There is no improvement in β parameter clustering.

4.6 Conclusion

In this chapter we considered two approaches to interpreting magnetics and TEM data sets: cooperative inversion and joint inversion. Both approaches utilize the ability of magnetics to accurately locate buried targets and the ability of TEM to recover the orientation of the target. Knowledge of the orientation of the target is required in order to uniquely determine the size and shape of the best fit spheroid. The accuracy of size and shape estimates of the spheroid depends on the amount of remnant magnetization in the target since we assume there is no remnant magnetization during the

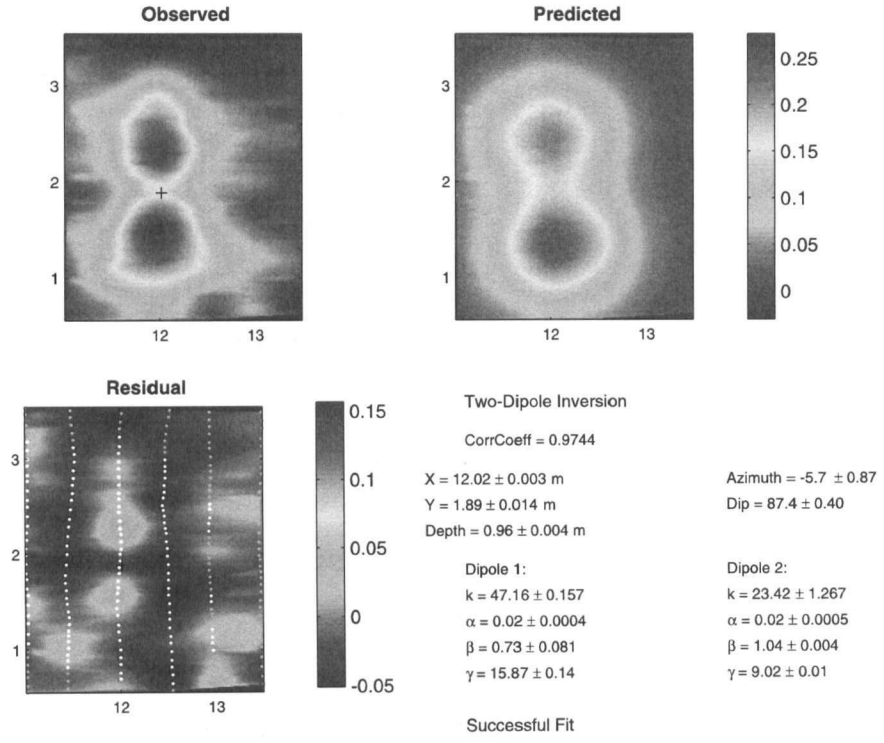

(a) Inversion of TEM data with no location constraints

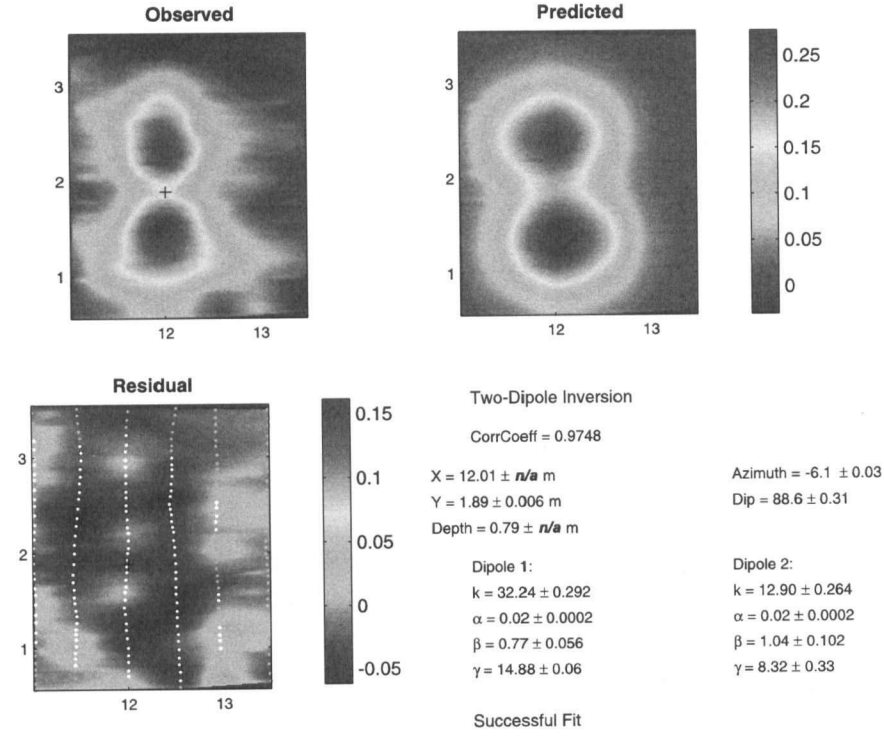

(b) Cooperatively inverted TEM data

Figure 4.11: TEM data fit and recovered dipole parameters when inverting the 105 mm M456 heat TEM data.

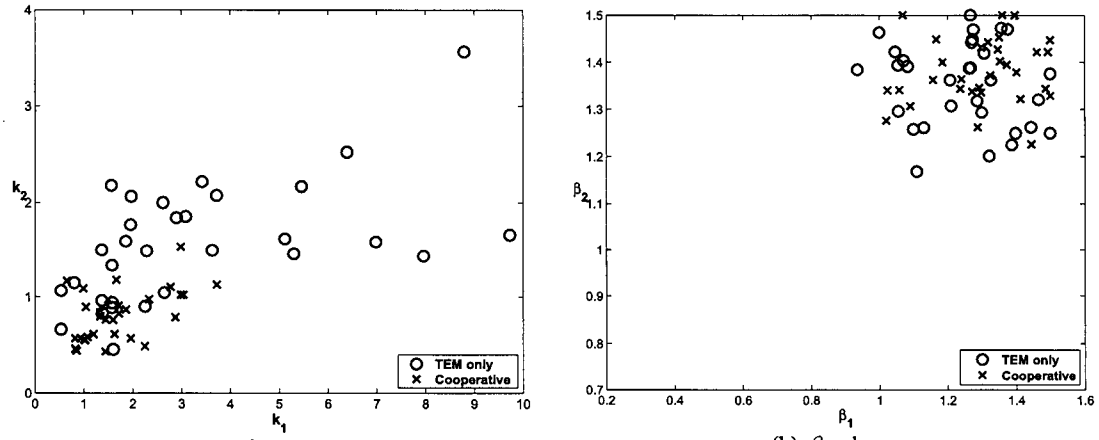

(a) k values (b) β values

Figure 4.12: Recovered k and β values when inverting spheres buried in the calibration grid.

calculation. Successful application of either the joint or cooperative inversion technique requires good absolute positioning of both the TEM and magnetic sensor data.

These techniques are demonstrated using synthetic magnetics and TEM data sets collected over a Stokes mortar. After demonstrating that individual inversions of the simulated data sets provided limited information on the buried target, we showed that both joint and cooperative inversions were able to estimate the size and shape of the buried target.

The cooperative inversion technique was demonstrated on data collected at the Yuma Proving Ground UXO Standardized Test Site Calibration Grid. Although more tests of the respective algorithms need to be conducted to assess performance in a field setting, the joint and cooperative inversion techniques have the potential to improve the current characterization and identification ability.

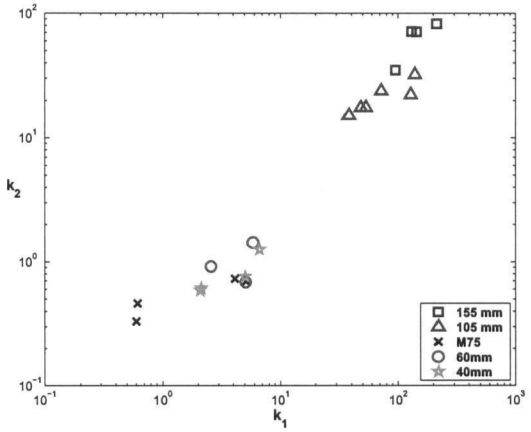

(a) Inversion of TEM data, no location constraints: k values

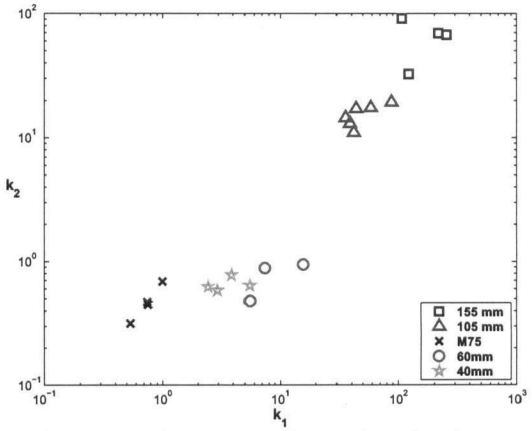

(b) Cooperatively Inverted TEM data: k values

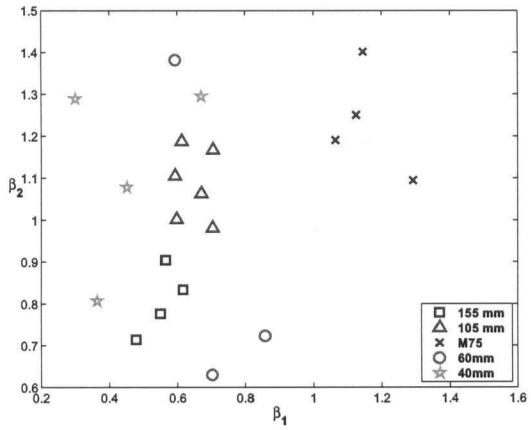

(c) Inversion of TEM data, no location constraints: β values

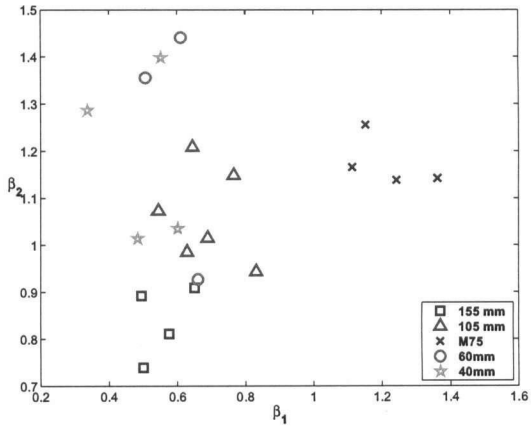

(d) Cooperatively Inverted TEM data: β values

Figure 4.13: Recovered k and β parameters when inverting TEM data anomalies from 155mm, 105mm, 60mm, 40mm, and M75 targets in the calibration grid.

Chapter 5

Application of a Simple Library Method for Identifying UXO

5.1 Introduction

The success of dipole model based discrimination algorithms depends on the accuracy with which the axial and transverse components of the polarization tensor can be estimated. In many cases the data are unable to constrain the inversion and hence the true polarization tensor could not be recovered (Pasion et al., 2004; Bell, 2005). Poor data quality, due to a low signal to noise ratio or survey design (for example, poor spatial coverage and inadequate illumination of both axial and transverse excitations), make the use of parameter estimation difficult. In such cases, a priori information can be introduced when searching model, or feature, space. Examples of a priori information include target location estimates from processing previously acquired data sets (for example, magnetics (Zhang et al., 2003; Pasion et al., 2003) or ground penetrating radar (Shamatava et al., 2004)), and restricting the model type to be rod-like targets. A further restriction in model space would be to assign higher probabilities to encountering specific targets. A simple implementation of this concept is to develop a list of candidate UXO likely to be encountered during a survey, then to determine, for each member of the library, the likelihood of generating the anomaly. Norton et al. (2001) and Riggs et al. (2001) use a frequency domain sounding collected at a single location for determining the optimal target from a library. For a single sounding, the measured response is a linear function of the dipole polarization tensor. Therefore these techniques are very fast, but do not utilize the additional information provided by utilizing data acquired a number of points spatially distributed on the surface above the target.

In this chapter we apply a simple library based technique to time domain electromagnetic data for the identification of UXO. High-quality test-stand data acquired over a collection of UXO are

inverted for polarization tensors. The polarization tensors are functions of the target only and, therefore, are used to characterize each member of the library. A simple matching scheme has been used to estimate the target type from measured TEM anomalies from this library of polarization tensors. For each polarization tensor within the library, a template is generated. The template is defined as the data predicted by the polarization tensor that best fits the observed data. Generating this template requires solving a non-linear inverse problem for the orientation and location of a target. Each of the data templates are then compared to the observed data. To determine if the anomaly is likely generated by one of the targets we can either find the template with the minimum error (for example, least squares) or the maximum correlation to the observed data. By not inverting for model parameters directly, we reduce trade-offs between polarization tensor values and orientation and position that can occur. This method is not meant to replace parametric inversion, but rather provides an additional analysis tool when working with data that does not support inverting for model parameters directly.

5.2 Method

The objective of our template matching analysis is to determine, from a list of M targets, the target that is most likely to have generated the observed data $\mathbf{d^{obs}}$. Each target in our list is characterized by its polarization tensor, which we represent by the vector $\mathbf{p}_i$. For each polarization tensor in our library, we determine the location r_i and orientation, represented by angles θ_i and ϕ_i, at which we can best fit the observed data $\mathbf{d^{obs}}$ by obtaining the maximum likelihood solution. The data predicted by this recovered model, $\mathbf{d_i^{pred}} = F[\mathbf{r}_i, \theta_i, \phi_i, \mathbf{p}_i] = F[\mathbf{m}_i]$, is referred to as the template for target i. The target template $\mathbf{d_i^{pred}}$ most similar to the observed data $\mathbf{d^{obs}}$ is selected as the most likely target.

There are several similarity measures with which we can compare the target templates with the observed data. Intuitively, these include measures of maximum correlation or minimum error. There are several ways with which to define the minimum error. Riggs et al. (2001) outlines the derivation of the minimum least squares from a generalized likelihood ratio test (GLRT) with Gaussian data

statistics. The likelihood ratio test for two targets is given by

$$\frac{p\left(\mathbf{d}_{obs}|\mathbf{p}_1\right)}{p\left(\mathbf{d}_{obs}|\mathbf{p}_2\right)} \underset{target2}{\overset{target1}{\lessgtr}} \frac{p\left(\mathbf{p}_2\right)\left(C_{01}-C_{11}\right)}{p\left(\mathbf{p}_1\right)\left(C_{12}-C_{22}\right)} \equiv \eta, \tag{5.1}$$

where C_{ij} is the cost of classifying the target as $\mathbf{p}_1$ when the target is $\mathbf{p}_2$, and $p\left(\mathbf{p}_i\right)$ is the prior probability. The GLRT is obtained by substituting the maximum likelihood estimate into (5.1). If we consider two targets with equal prior probability of producing the anomaly, and assuming that an incorrect classification produces the same cost, then $\eta = 1$. By taking the logarithm of the resulting expression, our decision criterion is to simply select the target that has the smallest least squares error

$$\|\mathbf{V_d}^{-1/2}\left(\mathbf{d^{obs}} - F[\mathbf{r}_1, \theta_1, \phi_1, \mathbf{p}_1]\right)\|^2 \underset{target2}{\overset{target1}{\lessgtr}} \|\mathbf{V_d}^{-1/2}\left(\mathbf{d^{obs}} - F[\mathbf{r}_2, \theta_2, \phi_2, \mathbf{p}_2)]\right)\|^2 \tag{5.2}$$

where $\mathbf{r}_i$, θ_i, and ϕ_i are the position and orientation that produces the best fits the observed data for the model $\mathbf{p}_i$. For multiple candidate targets we simply choose the target with smallest least squares misfit.

Application of the above algorithm to survey data requires establishing two thresholds. First, a minimum level of data quality must be established, since our confidence in identifying the correct target decreases with data quality. For data sets acquired with the same survey parameters (such as station density) for the entire data set, the critical measure of data quality is the signal to noise ratio. A second threshold to establish is a maximum misfit at which an anomaly can be labeled as a target within our library. Since the ability to distinguish differences between the observed data and the template data will depend on the quality of data, the minimum correlation threshold will also be dependent on the signal to noise ratio of the target. These thresholds can be established with training data or, if the survey noise can be accurately modeled, through simulations.

5.3 Results and Analysis

5.3.1 Development of a Target Library From Test Stand Data

Our UXO library consists 14 different targets: eleven items from the Aberdeen Test Center (ATC) Standardized UXO set and three ordnance from the Montana Army National Guard (MTARNG)

(Table 5.1). These items represent a cross section ordnance size from large to small and also include a few examples of sub-munitions. The ATC items were manufactured as inert UXO and have never been fired. The MTARNG items were fired and recovered from the Limestone Hills in Montana.

Table 5.1: Description of UXO in our target library.

Type	Description	Length (cm)	Diameter (cm)	Weight (lbs)
ATC 20 mm	20 mm M55	7.5	2.0	0.25
ATC 40 mm	40 mm M385	8.0	4.0	0.55
ATC M42	submunition	6.2	4.0	0.35
ATC BLU-26	submunition	6.6	6.6	0.95
ATC BDU-28	submunition	9.7	6.7	1.70
ATC MK118	MK118 rockeye	34.4	5.0	1.35
ATC 60 mm	60 mm M49A3	24.3	6.0	2.90
ATC 81 mm	81 mm M374	48.0	8.1	8.75
ATC M230	2.75" rockeye	76.1	7.5	18.20
ATC 105 mm	M456 heat rd	64.0	10.5	19.65
ATC 155 mm	155 mm M483A1	87.0	15.5	56.45
MTANG 76 mm	artillary	22.0	7.6	13.50
MTANG 81 mm	mortar	27.3	8.1	6.00
MTANG 96 mm	artillary	25.0	9.0	22.50

Geonics EM63 sensor time domain data were collected over each item at the U.S. Army Engineer Research and Development Center (ERDC) test stand facility in Vicksburg, MS. Each item was measured at three orientations and two depths. The test stand makes it possible to collect geophysical data with highly repeatable positional information. It also enables us to collect data in an environment free of background geologic responses with the ordnance placed at an accurately known position and orientation relative to the geophysical sensor. The sensor is mounted on a robotic arm that is controlled an external computer. Noise levels of the instrument were decreased by stacking multiple time domain decays at each sounding location.

The polarization tensors, represented by the set of decay parameters defined in equation 2.34, were determined by solving 3.11 for each set of data. Model constraints restricting the depth to within 10 cm of the true depth and orientation to within 5 degrees of the true orientation were implemented when inverting for the decay parameters. Figure 5.1 shows how the different targets separate within the (k_1, k_2) feature space. Each target is well grouped in this space, with some overlap. A rectangular box is drawn around each cluster. If the dipole model exactly described

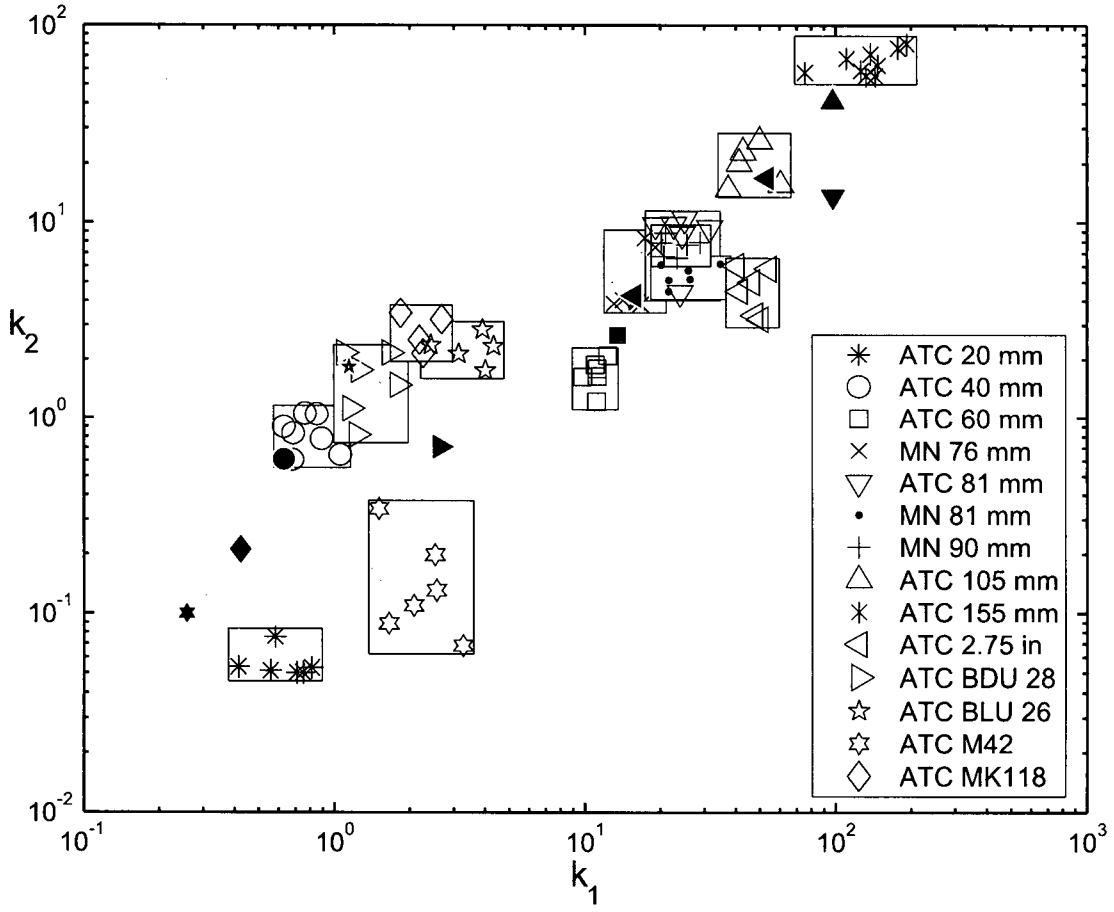

Figure 5.1: Comparison of k_1 and k_2 parameters derived from ERDC test stand data. Solid symbols represent results from inverting blind test data for the polarization tensor.

the response of each UXO, and if the data could constrain each inversion parameter, then each cluster would collapse to a single point in parameter space. We reduce the number of polarization tensors for each target in our library to a single polarization by using the median value of each decay parameter. Figure 5.2 plots the representative polarizations $L_1(t)$ and $L_2(t)$ for each target within the library.

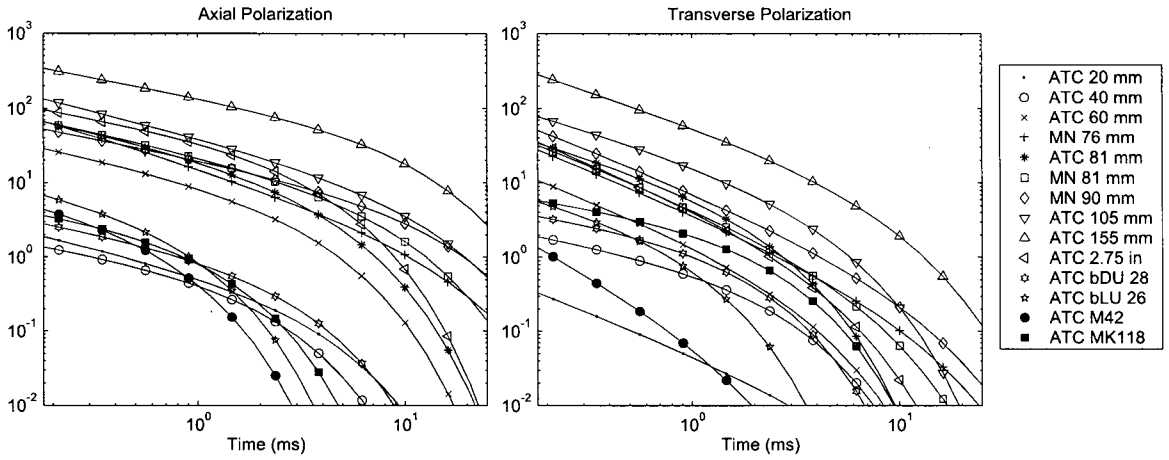

Figure 5.2: Axial ($L_1(t)$) and transverse ($L_2(t)$) polarization curves for targets within our library.

5.3.2 Application of the Library method to data collected at the Sky Research Ashland Test Plot Data

The library method was tested using data collected at the Sky Research UXO test plot in Ashland, Oregon (Figure 5.3). The test plot was seeded with a set of ordnance that included items from the ATC standardized test set, items from the MTARNG, as well as fragments of UXO. Multi-target and clutter scenarios are simulated within the test plot. The blind test, consisting of identifying the target present for ten anomalies within the test plot, was used to demonstrate the identification potential of the library procedure. This test represents the simplest identification problem for the library method since (1) each target was a member of the ordnance library and (2) each target anomaly was isolated (i.e., no overlapping signals due to nearby metal objects).

The library method was tested using dynamic and static collected data. Analysis of the statically collected data is carried out in Chapter 8. Dynamic data collection describes a typical detection survey data acquisition where an area is covered by a series of data transects. The Geonics EM63

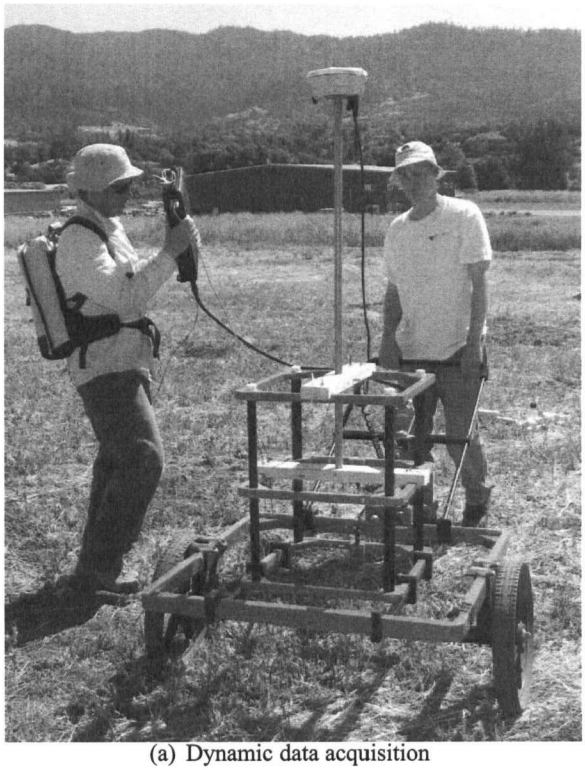

(a) Dynamic data acquisition

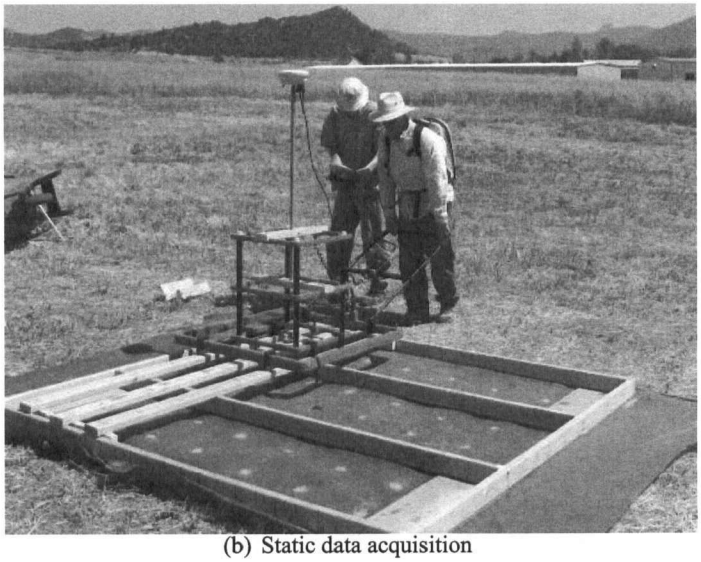

(b) Static data acquisition

Figure 5.3: Dynamic and static data acquisition modes using the Geonics EM63.

data were obtained with 0.5 m line spacing. A differential GPS was used for recording positioning. Long spatial wavelength background signal was removed from the data using a high pass filter.

In order to minimize equation (3.11), an estimate of the data covariance matrix V_d is required. For our data inversion we assume that the data errors are uncorrelated, and that the diagonal components of the covariance matrix are defined as $[V_d^{1/2}]_{ii} = 5\% \times d_i^{obs} + \sigma_i$, where σ_i is the standard deviation of the noise. The noise analysis in Walker et al. (2005a) is used for estimating σ_i. Figure 5.4 plots the signal to noise ratio for each time channel of the ten anomalies in the blind test. For each anomaly, only time channels with a signal to noise ratio greater than 5 were inverted. Data less than twice the standard deviation were not included in the inversion.

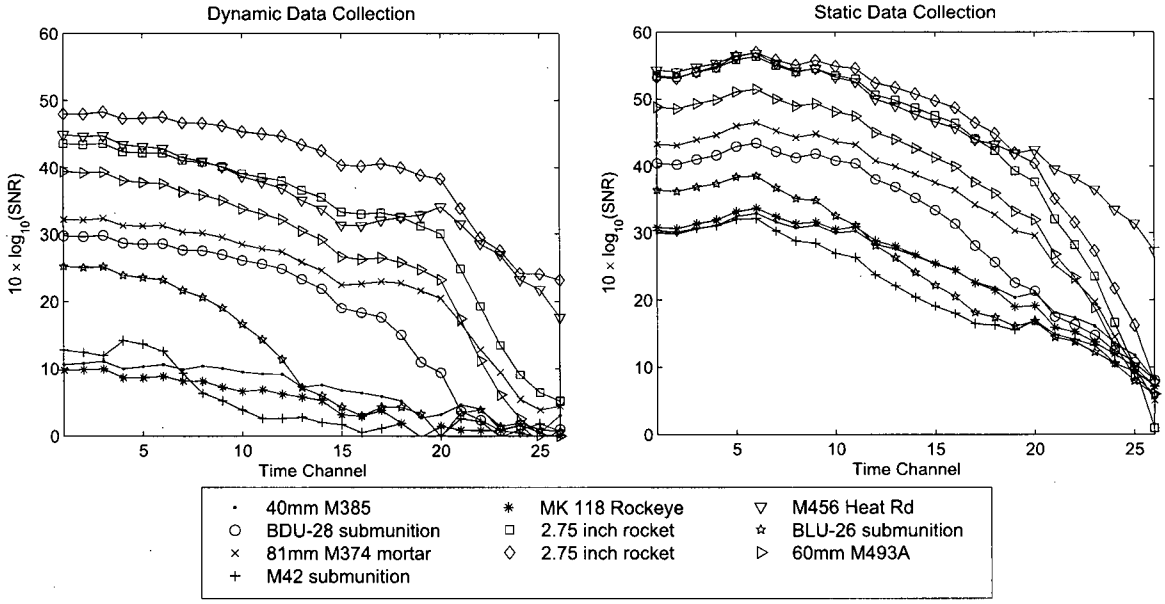

Figure 5.4: Comparison of signal noise ratio for data anomalies acquired statically and dynamically. The ten targets represent the targets in the blind test.

Figures 5.5 and 5.6 demonstrate the library technique on ATC M230 2.75 inch rocket data. The least squares solution was computed for each target in the library, and then the targets are ranked by their least squares misfit to the observed data. Figure 5.5 plots the fifteenth time channel of data of the observed data and the predicted data from the three targets that best fit the data. The quality of fit is quantified by the least squares misfit divided by the number of data N. Figure 5.6 shows the quality of fit of a TEM sounding measured directly above the target.

Results from applying the library technique to the dynamically collected data are summarized

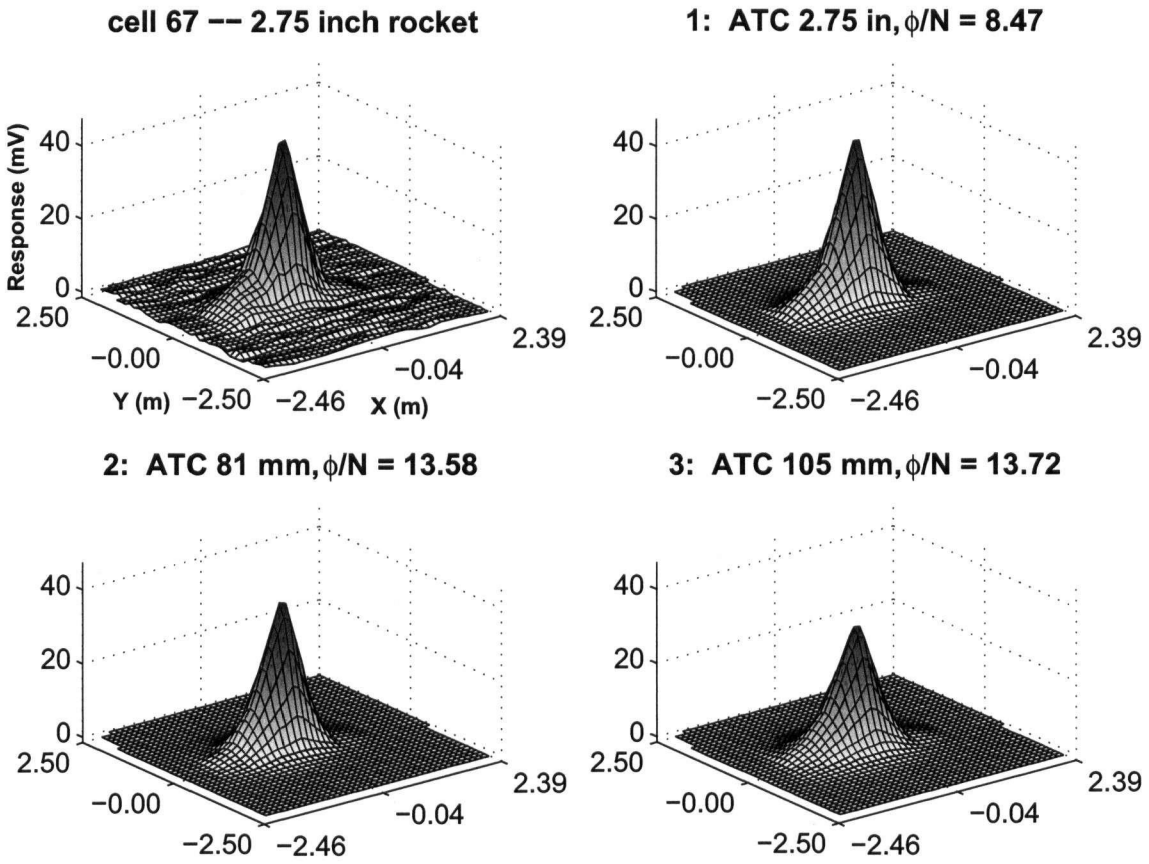

Figure 5.5: Application of the library method to dynamically collected data measured over an ATC M230 2.75 inch rocket. The upper left panel contains the fifteenth time channel of observed data. The remaining panels represent the three most likely targets, ranked according to the normalized misfit ϕ/N.

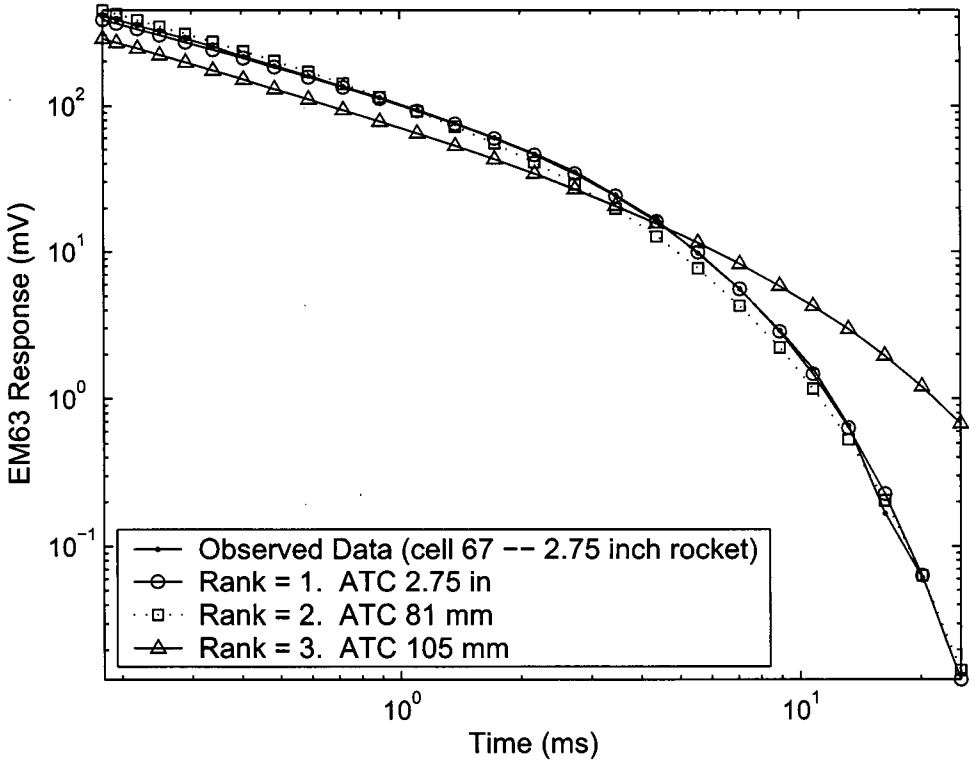

Figure 5.6: Application of the library method to dynamically collected data measured over an ATC M230 2.75 inch rocket. The best fit soundings observed at a point directly over the rocket is plotted.

in Table 5.2. A list of the library targets, sorted by each target's ability to fit the data, is formed

Actual Target	Estimated Target	Target List Rank	Normalized Misfit (ϕ/N)	Signal to Noise
ATC 40 mm M385	**ATC MK118 rockeye**	**3**	**0.8**	**241.0**
ATC BDU-28 submunition	**ATC MK118 rockeye**	**2**	**2.7**	**3007.1**
ATC 81 mm M374	ATC 81 mm M374	1	6.1	13046.7
ATC M42 submunition	ATC M42 submunition	1	0.7	203.9
ATC MK118 rockeye	ATC MK118 rockeye	1	0.6	243.1
ATC M230 2.75" rockeye	ATC M230 2.75" rockeye	1	8.5	50953.6
ATC M230 2.75" rockeye	ATC M230 2.75" rockeye	1	18.4	98099.4
ATC 105 mm M456 heat rd	ATC 105 mm M456 heat rd	1	8.9	69888.7
ATC BLU-26 submunition	ATC BLU-26 submunition	1	1.2	2011.4
ATC 60 mm M49A3	ATC 60 mm M49A3	1	4.1	14548.1

Table 5.2: Blind test results when inverting dynamically acquired data.

for each anomaly. The column labeled "Target Rank" indicates where the actual target was ranked by the algorithm. The column "Signal to Noise" is the sum of the signal to noise ratios calculated at each of the 26 time channels. The algorithm correctly identified 8 of 10 targets. The algorithm incorrectly classified the 40 mm as a MK118 Rockeye. This result is likely due to the anomaly from the 40 mm has a low signal to noise ratio (see Figure 5.4). The algorithm incorrectly classified BDU28 the anomaly as an MK118 Rockeye, while ranking the BDU28 as the second most likely target. Incorrect classification of the BDU28 may be due to similarities of the BDU28 and MK118 polarization tensors. Figure 5.1 shows an overlap of their respective k clusters.

For comparison purposes, the dynamically acquired data was also inverted for the polarization tensor. Figure 5.1 compares the recovered k values (plotted with solid symbols), with the k parameter clusters derived from the ERDC test stand data. If we define identification according to the cluster closest to the recovered parameter, then the inversion would have correctly identified three of the ten targets. Due to the noise levels of the data, parametric inversion on this dynamically collected data set is less successful than using the template approach.

Following the blind test, the library procedure was further tested by processing the remaining anomalies from the dynamically acquired test plot. The remaining anomalies include single isolated targets both belonging and not belonging to our library, and target anomalies obscured by responses from nearby sources. Table 5.3 summarizes the results of applying the method to the single, isolated test plot targets that are also members of the library. There are 41 anomalies from single, isolated

targets. Of these 41 anomalies, 29 were correctly identified, 6 of the anomalies had the correct target ranked second, and 3 of the anomalies had the correct target ranked third. Misclassified targets are generally due to low signal to noise ratios.

Cell	Actual Target	Rank	ϕ/N	SNR
56A	ATC 20 mm	7	1.1	176.7
56B	ATC 20 mm	1	2.4	2423.7
56C	ATC 20 mm	3	0.8	241.0
57A	ATC BDU 28	2	0.8	491.3
57B	ATC BDU 28	2	2.7	3007.1
57C	ATC BDU 28	4	2.2	2124.3
60	ATC 81 mm	1	6.1	13046.7
61	ATC 81 mm	2	1.1	2433.1
62	ATC 81 mm	1	7.2	57351.1
63	ATC 2.75 in	1	4.1	23445.1
64A	ATC 40 mm	3	0.8	533.6
64B	ATC 40 mm	2	1.4	939.5
64C	ATC M42	1	0.7	203.9
64D	ATC M42	1	1.4	768.7
65A	ATC MK118	1	0.6	243.1
65B	ATC MK118	3	0.6	503.3
65C	ATC MK118	1	1.4	4158.5
65D	ATC 60 mm	1	1.8	4602.7
67	ATC 2.75 in	1	8.5	50953.6
68	ATC 2.75 in	1	18.4	98099.4
69	ATC 105 mm	2	3.3	1395.2
70	ATC 105 mm	2	4.2	10556.9
71	ATC 105 mm	1	8.9	69888.7
72A	ATC M42	1	2.0	3022.0
72B	ATC bLU 26	1	1.2	2011.4
72C	ATC bLU 26	1	4.3	3839.7
72D	ATC bLU 26	1	2.3	2120.3
73A	ATC 60 mm	1	8.1	63828.2
73B	ATC 60 mm	1	4.1	14548.1
75	ATC 155 mm	1	6.5	17542.9
76	ATC 155 mm	1	8.2	74554.2
77	ATC 155 mm	1	16.0	347888.0
78	MN 76 mm	3	2.7	3073.5
79	MN 76 mm	1	1.9	15164.6
80	MN 76 mm	1	5.6	50001.3
81	MN 81 mm	1	8.5	3269.2
82	MN 81 mm	1	8.2	44246.4
83	MN 81 mm	1	4.5	32537.6
84	MN 90 mm	1	3.7	7038.2
86	MN 90 mm	4	4.9	64553.1
87	MN 90 mm	1	6.9	50964.7

Table 5.3: Blind test results when inverting static data.

In order for the library method to be an attractive technique for processing TEM data, we must be able to identify anomalies due to targets not included in our target library. Figure 5.7 has an example of fitting non-UXO scrap. The secondary anomaly in the data, to the right of the main peak, was assumed to be from an adjacent target and, therefore, not included in the data fitting. The metallic scrap is a fragment from a 105 mm white phosphorous round, and is not included in our library of targets. The normalized misfit is larger than most of the fits in Table 5.3, indicating that none of the templates from our library fits the data well. This suggests that a threshold on the normalized misfit could be established for classifying the target as a member of our library. However, the misfit is sensitive to non-dipolar features in the noise. For example, cell 68 containing a 2.75

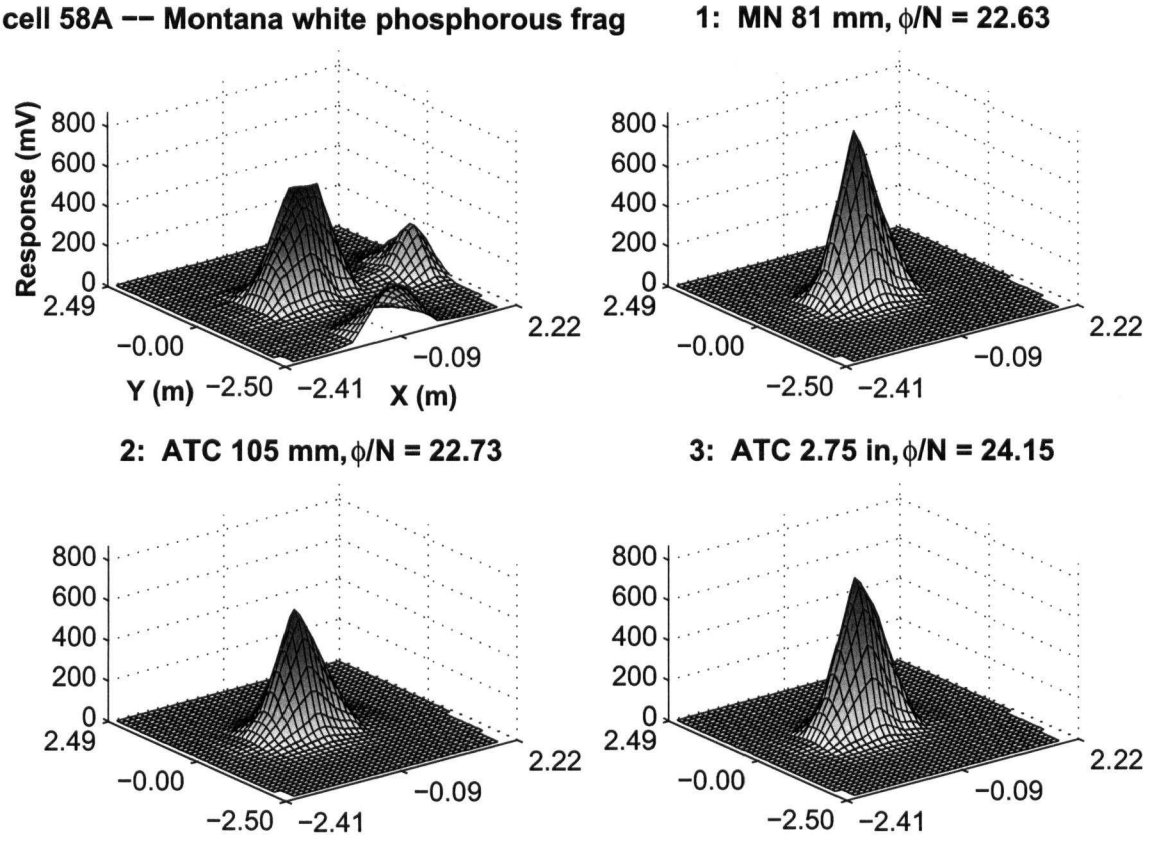

Figure 5.7: Fitting results when applying the library matching to a metal scrap not included in the library. The normalized misfit is higher than when fitting targets within the library.

inch rocket, has nearly the same normalized misfit due to signal at late time not being accurately modeled (Figure 5.8). There are not enough targets in this example to establish a reliable threshold. Application of this method to real world UXO applications should be preceded with careful noise analysis of the data and Monte Carlo studies for establishing a useful threshold for classification.

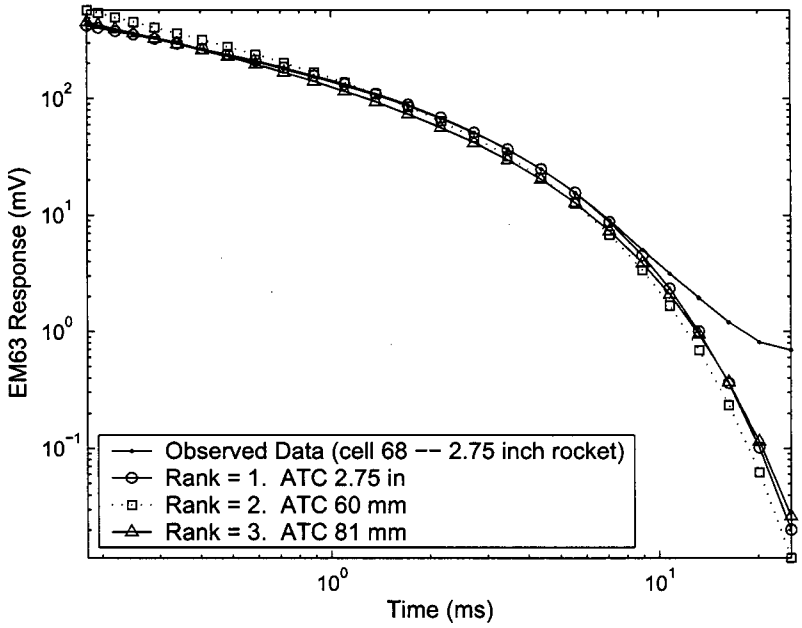

Figure 5.8: Application of the library method to cell 68 containing a 2.75 inch rocket. Even though the anomaly was correctly identified, the feature in the data at late time result in an atypically large misfit.

5.4 Fitting both dipole and soil parameters simultaneously

In this section, the statically collected data, representing a "cued interrogation" style of data acquisition, is processed. Static data were collected by placing a Geonics EM63 sensor without wheels on a portable test stand positioned over the target (Figure 5.3(b)). The test stand was used to increase positioning accuracy and to reduce instrument noise by stacking multiple TEM soundings. Data were collected over a 1.8 m square area with measurements on a uniform grid with 30 cm station spacing. When placed on the stand, the transmitter coil of the EM63 was located 15 cm from the ground. By being closer to the ground and being placed on a platform, the signal to noise ratio of the data is improved (Figure 5.4). However, the close proximity of the transmitter coil to the ground

produced a significant soil response. Since the data were collected over 1.8 m square areas, a high pass filter could not be used to remove the background response. Therefore when solving for the least squares misfit (equation 5.2) of each library target, a background soil model was included and the least squares problem is

$$\text{minimize} \quad \Phi(\mathbf{m}) = \frac{1}{2}\|\mathbf{V}_{\mathbf{d}}^{-1/2}\left[\mathbf{d}^{obs} - \left(F[\mathbf{m}] + \frac{A}{t}\right)\right]\|^2, \tag{5.3}$$

where $F[\mathbf{m}]$ represents a dipole forward model, and the soil model is represented by A/t. The A/t soil model is suitable for laterally uniform viscous remnant magnetic soil. This form of the soil model is explained in Chapter 7. Therefore, for each target in the library we solve for three location parameters, two orientation angles, and an amplitude of the background soil response. Similar to the dynamic case, data less than twice the standard deviation of the noise were not included in the inversion.

Results from applying the library technique to the statically collected data are summarized in Table 5.4. The algorithm correctly identified nine of the ten targets. The only misclassified anomaly was from a MK118 Rockeye. The algorithm classified the target as BDU28 submunition, while determining the MK118 Rockeye to be the fourth most likely library target. The data fit for this case is good as is demonstrated by Figure 5.9 and the low normalized misfit (Table 5.4). The incorrect identification of the MK118 Rockeye may be related to a tradeoff between the parameter modeling the relatively large background soil signal in the data (approximately 20 mV in the first time channel) and the polarization tensor (Figure 5.10). In addition, the anomaly was only partially sampled due to the test stand not being centered on the target, therefore less data is available to constrain the result.

5.5 Application to Field Data from Camp Lejeune, North Carolina

The library method was applied to Geonics EM63 data collected at the Marine Corps Base Camp Lejeune in North Carolina. Figure 5.11 contains a grayscale image of the gridded first channel of data. Red crosses indicate anomalies that were picked, and blue triangles represent locations at which there were groundtruth. Of the picked anomalies, 86 were excavated and verified (Figure 5.12). The 86 verified targets consisted of 15 UXO and 71 non-UXO, which included junk, OE

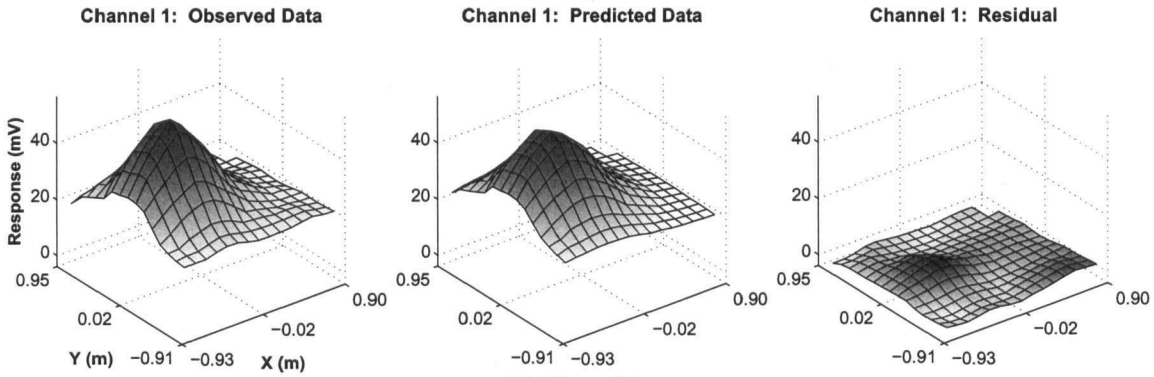

(a) Channel 1

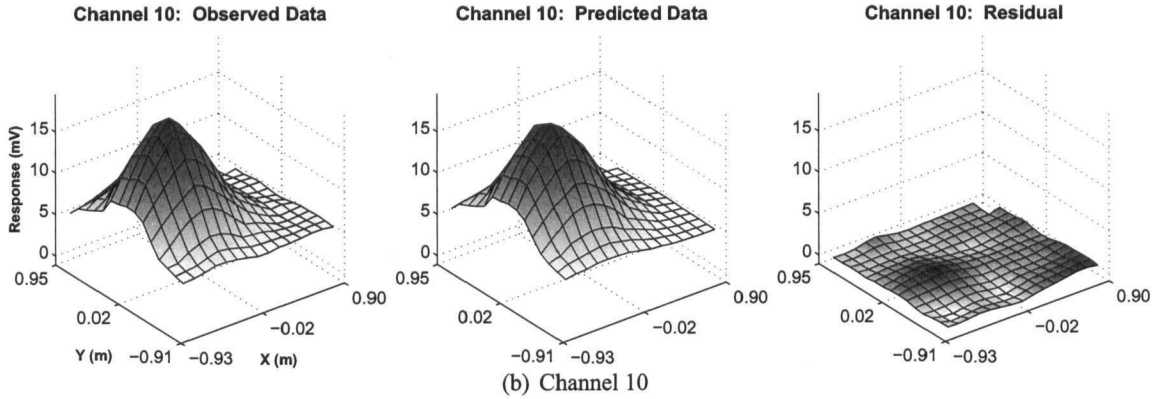

(b) Channel 10

Figure 5.9: Data misfit when applying the library method to data statically collected over an ATC MK118. The algorithm incorrectly classified this target.

Actual Target	Estimated Target	Target List Rank	Normalized Misfit (ϕ/N)	Signal to Noise
ATC 40 mm M385	ATC 40 mm M385	1	1.5	9596.3
ATC BDU-28 submunition	ATC BDU-28 submunition	1	1.1	100591.2
ATC 81 mm M374	ATC 81 mm M374	1	3.1	201625.7
ATC M42 submunition	ATC M42 submunition	1	0.9	6931.8
ATC MK118 rockeye	**ATC M230 2.75" rockeye**	**4**	**1.1**	**11010.5**
ATC M230 2.75" rockeye	ATC M230 2.75" rockeye	1	3.6	1972452.7
ATC M230 2.75" rockeye	ATC M230 2.75" rockeye	1	2.3	2382358.6
ATC 105 mm M456 heat rd	ATC 105 mm M456 heat rd	1	4.6	2135632.3
ATC BLU-26 submunition	ATC BLU-26 submunition	1	1.0	27950.4
ATC 60 mm M49A3	ATC 60 mm M49A3	1	1.2	619430.8

Table 5.4: Blind test results when inverting static data.

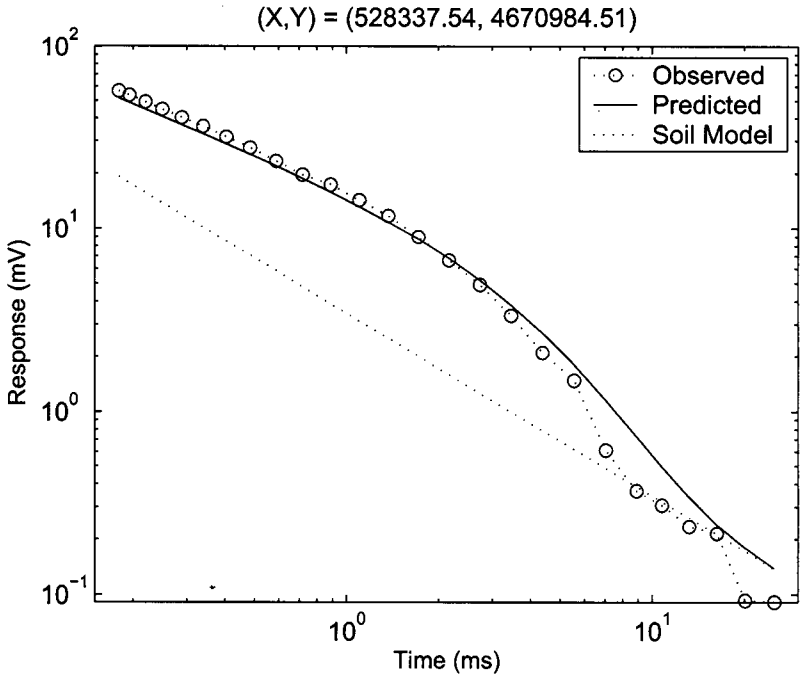

Figure 5.10: Data misfit for a sounding taken directly over an ATC MK118. The estimated soil noise is of approximately the same order as the data, possibly causing the difficulty in correctly identifying the target.

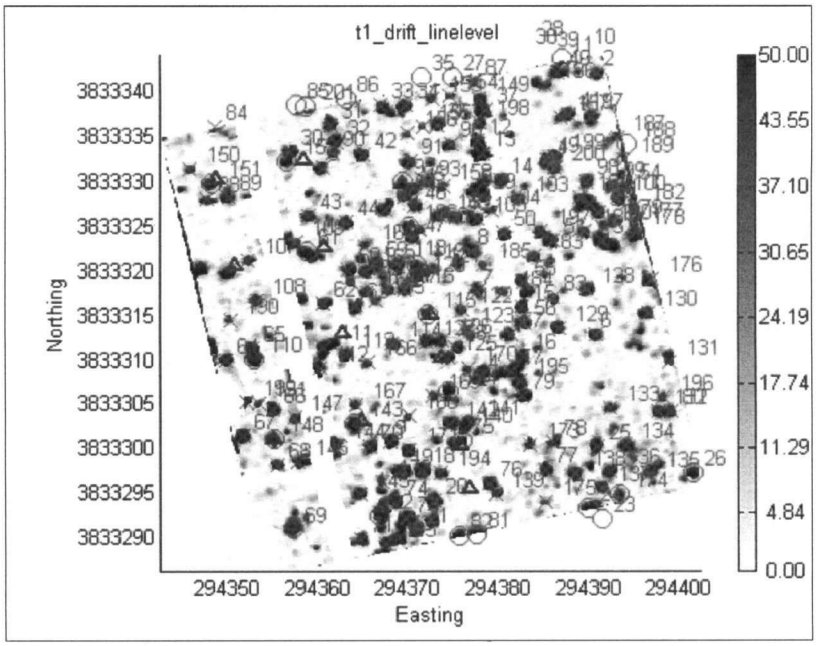

Figure 5.11: First channel of Geonics EM63 data collected on the Grid A1 at the Marine Corps Base Camp Lejeune in North Carolina. The red crosses are picked anomalies.

scrap, and adapters. The adapters are cylindrical pieces of aluminum that were discharged from guns when firing one of the ordnance types at the site. The adapters were the bulk of the non-UXO targets, and successful discrimination on this grid requires accurate classifying of anomalies due to adapters. This grid represented the optimal situation for discrimination since (1) the scrap consists of mainly a single target type, (2) since the adapter is aluminum, the decay characteristics of the main source of scrap will be very different from the steel UXO, and (3) the polarization tensor for this target could easily be determined through a few measurements.

The template matching algorithm was applied to data collected over Grid A1. The polarization library of consists of 6 items: ATC 40 mm, Montana 90 mm, Lejeune 3.5 inch rocket, Lejeune 105 mm, ATC 105 mm, and the Lejeune Adapter. The polarization tensors of the Lejeune items were derived from measurements made over a test pit at the site (Figure 3.17. The 86 anomalies with ground-truth were inverted. A dig list created by (1) classifying all anomalies whose best fit with the Adapter polarization to be non-UXO, and (2) sorting remaining anomalies by their misfit, such that those anomalies that could be well fit by one of the ordnance items in the library would be highly ranked. The receiver operator characteristic (ROC) curve of Figure 5.11 summarizes the performance of the fingerprint algorithm. A prioritized dig-list based on the fingerprint algorithm

(a) An adapter

(b) Photo of items excavated from Grid A1

Figure 5.12: Photos of adapters at the Camp Lejeune site.

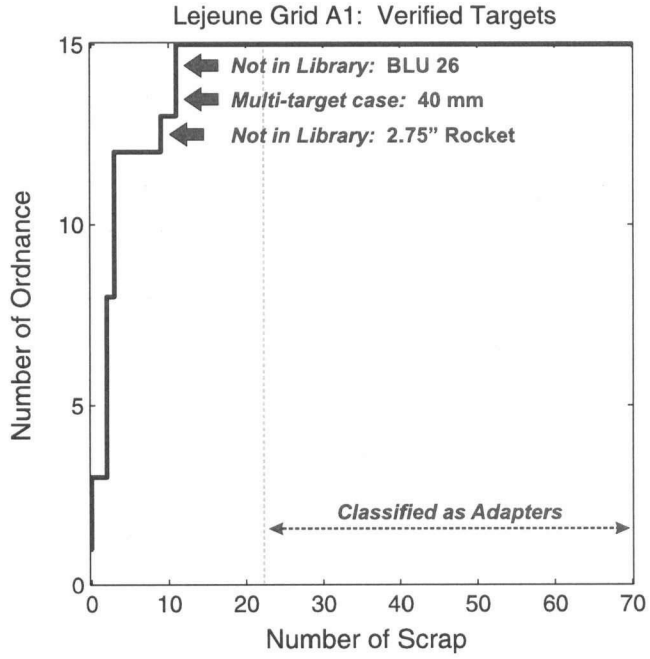

Figure 5.13: Receiver Operator Characteristic curve for the fingerprinting method applied to Grid A1.

would have resulted in all of the 15 UXO being recovered with only 11 scrap being excavated. The low false alarm rate can be attributed to the ability to correctly classify the numerous adapters. The UXO with the lowest priority for excavation are indicated by red arrows in Figure 5.13. These three targets had poorer misfits than the other UXO due to not being in the library of polarizations (BLU 26 and 2.75 inch rocket) or due to the target being an overlapping anomaly/multi-target case.

5.6 Conclusion

In this chapter we applied a simple library based technique for processing time domain electromagnetic data. This technique avoids direct inversion for polarization tensor parameters, making it more feasible for cases where sensor data quality might not be sufficient to support confident estimation of model parameters. The performance of the algorithm is limited by the data quality and the differences of polarization tensors for different targets. Targets with similar polarization tensors would be indistinguishable with this algorithm.

This library based technique can be applied to any type of electromagnetic sensor. Indeed, the performance of the technique would improve if the data were able to sense each of the three stages of the time decay, since the magnetic crossover time, the power law decay, and the fundamental time constant each contain information on the shape and material properties of the target. If the data were sensitive to non-dipole features of the response, non-dipole type models could be implemented. If these models had parameters that reflect the target shape features that produce higher order poles, there would likely be a greater separation within parameter space (compared to dipole polarization models) and better performance of the library technique.

Geonics EM63 data acquired in dynamic and static modes were used to test this technique. A blind test demonstrated an ability to accurately identify single targets when the target was a member of the UXO library. Misidentification of single targets was due to either low signal to noise ratios of data anomalies or because different items had similar polarization tensors. In cases where there was a significant background signal due to magnetic ground, the library technique showed improved performance by simultaneously solving for the best fit background soil model with the dipole parameters.

The library technique was applied to data collected at Marine Corps Base Camp Lejeune in

North Carolina. The method produced a a prioritized dig-list that resulted in all of the 15 UXO being recovered with only 11 scrap being excavated. The low false alarm rate can be attributed to having the most prevalent non-UXO target being part of the target library.

This summarizes some preliminary tests of the library method. Before this method can be implemented in a practical setting, tests are required to determine robustness to noise and other data quality factors, such as positional accuracy and spatial data coverage. Work is required to determine an optimal measure for determining whether we can classify an anomaly as coming from a target that is not a member of the library. A series of Monte Carlo style simulations should be carried out in order to investigate these questions.

Chapter 6

Establishing Data Quality Requirements for Inversion and Discrimination Using Simulations

The general approach to the interpretation of TEM data involves three steps: (1) detection, (2) inversion, and (3) discrimination. Detection involves identifying anomalies of interest within the TEM data. Inversion is the estimation of parameters that characterize the size, shape, and material properties of the target that produced the anomaly. In the case of TEM, the parameters most often inverted for are the elements of the magnetic polarization tensor of the induced electromagnetic dipole. A dipole's magnetic polarization tensor is a good candidate for inversion since the electromagnetic response measured by current sensors is primarily dipolar, and the elements of the tensor are functions of the size, shape, and material properties. Discrimination describes the process of determining the likelihood that a UXO produced the anomaly. A feature vector is defined which includes (but is not restricted to) the estimated parameters obtained from inversion. Physics-based or statistics based discrimination rules are developed that can be applied to the feature vectors of observed anomalies.

Discrimination performance is dependant on the ability to accurately determine a target's polarization parameters. The accuracy of the inverted polarization parameters depends directly on the quality of the TEM sensor data. Advanced discrimination routines utilizing parameters of a dipole model have been successfully demonstrated at a number of geophysical prove-out sites and demonstrations. However, surveying conditions at these seeded sites are atypical of field conditions. Not surprisingly, the transition of advanced discrimination techniques to real-world field sites have produced mixed, and often poor, results. Indeed, there have been instances of hospitable field conditions where data quality was still insufficient for implementation of advanced discrimination

techniques.

In order for inversion and characterization to become an effective and integral component of data processing strategies, the data must be of sufficiently high fidelity to support advanced discrimination. In this chapter we use Monte Carlo analysis to determine how variations in data noise and variations in survey parameters affect the ability to recover magnetic polarization tensor parameters from TEM data anomalies of single, isolated targets. In addition to identifying existing TEM data sets where inversion can be reliably applied, an understanding of data quality requirements will aid geophysicists in designing surveys that balance the cost of surveys with the savings achieved by having a reduced false alarm rate.

This chapter is drawn from the report *Guidelines On Data Quality Requirements for Advanced Discrimination of UXO* (Pasion et al., 2004). In the interest of space, additional supporting plots and figures that can be found in that report were not included here.

6.1 Factors affecting data quality

We define data quality in terms of the amount of information about the target that can be derived from the data. Factors that affect data quality include the choice of electromagnetic sensor, the method of mobilizing the sensor, the method for obtaining positional information, and survey design.

Choice of TEM sensor Sensor specific noise sources include the inherent instrument noise (i.e. noise measured in a static, target free setting) and motion related mechanical vibration noise. The design of transmitter, receiver and associated electronics can vary greatly across different models of TEM sensors. As a result the noise characteristics can be quite different for each sensor. Recently, EM sensors have been designed with the ability to change the direction of the illuminating field in an attempt to better illuminate the different polarizations of the target. In addition, sensors are now available with multiple receivers to measure the multiple components of the secondary field. These developments provide improvements in data quality.

Survey Design There are generally two modes of data collection: line data and cued interrogation. Line data is collected by a sensor platform moving along a series of lines. Line data is the most

commonly collected type of data due to the ease and efficiency of covering a survey area. Cued interrogation involves resurveying a target with a small grid of data. Data can then be acquired in a static mode, thereby improving positional information and reducing (or eliminating) vibration or motion induced noise.

Recording of positional information Sensor position and orientation are required for accurate modelling of data. Global Positioning System (GPS) and Robotic Total Station (RTS) are popular technologies for recording position, but they are not accurate and there is still random positioning error at each location. Dynamic platforms for sensors, such as wheeled carts, introduce additional positioning error due to the movement of the GPS antennas and RTS prisms relative to the sensor. If positioning is recorded via a cotton thread or wheel odometer, a more systematic error in positioning, where entire lines can shift, can be introduced.

Non-UXO signal sources During an EM survey, there are a number of signal sources that are not due to UXO. Examples include signal from power lines and the presence of geologic noise. These signals are listed as noise sources since they are not included in the forward modelling. Pre-inversion data processing is applied to reduce the effects of these noise sources on interpretation.

6.1.1 Signal to Noise Ratio

There are many different types of noise and each has its own mathematical representation. One of the most common ways of describing noise is to assume that it is random and can be represented by Gaussian statistics, $N(0, \sigma)$, that is unbiased noise with a standard deviation σ.

The random noise sources are quantified with the signal to noise ratio

$$SNR = \frac{E_s}{E_n}, \tag{6.1}$$

where the signal energy E_s for N observations of sensor data $d_n^{obs}, n = 1..N$, is

$$E_s = \sum_{n=1}^{N} \left(d_n^{obs}\right)^2. \tag{6.2}$$

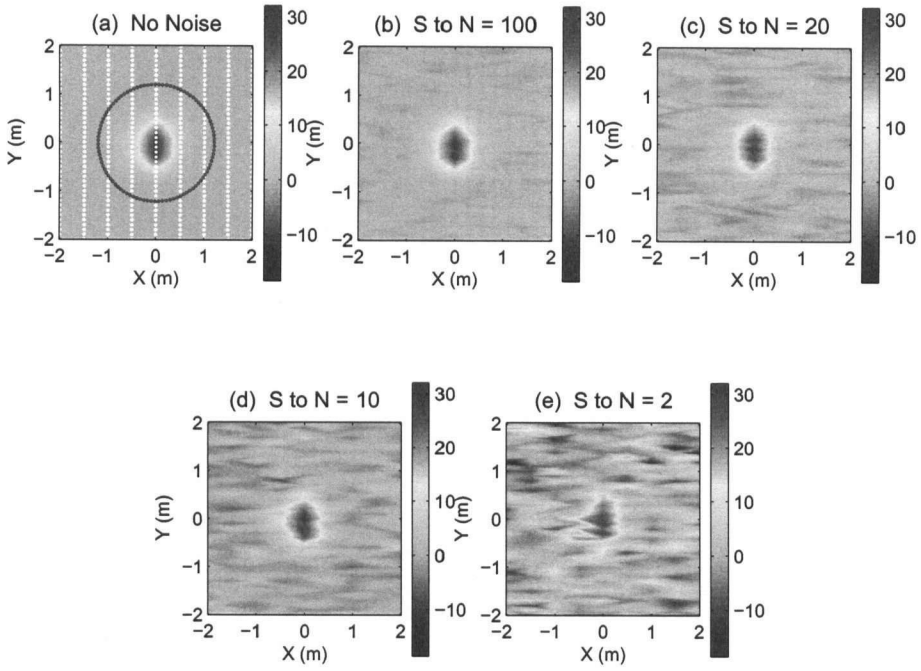

Figure 6.1: Comparison of different signal to noise ratios for a channel of EM61-MK2 data.

If all data are contaminated by the same level of noise, the expected noise energy will be

$$< E_n >= N\sigma^2 \tag{6.3}$$

Figures 6.1 and 6.2 compare a channel of synthetically generated EM61-MK2 data with different signal to noise ratios. Figure 6.1(a) is an image of the noise-free data that was generated assuming a target located 0.5 m below the plane of a transmitter/receiver pair. The red circle represents the amount of data that contains 97.5 percent of the signal energy, and the white dots mark the station locations. Figures 6.1(b) to (e) plot images of the data with signal to noise ratios of 100, 20, 10, and 2. Figure 6.2 plots profiles of the noisy data over the noise-free data.

Figure 6.3 compares the signal strength and background noise level for the first channel of EM63 data collected at the Yuma Proving Ground calibration grid. The data were collected on lines with 0.5 m spacing. We concentrate upon four regions. The first, labelled "Noise", is a region where the signal is assumed to be only noise, that is, there are no targets. The other regions (Signals 1, 2, and 3) are different size targets. A profile plot of a noise signal and Signals 1 and 2 are shown in Figure 6.3(b). By applying equations 6.1 to 6.3, Signals 1, 2, and 3 have SNR's of 150, 3, and 7750,

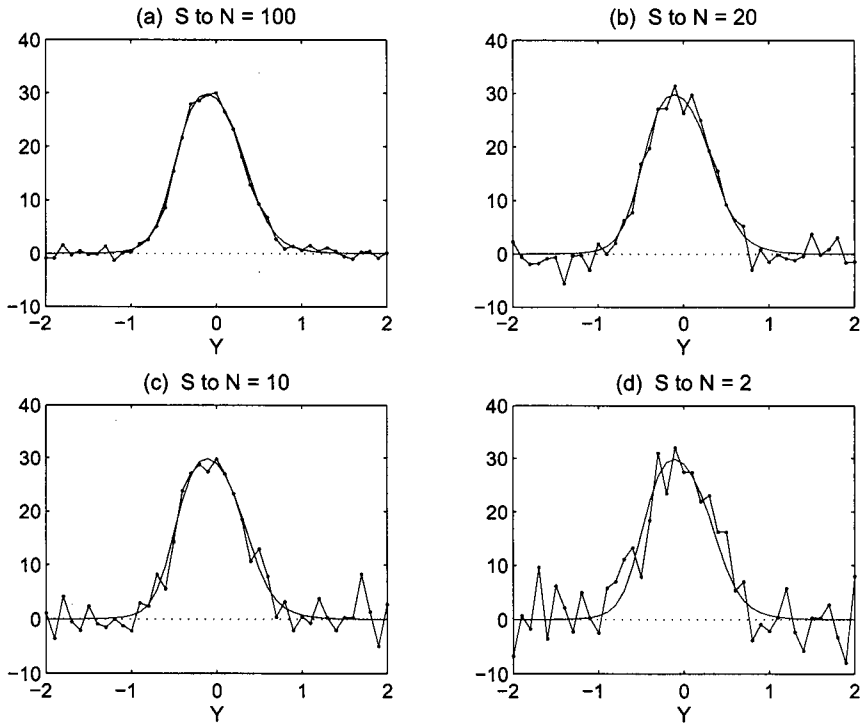

Figure 6.2: A line profile comparison of different signal to noise ratios for a channel of EM61-MK2 data.

respectively.

Figure 6.4 plots the first time channel of EM61-MK2 collected at the PIG discrimination test site at the Former Lowry Bombing Range. Data were collected on a uniform grid with station spacing of 0.61 m (2 feet). Unlike the Yuma proving ground data example, the instrument was stationary at each station location.

6.1.2 Errors due to inaccurate sensor positioning

Incorrect sensor positioning information introduce errors in the interpretation because it prevents accurate modelling of the data. Let us consider data collected on a grid with a line spacing of 0.5 m and a station spacing of 0.25 m, and over a target location 1 m from the plane of the sensor (Figure 6.5(a)). Figures 6.5(b) and (c) demonstrate how misrepresentation of the positional information can affect this data. Panel (b) was calculated with a random positional error with a standard deviation of 5 cm. Random positional error at each station would be encountered when using GPS or RTS for positioning. Panel (c) was calculated with a random positional error of 5 cm applied to all the data on each line.

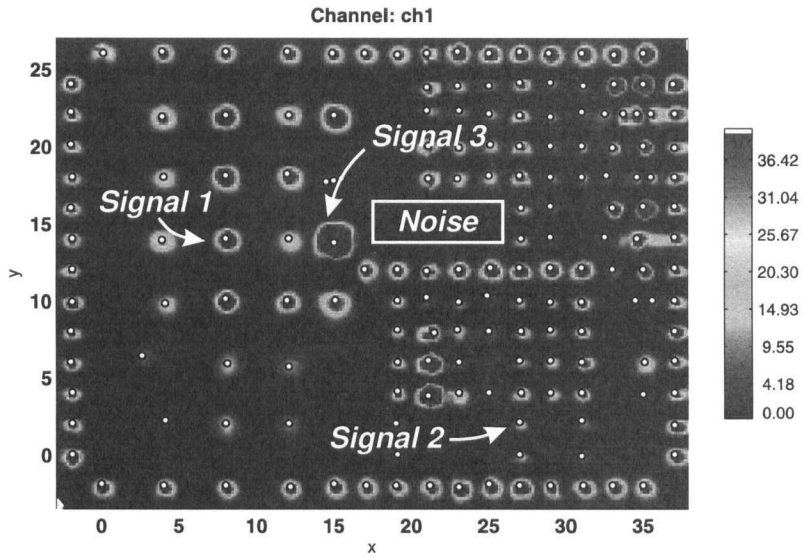

(a) Targets examined for signal to noise example

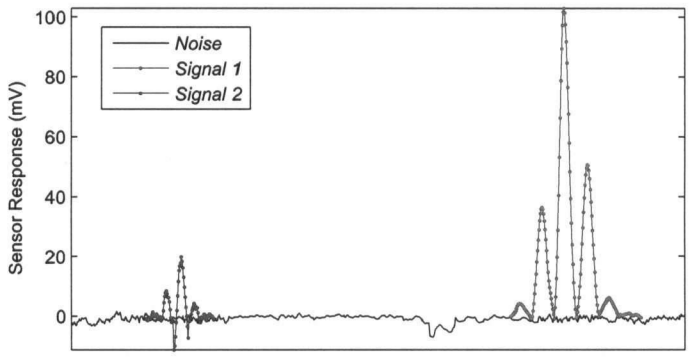

(b) Comparison of signal and background noise. Data values are plotted as a function of data point number.

Figure 6.3: (a) Data examples. (b) Comparison of signal strength to background noise. Signal 3 is not included since its amplitude is much larger than the Signals 1 and 2, and the noise.

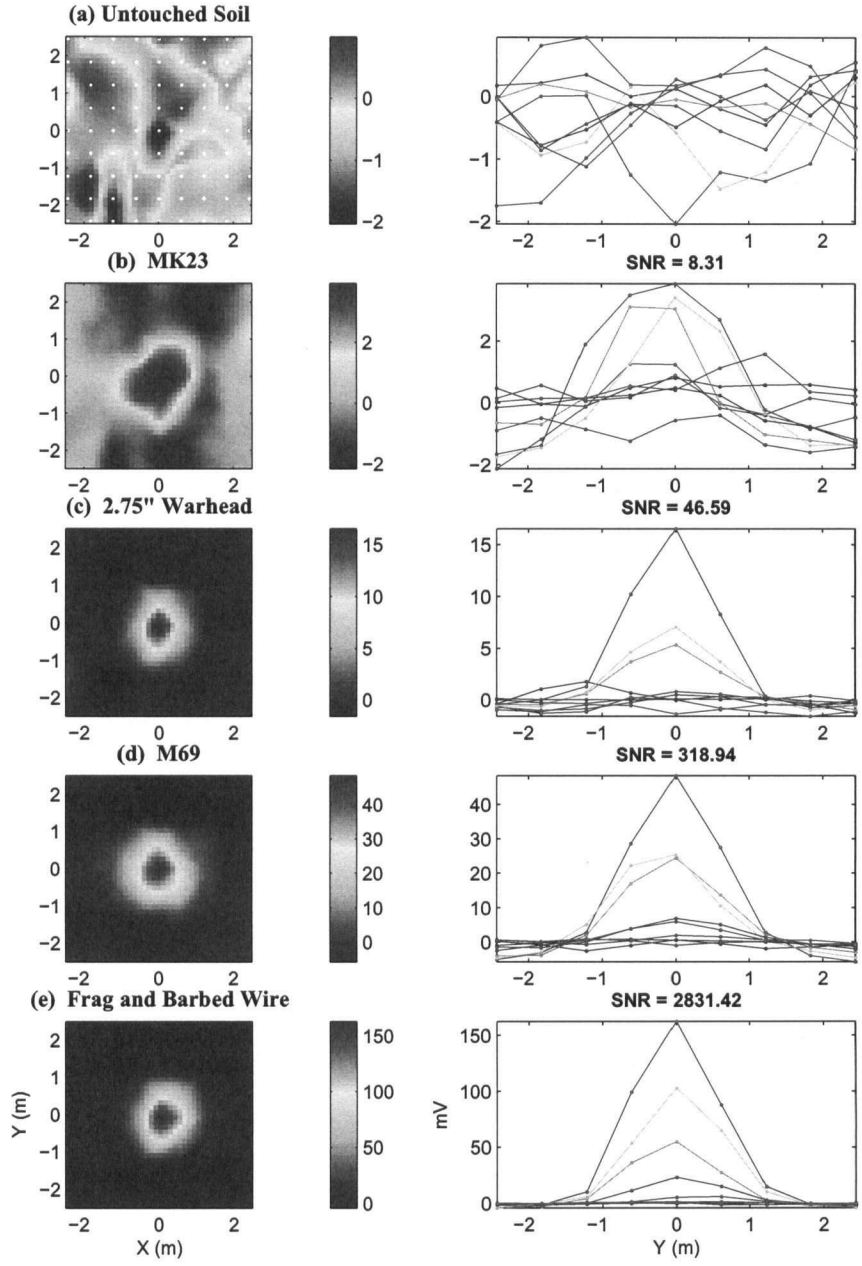

Figure 6.4: Comparisons of different signal to noise ratios for a channel of EM61-MK2 data. The different color profiles represent the North-South lines.

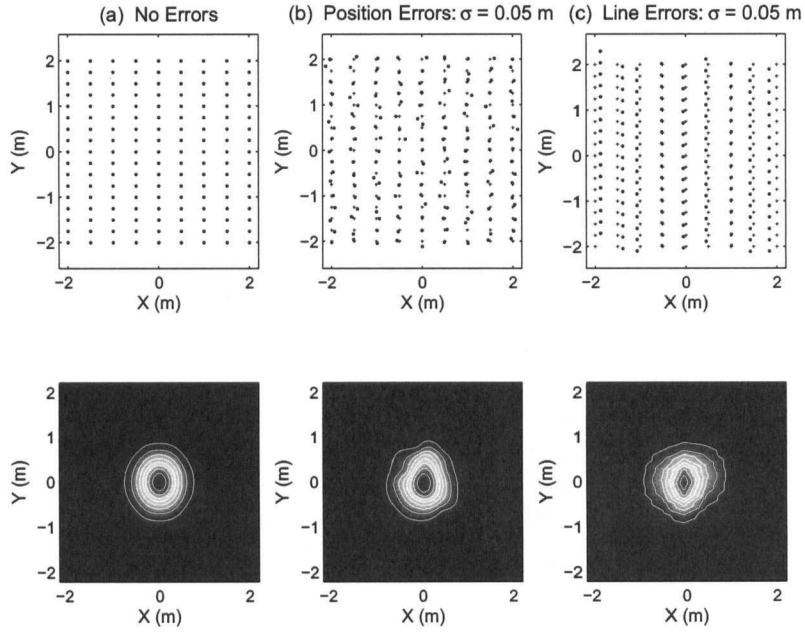

Figure 6.5: Effect of position errors on an anomaly.

6.2 Survey Design Parameters that Affect Detection

The focus of this Chapter is to define data requirements for discrimination. However, before discrimination techniques can be applied, target anomalies have to be detected from the sensor data. Anomaly detection requires a significant number of adjacent data points with a recorded value that is higher than the background noise. Therefore the density with which sensor data are collected is dependent upon the minimum size of anomaly expected in the survey. The observed size of an anomaly (areal extent and amplitude) depends upon size and configuration of the transmitter and receiver as well as on the details of the ordnance item (physical properties, depth of burial, and orientation). Modelling of target anomalies for different variations of target/sensor geometries and SNRs is used to investigate the effect of these variations on anomaly size, and therefore the minimum data density required for detection.

6.2.1 Receiver Loop Size

The time varying change of the secondary field $\mathbf{B}$ induces an EMF, ε, in the receiver loop according to Faraday's law:

$$\varepsilon = -\int_S \frac{\partial \mathbf{B}}{\partial t} \cdot d\mathbf{S}, \tag{6.4}$$

where S is the surface of the loop, and $d\mathbf{S}$ is normal to the surface of the loop. The component of the $\mathbf{B}$-field normal to the surface is integrated over the surface of the loop and the time rate of change of this flux generates a voltage in the loop. As a result of this integration, the measured voltage in the loop represents a smoothed version of the target's dipolar secondary field, and the amount of smoothing is proportional to the size of the loop. As the loop size is reduced to infinitesimal proportions, the measured response is representative of the secondary field at the receiver location.

The effects of different receiver coil sizes is substantial. Figure 6.6 shows images and profiles of the measured field over a vertical rod-like object located at 0.5 m below the coil. Configuration #1 involves integrating over a 1 m $\times$ 1 m coil and therefore has a broader, higher amplitude peak than the coil for configuration #4 which integrates over a much smaller area of 0.5 m $\times$ 0.5 m. Configuration #2 is the coil size of the EM61MK2 sensor. The response is asymmetric and has more smearing of spatial detail along the longer 1 m coil direction compared to the 0.5 m direction. The differences in the response for the different coils are considerably reduced when the target lies at

a depth of 1 m (Figure 6.7). This is due to the half-width of the anomaly becoming larger relative to the coil dimensions so that the response measured in the coil more closely reflects the true variation in the secondary magnetic field.

For the remaining tests and modelling presented here, we will assume EM61-MK2 dimension loops oriented such that the 0.5 m edge of the loop is parallel to the direction of travel.

6.2.2 Target depth and orientation

The location and orientation of a target will affect the anomaly size. Consider the case of a horizontal transmitter loop moving over a buried rod-like target. For rod-like targets, the axial polarization of the target (whose strength is represented by k_1 in equation (6.5)) is larger than the transverse polarization (whose strength is represented by k_2). When the transmitter loop passes directly over a vertical target, the axial (k_1) polarization will be excited since the field beneath a loop is predominantly along the axis of the loop. Excitation of the transverse (k_2) component will be excited when the transmitter loop is not directly over the target. When the target is horizontal, the transverse polarization will be excited when directly beneath the transmitter, and the axial polarization will be excited when the transmitter is not directly over the target. Since the axial polarization is stronger than the transverse polarization for rod-like targets (i.e., $k_1 > k_2$), the footprint of a horizontal target will be larger as a result of the comparatively larger excitation that occurs for the off-centered data. A vertical target will have a larger magnitude directly over the target, but off-centered data will have a small magnitude due to the smaller transverse polarization. Figure 6.8 demonstrates that the anomaly will be smaller if a rod-like target is vertical rather than horizontal. These concepts were also discussed earlier in Chapter 2.

Deeper targets produce wider anomalies. Figure 6.9 plots the profile view of a vertical target with a k_1/k_2 ratio of 5 for a number of depths below the plane of the transmitter and receiver. In the previous analysis of orientation effects on the anomaly, we saw that horizontal targets will produce anomalies with a larger spatial footprint. The profiles are normalized to unity at the maximum value of the anomaly. As the distance from the receiver increases, the anomaly radius increases.

6.2.3 Determining a maximum line spacing for detection

In order to establish station density guidelines for detection, we model the dipole response and calculate the anomaly radius for different target depths and signal levels. The anomaly radius is defined as the radius of the largest circle that contains only data that are larger than twice the standard deviation of the noise. Figures 6.10 and 6.11 demonstrate the relationship between signal noise, target depth, and the expected anomaly size. We remind the reader that the depth is defined relative to the horizontal plane in which the receiver moves. As the signal to noise ratio decreases, the size of the anomaly that sits above the background noise also decreases.

The maximum line spacing for reliable detection is constrained by vertical targets close to the surface. Therefore Figures 6.10(b) and 6.11(b) are the most useful figures for deciding data densities for detection. In order to use these figures, some knowledge of the targets that might be found in the survey and the noise level of the sensor are required to determine the SNRs of targets in the survey. Knowledge of the targets in a typical survey will allow a survey designer to determine the minimum signal to noise ratio that can be expected, and thus the radius of smallest anomaly. Once this radius is established, a line spacing can be chosen that ensures the sensor will sample every anomaly that sits above the survey noise level.

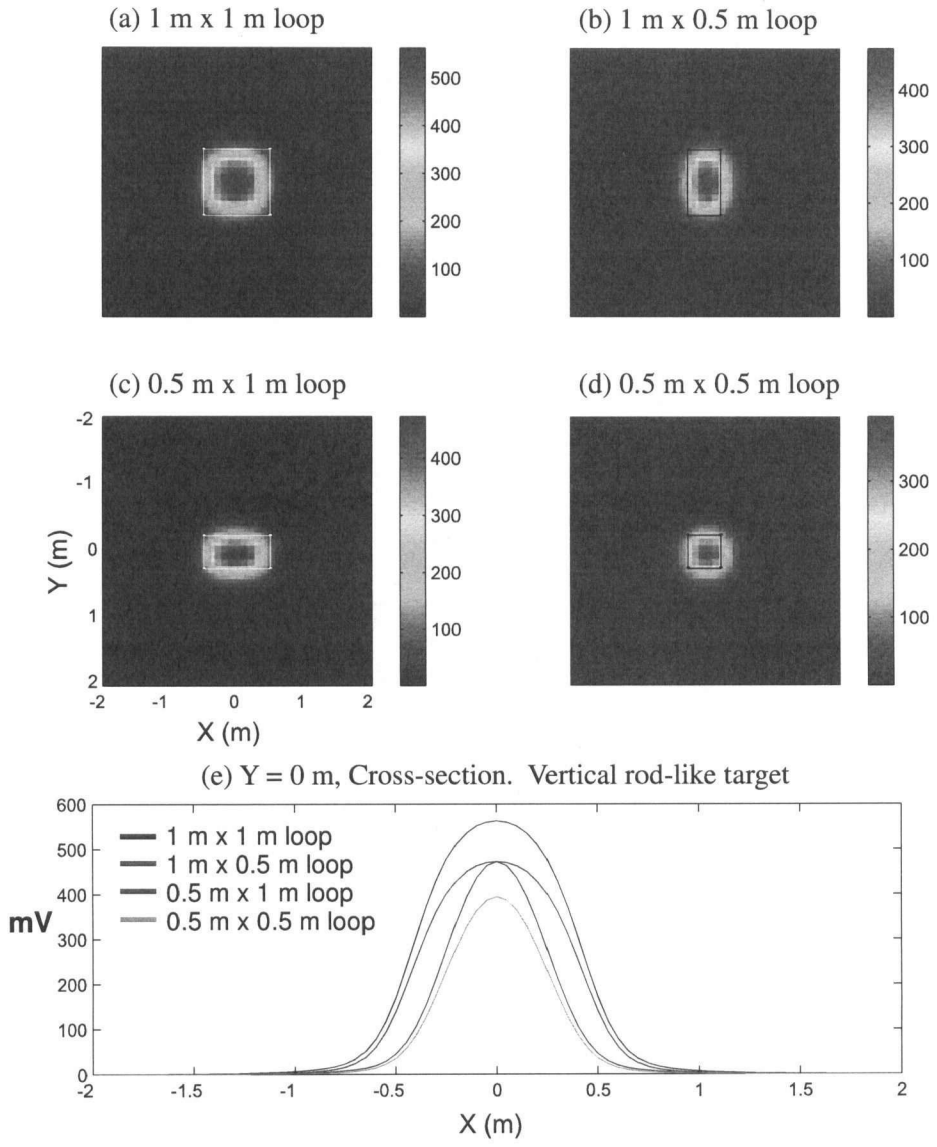

Figure 6.6: Images and profiles of the measured response for each coil configuration for a vertically oriented object at 0.5 m depth.

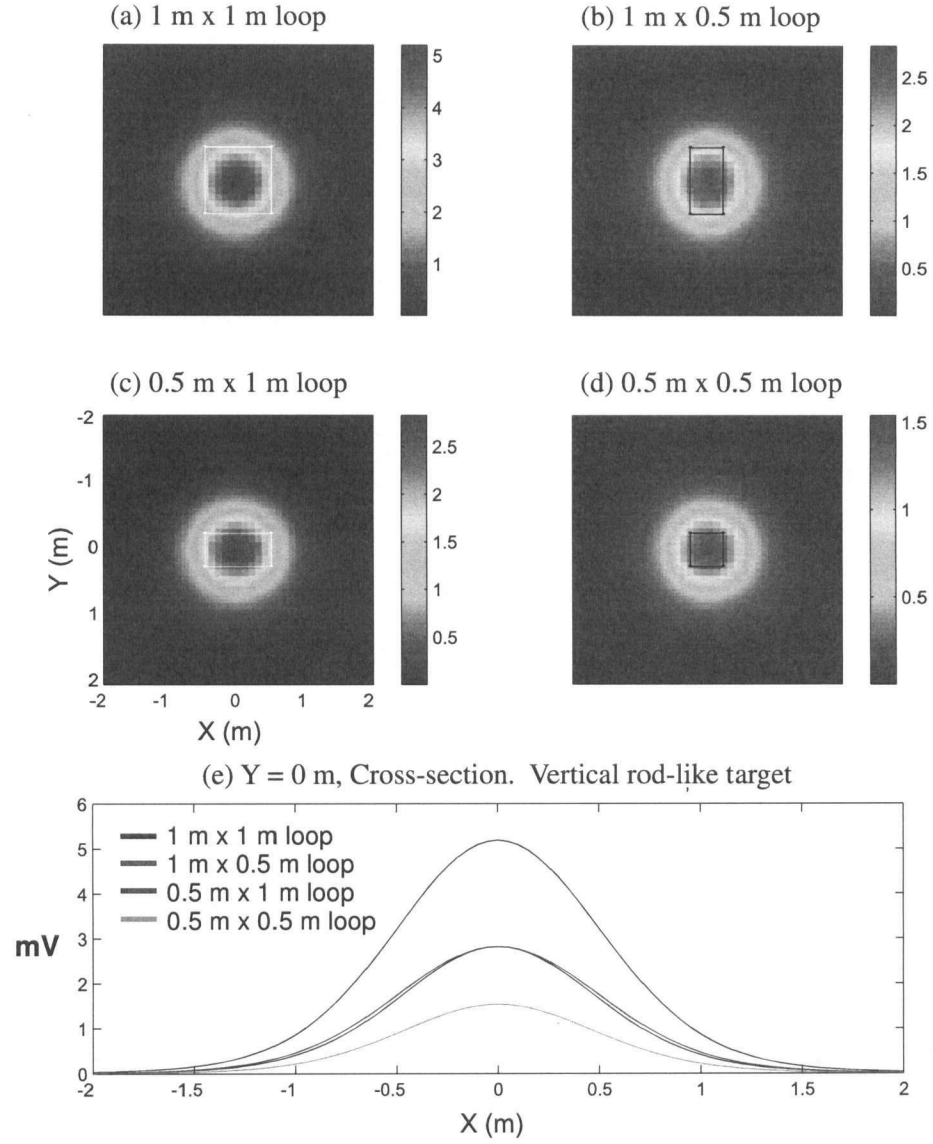

Figure 6.7: Images and profiles of the measured response for each coil configuration for a vertically oriented object at 1.0 m depth.

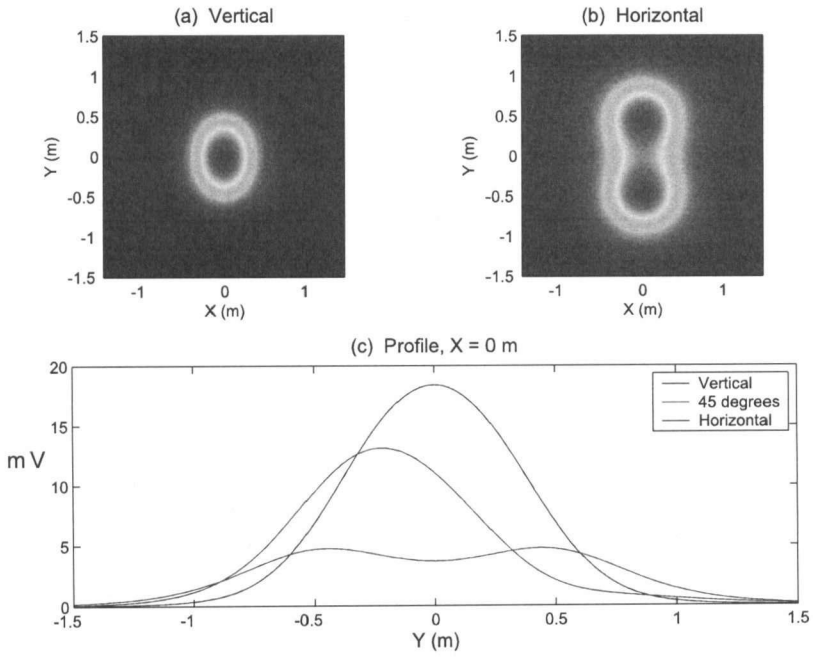

Figure 6.8: Width of an anomaly as a function of orientation.

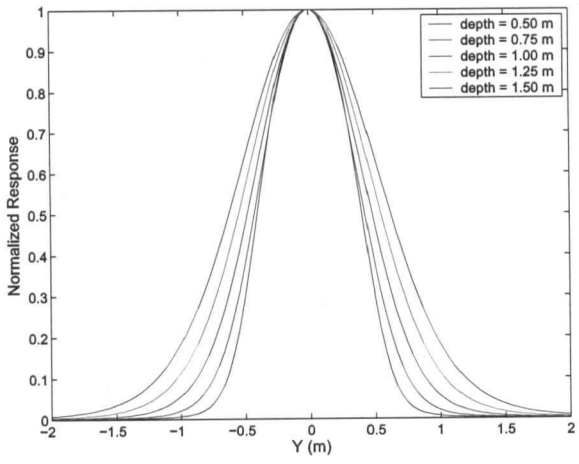

Figure 6.9: The width of an anomaly as a function of depth.

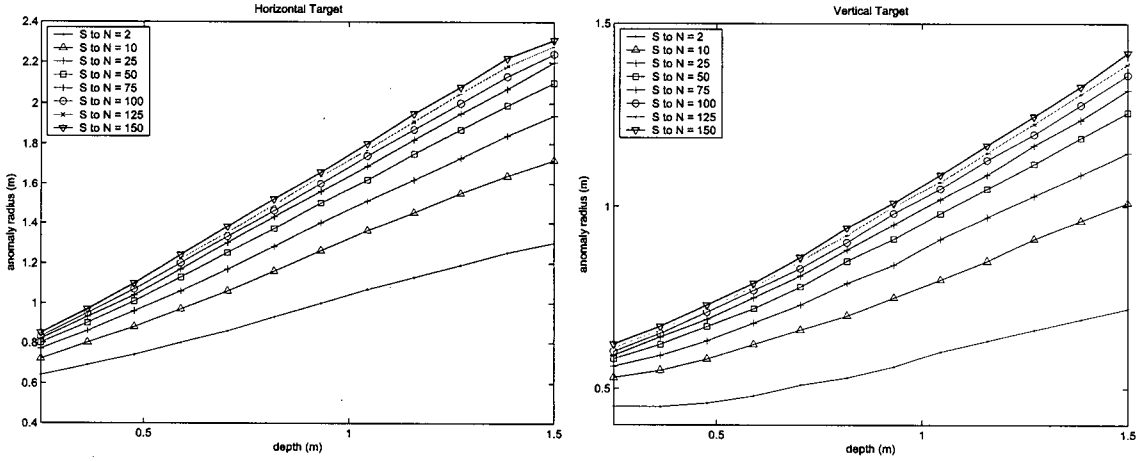

(a) Anomaly radius as a function of SNR and depth for a horizontal target

(b) Anomaly radius as a function of SNR and depth for a vertical target

Figure 6.10: The anomaly radius for an (a) horizontal and (b) vertical target as a function of depth for different signal to noise ratios.

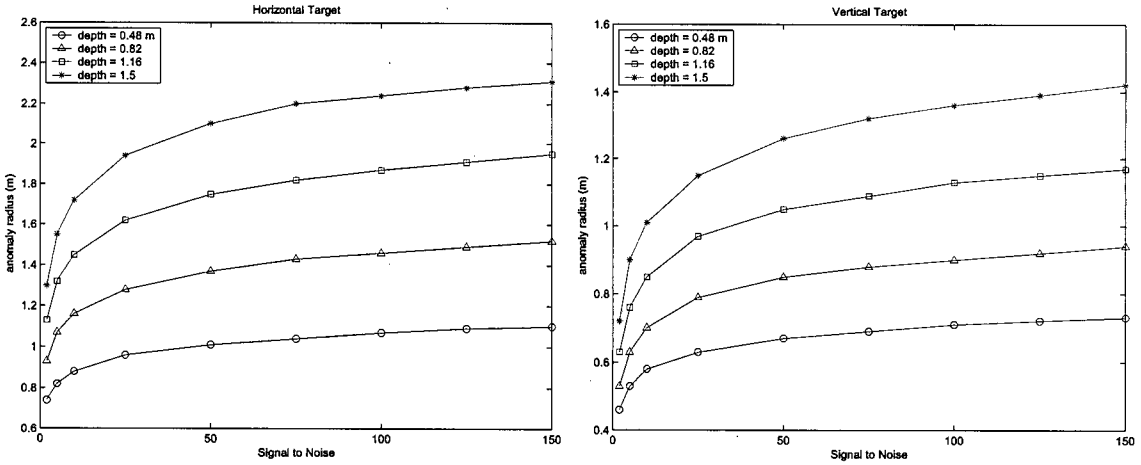

(a) Anomaly radius as a function of SNR and depth for a horizontal target

(b) Anomaly radius as a function of SNR and depth for a vertical target

Figure 6.11: The anomaly radius for an (a) horizontal and (b) vertical target as a function of depth for different signal to noise ratios.

6.3 Data Requirements for Discrimination

A buried target, UXO or scrap, will produce a data anomaly if located within the measurement range of the instrument. In order to determine the nature of the unknown buried target, we need to define feature vectors that are derived from the anomaly and formulate decision rules. These decision rules are based on feature vectors derived from data from known targets (training data). The decision rules can take the form of boundaries in feature space that separate classes of targets. The region in which feature vectors recovered from inversion of data anomalies then define the class to which the unknown target belong. Therefore, effective discrimination requires:

1. Definition of feature vectors for different classes that separate in feature space
2. Adequate training data to produce classification rules
3. Accurate recovery of feature vectors from data

In this section we study the ability to accurately recover feature vectors from data of varying quality. In particular we will use simulations to study the accuracy of recovered parameters. Each simulation involves inverting synthetically generated noisy data. We study the spread of inverted parameters from numerous simulations to determine the sensitivity of the dipole model parameters to variations in SNR, data coverage, and inaccuracy of positional information.

The survey design problem for TEM is similar in concept to that for magnetics but quantitative analysis is more difficult. Magnetic data are summarized in a single map, whereas there is a map of data for each time in a TEM survey. There are also more parameters to be determined in TEM inversion and the parameters can be related to the data in a very non-linear way.

To make the problem tractable, and at the same time extract some general conclusions that are applicable to TEM surveys using different instruments, we proceed as follows. We restrict ourselves to a single time channel. We use an approximate forward model that can adequately reproduce the measured electromagnetic anomaly with minimal computational effort. For a single time channel, we can rewrite the magnetic polarization tensor as

$$\mathbf{F} = \begin{bmatrix} k_2 & 0 & 0 \\ 0 & k_2 & 0 \\ 0 & 0 & k_1 \end{bmatrix}. \tag{6.5}$$

The parameter vector is then $\mathbf{m} = [X, Y, Z, \phi, \theta, k_1, k_2]$, where (X, Y) is the location of the target, Z is the depth of the target (relative to the receiver), (ϕ, θ) are angles that define the orientation of the target, and k_1 and k_2 represent the axial and transverse polarizations of the target.

6.3.1 Monte Carlo analysis

The sensitivity of the inversion procedure to data noise, sensor position inaccuracies, and data coverage are studied using a Monte Carlo analysis. Data were synthetically generated, with signal or positional noise added, for different target depths and data acquisition parameters.

Survey design variations Data were synthetically generated using the TEM dipole of equation 4.3. We consider two different survey acquisition modes: uniform grid surveys and line surveys. We model uniform survey grids with station spacing of 0.25, 0.5, 0.75, and 1.00 m. Line survey data was simulated using line spacings of 0.25, 0.5, 0.75, and 1.00 m, with along line station separation ranging from 0.10, 0.25, 0.5, 0.75 and 1.00 m.

There were three different position errors tested:

1. Random position errors: For these errors a random position error was added to the true position at each station location. Normally distributed errors with standard deviations of 0.02 and 0.05 m were added to the sensor locations.

2. Error on the sensor height: Normally distributed errors with standard deviations of 0.02, 0.05, and 0.10 m were added to the sensor heights when modelling the data.

3. Shifts of a line of data: A shift in the position of the entire line of data was added for this set of simulations. The amount of shift considered had standard deviations of 0.02, 0.05, 0.10 m.

Target variations

Target depths of 0.25, 0.5, 0.75, 1.0, 1.25, and 1.5 m were modelled, where the target depth is defined as the distance from the plane of the transmitter/receiver pair to the center of the target. The location of the target was randomly chosen within a square with sides equal to the line spacing (Figure 6.12). The polarizations k_1 and k_2 are a function of the size and shape of a target (see Figure 2.9). There are three different targets that are modelled in this study: (1) $k_1 = 2$ and $k_2 = 1$,

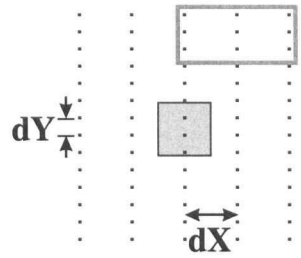

Figure 6.12: Location of target was chosen to be within a square with sides equal to the line spacing as indicated by the grey box. The line and station spacing is indicated by dX and dY, respectively. The orange rectangle represents the orientation relative to the line direction of the EM61-MK2's 1 m x 0.5 m receiver/transmitter.

(2) $k_1 = 5$ and $k_2 = 1$, (2) $k_1 = 10$ and $k_2 = 1$. A target with a ratio $k_1/k_2 = 5$ corresponds to a target with an aspect ratio of approximately 4:1, which corresponds to many UXO. The modelled secondary field is a linear function of k_1 and k_2, such that the results from this Chapter can be applied to targets by scaling.

Inversion Simulations

The sensitivity of the estimated k_1 and k_2 polarization values as a function of the survey type, target type, and data noise is studied by performing a number of simulations. For each survey specification (line spacing, station spacing, positional accuracy), target specification (depth and target type), and signal to noise ratio, the following procedure is used:

1. *Determine the true model.* The true model is the location (X, Y), depth (Z), orientation (θ, ϕ), and target type (k_1, k_2). The depth and target type remains the same for each set of simulations. The orientation is randomly generated, and the ordnance location is randomly chosen within a square with sides equal to the line spacing (Figure 6.12).

2. *Simulate data.* Data were simulated using equations (4.3), and (6.5). For this study we use transmitter and receiver sizes of the EM61MK2 sensor. The forward modelled data are then used to determine the radius of a circle that would capture 97.5% of the energy. If there are less than 9 stations that fall within the circle of data, we assume that no solution can be obtained and we return to Step 1.

3. *Add noise to data.* Gaussian noise is added to the data. The standard deviation of the noise is calculated using the predetermined signal to noise ratio and equations (6.1) to (6.3).

4. *Add positional uncertainty to station locations.* Positional errors are added as described on page 154.

5. *Invert noisy data for orientation and polarization factors.* For each data set we assume that the location and depth of the target is known. Therefore, each data set was inverted for a model vector $\mathbf{m} = [\phi, \theta, k_1, k_2]$, where (ϕ, θ) are angles that define the orientation of the target, and k_1 and k_2 represent the axial and transverse polarizations of the target. The data were fit by minimizing a least squares objective function using a local optimization algorithm. A number of rod-like targets at a number of orientations, are used as starting models for the inversion.

6. *Return to Step 1.*

These steps are repeated 750 times. I found that 750 iterations of the above procedure was enough to characterize the parameter distributions. That is, additional iterations did not change the shape of the parameter histograms and the standard deviations of the parameter distributions.

Difficulties

For many surveys the data quality is insufficient to constrain the model parameters. An obvious example would be the case when the signal is below the noise level of the instrument. A second example would be when line spacing is large enough such that anomalies will have poor spatial sampling, or even be missed altogether. In both cases the data are non-informative, and inversion will produce spurious results.

We want to minimize the inclusion of these spurious results in our analysis. We can define an inversion result as being "successful" when: (1) there are more than 8 data to be inverted whose amplitude is greater than 2σ, where σ is the standard deviation of the background noise, (2) the Matlab optimization algorithm is able to minimize the objective function (i.e., the optimization function does not return an indication that a solution could not be found) and (3) the data are able to constrain the recovered polarization parameters (k_1 and k_2) within their minimum and maximum

bounds. For a set of simulations, we define a "percent success" as the number of times these three criteria are satisfied divided by the total numbers of simulations. Figure 6.13 demonstrates how SNR and data coverage affect the ability of the inversion algorithm to return a successful result. The plots indicate that for larger line spacings, there is an increased chance that inversion will not produce a "successful" result since there is a lack of data coverage. The plots also reflect how shallower targets (with their smaller anomaly size) and target anomalies with a low SNR produce more cases of data with insufficient information for inversion.

Even when there is adequate data to provide an inversion result, it is possible that the recovered result is inaccurate due to the inability of the data to constrain the object's EM parameters. One source of non-uniqueness in the model parameters is due to shape of the primary field. The way with which a sensor illuminates the target is defined by the orientation and size of the transmitter. Figure 6.14 plots the shape of the primary field beneath a horizontal 1 m x 1 m loop located at a height of 40 cm over the surface. The field directly beneath the center of the loop is vertical. In order to illuminate a buried target with a non-vertical field requires obtaining soundings with the transmitter not directly over the target. However, the strength of the field is weaker away the center of the instrument and thus noise level of the instrument limits the distance at which target signal can be detected. Successful recovery of the polarization tensor elements require exciting and measuring both the transverse and axial polarizations of the target.

The limited view of the target provided by horizontal loop instruments (such as the EM61-MK2 sensor), can lead to ambiguities in the recovered model parameters. Figures 6.15 and 6.16 demonstrate the ambiguity for a target buried 0.50 m beneath the plane of the sensor loop. Figure 6.15 plots the k parameters for a target with $k_1 = 5$ and $k_2 = 1$. When the line spacing is 0.25, the recovered parameters are well constrained. However, when the line spacing is increased to 0.5, a small number of the simulated data sets can be well fit by a plate-like target with parameters of $k_1 \approx 1$ and $k_2 \approx 5$ and oriented such that the axis of symmetry (defined by $\hat{z}$ in Figure 2.11) is rotated 90 degrees into the plane of the transverse excitation. This ambiguity, and also the spread of the parameters, increases when the SNR decreases. The ambiguity is much worse when the k_1 and k_2 are less distinct, i.e. when the target has an aspect ratio closer to unity. Figure 6.16 plots the k parameters for a target with $k_1 = 2$ and $k_2 = 1$. There is a very distinct cluster at $k_1 \approx 1$ and $k_2 \approx 2$. For noisier data, it is safer to constrain the solution to rod-like targets. The constrained

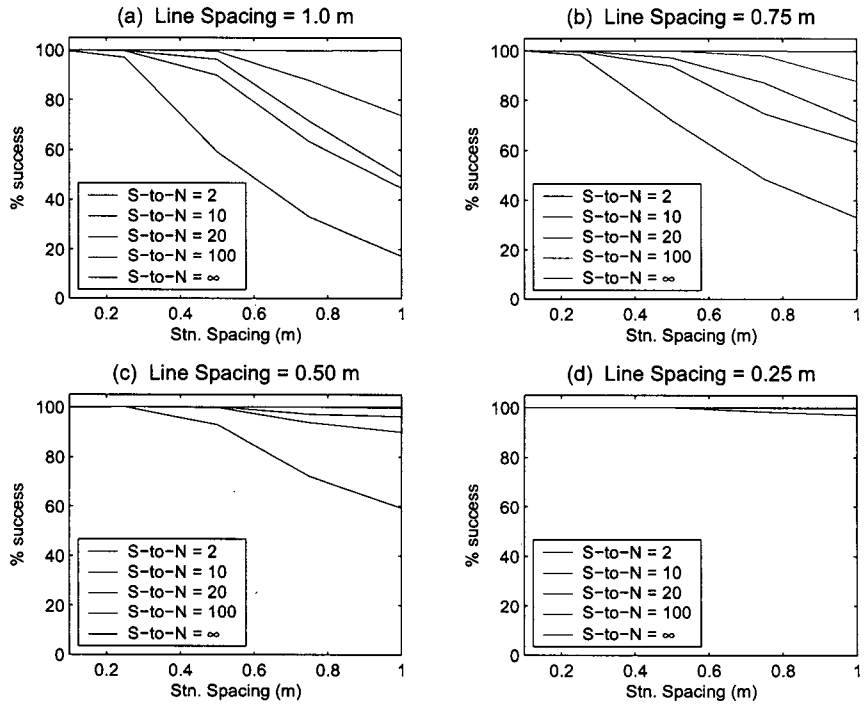

(a) Target at depth (from sensor) of 0.75 m.

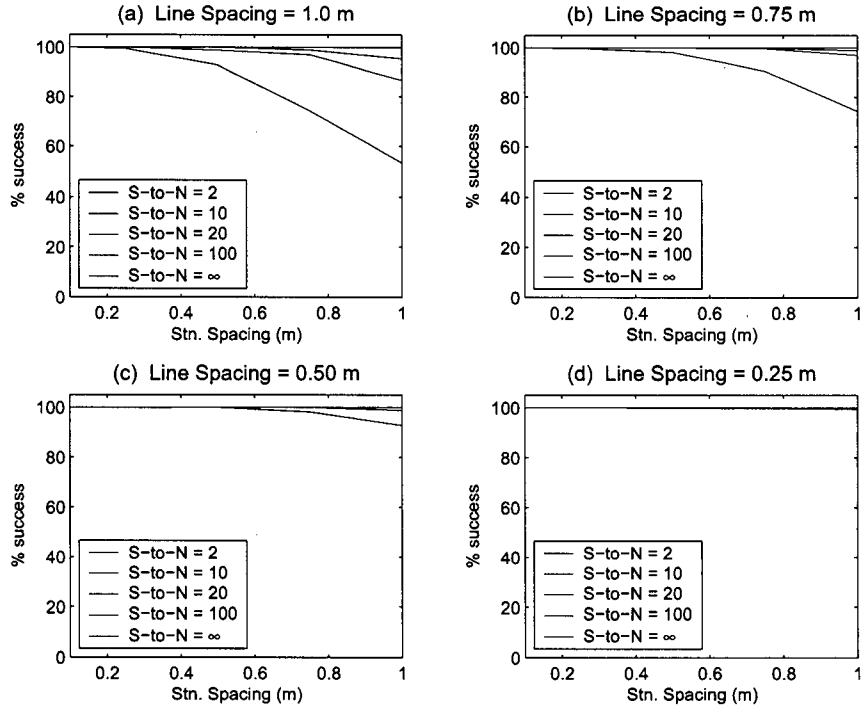

(b) Target at depth (from sensor) of 1.25 m.

Figure 6.13: Influence of line spacing, station spacing, target depth and signal to noise ratio on success rate for inversion.

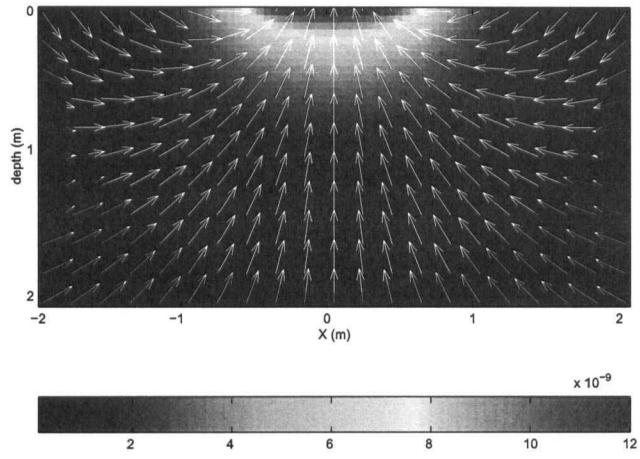

Figure 6.14: The primary field shape beneath a 1m x 1m transmitter loop.

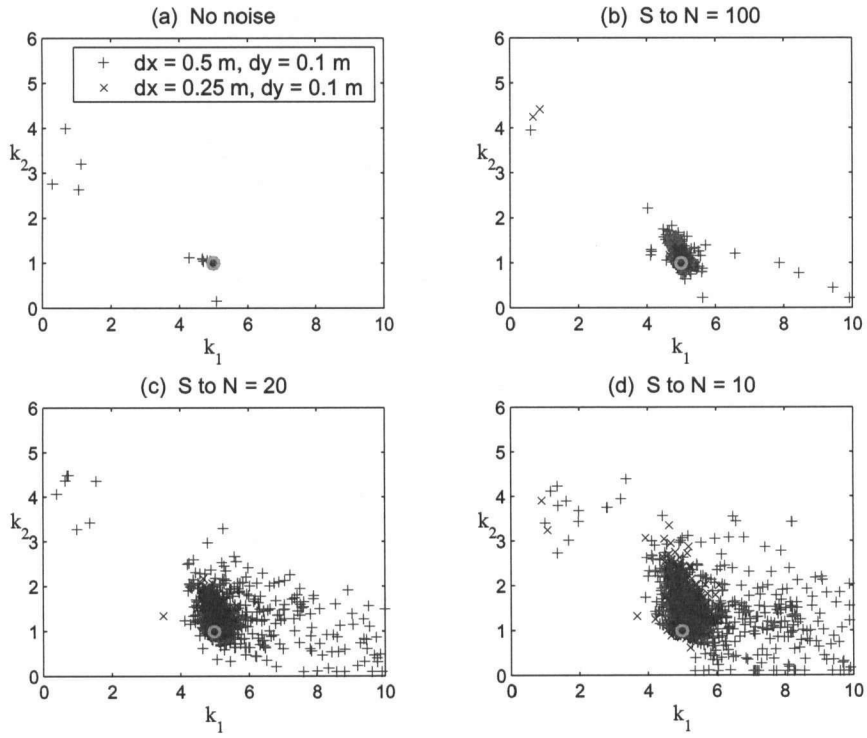

Figure 6.15: An example of ambiguities in the recovered model parameters. In this example $k_1/k_2 = 5$.

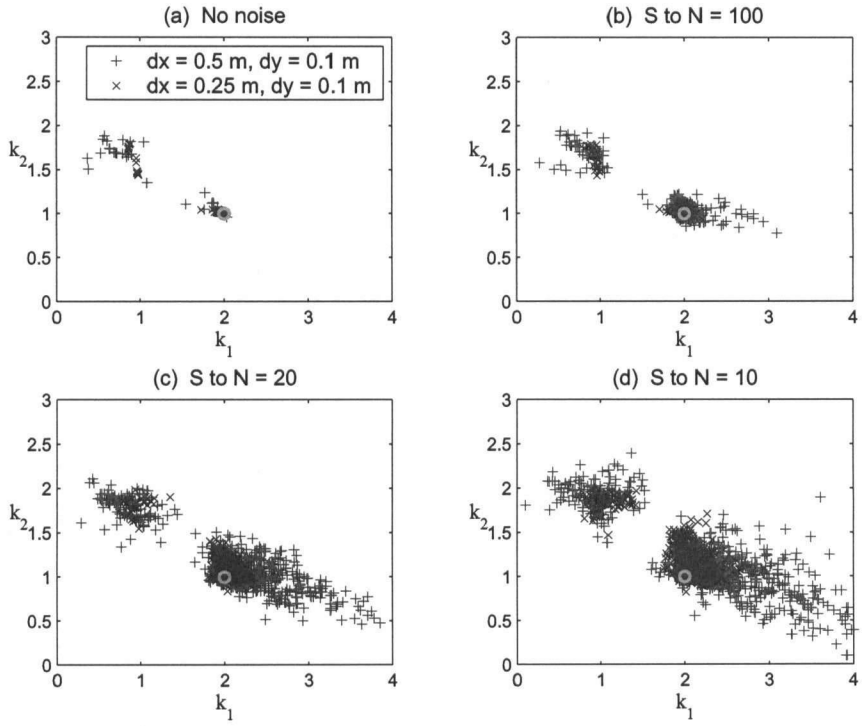

Figure 6.16: An example of ambiguities in the recovered model parameters. In this example $k_1/k_2 = 2$.

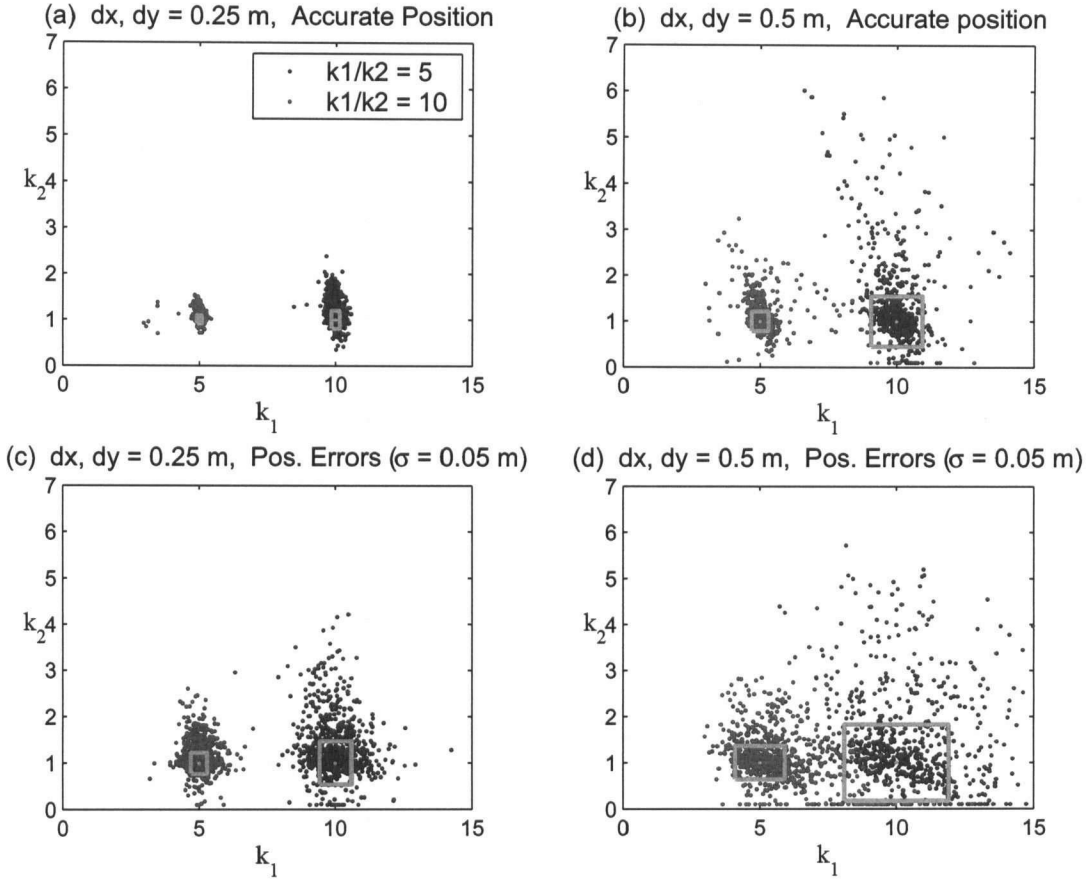

Figure 6.17: Example of the spread in k_1 and k_2 parameters for two different targets ($k_1 = 5, k_2 = 1$, blue dots; and $k_1 = 10, k_2 = 1$, red dots). As position errors and station spacing increases, the absolute deviation of the k_1 and k_2 parameters also increase.

inversion is obtained simply by applying a linear constraint to the k_1 and k_2 (i.e. $k_1 - k_2 > 0$). For this study, we simply choose the larger k parameter to be k_1, and the smaller k parameter to be k_2.

An example of simulation results

As an example of simulation results let us consider two targets. One target has parameters of $k_1 = 5$ and $k_2 = 1$, and the second target has parameters $k_1 = 10$ and $k_2 = 1$. Both targets are at a depth of 0.5 m from the transmitter/receiver loop. The recovered k_1 and k_2 parameters from data collected on uniform grids of $dx = dy = 0.25$ m and $dx = dy = 0.50$ m are plotted in Figure 6.17. The SNR for both targets is 100. The red dots represent inversion results for a target with $k_1 = 5$ and $k_2 = 1$, and blue dots represent inversion results for a target with $k_1 = 10$ and $k_2 = 1$. Green

	$k_1 = 5, k_2 = 1$			
	$dX = dY = 0.25$m		$dX = dY = 0.50$m	
	Δk_1	Δk_2	Δk_1	Δk_2
Accurate Positioning	0.10	0.09	0.31	0.21
$\sigma = 0.05$ m	0.30	0.23	0.92	0.37

Table 6.1: Summary of average absolute deviations for $k_1 = 5$ and $k_2 = 1$ results of Figure 6.17

	$k_1 = 10, k_2 = 1$			
	$dX = dY = 0.25$m		$dX = dY = 0.50$m	
	Δk_1	Δk_2	Δk_1	Δk_2
Accurate Positioning	0.15	0.20	0.93	0.55
$\sigma = 0.05$ m	0.58	0.47	1.90	0.83

Table 6.2: Summary of average absolute deviations for $k_1 = 10$ and $k_2 = 1$ results of Figure 6.17

rectangles are centered on the true parameters and have dimensions of $(2\Delta k_1) \times (2\Delta k_2)$. Panels (a) and (b) show the spread of parameters when the sensor position is accurately known. Panels (c) and (d) demonstrate how the spread of parameters increase when the method of determining sensor position has a normally distributed uncertainty with a standard deviation of 0.05 m.

The spread for each of a recovered parameter m_i is quantified by the average absolute deviation

$$\Delta m_i = \frac{1}{N} \sum_{j=1}^{N} |m_i^j - m_i^{true}|, \tag{6.6}$$

where N is the number of simulations, and m_i^j is the recovered parameter from the j^{th} simulation for the i^{th} recovered parameter.

The average absolute deviations for the example in Figure (6.17) are summarized in Tables (6.1) and (6.2). For this example, inaccurate knowledge of the sensor location would not affect greatly the ability to distinguish the two target types provided that the station spacing is 0.25 m (Figures 6.17(a) and (c)). However, when the station spacing is 0.5 m and the sensor location has a positional error of 0.05 m, we see that the data coverage is not sufficient enough to ensure good separation in the classes for the recovered parameters (Figures 6.17(b) and (d)). The probability of misclassification clearly increases with poorer data density.

6.3.2 Results

Due to the large number of plots that make up the results, I refer the reader to the report *"Guidelines On Data Quality Requirements for Advanced Discrimination of UXO"* (Pasion et al., 2004). In the aforementioned report, the simulation results of the different survey setups are summarized in Figures B.1 to B.45. Figures B.1 to B.15 have no positional error. Figures B.19 to B.45 have random error on each position. Figures B.46 to B.93 have random error on each line. Figures B.94 to B.135 have random error on the height at each station. Each page consists of 8 plots. The four rows of plots per page correspond to the four different line spacings (0.25, 0.5, 0.75, and 1.00 m) considered in the simulations. The left column of plots are the relative deviation of spread of k_1 and the right column of plots are the relative deviation of spread of k_2. The relative deviation is defined as

$$\frac{\Delta m_i}{m_i^{true}} = \frac{1}{m_i^{true} N} \sum_{j=1}^{N} |m_i^j - m_i^{true}|. \tag{6.7}$$

6.3.3 Utilizing simulation results

The objective of this study was to provide guidance when planning EM surveys. However, generating specific guidelines for EM data acquisition is difficult due to the numerous variations in survey design, target types, instrumentation, and noise. Our simulations represent a simplification of the general EM problem. We have restricted our simulations to the inversion of a single channel of Geonics EM61Mk2 data for orientation values and polarization values. Even with these simplifications, there are still numerous measurement variations that we considered.

One possible way of determining minimum requirements for EM survey design is to define a Figure of Merit that summarizes the data quality, and relate this number to the spread in recovered parameters. For the case of accurate positioning, the Figure of Merit would reflect the SNR of the anomaly and the data coverage. One possible definition of a Figure of Merit is

$$\xi = SNR \times (\max[0, 1 - dx/R])^4 \times \sqrt{\frac{dx}{dy}}, \tag{6.8}$$

where dx represents the line spacing, R is the radius of the anomaly, and dy is the station spacing. The term $\max[0, 1 - dx/R]$ is a function that reflects the spatial density with which data is collected over the target. The minimum value of 0 indicates poor sampling, while the maximum value of 1

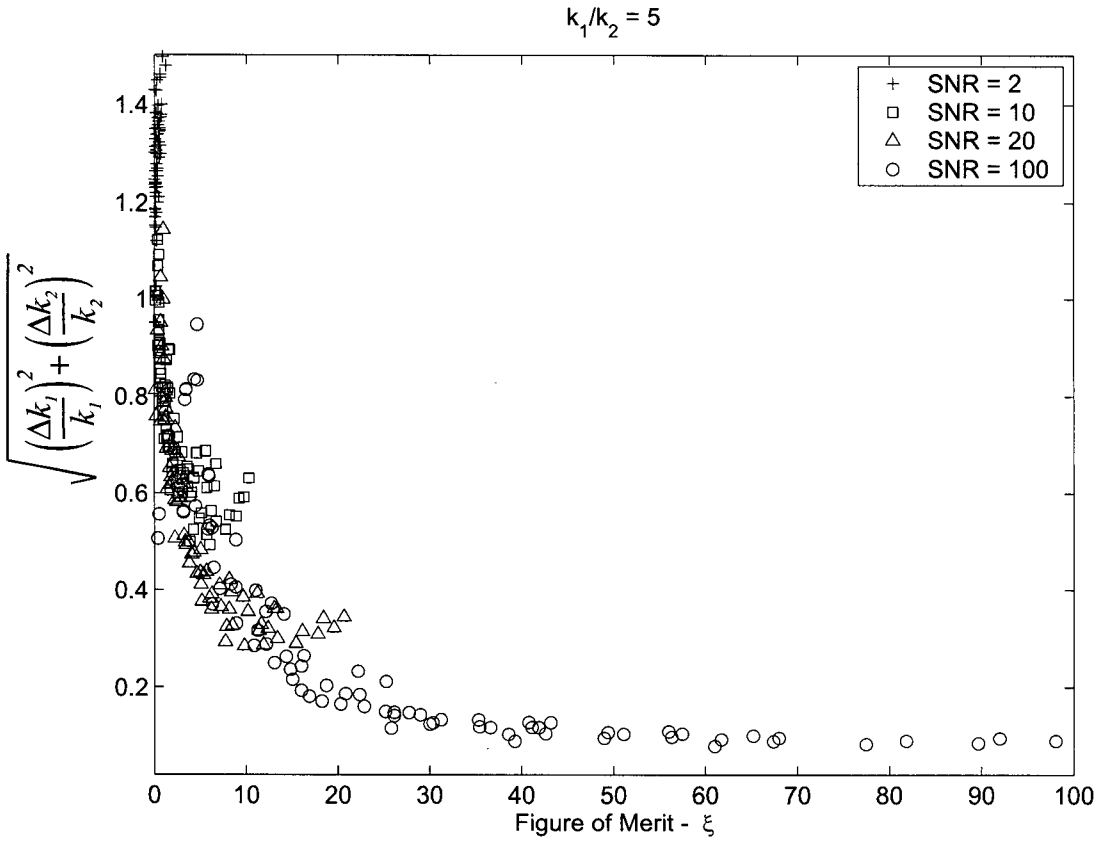

Figure 6.18: A plot of the relationship between the Figure of Merit, ξ, and the square root of the sum of squares of the average relative deviations for a target with $k_1 = 5$ and $k_2 = 1$.

indicates station separation approaching 0. The fourth power was arbitrarily chosen. The term $\sqrt{dx/dy}$ reflects how uniformly the sensor samples the anomaly. Dense sampling along lines (i.e. $dx \ll dy$) is less desirable than uniformly sampling ($dx \approx dy$).

Figure 6.18 plots the relationship between the Figure of Merit defined in (6.8), and the square root of the sum of squares of the average relative deviation (defined in Equation 6.7). Figure 6.18 includes results from simulations where there are no positional errors, and for targets with $k_1 = 5$ and $k_2 = 1$. Clearly, as the Figure of Merit increases, there is reduction in the spread of parameters. Figure 6.19 plots only points from Figure 6.18 where the line spacing is 0.5 m. The plot shows how the different SNR's and depths relate to the Figure of Merit and parameter spread. The three points on the line segment correspond to station spacings of $dy = 0.5, 0.25, 0.1$ m.

There are different ways this plot could be used. As a first example, consider the goal of recov-

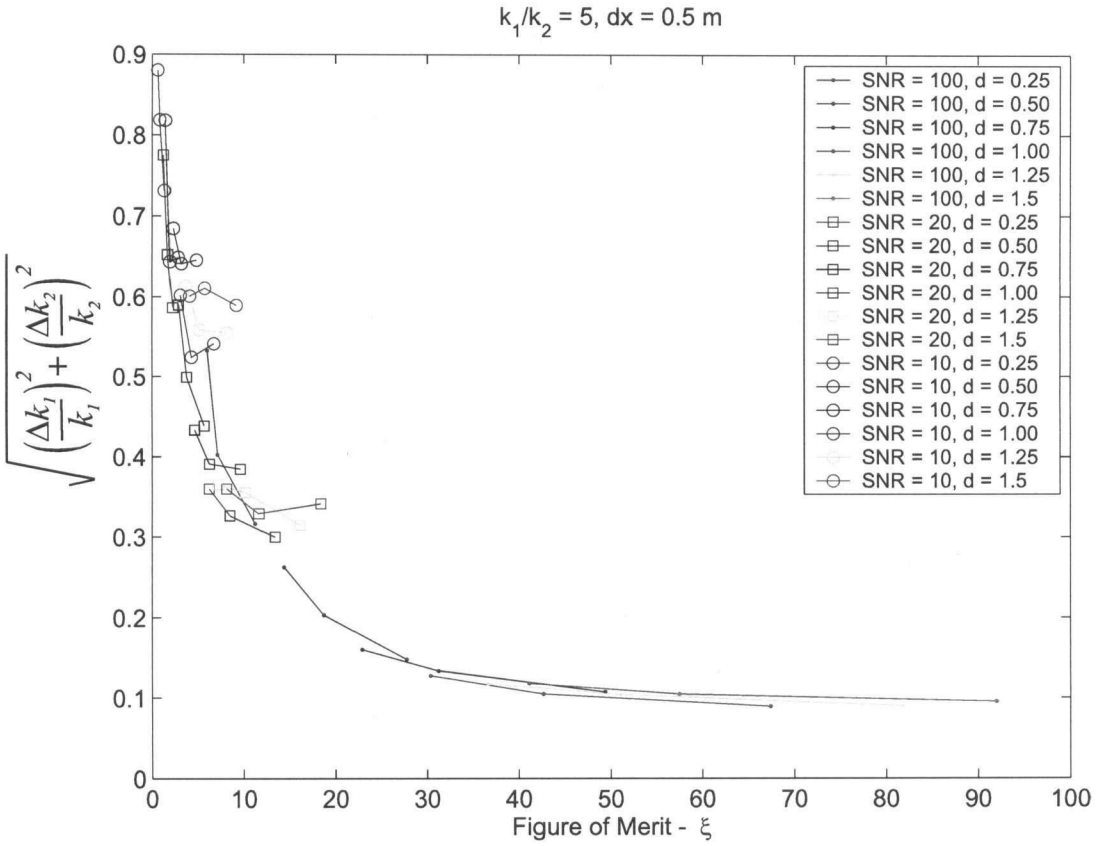

Figure 6.19: A plot of the relationship between the Figure of Merit, ξ, and the square root of the sum of squares of the average relative deviations for a target with $k_1 = 5$ and $k_2 = 1$. Only simulations with a line spacing of 0.5 m are plotted.

ering parameters for a target (with $k_1/k_2 = 5$) such that the average relative deviation for each is 0.25. The square root of the sum of squares of the average relative deviations would be 0.35. From Figure 6.18, we see that in order to achieve the desired spread in parameters, the Figure of Merit must be greater than approximately 15. From the graph, we see that anomalies with an SNR of 10 or 2 will not recover the parameters with the desired average relative deviation. For given estimates of SNR and anomaly radius, a line and station spacing can be chosen that will allow us to recover parameters within our desired accuracy. Alternatively, once the station and line spacing is set, we can use the Figure of Merit to determine which anomalies can be reliably interpreted. Anomalies that do not meet the Figure of Merit standard with the available data, could be re-surveyed in a cued interrogation sense where the SNR would be decreased and the data density could be increased.

Figure 6.20 demonstrates the relationship between Figure of Merit and the parameter spread for all the target types simulated in this analysis. The target with $k_1/k_2 = 10$ corresponds to the most elongated target. Since the transverse polarization of this target is the most difficult to resolve (due to its much smaller size relative to the axial polarization), the spread in the recovered polarization parameters will be greater.

6.4 Conclusion

A Monte Carlo methodology was used for TEM data. The EM situation is complex because:

1. Multi-time channels are recorded, and the number varies with the sensor (e.g. EM63, EM61MK2, etc.).

2. There are different ways to establish a relationship between the UXO and data. (e.g. dipole models, more rigorous numerical electromagnetic modelling,etc.). Even if we choose to adopt a dipole model, then various scenarios are possible. If data at many time channels are obtained then all parameters of the dipole model can be estimated. Alternatively, each time channel can be inverted separately to yield amplitudes of the representative dipole polarizations.

3. There are different choices for selecting features for discrimination. For example, one can choose the magnitude of k_1, k_2 (strengths of the axial and transverse dipole polarizations) or their ratio.

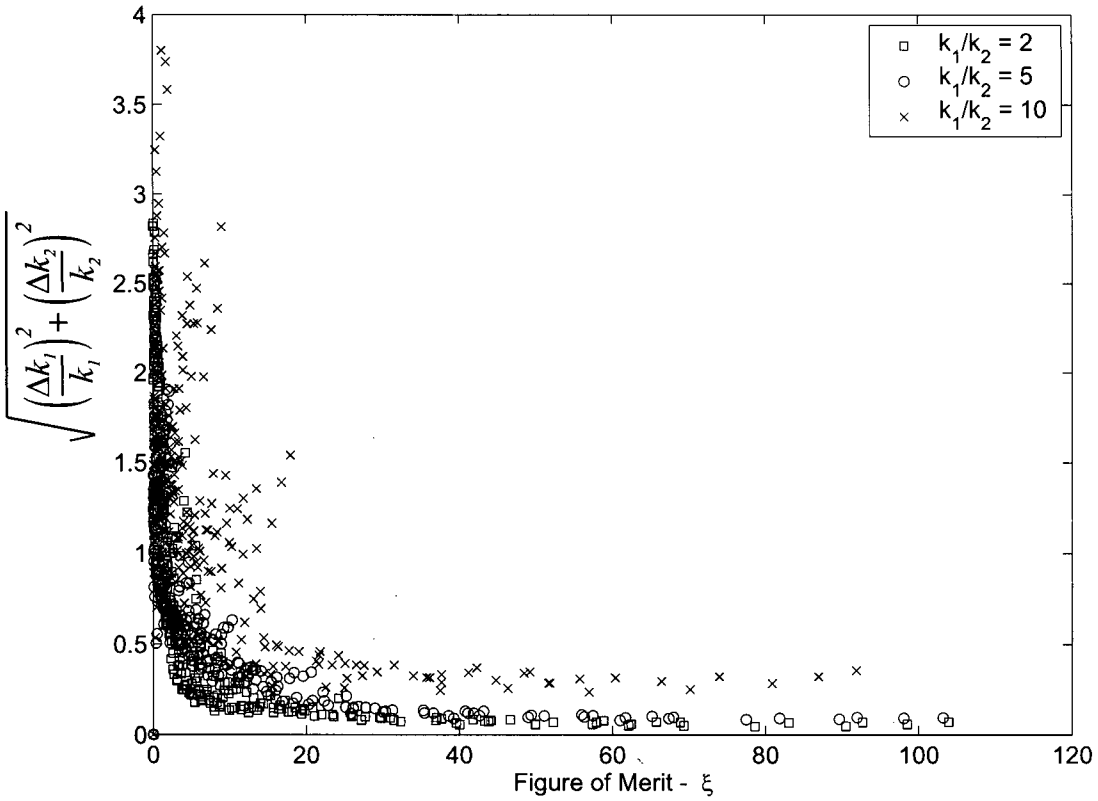

Figure 6.20: A plot of the relationship between the Figure of Merit, ξ, and the square root of the sum of squares of the average relative deviation for all targets simulated in this analysis. For the simulations in this plot there were no sensor positioning errors.

4. System noise, orientation errors, cultural noise are generally more complicated for EM measurements.

Attempts to account for all realistic scenarios encompassed by the above items leads to consideration of too many variables. For any field survey there is only a subset of the above possible scenarios that are important. Once these are identified, then Monte Carlo simulations can be generated to quantify the importance of various acquisition parameters or signal/noise ratios. The ideal goal would be to assess how specific choices of the above scenarios affect the final receiver operating characteristic (ROC) curves.

We conclude that it would be more useful to develop software to simulate various realistic scenarios regarding:

1. Acquisition parameters and uncertainties;
2. Specific ordnance items and their depth ranges;
3. Specifics of the instrumentation (frequency domain, time domain, number of channels);
4. Choice of parameterization for forward modelling;
5. Choice of which features (inversion parameters, ratios of parameters etc) are to be used in discrimination.

The results presented in this Chapter represent analysis of a single time channel of Geonics EM61MK2 data. Therefore, these results can immediately help determine design parameters for EM61MK2 data collection surveys. In addition, these results can be used to help establish which anomalies within an EM61MK2 survey are candidates for inversion and discrimination, and which anomalies may require higher quality data from a follow-up cued interrogation survey.

Chapter 7

Detection of Unexploded Ordnance in Magnetic Environments

This chapter is organized into three parts. First, we review the theory of viscous remanent magnetization and derive expressions for the time dependent magnetization for a collection of single domain magnetic grains. Second, we review complex susceptibility models for single domain grains, and utilize these models in simulating responses of a loop on a magnetic viscous half-space. The modelling allows us to investigate the relative contributions of magnetic viscosity and eddy current induction on the half-space response. We also compare the magnitude and character of half-space and spheroid responses. In the final part of the chapter, a pair of field examples are used to illustrate the effect of magnetic viscosity on electromagnetic measurements. For the first example we consider time domain electromagnetic data acquired on seeded test plots on Kaho'olawe Island, Hawaii 7.1. Due to basalt-derived magnetic soils, 30% of identified anomalies later turned out to be from geology (Putnam, 2001). Figure 7.2 contains an image of the first channel of Geonics EM63 time domain electromagnetic data collected over a Kaho'olawe test grid.

The second example we consider is from the International Test and Evaluation Program for Humanitarian Demining (ITEP). ITEP constructed landmine testing lanes to study the effect of

Figure 7.1: Seeded UXO test grid located on Kaho'olawe Island, Hawaii.

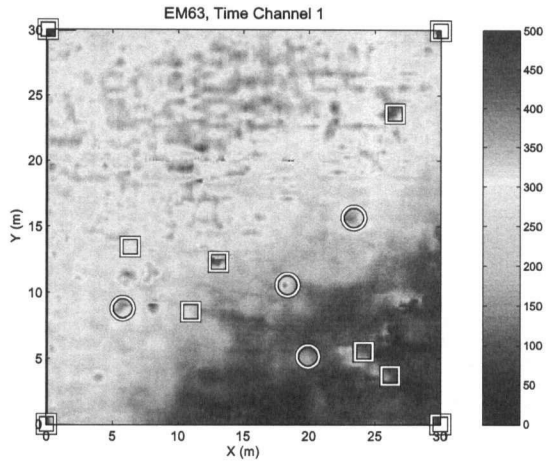

Figure 7.2: Geonics EM63 data acquired on Kaho'olawe island, Hawaii.

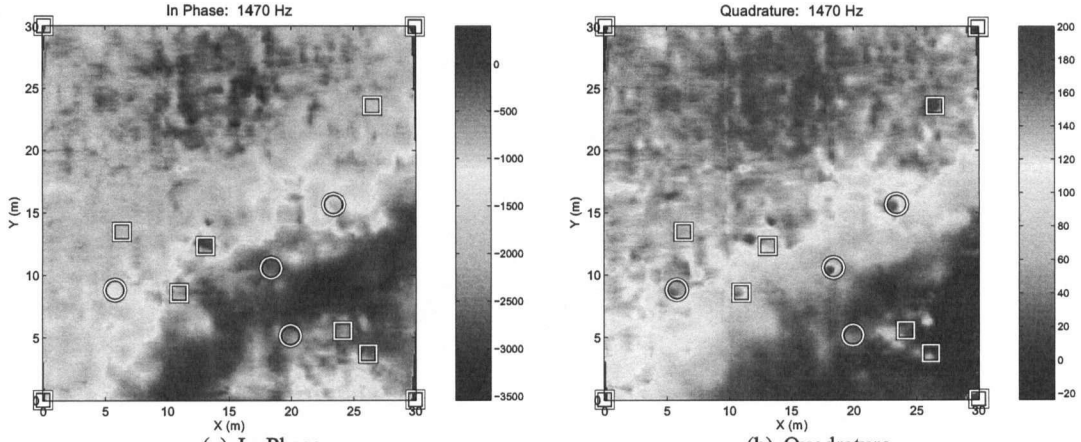

(a) In-Phase (b) Quadrature

Figure 7.3: GEM data acquired on Kaho'olawe island, Hawaii.

different soil types on the response of typical metal detectors used for humanitarian demining. Table 7.1 summarize the susceptibility measurements of three of the lanes. The ground reference height (GRH) refers to the maximum height at which a calibrated Scheibel pulse induction sensor is sensitive to the background soil, and is therefore a crude measure of the background soil noise (Müller et al., 2003). The ITEP trials demonstrated that it is the change in the magnetic susceptibility with frequency, and not the magnitude, of the susceptibility that is the important parameter determining the electromagnetic response of the soil host. In this chapter, we show that magnetic viscosity from non-interacting single domain grains can quantitatively explain the results observed at Oberjettenberg, Germany and Benkovac, Croatia.

Sample	χ_{980Hz}	$\Delta\chi$	GRH (cm)
Oberjettenberg	3000 ± 500	5.6 ± 7	4.5
Benkovac	154 ± 13	25.5	19.0

Table 7.1: Frequency dependent susceptibilities and ground reference heights (GRH) for a pair of landmine test lanes in Oberjettenberg, Germany and Benkovac, Croatia. The column titled $\Delta\chi$ contains the difference in susceptibility measured by the Bartington MS2D meter.

7.1 Magnetic Properties of Soils

The magnetic properties of soils are mainly due to the presence of iron. Hydrated iron oxides such as muscovite, dolomite, lepidocrocite, and geothite are weakly paramagnetic, and play a minor role in determining the magnetic character of the soil. The most important determinants of the magnetic character are the ferrimagnetic minerals, maghaemite (αFe_2O_4) and magnetite (Fe_3O_4). Maghaemite is the most important of the minerals for archaeological prospecting applications as fire pits and ovens that heat the soil can result in a conversion of minerals to maghaemite (Scollar et al., 1990). Magnetite is the most magnetic of the iron oxides, and is the most important mineral when considering the effects of magnetic soils on EM measurements.

Ferrimagnetic minerals are characterized by anti-parallel alignment of unequal magnetic moments which result in a permanent magnetic moment. When these minerals are exposed to a magnetic field, there is a corresponding change in magnetization. Viscous remanent magnetization, or magnetic after-effect, refers to the non-instantaneous nature of magnetization change. The viscous remanent magnetic behavior is correlated with magnetic grain size. Very small magnetic grains cannot retain a coherent alignment of atomic moments; they are superparamagnetic. This behavior occurs for magnetite grains with radii of the order of 250 angstrom or less as they are unable to accommodate a complete domain (Dunlop and Ozdemir, 1997). Grains that are large enough to accommodate a single domain of magnetization are referred to as "single domain" grains and are very stable carriers of magnetization. The magnetization of the single domain can rotate under the influence of an applied magnetic field, large stress, or an elevated temperature. Larger grains may have more than one domain, and are referred to as "multi-domain" grains. If the grain exhibits both single-domain and multi-domain behavior the grain is a "pseudo-single-domain" grain. The magnetization of multi-domain grains changes in the presence of an applied field by the growth of

some domains, at the expense of others, via the motion of domain walls. For large applied fields the magnetization within the domains may rotate. Although domain wall movement is a frequency dependent process (Klein and Santamarina, 2000), it is an effectively instantaneous behavior relative to our frequency range of interest. Thus it does not contribute to the viscous part of the magnetization that we model. Measurements taken on a multi-domain grain sample of magnetite have shown no measurable variation of susceptibility with frequency and no quadrature susceptibility (Bhatal and Stacey, 1969).

7.2 Viscous Remanent Magnetization of a Collection of Single Domain Grains

Suppose that we apply a magnetic field H to a magnetic material at a time $t = 0$. The magnetization vector will try to adjust to align itself with the exciting field. At the instant the magnetic field is applied there is an immediate change in magnetization M_i, which we refer to as instantaneous magnetization. The time dependent change of magnetization is represented by $M_n(t)$. A time constant τ is used to characterize the time for the magnetization vector to rotate from its minimum energy orientation prior to $t = 0$, to its new orientation.

Neel (1949) developed a simple theory to describe the magnetization of an ensemble of non-interacting single domain grains. The magnetization vector will rotate to a new orientation if the total available energy provided by the inducing field exceeds an energy barrier $\Delta E = KV$, where K is the anisotropy constant for the domain's composition and lattice, and V is the volume of that domain. In strong fields the magnetization takes place almost immediately after application of the field. In weak fields the energy provided by the field may not be sufficient to provide an instantaneous change in magnetization. Instead, thermal vibrations kT, where k is the Boltzmann constant and T is temperature, gradually provide the energy for the magnetization change. The relaxation time is given by

$$\frac{1}{\tau} = \frac{1}{\tau_o} \exp\left(\frac{-\Delta E}{kT}\right) \tag{7.1}$$

where ΔE is the height of the energy barrier for a rotation in magnetization, and $\tau_o \approx 10^{-9}$ is the atomic reorganization time (Dunlop and Ozdemir, 1997). The exponential form of equation 7.1 demonstrates the sensitivity of relaxation times to grain sizes and also to temperature. When the

particle size becomes small enough, the thermal energy will become sufficient to spontaneously switch the magnetic moments immediately.

Let us consider a situation where field H has been instantly switched off at $t = 0$, and the equilibrium magnetization is zero. The resulting decay of the magnetization is

$$M(t) = H\chi_o F(t) \tag{7.2}$$

where χ_o is the susceptibility and $F(t)$ is the after-affect function. With a single relaxation time, the after-effect function $F(t) = \exp(-t/\tau)$. When the relaxation times are distributed with the weight function $f(\tau)$ the after-effect function becomes

$$F(t) = \int_0^\infty f(\tau)\exp(-t/\tau)\mathrm{d}\tau \tag{7.3}$$

Thus, it is evident that the distribution of the relaxation times will be critical in determining the behavior of the system. If we assume a uniform distribution of energy barriers between finite limits, then we have a log-uniform distribution for the time constants. The log-uniform distribution is

$$G(\ln\tau) = \begin{cases} \dfrac{1}{\ln(\tau_1/\tau_2)} & \tau_1 < \tau < \tau_2, \\ 0 & \text{otherwise.} \end{cases} \tag{7.4}$$

The appropriate distribution function is obtained through a change in variables:

$$G(\ln\tau) = f(\tau)\left|\frac{d\tau}{d(\ln\tau)}\right|^{-1} = \tau f(\tau) \tag{7.5}$$

Therefore, the distribution function is

$$f(\tau) = \frac{1}{\tau\log(\tau_2/\tau_1)} \text{ for } \tau_1 \le \tau \le \tau_2 \tag{7.6}$$

and zero everywhere else, where τ_1 is the lower and τ_2 is the upper time-constant in the system. The weight function in (7.6) has a log-uniform distribution of time constants ($f(\log\tau)\mathrm{d}(\log\tau) = \text{const}$).

Combining equations (7.2)-(7.6) gives the time dependent magnetization as

$$M(t) = \frac{H\chi_o}{\log(\tau_2/\tau_1)} \int_{\tau_1}^{\tau_2} \frac{\exp(-t/\tau)}{\tau} \mathrm{d}\tau \tag{7.7}$$

Assuming $\tau_2 >> \tau_1$, then within the range $1/\tau_2 << t << 1/\tau_1$, it follows that

$$M(t) \approx \frac{H\chi_o}{\log(\tau_2/\tau_1)} (-\gamma - \log t - \log \tau_2) \tag{7.8}$$

where $\gamma \approx 0.577$ is the Euler constant. Most metal detectors measure $\partial H/\partial t$ so that the sensor reading is proportional to the change in the ferrite magnetization over-time. Within the same range where the $\log t$ behavior is evident in the H-field,

$$\frac{\mathrm{d}M(t)}{\mathrm{d}t} \propto \frac{-H\chi_o}{\log(\tau_2/\tau_1)} \frac{1}{t} \tag{7.9}$$

Consequently, the time derivative of the decaying magnetic field produced by the magnetization decays as t^{-1}. This t^{-1} decay has been observed in archaeological prospecting (Colani and Aitken, 1966), time domain electromagnetic (TEM) surveys carried out over laeteritic soils for mineral exploration (Buselli, 1982), and also in TEM surveys carried out on Kaho'olawe Island, Hawaii (Ware, 2003).

7.3 The Magnetic Susceptibility of a Collection of Single Domain Grains

If the acquisition and decay of magnetization is not instantaneous, then a complex frequency-dependent susceptibility is required to explain the behavior of a system exhibiting viscous magnetization. The frequency dependent susceptibility is the one-sided Fourier transform of the impulse response (equivalent to the derivative of the step-off after-affect function),

$$\frac{\chi(\omega)}{\chi_o} = -\int_0^{\infty} \frac{\mathrm{d}F(t)}{\mathrm{d}t} \exp(-i\omega t)\mathrm{d}t \tag{7.10}$$

(Fannin and Charles, 1995). An elementary Fourier integral can be used to show that for a single relaxation time the complex susceptibility model is

$$\chi(\omega) = \frac{\chi_o}{1 + i\omega\tau} \tag{7.11}$$

This model is the well known Debye model (Debye, 1928).

In more general terms, if the relaxation times are distributed with the weight function $f(\tau)$ then the complex susceptibility model becomes

$$\chi(\omega) = \chi_o \int_0^\infty \frac{f(\tau)}{1 + i\omega\tau} \mathrm{d}\tau \tag{7.12}$$

Assuming a log-uniform distribution of time constants (Fannin and Charles, 1995; Lee, 1983) the complex susceptibility becomes

$$\chi(\omega) = \chi_o \left(1 - \frac{1}{\log(\tau_2/\tau_1)} \log\left(\frac{1 + i\omega\tau_1}{1 + i\omega\tau_2}\right)\right) \tag{7.13}$$

Within a certain range of frequencies determined by the end-member time constants, the in-phase susceptibility will vary linearly with the logarithm of the frequency while the quadrature susceptibility is constant with frequency. Furthermore, for $\tau_2 \gg \tau_1$ the slope of the in-phase and value of the quadrature susceptibility are related by

$$\frac{\partial \mathrm{Re}[\chi(\omega)]}{\partial \log \omega} = \frac{2}{\pi} \mathrm{Im}[\chi(\omega)] = -\frac{\chi_o}{\log(\tau_2/\tau_1)} \tag{7.14}$$

From analysis of a wide range of soils, (Dabas et al., 1992) found that most could be explained with the above susceptibility model. However, there were some soils that did not fit the model so well, which may indicate that a log-uniform distribution of time constants may not always be appropriate.

The Cole-Cole frequency distribution has also been used to represent magnetic susceptibility (for example Olhoeft and Strangway, 1974; Dabas et al., 1992). The Cole-Cole model for magnetic susceptibility is

$$\chi(\omega) = \chi_\infty + \frac{\chi_o - \chi_\infty}{1 + (i\omega\tau_c)^{1-\alpha}}. \tag{7.15}$$

where χ_∞ is the susceptibility as frequency approaches infinity (therefore characterizing the instan-

taneous magnetization) and χ_o is the susceptibility as frequency approaches zero. The imaginary part of the susceptibility is zero in the limits of zero and infinite frequency. The value of α controls the distribution of relaxation times. The limits of α are $\alpha = 0$ for a single Debye relaxation mechanism and $\alpha = 1$ for an infinitely broad distribution of relaxation times. The time constant τ_c controls the location of the peak of the imaginary part of the susceptibility, with the peak occurring at $\omega = 1/\tau_c$. For a large α the Cole-Cole model yields a straight line for the real part and a constant negative value for the imaginary part, thus it is similar to our model in equation 7.15

It has been suggested that a Log-Normal distribution would best describe the distribution of time constants (Cross, 2006). Figure 7.4 compares the Cole-Cole, Log-Uniform, and Log-Normal distributions. Clearly, the log-normal distribution can be well approximated by a Cole-Cole model with the appropriate parameters. Figure 7.4(a) plots the Log-Uniform, or Frohlich, distribution of

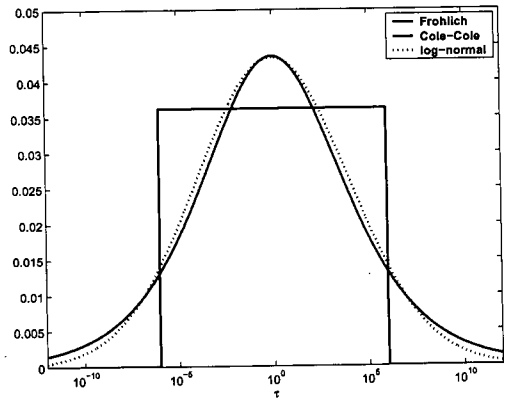

(a) Comparison of a Log-Uniform (or Frohlich) time constant distribution to the Cole-Cole and Log-Normal distributions.

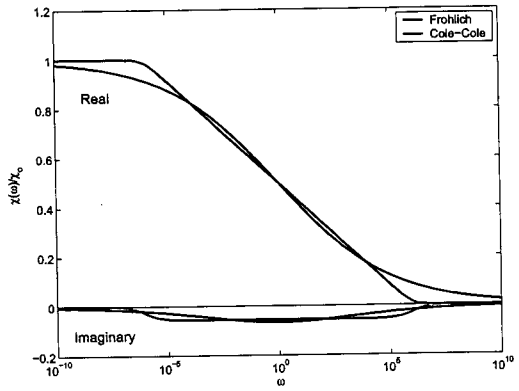

(b) Comparison of the resulting magnetic susceptibility from the distributions in (a). For the Cole-Cole model we assume that $\chi_\infty = 0$.

Figure 7.4: Comparison of the Log-Uniform (or Frohlich) distribution and the Cole-Cole distribution.

Equation 7.4 with bounding time constant values of $\tau_1 = 10^{-6}$ and $\tau_2 = 10^6$. The expression for the log distribution of the Cole-Cole model is

$$G(\ln \tau) = \frac{1}{2\pi} \frac{\sin(\pi\alpha)}{\cosh((1-\alpha)\ln(\tau_o/\tau)) - \cos(\pi\alpha)} \tag{7.16}$$

(see, for example, Fannin and Charles (1995)). If we assume, that $\chi_\infty = 0$, $\tau_o = 1$, and $\alpha = 0.83$, we obtain the distribution plotted in blue in Figure 7.4(a).

Sample	Low Frequency (0.46 kHz)	High Frequency (4.6 kHz)
7462-2728A-6"	3554	3311
7462-2728A-24"	3022	2771
7462-2728B-6"	1046	1001
7468-2734AP-6"	1726	1630
7468-2734AP-18"	1529	1448
7468-2734BP-12"	2807	2634
7468-2734BP-24"	1920	1807
7468-2734AB-6"	845	805
7468-2734BB-8"	1795	1707

Table 7.2: Susceptibility measurements ($\times 10^{-5}$ S.I.) at the Seagull Site.

The different time constant distributions produce different magnetic susceptibilities. Figure 7.4(b) compares the resulting magnetic susceptibilities from the Log-Uniform and Cole-Cole distributions of Figure 7.4(a). The continuous and smooth time constant distribution of the Cole-Cole model produces a smoother susceptibility model.

A model for the frequency dependent susceptibility of soils is required to investigate magnetic noise problems through forward modelling. For the modelling examples of this paper we will use magnetic susceptibility measurements taken on soil samples from Kaho'olawe Island, Hawaii. The Bartington MS2B susceptibility meter was used for the measurements. The MS2B measures the susceptibility of a 30 ml sample at 4.6 and 0.46 kHz. Table 7.2 lists measurements of the magnetic susceptibility for soil samples at the Seagull site on Kaho'olawe. These measurements provide us with the real part of the complex susceptibility at two frequencies. Given this limited information of the soil's magnetic characteristics, we need to make some assumptions before generating a susceptibility model. First, we assume that the two measuring frequencies are within the frequency range where the in-phase component decreases linearly with the logarithm of frequency ($\tau_2^{-1} \ll \omega \ll \tau_1^{-1}$). Second, we assume that all the frequencies of interest fall within this range of frequencies. With these two assumptions, we can model the real part of the susceptibility as a straight line. Furthermore, we can use equation 7.14 to predict the quadrature component of the susceptibility from the slope of the in-phase component. Figure 7.5 shows the susceptibility model assumed for soil sample 7468-2734AP-6".

In addition to the log-uniform distribution model for the soil susceptibility, we also plot in figure 7.5 the best fit Cole-Cole model. To obtain a unique model, we assume that the peak of

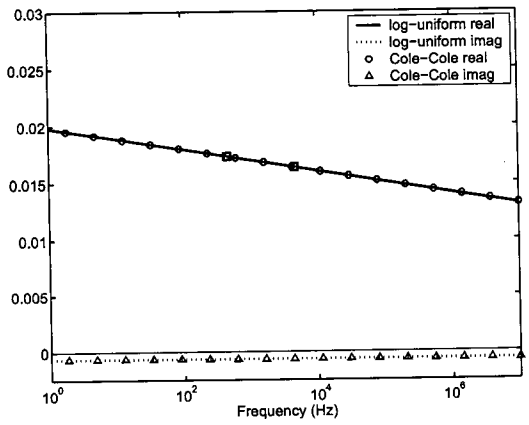

Figure 7.5: Frequency dependent susceptibility models for sample 7468-2734AP-6".

the imaginary part of the susceptibility is located between the two measurement frequencies of the MS2B (i.e. $\tau = 1.08 \times 10^{-4}$). We also assume no instantaneous magnetization (i.e. $\chi_\infty = 0$). For the soils sample of figure 7.5, $\chi_0 = 5441 \times 10^{-5}$ S.I. and $\alpha = 0.94$. The large value of α indicates a broad distribution of time constants.

Complex susceptibility measurements of a number of soil samples from the Navy UXO QA grid were carried out using a LakeShore Cryotronics AC Susceptometer at the University of Minnesota's Institute for Rock Magnetism (IRM) (Li et al., 2005). Figure 7.6 contains a typical measurement for the Kaho'olawe soil samples. The susceptibility of the Kaho'olawe soil samples exhibit a strongly frequency-dependent real component and a much smaller, and nearly constant, imaginary component. The best fit log-uniform time constant susceptibility model of equation 7.13 is plotted as a solid line.

7.4 Modelling the Electromagnetic Response of Viscous Remanent Soil

7.4.1 The Electromagnetic Response of a 1-D Layered Earth

In order to examine the effect of viscous remanently magnetized soils on EM sensors, we consider the response of a half-space with the frequency dependent susceptibility of Figure 7.5. Forward modelling in 1D is solved in the frequency domain using a propagation matrix formalism (Farquharson et al., 2003). Let us consider a circular transmitter loop of radius a, carrying a current

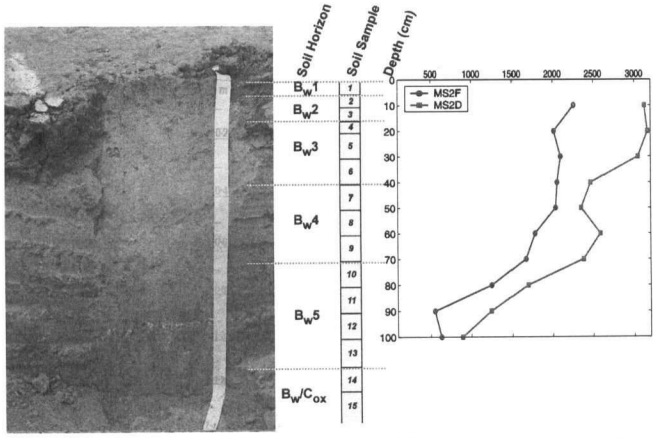

(a) A soil pit dug at approximately the center of the site. The plot to the right indicate the magnetic susceptibility measured by Bartington MS2D (blue line, 0.958 kHz) and MS2F (green line, 0.58 kHz) susceptibility meters.

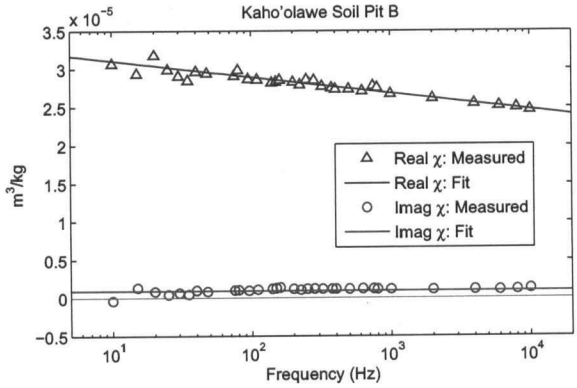

(b) Susceptibility measurement of a surface soil sample from Kaho'olawe Navy QA grid. The measured susceptibility values are fit assuming a log-uniform time constant susceptibility model.

Figure 7.6: Susceptibility analysis of a soil pit in Grid 2E at Kaho'olawe.

I, and at a height h above a 1-D layered earth. At an observation point z above the ground and a radial distance ρ from the axis of circular transmitter loop, the radial component H_ρ and the vertical component H_z of the **H**-field are

$$H_\rho(\omega) = \frac{Ia}{2}\int_0^\infty \left[e^{-u_o(z+h)} - \frac{P_{21}}{P_{11}}e^{u_o(z-h)}\right]\lambda J_1(\lambda a)\, J_1(\lambda\rho)\, d\lambda \tag{7.17}$$

$$H_z(\omega) = \frac{Ia}{2}\int_0^\infty \left[e^{-u_o(z+h)} + \frac{P_{21}}{P_{11}}e^{u_o(z-h)}\right]\frac{\lambda^2}{u_o} J_1(\lambda a)\, J_o(\lambda\rho)\, d\lambda \tag{7.18}$$

where $u_o = \sqrt{\lambda^2 - k_o^2}$, k_o is the wave number of the air, and J_o and J_1 are the zeroth and first order Bessel functions, respectively. P_{21} and P_{11} are elements of the matrix $\mathbf{P}$:

$$\mathbf{P} = \mathbf{M}_1 \prod_{j=2}^{m} \mathbf{M}_j \tag{7.19}$$

where

$$\mathbf{M}_1 = \begin{bmatrix} \frac{1}{2}\left(1+\frac{\mu_0 u_1}{\mu_1 u_0}\right) & \frac{1}{2}\left(1-\frac{\mu_0 u_1}{\mu_1 u_0}\right) \\ \frac{1}{2}\left(1-\frac{\mu_0 u_1}{\mu_1 u_0}\right) & \frac{1}{2}\left(1+\frac{\mu_0 u_1}{\mu_1 u_0}\right) \end{bmatrix} \tag{7.20}$$

$$\mathbf{M}_j = \frac{1}{2}\begin{bmatrix} \left(1+\frac{\mu_{j-1} u_j}{\mu_j u_{j-1}}\right) & \left(1-\frac{\mu_{j-1} u_j}{\mu_j u_{j-1}}\right) \\ \left(1-\frac{\mu_{j-1} u_j}{\mu_j u_{j-1}}\right) e^{-2u_{j-1}t_{j-1}} & \left(1+\frac{\mu_{j-1} u_j}{\mu_j u_{j-1}}\right) e^{-2u_{j-1}t_{j-1}} \end{bmatrix} \tag{7.21}$$

The thickness of the j^{th} layer is t_j, and μ_j is the magnetic permeability of the layer.

In this study we will consider measurements of the secondary field at the center of the transmitting loop. The fields at the center of the transmitter loop are calculated by setting $\rho = 0$ and $z = -h$. These substitutions give

$$H_\rho(\omega) = 0 \tag{7.22}$$

$$H_z(\omega) = \frac{Ia}{2}\int_0^\infty \left[1 + \frac{P_{21}}{P_{11}}e^{-2u_o h}\right]\frac{\lambda^2}{u_o} J_1(\lambda a)\, d\lambda \tag{7.23}$$

Therefore, as the symmetry of the 1-D would also suggest, there is no horizontal component to the **H**-field response at the center of the transmitter loop. The time domain solution is obtained by calculating Fourier transformations of the frequency response for a causal step turn-off.

7.4.2 The Effect of Magnetic Susceptibility on the Electromagnetic Response

Figure 7.7 shows the modelled electromagnetic response at the center of a circular transmitter loop of radius $a = 25$ m and carrying a current of 1 A placed on the surface of a half-space. This arrangement is typical of large loop electromagnetic soundings carried out in exploration geophysics. We consider three half-space conductivities (σ =0.01, 0.1 and 1.0 S/m). The smaller conductivity is applicable to the soils on Kaho'olawe Island, Hawaii, while 1.0 S/m represents a soil with a very high conductivity. In each model we use the susceptibility of sample 7468-2734AP-6" (figure 7.5).

Figure 7.7(a) shows the time domain response to a step-off transmitter current. In general, the time-domain response consists of three stages. At the earliest times the eddy currents are distributed on the surface of the half-space and the $\partial H_z/\partial t$ response is flat. This corresponds to the so called inductive limit. At intermediate times, the current starts to move downwards and spreads out, with the $\partial H_z/\partial t$ response at the center of the loop decaying as

$$\frac{\partial H_z}{\partial t} = \frac{I\sigma^{3/2}\mu^{3/2}a^2}{20\sqrt{\pi}} t^{-5/2} \tag{7.24}$$

This intermediate time response is referred to as the ground effect (Ward and Hohmann, 1991) and has a characteristic decay of $t^{-5/2}$. The ground effect extends later into time with higher conductivity soils, higher susceptibility soils, or larger loop size. The third stage is the late-time response which is dominated by the magnetic viscosity and displays the characteristic $1/t$ decay derived in equation 7.9.

The secondary H-field frequency domain response for the three half-space models are plotted in Figure 7.7(b). At high frequencies the secondary H-field asymptotes to the half-space inductive limit. At the inductive limit currents are induced on the surface of the half-space to cancel the primary field, thus producing a secondary field that is (1) the negative of the primary field ($H_z = -I/(2a)$ at the loop center) and (2) in-phase with the primary field (i.e. no imaginary component).

The low frequency response corresponds to the resistive limit. At the center of a circular loop on a half-space this can be determined by taking the low frequency limit of equation 7.23:

$$\lim_{\omega \to 0} H_z = \frac{I}{2a}\left(\frac{\chi}{2+\chi}\right). \tag{7.25}$$

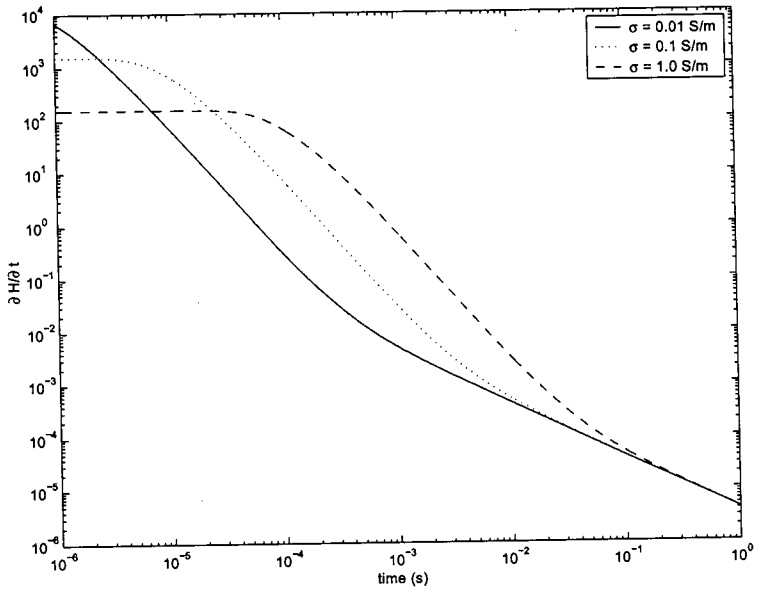

(a) Time domain response.

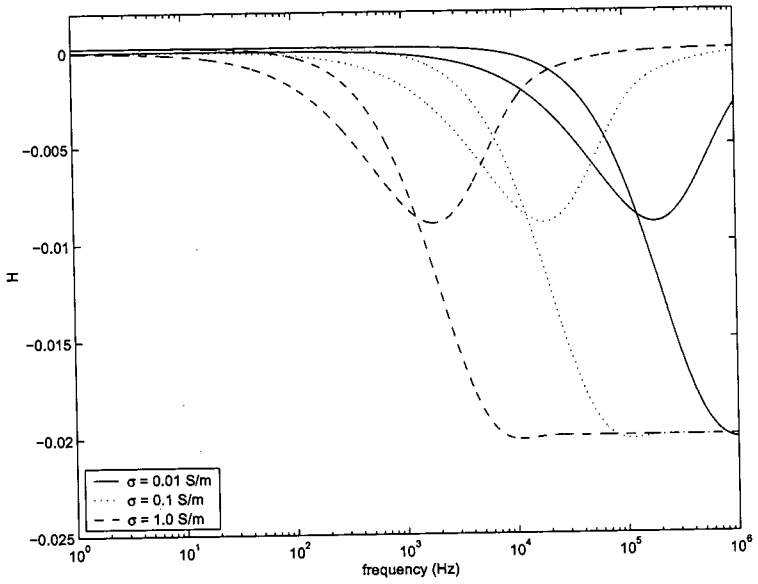

(b) Frequency Domain Response

Figure 7.7: Forward modelled electromagnetic responses for half-spaces with magnetic viscosity and conductivities of σ =0.01, 0.1 and 1.0 S/m.

It is clear from equation 7.25 that for a non-magnetic half-space ($\chi = 0$), both real and imaginary components asymptote to zero at low frequencies. The resistive limit response of half-space with a non-frequency dependent, non-complex magnetic susceptibility ($\chi(\omega) = \chi_o$) has a non-zero real component and is in-phase with the primary field (i.e. no imaginary component). For the case of a viscous magnetic earth, characterized by a complex, frequency dependent susceptibility, the real component of the field has a positive asymptote and the imaginary component has a negative asymptote. The resistive limit characteristics are seen more clearly in Figure 7.8, where the response of a half-space with conductivity of 0.1 S/m is plotted.

Figures 7.8 and 7.9 show the electromagnetic responses that occur for (1) no magnetic viscosity ($\chi = 0$, the conductive response) and (2) no eddy currents ($\sigma = 0$, the magnetic response). Note that the oscillations at early time for the magnetic response are artifacts of the filter we used convert to the time domain. The full modelling results, which include both the eddy current and magnetic viscosity response are plotted as solid black lines. At low frequencies and, correspondingly, late times the full modelled response is dominated by the magnetic response. At high frequencies and early times the full modelled response is dominated by the eddy current response. Figure 7.9(b) shows that for smaller loop sizes (in this case, $a = 0.5$ m) that the ground response is not evident within the plotted time range. The dependence of loop size and amplitude of ground response is reported in equation 7.24.

When the independently computed conductive and magnetic viscosity responses are added together, the time-decay is almost exactly the same as the full modelling results which incorporated the eddy current plus magnetic viscosity response. Therefore we conclude that there is no appreciable interaction between the eddy-current response and the magnetic relaxation; at the most the interaction is a second order effect. Since the geometry dependent eddy current response does not appreciably interact with ferrite response, the decay will always be $1/t$ regardless of the spatial distribution of magnetic soil. The amplitude of the $1/t$ response will change with variations in the ferrite concentration.

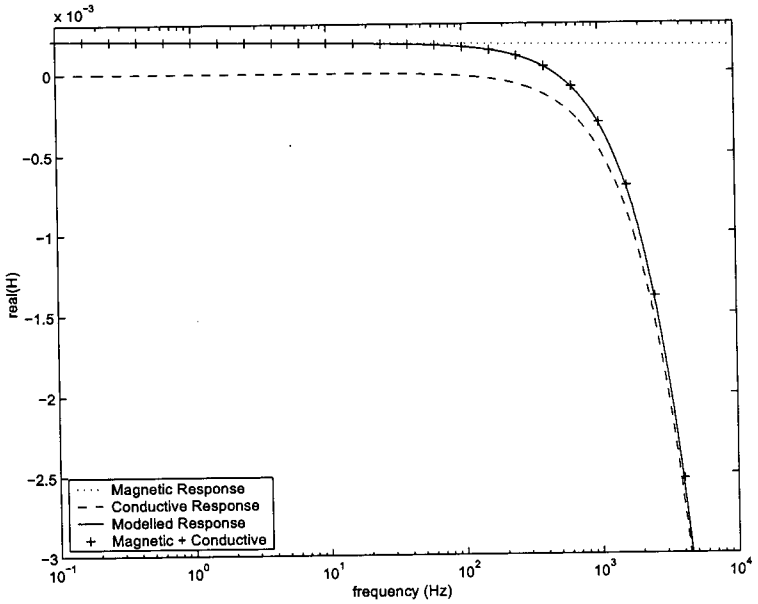

(a) Frequency domain response: Real component

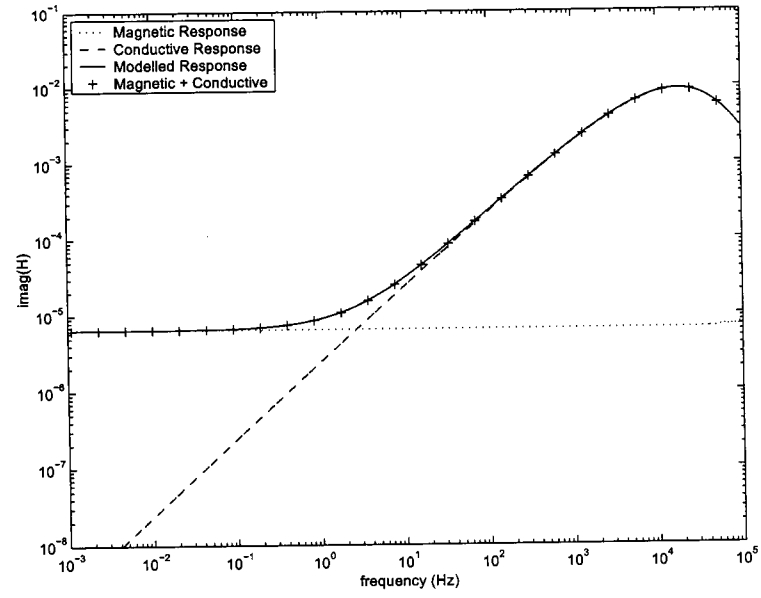

(b) Frequency Domain Response: Imaginary component

Figure 7.8: Forward modelled frequency domain electromagnetic responses to a step-off transmitter current for a half-spaces with magnetic viscosity and a conductivity of σ =0.1 S/m.

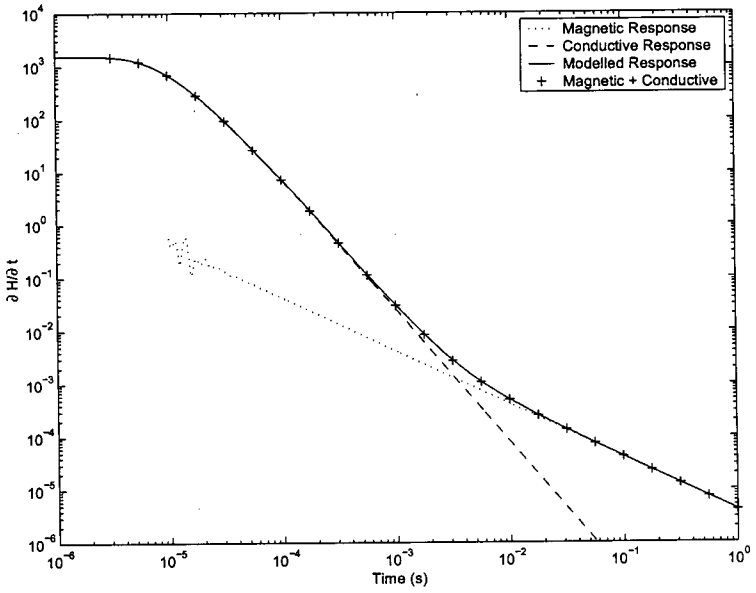

(a) Time domain response. $a = 25$ m

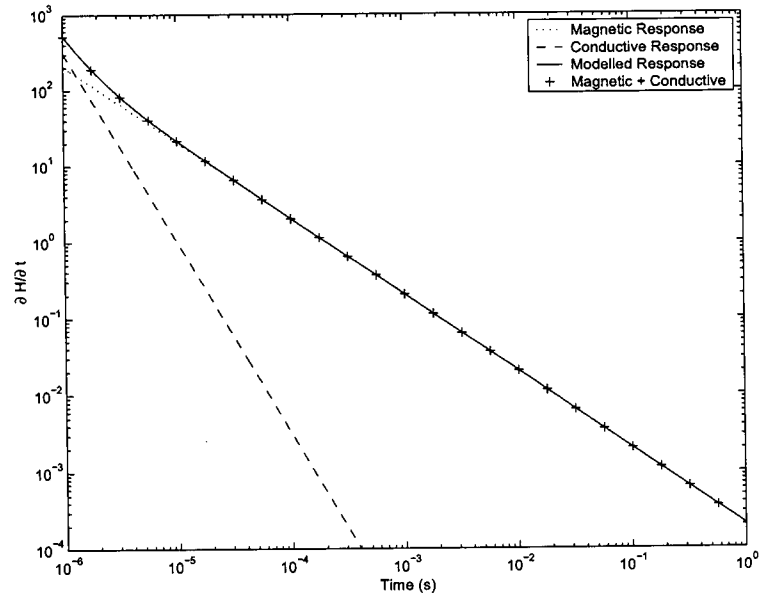

(b) Time Domain Response. $a = 0.5$ m

Figure 7.9: Forward modelled time domain electromagnetic responses to a step-off transmitter current for half-spaces with magnetic viscosity and a conductivity of σ =0.1 S/m.

7.4.3 Comparing the Electromagnetic Response of a Steel Object and Viscous Remanent Magnetic Soils

In landmine and UXO detection applications, electromagnetic sensors are used for detecting steel targets. In Figures 7.10 and 7.11, we compare the EM response of soils exhibiting viscous remnant magnetization (VRM) with the EM response of a steel spheroid in the frequency and time domain, respectively. We consider a horizontal loop transmitter with a diameter of 50 cm located 40 cm above a half-space with a conductivity of 0.01 S/m and a susceptibility of sample 7468-2734AP-6" (Figure 7.5). The responses for a spheroid with a length of 24 cm and a width 6 cm are calculated using the method of auxiliary moments (MAS) methodology (Shubitidze et al., 2002b). We assume that the spheroid sits in a uniform primary field in free space ($\sigma = 0$ S/m and $\mu = \mu_o$) and the center of the spheroid is located 70 cm below the measuring point. We assume that the steel conductivity is $\sigma = 1 \times 10^6$ S/m and magnetic permeability is $\mu = 250\mu_o$. The in-phase part of the response

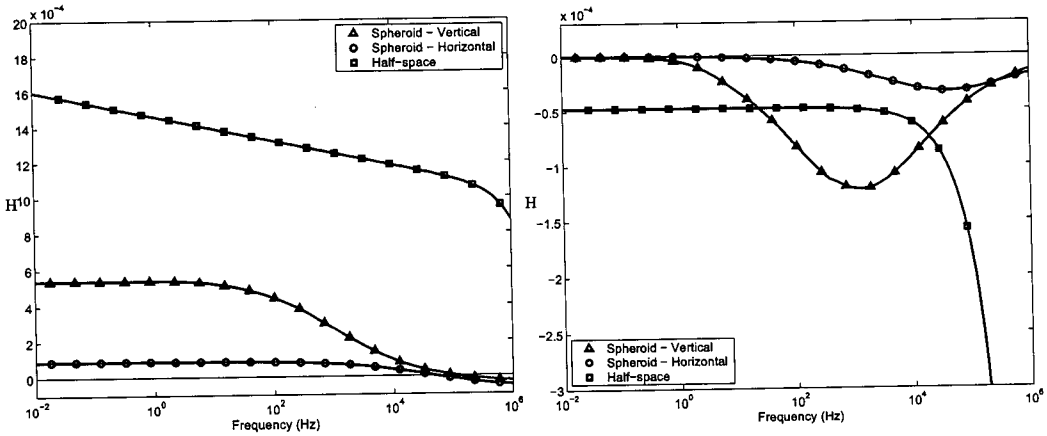

(a) The real, or in-phase, component of the frequency response.

(b) The imaginary, or quadrature, component of the frequency response.

Figure 7.10: Comparing the frequency domain responses of a steel spheroid and a complex susceptibility half-space .

(Figure 7.10(a)) is greater for the half-space than either the vertical or horizontal spheroids. At low frequencies the electromagnetic response approaches the magnetostatic limit for the half-space and spheroid. Although the magnetic susceptibility of the spheroid is much greater than for the half-space, the half-space response is greater than the spheroid due to the volume of magnetic material making a contribution to the secondary field. The differences in the quadrature response of the

half-space and spheroid can be observed in Figure 7.10(b). At low frequency the imaginary part of the spheroid response is zero while the soil response, due to its complex susceptibility, is non-zero. Within the frequency range of typical UXO detection electromagnetic induction sensors, the complex susceptible soil response is flat, while the spheroid response exhibits a resonance peak. The resonance peak of the half-space occurs at a much higher frequency than the steel spheroid. This characteristic has been exploited for detection using frequency domain sensors of metallic targets within magnetic soil (Wright et al., 2001; Huang and Won, 2004).

The time decay response for the half-space and spheroid are compared in Figure 7.11. The $1/t$ time decay of VRM soils is similar in magnitude to the steel spheroids. Unlike the half-space, the spheroid response does not follow a power law decay for the entirety of the time range. The response of the half-space is greater than the horizontal spheroid at all time channels. The response of the half-space is greater than the vertical spheroid at early and late times, with the spheroid having a larger response at intermediate times.

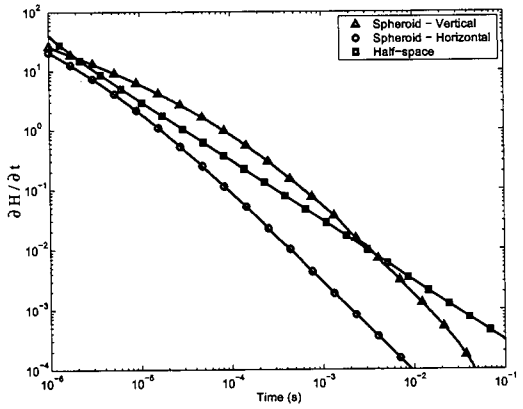

Figure 7.11: Forward modelled time domain electromagnetic responses of a steel spheroid and a complex susceptibility half-space.

7.5 Application to ITEP Landmine Test Lanes

The International Test and Evaluation Program for Humanitarian Demining (ITEP) constructed landmine testing lanes to study the effect of different soil types on the response of typical metal detectors used for humanitarian demining. ITEP have considered a simple, empirical method for quantifying the amount of signal noise from the soil host (Müller et al., 2003). In this method a

metal detector without soil compensation is calibrated and a signal sensitivity is set such that the sensor responds to a predefined minimum signal. The maximum height at which the sensor reports a signal, referred to as the *ground reference height*, is then an indicator of the background soil noise. A Schiebel time domain pulse induction metal detector was used for the ground height measurement.

We investigate the relationship between ground reference height and susceptibility change by considering data collected from a pair of test lanes in trials performed at Benkovac, Croatia and Oberjettenberg, Germany. The Benkovac test lane contained red, bauxite soil which was classified as being uncooperative (i.e. the background soil produced a large background signal). The Oberjettenberg test lane soil consists of magnetite mixed with coarse sand, and has a relatively low background signal. The change in magnetic susceptibility of each lane was measured using a Bartington MS2B susceptibility meter. A susceptibility measurement was obtained with the MS2D susceptibility probe was used to determine the susceptibility at 980 Hz. Table 7.1 summarizes the susceptibility measurements of the lanes and the ground height measurement.

The Benkovac lane has a larger ground reference height (and therefore a larger magnetic soil signal) than the Oberjettenberg lane, even though the absolute susceptibility of the Oberjettenberg lane ($\chi_{980Hz} = 3000 \pm 500 \times 10^{-5}$SI) is much greater than the absolute susceptibility of the Benkovac lane ($\chi_{980Hz} = 154 \pm 13 \times 10^{-5}$SI). We can see how the change in susceptibility with frequency affects the magnitude of the measured response, and therefore the ground reference height measurement by modelling the susceptibility of each lane as a complex, frequency dependent quantity (figure 7.12). It is clear from figure 7.12 that the amplitude of $1/t$ characteristic soil decay of the Benkovac test lanes is much greater than the amplitude for the Oberjettenberg decay, indicating the less cooperative nature of the soil with larger $\Delta\chi$.

To simulate the ground reference height test we calculate the signal as a function of sensor height above the surface at 45 microseconds after the transmitter step off. Figure 7.13(a) shows that, for the Benkovac and Oberjettenberg soils, the height at which a sensor measures a defined response magnitude is indicative of the soil noise. We generalize this result in Figure 7.13(b) by plotting the ground reference height as a function of $\Delta\chi$ for a number of soils varying in susceptibility magnitude. There exists a one-to-one relationship between the ground reference height and the change of susceptibility. This relationship is nearly independent of the magnitude in susceptibility.

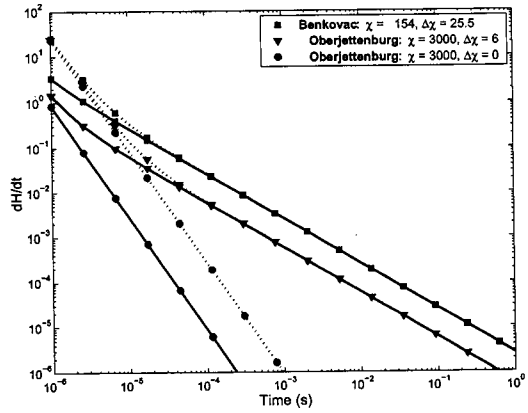

Figure 7.12: Forward modelled time domain electromagnetic responses for half-space models with susceptibility models based on soil susceptibility measurements of Oberjettenberg and Benkovac landmine test lanes.

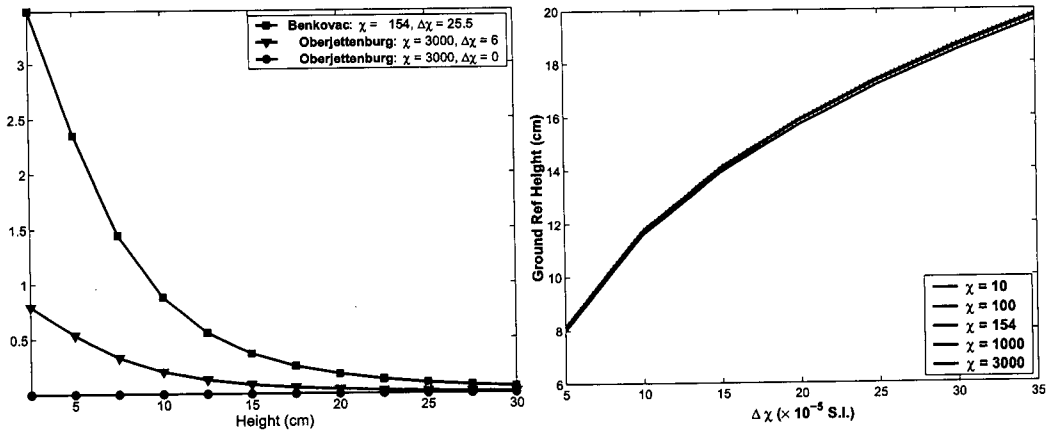

(a) The modelled time domain response at 45 croseconds.

(b) Relationship between the ground reference height and the change in susceptibility.

Figure 7.13: Comparison of the Benkovac and Oberjettenberg soil responses as a function of sensor height.

The $\Delta\chi$ measurements and ground reference heights reported in Table 7.1 approximately match the modelled ground reference heights of Figure 7.13.

7.6 Conclusion

This chapter demonstrated that the theory of viscous remnant magnetization can be used to explain the characteristics of electromagnetic sensor data acquired in magnetic settings. Magnetic susceptibility models based on magnetic particles with a log-uniform distribution of time constants are considered. We generated complex susceptibility models from measurements under the assumption that, within the frequency range of electromagnetic sensors used for UXO detection, the complex susceptibility has a constant imaginary component and a real component that decreases linearly with the logarithm of frequency. Recent multi-frequency measurements of the complex susceptibility have confirmed this characteristic (Li et al., 2005). Forward modelling of susceptibility models derived from Bartington MS2B measurements of Kaho'olawe soil have shown good quantitative agreement with measured data. A complex and frequency dependent magnetic susceptibility model is required to represent the magnetic characteristic of a viscous remanent magnetized subsurface. Our modelling helped explain results observed in field data sets acquire in Kaho'olawe and in test lanes built by ITEP.

Chapter 8

Processing of Data Acquired in Magnetic Settings

Detection and identification of UXO at sites with large geologic background signals can be very difficult. Figures 7.2 and 7.3 contain images of TEM and FEM data collected on the island of Kaho'olawe. The large frequency dependent component of susceptibility of Kaho'olawe soils produce background responses of the same order of magnitude of UXO.

Consider a target buried in a halfspace. The measured sensor data can be written as

$$\mathbf{d}^{obs} = \mathcal{F}\left[target, host\right] + \text{noise}, \tag{8.1}$$

where $\mathbf{d}^{obs}$ is the observed sensor data and $\mathcal{F}\left[target, host\right]$ represent the forward model that is function of the target and host. If the response of the target and host are approximately additive, we can write

$$\begin{aligned} \mathbf{d}^{obs} &= \mathcal{F}^{bg}\left[host\right] + \mathcal{F}^{t}\left[target\right] + \text{noise} \\ &= \mathbf{d}^{bg} + \mathbf{d}^{target} + \text{noise} \end{aligned} \tag{8.2}$$

where $\mathbf{d}^{bg} = \mathcal{F}^{bg}\left[host\right]$ is the response due to the background host, $\mathbf{d}^{target} = \mathcal{F}^{t}\left[target\right]$ is the response due to the target, $\mathcal{F}^{int}\left[target, host\right]$ represents the interaction between target and host. In most cases $\mathcal{F}^{t}\left[target\right]$ is chosen to be a dipole model representation of the target.

A method of simultaneous estimating the parameters for the target and host was presented in Chapter 5. However, the most common approach to processing is to develop filtering techniques such that the background response $\mathbf{d}^{bg}$ can be estimated, and subsequently subtracted from the data. These filtering methods assume that the geologic, and therefore electromagnetic, properties of the host material are spatially slowly varying, while the anomalies of compact targets have a relatively

smaller spatial wavelength. The filtered data is then inverted with the physical model $\mathcal{F}^T\,[target]$ for the UXO response in free space. One of the major difficulties with this approach is the accuracy with which the background response $\mathbf{d}^{bg} = \mathcal{F}^{bg}\,[host]$ can be estimated. In particular, movement of the transmitter and receiver relative to magnetic ground can produce significant small wavelength anomalies in the data (Walker et al., 2005b; Foley et al., 2005). High pass filters will have limited success in these cases. Our preferred approach to processing these data is to estimate a smoothly varying background geology, that is subsequently removed from the data. This approach requires accurate sensor positioning and orientation information to model the small wavelength variations.

Techniques for processing data collected at remediation sites with large geologic background signals are considered in this chapter. A number of synthetic data will be used to demonstrate filtering, target picking, and parameter estimation of data collected in a magnetic geology setting. The objective is to determine what type of information can be recovered from electromagnetic data collected in regions with highly magnetic geology.

8.1 The Electromagnetic Response of a Viscous Remnant Magnetic Halfspace

In the previous chapter we outlined the equations for modelling the response over a layered earth. Let us consider a circular transmitter loop of radius a, carrying a current I, and at a height h above a 1-D layered earth. At an observation point at the center of the transmitter loop, the vertical component H_z and the radial component H_ρ of the **H**-field are

$$H_\rho\,(\omega) = 0 \tag{8.3}$$

$$H_z\,(\omega) = \frac{Ia}{2}\int_0^\infty \left[1 + \frac{P_{21}}{P_{11}}e^{-2u_o h}\right]\frac{\lambda^2}{u_o}J_1\,(\lambda a)\,d\lambda \tag{8.4}$$

where $u_o = \sqrt{\lambda^2 - k_o^2}$, k_o is the wave number of the air, and J_1 is the first order Bessel function. P_{21} and P_{11} are elements of the propagation matrix $\mathbf{P}$.

For a half-space we can write

$$H_z\,(\omega) = \frac{Ia}{2}\int_0^\infty \left[1 + \frac{\mu_1 u_0 - \mu_0 u_1}{\mu_1 u_0 + \mu_0 u_1}e^{-2u_o h}\right]\frac{\lambda^2}{u_o}J_1\,(\lambda a)\,d\lambda \tag{8.5}$$

If we make the quasi-static assumption and assume a non conductive half-space, then $u_o = u_1 = \lambda$. The field is then

$$H_z(\omega) = \frac{Ia}{2}\int_0^\infty \left[1 + \frac{\mu_1 - \mu_0}{\mu_1 + \mu_0} e^{-2u_o h}\right] \lambda J_1(\lambda a)\, d\lambda \tag{8.6}$$

We first split the equation into a couple of terms:

$$H_z(\omega) = \frac{Ia}{2}\left(\frac{\chi}{2+\chi}\right)\int_0^\infty e^{-2h\lambda}\lambda J_1(\lambda a)\, d\lambda + \frac{Ia}{2}\int_0^\infty \lambda J_1(\lambda a)\, d\lambda \tag{8.7}$$

and with the integrals carried out analytically, we obtain

$$H_z(\omega) = \frac{Ia}{2}\left(\frac{\chi}{2+\chi}\right)\frac{a}{\left[a^2 + (2h)^2\right]^{3/2}} + \frac{Ia}{2}\left[\frac{1}{a^2}\right] \tag{8.8}$$

The second term in Equation 8.8 is equal to the primary field. Therefore, the secondary field is

$$H_z^s(\omega) = \frac{Ia}{2}\left(\frac{\chi}{2+\chi}\right)\frac{a}{\left[a^2 + (2h)^2\right]^{3/2}} \tag{8.9}$$

In cases where $\chi \ll 2$,

$$H_z^s(\omega) \approx \frac{I}{4}\frac{a^2}{\left[a^2 + (2h)^2\right]^{3/2}}\chi(\omega) \tag{8.10}$$

Therefore the resistive limit response is approximately proportional to the susceptibility. If we represent the magnetic susceptibility with equation 7.13 and assume that $\tau_2 \gg \tau_1$, then the field can be written as

$$H_z^s(\omega) \approx \frac{I}{4}\frac{a^2}{\left[a^2 + (2h)^2\right]^{3/2}}\frac{\chi_o}{\ln(\tau_2/\tau_1)}\left(1 - \ln(\omega\tau_2) - i\frac{\pi}{2}\right) \tag{8.11}$$

The corresponding result in the time domain can be obtained by taking the sine transform of the imaginary component of the secondary field. The step-off response of the time derivative of the H field is

$$\frac{\partial H}{\partial t} = \frac{2}{\pi}\int_0^\infty \Im[H(\omega)]\sin(\omega t)\, d\omega \tag{8.12}$$

Substitution of the imaginary component of Equation 7.13 into equation 8.12 gives

$$\frac{\partial H}{\partial t} = -\frac{2}{\pi}\frac{I}{4}\frac{a^2}{\left[a^2+(2h)^2\right]^{3/2}}\frac{\chi_o}{\ln(\tau_2/\tau_1)}\int_0^\infty \left[\tan^{-1}(\omega\tau_2)-\tan^{-1}(\omega\tau_1)\right]\sin(\omega t)\,d\omega \quad (8.13)$$

where a log-normal distribution of time constants is assumed. The sine transform identity

$$\frac{\pi}{2\omega}e^{b\omega} = \int_0^\infty \tan^{-1}\left(\frac{x}{b}\right)\sin(\omega x)\,dx \quad (8.14)$$

can be rewritten as

$$\frac{\pi}{2t}e^{-t/b} = \int_0^\infty \tan^{-1}(\omega b)\sin(\omega t)\,d\omega. \quad (8.15)$$

Therefore the step-off response can be written

$$\frac{\partial H}{\partial t} = -\frac{I}{4}\frac{a^2}{\left[a^2+(2h)^2\right]^{3/2}}\frac{\chi_o}{\ln(\tau_2/\tau_1)}\frac{1}{t}\left(e^{-t/\tau_2}-e^{-t/\tau_1}\right) \quad (8.16)$$

For $t \ll \tau_2$ and $t \gg \tau_1$,

$$\frac{\partial H}{\partial t} \approx -\frac{I}{4}\frac{a^2}{\left[a^2+(2h)^2\right]^{3/2}}\frac{\chi_o}{\ln(\tau_2/\tau_1)}\frac{1}{t} \quad (8.17)$$

Equations 8.11 and 8.17 will be used as soil models.

For constant sensor height and orientation, the measured time domain response and frequency domain response are proportional to $G(\chi) = \chi_o/\log(\tau_2/\tau_1)$. Therefore, in areas of low conductivity soil, electromagnetic sensors act as viscous remnant susceptibility meters. To demonstrate this, we can compare susceptibility measurements with sensor data collected on Kaho'olawe. As part of SERDP project MM-1414 (Li et al., 2005), surface soil samples were collected from Grid 2E and their susceptibility measured with a Bartington MS2B susceptibility meter. Comparisons of the susceptibility measurements and sensor data are shown in Figure 8.1. Figure 8.1(a) is a gridded image of the difference in the susceptibility $\Delta\chi$ measured by the Bartington MS2B susceptibility meter at frequencies of 4.7 kHz and 0.47 kHz. If we assume the susceptibility model of equation 7.13, we can show that the

$$\Delta\chi \approx \frac{\chi_o}{\log(\tau_2/\tau_1)}\log(0.47kHz/4.7kHz)\,. \quad (8.18)$$

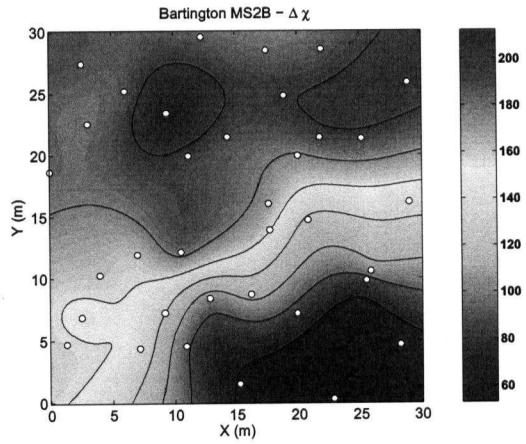

(a) Bartington MS2B susceptibility measurements ($\Delta\chi$). White circles indicate sampling points.

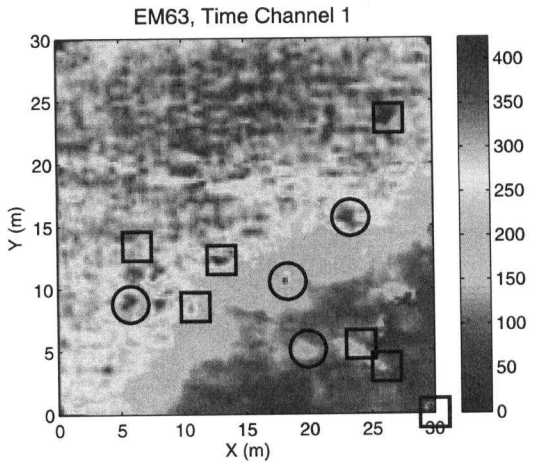

(b) First channel of Geonics EM63 data ($t = 0.18$ ms)

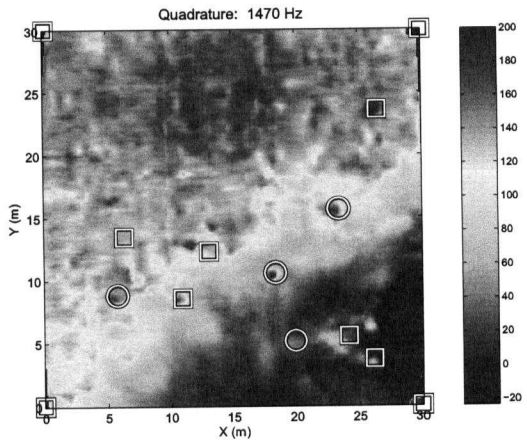

(c) Geophex GEM3 quadrature component data ($f = 1470$ kHz)

Figure 8.1: Comparison of Bartington MS2B susceptibility measurements with electromagnetic sensor data. Data collected on the Kaho'olawe Grid 2E are presented.

EM63 and quadrature component GEM3 data are plotted in Figure 8.1(b) and (c), respectively. Clearly the three images of Figure 8.1 are similar to within a scaling factor.

In the frequency domain, the response is proportional to the susceptibility (Equation 8.10) and not the susceptibility difference. Bartington MS2D measurements were taken on Grid 2E. The Bartington MS2D is a portable susceptibility meter that measures the modulus of the complex susceptibility at frequency $f = 0.98$ kHz. Figure 8.2 compares measurements from Kaho'olawe Grid 2E made by the Bartington MS2D sensor with the amplitude of the GEM3 data at 1470 Hz. Both the GEM3 and Bartington measurements identify an increase in signal in the lower right portion of the grid that was not evident in Figure 8.1. This increase in signal is not seen in the susceptibility and sensor data of Figure 8.1 since the increase is likely due to an increase in the static susceptibility.

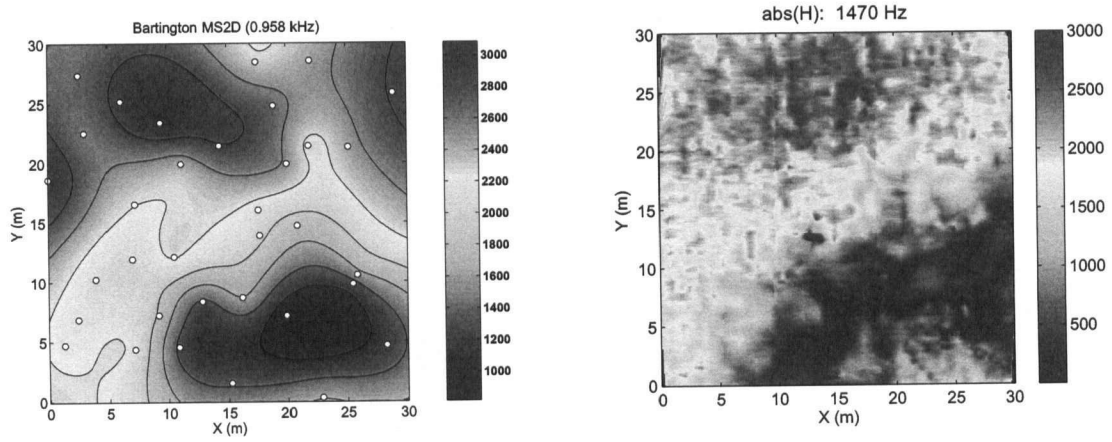

(a) Bartington MS2D measurements

(b) Geophex GEM3 magnitude FEM data

Figure 8.2: Comparison of Bartington MS2D susceptibility measurements with the inphase component of GEM3 data. The MS2D measures the phasor sum of the complex susceptibility at $f = 0.98$ kHz.

8.2 The Effect of Height Variations on the Sensor Response

We can use equations 8.10 and 8.17 to demonstrate the importance of sensor height accuracy. In both the frequency and time domain, the magnitude of the background response is scaled by the function

$$\text{Scale Factor } (SF) = \frac{a^2}{\left[a^2 + (2h)^2\right]^{3/2}} \tag{8.19}$$

Figure 8.3 plots this function for a loop with radius a=0.5m, normalized by the value at h = 0.3 m. Changes in height of only a few centimeters can change the signal by tens of percent. This formula can be used to study the effect of sensor height on the measured data.

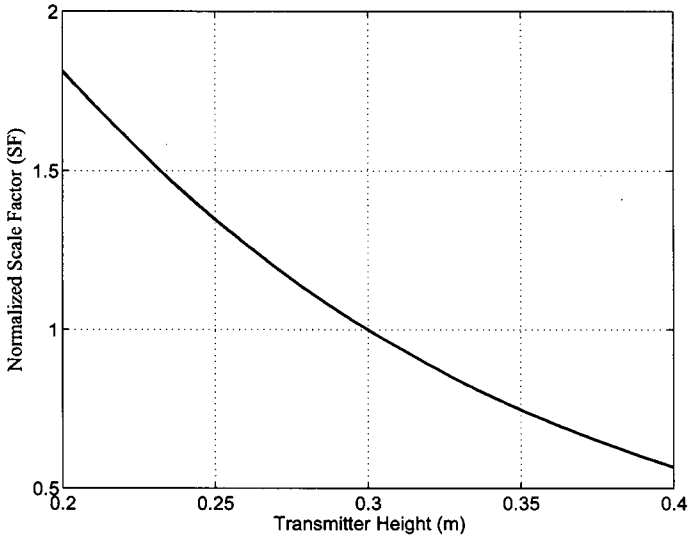

Figure 8.3: Scale factor normalized so the response is unity for a loop of radius a = 0.5 m and height h = 0.3 m.

Example 1: A Simulation of VRM geologic background response due to height variations

To demonstrate the importance of measuring the height of the sensor accurately, we forward model simulated height measurements. For this example we simulate heights based on the measurements made during a Geonics EM63 survey carried out on the FLBGR. Figure 8.4 has photographs of the GPO site. The site is relatively flat, but there are small "clumps" of dirt and grass that causes height and orientation variations in the EM63 cart.

The height of the sensor was measured using a Trimble RTS laser positioning system. Figure 8.5(a) shows the elevation measured during the survey, indicating the slight decease in elevation from the Northwest to Southeast corner (as is seen in Figure 8.4). The long wavelength elevation information is obtained through the application of a Butterworth filter (Figure 8.5(b)), and the short wavelength variations are obtained by subtracting the long wavelength component from the raw data.

A new elevation dataset is constructed by estimating the power spectra of the detrended eleva-

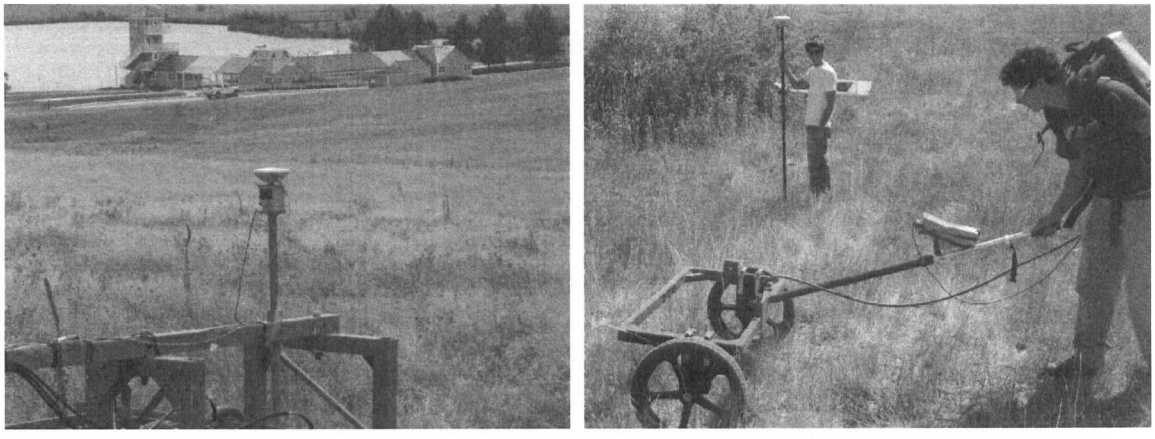

(a) View of GPO towards the southeast corner. (b) Close up of ground

Figure 8.4: On the left is a photograph of the FLBGR GPO looking southeast. The elevation of the grid decreases as we move from the Northwest corner to the Southeast corner. The photo on the right shows the small scale topography

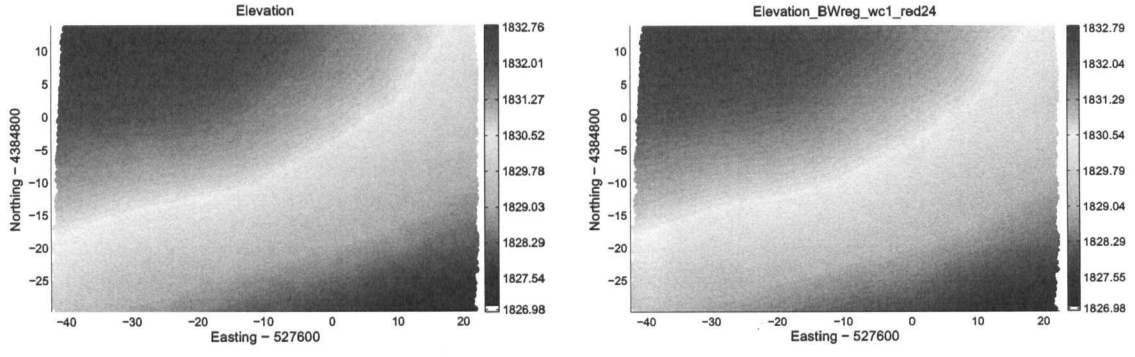

(a) Measured elevation (b) Low-pass filtered elevation values

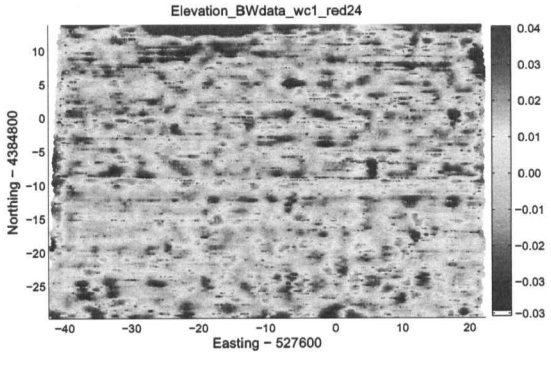

(c) Detrended elevation

Figure 8.5: Elevation data measured using an RTS at the FLBGR. The bottom plot portrays small scale height variations that will be used for simulating height variations in our synthetic modeling.4 All elevations are in meters.

tion, and adding a random phase to the FFT (Sinex, 2006). An inverse FFT produces elevation data with the same power spectrum as the measured elevation data. Figure 8.6 shows an example of the correlated random number procedure. We assumed that the error had a standard deviation of 2 cm. The bottom image of Figure 8.6 contains the corresponding response expressed as a percentage of the uniform VRM background. The bottom image was constructed by assuming a mean cart height of 30 cm.

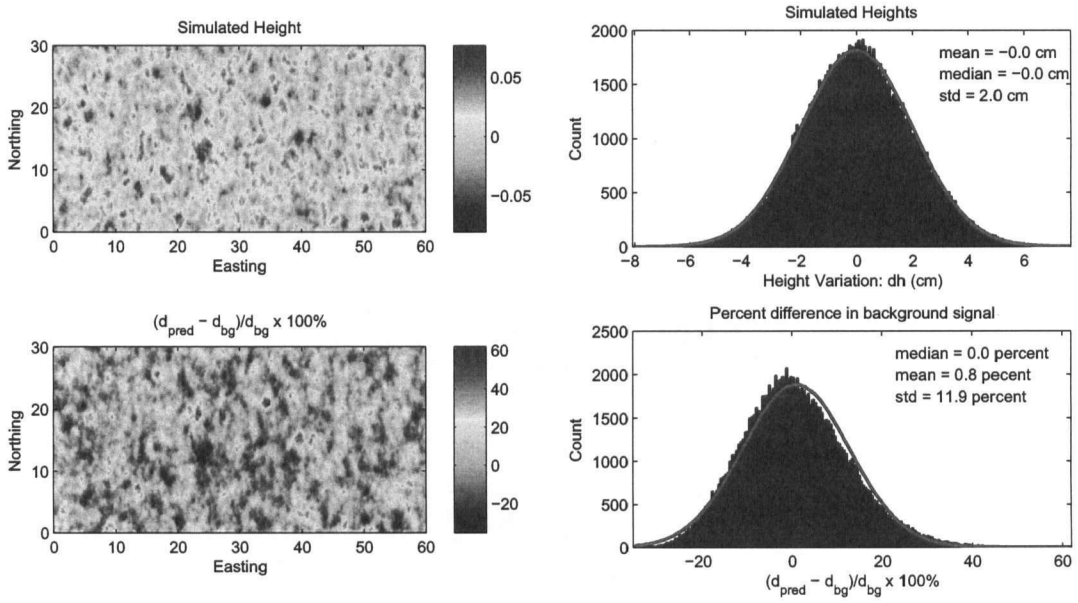

(a) Height simulations and calculated response

(b) Distribution of simulated height and response

Figure 8.6: Simulated height values ((a), top) and the corresponding response expressed as a percent of the uniform VRM background response ((a), bottom). Heights are simulated using correlated random numbers generated from the power spectra estimated from Geonics EM63 height data. The distribution of simulated heights and corresponding response are plotted in (b).

Example 2: Examining the relationship between height errors and data variances

Figure 8.7 shows how different height errors translate to uncertainties in a channel of the measured sounding. For small changes in height the relationship between data error and height variation is approximately linear. A random height uncertainty of 2 cm (which will be assumed in these initial tests) produces a data uncertainty of 10 percent. However, the relationship becomes non-linear as

height variations increase. This is a reflection that the value measured by the sensor increases rapidly as the sensor gets closer to the ground. As the standard deviation of the height error increases, the uncertainty in the measured data is no longer adequately described by a Gaussian. The associated probability density for the errors will be non-symmetric. This example highlights the importance of filtering the measured height to help reduce the random uncertainty in height. However, filtering may not be possible in cases where cart data are acquired where there is significant small wavelength topography, such as small holes and bumps. In such cases, there will be small wavelength features in the data that reflect the height variations of the sensor.

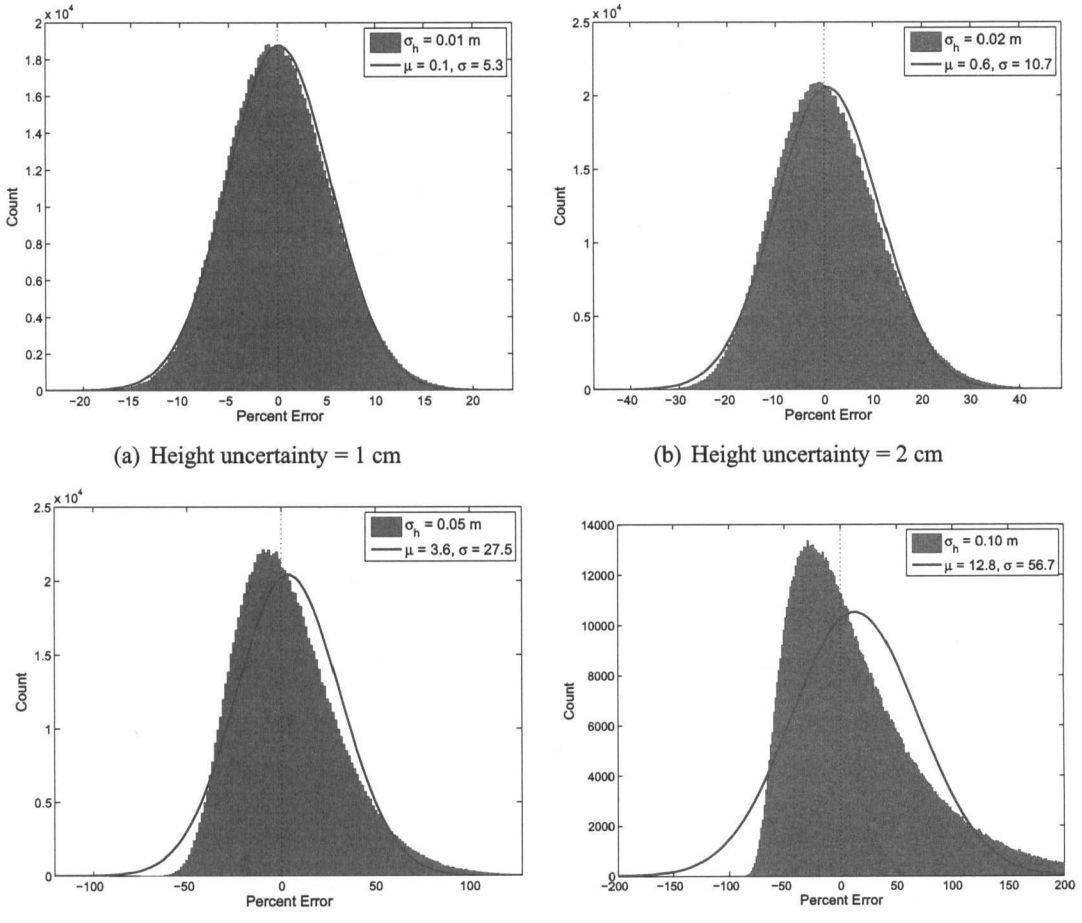

(a) Height uncertainty = 1 cm

(b) Height uncertainty = 2 cm

(c) Height uncertainty = 5 cm

(d) Height uncertainty = 10 cm

Figure 8.7: Effect of height errors on sensor data acquired over VRM soils. The red line indicates a best fit Gaussian. For large height errors the histogram for data errors is asymmetric and even a biased Gaussian is a poor representation.

Example 3: Examining the relationship between sensor height and orientation on VRM response

A series of tests were carried out to investigate the effect of micro-topography and coil orientation on TEM data collected on Kaho'olawe island. These tests were a part of investigations MM-1414 "Improving Detection and Discrimination of UXO in Magnetic Environments " and UX-1355 "UXO Target Detection and Discrimination with Electromagnetic Differential Illumination", both funded by the Strategic Environmental Research and Development Program (SERDP). The results of these tests are summarized in Walker et al. (2005b) and Foley et al. (2005).

Both a coil tilt test and a coil height test were performed with a Geonics EM61 MK2 sensor in a highly magnetic area of Kaho'olawe. During the tilt test, data were collected with the coil at seven tilt angles (Figure 8.8). At the largest angle, the edge of the EM61 transmitter coil was

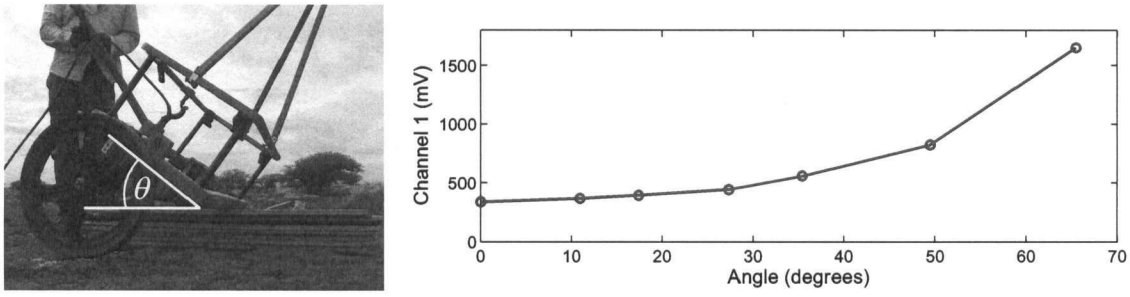

(a) Photo of Geonics EM61 Mark2 tilt test. The tilt angle is indicated by θ.

(b) Measured data

Figure 8.8: Tilt test carried out on Kaho'olawe Island using a Geonics EM61 Mark 2.

in contact with the ground. Tilting the coil 10 degrees forward results in an amplitude increase of approximately 30 mV. The height test varied the height of a horizontal Geonics EM61 with the ground (Figure 8.9). This was repeated for eleven heights ranging from 0 (EM61 coils resting on the ground) to 64 cm. As an example of how dramatic the effect of coil height can be, a coil positioned at 36 cm instead of the normal survey height of 40 cm, will have an amplitude increase of approximately 80 mV. The height test measurements were modelled using viscous remnant magnetic halfspace. The modelled behaviour of the signal with height (the blue curve in Figure 8.9) diverges from the measured response as the coil is closer to the ground. This may be due to the response of the coil being approximated using the field at the center of the receiver loop rather than explicitly integrating the flux over the loop. The effect of loop height is much more dramatic than

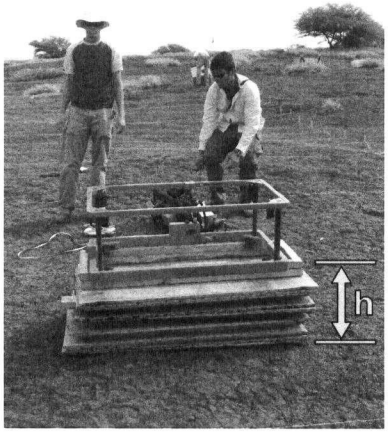

(a) Photo of Geonics EM61 Mark2 tilt test. The height of the coil indicated by h.

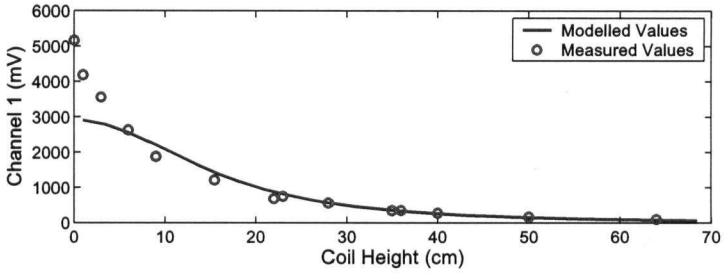

(b) Measured (red dots) and modelled (blue line) height test data.

Figure 8.9: Height test carried out on Kaho'olawe Island using a Geonics EM61 Mark 2.

sensor orientation differences.

8.3 The Additivity of Background and Target Responses

Throughout this thesis we assume that the response of a target in a halfspace can be approximated well by adding the response of the target in free space and the response of the halfspace. The extent to which the additive assumption is appropriate can only be rigorously tested through the numerical modelling of Maxwell's equations. We can use the methodology of Das (2006) to estimate the first order effects of the background host on the target response. Das (2006) studies the effect of the background host material on the response function (for example see Grant and West, 1965) of a sphere, by (1) taking into account how the host material alters the primary field that illuminates the sphere and (2) taking into account how the host material alters the secondary field generated by the sphere that is measured at the receiver coil.

Figure 8.10 demonstrates how the polarization tensor for a sphere would change for 3 different scenarios: (1) A non conductive background host with a magnetic susceptibility model based on Kaho'olawe sample 7468-2734BP-12" from Table 7.2 ($\chi\,(f = 0.46\text{kHz}) = 0.02807, \chi\,(f = 4.6\text{kHz}) = 0.02634$), (2) A non conductive background host with a static susceptibility of $\chi = 0.1$, and (3) A non-magnetic host with a halfspace conductivity of 0.01 S/m. For these results a sphere with a ra-

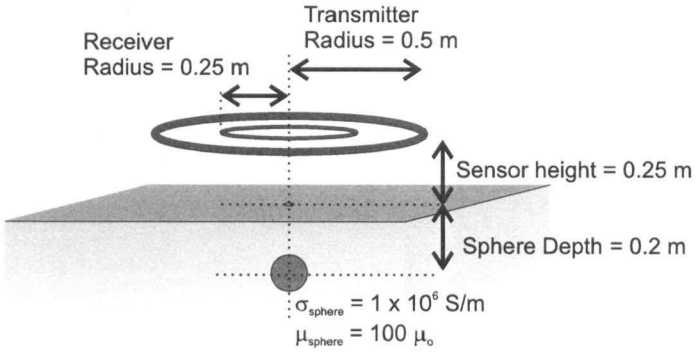

(a) Geometry of the test. The diameter of the sphere is assumed to be 5 cm, with a conductivity of 1×10^6 S/m, and a magnetic permeability of $\mu = 100\mu_o$.

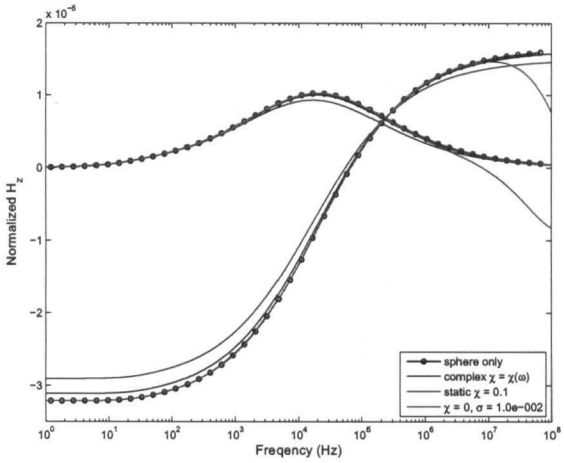

(b) Frequency domain response of the sphere's polarization tensor

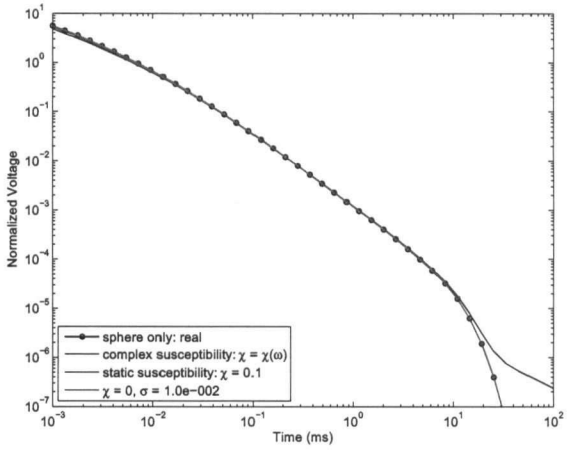

(c) Time domain response of the sphere's polarization tensor, obtained through a Fourier transform of the spectral response in (b).

Figure 8.10: Studying the effect of a conductive or magnetic background halfspace on the dipole polarization tensor of a sphere using the formulation of Das (2006). Deviations from the sphere in free space polarization indicate non-additive interactions with the background host. Although there are some differences in the spectral (frequency domain) response, the time domain response is not significantly altered.

dius of 5 cm is placed at a depth of 0.2 m. The height of the co-axial transmitter and receiver loops is 0.25, and the radius of the transmitter and receiver loops are 0.5 m and 0.25 m, respectively.

Frequency domain response of the sphere's polarization tensor in free space and in the three different background geologies are plotted in Figure 8.10(b). The curves for the complex susceptible magnetic, static susceptible magnetic and conductive background cases represent the response of the sphere in the background host with the response of the halfspace subtracted. If the background response and sphere response were truly additive, each of the four different lines in Figure 8.10(b) would be equal. At lower frequencies the polarization tensor for sphere is affected by the presence of magnetic materials, while at higher frequencies, the response is altered more by the presence of a conductive background. These spectral responses are transformed to the time domain via a Fourier transform. Although there are some changes in the spectral (frequency domain) response, the time domain response is not significantly altered.

8.4 Estimating the response of the background geology

Our general approach to processing electromagnetic data is to invert data for model parameters $\mathbf{m}$ that are representative of the physical characteristics of the target. Since our forward modeling function $\mathcal{F}(\mathbf{m})$ is for a dipole in free space, we must estimate and remove the response due to geology. We assume that the response of the background geology and target response is additive

$$\mathbf{d}^{obs} = \mathbf{d}^{bg} + \mathbf{d}^{target} + noise \tag{8.20}$$

The background response $\mathbf{d}_{bg}$ is estimated by fitting a soil model at each station to obtain $G(\chi)$. A low pass filter is applied to $G(\chi)$, and the predicted soil response $\mathbf{d}_{bg}$ is subtracted from $\mathbf{d}_{obs}$ to obtain the target data $\mathbf{d}_{target}$.

This approach relies on the assumption that the small wavelength components in the data are due to compact targets, and not the geology. However, even if the magnetic properties of the soil are slowly varying, variations in cart height due to topography and topography itself, can add a significant high frequency component to the data. Therefore, our preferred approach is to estimate

a soil model from the data.

$$V_{soil}(t) = R(orientation, height)\, G(\chi)\, f(t) \tag{8.21}$$

where $G(\chi) = \chi_o / \ln(\tau_2/\tau_1)$ for a half-space, and $f(t) = 1/t$ for a step-off response. The function $G(\chi)$ is assumed to be spatially smooth, while the function R can have high frequency spatial variations due to sensor position and orientation variations. If we assume a half-space model for the soil, then a single parameter that is a function of the low frequency magnetic susceptibility and upper and lower limits of the soil decay time constants characterizes the response at each station location. We estimate this parameter such that it is laterally smooth. This is achieved by fitting each sounding independently, then applying a low pass filter to the $G(\chi)$, i.e. the susceptibility spatial distribution, rather than to the data directly.

The tilt and height tests illustrate that even small changes in coil orientation and the distance between the coil and a highly magnetic sub-surface can produce significant amplitude variations. Therefore, the amount of processing carried out on data is dependent on the accuracy of the sensor positioning and orientation. If the positioning and orientation of the sensor is sufficient to model the high spatial frequency components of the background response, then the approach of subtracting a background signal followed by parameter estimation can be considered. Otherwise, the background noise that can be encountered would likely limit the amount of target information that could be extracted from the data. In such a case, the data processing should focus on improving target detection and reducing false negatives due to soil, rather than determining shape and size characteristics through inversion.

Figure 8.11 summarizes a procedure for processing data that incorporates background subtraction. Once data have been collected, the data are then pre-processed to remove sensor related data artifacts (e.g. sensor drift), and to integrate positioning information. These data can then be used to estimate a soil susceptibility model. Estimation of a soil susceptibility is complicated by the presence of dipole signals due to compact metallic objects and the quality of sensor position and orientation information. The data predicted by the soil susceptibility can then be subtracted from the pre-processed data:

Good Sensor Position Orientation Information: In this case, the small spatial wavelength

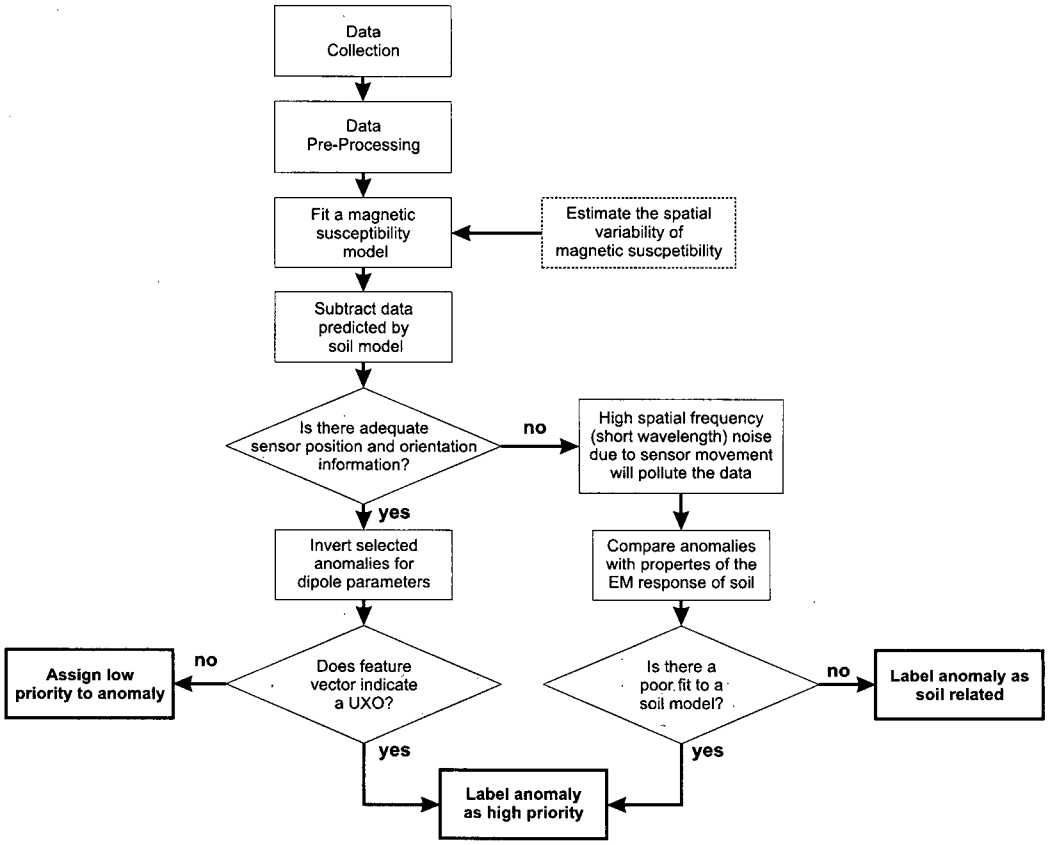

Figure 8.11: Processing EMI data in a magnetic setting.

signal due to sensor motion can be predicted. The anomalies in the background-subtracted data are then inverted for dipole parameters. The resulting dipole parameters can then be incorporated into a feature vector for statistical classification.

Poor Sensor Position and Orientation Information: In this case we would likely have to assume a constant elevation and orientation for the transmitter and receiver coils. The anomalies in the background-subtracted data may have a large amount of high spatial frequency (short wavelength) noise due to the unmodelled sensor motion. For this case, the objective should be simply to minimize the number of targets due to soil.

8.5 Testing EMI Processing Methods using simulated TEM Data

In this section I outline the generation of simulated data sets that I will later use to investigate different processing techniques applied to electromagnetic data. These simulations are also included in the Strategic Environmental Research and Development Program (SERDP) funded project "Improving UXO Detection and Discrimination in Magnetic Environments (SERDP Project MM-1414)" we are using data inversion simulations to quantify the effectiveness of different processing techniques applied to frequency domain and time domain electromagnetic data contaminated by magnetic geologic noise (Li et al., 2005, 2006). The project is a joint research effort involving the University of British Columbia Geophysical Inversion Facility, the Colorado School of Mines, New Mexico Tech, and Michigan State University.

Objective of our simulations include

1. Assessing our ability of spatial filtering, used in conjunction with soil models, to estimate background geologic response, and

2. Determining how the variance of class clusters in feature space is affected by filtering techniques, target geometries, and magnetic susceptibility characteristics.

These simulations will help us optimize the processing methods for data sets with significant geologic noise.

Due to the different possible survey modes, target types and geometries, and geologic signal variation characteristics, there are numerous data set types that can be modeled. A number of different survey parameters will be varied:

- **Target type:** Targets from the ATC standardized test set will be modeled. Dipole models will be used to approximate the EM response, with polarization parameters being derived from data acquired on the ERDC UXO test stand. Figure 8.12 has pictures of some of the different ordnance that will be studied. These are overlaid on a feature space plot containing parameters that describe the polarization tensor magnitude. Within each grid, targets are placed at depths of 0.25 and 0.5 m. The targets are randomly oriented.

- **Background Geology:** For all the simulated data sets, we will assume that the response of a UXO in a magnetic soil is the sum of the individual responses.

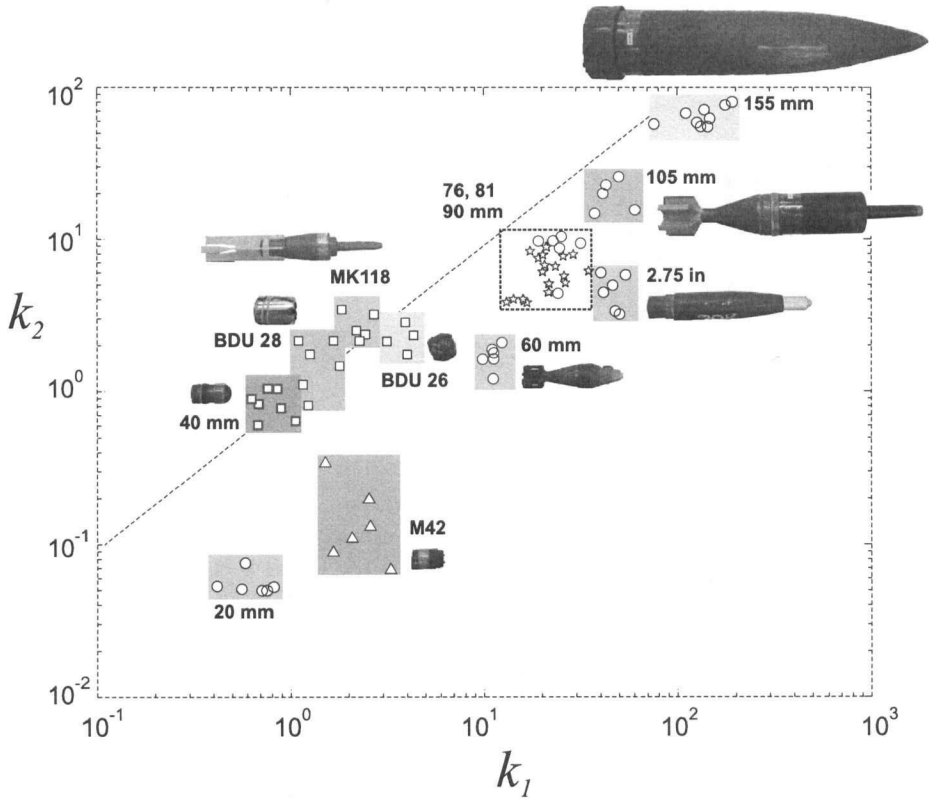

Figure 8.12: Example of recovered values for different targets. Parameters were estimated through inversions of Geonics EM63 data that were acquired on the USACE ERDC test stand in Vicksburg, MS.

- **Sensor Type:** We are simulating data from multi-channel EMI sensors, since we want to exploit the time and frequency domain characteristics of soils to improve detection. In particular we are focusing on the Geophex GEM3 and Geonics EM63 sensor.

- **Survey Geometry:** Data will be modeled on 70 m square grids. For our initial simulations we focus on single sensors acquiring data along survey lines. We assume the commonly adopted survey acquisition parameters of 50 cm for line spacing and 10 cm along line for the station spacing. A sensor height of 30 cm is assumed.

In this chapter, processing is applied to data simulated Geonics EM63 data for a 40 mm projectile and 60 mm mortar (see Figure 8.12 for photos). The 40 mm projectile is buried at a depth of 25 cm and the 60 mm mortar is buried at a depth of 50 cm.

8.5.1 Simulated Noise

The inverse problem for estimating dipole parameters can be cast as an optimization problem. The mathematical background for this was presented in Chapter 3. Here we briefly present some essential points. For the data of this study we only consider uniform priors such that our problem is to minimize a data misfit function subject to box constraints:

$$\text{minimize} \quad \phi(\mathbf{m}) = \frac{1}{2}\|V_d^{-1/2}\left(\mathbf{d}^{obs} - \mathcal{F}(\mathbf{m})\right)\|^2 \text{subject to} \quad m_i^L \leq m_i \leq m_i^U \tag{8.22}$$

where i represents model parameters which have upper and lower bounds. Finding a model that minimizes the above equation involves defining a data covariance vector V_d, the data vector $\mathbf{d}^{obs}$, the forward modeling function $\mathcal{F}(\mathbf{m})$, the constraints m_i^L and m_i^U, and a numerical optimization procedure. The data vector $\mathbf{d}^{obs}$ is typically contaminated with noise:

$$d_i^{obs} = d_{dipole} + e_i \tag{8.23}$$

where e_i is the noise on the i^{th} datum.

The source of data errors can generally be categorized as being components of the data that can not be modeled with the dipole forward modeling function F(m). The components of e_i include modeling errors, sensor noise from natural and cultural sources, and processing artifacts. As e_i

increases, the variance of the recovered parameters $\mathbf{m}$ increases. For example, for deeper targets the relative value of the data error compared to the target signal increases, and the ability to constrain the model parameters decreases. The choice of the least squares objective function is optimal when the errors e_i are Gaussian. Biased components of e_i will reduce the quality of the estimates of $\mathbf{m}$. The relationship between the data error bias and estimated values of $\mathbf{m}$ requires numerical simulations. A couple of examples of where biased components could be introduced include using a dipole model where the target response contains significant multipole components, and when background removal filtering produces data artifacts. In this section we describe how the noise is included in the simulated data.

8.5.2 Baseline noise

We define baseline noise to be the random signal produced in the sensor in the absence of nearby conductive bodies. There are numerous sources of EMI noise (for example Nabighian and Macnae (1991)). Efferso et al. (1999) examined the effect of AM and very low frequency (VLF) electromagnetic transmitters on TEM measurements. They observed for their particular TEM instrument that the standard deviation voltage signal exhibits a $1/t$ proportionality when AM transmitter noise is log-gated and stacked. Munkholm and Auken (1996) showed that log-gated and stacked white noise maps onto the TEM response as errors with a standard deviation exhibiting a $1/\sqrt{t}$ decay. Figure 8.13 shows a calculated noise floor (in green) for a grid of Geonics EM63 data acquired at FLBGR and the theoretical $1/\sqrt{t}$ decay due to Gaussian input noise. The magnitude of the noise was estimated by calculating data statistics from regions on the grid where there were no UXO anomalies. For these simulations, we assume that the baseline error can be characterized by a single standard deviation for the entire grid (although past experience has shown that the magnitude of the baseline noise can vary as a function of Geonics EM63 survey event). Figure 8.13 plots realizations of the synthetic noise as a function of time channel.

8.5.3 Sensor Position Uncertainty

Sensor position and orientation are generally recorded with some combination of GPS, robotic total station, and IMU sensor. Inaccurate position and orientation information are sources of modeling error. For these simulations we assume that the pitch, roll and yaw can be measured to within an

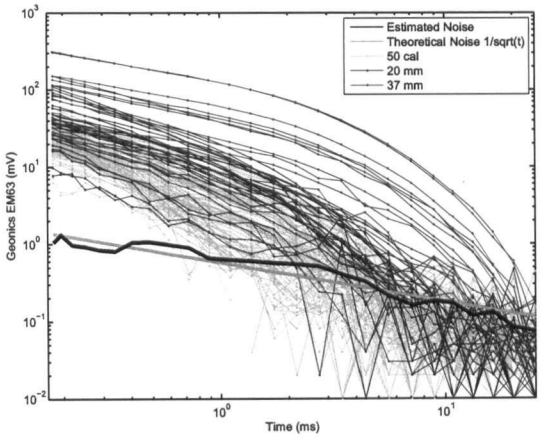

(a) Calculated and theoretical noise floor for Grid 1914 at FLBGR. The calculated noise floor was based on Geonics EM63 data collected over areas where there were no UXO anomalies. Data over validated 50 calibre bullets, and 20 mm and 37 mm projectiles are also plotted.

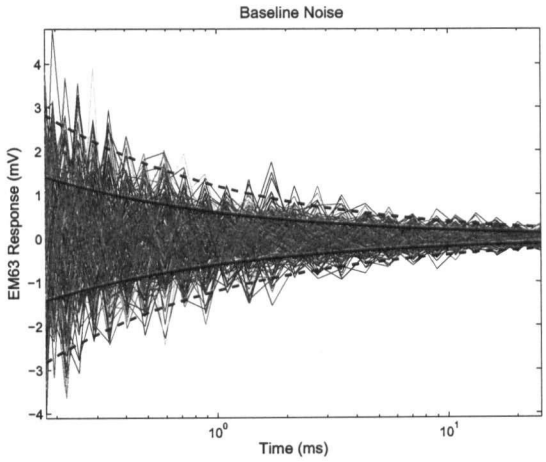

(b) Simulated baseline noise for the Geonics EM63. The standard deviation of the noise for each time channel is the same as the noise from data acquired at FLBGR. At each time channel the realizations shown in the Figure are represented by a Gaussian probability. The dark and dashed lines respectively correspond to 1 and 2 standard deviations.

Figure 8.13: Baseline noise for magnetic soil simulations.

accuracy of 2 degrees. We assume the position errors are normally distributed with 2 cm standard deviation in northing, easting, and height. Our past tests have shown that the sensor data are more sensitive to sensor height variations than to position and orientation errors.

8.5.4 Simulating the Magnetic Background Signal

We assume that there are two components of the background geologic response: (1) A long wavelength variation due to changes in magnetic susceptibility associated with geologic and/or weathering features, and (2) Short wavelength variations due to topography and sensor motion relative to the surface.

For the long wavelength variation, we assume that susceptibility decreases smoothly from a maximum at the South (y= 0 m) end of the grid to a minimum at the North (y = 70 m) end of the grid (Figure 8.14). There are three different magnitudes of background response considered. Background responses of 100 mV, 50 mV, and 20 mV in the first time channel are constructed. The response at the North end of the grid is one-half the value of the response at the South end of the grid. The time decay of the background response has a $1/t$ magnitude.

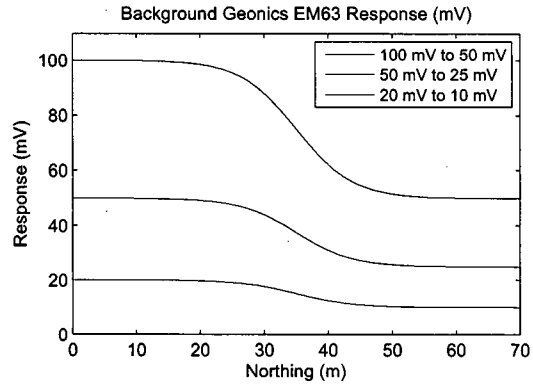

Figure 8.14: Variation of geologic background responses along a North/South line. The background response with a maximum of 50 mV and minimum of 25 mV is used for the examples of this chapter.

Smaller wavelength variations in the background response are assumed to be from either cart positioning (i.e., height and orientation) or from small topographic features, such as surface depressions (e.g. potholes) or small mounds of soil. For this first set of simulations, the recorded height has a 2 cm standard deviation noise added to the nominal height 30 cm. A shorter wavelength background response is simulated by using correlated random numbers (Sinex, 2006). The smaller wavelength variations in the background response are simulated from the estimated power spectra of Kaho'olawe test plot data. The standard deviation of the small wavelength background response is set to be 15 percent of the background response.

8.5.5 Examples of Simulated Data Sets

In this chapter, simulated data from a 40 mm M385 projectile and a 60 mm mortar are used to demonstrate filtering and inversion. Figure 8.15(a) shows the first channel of modeled data from a 40 mm projectile buried at a depth of 25 cm and randomly oriented at 36 locations in a rectangular grid. The free-space response of the 40 mm projectiles has a maximum first time channel value of 15 mV (Figure 8.15, upper left). The long wavelength background response decreases from a maximum of 50 mV at the South end of the grid, to a minimum of 25 mV at the North end of the grid. The standard deviation of the correlated noise is defined to be 15 percent of the long wavelength regional response. Fifteen percent corresponds to a height variation of approximately 3 cm. The spatial characteristics of the modeled response are based on Geonics EM63 data acquired

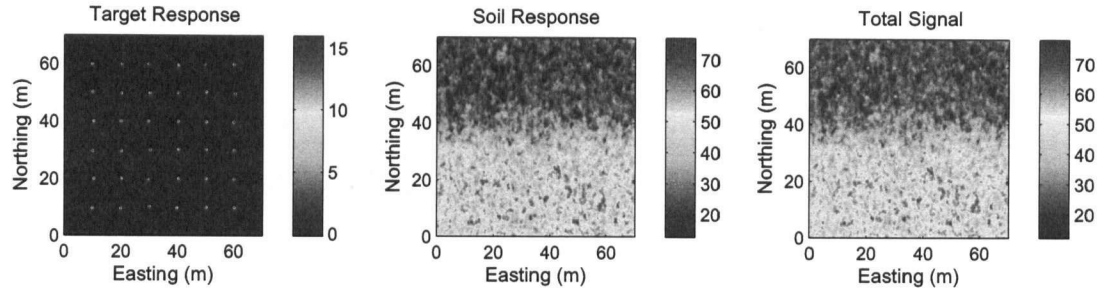

(a) ATC 40 mm M385 simulated data

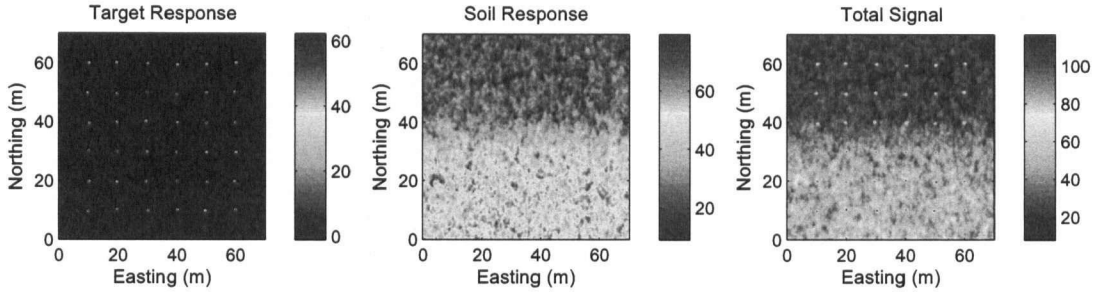

(b) ATC 60 mm mortar simulated data

Figure 8.15: Data simulated for a 40 mm buried at a depth of 50 cm. The first time channel of data is plotted. UXO are placed at all points on the grid in the upper left plot. The simulated soil response is shown in the top right, and simulated survey data are shown at the bottom.

on Kaho'olawe. A radial power spectra was estimated for a region within a Kaho'olawe grid with a background of approximately 50 mV. The total soil (i.e., non-target) response is plotted in the upper right of Figure 8.15. The total signal is plotted in the bottom image of Figure 8.15. The responses of the 40 mm projectiles are not easily identified in the total signal. The 40 mm projectile has a weak small amplitude signal due to its small size, aluminum construction and, of course, its distance from the sensor.

The different components of simulated data for a 60 mm mortar buried at 50 cm in a background that has a maximum response of 50 mV in the first time channel is shown in Figure 8.15(b).

8.6 Picking Targets in highly magnetic soils

The goal of target picking is to generate a list of survey locations at which there is a high probability that a target is present. The data can be written as

$$\mathbf{d}^{obs} = \mathbf{d}^{target} + \text{noise}. \tag{8.24}$$

In this case, we define the noise to be the random baseline noise of the instrument and the spatially correlated signal from topography and sensor movement. Since we are not fitting the data with a model, modeling error is not considered a noise source. Fundamentally, target picking labels a survey location as a potential target when the sensor data $\mathbf{d}^{obs}$ exceeds some threshold level. The choice of threshold depends on the characteristics of the noise and the target signal.

Target picking is an example of signal detection theory and hypothesis testing. The null hypothesis $\mathcal{H}_0$ is that the signal is due to noise. The alternative hypothesis $\mathcal{H}_1$ is that the signal is from a buried target. Let $p\left(x|\mathcal{H}_0\right)$ be the pdf of x under $\mathcal{H}_0$, i.e., the pdf of the noise. The variable x is some test statistic of the data (which can be the data itself). Let $p\left(x|\mathcal{H}_1\right)$ be the pdf of x under $\mathcal{H}_1$, i.e. the pdf of the target. For a threshold level τ, the probability of false alarm P_{FA} and the probability of detection P_D is defined as

$$P_{FA} = P\left[x > \tau; \mathcal{H}_0\right] \tag{8.25}$$

$$P_D = P\left[x > \tau; \mathcal{H}_1\right], \tag{8.26}$$

where the test statistic is x. The definitions of P_D and P_{FA} are expressed graphically for the example of a 40 mm projectile buried at a depth of 25 cm in a background geology whose mean response in the first time channel is 20 mV in Figure 8.16(a). The curves in Figure 8.16 were generated through simulations and fitting the experimental histograms with log-normal distributions. The ability to detect the 40 mm projectile is characterized by the width and separation of the two pdfs. As the depth of the target decreases, the signal-to-noise ratio of the anomaly will increase. The anomalies for these shallower targets will have a poorer fit to the soil model and the soil and target distributions will have greater separation. The ability to discriminate is summarized with a receiver operator characteristic (ROC) curve (Figure 8.16(b)). An ROC curve is constructed by plotting the

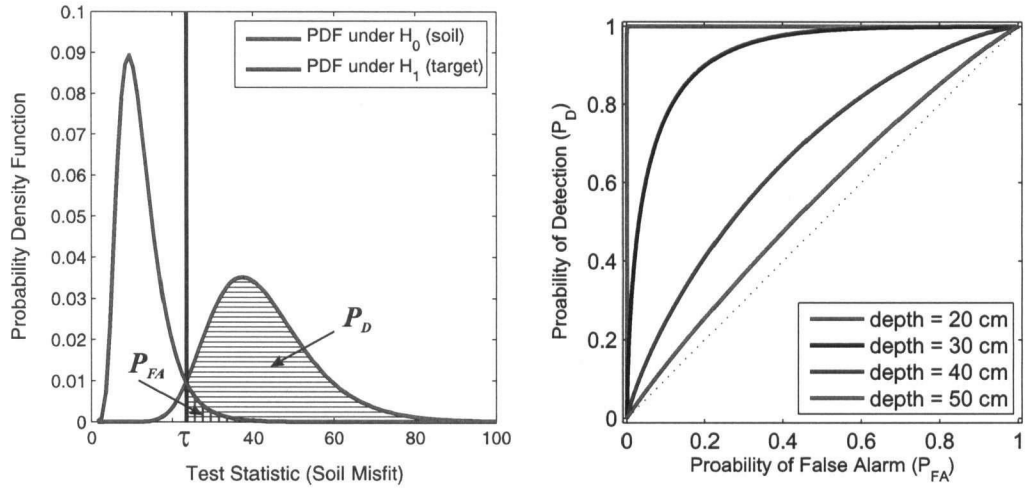

(a) The pdf for a depth of 25 cm.

(b) ROC curve for different target depths

Figure 8.16: Soil fitting results for data simulated for a 40 mm projectile in a background geology whose mean response in the first time channel is 20 mV.

P_{FA} against the P_D as a function of the test statistic. As we vary the soil misfit test statistic, a smooth curve is traced. It is clear that as depth decreases, the ability to discriminate improves. For a depth of 20 cm, it is possible to define an operating point such that all the 40 mm projectiles can be identified without detecting soil.

In general, types of targets to be found in a survey are not known ahead of time and, thus, $p(x|\mathcal{H}_1)$ is generally unknown. In this case, the natural approach is to simply sort prospective targets by there probability of false alarm. For the single time channel case, this means picking points on a map where the measured data exceeds some threshold and sorting those values by the amplitude.

Target picking using a single channel of data

To study target picking using a single time channel case, let us use the first time channel of the synthetic data sets (Figures 8.15(a) and (b)). We assume that the sensor height is 30 cm and the transmitter is horizontal, such that R is constant. Due to the spatially varying long wavelength background response we must either (1) define a spatially varying threshold must be defined, or (2) remove the background response through filtering. We choose to remove the background response for these example.

Figure 8.17 demonstrates the application of a simple low pass Butterworth filter to the image of gridded raw first time channel data image, and the subsequent picking based on the filtered image. Each image contain 10 cm square pixels. The gridded raw data are shown in each of the aforementioned figures upper left panel, with the low pass image plotted in the top right panel. Targets are picked using the image of high passed data, and the results are plotted in the bottom right corner. The criteria for labelling an anomaly are: (1) the pixel value is greater than a threshold of 10 mV and (2) there are at least 3 connected pixels that exceeds the threshold. The small wavelength variations due to cart motion and topography are often picked. The number of non-UXO target picks increases in the South end of the grid, where the magnitude of the VRM is the highest.

Target picking using the misfit to a soil model

With only a single time channel of data, we cannot use the characteristic temporal or frequency response of soil to reduce the number of geologic related peaks. Here we use the Geonics EM63 with potentially 26 time channels of data. If we fit a soil model to the data picks, we would expect that the misfit would be larger when the anomalies are due to UXO. The fitting procedure involves solving for a soil model that minimizes the least squares misfit between the measured sounding and soil response. The soil response is given by a characteristic soil decay multiplied by an amplitude A, i.e., $\mathcal{F}^{soil} = Af(t)$. Figures 8.18 and 8.18 shows the misfit of the 40 mm and 60 mm data sets to the soil response. The soil misfit image is much more useful for target picking than using simply a single time channel of data.

From these results, we can conclude that target picking can be improved by using the soil misfit as a test statistic. Simulations can be used to study the effectiveness of this strategy for a given target and background response. Let us consider data simulated for a 40 mm projectile buried at a depth of 25 cm and in a background geology whose mean response is 20 mV, and has a short wavelength background noise with the same correlation lengths of Kaho'olawe data. The standard deviation of the short wavelength noise is 15 percent of the long wavelength response (i.e., 3 mV). Soundings with and without a target present are fit with a soil model, and are then used to estimate the pdf for soundings from soil ($p(\phi; \mathcal{H}_0)$) and pdf for soundings from the 40 mm projectile ($p(\phi; \mathcal{H}_1)$). Figure 8.20 compares both soil and 40 mm misfit distributions as a function of the misfit (Figure 8.20(a)) and the log of the misfit (Figure 8.20(b)). The log normal distribution is a

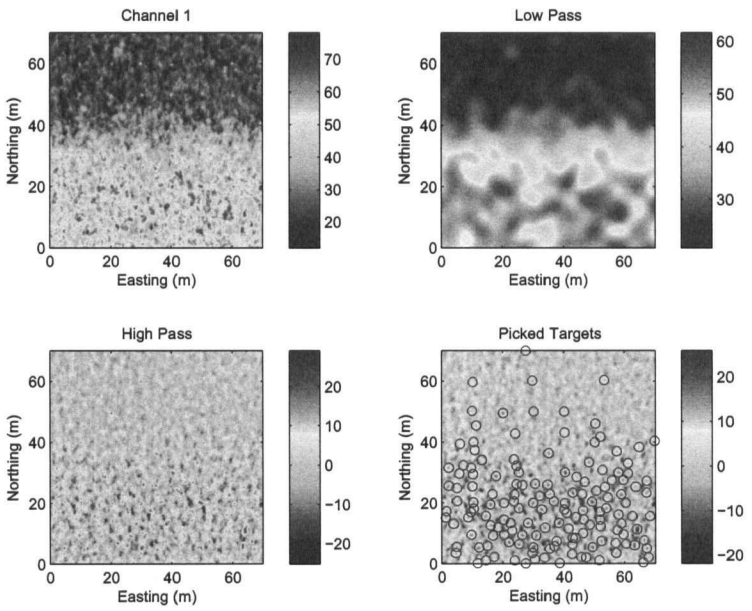

(a) ATC 40 mm M385

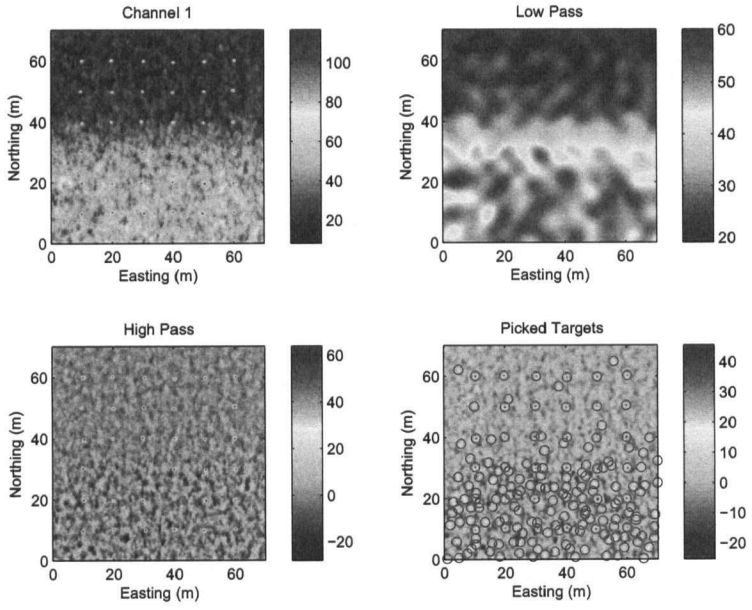

(b) ATC 60 mm mortar

Figure 8.17: Target Picking results for a 40 mm projectile and 60 mm mortar buried in a magnetic background. For both data sets a 3 pixels must exceed the picking threshold of 10 mV to be picked. Target picking using the high pass filter results in many false positives due to large magnitude of the spatially correlated background response.

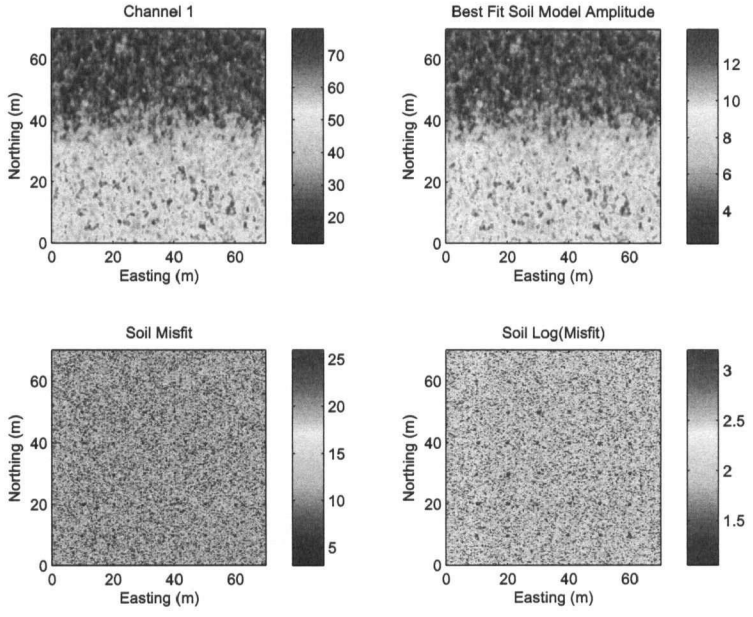

(a) The amplitude of the soil response is plotted in the top right image, with the misfit and log-misfit to the soil response plotted in the bottom two plots.

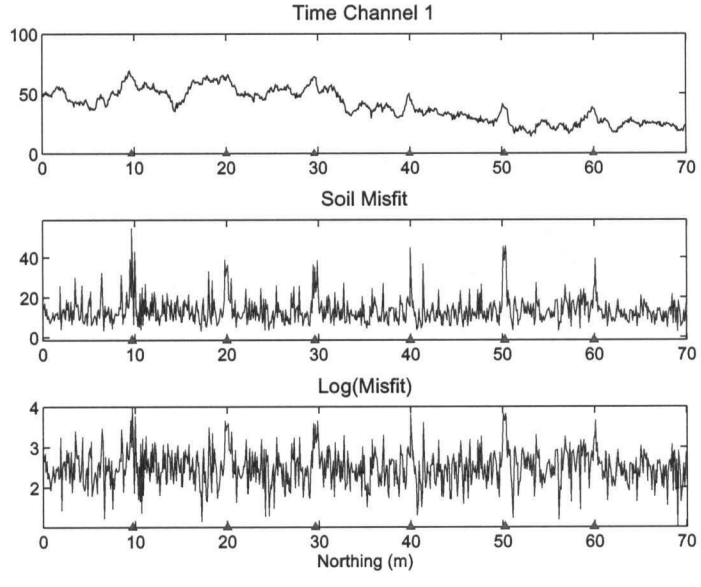

(b) Comparison of the first time channel raw data with the soil misfit along the line Easting = 10 m. The red triangles indicate the location of targets.

Figure 8.18: Soil fitting results for the 40 mm projectile data. At each location, the sounding data from the EM63 is inverted to find a best fitting soil model. It is clear the magnitude of the 40 mm response is similar to the soil response, and that the fitting of a soil model provides limited advantages for target picking purposes.

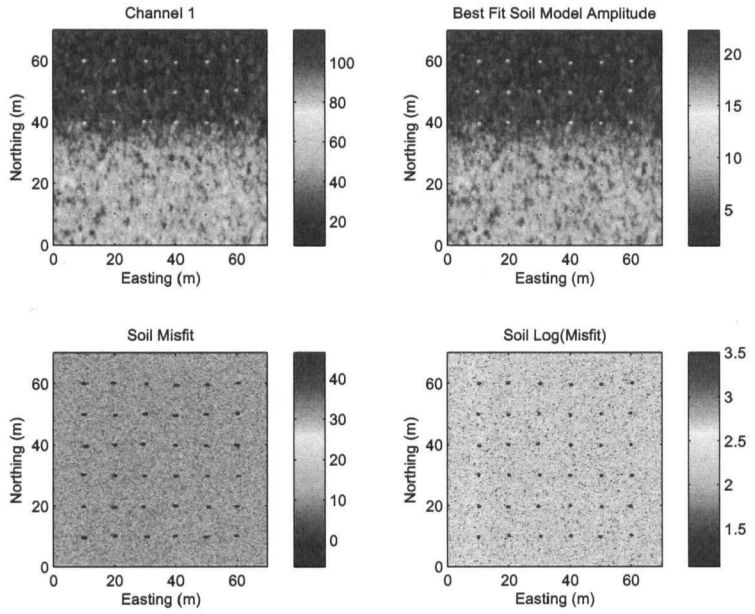

(a) The amplitude of the soil response is plotted in the top right image, with the misfit and log-misfit to the soil response plotted in the bottom two plots.

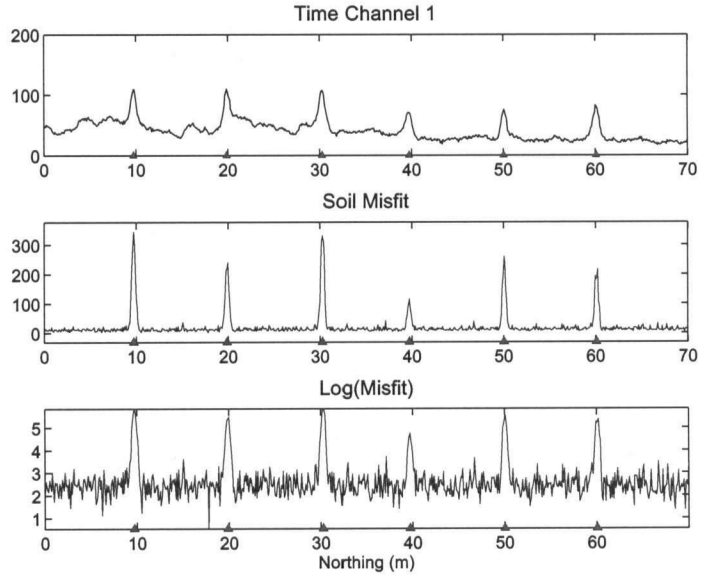

(b) Comparison of the first time channel raw data with the soil misfit along the line Easting = 10 m. The red triangles indicate the location of targets.

Figure 8.19: Soil fitting results for the 60 mm mortar data. At each location, the sounding data from the EM63 is inverted to find a best fitting soil model. The 60 mm mortar is a much larger target than the 40 mm projectile, and therefore is much easier to detect in the raw data. The soil misfit has very distinct anomalies over each of the buried 60 mm.

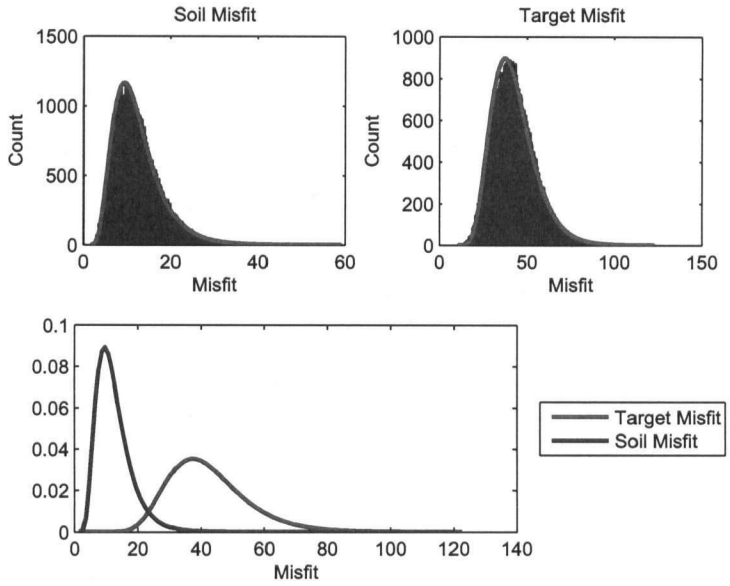

(a) Soil misfit ϕ

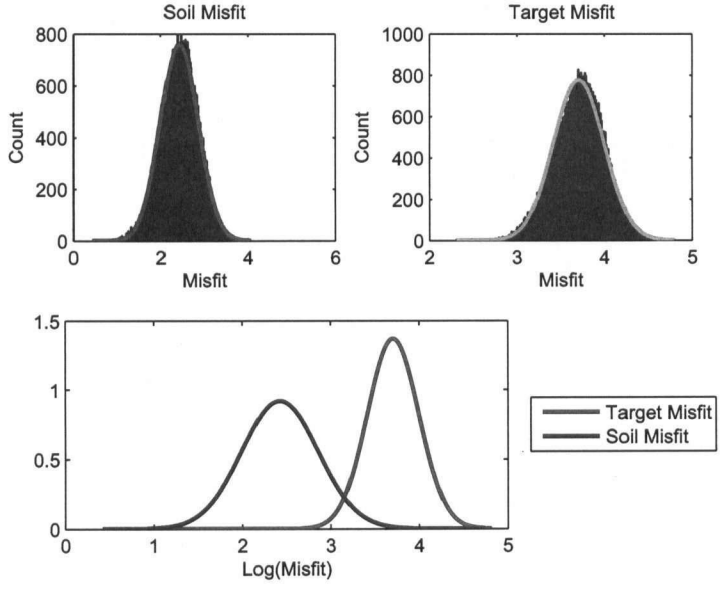

(b) Log of the soil misfit log (ϕ)

Figure 8.20: Soil target histograms for a ATC 40 mm projectile buried at a depth of 25 cm. The long wavelength background response is 20 mV.

good representation of the pdf of the soil misfit. The experimental cumulative distribution function (i.e. the cdf obtained by binning and summing the soil misfit) and the theoretical log normal cdf are compared in Figure 8.21.

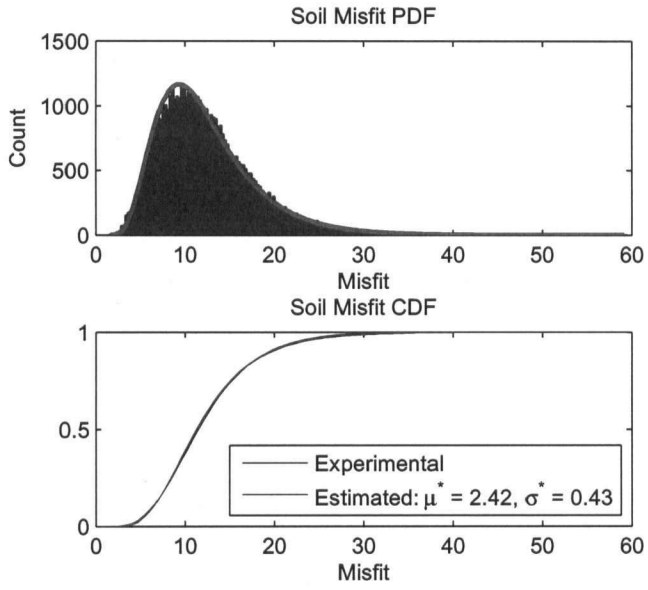

Figure 8.21: The pdf and cumulative distribution for a 40 mm buried at a depth of 25 cm in a magnetic background that has a response of 20 mV in the first time channel. The quantities μ^* and σ^* are the mean and standard deviation of $log\,(\phi)$.

The ability to accurately pick targets depends on the separation and widths of the soil and 40 mm pdfs. As the overlap of the pdfs for soil and target misfits decreases, so does the probability of false negatives and misses. For a given geologic setting (and therefore soil pdf) the effectiveness of target picking relies on (1) the similarity of the target response to the soil model and (2) the signal strength. The main influence on signal strength is the depth of the target. Figure 8.22 compares the pdfs for a 40 mm at depths of 25 cm and 50 cm. The pdf for the 40 mm at 50 cm is very similar to the pdf of the soil, thereby indicating that using the soil misfit for detecting this target will not be successful. The ROC curve for a number of different 40 mm depths are plotted in Figure 8.16(b). The ROC curve is diagnostic of the performance of a classifier as a tradeoff between the probability of false alarm and probability of detection. The ROC curve shows that a 40 mm at 50 cm has a ROC curve that nearly follows the line $P_{FA} = P_D$, which indicates that when the 40 mm is at 50 cm deciding whether a anomaly is due to soil or a target with soil misfit will not perform much better

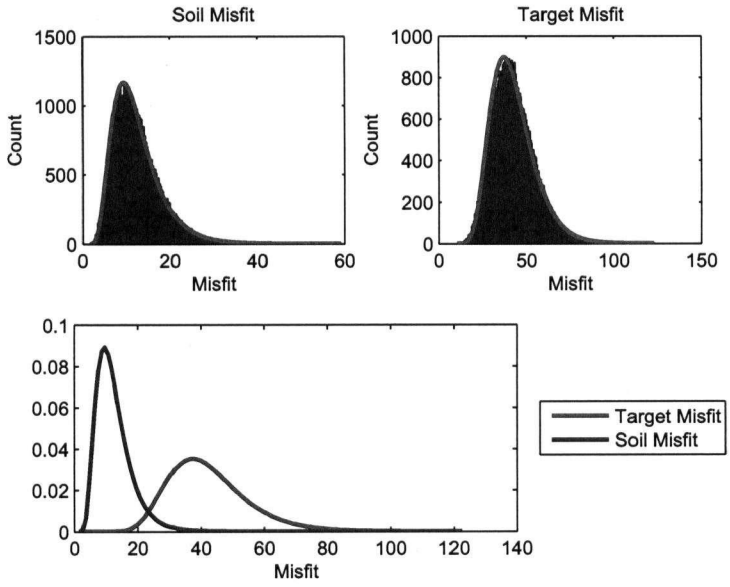

(a) Soil misfit distributions for depth of 25 cm.

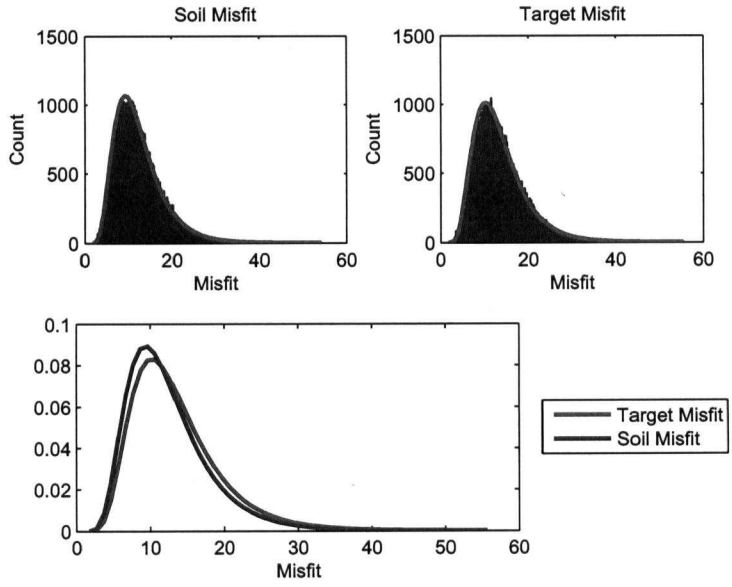

(b) Soil misfit distributions for depth of 50 cm.

Figure 8.22: Soil target histograms for a ATC 40 mm projectile buried at a depth of (a) 25 cm and (b) 50 cm. The long wavelength background response is 20 mV. The pdf for the soil and target nearly overlap when the 40 mm is 50 cm deep.

than simply flipping a coin. In contrast, a 40 mm at 20 cm has the perfect rock curve, with no false alarms prior to picking every all the targets.

8.7 The accuracy of filtering when estimating the background response

Since our forward modeling function $\mathcal{F}(\mathbf{m})$ is for a dipole in free space, we must estimate and remove the response due to geology. We assume that the response of the background geology and target response is additive

$$\mathbf{d}^{obs} = \mathbf{d}^{bg} + \mathbf{d}^{target} + noise \tag{8.27}$$

The background response $\mathbf{d}^{bg}$ is estimated by fitting the soil model of equation 8.17 at each station to obtain $G(\chi)$. A low pass filter is applied to $G(\chi)$, and the predicted soil response $\mathbf{d}^{bg}$ is subtracted from $\mathbf{d}^{obs}$ to obtain the target data $\mathbf{d}^{target}$. The inverse problem is then to minimize the data misfit

$$\begin{aligned} \phi &= \frac{1}{2}\| V_d^{-1/2} \left(\mathbf{d}^{target} - \mathcal{F}(\mathbf{m}) \right) \|^2 \\ &= \frac{1}{2}\| V_d^{-1/2} \left(\left(\mathbf{d}^{obs} - \mathbf{d}^{bg} \right) - \mathcal{F}(\mathbf{m}) \right) \|^2 \end{aligned} \tag{8.28}$$

In this section we filter the data sets of Figure 8.15. Results are shown in Figure 8.23. A simple Butterworth filter is used to estimate the background response. The low amplitude signal from the 40 mm projectile, and the similarity between the spatial wavelength of the background response and target anomaly result in a very poor recovery of the target anomalies. Filtering the 60 mm projectile data produces better results.

We quantify the ability to recover the true target data by calculating the difference between the estimated and true target data (Figure 8.24). We call this value the"absolute error" (as opposed to a relative, or percent error). The "absolute error" for the first time channel of data is shown in Figure 8.24. Data from a 5 m square region about each target is used for the calculation. The three histograms of Figure 8.24 show: (a) the distribution of the error for targets in the region when the average background response is 25 mV ($y > 45$), (b) the error distribution for targets in the region where the average background response is 50 mV ($y < 25m$), and (c) the error for all the targets within the 70 m grid. The histograms confirm that the error is greater in areas where the magnetic background response is larger. In addition, there is a slight negative bias in the "absolute error" distribution, suggesting that we are underestimating the contribution of the background response.

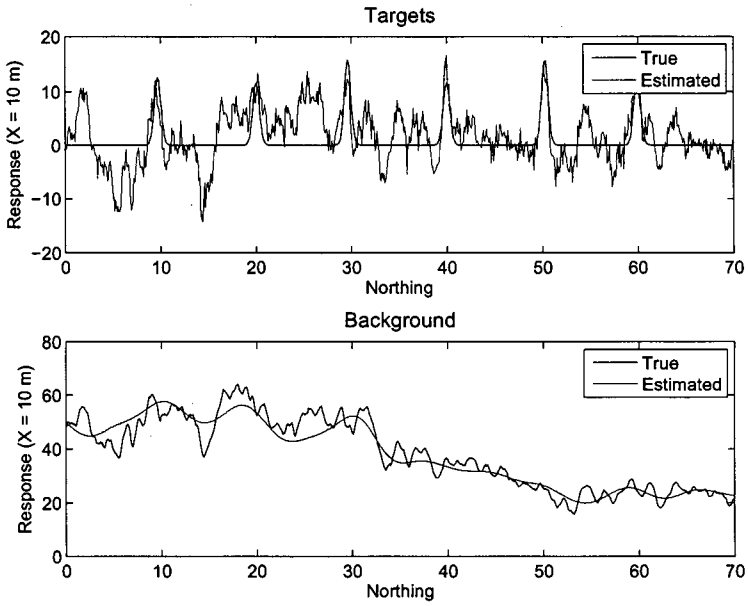

(a) 40 mm projectiles

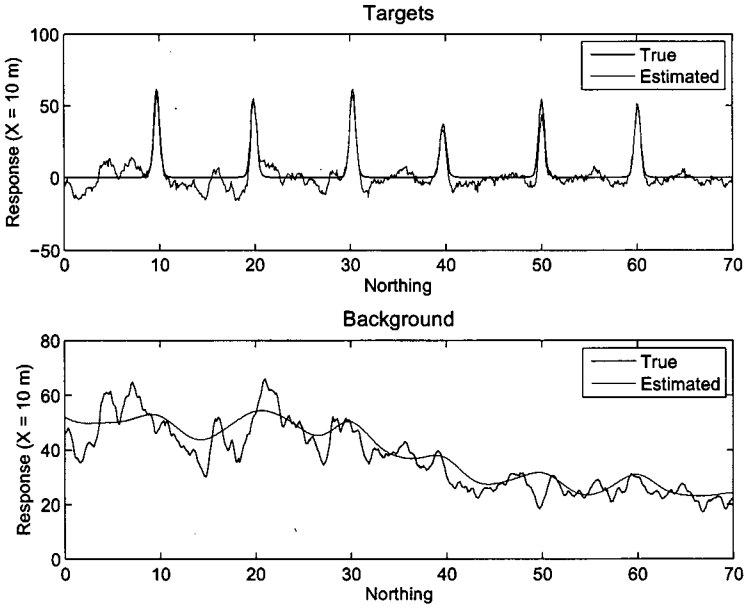

(b) 60 mm projectiles

Figure 8.23: Estimation of target signals through high-pass filtering of the data. Filtering results along the line Easting = 10 m are plotted.

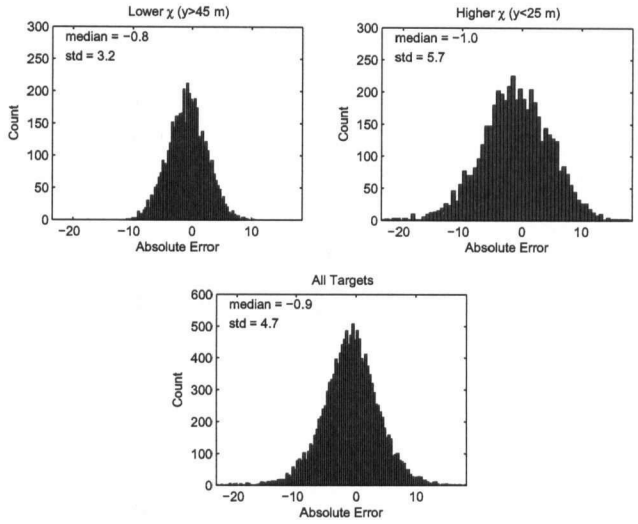

(a) A 40 mm projectile buried at a depth of 25 cm.

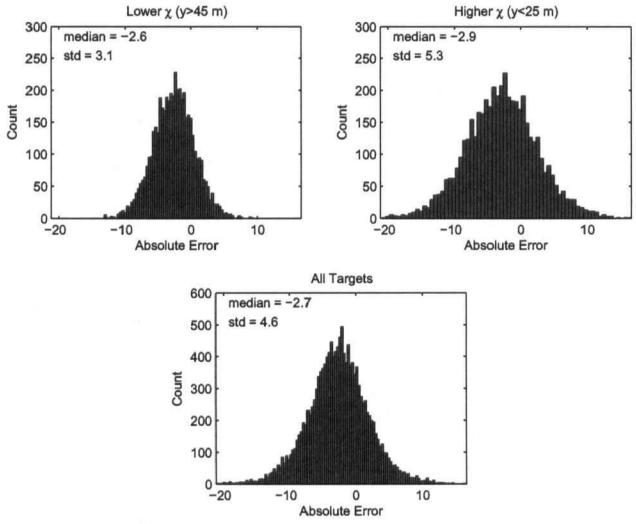

(b) A 60 mm mortar buried at a depth of 50 cm.

Figure 8.24: Accuracy of estimating target anomalies by subtracting a smoothly varying background response. Absolute error is defined as the estimated background minus the true target data. Data are within a 5 m square centered on the target.

8.8 The effect of VRM noise on recovered model parameters

The success of dipole model based discrimination algorithms depends on the ability of the data to constrain the inversion for the dipole parameters. To demonstrate this process we process synthetic data collected over a 60 mm mortar. We compare results from inverting: (a) synthetically generated data for 60 mm mortars buried in a non-magnetic background and (b) data with a background geology. The synthetic data set is 70 m square, with a long wavelength background geologic response that decreases smoothly from 50 mV at the south end of the grid, and 25 mV at the north end of the grid. Correlated noise is added in the same manner as the examples presented earlier. The 60 mm mortars are buried at a depth of 50 cm.

The background geology was estimated by using a low pass Butterworth filter. The background response is subsequently subtracted from the observations (Figure 8.25). Data within a 1.5 m cir-

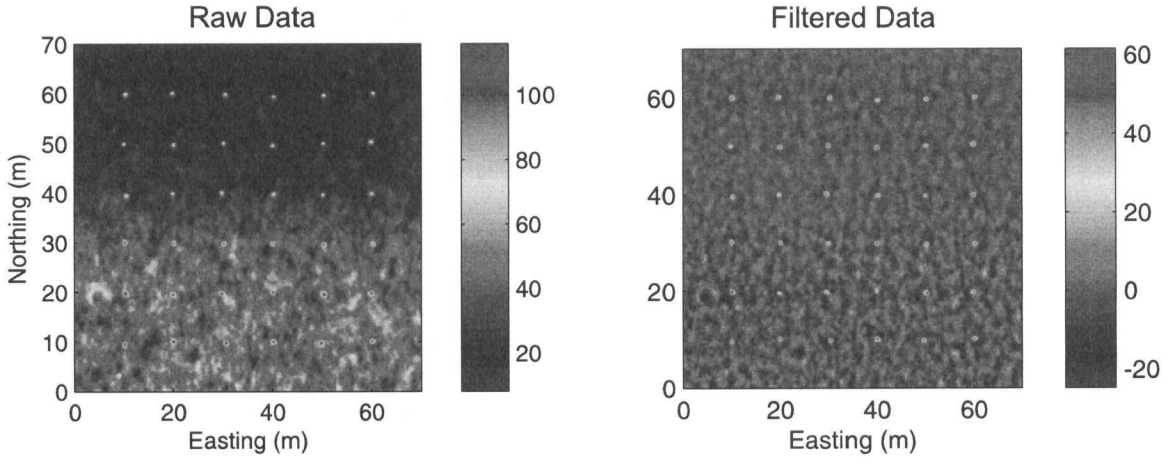

Figure 8.25: Data set with magnetic geology (left) and with the magnetic geology filtered and subtracted (right).

cle radius centered about the picked targets were inverted for the dipole polarization tensor. The axial and transverse components are parameterized with the function $L(t) = kt^{-\beta}\exp(-t/\gamma)$. The dipole parameters are obtained through the parameter estimation techniques of Chapter 3. Figures 8.26(a) and (b) shows the data fit for a 60 mm mortar in a non-magnetic background and magnetic background, respectively. In the non-magnetic background case, the residual appears random. The magnetic background case was taken in a part of the grid where the mean background response is 50 mV. When inverting this anomaly, the residual shows background noise that appears

spatially correlated.

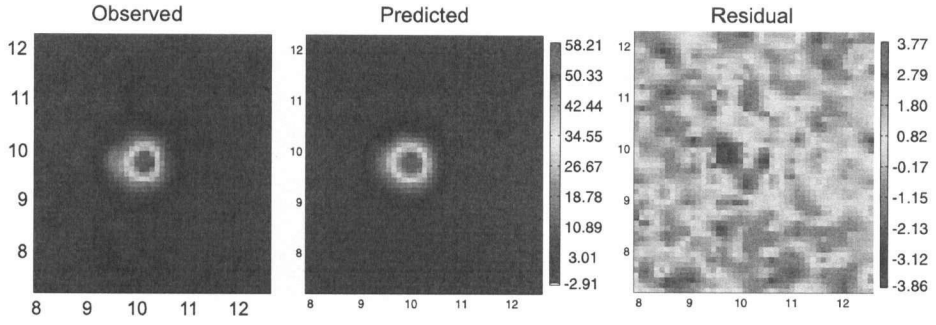

(a) Example of an inversion of data with a non-magnetic background

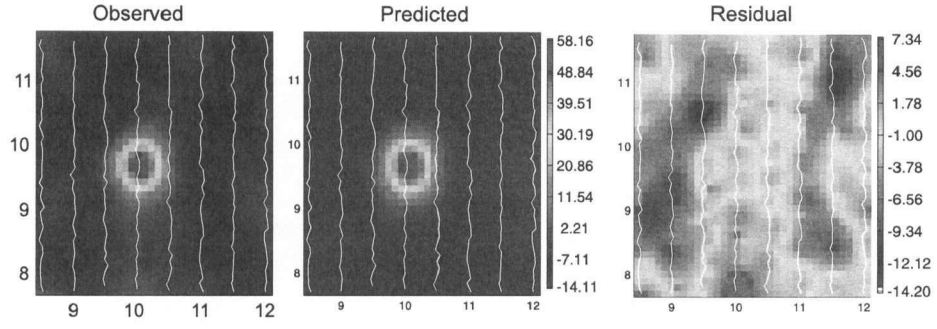

(b) Example of inversion of data with magnetic background filtered.

Figure 8.26: Inversion of synthetically generated 60 mm mortar data. The white lines in (b) indicate the synthetically generated cart locations.

Table 8.1 lists the recovered parameters for the data fits in Figure 8.26. The inversion of data without a magnetic background host clearly recovers the 60 mm parameters more accurately than the inversion of data where a magnetic background response was removed via filtering. In particular the depth derived from the filtered data is shallow, resulting in low estimates of the polarization magnitudes k_1 and k_2. Inversion results for all the targets are plotted in Figures 8.27 to 8.29. Parameters derived from the non-magnetic background data are plotted using blue circles and parameters derived from the filtered magnetic background are data plotted using red triangles. The true values are indicated by a green box. Some observations:

- The SNR for both data sets was not high enough to constrain the estimated depth. Figure 8.27 plots the estimated depth vs. k_1, i.e., the magnitude of the axial polarization. It is clear that there is a trade-off between the depth and the magnitude of the axial polarization.

- The non-magnetic background data produces a cluster near the true polarization amplitudes

Table 8.1: Comparing recovered parameters for data in Figure 8.26.

Parameter	Known values	Non-Magnetic Background		Magnetic Background Filtered	
		Recovered Parameters	Standard Deviation	Recovered Parameters	Standard Deviation
Northing x (m)	9.96	9.93	0.02	10.02	0.01
Easting y(m)	9.73	9.77	0.02	9.73	0.02
Depth z (m)	0.50	0.51	0.03	0.05	0.02
ϕ (degrees)	-	-1.0	65.2	6.3	4.2
θ (degrees)	-	4.9	3.4	127.6	2.5
k_1	11.17	11.28	2.23	0.40	0.41
β_1	0.58	0.61	0.02	0.30	0.70
γ_1	3.21	3.44	0.33	1.24	1.25
k_2	1.83	1.26	0.24	0.37	0.03
β_2	1.08	1.24	0.12	0.78	0.03
γ_2	2.89	16.33	44.76	12.65	4.34
CorrCoeff		0.945		0.873	
Φ/N		0.857		0.888	

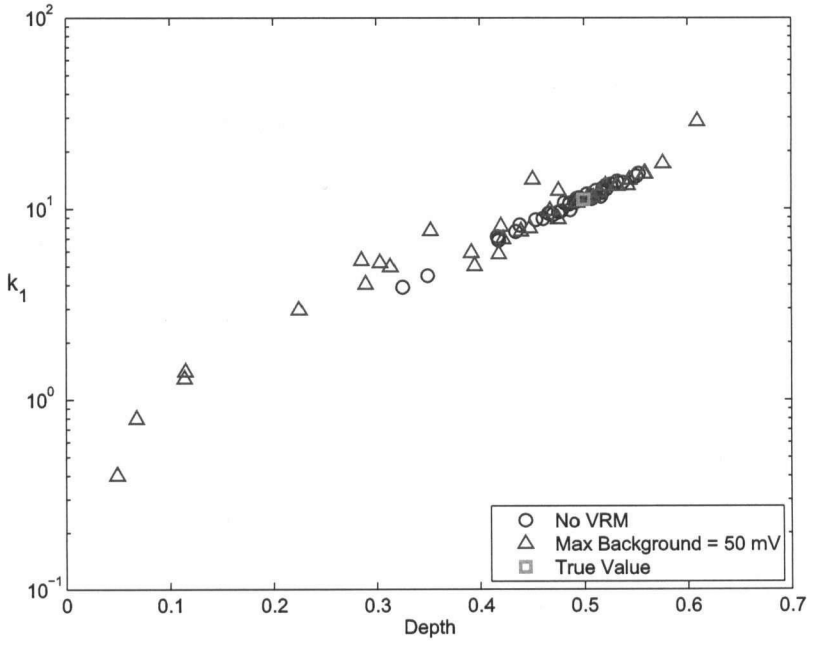

Figure 8.27: Magnitude of the axial polarization (k_1) and depth.

k_1 and k_2 values (Figure 8.28(a)). Accurate estimation of the polarization amplitudes are not possible with the filtered data.

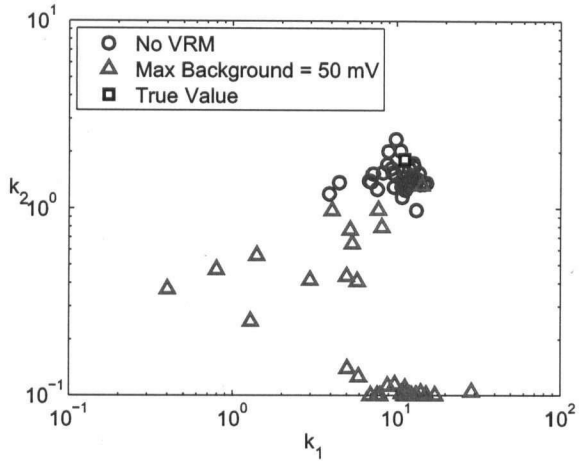

(a) Magnitude of the axial (k_1) and transverse (k_2) polarizations.

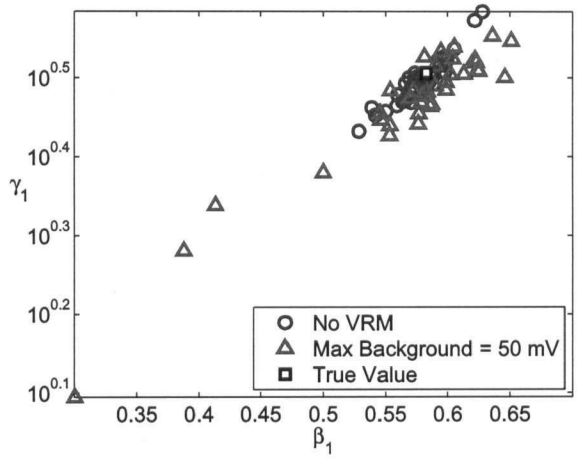

(b) Example of inversion of data with magnetic background filtered.

Figure 8.28: Inversion of synthetically generated 60 mm mortar data.

- Although the amplitude of the axial polarization is not well constrained by the filtered magnetic data, the decay parameters γ_1 and β_1 are relatively well constrained (Figure 8.28(b)), will likely be the best derived parameters for identification.

- Figure 8.29 shows the recovered polarization curves, confirming that the filtered magnetic background data are unable to estimate the amplitude of the axial components while correctly

estimating its decay characteristics, and the transverse components of the data are poorly constrained.

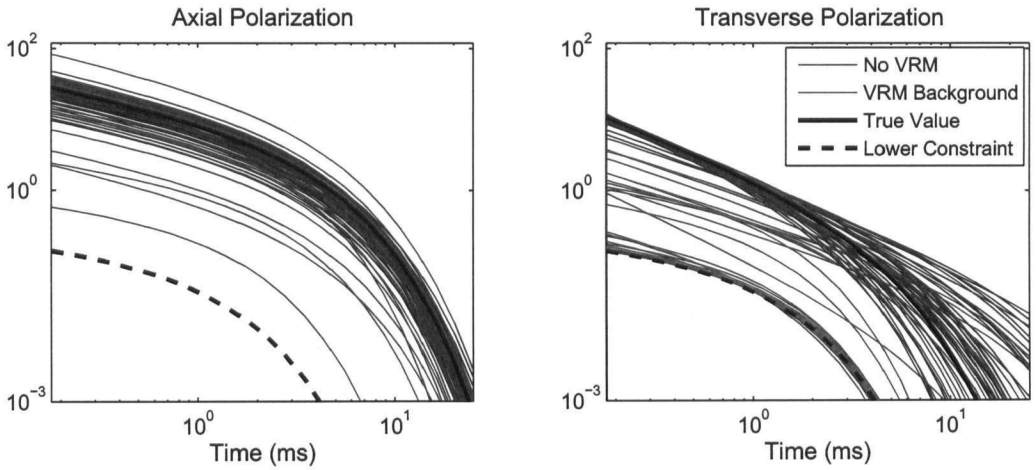

Figure 8.29: Recovered polarizations when inverting the 60 mm mortar data. The amplitude of the axial polarization is poorly constrained by the filtered data. Neither the amplitude nor decay behavior of the transverse polarization is well constrained by the filtered data.

8.9 Processing of data collected on Kaho'olawe Island, Hawaii

Geophysical data were collected on the island of Kaho'olawe, Hawaii as part of an Environmental Security Technology Certification Program (ESTCP) project to determine the effectiveness of EMI sensors fielded in areas with a large background geologic response (Cargile et al., 2004). Ordnance and ordnance related scrap were emplaced in a number of test plots. In this section we will apply target picking techniques on Geonics EM63 time domain and Geophex GEM3 frequency domain electromagnetic data collected over ESTCP Grid 2D and 2E (Table 8.2).

Table 8.2: Ground truth for Grids 2D and 2E.

Label	Target Name	X (m)	Y (m)	Depth (m)
1	Grid stake	0.00	0.00	0.00
2	Small Frag	29.04	1.36	0.15
3	2.75 ROCKET WARHEAD	56.17	3.70	0.38
4	MK-82 P. B. W/CON FINS	9.72	4.32	1.22
5	Large Frag	49.92	5.15	0.65
6	LAAW	54.15	5.52	0.13
7	Small Frag	4.58	5.70	0.10
8	Small Frag	22.31	5.82	0.10
9	81 mm Mortar	40.96	8.56	0.35
10	Med Frag	35.79	8.79	0.35
11	Large Frag	13.69	9.20	0.90
12	MK 76 P.B. (BDU 33)	23.32	10.20	0.71
13	Med Frag	48.35	10.56	0.20
14	5" HE PRACTICE	43.08	12.31	0.91
15	MK-3 PRACTICE BOMB	15.96	12.75	0.23
16	MK-81 P. B. W/S.E. FINS	7.92	12.77	1.02
17	20 MM	36.36	13.45	0.15
18	Large Frag	53.41	15.64	0.55
19	2.75" ILLUM	20.96	16.04	0.15
20	60 MM	12.63	16.21	0.20
21	SMAW ROCKET	4.40	20.86	0.76
22	Large Frag	10.15	20.94	0.70
23	MK 76 P.B. (BDU 33-(NOSE)	56.52	23.60	0.23
24	60 MM	28.32	26.63	0.15
25	Grid stake	60.07	30.02	0.00
26	Grid stake	30.09	30.03	0.00
27	Grid stake	0.08	30.04	0.00
28	Grid stake	30.00	0.00	0.00
29	Grid stake	60.00	0.00	0.00

8.9.1 Geonics EM63 TEM data

Naeva Geophysics, Inc. collected Geonics EM63 data at the ESTCP test site. Data on Grids 2D and 2E were collected on 60 m long, east-west lines with a linespacing of 50 cm. Data were collected in three 10 m wide sections. Before and after each section data were collected with the EM63 sensor elevated such that an in air measurement could be recorded, and sensor drift could be estimated and removed.

Sensor positioning were recorded with a GPS unit. Sensor orientation and height information were not provided with the data we received. For this analysis, we assume that the transmitter loop is at a height of 40 cm, and we assume that the loop is perfectly horizontal. Since we do not have accurate height and orientation information will not attempt to estimate the background response through the use of a low pass filter.

Figure 8.30 contains a plot of the sensor response for the first and tenth time gates, centered at t=0.18 ms and t=0.72 ms respectively. The weathering characteristics of the area results in a zone of high susceptibility that runs diagonally from the lower left to the upper right corners of the gridded data images (Li et al., 2005). The high susceptibility causes background responses of greater than 300 mV in the first time channel of the EM63 data. The lowest level of background responses are approximately 50 mV in the lower right corner of the grid.

A soil model is fit to each of the soundings recorded within the grids. The fitting procedure involves solving for a soil model that minimizes the least squares misfit between the measured sounding and soil response. The soil response is given by a characteristic soil decay multiplied by an amplitude A, i.e. $\mathcal{F}^{soil} = Af(t)$. Therefore, the fitting involves solving for a single amplitude parameter A. Figure 8.31 contains gridded images of the best fit amplitude A and misfit ϕ. The different sections of data being joined at $y = 10$ m and $y = 20$ m produce overlapping lines which result in some gridding artifacts. Several of the anomalies in the soil misfit image correspond to buried items (see Figure 8.34 for locations of known buried items). Anomalies not corresponding to emplaced items may be due to a buried metallic target, since it is possible that the site was not completely cleared of metal prior to preparing the test site.

Although it appears that several of the anomalies in Figure 8.31 correspond to emplaced items, we will not use the image for target picking purposes. Instead, our approach is to determine, for each sounding within the grid, the probability that the signal is due to soil (i.e. the null hypothesis).

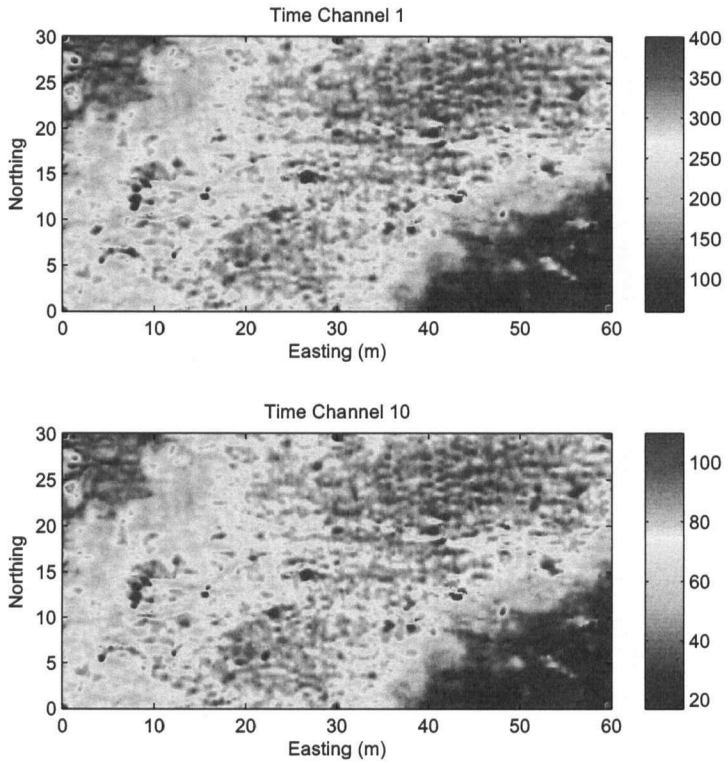

Figure 8.30: The first and tenth time channel of Geonics EM63 data collected over Grid 2D and 2E on Kaho'olawe Island, Hawaii.

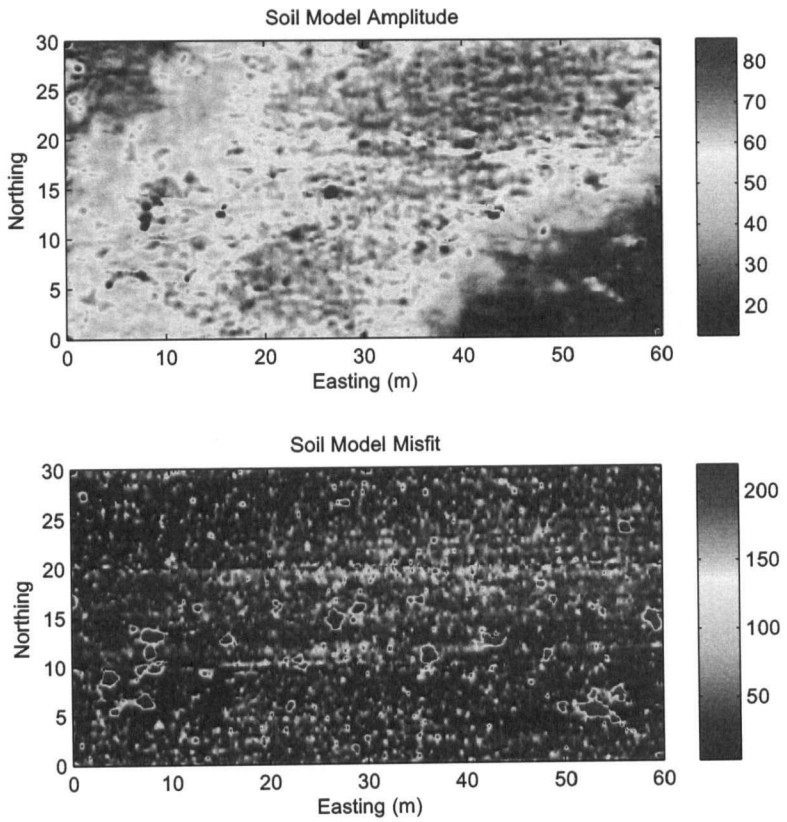

Figure 8.31: The soil model amplitude A and misfit ϕ for Geonics EM63 data collected on Kaho'olawe.

Since we do not have prior knowledge of the target types in the grid, we do not have an estimate of the pdf for the target misfits. Therefore we base our picks on the probability of false alarm P_{FA}. Calculating P_{FA} requires an estimate of the statistics of the soil misfit for the data set. The estimated probability density function and corresponding cumulative distribution function allows us to estimate the probability of false alarm P_{FA} for each sounding. That is, if a sounding has a soil misfit that is unlikely to belong to the distribution of soil misfits, then it will be classified as a target.

Figure 8.32 contains plots of the misfit distributions. The upper plot shows a histogram of the

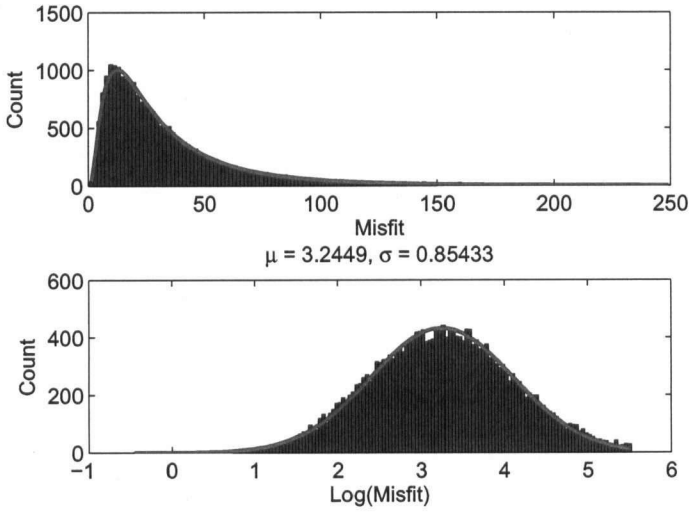

Figure 8.32: Values of misfits when fitting Geonics EM63 soundings in Grids 2D and 2E with a soil model.

raw misfit values and the lower plot shows a histogram of the log of the misfit values. Values of misfit greater than 250 are considered to be non-soil and are therefore not included when calculating the distribution statistics. Similar to the synthetic data results, the distribution of misfit values are well modelled with a log normal distribution. The mean of $\log(\phi)$ is 3.24 and its standard deviation is 0.85. The red lines plotted on the histograms are distributions with this mean and standard deviation. The estimated cumulative distribution function is plotted in Figure 8.33. For each sounding a best fit soil model is calculated, and the misfit of the soil model is used to calculate probability of false alarm

$$P_{FA} = \int_{\phi}^{\infty} p(x)\, dx = 1 - cdf(\phi) \tag{8.29}$$

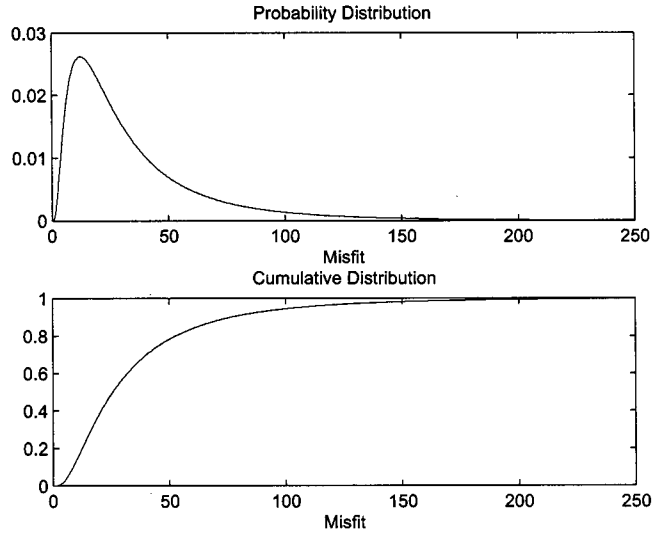

Figure 8.33: Estimated probability density function and cumulative density function for the soil misfit of the Kaho'olawe EM63 data.

Figure 8.34(a) plots results of target picking according to P_{FA}. Grey dots mark locations of each sounding and the emplaced items, listed in Table 8.2, are indicated by circles (fragments and scrap items) and squares (ordnance items or corner grid stakes). Two thresholds for P_{FA} are plotted; soundings with $P_{FA} < 0.005$ are identified by blue circles, and soundings with $P_{FA} < 0.001$ are identified by red stars. A good target picking algorithm would be able to identify all the known targets (i.e. minimizing false negatives), with a minimal number of picked targets resulting from non-metallic items (i.e. false positives). It is difficult to determine the number of false positives in this example, since there are possibly targets present that were not cleared prior to preparing the test site. Indeed, when I visited Kaho'olawe, I found that there were pieces of metal present in areas that were classified as cleared.

In any case, let us compare the picked targets with the locations of the known emplaced items. Setting a threshold of $P_{FA} < 0.005$ results in correctly locating all but 3 items: Targets 4, 17, and 21. Target 21 is a Shoulder launched Multi-purpose Assault Weapon (SMAW) Rocket. A SMAW rocket has a diameter of 84 mm. This particular rocket was reported to be buried at 76 cm which, due to its size, would be difficult to detect. Target 17 is a 20 mm projectile at a depth of 15 cm. Missing the 20 mm projectile is not unexpected, as the spatial size of the anomaly and the anomaly magnitude would be quite small. Target 4 is listed as a MK-82 at a depth of 1.22 m. Although 1.22

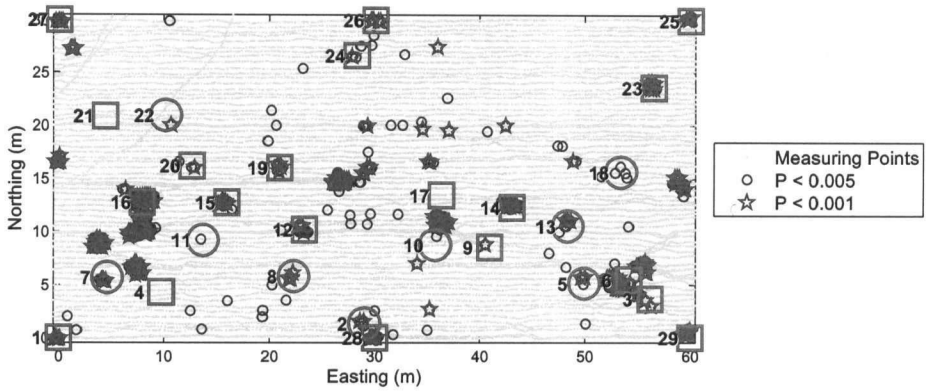

Figure 8.34: Target picking results when using the P_{FA}. Sounding locations are indicated by gray dots. Gray circles indicate emplaced non-UXO items such as frag, while gray squares indicate emplaced UXO items.

m is considered to be at the limit of detection depth for a Geonics EM63 sensor, the MK-82 is a type of 500 lb bomb that is 2.21 m long and 10.75 inches (221 mm) in diameter. There are a few reasons why the target picking might not of been able to identify the MK-82. It is possible that the anomaly within a couple of meters to the northwest of the groundtruth location is due to the buried MK-82. In addition, the MK-82 buried may be corroded, and thus have a weak signal. A final possibility is that the measured decays of the MK-82 may be similar to the characteristic soil decay. As the EM63 moves above a non-spherically symmetric target, the axial and transverse components will be "illuminated" at different angles by the primary field. This results in the observed decay (which is a linear combination of the target's axial and transverse polarizations) varying with position. However, if the signal-to-noise ratio of an anomaly is too low to allow for the collection of data at a number of locations, then the response might not change appreciably. If this response happens to be similar to the soil, the target will not be identified using a soil model misfit. This mechanism for false negatives is unavoidable. Responsible application of this method requires modelling the soil misfit for targets that may be encountered in a survey, and then generating receiver operator characteristic curves to quantify the success of the method.

When using $P_{FA} < 0.005$ as a threshold, we see that there are a number of false positives. Decreasing the threshold to 0.001 (red stars) reduces the number of false positives to 7, but also increases the number of misses. In particular, targets 11 and 18 are no longer picked when the threshold is decreased. For these data, rather than decreasing the threshold to reduce false positives,

it would be a better idea to recognize that targets generally have more than one sounding in which the soil misfit is large. If we look at the false positives for the $P_{FA} < 0.005$ target list, we see that majority of them are isolated soundings. Removing target picks associated with isolated soundings having a poor misfit reduces the number of false positives (Figure 8.35). However, requiring more

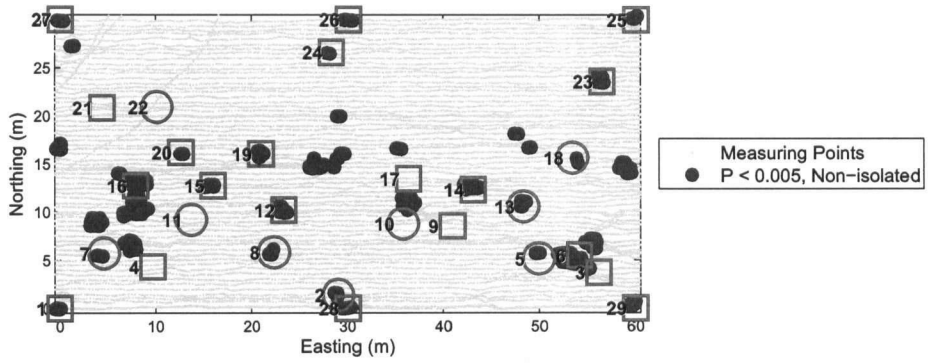

Figure 8.35: Target picking results when choosing anomalies whose $P_{FA} < 0.005$. Target picks where there is only a single sounding has a misfit falling below the threshold are removed from the list.

than one sounding to define a target results in Targets 9, 11, and 22 no longer being picked as targets. Targets 11 and 22 are deep fragments (90 and 70 cm depth, respectively). Target 9 is an 81 mm mortar buried at a depth of 35 cm. Target 9 has a single sounding with a misfit that falls below both the $P_{FA} < 0.005$ and $P_{FA} < 0.001$ thresholds.

Comparing our target picking results to the known emplaced items have shown that using the misfit of a soil model can be effective in improving detection when processing multiple time channel TEM data.

8.9.2 Geophex GEM3 Frequency Domain Electromagnetic Data

Frequency domain electromagnetic data were collected at Kaho'olawe using the Geophex GEM-3 sensor 8.36. The GEM-3 consists of a co-axial transmitter and receiver loops that simultaneously collects the frequency domain response at frequencies determined by the operator (Won et al., 1997). For the ESTCP demonstration the GEM-3 was mounted on a wheeled cart, and configured to collect

Figure 8.36: A photo of Alex Oren from Geophex Ltd. collecting data at the Kaho'olawe UXO test site. Data were collected with cart mounted version of the GEM-3. A 1 m circular transmitter loop was used for the demonstration.

data at 10 frequencies located at 90, 150, 390, 750, 1470, 2970, 5910, 11910, 23850 and 47940 Hz. A 1 m circular transmitter loop was used. Data were collected by Geophex Ltd. and they provided us with sensor drift collected data from grid 2E. Grid 2E was surveyed in 3 parts. Each section was 10 m wide, with lines running in a north-south direction with a line spacing of 0.5 m.

Gridded images of the inphase (real) and quadrature (imaginary) components of the fifth frequency (1470 Hz) data are plotted in Figures 8.37(a) and (b), respectively. Compact anomalies due to several of the emplaced ordnance items can be observed in the quadrature component of the data. However, the high susceptibility zone that runs diagonally from the lower left to the upper right corners of the grid dominate the sensor response. Figures 8.37(c) and (d) show the long wavelength component of the data estimated using a 2D median filter. Subtraction of this background response produces the detrended versions of the data (Figures 8.37(e) and (f)). As was the case with the time

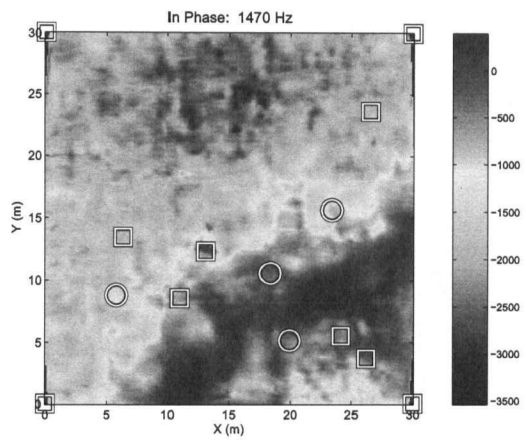

(a) In Phase (Real) data for $f = 1470$ Hz

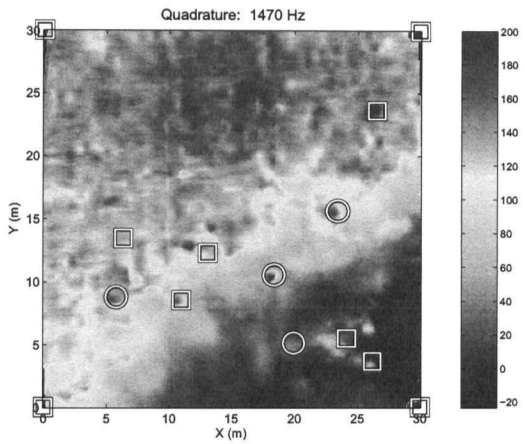

(b) Quadrature (Imaginary) data for $f = 1470$ Hz

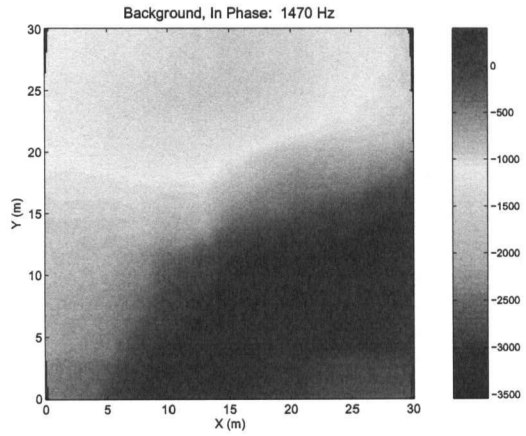

(c) Median filter estimate of the in phase data for $f = 1470$ Hz

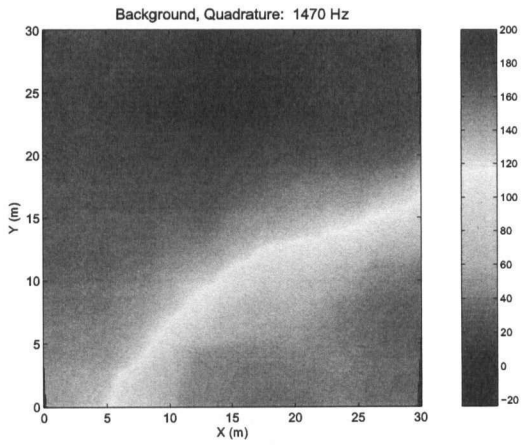

(d) Median filter estimate of the quadrature data for $f = 1470$ Hz

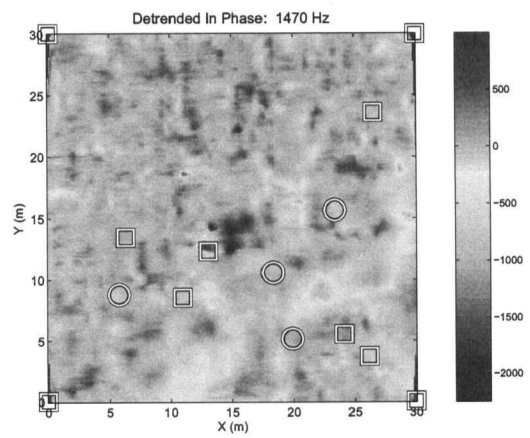

(e) Detrended in phase data

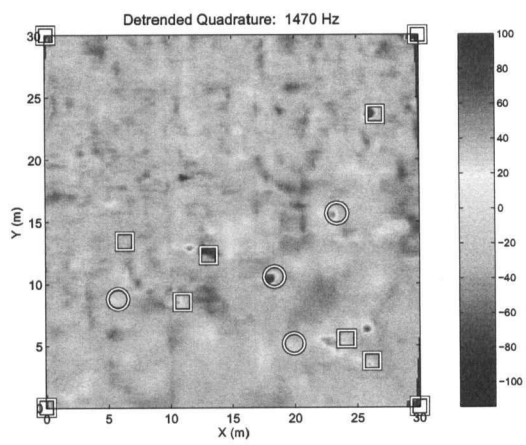

(f) Detrended quadrature data

Figure 8.37: Geophex GEM3 data collected over grid 2E at Kaho'olawe.

domain case, the detrended data contain numerous soil related small wavelength anomalies due to sensor movement and topography.

We process the GEM3 data by fitting a soil model. We fit the inphase and quadrature components of each FEM sounding with the following soil model:

$$H^{real} = m_1 \ln(\omega) + m_2 \tag{8.30}$$

$$H^{imag} = m_1 \tag{8.31}$$

Therefore, we have a two element model vector $\mathbf{m} = [m_1, m_2]^T$ which we estimate through minimizing a least squares objective function

$$\phi = \frac{1}{2}\|\mathcal{F}[m_1, m_2] - \mathbf{d}^{obs}\|^2 \tag{8.32}$$

where $\mathbf{d}^{obs} = \left[H^{real}, H^{imag}\right]^T$. The lowest two frequencies ($f = 90$ and 150 Hz) and the highest frequency ($f = 47940$ Hz) are not included in the data vector due to the noise in these data. The gridded image of the log of the soil misfit ($\log(\phi)$) is plotted in Figure 8.38. Figure 8.38 clearly

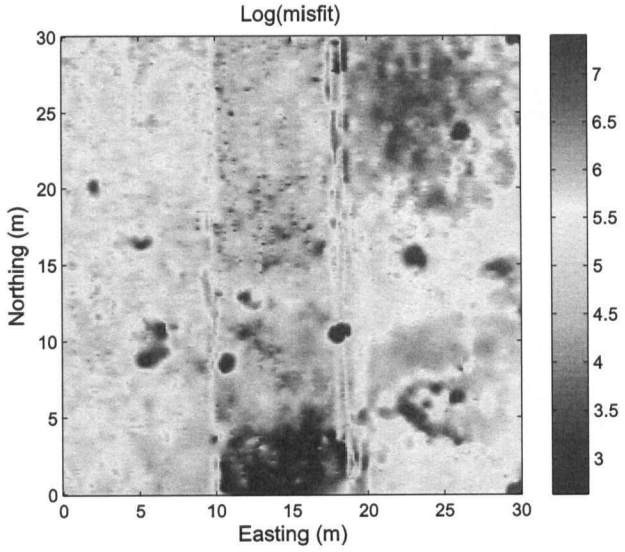

Figure 8.38: The calculated log of the misfit from fitting the model of equation 8.31 to the GEM3 data. The three separate survey events are clearly seen.

shows the three separate surveys that make up the Grid 2E data. The noise characteristics of the

instrument is clearly different for each survey. The middle section of data is clearly distinguished by its relatively lower misfit. The rightmost section of data ($x > 20$ m), has a misfit that is correlated with the amplitude of the soil response.

We will use the soil misfit results of Figure 8.38 in two ways: (1) Estimate the probability of false alarm for each sounding (as we did with the time domain data), and (2) Remove the long wavelength components of the soil misfit, and pick from the gridded image of the detrended data.

Target picking by calculating the probability of false alarm: Since the soil misfit distributions for the GEM data are different for each of the three sections (Figure 8.39), we calculate a unique soil misfit distribution for each section. Figure 8.39 contains the histograms for the soil misfit in each of the three surveys. The histograms are fit with log normal distributions, and their respective

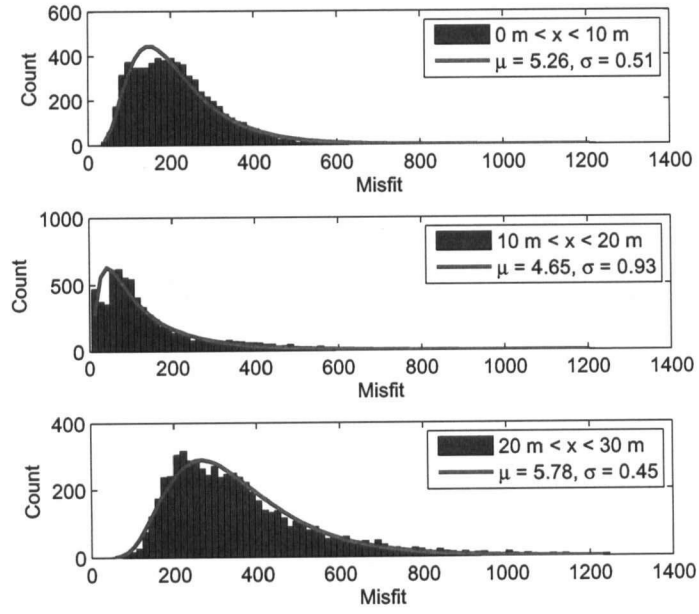

Figure 8.39: Histograms of the 3 surveys that make up the Grid 2E dataset.

cumulative distributions are computed (Figure 8.40). Figure 8.41 shows target picking results with two threshold values: $P_{FA} < 0.001$ and $P_{FA} < 0.005$. The picked targets correspond well with the ground truth. Target 17, a 20 mm projectile buried at a depth of 15 cm, was the only non-scrap emplaced item undetected by this method. Due to its small size, Target 17 was also missed when

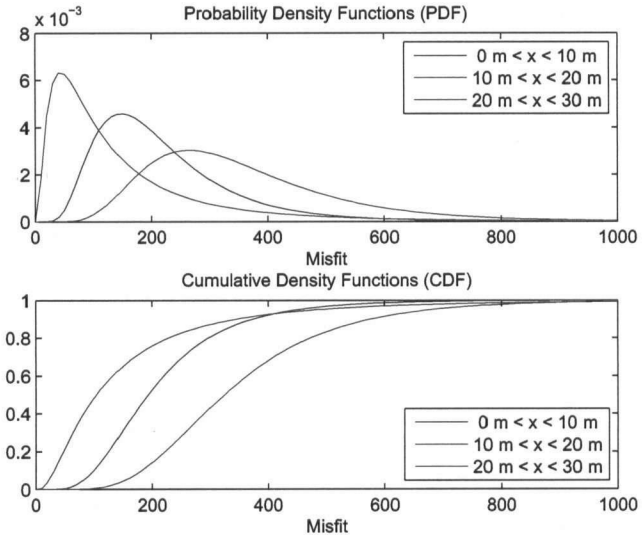

Figure 8.40: Probability density functions and cumulative density functions for the soil misfit of the three surveys of Grid 2E.

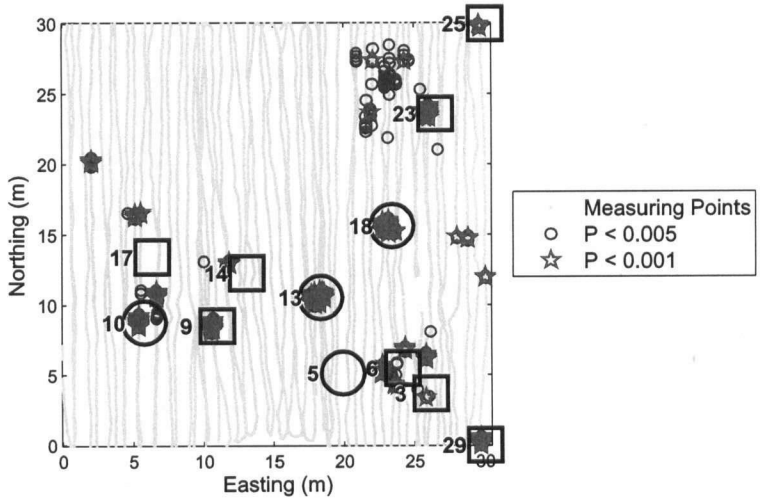

Figure 8.41: Target picking results when using P_{FA} for detection. The positions of the GEM3 sensor are indicated by grey points.

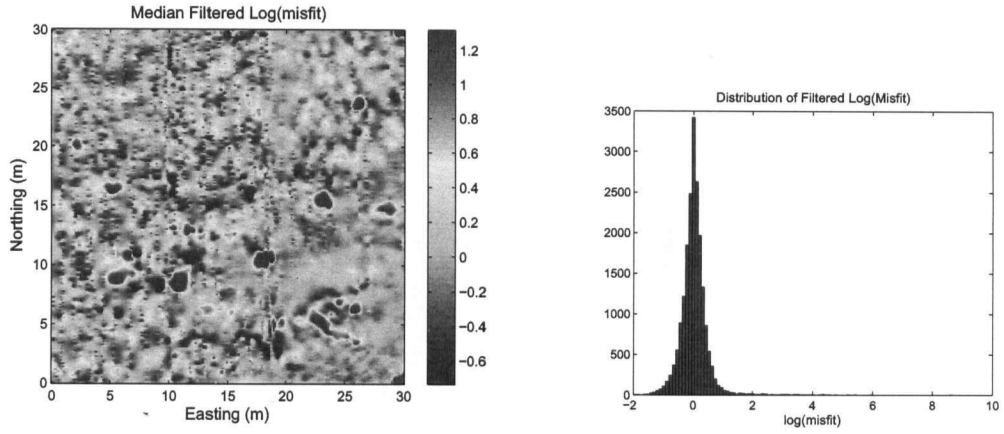

(a) Gridded image of median filtered log of the soil misfit. (b) Histogram of the filtered log of the soil misfit

Figure 8.42: Results from median filtering data from Figure 8.38.

the target picking technique was applied to the Geonics EM63 data. Target 5 was undetected, but, after taking a closer look at the GEM3 sounding positions in the vicinity of the target, the miss may be due to inadequate spatial coverage. Target 9 (81 mm) is clearly identified by the picking method, although it was missed when processing the EM63 data.

Target picking from the log-misfit image: An alternative to examining the soil misfit for each sounding is to work with the gridded image of the soil misfit. We will work with the log of the misfit. Due to the different dc offsets of the soil misfit for the three survey sections making up Grid 2E, we apply an along line median filter for each survey sections. A 2D filter was not used due to the relatively narrow width of the data swath. Gridding the high-passed results produces the image in Figure 8.42(a). A pixel size of 0.125 m was chosen for the gridding. In order to determine a reasonable threshold for $\log(\phi)$, we histogram the log of the misfits (Figure 8.42(b)).

Figure 8.43(a) contains gridded images where pixels with values less than or equal to unity are colored gray. Targets are chosen to be those anomalies that have at least 9 connected pixels that exceed the threshold $\log(\phi) > 1$ (Figure 8.43(b)). The performance of target picking from the soil misfit image is, in this example, approximately equivalent to using P_{FA} of each sounding.

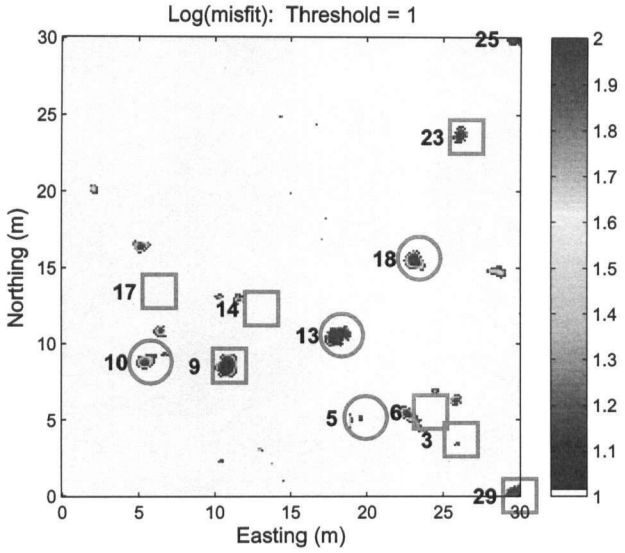

(a) Anomalies in the image of Figure 8.42 that are greater than unity, i.e. $\ln(\phi) > 1$.

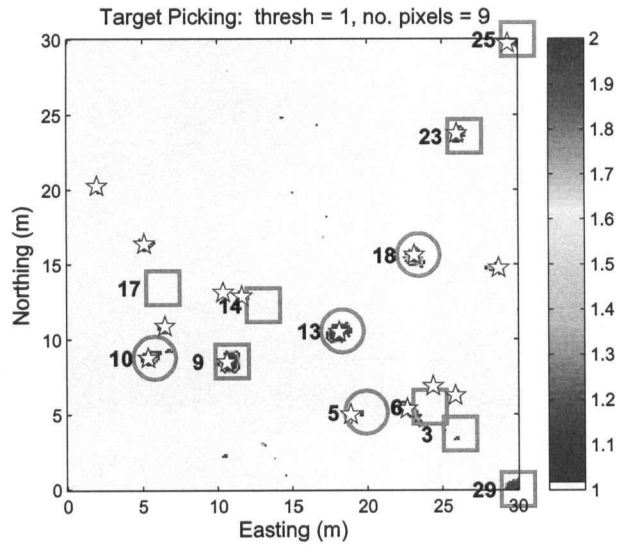

(b) Anomalies that have more than nine pixels greater than unity.

Figure 8.43: Target picking using the median filtered version of the log of the soil misfit ϕ. A target is defined when a $\log(\phi)$ anomaly has three pixels greater than one.

8.10 Improving detection and identification by using horizontal components of the secondary field

As the symmetry of the 1-D model would also suggest, there are no horizontal components to the H-field response at the center of a transmitter loop (see equations 8.3 and 8.4). This is an important point because it shows, for the case where the fields are measured along the axis of the transmitter loop, that the effects of magnetic susceptibility will appear only in the vertical component. Figure 8.44 plots the horizontal and vertical components from a field data set acquired using the Zonge NanoTEM time domain sensor. The magnetic ground on the right portion of the survey is clearly detectable in the vertical component of the data, but is less evident in the horizontal component. In this section we present a method that first uses the horizontal component of the secondary field.

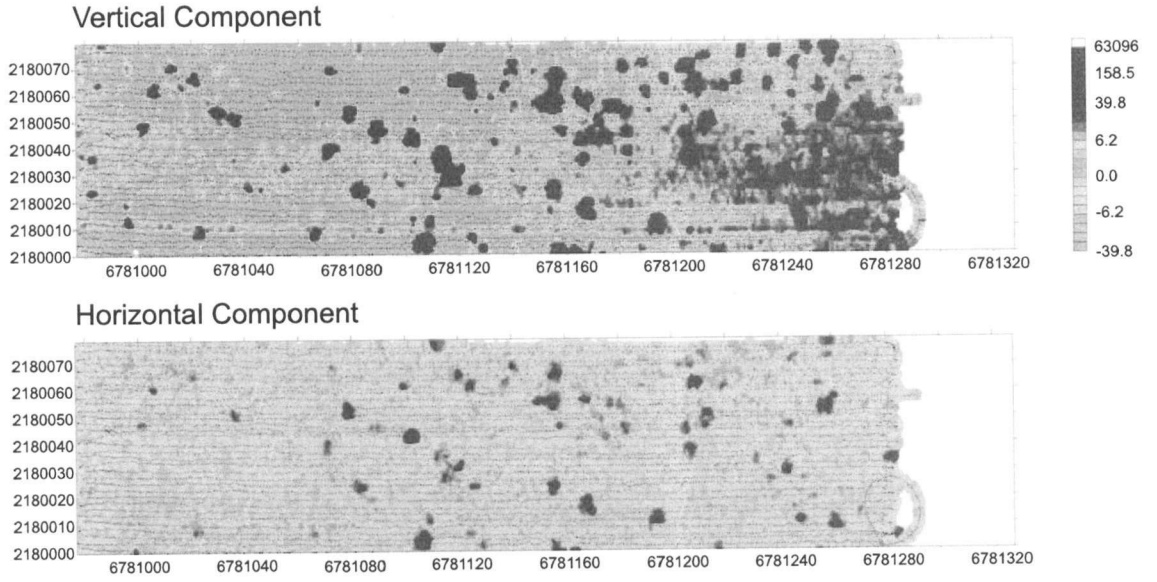

Figure 8.44: Field TEM data collected by the Zonge NanoTEM. The magnetic materials at the right hand portion of the survey are less evident in the horizontal component.

As our modelling suggests, the presence of magnetic soils will produce a t^{-1} signal in the vertical component of the measured secondary field. The difficulty in removing this signal lies in identifying whether the measured response arises only from the soil or from a combination of soil and a metallic target. The absence of the soil signal in the horizontal components suggest that they can be used as part of a pre-processing step to help determine where and how we should attempt to remove the soil signal in the vertical component. One possible (and simple) way of doing this would be to

1. Calculate the horizontal component of the data at the first time channel:

$$d^h(t_1) = \sqrt{d_x^2(t_1) + d_y^2(t_1)} \tag{8.33}$$

2. At each sounding, if d^h is less than some threshold value (e.g. $d^h < 2\text{mV}$) then identify this station as unlikely to contain signal from a target. We can proceed to fit At^{-1} to the data at this station and subtract from the data.

3. At soundings where d^h is greater than the threshold, we can then subtract $A^\dagger t^{-1}$ where $A^\dagger$ is determined from interpolation of the A values from the previous step.

8.10.1 Application to Synthetic Data

Although 3-component sensors have been developed by Geonics Inc. (EM61-3D) and Zonge Engineering (NanoTEM), testing of either sensor has been limited. Field data, in particular data acquired over magnetic soils, are not readily available. Therefore, to investigate the effects of the magnetic soils we must generate synthetic data sets. We assume that the secondary field is a linear sum of the response of the buried metallic target, the response of the magnetic soil and Gaussian noise. We use the conclusion, arrived at earlier, that the magnetic soils affect only the vertical component of the receiver if the receiver is on the axis of the transmitter.

The buried target response is calculated by using the decaying two-dipole approximation outlined in Pasion and Oldenburg (2001a). For the examples in this chapter, we will forward model the response for the Stokes mortar of Figure 8.45. Data will be generated for a 4 m $\times$ 4 m survey

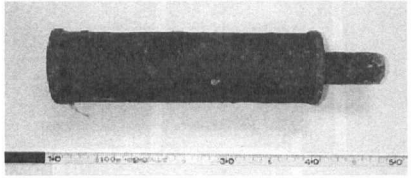

Dipole 1	
k_1	43.9
α_1	0.02
β_1	0.73
γ_1	9.1

Dipole 2	
k_2	4.9
α_2	0.001
β_2	1.09
γ_2	10.8

Figure 8.45: Photo and Decay Constants for a Stokes mortar.

area, with lines collected at 0.5 m separation, and soundings collected every 10 cm along each line. The mortar is placed at (X, Y) =(2m, 2m) and at a depth of 40 cm. The target is oriented such that (θ, ϕ) =(30 degrees, 70 degrees).

To model horizontal variation of magnetic soils we assume that the magnetic soil response is

$$F^{soil} = A(x, y)\, t^{-1} \tag{8.34}$$

where the amplitude $A(x, y)$ can vary across the survey area. Figure 8.46 contains data collected on Kaho'olawe with a Geonics EM63 TEM sensor. From the plotted decay curves, we see that the basaltic soils produces a response of approximately 100mV at the first time channel (180 μsec). The amplitude $A(x, y)$ is defined as

$$A(x, y) = \frac{k}{2}\left[1 + \tanh\left(2\left(x - \frac{3}{2}\right)\right)\right] \tag{8.35}$$

where k is chosen such that at the first time channel the background soil response is 50 mV at $Y = 0$m and increases to 100 mV at $Y = 4$m.

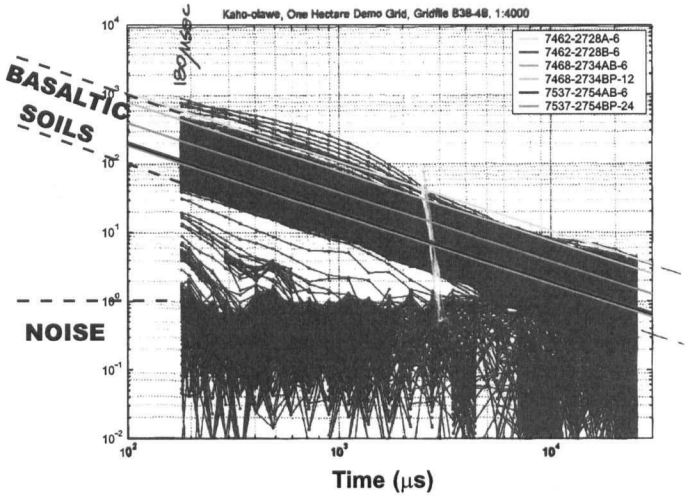

Figure 8.46: Geonics EM63 TEM data collected on Kaho'olawe island. Overlaid on the data are modelled responses of two layer models.

Finally noise with a standard deviation of 5% of the data plus 0.5 mV are added to the sum of the basalt response and the dipole response. Figure 8.47 plots the synthetic data at $t = 180\mu$sec.

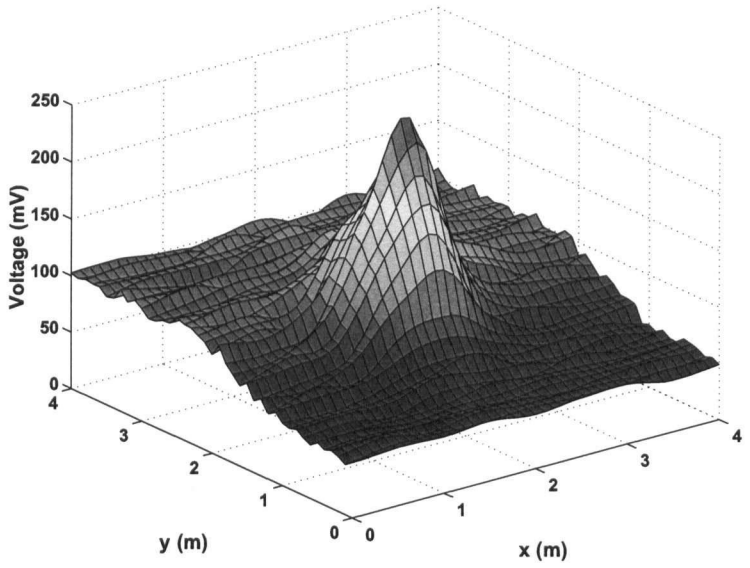

Figure 8.47: First time channel of synthetic data.

8.10.2 Inversion Results

The synthetic data were inverted for the 13 parameters of the two dipole model. Three data sets we considered are: (1) Stokes mortar without magnetic soil response, (2) Stokes mortar with the magnetic soils noise model, and (3) Stokes mortar with a magnetic soil background, where the data has been pre-processed using the horizontal components to remove the response from the vertical components. The results of inverting the data sets are shown in Table 8.3. The inversion was successful in recovering the location, orientation, and dipole parameters without the magnetic soil signal, and when the data was pre-processed as described in the previous section. The inversion of the un-preprocessed data set that contained the magnetic soil signal, was not successful in recovering the dipole decay parameters.

8.10.3 Summary

One-D forward modelling of this susceptibility model reveals that the horizontal components of data measured along the axis of a transmitter loop are not sensitive to magnetic soils provided that the subsurface properties can be adequately represented by a 1D layered model. As a consequence, when inverting the three component sensor data collected over a target buried in magnetic soil,

	Real Params	No Basalt	w/ Basalt Model	Basalt Removed
X	2	2.00	2.08	2.02
Y	2	2.00	2.00	1.98
depth	0.4	0.40	0.58	0.42
ϕ	30	29.9	41.1	38.2
θ	70	70.0	74.2	69.3
k_1	43.9	45.35	125.69	47.45
α_1	0.02	0.02	0.00	0.02
β_1	0.73	0.73	0.71	0.72
γ_1	9.1	9.17	29.31	9.04
k_2	4.9	4.96	26.05	6.62
α_2	0.001	0.02	0.00	0.02
β_2	1.09	1.16	0.80	1.04
γ_2	10.8	12.69	29.23	15.06

Table 8.3: Inversion Results for a Stokes Mortar buried in a background of magnetic soils.

the information provided by the horizontal components of data may: (1) improve detection, (2) be exploited in developing processing routines to aid in the removal of the magnetic soil response in the vertical component of data, and (3) help constrain the inversion to more reliably recover dipole model parameters.

8.11 Conclusion

The most common approach to processing is to: (1) develop a target list based on a property of the data, (2) develop filtering techniques such that the background response can be estimated, and subsequently subtracted from the data, and (3) the spatially filtered data is then inverted with the physical model for the UXO response in free space. In this chapter, we looked at different aspects of processing electromagnetic data collected in regions with highly magnetic geology. Synthetic data sets were generated to help study the effectiveness of filtering, target picking, and inversion.

We showed that sensor height changes of only a few centimeters can change the measured soil signal by tens of percent. Therefore, in regions where there is a significant VRM response, accurate sensor positioning and orientation information are required to model the measured data. The standard high pass filter approach will have limited success due to the high spatial frequency components of the data introduced by the sensor movement and small scale topography. Instead of

filtering the data directly, an improved approach would be to include sensor position information in estimates of the soil properties. These soil properties can then be filtered if the assumption that the soil properties of the host medium is smooth is valid.

In general, TEM data is not collected with accurate sensor position and orientation information. Sensor movement then leads to the numerous anomalies that are similar to those from UXO. When the number of soil anomalies make the target picking directly from the data ineffective, the misfit of the measured time or frequency sounding to a soil model is a potential diagnostic for determining if a sounding is from soil or metal. The use of the soil model misfit was shown to be effective for picking targets in Geonics EM63 and Geophex GEM3 data acquired on Kaho'olawe.

An analysis of how noise due to the background response affects dipole inversion parameters. Data collected at magnetic sites with very accurate sensor motion information was not available when writing this chapter. Therefore our analysis focussed on the effects of not including the sensor motion information into the processing. Inversion of synthetic data showed that not included including this information leads to inaccurate recovery of the polarization tensor magnitude. The decay characteristics of the axial polarization tensor appears to be better constrained than the amplitude. The transverse component is not recovered well.

The final example of this chapter showed that an estimate of the background response could be improved with the use of horizontal component data. Target picking on the horizontal component can be an effective in highly magnetic soil since no spatial filtering is required. The effectiveness of using the horizontal component is limited by the smaller signal to noise ratio of the horizontal component.

Chapter 9

Conclusions

Remediation of UXO contaminated sites is a multi-stage process consisting of detection, discrimination, and excavation. In the traditional "Mag and Flag" approach, analog metal detectors are used to locate the presence of metallic objects and a flag is placed at each detection location for excavation. The integration of digital geophysics and the application of geophysical data processing techniques into the UXO remediation process has led to the development of discrimination techniques. Indeed, at sites where digital geophysical data can be acquired, it is no longer considered sufficient to provide EOD technicians with a list of possible UXO for excavation. Geophysicists are expected to apply data processing techniques that can prioritize the target list by estimating, for each target, the likelihood of it being a UXO. Being able to recognize which anomalies are not likely UXO reduces the number of UXO excavations and, therefore, reduces the cost of UXO remediation.

UXO discrimination is achieved by extracting parameters from geophysical data that reflect characteristics of the target that generated the measured signal. These parameters come in two forms: (1) data-based parameters that are based solely on the data, such as amplitude and energy (2) model-based parameters which are inputs to a mathematical forward model (such as the dipole model) that can reproduce the data. Data and model based parameters can then be used as input to statistical classification methods (such as support vector machines and neural networks) to determine the likelihood that the target is, or is not, a UXO.

The focus of this thesis was the extraction of physics-based model parameters from time domain electromagnetic data. Pasion (1999) suggested that a buried target's dipole polarization tensor could be extracted from multi-channel time domain electromagnetic data, and the decay characteristics of the polarization tensor could be diagnostic of the targets size and shape. We believe that the dipole model strikes a reasonable balance between model complexity and accuracy for the majority of geometries encountered in UXO remediation, without being computationally intensive. In this thesis we further developed the dipole modelling and inversion methodologies described in Pasion

(1999) for application to real-world UXO remediation projects.

An understanding of the dipole model was developed in this thesis (Chapter 2). We examined how sensor geometry illuminates the axial and transverse components of the dipole model, and how these components contribute to the measured dipole field. The axial and transverse components of the dipole polarization tensor decay with time, and we define a parameterization for the axial and transverse decay that are related to the conductivity, permeability, shape, and size of the buried object. The suitability of these parameterizations have been confirmed through the fitting of numerous TEM data anomalies measured over UXO.

Several different inversion techniques for estimating dipole parameters were developed for TEM sensor data (Chapters 3 to 5). Inversion was first carried out on high quality data sets acquired by slowly moving the Geonics EM63 sensor, thereby minimizing survey errors and additive noise. With the exception of cued interrogation surveys, these survey conditions are not typical of UXO surveys. The anomalies acquired in this manner were characterized by high signal to noise ratios, excellent position and orientation information for the sensor, and excellent spatial coverage. Unconstrained minimization was carried out using both local Newton-type methods and the global Neighbourhood Algorithm method of Sambridge (1999a). The local and global approaches produced similarly good results for the estimated parameters, although variances for local approaches were smaller than those from global methods. These successful inversions allowed us to proceed to more realistic, and challenging, data sets.

There are two main difficulties with field data: (1) field data are collected in a dynamic mode, which reduces signal to noise ratio data and decreases the accuracy sensor position and orientation information, and (2) filtering designed to remove non-target signal such sensor drift and geology can often leave artifacts in field data. Recognizing that lower signal to noise data will often be unable to constrain parameters, we considered two types of a priori information that could be included in the inversion. In Chapter 4 we tested joint and cooperative inversion techniques where position information from magnetics data was used to constrain TEM inversions. Examples showed that the addition of target position information reduced the variance of target cluster classes. Obviously, the success of jointly and cooperatively inversion is sensitive to the ability to co-register the multiple data sets. Knowledge of the different types of UXO expected at a site was the second type of prior information considered. This type of prior information led to the implementation of a fingerprinting

style discrimination approach in which a generalized likelihood ratio test (GLRT) determined the most likely UXO to generate the target anomaly (Chapter 5). Future refinements could include the cost of misclassifying a UXO, or include prior probabilities of different target types into the GLRT formulation. In the GLRT approach, targets are ranked according to their misfit. The fingerprinting approach is most effective in cases where one of the members of the target library represents targets that should not be excavated.

There exists instances where a combination of target types, signal to noise ratio, and survey parameters do not support data inversion. We investigated the ability to constrain dipole parameters using Monte Carlo type simulations (Chapter 6). Numerous synthetic data sets with different noise, survey parameters and target types were generated and inverted. Relationships between the spread of recovered parameters and survey characteristics were established for a single channel of Geonics EM61-MK2. A figure of merit that quantifies these relationships was proposed.

If the host material in which the UXO is buried is conductive or magnetic, then the EM signals will be altered as they travel from the transmitter to the target and from the target back to the receiver. If these effects are significant, but not accounted for, the performance of the inversion algorithms will be degraded. In particular, soils that display viscous remnant magnetization are problematic (Chapter 7). In such circumstances, there are two options. We can either include the effects of the magnetic soils in the forward modelling and inversion, or we can attempt to remove the soil properties, with the application of various filters, and then invert the processed data.

Two data processing strategies for electromagnetic data acquired magnetic geology are explored in this thesis: (1) Improve estimates of the background geologic signal, which are then subtracted from the data (Chapter 8), and (2) Use a forward model that includes the geologic response (Chapter 5). The first technique is most commonly used in current UXO data processing. For single time channel data the most common procedure is to apply a low pass filter to the data to estimate the soil response. This approach relies on the assumption that the small wavelength components in the data are due to compact targets, and not the geology. However, even if the magnetic properties of the soil are slowly varying, variations in cart height due to topography and topography itself, can add a significant high frequency component to the data. Therefore, our preferred approach is to estimate a soil model from the data. Our soil model consists of a single parameter at each spatial location that is a function of the low frequency magnetic susceptibility and upper and lower limits of the soil

decay time constants. We estimate this parameter such that it is laterally smooth. This is achieved by fitting each sounding independently, then applying a low pass filter to the soil. In regions of large background geologic signal it is important to include sensor height and orientation information to model the high frequency signal due to sensor movement. Without height and orientation information a significant high frequency noise will remain in the data, and dipole parameter estimates will not be accurate.

Much of the work in this thesis has been implemented in the software package UXOLab, first developed at the University of British Columbia by the University of British Columbia Geophysical Inversion Facility. UXOLab enables users to import sensor data, perform pre-inversion processing steps such as simple filtering and target detection, estimate dipole parameters and apply statistical discrimination algorithms. The unconstrained, linearly constrained, cooperative, and library methods for estimating dipole parameters have been implemented in UXOLab. These TEM inversion techniques developed in this thesis are currently being tested as part of a number of research projects funded by Environmental Security Technology Certification Program (ESTCP), in particular, Practical Discrimination Strategies for Application to Live Sites, ESTCP MM-0504 (Billings, 2007).

Part I

Appendices

Appendix A

Comparison of the Dipole Model and Data collected at the U.S. Army Engineer Research and Development Center (ERDC)

In Chapter 2 an approximate forward model was proposed for the TEM response of a buried axi-symmetric metallic target. In this forward model, the secondary field is approximated by a pair of orthogonal and independently decaying dipoles, whose strengths are proportional to the projection of the primary field onto their direction. The decay of each dipole moment is governed by the magnetic polarization tensor $\bar{\bar{M}}$. The magnetic polarizability tensor is independent of transmitter/receiver/target geometry and is a function of the physical characteristics of the target alone. In our previous work we outlined a technique for exploiting $\bar{\bar{M}}$ as a tool for characterizing the shape of target as either rod-like or plate-like, and if the target is ferrous or nonferrous (Pasion, 1999). These results can only be applied with confidence for measurement configurations where the forward modelling is applicable.

This appendix summarizes a series of tests designed to verify that the magnetic polarization tensor is indeed independent of transmitter/receiver/target geometry. Each test follows the same procedure. First, the target is measured in two orientations: with the axis of symmetry parallel to the primary field and then perpendicular to the primary field. These measurements allow us to extract the target's two characteristic decay curves $L_1(t)$ and $L_2(t)$ that define the magnetic polarization tensor. Equipped with $\bar{\bar{M}}$, we can then predict the TEM response for various locations and orientations and compare these results with measured data. In this section we evaluate the

accuracy of these predictions.

This appendix is part of the report "Locating and Characterizing Unexploded Ordnance Using Time Domain Electromagnetic Induction" (Pasion and Oldenburg, 2001b) which summarized the data acquisition at the U.S. Army Engineer Research and Development Center and their subsequent processing. In the interest of space, we do not present the majority of Geonics EM63 data and any of inversion results here.

A.1 TEM Data Collection at the U.S. Army Engineer Research and Development Center (ERDC) Unexploded Ordnance (UXO) Test Site

Between April 5 and April 21, 2000, I carried out a series of TEM measurements at the Engineering Research Development Centre in Vicksburg, Mississippi. The Geonics EM63 TEM sensor was used for all the data collection in this investigation. The EM63 is a multi-time channel time domain unit consisting of a 1 $\times$ 1 m square transmitter coil and a co-axial, horizontal $50cm$ diameter receiver coil mounted on a two-wheel trailer. More information about the EM63 sensor can be found in "EM63 Full Time Domain Electromagnetic UXO Detector: Operating Instructions" (2000).

A.1.1 Plan Measurements

A series of surveys were conducted over single targets seeded at the WES UXO test site (Figure A.1). A $4m \times 4m$ square centered at ($18m\,N$, $24m\,E$) was chosen for the surveys. Prior to seeding the individual targets, EM63 and EM61-HH surveys were carried out to ensure that the area was "quiet", i.e. to ensure the area did not contain metallic scrap. The borders of the $4m \times 4m$ square were marked with string to indicate the extent of the survey area. Lines for each survey were run in a $N - S$ direction with a line spacing of $50cm$. The location of the sensor was measured more accurately by marking survey lines at $1m$ spacing with string and by dropping a plumb line from the center of the receiver/transmitter loop pair. The EM63 was set to record a time decay curve at $10cm$ intervals triggered by the odometer in the EM63 trailer wheels.

Targets measured in this survey setup included several UXO (37 mm projectile, 60 mm mortar, 81 mm mortar, stokes mortar, 105 mm mortar projectile, 155 mm projectile) and a variety of scrap

items excavated during a UXO remediation project at Camp Croft, Maryland. These targets were placed at approximately the center of the grid $(2mN, 2mE)$, and at depths up to $75cm$. In all cases the strike of the target was parallel to the line direction. In order to save time, the soil, removed when digging a hole for the target, was not replaced over the target. A wooden plank was placed over the hole in which the object was laid. Targets were generally measured in three orientations: horizontal, vertical, and an intermediate angle.

Target	Mass (kg)	Length (cm)	Width /Thickness (cm)
155 mm		60	15.5
105 mm	14.05	21	10.5
Stokes Mortar	3.55	36	16
81 mm (no fins)	3.3	26	8.1
Rusted Mortar	2.85	36	29
60 mm	1.352	26	6
37 mm	0.839	11.4	3.6
Disk	0.88	8 (diameter)	2.2 thick
Scrap 1	0.08	13 (diameter)	~2 thick
Scrap 2	0.026	6.4	6.3
Scrap 3	0.055	11	6.4
Scrap 4	0.091	19.4	2.5
Scrap 5	0.172	16.5	3
Scrap 6	0.256	21	4.8
Scrap 7	0.069	12.5	2
Scrap 8	0.075	7	3
Scrap 9		19	9
Scrap 10	0.032	5	3.5
Scrap 12	0.186	9.6	4.4
Rocket Fins (Scrap 13)	0.83	21.4	6.5
Blown Mortar (Scrap 14)	0.939	16	7
Scrap 15	0.431	16	5.6

A.1.2 Decay Measurements

A controlled set of experiments was carried out to carefully examine how the secondary field of a target decays as a function of depth and orientation. For these experiments we required measurements with the EM63 transmitter/receiver coil directly above the center of various targets positioned at several depths and orientations.

In order to accurately and quickly position each target, Jose Llopis at WES designed and built a target holder (Figure A.2(a)). The jig was made of wood and glue, contained no metallic materials, and could orient each target at 15 degree increments from vertical to horizontal. The size of the jig made it difficult to bury. Therefore the jig was only partially buried and 2×6 planks were used to adjust the height between the EM63 and the target (Figure A.2(b)). The height of the planks was varied by changing the number of cinder blocks used to elevate the planks. The majority of measurements were taken at two sensor heights: $Z \sim 50cm$ and $Z \sim 100cm$ from the center of the receiver to the center of the target, where Z is the vertical distance from the center of the target to the center of the receiver loop. Additional measurements with $Z \sim 75cm$ were made on a subset of the targets. TEM soundings were recorded for several UXO items ranging from a 37 mm projectile to a 105 mm, as well as several scrap items. Samples soundings are plotted in Figure A.3.

Several of the smaller, non-UXO items did not produce a significant response when placed in the jig. Therefore, they were measured using the setup of Figure A.4(a). Each target was placed in two orientations and at ground level. To facilitate the collection of cleaner data, a pair of 6×2 inch planks was placed on the ground to provide a level surface for the EM63 to be pulled along. The measured voltage curves for scrap targets 1 to 8 are plotted in Figures A.4(b) and (c). The line profiles for the first time channel ($t = 180\mu s$) and the tenth time channel ($t = 0.72msec$) are plotted in Figure A.5.

A.1.3 Analysis

Obtaining the Polarizability Tensor

Constructing the polarizability tensor $\bar{\bar{\mathbf{M}}}$ requires obtaining the dipole decay functions $L_1(t)$ and $L_2(t)$. The decay functions can be isolated by making two measurements: (1) primary field B^P parallel to the $\hat{\mathbf{z}}'$ axis of symmetry, and (2) primary field perpendicular to the $\hat{\mathbf{z}}'$ axis of symmetry.

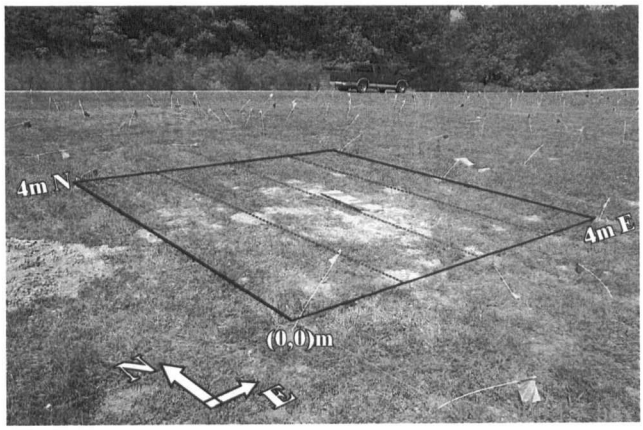

Figure A.1: $4m \times 4m$ area on which a series of EM63 surveys were taken over different targets at several depths and orientations.

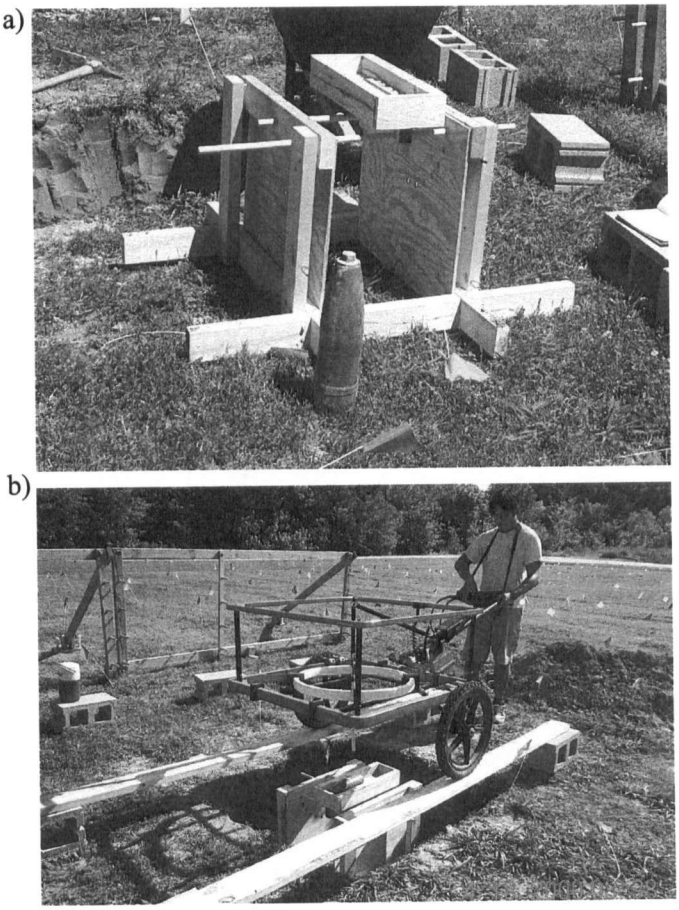

Figure A.2: (a) Photograph of the wooden target holder for EM63 measurements. A 105mm projectile is standing beside the jig. (b) Measurement procedure when using the jig.

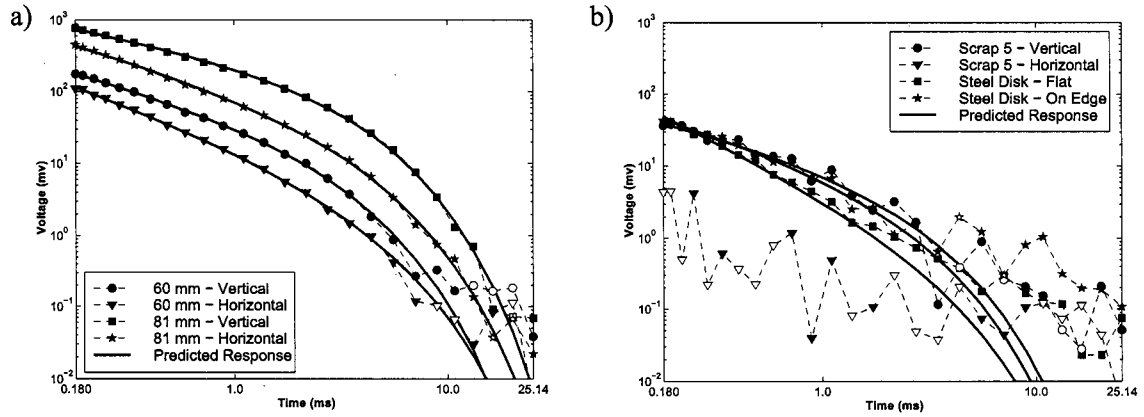

Figure A.3: (a) Measurement of a 60 mm and 81 mm in jig. (b) Measurement of Scrap 5 and a Steel Disk. Unfilled symbols (e.g. 'o') indicate negative data that has its absolute value plotted. Predicted response is obtained by fitting the measurement with Equation A.1.

Figure A.6 illustrates the arrangement of the EM63 and target that we used to obtain the decay functions. In this geometry, the measured voltage is then:

$$V(t) = \kappa \frac{B^P(Z)}{Z^3} 2\left[L_1(t)\cos^2\theta + L_2(t)\sin^2\theta\right] \tag{A.1}$$

where Z is the distance between the center of the receiver loop and the center of the target, and κ is a constant that depends on the size of the receiver and transmitter loops, the number of turns in each loop, and the transmitter current.

When the target's $\hat{\mathbf{z}}'$ axis of symmetry is parallel to the inducing field ($\theta = 0$ degrees, Figure A.6a), only the $\mathbf{m}_1(t)$ dipole is excited, and the measured voltage is

$$V^{\parallel}(t) = \kappa \frac{B^P(Z)}{Z^3} 2L_1(t) = \left[2\kappa \frac{B^P(Z)}{Z^3}\right] k_1 (t+\alpha_1)^{-\beta_1} e^{-t/\gamma_1} \tag{A.2}$$

and when the target's $\hat{\mathbf{z}}'$ axis of symmetry is perpendicular to the inducing field ($\theta = 90$ deg, Figure A.6b), then only the $\mathbf{m}_2(t)$ dipole is excited and the observed voltage is:

$$V^{\perp}(t) = \kappa \frac{B^P(Z)}{Z^3} 2L_2(t) = \left[2\kappa \frac{B^P(Z)}{Z^3}\right] k_2 (t+\alpha_2)^{-\beta_2} e^{-t/\gamma_2} \tag{A.3}$$

The voltage curves recorded by the EM63 for the parallel and perpendicular responses can be obtained by using a scaled down version of the inversion algorithm to recover the decay parameters

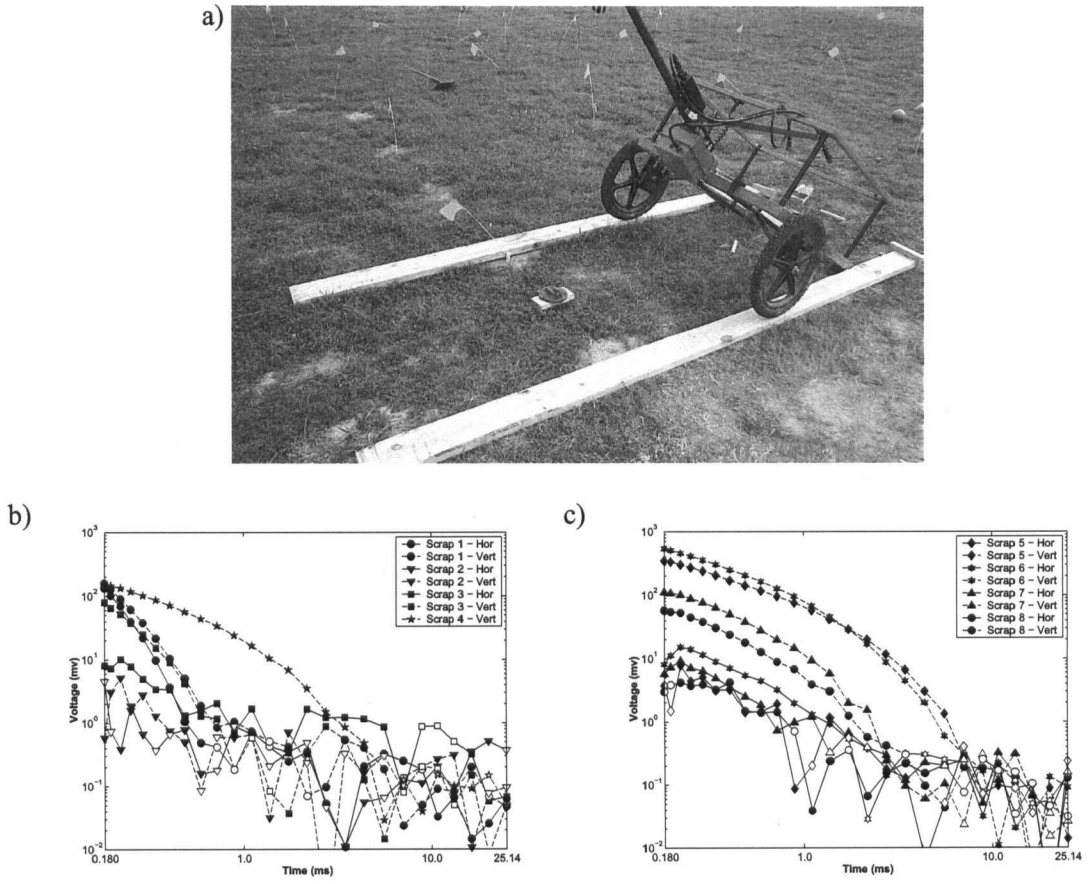

Figure A.4: (a) Photograph of setup used to measure response of smaller scrap targets. (b) Voltage decay measurements for scrap targets 1 to 4. (c) Voltage decay measurements for scrap targets 5 to 8. Unfilled symbols (e.g. 'o') indicate negative data that has its absolute value plotted.

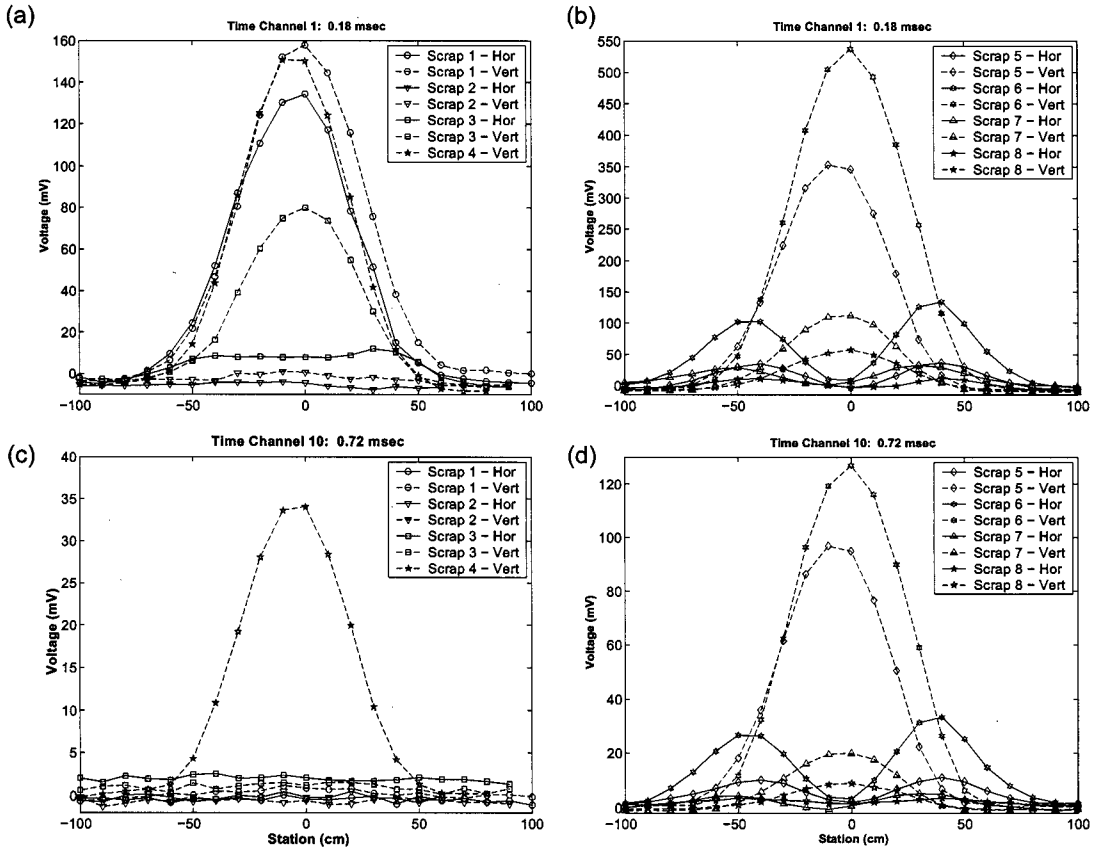

Figure A.5: Measured response of scrap targets 1 to 8 along a line. Panel (a) and (b) plot the response along a line for the first time channel ($t = 0.18msec$). Panel(c) and (d) plot the response along a line for the tenth time channel ($t = 0.72msec$). Each target is located at station $0cm$.

(Pasion 1999). Figures A.6c and d give the result of this procedure applied to a 105 mm projectile and scrap 14. As expected for a rod-like target the L_1 component of the polarization tensor has a greater magnitude than the L_2 component. Figure A.7 has the recovered $L_1(t)$ and $L_2(t)$ for the targets placed in the jig. Several of the curves have been extended by a "dash-dot" line that indicates an extrapolated portion of $L_1(t)$ and $L_2(t)$.

The accuracy of this procedure to obtain $L_1(t)$ and $L_2(t)$ will depend on experimental error and model error. Possible experimental errors include: (1) inaccurate measurement of Z; (2) inaccurate placement of the target beneath the receiver loop, i.e., the center of the target must be placed along the vertical axis passing through the center of the loop; (3) tilting of the EM63 trailer such that the primary field isn't vertical. Modelling errors describe instances where assumptions of the forward model are violated, such as: (1) uniformity of the primary field in the volume of the target; (2) representing the response as a point dipole; and (3) absence of fore-aft symmetry.

Test 1: Reproducing the Time Sounding at Intermediate Orientation

Once we determine the parameters of the magnetic polarization tensor, we can forward model the parameters to obtain the TEM response for any location, depth, and orientation. In this test we investigate how accurately we could predict the decay of the secondary field at an arbitrary orientation for a recovered magnetic polarization tensor.

Equation A.1 describes the measured voltage in a receiver coil directly above a target illuminated by a purely vertical primary field. Using Equation A.1 and the decay functions $L_1(t)$ and $L_2(t)$ obtained in the analysis of the previous section, we predict the voltage response and compare it to measurements using the EM63. The set of measurements we use for comparison were those obtained using the target holder. Figures A.8 and A.9 compare the measured responses at different angles and the response predicted by the forward model for an 81 mm mortar without fins. Figure A.8 has the measured voltage curves at different heights from the sensor. $L_1(t)$ and $L_2(t)$, obtained by fitting these curves with Equations A.2 and A.3, are then forward modelled and plotted in Figure A.9. The top two panels of Figure A.9 demonstrate the procedure on an 81 mm mortar (without fins) located approximately 55 cm beneath the receiver loop. At this distance (equivalent to approximately 10 cm below the surface) we see that the representation is only moderately good at reproducing the data at the different angles. When we repeat the procedure for data collected

approximately $100cm$ beneath the receiver, we see that the model does a better job of predicting the data. This is not surprising, since we would expect the modelling of a compact metallic object as a dipole to become more applicable as we move further from the source/receiver loop. Figure 21 demonstrates the procedure for predicting the measured voltage decay curves for Scrap 5 using the dipole model.

Test 2: Reproducing the spatial behavior

In our second test, we focus on how accurately we could predict the spatial response of a target using the dipole model. For this investigation we first use a target's magnetic polarization tensor, obtained in the manner described in the previous section, to predict the secondary field over a survey line that passes directly over the target. In each case, the survey line is co-aligned with the target. This predicted response is then compared with the measured response.

In Figures A.11 to A.19, the predicted and measured responses along a line are plotted for several targets in three orientations: vertical, horizontal, and at an intermediate dip angle. At intermediate angles the target dips toward the end of the line (i.e., dips downward to the right in Figures A.11 to A.19). Figures A.11 to A.19 indicate the model is successful in predicting the response along each survey line.

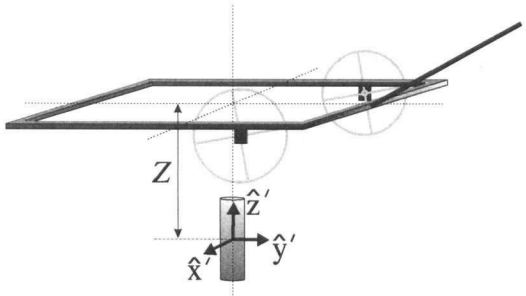

(a) EM63 and target geometry used to obtain $L_1\,(t)$.

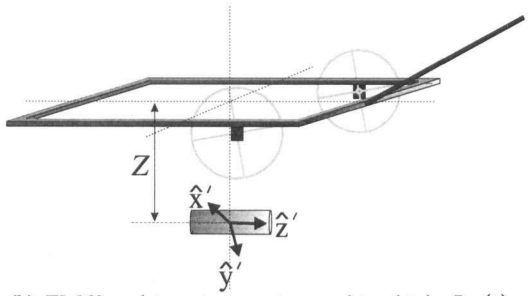

(b) EM63 and target geometry used to obtain $L_2\,(t)$.

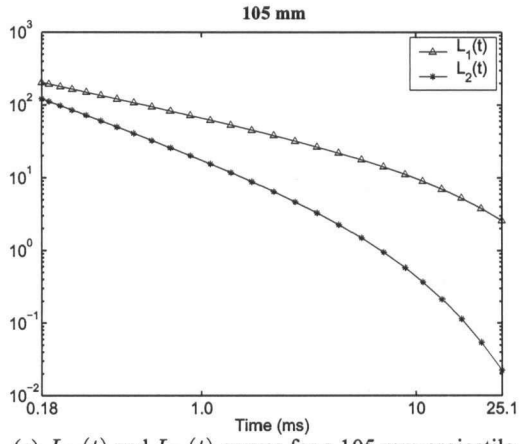

(c) $L_1\,(t)$ and $L_2\,(t)$ curves for a 105 mm projectile.

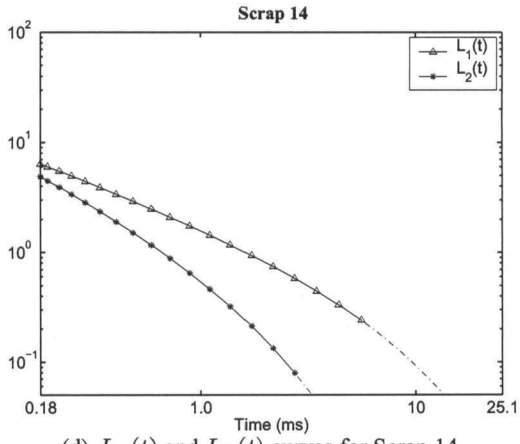

(d) $L_1\,(t)$ and $L_2\,(t)$ curves for Scrap 14.

Figure A.6: Arrangement of EM63 and target for obtaining decay functions.

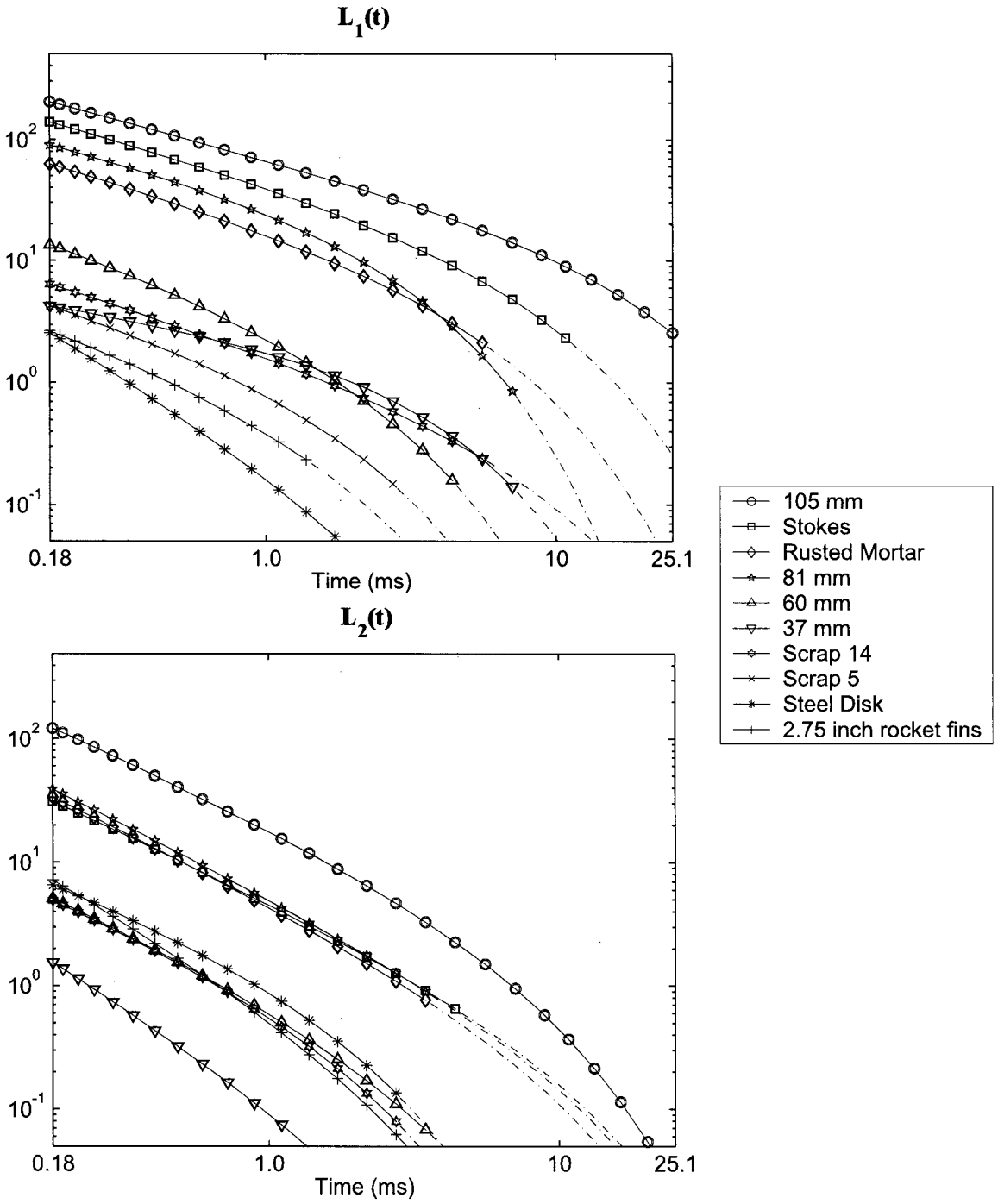

Figure A.7: $L_1(t)$ and $L_2(t)$ decay functions for different targets.

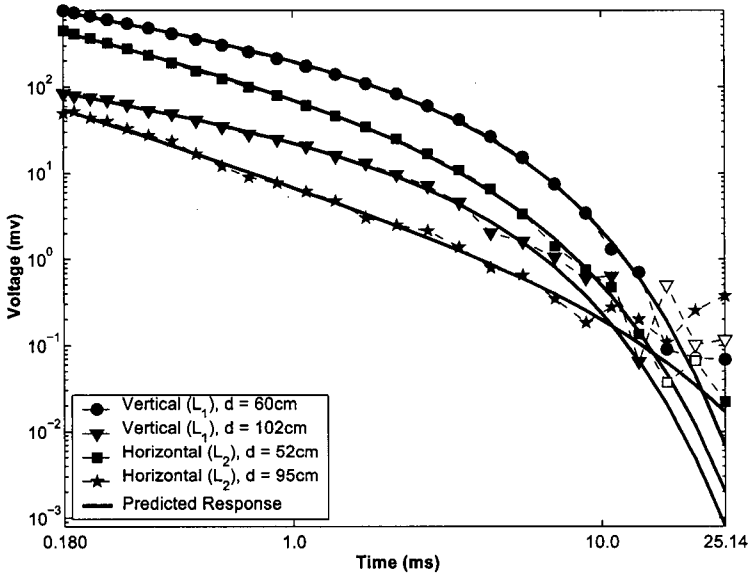

Figure A.8: Measured voltage curves for a 81 mm Mortar without fins at different heights from the sensor. Unfilled symbols (e.g. '□') indicate negative data that have absolute value plotted. These curves were inverted to obtain $L_1(t)$ and $L_2(t)$. Clearly, the decay nature of the signal changes when the mortar is brought close to the sensor. The resulting $L_1(t)$ and $L_2(t)$ curves are used to predict the decay at intermediate angles in Figure A.9.

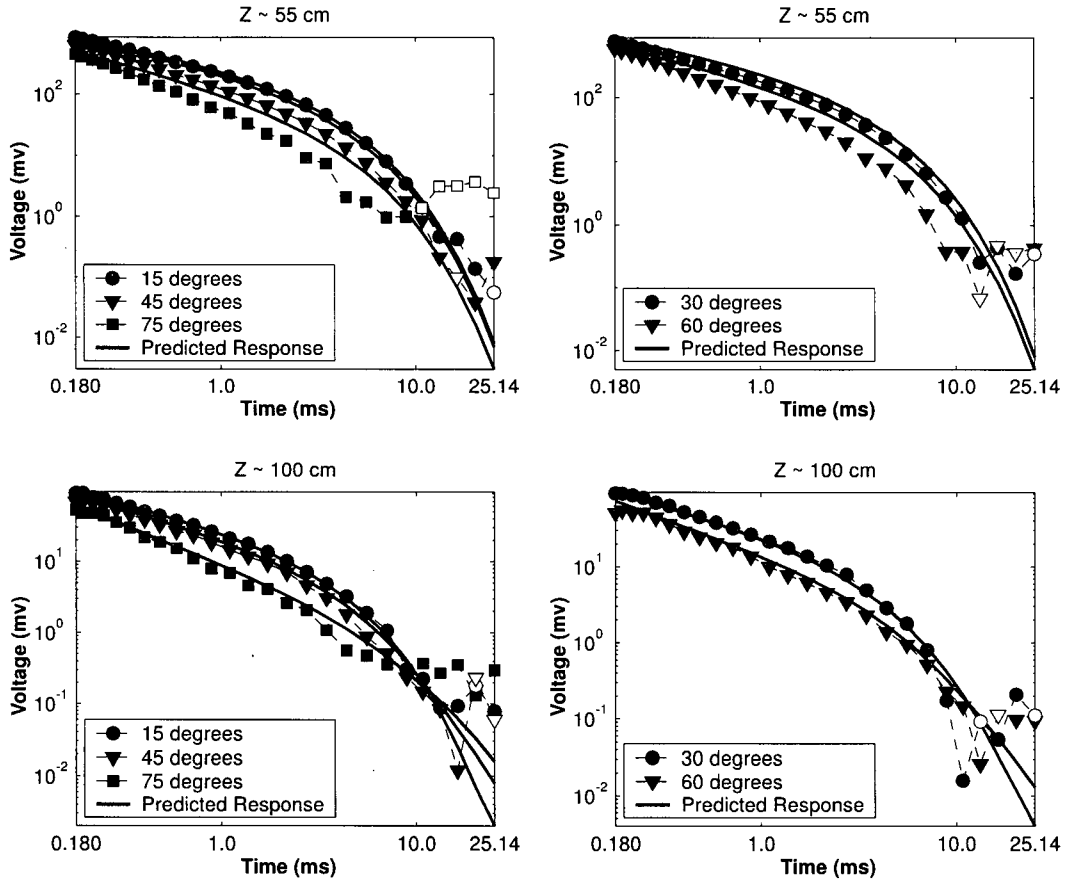

Figure A.9: Predicting the measured voltage decay curves for an 81 mm mortar without fins at different orientations θ. Unfilled symbols (e.g., '□') indicate negative data that have absolute value plotted. The $L_1(t)$ and $L_2(t)$ decay curves recovered from measurements with Z=60 cm and Z=52 cm (Figure A.8), respectively, are used to predict the voltage curves in the top two panels. The $L_1(t)$ and $L_2(t)$ decay curves recovered from measurements with Z=102 cm and Z=95 cm, respectively, are used to predict the voltage curves in the bottom two panels. The prediction of the measured curves is more successful when the target is farther away from the sensors.

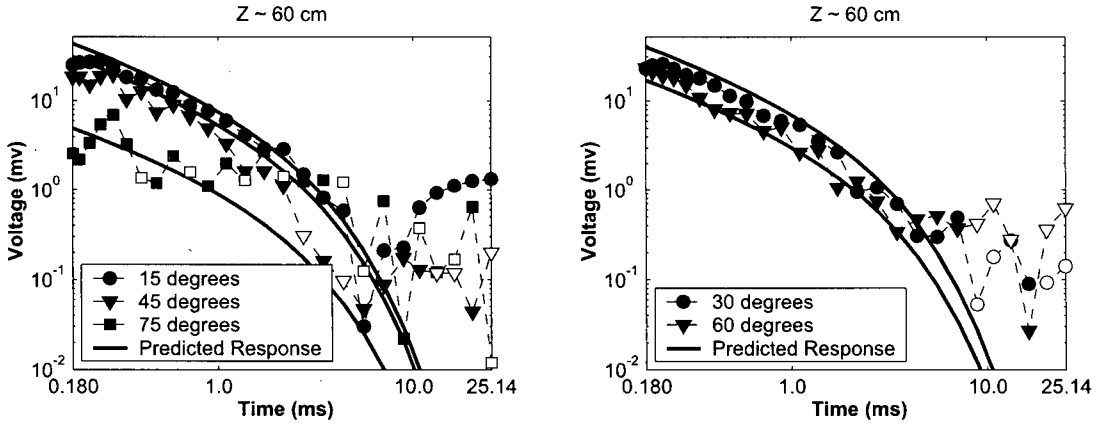

Figure A.10: Predicting the measured voltage decay curve for Scrap 5 using the dipole model.

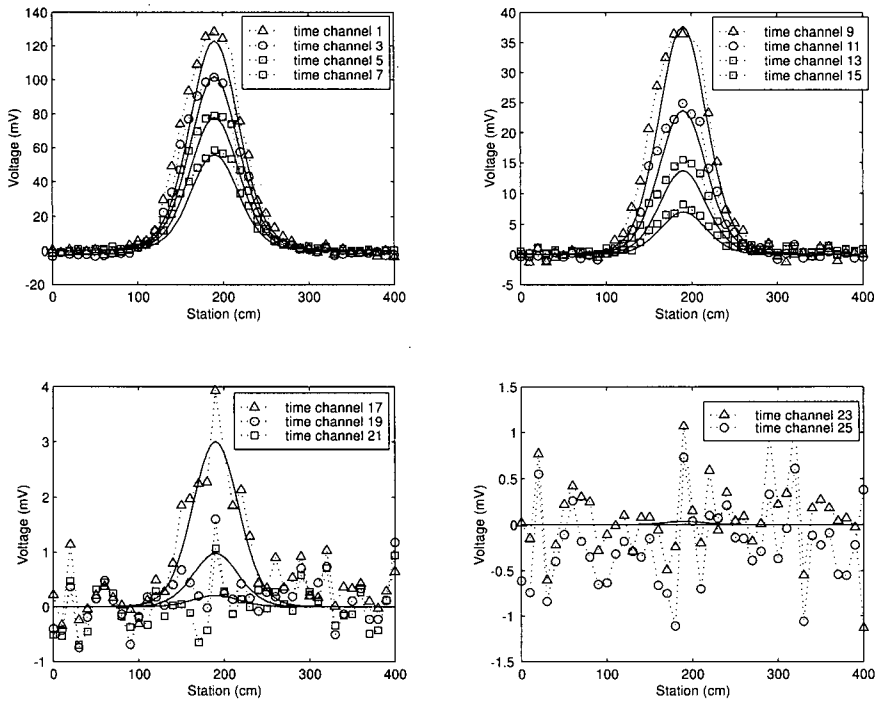

Figure A.11: Geonics EM63 data acquired over a 60 mm mortar: $\theta = 0$ deg (vertical), Z=73 cm.

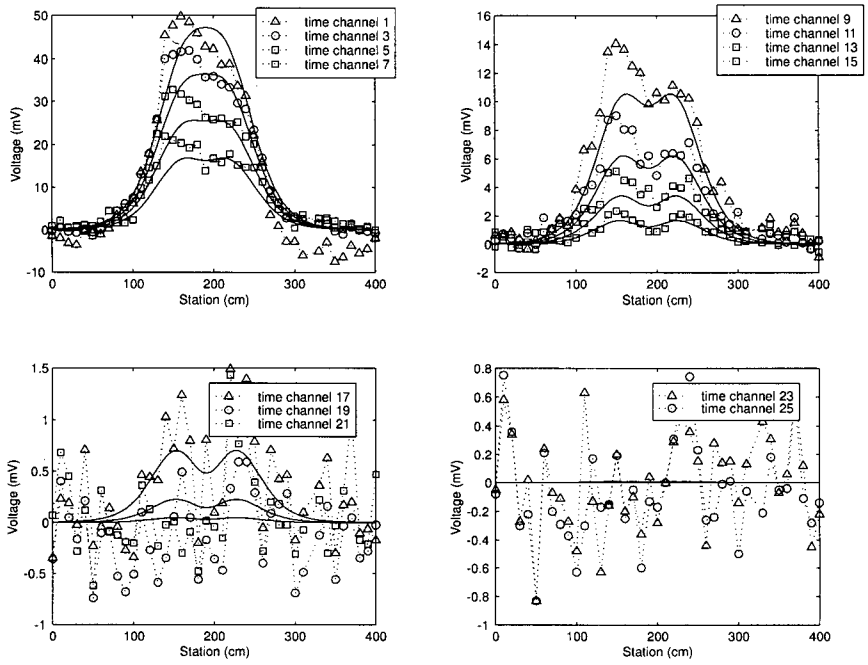

Figure A.12: Geonics EM63 data acquired over a 60 mm mortar: $\theta = 90$ deg (horizontal), Z=73 cm.

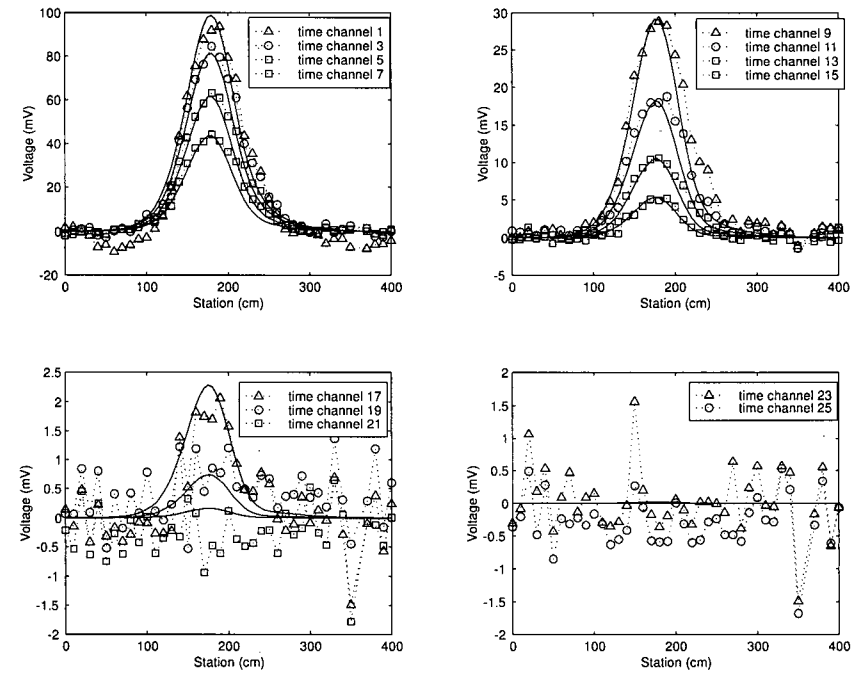

Figure A.13: Geonics EM63 data acquired over a 60 mm mortar: $\theta = 40$ deg, Z=75 cm.

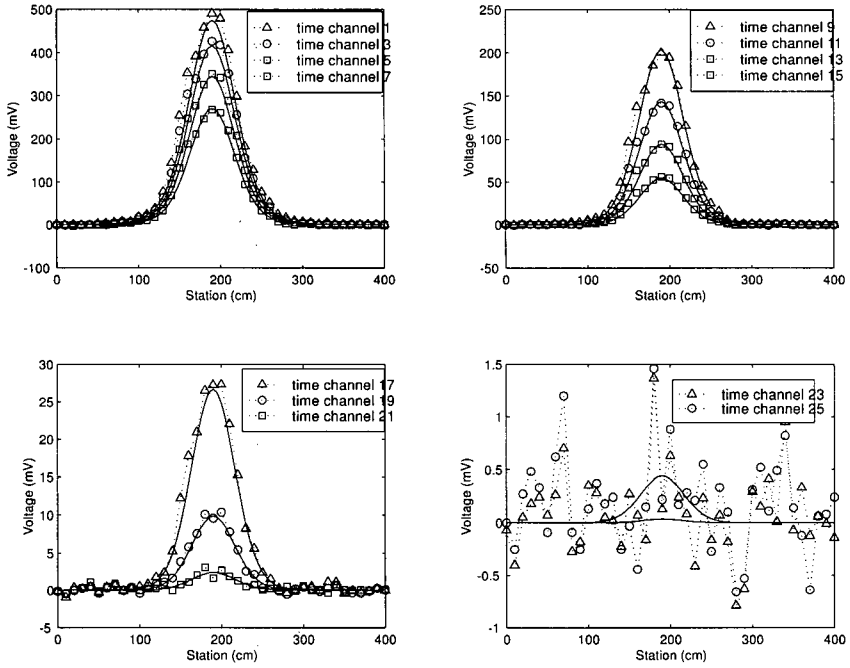

Figure A.14: Geonics EM63 data acquired over an 81 mm mortar: $\theta = 0$ degrees (vertical), Z=73 cm.

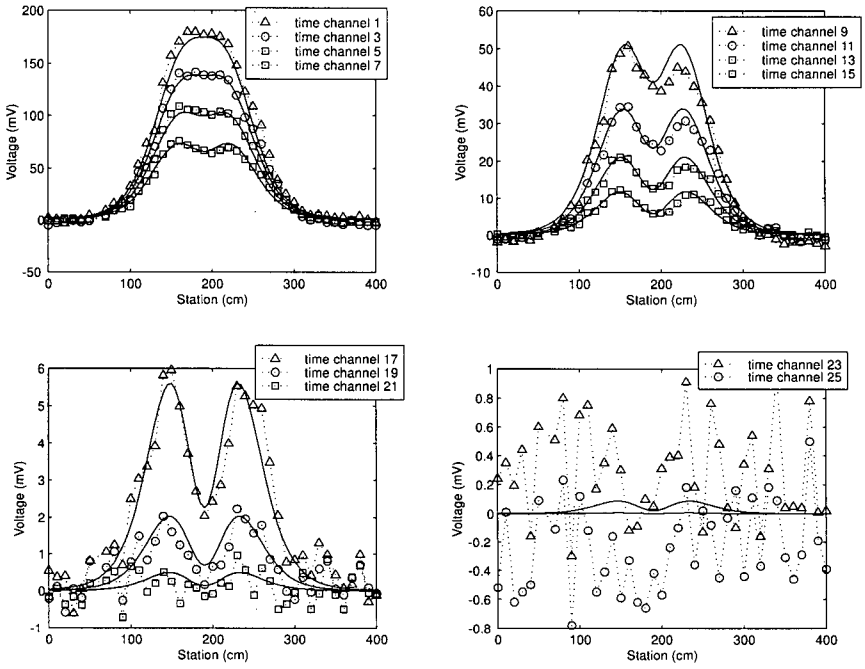

Figure A.15: Geonics EM63 data acquired over an 81 mm mortar: θ = 90 degrees (horizontal), Z=73 cm.

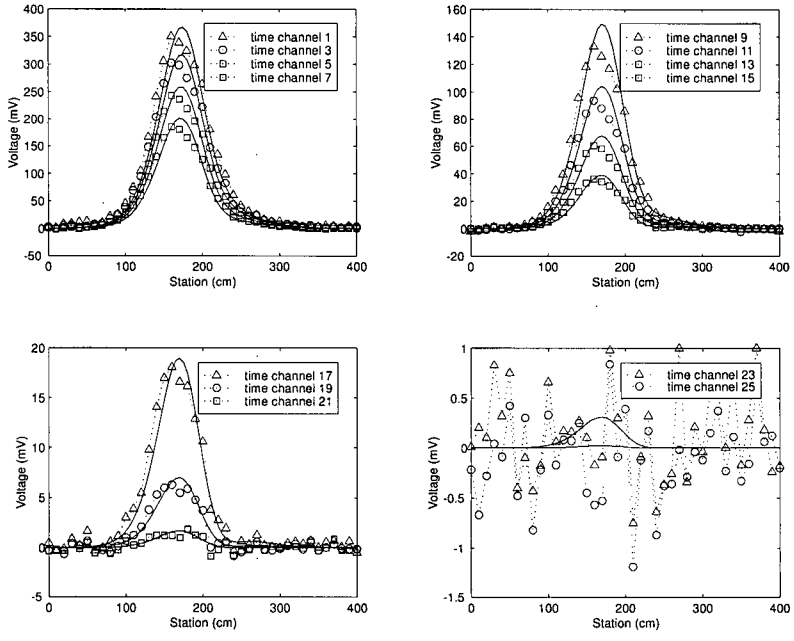

Figure A.16: Geonics EM63 data acquired over an 81 mm mortar: θ = 43 degrees, Z=74 cm.

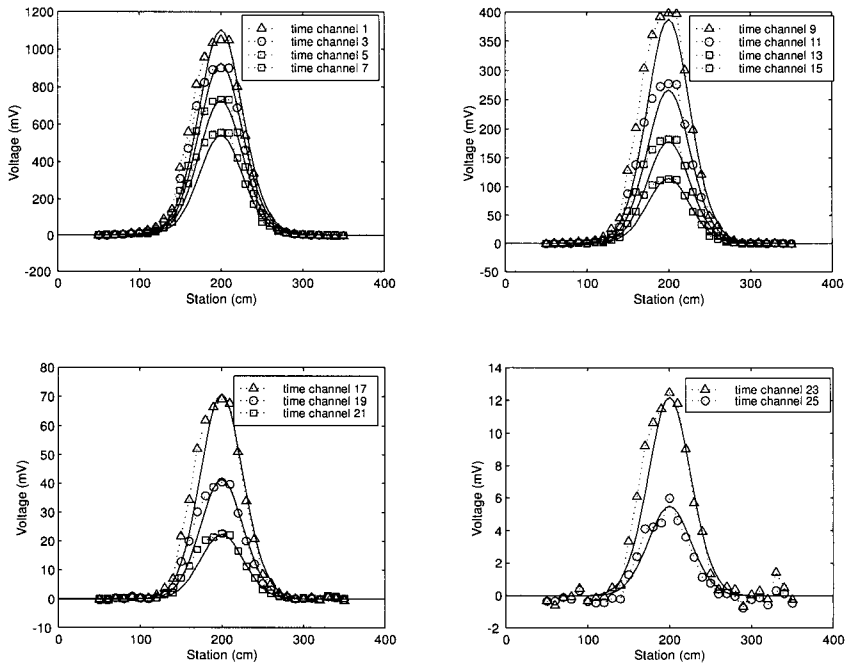

Figure A.17: Geonics EM63 data acquired over a Stokes mortar: $\theta = 0$ deg (vertical), Z=73 cm.

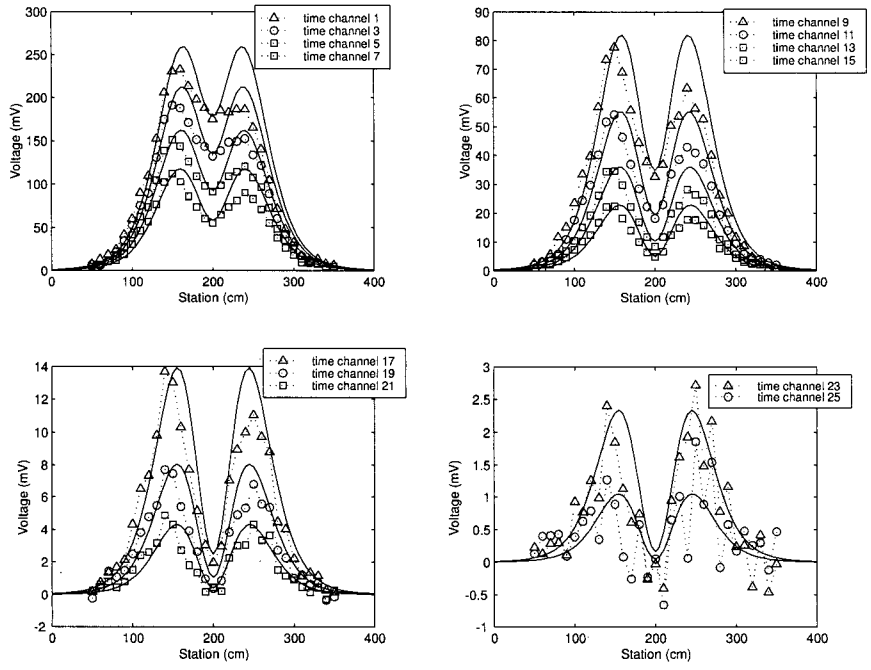

Figure A.18: Geonics EM63 data acquired over a Stokes mortar: $\theta = 90$ deg (horizontal), Z=73 cm.

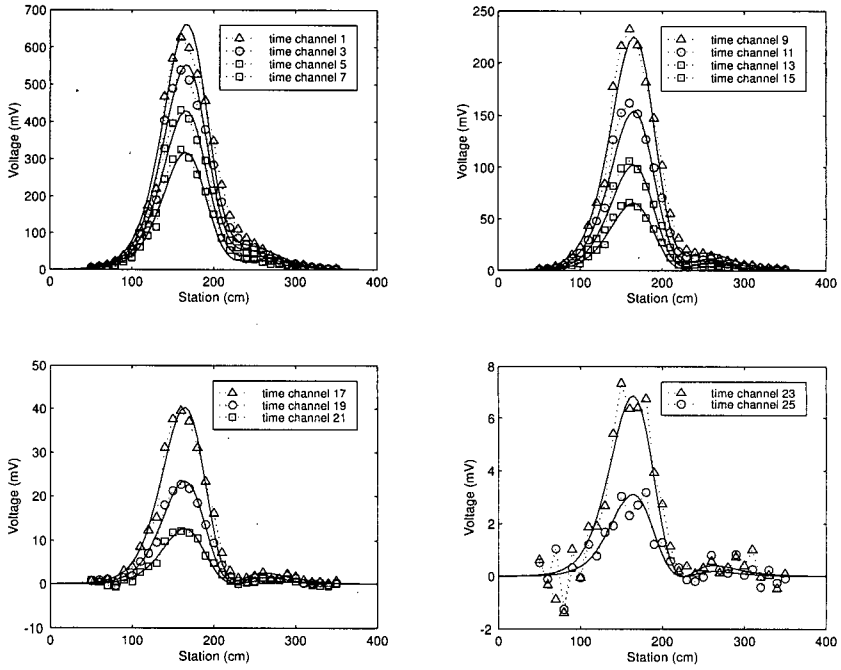

Figure A.19: Geonics EM63 data acquired over a Stokes mortar: $\theta = 54$ deg, Z=73 cm.

Appendix B

A Differential Electromagnetics Approach for Detecting UXO in Magnetic Geology

B.1 Introduction

In this appendix, we study the effectiveness of varying the transmitter waveform characteristics applied to an EM61-MK2 sensor. This study is motivated by several practical and theoretical reasons. Although the Minelabs F14A sensor is effective in detecting small targets in a VRM soil setting, it has problems seeing larger deep targets. In addition, it is difficult to perform advanced processing, in particular inversion, on Minelabs F14A data due to proprietary on-board data processing. The EM61-MK2 is the most common EM tool used in UXO remediation. It has a greater depth of investigation than the Minelabs F14A, and is a much lighter, field ready alternative to the EM63. Although the EM61-MK2 only has four channels, the addition of multiple pulse widths provides additional data that will enhance the differences between a metal target decay to a soil decay. We study soil and metal TEM responses and show how these responses differ as a function of the transmitter waveform. We investigate how size variations in the buried metal targets affect the effectiveness of the differential illumination technique.

This appendix is part of the report "UXO Target Detection and Discrimination with Electromagnetic Differential Illumination" (Foley et al., 2005).

B.2 The TEM Response of VRM soils and Metallic Objects

Our analysis in Chapter 7 showed that rate of change of the secondary magnetic field due to a VRM soil with a collection of grains with time constants distributed log-uniformly between τ_1 and τ_2 is

$$\frac{\partial M}{\partial t} \propto \frac{-H\chi_o}{\log(\tau_2/\tau_1)}\frac{1}{t} \tag{B.1}$$

The theory of the TEM response of metal targets is well understood. Similar to the response of VRM soils, the response of a compact metal target can be expressed as a function of time constants. Kaufman (1994) derived a general form for the field caused by currents induced in a confined conductor. By assuming quasi-static fields, the secondary field produced by currents in a confined conductor can be written as

$$H_{\hat{1}}(t,p) = \left(\mathbf{H}^P \cdot \hat{1}\right) \sum_{n=1}^{\infty} d_{n\hat{1}}(p) \exp\left(\frac{-t}{\tau_n}\right) \tag{B.2}$$

where $H_{\hat{1}}(t,p)$ is the secondary field in the $\hat{1}$ direction, observed at a point p, and at a time t following the termination of the primary field. The coefficients $d_{n\hat{1}}(p)$ depend on the target location, size and shape, and upon the geometry of the primary field. The time constants τ_n are also dependent on the permeability, size and shape of the target, but not the target location and geometry of the primary field. The largest time constant, τ_1, determines the onset of the late time, exponential stage of the decay and is referred to as the diffusion time constant of the conductor. The form of the time constant is $\tau_1 = L^2\mu\sigma/\pi^2$ where L is a target diameter, μ is the target's magnetic permeability, and σ is the target conductivity. Prior to the late time stage, the cumulative effect of the summed exponentials produces a power law decay. The power law behavior has been verified experimentally and theoretically. Measurements have shown that a combination of a power law and exponential, $V(t) = kt^{-\beta}exp(-t/\tau)$, can be used to model the decay observed within the time range of the Geonics EM63 sensor (Pasion and Oldenburg, 2001b). The power law exponent β is a function of the shape of the target, and we have observed β values ranging from 1/2 to 3/2 for metallic targets.

Equations B.1 and B.2 assume a step-off transmitter field. For an arbitrary waveform $g(t)$ that turns off at time $t = 0$, the measured response is obtained by convolution of the waveform with the

impulse response

$$\frac{\partial H(t)}{\partial t} = \int_{-\infty}^{0} g(t') \frac{\partial H^I(t-t')}{\partial t} dt' \tag{B.3}$$

where $\partial H^I(t)/\partial t$ is the time derivative of the impulse response. Appendix D lists the form of the VRM decay for a finite pulse and a ramp on pulse for log-uniform distribution of time constants. For this chapter, we will study the effectiveness of varying the transmitter waveform characteristics applied to an EM61-MK2 time domain electromagnetic sensor. The waveforms that we will be considered consists of an exponential current increase followed by a linear ramp off:

$$g(t) = \begin{cases} 1 - \exp\left[-\frac{(t+T_a+T_b)}{Tx}\right] & ,\text{if} -(T_a+T_b) < t < -T_b \\ -\frac{[1-\exp(-T_a/T_x)]}{b}\ t & ,\text{if} -T_b \le t < 0 \end{cases} \tag{B.4}$$

where T_a is the length of the exponential charge up, T_x is the time constant of the transmitter loop, and T_b is the length of the turn-off ramp. Convolving the impulse response with the exponential increase/linear ramp off waveform gives:

$$\frac{dM(t)}{dt} \approx \frac{-\chi_o}{\ln(\tau_2/\tau_1)} \left[\frac{e^{\left(-\frac{t+T_a+T_b}{T_x}\right)}}{T_x} \left(Ei\left(\frac{t+T_b}{T_x}\right) - Ei\left(\frac{t+T_a+T_b}{T_x}\right)\right) + \frac{\alpha}{T_b} \ln\left(1+\frac{T_b}{t}\right) \right] \tag{B.5}$$

where Ei is the exponential integral and $\alpha = 1 - \exp(-T_a/T_x)$. We note that the expression for a finite length pulse can be obtained by taking the limit as $T_b \to 0$ (i.e. ignoring the ramp-off part of the transmitter waveform) and $T_x \to 0$ (i.e. assuming an instantaneous current turn-on). The expression for a ramp on current can be obtained from (B.5) by taking the limit as $T_b \to 0$ and assuming T_x is large enough relative to T_a and t such that the transmitter waveform is approximately a ramp on. In such a case, we can apply expansions $e^x \approx 1 + x$ and $Ei(x) \approx \gamma + \ln(x) + x$.

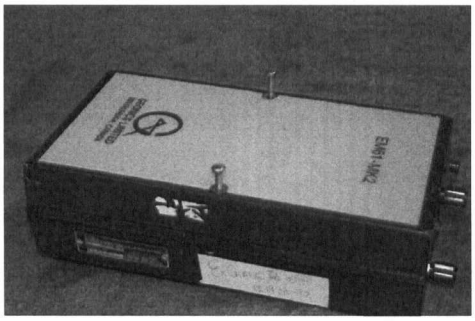

(a) Plastic casing EM61 MK2 electronics unit.

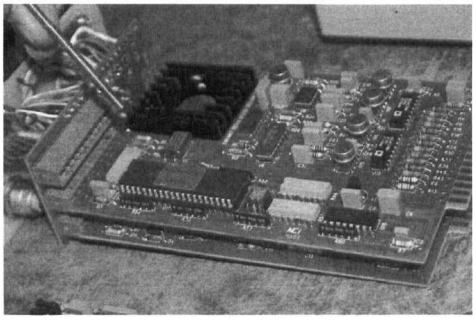

(b) Electronics for the EM61 MK2. The chip with red mark controls on the charge-up times of the transmitter

Figure B.1: Electronics for the modified EM61 MK2 sensor.

B.3 Soil Compensation Processing Applied to Variable Transmitter Waveform TEM Data

B.3.1 Instrumentation

Data from a Geonics EM61MK2 will be used in this chapter. The EM61MK2 was chosen for this project since it is one of the most common EM instruments used for UXO remediation projects. The design of the EM61 is such that a single electronics chip controls the transmitter waveform characteristics and the receiver times (Figure B.1). Since it was not possible to transmit different charge-up times using a single chip, Geonics produced four chips, each with a different transmitter waveform and receiving times. The on times of the chips were 10ms, 4ms, 2ms and 1ms. The 1 ms chip, was not used in this study due to its inability to produce a stable signal. The different transmitter waveforms, with their specific on-times and measurement times are shown in Figure B.2. The modified chips represent the largest possible range of on-times and measurement windows for the EM61MK2 sensor. The turn-on for each of the waveforms has the same exponential time constant of 3.46 ms and approximately the same linear ramp slope.

Figure B.3 illustrates how the transmitter waveforms described in Figure B.2 alters the $V(t) = 1/t$ step-off soil response and the $V(t) = kt^{-\beta}\exp(-t/\tau)$ step-off metallic target response. For this example, the metallic response is calculated using time constants of $\tau = 0.1$, 1, and 10 ms, and a power law with $\beta = 1/2$. In evaluating (B.3) we differentiate $V(t)$ to get the impulse response. In order to compare the changing decay characteristics due to the different waveforms, the metal

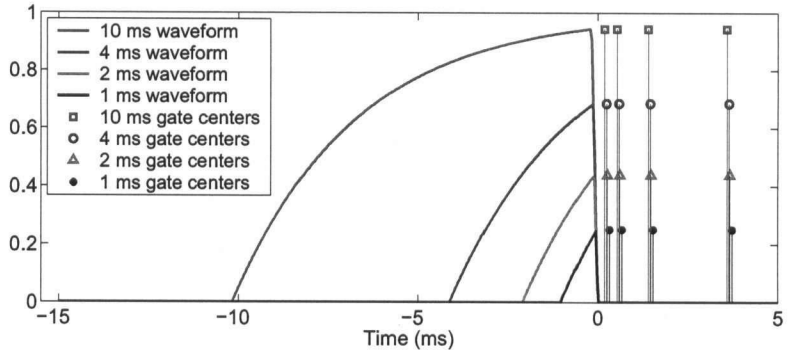

(a) Waveforms and measurement gate centers for the different chips.

Charge Time	Ramp Length	t1	t2	t3	t4
10	0.178	0.190	0.540	1.415	3.600
4	0.121	0.247	0.597	1.472	3.657
2	0.093	0.267	0.617	1.492	3.677
1	0.032	0.328	0.678	1.553	3.738

(b) Timing details for the different chips (all times in milliseconds)

Figure B.2: Transmitter waveforms for the four Geonics EM61MKII chips.

and soil responses are normalized to unity at 1ms.

Figure B.3 indicates that a target's time constant size, relative to the transmitter on-time, controls how the target decay varies with the length of transmitter on-times. Targets with small time constants are less sensitive to changes in transmitter on-time. The target with $\tau = 0.1$ ms has the same decay for each waveform since the transmitter on-times for each waveform is greater than 0.1 ms. Targets with larger time constants demonstrate increased sensitivity to the changes in on-time. The response of VRM soil response is also sensitive to the changes in transmitter on-time since the VRM soil response is due to a collection of magnetic grains with a log-uniform distribution of time constants.

The smaller change of the TEM response for short time constant targets illuminated by different on-times compared to the larger changes in the soil response, suggests that variable waveform instrument responses could be effective for detecting small targets in a magnetic soil background. However, time constants for steel targets are large relative to the transmitter on-times that we are considering. For example, due to the large magnetic permeability of steel ($> 200\mu_o$), a steel sphere with a diameter of 5 cm has a time constant of 40ms.

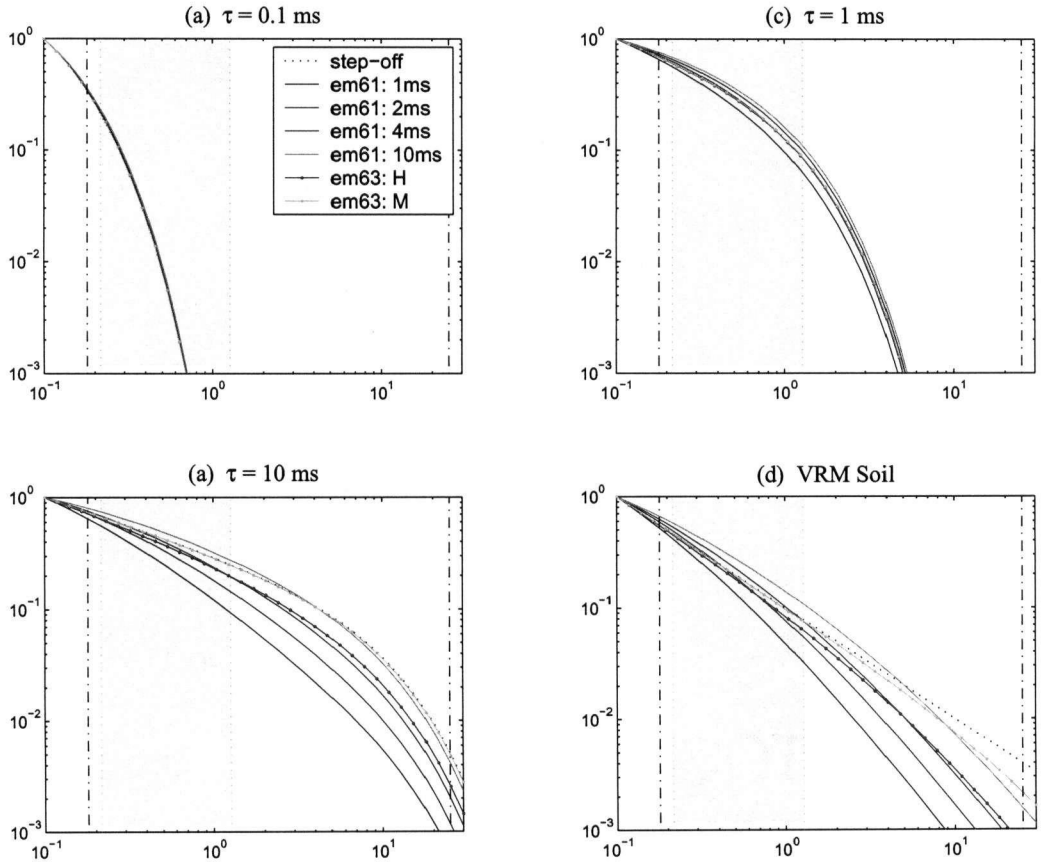

Figure B.3: The effect of different waveforms on different time constant targets. The grey area represents the measurement range of the standard EM61Mk2 TEM sensor.

B.3.2 Soil Model Fitting

Fitting measured data to a soil model is a simple way of determining which soundings are background responses and which soundings have a contribution from the presence of a metal body. If the observed sounding can be well fit with the response of the soil, then the measured response is likely from the background soil only. If we assume that the magnitude of the soil and metal target responses are independent, we can write the measured sounding from a particular chip as $V(t) = \alpha S(t) + T(t)$, where $V(t)$ is the observed decay, $S(t)$ is the characteristic soil response, and $T(t)$ is the response due to a metal target. The coefficient α is included because any observed soil response will be a multiplicative factor of $S(t)$. Since the coefficient α is a function of the soil characteristics, it is independent of the sensor characteristics (i.e. it will be the same for all chips).

There are two potential problems in fitting a soil model and analyzing a data misfit. Firstly, if the background soil response $\alpha S(t)$ is large relative to the target response, then there is a potential of obtaining a good fit to the data. In order to avoid this problem, an estimated soil response is subtracted from the data prior to fitting. A second potential problem would be if the decay of $T(t)$ is similar to the soil decay. We noted earlier that the variable waveform has the potential to alleviate this problem, but this would not be possible here due to the transmitter waveforms used in this study and the size of targets that can be detected by our sensor. However, the hope is that sampling 4 points of the decay curve will be sufficient in observing differences in soil and metal decays.

The fitting of the soil model represents the simplest of inverse problems: determine a single parameter by fitting multiple data. We define data vector where the TEM decays are normalized by the first time channel:

$$\mathbf{d} = \left[\tilde{V}^i(t_j)\right], \tag{B.6}$$

where $\tilde{V}^i(t_j) = Vi(t_j)/Vi(t_1)$ for time channels $j = 1..4$, and $i = 1, 2, 3$ representing data from the 2, 4, and 10 ms waveforms. We fit the data vector with a normalized soil model, with elements $\tilde{S}^i(t_j)$, multiplied by a parameter β. A coefficient β is determined by dividing the data vector by the soil model element by element, and then taking the median of the quotients. To quantify the fit we use a least squares measure of the misfit

$$\text{misfit} = \frac{1}{4N}\sum_{i=1}^{N}\sum_{j=1}^{4}\left[\tilde{V}^i(t_j) - \beta\tilde{S}^i(t_j)\right]^2 \tag{B.7}$$

where $N = 3$ if we use all of the three different chips for fitting.

B.3.3 Differential Analysis

As we saw in Figure B.3, short time constant targets have a small change in response with different on times, while the large time constant targets and VRM soil have a large change in response with different on times. Soil fitting does not attempt to take advantage of this differential effect. Soil fitting uses measurements from additional waveforms only as extra data when calculating the misfit to the characteristic VRM response. An example of a procedure that uses the differential effect for reducing soil anomalies is:

1. Measure the TEM response from one waveform.
2. Assume the measured response is from soil, then use the measured response to predict the response from a waveform with a different on-time.
3. Compare the predicted response with the observed response. If the observed response matches well with the predicted response, then the sounding is likely from soil.

The success of this procedure depends entirely on the time constant of the target. Short time constant targets would have the largest misfit between the observed data (which would have a small differential effect) and the predicted data (which would model the data as having the large differential effect of soil). However, relative to our measurement times, most targets of interest would have a large time constant that would make the differential effect minimal.

This technique is difficult to implement with our equipment due to the sensitivity of the signal to the relative position between sensor and the ground and our need to perform different surveys for each different waveform. It is impossible to ensure perfectly repeatable sensor position and orientation. The changes in sensor position and orientation would produce changes in data amplitude, and compromise our ability to model the data. However, we should point out that we are, at this point, only conducting a feasibility study whereby the differential measurements are collected on consecutive passes. Ideally, the data would all be collected in a single pass by varying the transmitter characteristics on neighboring measurements.

B.3.4 Kaho'olawe Island Navy QA Grid Data

In Chapter 8 we demonstrated that small sensor movements produced large changes in the measured voltage in the hostile soil environment of Kaho'olawe Island. In order to compare relative differences in signal due to transmitter waveform changes, we needed to minimize changes in sensor location and orientation when repeating measurements with different chips. For single soundings, marks were painted on the ground for accurate placement of the sensor. To replicate a multiple line grid survey, we placed wooden planks on the ground to provide an easily repeatable wheel path for the EM61MK2 cart (Figure B.4). The planks also minimized sensor orientation changes due to topographic variations. Differences in line paths over successive surveys were within a few

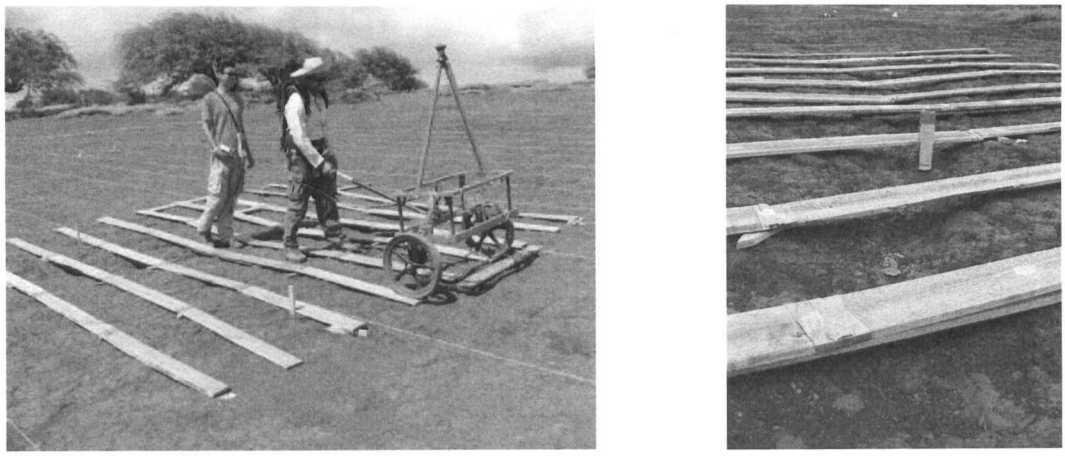

(a) The plank grid

(b) Close up of the rivulet that runs through the grid.

Figure B.4: Photographs of the detailed grid of planks established to investigate coil orientation within Grid 2E.

centimeters. The data from the different chips surveys were linearly interpolated to the same station locations.

Two sets of data were acquired at the Navy QA grid on Kaho'olawe. The first set was collected along the planks with each of the 10, 4, and 2 ms chips (Figures B.6(a)-(c)). This background measurement show the large background signal due to the soil and the large variations in signal simply due to the topography within the survey area. The surveys were then repeated with a small nut (Figure B.5(a)) placed on the surface at $(X, Y) = (0.56, 2.32)$m and a 90 mm projectile (Figure B.5(b)) placed on the surface at $(X, Y) = (2.92, 1.81)$m (Figures B.6(d)-(f)). Since the 90 mm target was

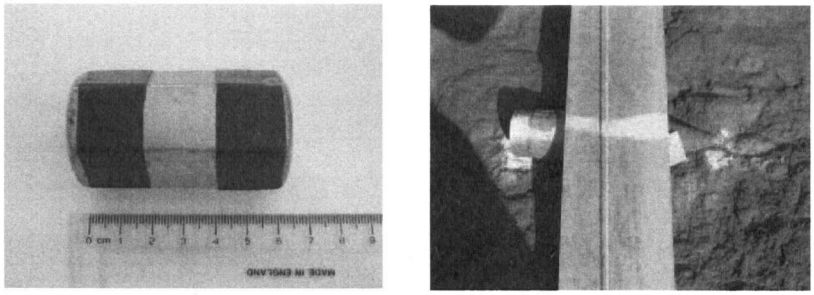

(a) Photo of steel nut (b) Photo of 90 mm uxo

Figure B.5: Targets measured in plank survey. (a) Photo of the steel nut placed on the surface. (b) Photo of the 90 mm projectile placed on the surface.

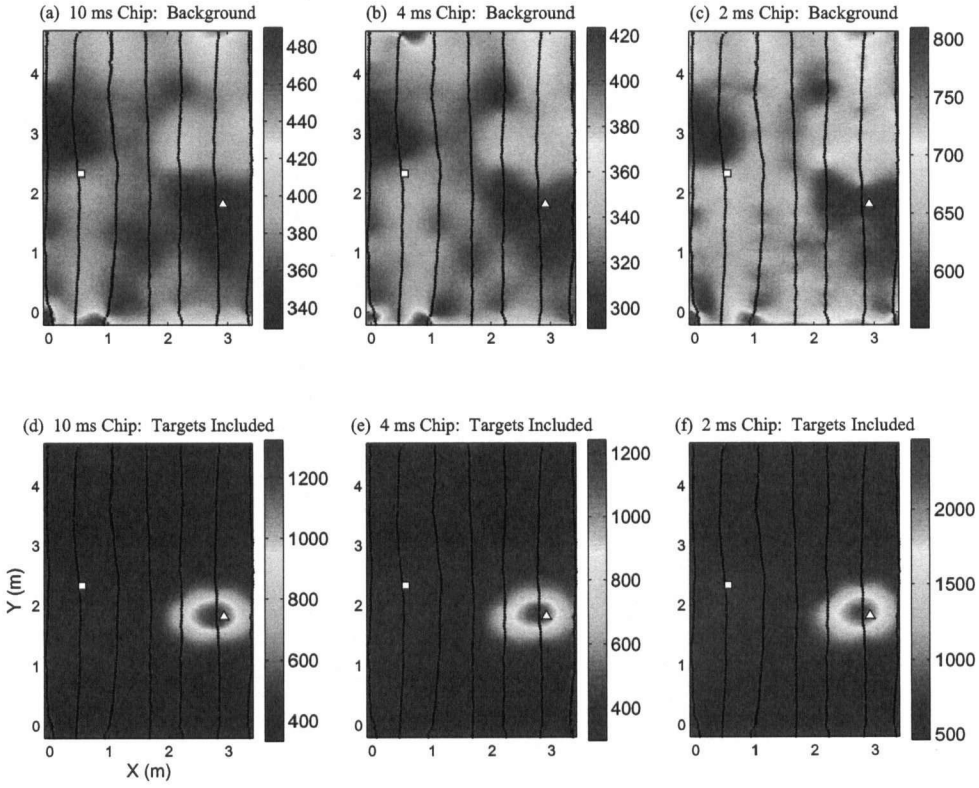

Figure B.6: The first channel of TEM data interpolated to common locations. The steel nut and 90 mm projectile locations are indicated by the '□' and '△' symbols, respectively.

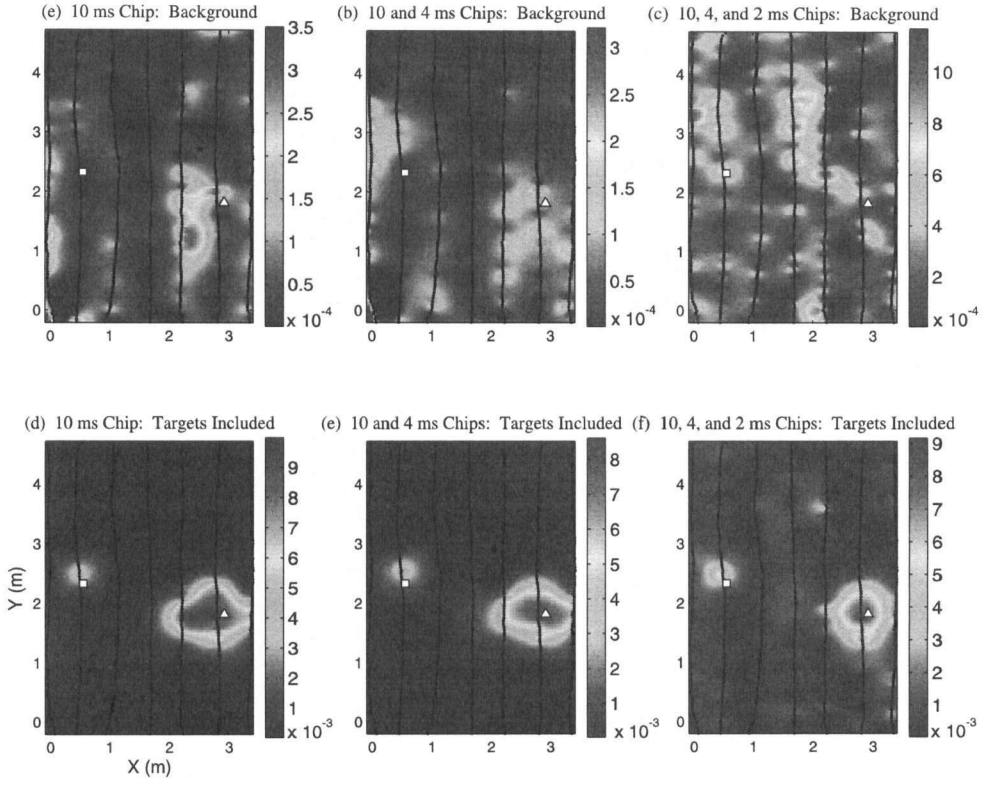

Figure B.7: Misfit comparison.

placed on the surface, its anomaly dominates the gridded data.

Soil Fitting Results

Figures B.7 to B.9 plots the soil modelling misfit on the data with, and without, metal targets placed on the surface. We compare fitting results using: (1) data from the 10 ms chip only, (2) data from the 10 ms and the 4 ms chip, and (3) data from the 10 ms, 4 ms, and 2 ms chips to fit the soil model. Regardless of how many chips we use in the fitting, the misfit provides a clear indicator of the presence of metal targets. Although we would expect that using data from all the chips would best detect the metal targets, the higher noise levels of the 2 ms chip degrades the performance when using all the chips.

Figure B.8 compares the characteristic soil model with soundings recorded with and without a metal target present, at the location of the bolt and the location of the 90 mm. The observed soundings of the background soil (Figure B.8(a) and (b)) fits the 10 ms and 4 ms data quite well, but

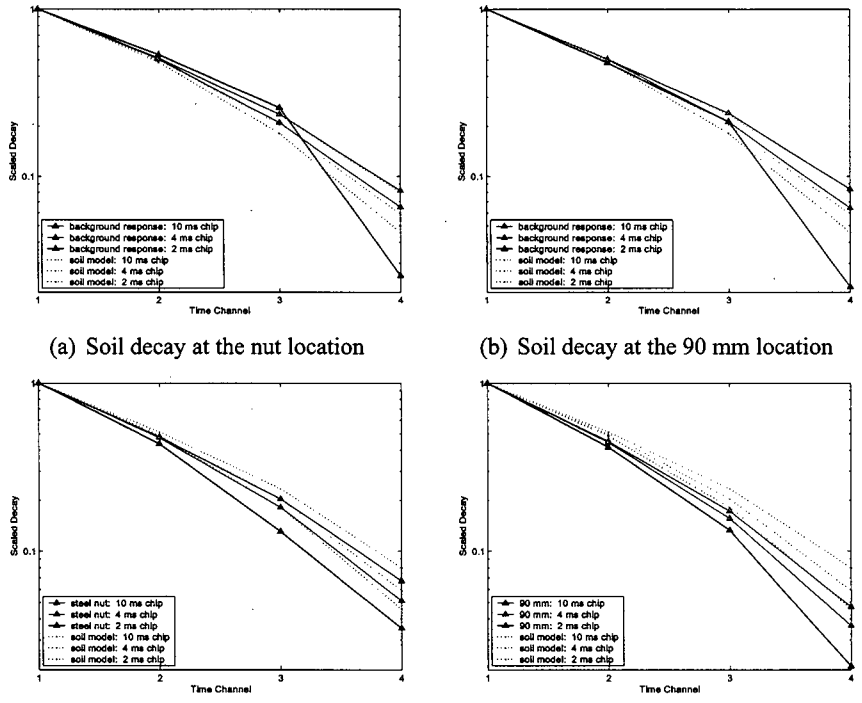

(a) Soil decay at the nut location

(b) Soil decay at the 90 mm location

(c) Soil and nut decay comparison

(d) Soil and 90 mm decay comparison

Figure B.8: Decay comparisons.

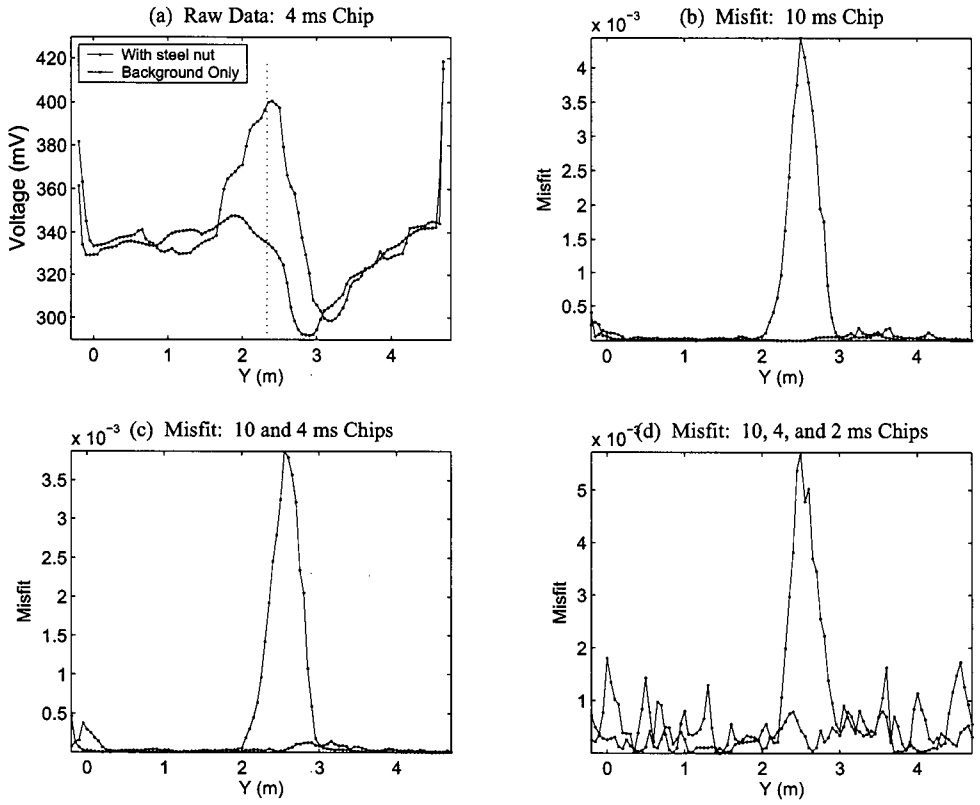

Figure B.9: Line 2 misfit comparison.

the noise level of the 2 ms data makes it difficult to fit. The inability to fit the observed decay with a soil model is clear when a metal target is present.

An indication of potential advantages of using soil model fitting rather than raw data for detection can be obtained by looking at line profiles. Figure B.9 compares the misfit calculated along the second line of data ($X \approx 0.5$). The red lines indicate data with the nut present and the blue lines are fit without the nut. Panel (a) contains the raw data. The large jump in amplitude at the beginning and end of each line is due to the EM61MK2 cart rolling onto and off of the planks. The dip in amplitude at approximately $Y = 3$ m is due to a small rivulet. Panels (b) to (c) plot the misfit along the line. The steel nut appears clearly, even when including the noisy 2ms data in the fitting procedure. The misfit plots are insensitive to the changes in the raw data due to topography. Figure B.10 plots the data from the 4 ms chip and the misfit using the 10 ms and 4 ms data. The misfit is shown on a scale similar to figure B.9. The large variation due to topography is not reflected in the misfit plot. This emphasizes the utility of the misfit as a means of reducing the amount of geologic anomalies

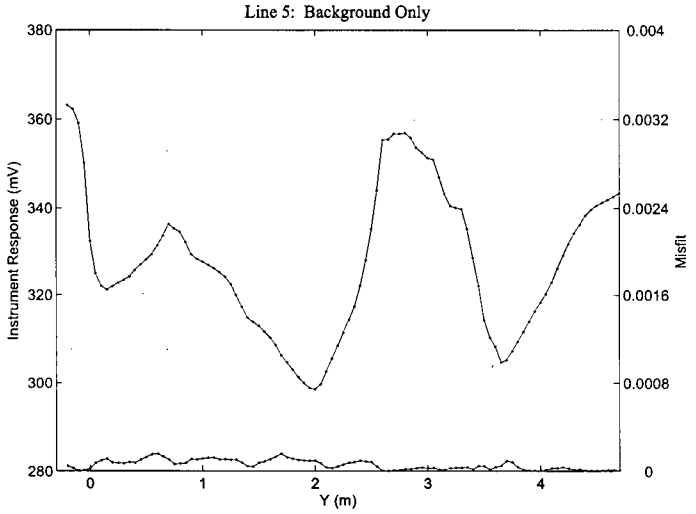

Figure B.10: Line 5 signal/misfit comparison.

chosen as potential targets.

Differential Analysis Results

The procedure outlined in Section B.3.3 was applied to data collected on the planks. The data collected with the 10 ms chip were used to predict the data from the 4 and 2 ms chips. Figures B.11 and B.12 compare the observed data (left column), predicted data (middle column), and residual (right column) for data collected with the 4 ms over the planks with no targets emplaced. The residual is defined as

$$R(t_j) = \log\left(V^{obs}(t_j)\right) - \log\left(V^{pred}(t_j)\right) \tag{B.8}$$

where $j = 1..4$ represents the time channel. The 4 ms and 2 ms data predicted from the 10 ms data closely matches the measured data when there is only soil response (no metal targets). The observed 2 ms data are much noisier than the predicted 2 ms data since the 10 ms chip is less noisy than the 2 ms chip.

The comparison of the predicted and observed data when metal targets are emplaced is shown in Figures B.13 and B.14. The 4 and 2 ms data are again accurately predicted by the 10 ms chip data, indicating that there is little observed differential effect. Figures B.15 and B.16 clearly demonstrates this by comparing the predicted and observed data along the lines containing the emplaced nut and UXO.

The observed and predicted decays directly over the nut and UXO (Figure B.17) are nearly the same, indicating that the soil and targets had the same change in response to the different waveforms.

The difference between predicted and observed data is quantified by a misfit function:

$$\text{misfit} = \frac{1}{4}\sum_{j=1}^{4}\left[\log\left(V^{obs}(t_j)\right) - \log\left(V^{pred}(t_j)\right)\right]^2 \tag{B.9}$$

The logarithm of the data in used order to account for the (potentially) large change in magnitude in a single decay. Figure B.18 plots the misfit for the 4 ms and 2 ms chip data both with and without the emplaced targets. The nut does not produce an anomaly in the gridded misfit, and the UXO does not produce a distinct anomaly in the gridded misfit. We conclude that there is minimal differential effect recorded in the data.

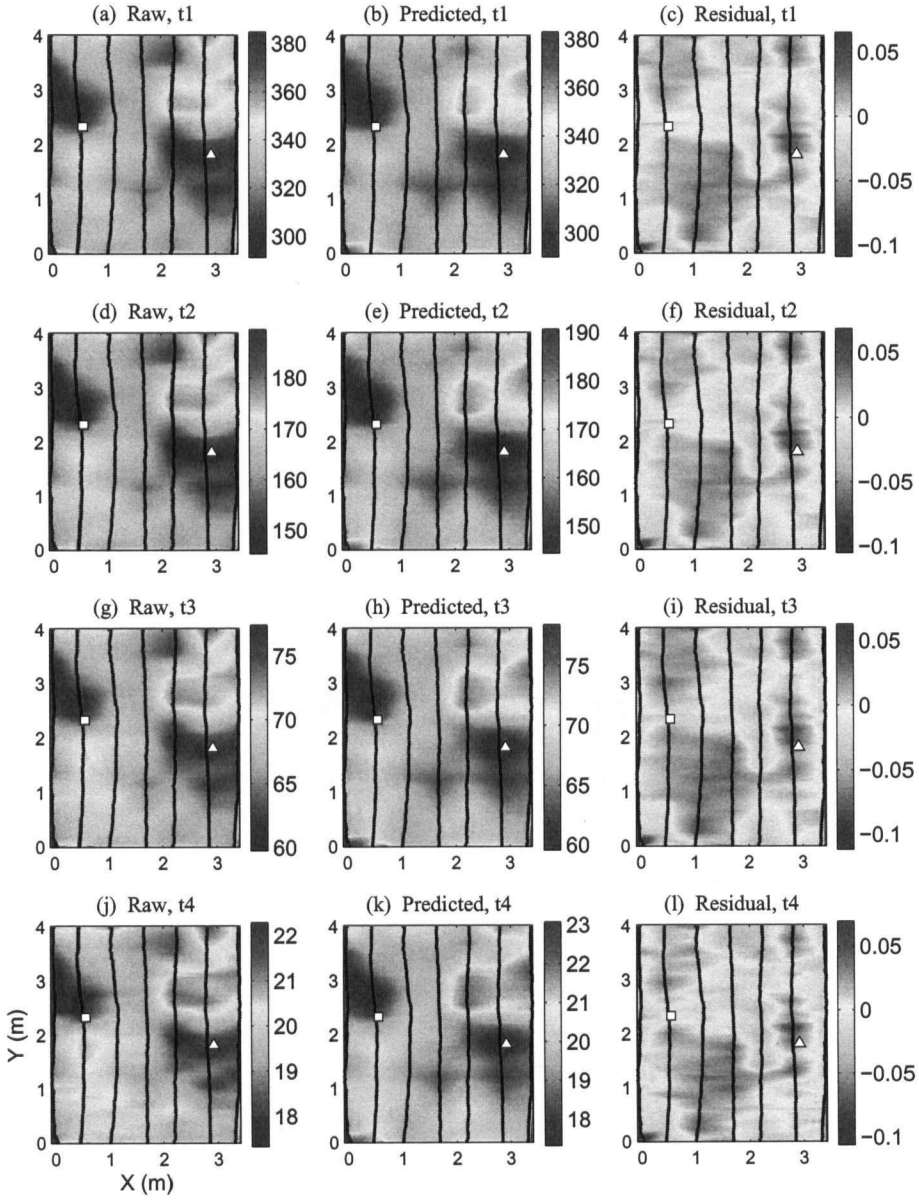

Figure B.11: Comparison of 4ms chip raw data and the 4ms data predicted from the 10 ms chip data. The bolt and UXO are not present for this data.

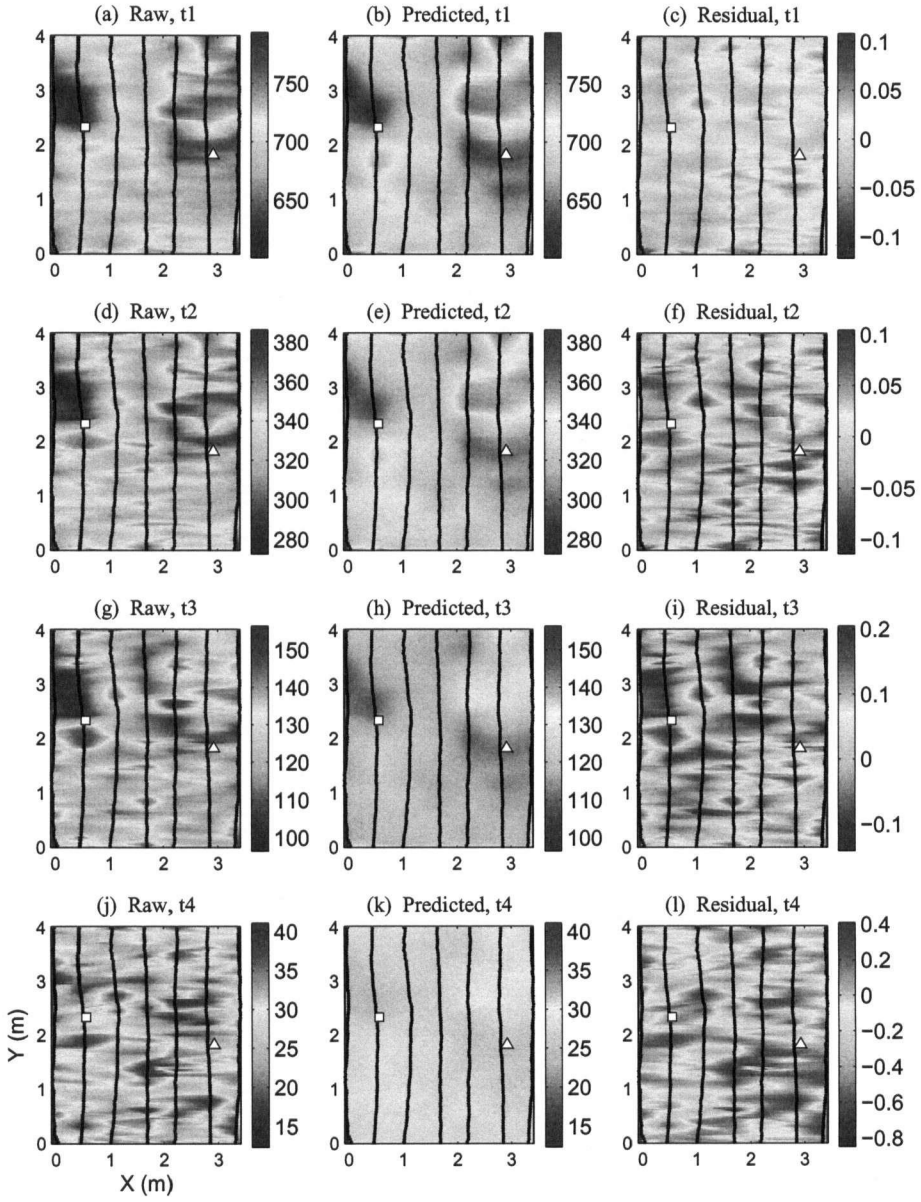

Figure B.12: Comparison of 2ms chip raw data and the 2ms data predicted from the 10 ms chip data. The bolt and UXO are not present for this data.

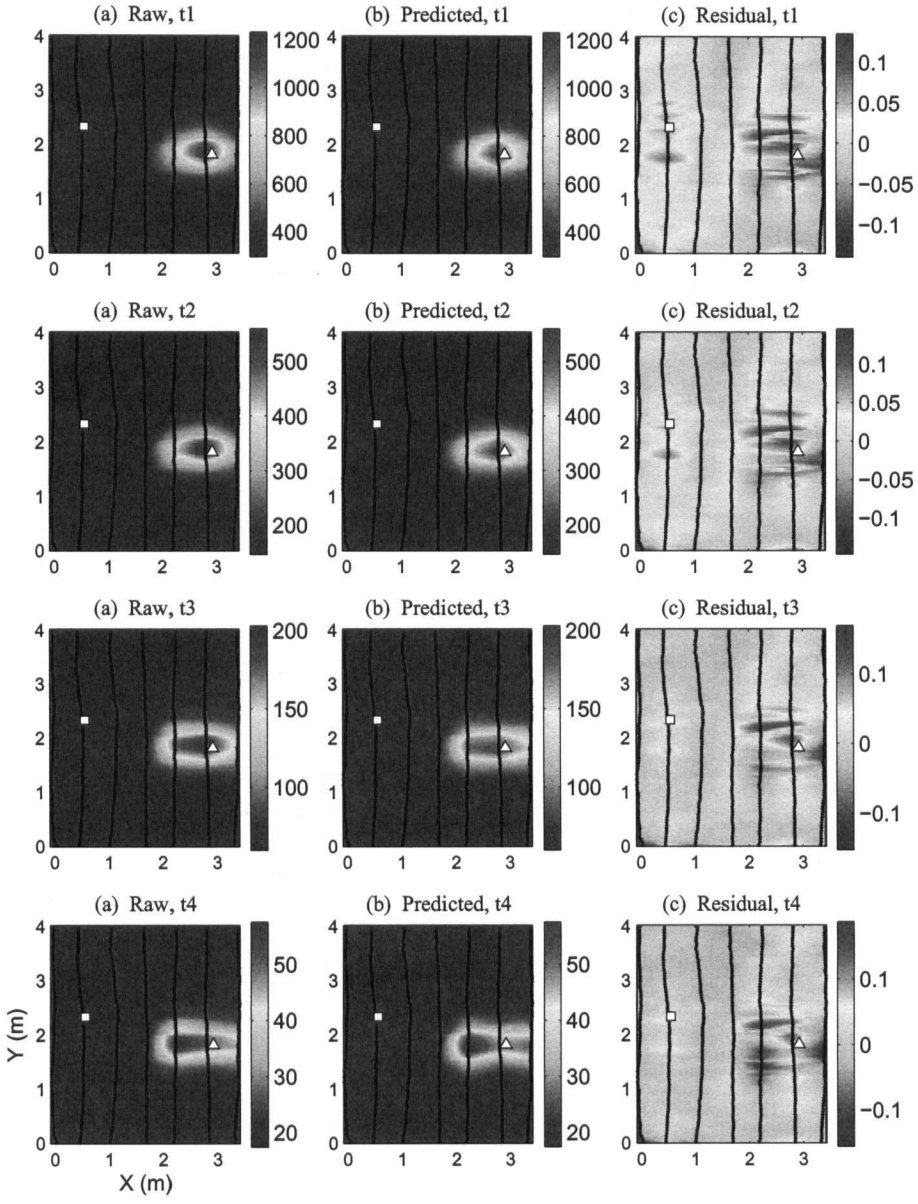

Figure B.13: Comparison of 4ms chip raw data and the 4ms data predicted from the 10 ms chip data. The bolt and UXO are present for this data.

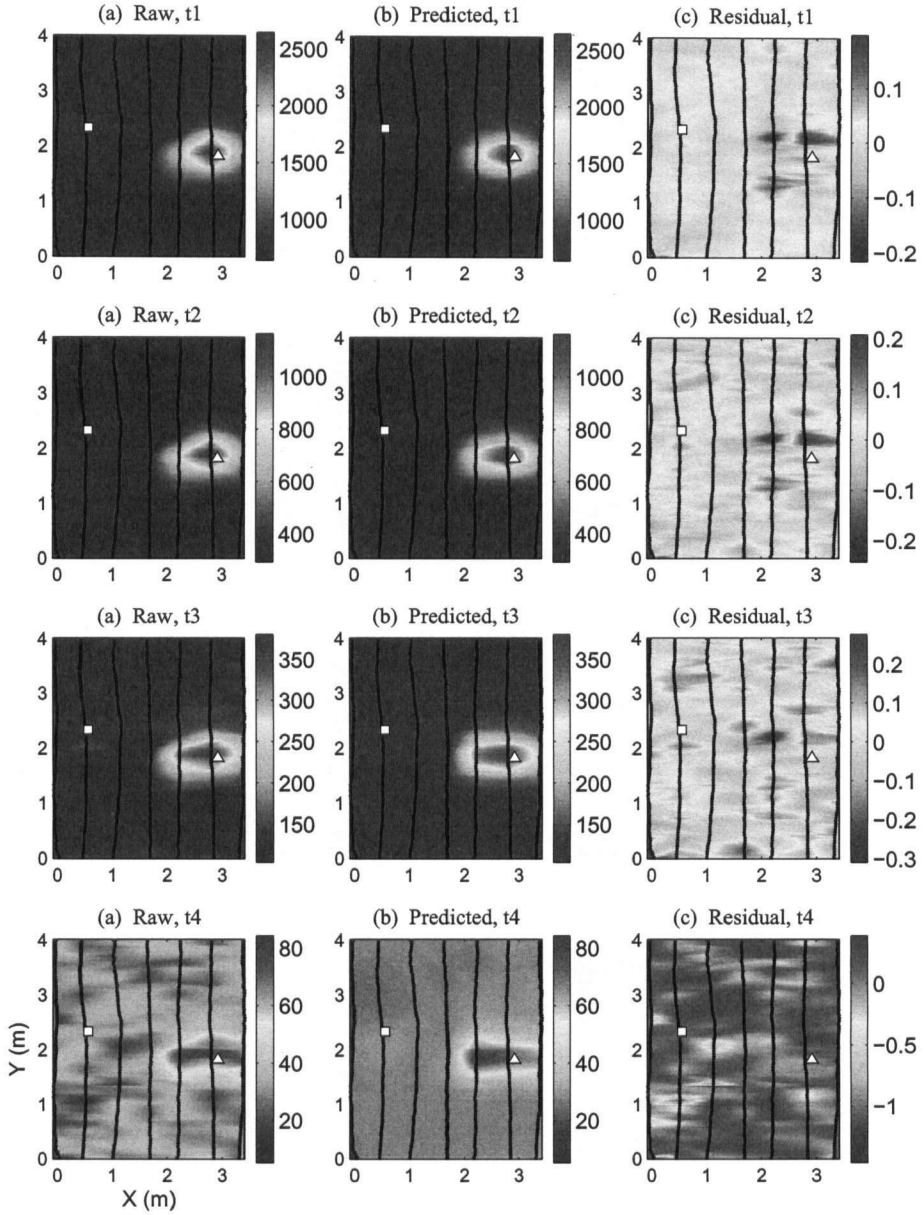

Figure B.14: Comparison of 2ms chip raw data and the 2ms data predicted from the 10 ms chip data. The bolt and UXO are present for this data.

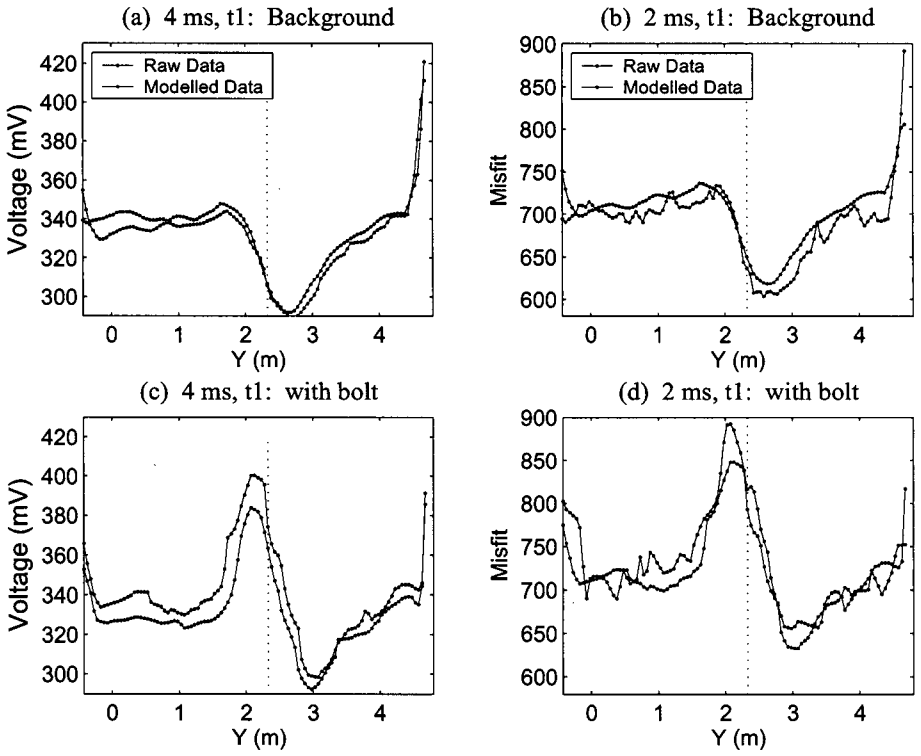

Figure B.15: Comparison of 4ms chip raw data and the 4ms data predicted from the 10 ms chip data. The bolt and UXO are not present for this data.

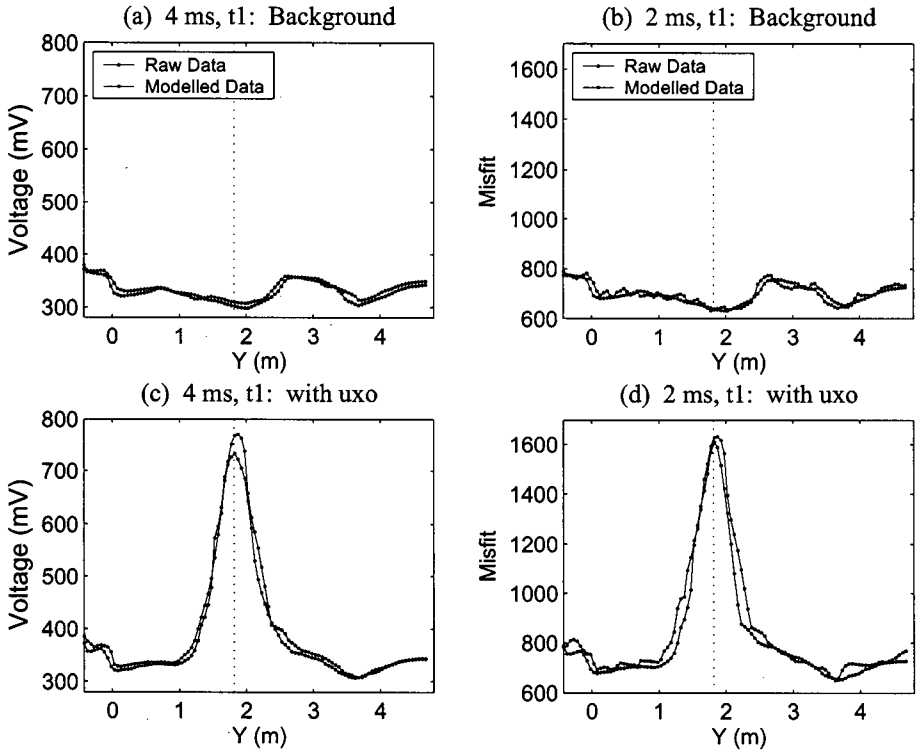

Figure B.16: Comparison of 4ms chip raw data and the 4ms data predicted from the 10 ms chip data. The bolt and UXO are present for this data.

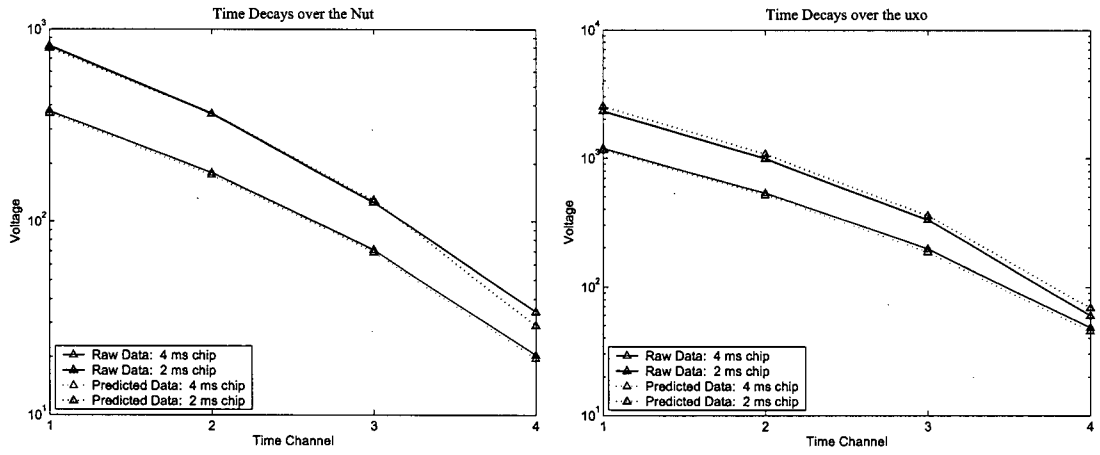

(a) Soil decay at the nut location

(b) Soil decay at the 90 mm location

Figure B.17: Decay comparisons.

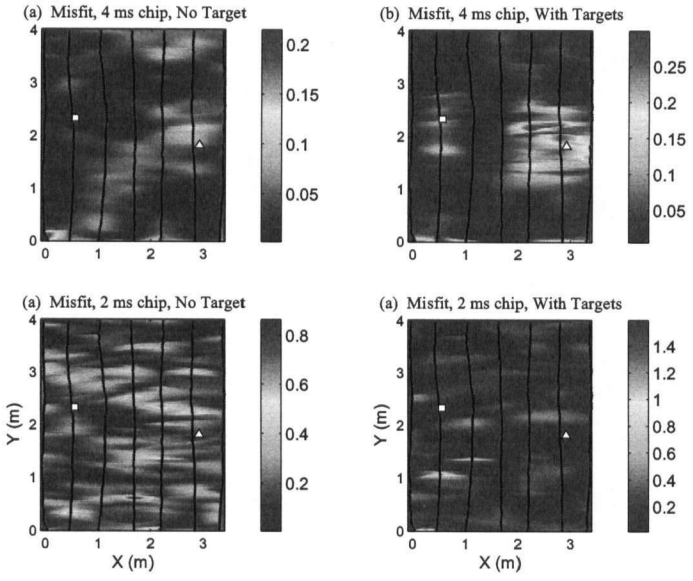

Figure B.18: Comparison of misfits when applying the differential.

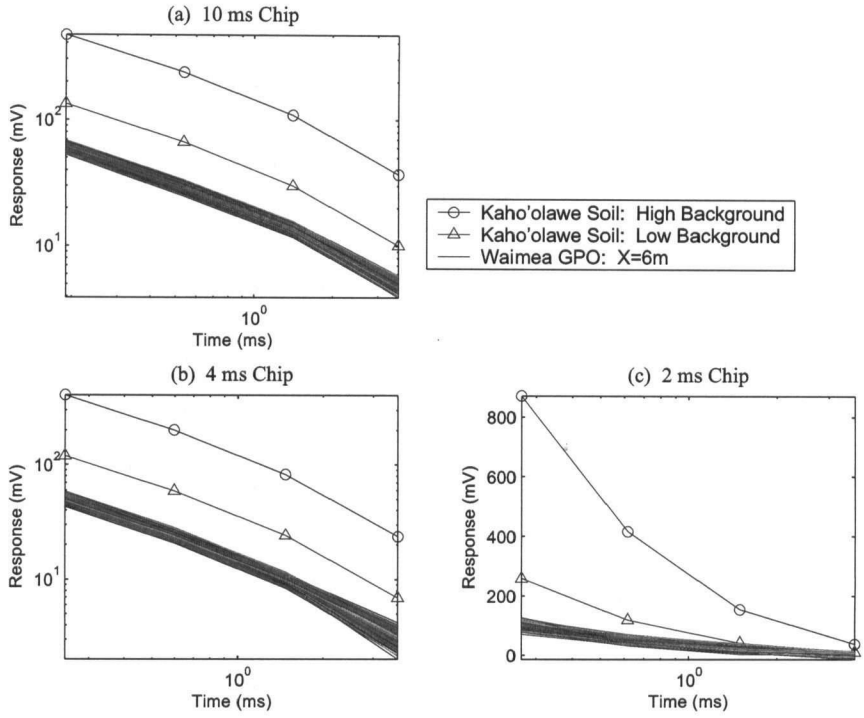

Figure B.19: Comparison of background soil signal strengths at Kaho'olawe and Waimea.

B.3.5 Waimea Geophysical Proveout at the Former Waikaloa Maneuver Area

Modified EM61MK2 data were collected at the Waimea GPO. The site has a much smaller background magnetic geologic response than Kaho'olawe. Figure B.19 compares decays measured on the Waimea GPO, with a decay measured in the area of the Navy QA with the highest background magnetic response and with a decay measured in the areas with the lowest response. The small wavelength data anomalies and noise due to sensor orientation and position changes will be smaller in magnitude compared to Kaho'olawe.

We will focus on modified EM61MK2 data collected on a 30 m x 6.5 m section of the Waimea GPO. Within this area there are 18 emplaced UXO targets. Data for the 10, 4, and 2 ms chips are plotted in Figures B.20 to B.22. Unlike the Kaho'olawe plank data, the Waimea data were collected on a large enough survey area such that we can apply a 2D median filter to remove the long wavelength background signal. Figure B.23 demonstrates the effect of a median filter with a 5 m square window on the first time channel of the 10 ms chip data. The middle panel contains the median values which show that the background response ranges from 52 to 70 mV in the first time

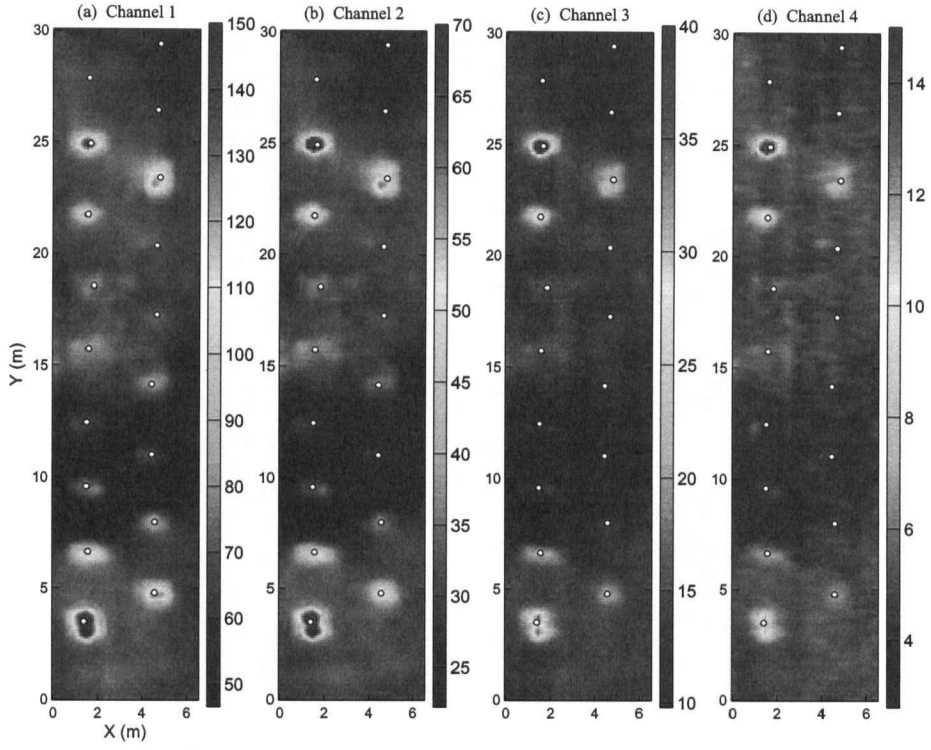

Figure B.20: Waimea raw data 10 ms. White circles indicate emplaced items.

channel of the 10 ms chip data (compared to greater than 300 mV measured on Kaho'olawe). The detrended data for each of the chips are plotted in Figures B.24 to B.26; Each of the detrended data sets clearly show the majority of the emplaced UXO.

We can use the data collected away from the known UXO to determine the background noise levels of the detrended data. Figures B.27 to B.29 contain histograms of the background noise levels. Once data above the noise are identified, the usual course of action is to use a target picking algorithm to determine the presence of anomalies. The selected anomalies can then be inverted for model parameters to determine the identification of the target. For this example, we proceed in the same manner as the Kaho'olawe plank data and compare the data above the noise to a soil model (Figures B.30 to B.32). By plotting the misfit to a soil model nearly all the non-uxo related anomalies have been eliminated. The misfit calculated from the 10 ms chip was able to produce a misfit at all but three of the UXO. Due to noise, the processed 2 ms chip data was not as effective in detecting the emplaced targets.

Let us label the left row of targets 1 to 9, with label number increasing with y. If we look at

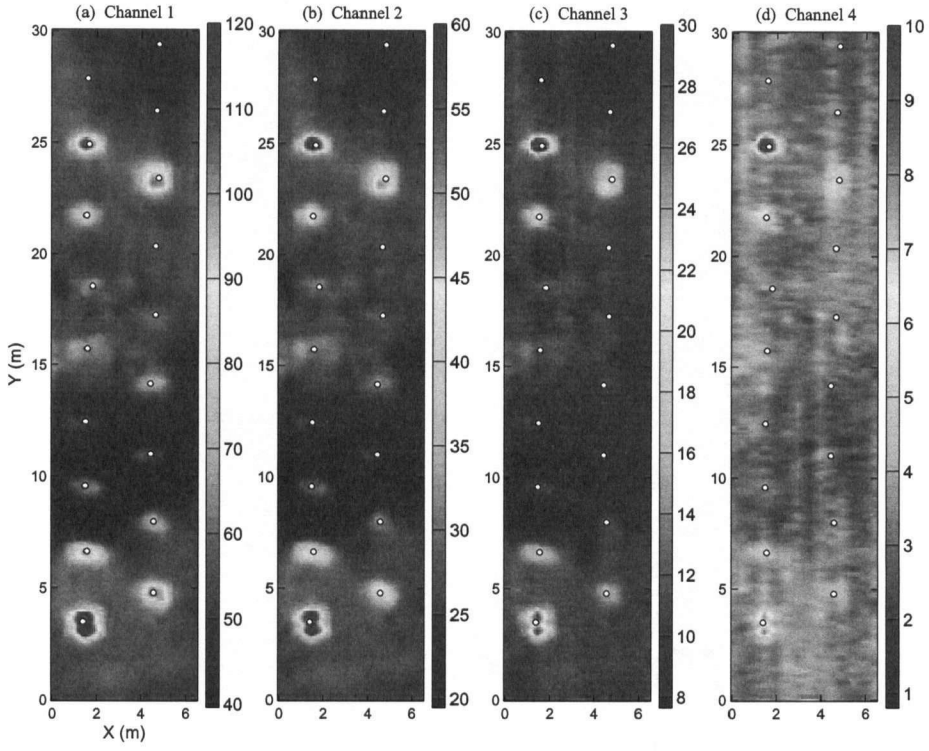

Figure B.21: Waimea raw data 4 ms. White circles indicate emplaced items.

the four emplaced targets at the top of the row, we notice that targets 6, 7, and 8 produce distinct anomalies in the detrended data, while target 9 produces a very weak anomaly. When proceeding with the soil fitting analysis and gridding the misfit, target 9 does not produce an anomaly and target 6 produces a weak, incoherent response. To see why this is let us look at the soundings over targets 6 to 9 (Figure B.33. The soundings measured by both the 10 ms and 4 ms chips indicate that the decay of targets 7 and 8 is slower than the background soil response, and therefore produces a significant misfit to the soil model. Target 9 does not produce an appreciable misfit since its response is nearly identical to the background when measured by the 10 ms chip, and the response is in the noise of the data when measured by the 4 ms chip. Target 6, which had an appreciable anomaly in the detrended data, has only a weak anomaly in the soil misfit map because its decay nearly matches the decay of the soil. If we decided to reduce the number of picks in the detrended data set by selecting targets based on the misfit map we would possibly have omitted target 6, which would have produced a false negative result.

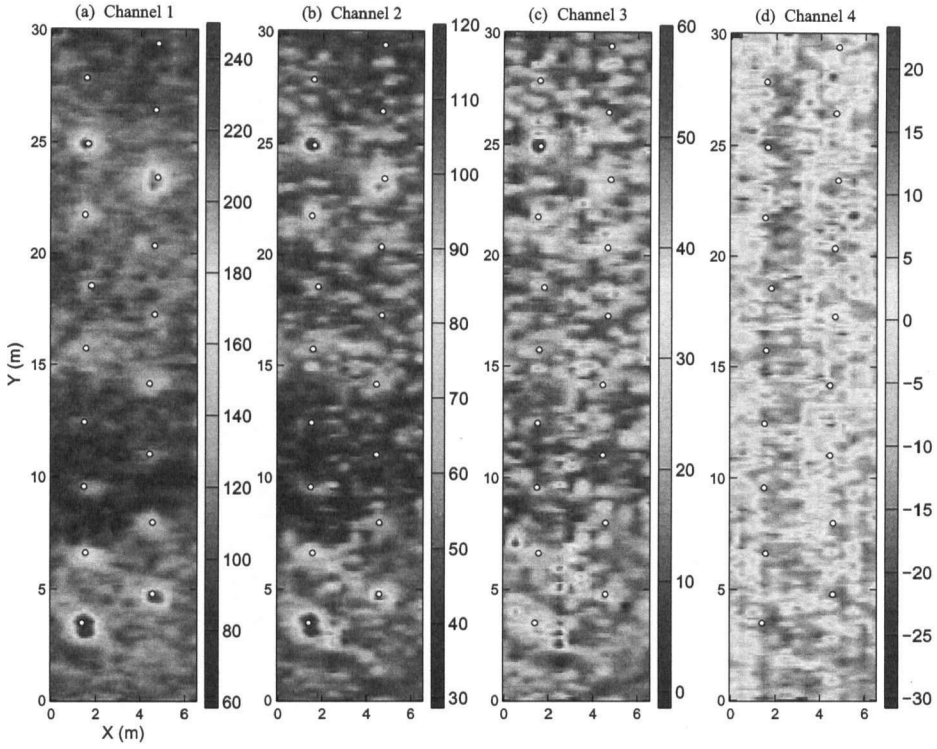

Figure B.22: Waimea raw data 2 ms. White circles indicate emplaced items.

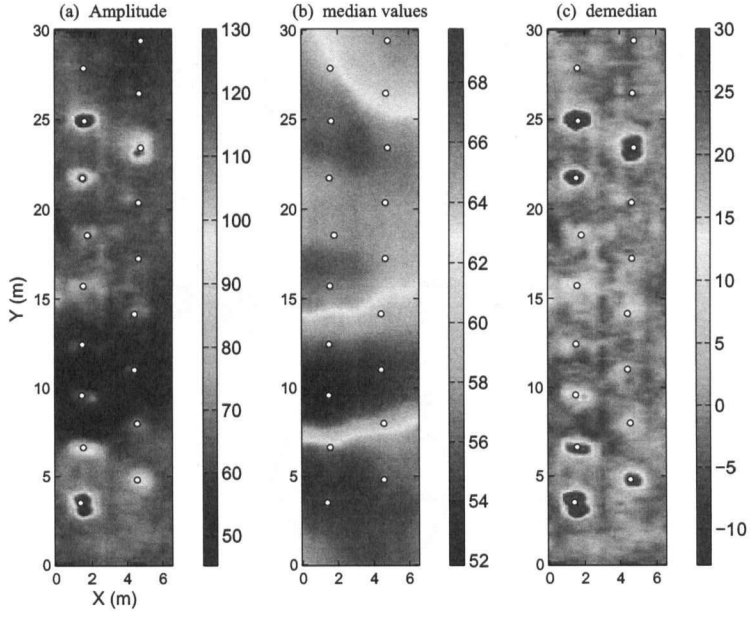

Figure B.23: Waimea detrending example on the 10 ms chip data.

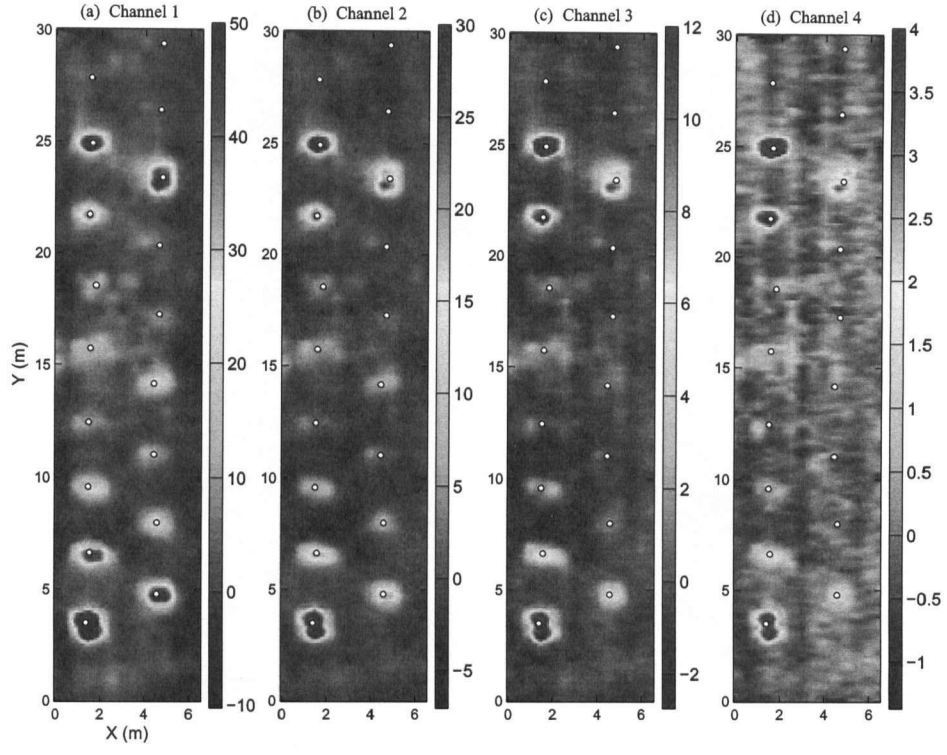

Figure B.24: Detrended Waimea data from the 10 ms chip.

B.4 Conclusion

In this appendx, we presented analysis of multi-waveform TEM data. Modelling was used to determine how a measured decay curve is altered by changing the length of the transmitter on-time. As expected, we saw that the response of targets with time constants less than transmitter on-times is less sensitive to the length of the on-time than the response of targets with larger time constants. We showed that the time constants of typical UXO targets would need to be large to have a differential effect when measuring data from different waveforms. The lack of a differential effect was evident when analysing the field data from Kaho'olawe and the Waimea GPO on the Waikaloa Maneuver Area. When soil model fitting was applied to the data, the inability of the soil model to fit the observed data proved to be a good indicator of the presence of metal. However, we saw instances where the target response was close to the background response. In such a case, false negatives may occur when using the soil misfit as a means of detection.

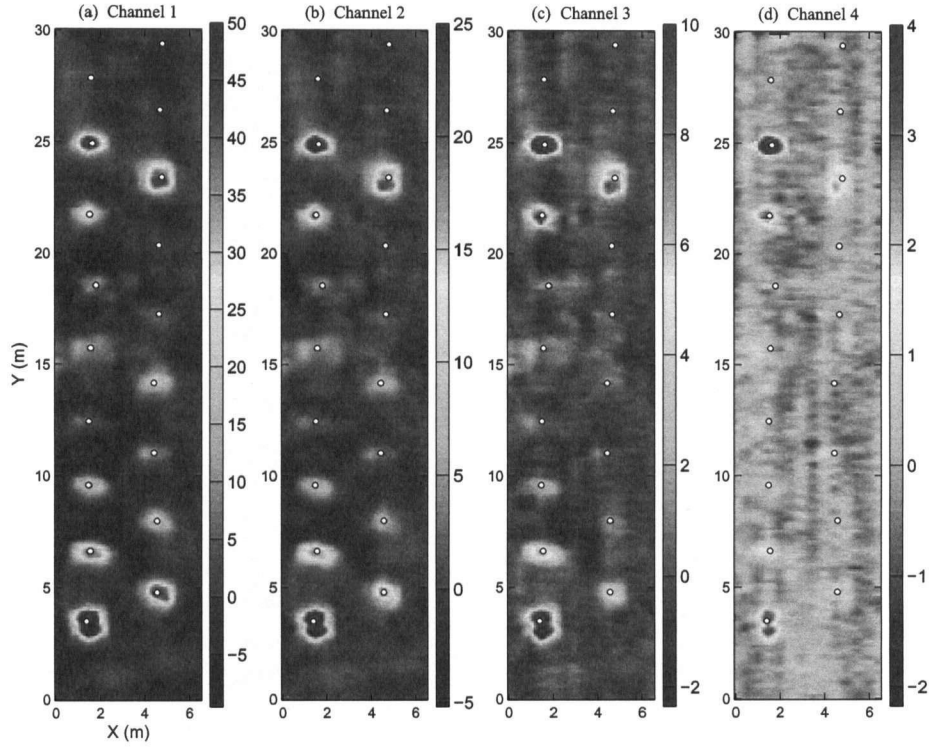

Figure B.25: Detrended Waimea data from the 4 ms chip.

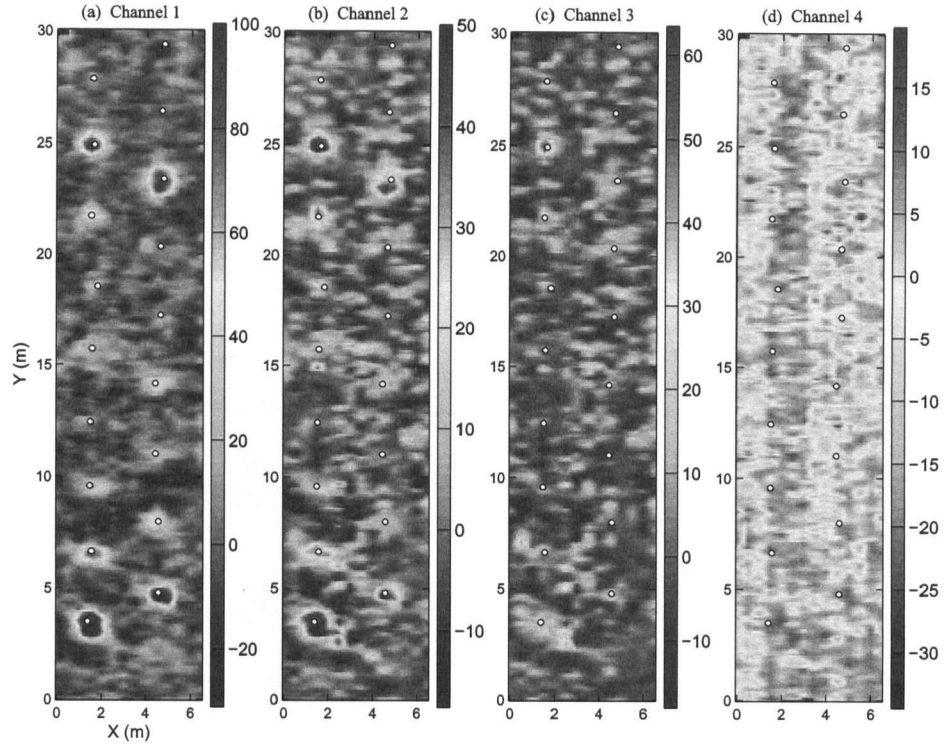

Figure B.26: Detrended Waimea data from the 2 ms chip.

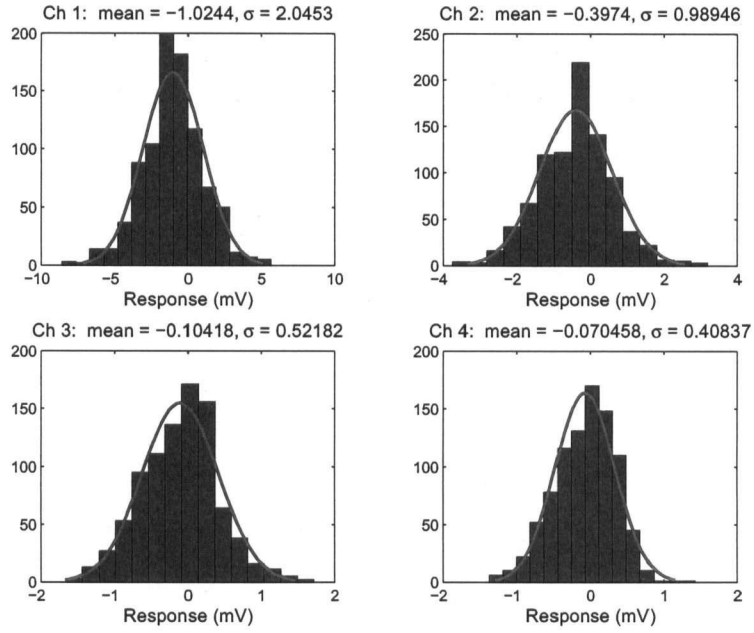

Figure B.27: Waimea Soil Histogram for the 10 ms chip data.

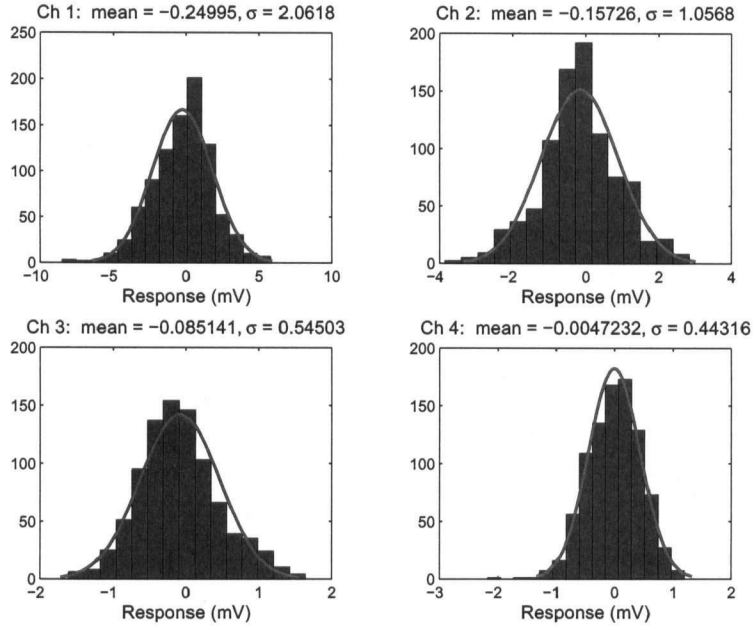

Figure B.28: Waimea Soil Histogram for the 4 ms chip data.

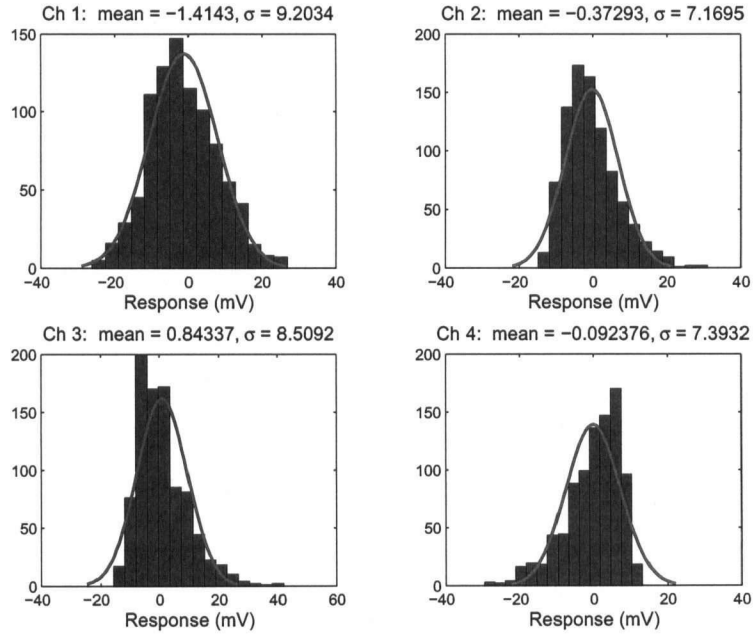

Figure B.29: Waimea Soil Histogram for the 2 ms chip data.

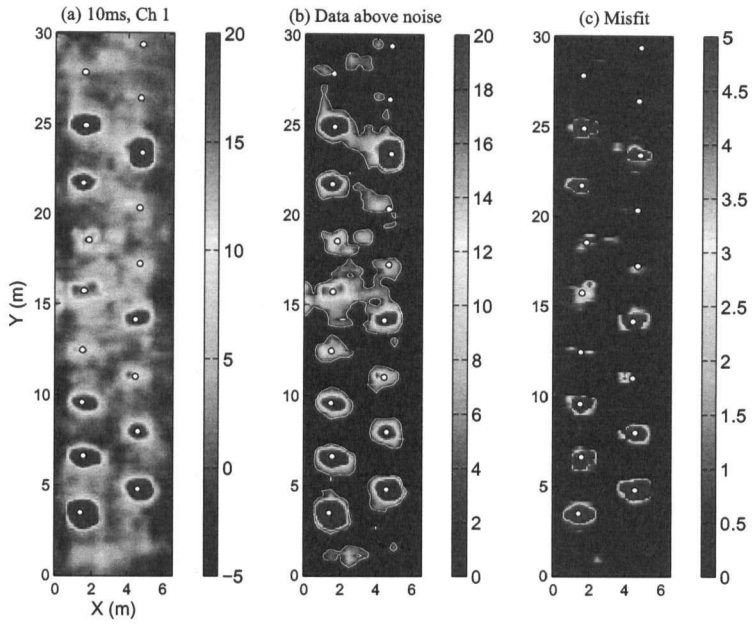

Figure B.30: (a) Raw 10 ms chip data for the first time channel. (b) Data greater than twice the standard deviation of the background noise. (c) The soil misfit calculated for the data above the background noise.

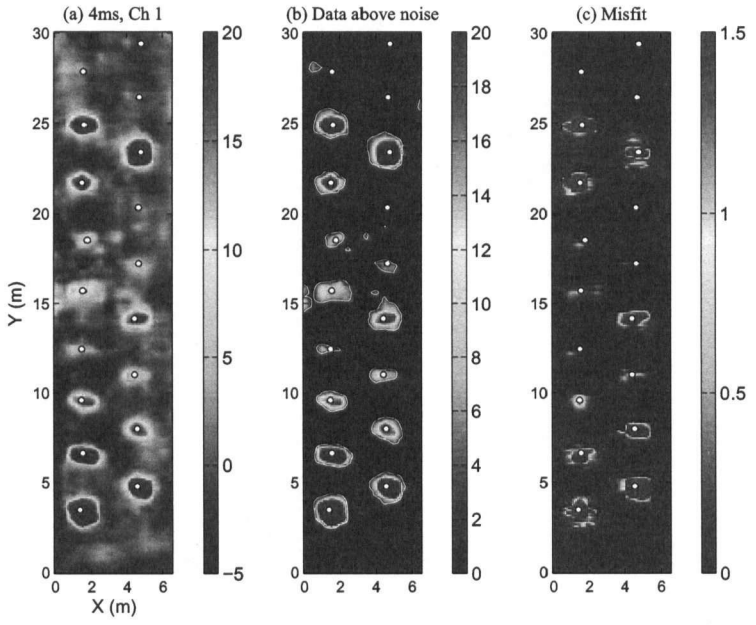

Figure B.31: (b) Raw 4 ms chip data for the first time channel. (b) Data greater than twice the standard deviation of the background noise. (c) The soil misfit calculated for the data above the background noise.

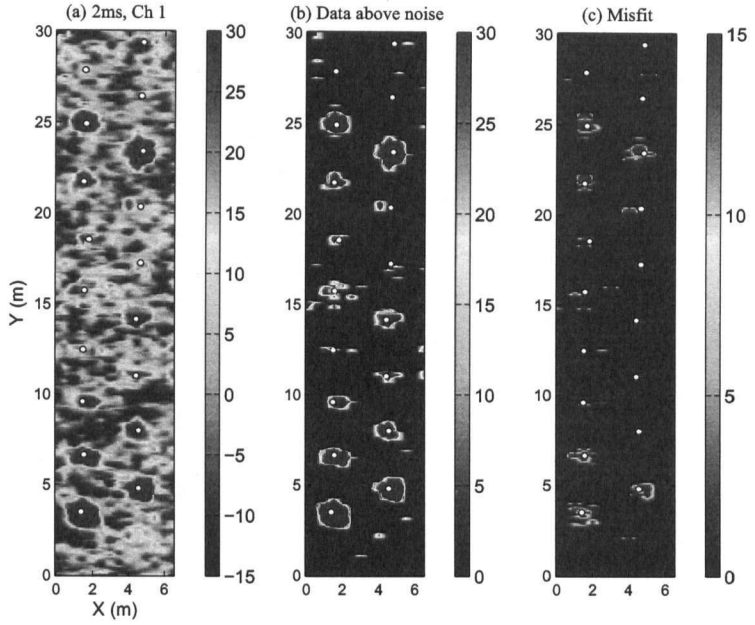

Figure B.32: (a) Raw 2 ms chip data for the first time channel. (b) Data greater than twice the standard deviation of the background noise. (c) The soil misfit calculated for the data above the background noise.

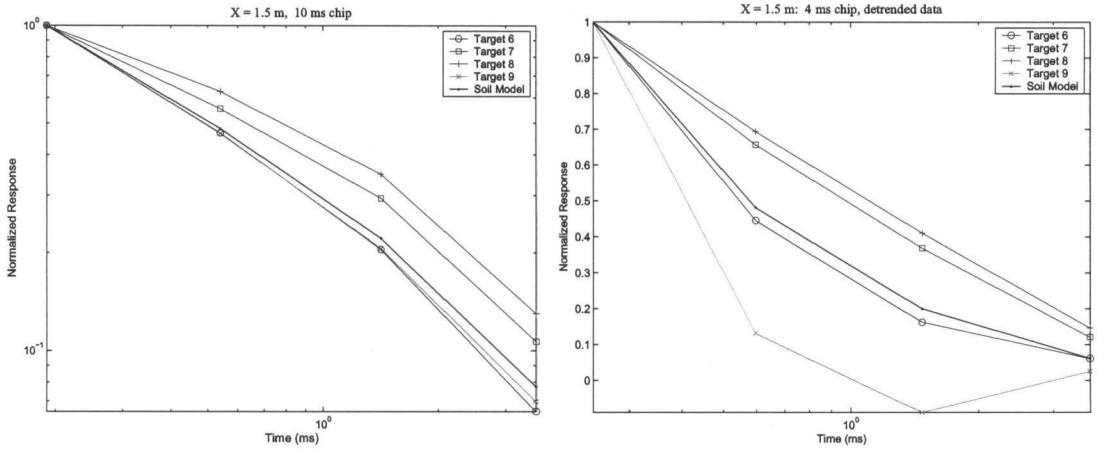

(a) Soil decay for the 10 ms chip

(b) Soil decay for the 4 ms chip

Figure B.33: Decay comparisons.

Appendix C

The Effect of Transmitter waveform on the TEM Response

Chapter 2 proposed parameterizations for the decay of the polarization to a step-off response. In a typical TEM system, a the waveform consists of a series of bipolar or unipolar pulses, with the secondary field being measured in the off-time between pulses. The Geonics EM63 and Geonics EM61 sensors are examples of this type of pulse TEM systems. The inductance of the transmitter loop does not allow for an instantaneous introduction or removal of current. The step-on of the transmitter current is exponential, with a time constant proportional to the inductance and inversely proportional to the resistance. In order to turn off the primary field quickly, the transmitter current is turned off using a linear ramp (Figure C.1). In this appendix we study how the transmitter waveform affects the measured signal. In particular, we would like to determine if the parameterizations we propose for the step-off response can be used for modelling responses due to transmitter waveforms like those in Figure C.1.

C.1 Effect of Tx pulse length

The first property of the transmitter waveform that we study is the pulse length. Consider a single rectangular pulse with a width of Δt (Figure C.1(b)):

$$g(t) = \begin{cases} H_1 & \text{if } -\Delta t < t < 0 \\ 0 & \text{otherwise} \end{cases} \tag{C.1}$$

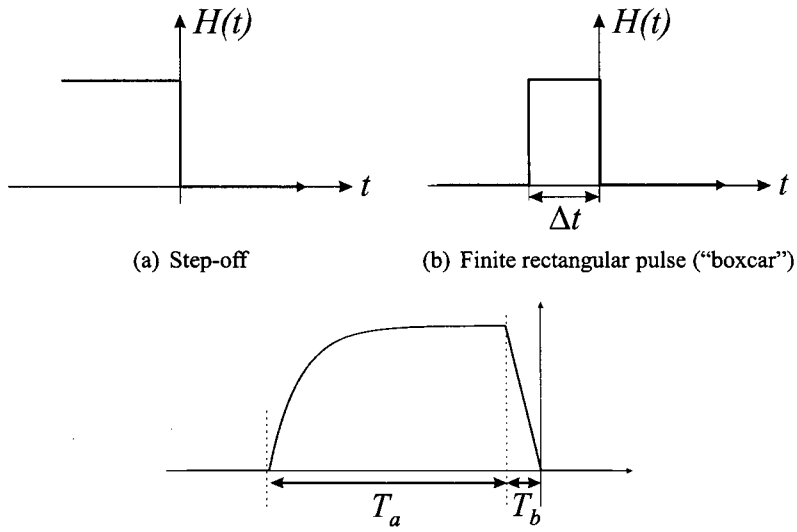

(a) Step-off

(b) Finite rectangular pulse ("boxcar")

(c) A TEM sensor exponential on/ramp off transmitter pulse.

Figure C.1: Examples of TEM transmitter waveforms (a) A step-off waveform (b) A single rectangular pulse (c) A typical exponential on/ramp off transmitter pulse commonly used in TEM sensors that measure in the off-time. T_a is the length of the exponential increase in transmitter current and T_b is the length of the linear turn-off ramp.

Let us consider a test step-off response

$$L(t) = \frac{1}{t}\exp\left(-\frac{t}{\gamma}\right) \tag{C.2}$$

This function is simply equation 2.17, with $k = \beta = 1$. To obtain the response due to a transmitter waveform $g(t)$, we convolve the impulse response $L^I(t) = -\partial L/\partial t$ with the waveform:

$$L^g(t) = \int_{-\infty}^{t} g(t')\, L^I(t - t')\, dt' \tag{C.3}$$

Substitution of the impulse response and rectangular pulse waveform into equation C.3 gives

$$L^g(t) = H_1\left[\frac{1}{t}\exp\left(-\frac{t}{\gamma}\right)\right] - H_1\left[\frac{1}{t+\Delta t}\exp\left(-\frac{t+\Delta t}{\gamma}\right)\right] \tag{C.4}$$

As expected, equation C.4 shows that for a large Δt relative to the target time constant γ, the single pulse response will have approximately the same form as the step-off response. Figure C.2 demonstrates how the pulse lengths affect the time decay function when a target has a time constant

$\gamma = 5$ ms.

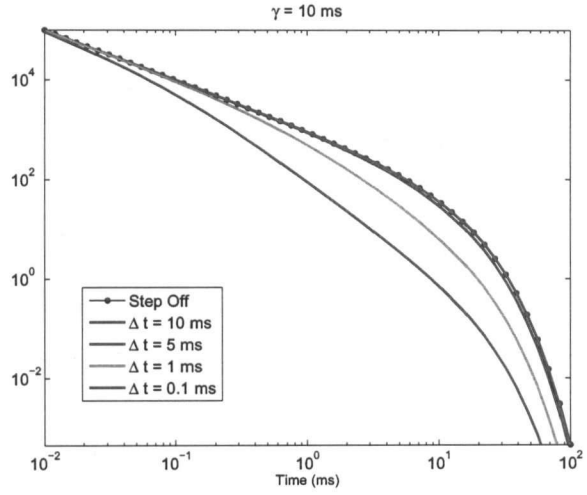

Figure C.2: Effect of pulse length on the time decay function $L(t)$ of equation C.2, where $\gamma = 10$ ms.

We can not expect to accurately estimate the true time constant of a target, when the time constant is greater than the pulse length.

C.2 Effect of Tx Pulse Ramp off

In order to turn off the primary field quickly, the transmitter current is turned off using a linear ramp. In order to study how the linear ramp affects the TEM signal, consider the following waveform $g(t)$:

$$g(t) = \begin{cases} H_1 & \text{if } t < -\Delta t \\ -\dfrac{H_1}{\Delta t}\, t & \text{for } -\Delta t < t < 0 \end{cases} \tag{C.5}$$

The length of the ramp is Δt. Examples of linear ramp waveforms are plotted in figure C.3(a).

We use two step-off functions to help study the effect of the linear ramp. The first step-off function we consider is $L_1(t) = 1/t$. Substitution of the impulse response and equation C.5 gives

$$L_1^g(t) = H_1 \frac{1}{\Delta t} \left[\ln(t + \Delta t) - \ln(t)\right] = H_1 \frac{1}{\Delta t} \ln\left(1 + \frac{\Delta t}{t}\right) \tag{C.6}$$

The second function we consider is $L_2(t) = 1/\sqrt{t}$, which is the early time behaviour for non-

permeable conductive items. The response due to a linear-ramp off waveform is

$$L_2^g(t) = H_1 \frac{2}{\Delta t}\left(\sqrt{t+\Delta t} - \sqrt{t}\right) \tag{C.7}$$

We note that for small Δt, and therefore a very fast ramp, equations C.6 and C.7 have the form of the derivative of $\ln(t)$ and $\sqrt{t}$, respectively. If we take the limit of $\Delta t \to 0$, then

$$\lim_{\Delta t \to 0} L_1^g(t) = H_1 \frac{1}{t} \tag{C.8}$$

and

$$\lim_{\Delta t \to 0} L_2^g(t) = H_1 \frac{1}{\sqrt{t}} \tag{C.9}$$

which are the step-off responses. Equation C.6 shows that for larger Δt and smaller t (i.e. early times) the response will deviate from the step-off response. At later times the response transitions to the step-off response (Figure C.3). An erroneous early time transition might be assumed if the measurement time is early, and the ramp is large. In such cases, parameterizations that estimate the magnetic crossover may have inaccurate estimates.

C.3 Effect of Tx Pulse time constant

A standard transmitter coil has an exponential charge up due to the resistance and inductance of the coil. The expression for an exponential on and step off current is

$$g(t) = \begin{cases} 1 - \exp\left(-\dfrac{t+\Delta t}{\tau}\right) & \text{, if} -\Delta t < t < 0 \\ 0 & \text{, otherwise} \end{cases} \tag{C.10}$$

where τ is the time constant of the transmitter current. A signal that has a step-off response of C.2, will have the following response to Equation C.10:

$$L^g(t) = H_1\left[\frac{1}{t}\exp\left(-\frac{t}{\gamma}\right)\right] - H_1\left[\frac{1}{t+\Delta t}\exp\left(-\frac{t+\Delta t}{\gamma}\right)\frac{1-\exp\left(-\Delta t/\tau\right)}{1-\exp\left(-\Delta t\left(\frac{1}{\tau}-1\right)\right)}\right]$$
$$+ H_1\left[\frac{\exp(-t)}{1-\exp(\Delta t/\tau)}\left(Ei\left[(t+\Delta t)\left(1-\frac{1}{\gamma}\right)\right] + Ei\left[t\left(1-\frac{1}{\gamma}\right)\right]\right)\right] \tag{C.11}$$

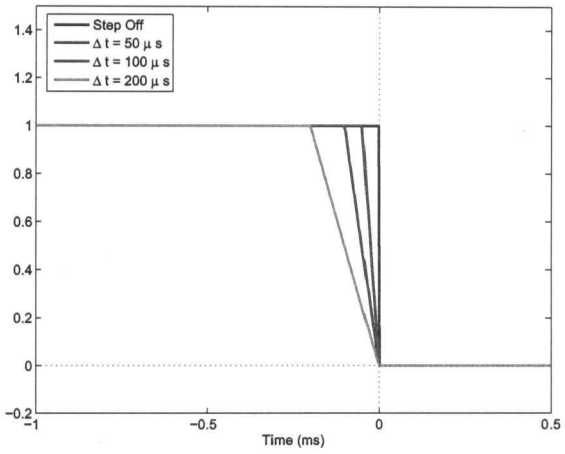

(a) Example of ramp-off waveforms

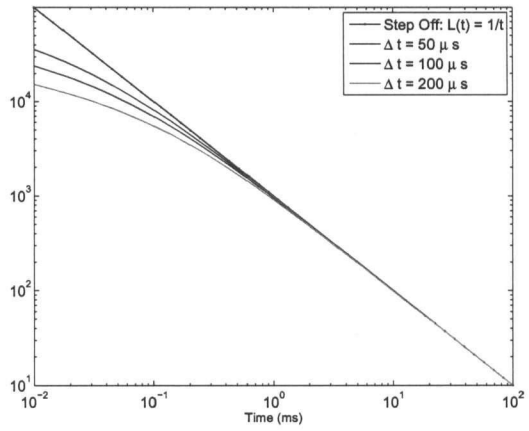

(b) Ramp-off responses for a target with a step-off response of $L(t) = 1/t$.

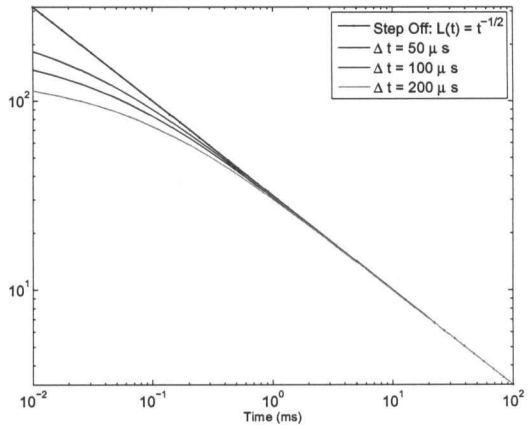

(c) Ramp-off responses for a target with a step-off response of $L(t) = 1/\sqrt{t}$.

Figure C.3: Responses due to different lengths of linear turn-off. A linear ramp will change the

As expected, equation C.11 simplifies to equation C.4 in the limit that $\tau \rightarrow 0$. Figure C.4 shows the effect of the transmitter current time constant on the response. Clearly the time constant has very

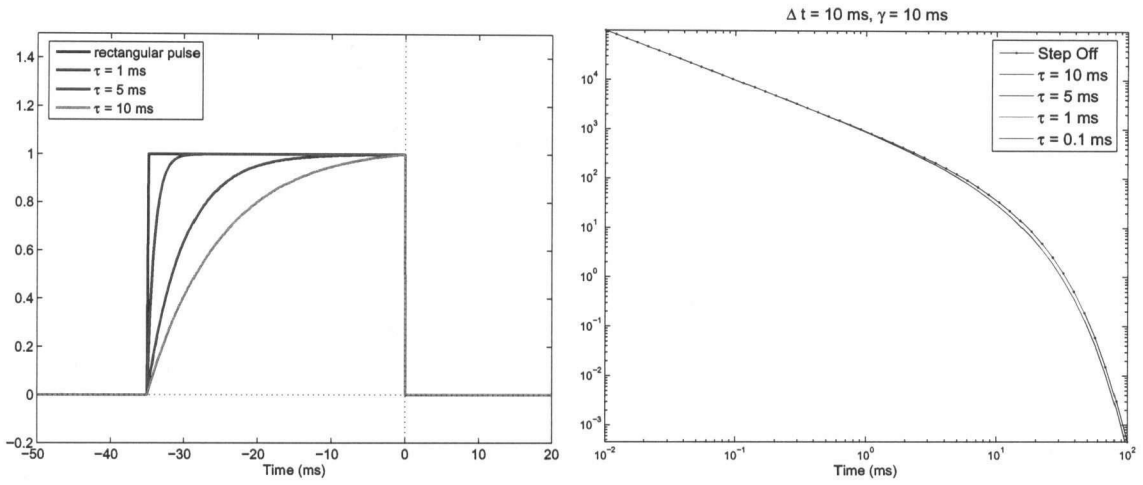

(a) Waveforms for testing the effect of the exponential on time constants. The on-time is $\Delta = 35$ ms.

(b) Effect of different exponential-on time constants τ on the response. The pulse on-time is $\Delta = 10$ ms.

Figure C.4: Examples of how the step-off response affected by the exponential time constant τ of the waveform pulse. The time constant of the waveform has less impact on the signal.

little impact.

C.4 Effect of Previous pulses

The waveform of pulse induction systems consists of a series of bipolar or unipolar pulses. Targets that have time constants of the order of the length of time between these pulses are sensitive to multiple pulses. Figures C.5 and C.6 demonstrate this effect for a pair of bipolar and unipolar pulses, respectively. For the bipolar pulse example, an on time of 30 ms and a 50 percent duty cycle waveform is convolved with the impulse response of the step-off test function of Equation C.2. For the unipolar example a 25 percent duty cycle waveform with an on time of 15 ms is modelled. The influence of a previous pulse is very small for both cases. For the bipolar pulse example, the effect of the previous pulse is a reduction in the signal at late times. There is an increase in the signal for unipolar pulses. These effects are seen only for longer time constant targets.

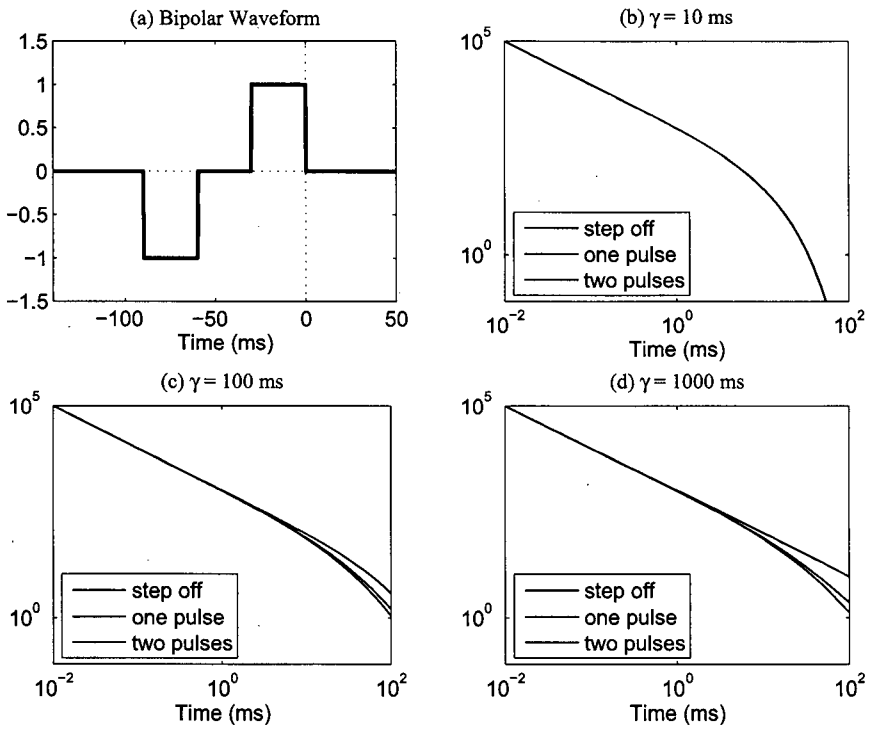

Figure C.5: Effect of a pair of bipolar pulses on a step-off response. The on time for these pulses is 30 ms and the waveform has a 50 percent duty cycle. Targets with time constants of (b) $\tau = 10$ ms, (c) $\tau = 100$ ms, and (d) $\tau = 1000$.

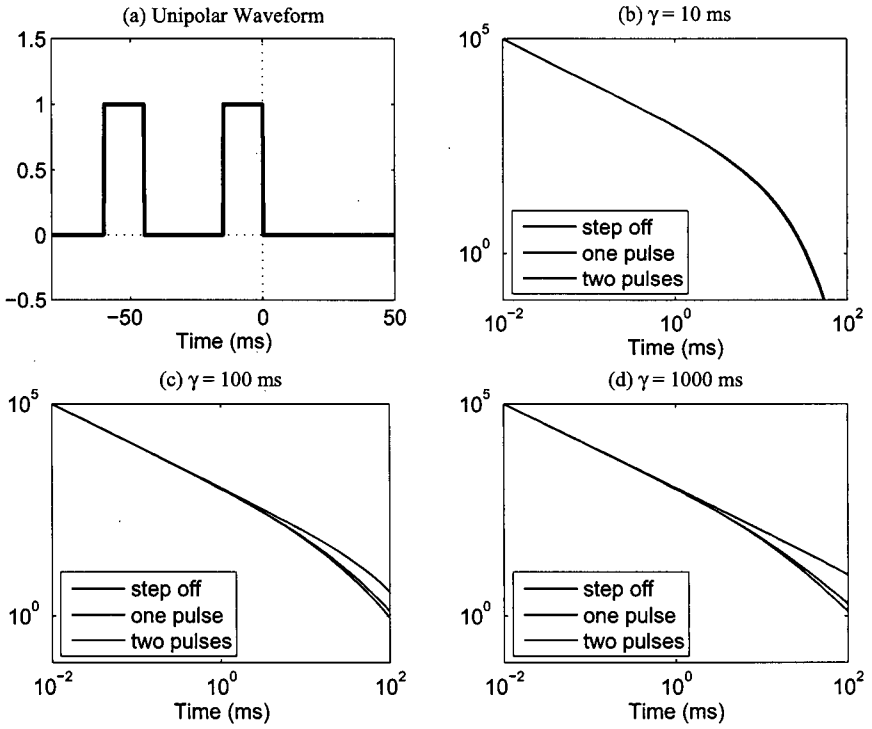

Figure C.6: Effect of a pair of unipolar pulses on a step-off response. The on time for these pulses is 15 ms and the waveform has a 25 percent duty cycle.

C.5 Response due to the EM63 and EM61 pulse

The majority of data examples in this thesis are from the EM61-MK2 sensor and EM63 time domain electromagnetic sensor. The waveforms are an exponential current increase followed by a linear ramp off:

$$g(t) = \begin{cases} 1 - \exp\left[-\frac{(t+T_a+T_b)}{Tx}\right] & , \text{if} -(T_a+T_b) < t < -T_b \\ -\frac{[1-\exp(-T_a/T_x)]}{b} \; t & , \text{if} -T_b \leq t < 0 \end{cases} \tag{C.12}$$

where T_a is the length of the exponential charge up, T_x is the time constant of the transmitter loop, and T_b is the length of the turn-off ramp.

A signal that has a step-off response of C.2, will have the following response to Equation C.12:

$$L^g(t) = \frac{-1}{1-\exp(-T_a/T_x)} \frac{1}{T_x} \exp\left[-\frac{(t+T_a+T_b)}{T_x}\right] \times \left(Ei\left[(t+T_b)\left(\frac{1}{\gamma}\right) - \frac{1}{T_x}\right] + Ei\left[(t+T_a+T_b)\left(\frac{1}{\gamma}\right) - \frac{1}{T_x}\right]\right) + \frac{1}{T_b}\left[Ei\left(\frac{t}{\gamma}\right) - Ei\left(\frac{t+T_b}{\gamma}\right)\right] \tag{C.13}$$

Figure C.7 plots the responses described by C.13 for a target with a time constant of 10 ms. There

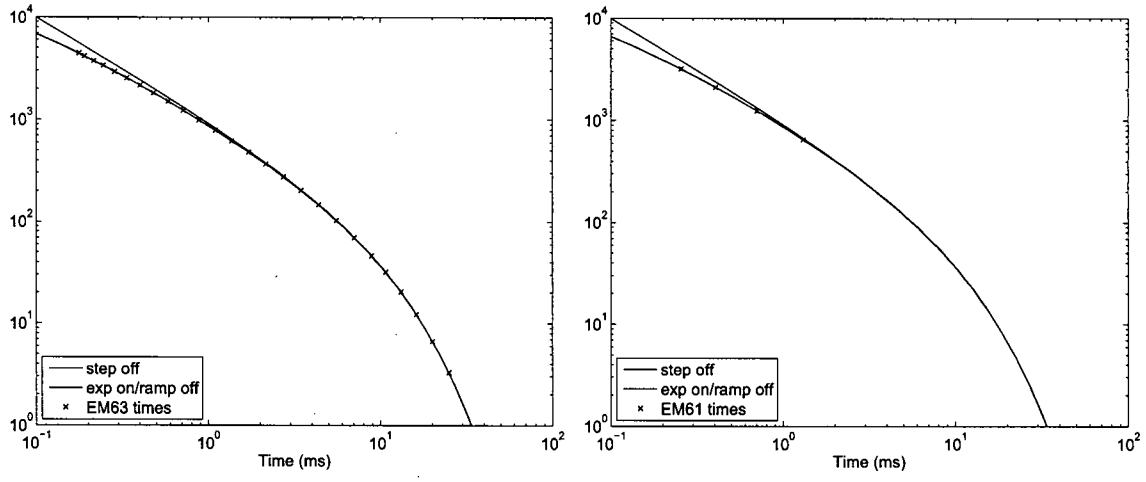

(a) Effect of a single Geonics EM63 pulse

(b) Effect of a single Geonics EM61 pulse

Figure C.7: Effect of a single Geonics EM63 and EM61 pulse on a step off response.

is a minor change in the response at early time.

C.6 Summary

The transmitter waveforms of TEM sensors will impact the measured decay of the target. In this section, the impact of the transmitter waveform was studied by convolving the impulse response with different transmitter waveforms. We found that for the parameterizations we propose for the step-off response can be used for modelling responses due to transmitter waveforms we would expect from a Geonics EM63, which is the sensor used to collect most of the data presented in thesis.

Appendix D

The magnetization decay for different waveforms

In this appendix we derive the expressions for the magnetization due to a collection of non-interacting single domain grains. We assume that the distribution of time constants are log-uniformly distributed. We derive expressions for a finite width pulse and ramp-on pulse D.1.

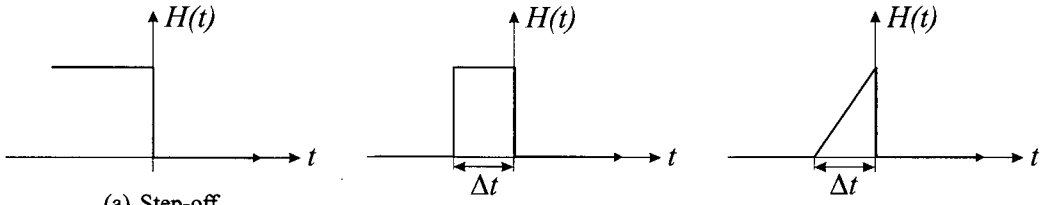

(a) Step-off (b) Finite pulse (c) Ramp on

Figure D.1: Waveforms

D.1 The Magnetization decay $M(t)$ for Finite width pulse

The magnetization of a step off field H can be written as

$$M(t) - M_o = H\chi_o F(t) \tag{D.1}$$

where χ_o is the DC susceptibility, and $F(t)$ is the after effect function. In the following treatment, we assume that $M_o = 0$ and the aftereffect function for a single relaxation time can be represented as $F(t) = \exp(t/\tau)$. The impulse response for a single relaxation time is then

$$F^i(t) = \frac{\partial F(t)}{\partial t} = \frac{1}{\tau}\exp(t/\tau) \tag{D.2}$$

Substitution of equation D.2 into (D.1) gives

$$\begin{aligned} M^i(t) &= \frac{H\chi_o}{\tau}\int_{-\infty}^{0} g(t')\exp\left[-\frac{(t-t')}{\tau}\right]dt' \\ &= \frac{H\chi_o}{\tau}\int_{-\Delta t}^{0}\exp\left(\frac{-t}{\tau}\right)\exp\left(\frac{t'}{\tau}\right)dt' = \frac{H\chi_o}{\tau}\exp\left(\frac{-t}{\tau}\right)\int_{-\Delta t}^{0}\exp\left(\frac{t'}{\tau}\right)dt' \\ &= \frac{H\chi_o}{\tau}\exp\left(\frac{-t}{\tau}\right)\left[\tau\exp\left(\frac{t'}{\tau}\right)\right]_{-\Delta t}^{0} = \frac{H\chi_o}{\tau}\exp\left(\frac{-t}{\tau}\right)\left[1-\exp\left(\frac{-\Delta t}{\tau}\right)\right] \\ &= \frac{H\chi_o}{\tau}\left[\exp\left(\frac{-t}{\tau}\right)-\exp\left(\frac{-(t+\Delta t)}{\tau}\right)\right] \end{aligned} \tag{D.3}$$

We then integrate over a uniform log distribution of time constants. Substitution of the appropriate distribution function is

$$f(\tau) = \frac{1}{\tau}\frac{1}{\ln(\tau_2/\tau_1)} \tag{D.4}$$

for $\tau_1 \leq \tau \leq \tau_2$, and integrating gives

$$\begin{aligned} M^i(t) &= \frac{H\chi_o}{\ln(\tau_2/\tau_1)}\left[\int_{\tau_1}^{\tau_2}\exp\left(\frac{-t}{\tau}\right)-\int_{\tau_1}^{\tau_2}\exp\left(\frac{-(t+\Delta t)}{\tau}\right)\right] \\ &= \frac{H\chi_o}{\ln(\tau_2/\tau_1)}\left[E_1\left(\frac{t}{\tau_2}\right)-E_1\left(\frac{t}{\tau_1}\right)-E_1\left(\frac{(t+\Delta t)}{\tau_2}\right)+E_1\left(\frac{(t+\Delta t)}{\tau_2}\right)\right] \end{aligned} \tag{D.5}$$

where E_1 is the exponential integral. Asymptotic and series expansions of the exponential integral are used to evaluate D.5. The asymptotic expansion of E_1 is

$$E_1(z) = \frac{e^{-z}}{z}\left(1-\frac{1}{z}+\frac{2}{z^2}-\frac{6}{z^3}+\ldots\right) \tag{D.6}$$

The asymptotic expansion is suitable for large z. The series expansion of E_1 is

$$E_1(z) = -\gamma-\ln(z)-\sum_{n=1}^{\infty}\frac{(-1)^n z^n}{nn!} \tag{D.7}$$

where γ is the Euler constant $\gamma = 0.577\ldots$. The series expansion is suitable for small z.

Since $t \ll \tau_2$, $E_1(t/\tau_2)$ is evaluated with the series expansion:

$$\begin{aligned} E_1\left(\frac{t}{\tau_2}\right) &= -\gamma - \ln\left(\frac{t}{\tau_2}\right) - \left[\frac{(-1)(t/\tau_2)}{1} + \frac{(-1)^2(t/\tau_2)^2}{2\,2!} + \ldots\right] \\ &\quad -\gamma - \ln\left(\frac{t}{\tau_2}\right) + \frac{t}{\tau_2} - \left(\frac{t}{\tau_2}\right)^2 \frac{1}{4} + \ldots \\ &\approx -\gamma - \ln\left(\frac{t}{\tau_2}\right) \end{aligned} \tag{D.8}$$

Since $t \gg \tau_1$, $E_1(t/\tau_1)$ is evaluated with the asymptotic expansion:

$$\begin{aligned} E_1\left(\frac{t}{\tau_1}\right) &= \exp\left(\frac{-t}{\tau_1}\right)\left(\frac{\tau_1}{t}\right)\left(1 - \left(\frac{\tau_1}{t}\right) + 2\left(\frac{\tau_1}{t}\right)^2 - \ldots\right) \\ &\approx 0 \end{aligned} \tag{D.9}$$

Substitution of D.8 and D.9 the into D.5 leads to an expression of the magnetization decay due to a finite pulse:

$$\begin{aligned} M^{pulse}(t) &\approx \frac{H\chi_o}{\ln(\tau_2/\tau_1)}\left[\left(-\gamma - \ln\left(\frac{t}{\tau_2}\right)\right) - \left(-\gamma - \ln\left(\frac{t+\Delta t}{\tau_2}\right)\right)\right] \\ &= \frac{H\chi_o}{\ln(\tau_2/\tau_1)}\left[\ln(t+\Delta t) - \ln(t)\right] \\ &= \frac{H\chi_o}{\ln(\tau_2/\tau_1)}\ln\left(1 + \frac{\Delta t}{t}\right) \end{aligned} \tag{D.10}$$

D.2 The $\partial M/\partial t$ response for a finite width pulse

Most metal detectors measure the time derivative of the secondary magnetic field, such that the sensor response is proportional to the change in the ferrite magnetization over time. The impulse of the $\partial M/\partial t$ response requires two derivative (one to get the impulse and the second to get the derivative):

$$\frac{\partial^2 F(t)}{\partial t^2} = -\frac{1}{\tau^2}\exp\left(-\frac{t}{\tau}\right) \tag{D.11}$$

Therefore, the impulse response for the derivative of the magnetization is

$$\frac{\partial M^I}{\partial t} = -\frac{H\chi_o}{\tau^2}\exp\left(-\frac{t}{\tau}\right) \tag{D.12}$$

Following the same steps as in the previous section, we convolve to determine the response:

$$\begin{aligned}\frac{\partial M}{\partial t} &= -\frac{H\chi_o}{\tau^2}\int_{-\infty}^{0} g\left(t'\right)\exp\left[-\frac{(t-t')}{\tau}\right]dt' \\ &= -\frac{H\chi_o}{\tau^2}\int_{-\Delta t}^{0}\exp\left[-\frac{(t-t')}{\tau}\right]dt' = -\frac{H\chi_o}{\tau^2}\exp\left(\frac{-t}{\tau}\right)\int_{-\Delta t}^{0}\exp\left(\frac{t'}{\tau}\right)dt' \\ &= -\frac{H\chi_o}{\tau^2}\exp\left(\frac{-t}{\tau}\right)\left[\tau\exp\left(\frac{t'}{\tau}\right)\right]_{-\Delta t}^{0} = -\frac{H\chi_o}{\tau^2}\exp\left(\frac{-t}{\tau}\right)\left[1-\exp\left(\frac{-\Delta t}{\tau}\right)\right] \\ &= -\frac{H\chi_o}{\tau^2}\left[\exp\left(\frac{-t}{\tau}\right)-\exp\left(\frac{-(t+\Delta t)}{\tau}\right)\right]\end{aligned} \tag{D.13}$$

We now integrate D.13 over a log-uniform distribution, and apply the same assumptions (i.e. $t \gg \tau_1$ and $t \ll \tau_1$) to obtain the final expression:

$$\begin{aligned}\frac{\partial M}{\partial t} &= -\frac{H\chi_o}{\ln\left(\tau_2/\tau_1\right)}\left[\frac{1}{t}\exp\left(\frac{-t}{\tau}\right)-\frac{1}{(t+\Delta t)}\exp\left(\frac{-(t+\Delta t)}{\tau}\right)\right]_{\tau_1}^{\tau_2} \\ &= -\frac{H\chi_o}{\ln\left(\tau_2/\tau_1\right)}\left[\frac{1}{t}-\frac{1}{t+\Delta t}\right]\end{aligned} \tag{D.14}$$

D.3 The $\partial M/\partial t$ response for a ramp-on response

Candy (1996) derived the expression for the time derivative of magnetization for a ramp-on response. The ramp-on waveform can be written as

$$g\left(t'\right) = H\left(t'+\Delta\right) \tag{D.15}$$

Convolving the impulse response with the waveform gives

$$\begin{aligned}\frac{\partial H}{\partial t} &= \frac{H\chi_o}{\tau^2}\int_{-\infty}^{0} g\left(t'\right)\exp\left(\frac{-(t-t')}{\tau}\right)dt' \\ &= \frac{H\chi_o}{\tau^2}\int_{-\Delta t}^{0}\left(t'+\Delta t\right)\exp\left(\frac{-(t-t')}{\tau}\right)dt'\end{aligned} \tag{D.16}$$

For convenience, we split the integral into two terms:

$$\begin{aligned}\frac{\partial H}{\partial t} &= \frac{H\chi_o}{\tau^2}\Delta t\int_{-\Delta t}^{0}\exp\left(\frac{-(t-t')}{\tau}\right)dt' + \frac{H\chi_o}{\tau^2}\int_{-\Delta t}^{0} t'\exp\left(\frac{-(t-t')}{\tau}\right)dt' \\ &= I_1 + I_2\end{aligned} \tag{D.17}$$

The integral I_1 was solved earlier (without the $-\Delta t$) when deriving the $\partial H/\partial t$ field from a box-car pulse:

$$I_1 = H\chi_o \Delta t \left[\frac{1}{\tau}\exp\left(\frac{-t}{\tau}\right) - \frac{1}{\tau}\exp\left(\frac{-(t+\Delta t)}{\tau}\right)\right] \tag{D.18}$$

Solving I_2:

$$\begin{aligned} I_2 &= \frac{H\chi_o}{\tau^2}\int_{-\Delta t}^{0} t' \exp\left[\frac{-(t-t')}{\tau}\right] dt' = \frac{H\chi_o}{\tau^2}\exp\left(\frac{-t}{\tau}\right)\int_{-\Delta t}^{0} t' \exp\left(\frac{t'}{\tau}\right) dt' \\ &= \frac{H\chi_o}{\tau^2}\exp\left(\frac{-t}{\tau}\right)\left[\tau^2 \exp\left(\frac{t'}{\tau}\right)\left(\frac{t'}{\tau}-1\right)\right]_{-\Delta t}^{0} \\ &= -H\chi_o\left[\exp\left(\frac{-t}{\tau}\right) - \frac{\Delta t}{t}\exp\left(\frac{-(t+\Delta t)}{\tau}\right) - \exp\left(\frac{-(t+\Delta t)}{\tau}\right)\right] \end{aligned} \tag{D.19}$$

Putting I_1 and I_2 together:

$$\begin{aligned} \frac{\partial M}{\partial t} &= H\chi_o[\frac{\Delta t}{\tau}\exp\left(\frac{-t}{\tau}\right) - \frac{\Delta t}{\tau}\exp\left(\frac{-(t+\Delta t)}{\tau}\right) - \\ &\quad \exp\left(\frac{-t}{\tau}\right) + \frac{\Delta t}{\tau}\exp\left(\frac{-(t+\Delta t)}{\tau}\right) + \exp\left(\frac{-(t+\Delta t)}{\tau}\right)] \\ &= H\chi_o\left[\frac{\Delta t}{\tau}\exp\left(\frac{-t}{\tau}\right) - \exp\left(\frac{-t}{\tau}\right) + \exp\left(\frac{-(t+\Delta t)}{\tau}\right)\right] \end{aligned} \tag{D.20}$$

Now integrate over the time constants

$$\begin{aligned} \frac{\partial M}{\partial t} = \frac{H\chi_o}{\ln(\tau_2/\tau_1)}[\Delta t\int_{\tau_1}^{\tau_2}\frac{1}{\tau^2}\exp\left(\frac{-t}{\tau}\right)d\tau - \int_{\tau_1}^{\tau_2}\frac{1}{\tau}\exp\left(\frac{-t}{\tau}\right)d\tau + \\ \int_{\tau_1}^{\tau_2}\frac{1}{\tau}\exp\left(\frac{-(t+\Delta t)}{\tau}\right)d\tau] \end{aligned} \tag{D.21}$$

These integrals have been evaluated earlier. Therefore the expression for the time derivative of the magnetization is

$$\begin{aligned} \frac{\partial M}{\partial t} = \frac{H\chi_o}{\ln(\tau_2/\tau_1)}[\Delta t\left[\frac{1}{t}\exp(-t/\tau_2) - \frac{1}{t}\exp(-t/\tau_1)\right] - \\ \left[E_1\left(\frac{t}{\tau_2}\right) - E_1\left(\frac{t}{\tau_1}\right)\right] + \left[E_1\left(\frac{(t+\Delta t)}{\tau_2}\right) - E_1\left(\frac{(t+\Delta t)}{\tau_1}\right)\right]] \end{aligned} \tag{D.22}$$

Similar to section D.1, we use approximations for the exponential integral

$$\begin{aligned}\frac{\partial M}{\partial t} &= \frac{H\chi_o}{\ln(\tau_2/\tau_1)}\left[\Delta t\left(\frac{1}{t}-0\right)-[(-\gamma-\ln(t/\tau_2))-0]+[(-\gamma-\ln((t+\Delta t)/\tau_2))-0]\right] \\ &= \frac{H\chi_o}{\ln(\tau_2/\tau_1)}\left[\frac{\Delta t}{t}+\ln(t)-\ln(t+\Delta t)\right] \\ &= -\frac{H\chi_o}{\ln(\tau_2/\tau_1)}\left[\ln\left(1+\frac{\Delta t}{t}\right)-\frac{\Delta t}{t}\right]\end{aligned} \tag{D.23}$$

Bibliography

T.W. Altshuler. Shape and orientation effects on magnetic signature prediction for unexploded ordnance. In *Proceedings of the 1996 UXO Forum*, 1996.

G. B. Arfken. *Mathematical Methods for Physicists*. Academic Press, New York, N. Y., third edition, 1985.

C.E. Baum. *Detection and Identification of Visually Obscured Targets*, chapter The Magnetic Polarizability Dyadic and Point Symmetry, pages 219–242. Taylor and Francis, 1999.

T. Bell. Geo-location requirements for UXO discrimination. In *SERDP & ESTCP Geolocation Workshop*, 2005.

T. Bell, B. Barrow, J. Miller, and D. Keiswetter. Time and frequency domain electromagnetic induction signatures of unexploded ordnance. *Subsurface Sensing Technologies and Applications*, 2(3):153 – 175, 2001a.

T. Bell, B. Barrow, and J.T. Miller. Subsurface discrimination using electromagnetic induction sensors. *IEEE Transactions Geoscience & Remote Sensing*, 39:1286–1293, 2001b.

A. Benavides and M. E. Everett. Non-linear inversion of controlled source multi-receiver electromagnetic induction data for unexploded ordnance using a continuation method. *Journal of Applied Geophysics*, 61(3):243–253, 2006.

L. Beran. Classification of unexploded ordnance. Master's thesis, University of British Columbia, 2005.

R.S. Bhatal and F.D. Stacey. Frequency independence of low-field susceptibility of rocks. *Journal of Geophysical Research*, 74:2025–2027, 1969.

S. Billings. Demonstration report for the former lowry bombing and gunnery range for estcp project 200504: Practical discrimination strategies for application to live sites. Technical report, ESTCP, 2007.

S. D. Billings. Discrimination and classification of buried unexploded ordnance using magnetometry. *IEEE Transactions Geoscience & Remote Sensing*, 42:1241 – 1251, 2004.

S.D. Billings, L. R. Pasion, and D. W. Oldenburg. Discrimination and identification of UXO by geophysical inversion of total-field magnetic data. Technical report, U.S. Army Research and Development Center, Vicksburg, MS, 2002. ERDC/GSL TR-02-16.

S.D. Billings, L.R. Pasion, and D.W. Oldenburg. Discrimination and classification of UXO using magnetometry: inversion and error analysis using robust statistics. In *Proceedings from SAGEEP 03*, 2003.

S.D. Billings, L. R. Pasion, and D. W. Oldenburg. Progress in inversion methodeologies for magnetic and electromagnetic discrimination of unexploded ordnance. Technical report, U.S. Army Research and Development Center, Vicksburg, MS, 2004.

G. Buselli. The effect of near surface superparamagnetic material on electromagnetic measurements. *Geophysics*, 47(9):1315–1324, September 1982.

D.K. Butler, E.R. Cespedes, C.B. Cox, and P.J. Wolfe. Multisensor methods for buried unexploded ordnance detection, discrimination, and identification. Technical Report T.R. SERDP-98-10, U.S. Army Corps of Engineers Waterways Experiment Station, 1998.

B. Candy. Pulse induction time domain metal detector. U.S. Patent 5,576,624, 1996.

D.M. Cargile, H.H. Bennett, R.A. Goodson, T.A. DeMoss, and E.R. Cespedes. Advanced UXO detection/discrimination technology demonstration – Kaho'olawe, Hawaii. Technical report, U.S. Army Research and Development Center, Vicksburg, MS, 2004. ERDC/EL TR-04-1.

L. Carin. FEM modelling of the EMI response of general UXO targets. In *Proceedings of UXO/Countermine Forum 2000*, 2000.

L. Carin, H. Yu, Y. Dalichaouch, A. R. Perry, P. V. Czipott, and C. E. Baum. On the wideband emi response of a rotationally symmetric permeable and conducting target. *IEEE Transactions on Geoscience and Remote Sensing*, 39(6):1206–1213, June 2001.

K. F. Casey and B. A. Baertlein. *An Overview of Electromagnetic Methods In Subsurface Detection*, chapter The Magnetic Polarizability Dyadic and Point Symmetry, pages 9–46. Taylor and Francis, 1999.

C. Colani and M. J. Aitken. Utilization of magnetic viscosity effects in soils for archaeological prospection. *Nature*, 1966.

T. F. Coleman and Y. Li. On the convergence of interior-reflective newton methods for nonlinear minimization subject to bounds. *Math. Program.*, 67(2-17):189–224, 1994. ISSN 0025-5610.

T. F. Coleman and Y. Li. A reflective Newton method for minimizing a quadratic function subject to bounds on some of the variables. 6(4):1040–1058, November 1996. ISSN 1052-6234 (print), 1095-7189 (electronic). doi: http://dx.doi.org/10.1137/S1052623494240456. URL `http://epubs.siam.org/sam-bin/dbq/article/24045`.

L.M. Collins, Y. Zhang, J. Li, H. Wang, L. Carin, S.J. Hart, S.L. Rose-Pehrsson, H.H. Nelson, and J.R. McDonald. A comparison of the performance of statistical and fuzzy algorithms for unexploded ordnance detection. *IEEE Transactions on Fuzzy Systems*, 9(1):17–30, February 2001.

G. Cross, 2006. personal communication.

M. Dabas, J. Jolivet, and A. Tabbagh. Magnetic susceptibility and viscosity of soils in a weak time varying field. *Geophysical Journal International*, 108:101–109, 1992.

Y. Das. Effects of soil electromagnetic properties on metal detectors. *IEEE Transactions on Geoscience and Remote Sensing*, 44(6):1444–1453, 2006.

Y. Das, J. E. McFee, J. Toews, and G. C. Stuart. Analysis of an electromagnetic induction detector for real-time location of buried objects. *IEEE Transactions on Geoscience and Remote Sensing*, 28(3):278–287, 1990.

P. Debye. *Polar Molecules*. Dover Publications, 1928.

Defense Science Board. Report of the defense science board task force on unexploded ordnance. Technical report, Office of the Under Secretary of Defense For Acquisition, Technology and Logistics, 2003.

J. E. Dennis and R. B. Schnabel. *Numerical Methods for Unconstrained Optimization and Nonlinear Equations*. Prentice–Hall, 1983.

D.J. Dunlop and O. Ozdemir. *Rock Magnetism: Fundamentals and frontiers*. Cambridge University Press, 1997. ISBN 0 521 00098 X.

F. Efferso, E. Auken, and K. I. Sorensen. Inversion of band-limited TEM responses. *Geophysical Prospecting*, 47:551–564, 1999.

P. C. Fannin and S. W. Charles. On the influence of distribution functions on the after-effect function of ferrofluids. *Journal of Physics D*, 28:239–242, 1995.

C. G. Farquharson, D. W. Oldenburg, and P. S. Routh. Simultaneous one-dimensional inversion of loop-loop electromagnetic data for both magnetic susceptibility and electrical conductivity. *Geophysics*, 68:1857–1869, 2003.

J. Foley, S. Billings, L. Pasion, S. Walker, and C. Pasion. UXO target detection and discrimination with electromagnetic differential illumination. Technical report, Strategic Environmental Research and Development Program (SERDP), 2005.

E. Gasperikova, J.T. Smith, F. Morrison, and A. Becker. Berkeley UXO discriminator (BUD) for UXO detection and discrimination. In *Partners in Environmental Technology Technical Symposium and Workshop*, November 2006.

P. E. Gill, W. Murray, and M. H. Wright. *Practical Optimization*. Academic Press, 1981.

F. S. Grant and G. F. West. *Interpretation Theory in Applied Geophysics*. McGraw-Hill Book Company, 1965.

R. E. Grimm, M. W. Blohm, and E. M. Lavely. UXO characterization using multicomponent, multichannel time-domain electromagnetic induction. In *Proceedings of UXO Forum '97*, 1997.

E. Haber, U. M. Ascher, and D. W. Oldenburg. Fast simulation of 3d electromagnetic problems using potentials. *Journal of Computational Physics*, 163(1):150–171, 2000.

R. Hiptmair. Multigrid method for Maxwell's equations. *SIAM Journal of Numerical Analysis*, 36:204–225, 1998.

H. Huang and I. J. Won. Detecting metal objects in magnetic environments by broadband electromagnetic method. *Geophysics*, 68(6):1877–1887, 2004.

A. A. Istratov and O. F. Vyvenko. Exponential analysis in physical phenomena. *Review of Scientific Instruments*, 70(2):1233–1257, 1999.

J. D. Jackson. *Classical Electrodyamics*. John Wiley and Sons, 1975.

A. A. Kaufman. *Geophysical Field Theory and Method.* Academic Press, 1994.

A. A. Kaufman and G. V. Keller. *Inductive Mining Prospecting.* Elsevier, 1985.

K. Klein and J. C. Santamarina. Ferromagnetic inclusions in geomaterials: Implications. *Journal of Geotechnical and Geoenvironmental Engineering*, 126(2):167–179, 2000.

Landmine Action. Explosive remnants of war: Unexploded ordnance and post-conflict communities. Technical report, Landmine Action (UK), 2002.

J.D. Lathrop, H. Shih, and W.M. Wynn. Enhanced clutter rejection with two-parameter magnetic classification for UXO. In *SPIE Conference on Detection and Remediation Technologies for Mines and Minelike Targets IV*, volume 3710, pages 37–51. The International Society for Optical Engineering, 1999.

T. Lee. The effect of a superparamgnetic layer on the transient electromagnetic response of a ground. *Geophysical Prospecting*, 32:480–496, 1983.

Y. Li, R. Kahenbuhl, T. Meglich, L. Pasion, D. Oldenburg, S. Billings, D. Sinex, and S. Walker. Improving UXO detection and discrimination in magnetic environments (SERDP project MM-1414) year 1 annual report. Technical report, Strategic Environmental Research and Development Program, 2005.

Y. Li, R. Kahenbuhl, T. Meglich, L. Pasion, D. Oldenburg, S. Billings, and D. Sinex. Improving UXO detection and discrimination in magnetic environments (SERDP project MM-1414) year 2 annual report. Technical report, Strategic Environmental Research and Development Program, 2006.

J. MacDonald, D. Knopman, N. Clancy, J. McEver, and H. Willis. Transferring army BRAC lands containing unexploded ordnance: Lessons learned and future options. Technical report, RAND Corporation, 2004.

The Mathworks. *Optimization Toolbox For Use with MATLAB*, 2nd edition, 2002.

J.E. McFee. Electromagnetic remote sensing: Low frequency electromagnetics. Technical Report 124, Defence Research Establishment Suffield, Ralston, Alberta, January 1989.

W. Menke. *Geophysical Data Analysis: Discrete Inverse Theory*. Elsevier, 1989.

J. T. Miller. Detection of copper rotating bands on buried ordnance using wide-band electromagnetic induction. In *Proceedings of UXO/Countermine Forum 2000*, 2000.

Richard Moyes. Explosive remnants of war and mines other than anti-personnel mines: A global survey 2003-2004. Technical report, Landmine Action (UK), Mines Action Canada and Actiongroup Landmine.de (Germany), 2005.

C. Müller, M. Scharmach, M. Gaal, D. Guelle, A. Lewis, and A. Sieber. Proposals for performance demonstration and modular reliability assessment for humanitarian demining. In *Internation Conference on Requirements and Technologies for the Detection, Removal and Neutralization of Landmines and UXO*, pages 233–241. Brussels, September 2003.

M. S. Munkholm and E. Auken. Electromagnetic noise contamination on transient electromagnetic soundings in culturally disturbed environments. *Journal of Engineering and Environmental Geophysics*, 1(2):119–127, 1996.

M. N. Nabighian and J. C. Macnae. *Electromagnetic Methods In Applied Geophysics: Applications*, volume 2, chapter Time Domain Electromagnetic Prospecting Methods, pages 427–520. Society of Exploration Geophysicists, 1991.

L. Neel. Theorie du trainage magnetique des ferromagnetiques en grains fins avec applications aux terres cuites. *Ann. Geophys.*, 5:99–136, 1949.

H.H. Nelson and J.R. McDonald. Target shape classification using the MTADS. In *Proceedings of UXO Forum '99*, 1999.

H.H. Nelson, T.W. Altshuler, B. Barrow E.M. Rose, J.R. McDonald, and N. Khadr. Magnetic modeling of UXO and UXO-like targets and comparison to targets measured by MTADS. In *Proceedings of the UXO/Countermine Forum*, 1998.

H.H. Nelson, J.R. McDonald, and D. Wright. Airborne UXO surveys using the MTADS. Technical Report NRL/MR/6110–05-8874, Naval Research Laboratory, 4555 Overlook Avenue, SW, Washington, DC 20375-5320, April 2005.

S.J. Norton, I.J. Won, and E.R. Cespedes. Spectral identification of buried unexploded ordnance from low-frequency electromagnetic data. *Subsurface Sensing Technologies and Applications*, 2 (3):177–189, 2001.

G. R. Olhoeft and D. W. Strangway. Magnetic relaxation and the electromagnetic response parameter. *Geophysics*, 39(3):302–311, 1974.

L. R. Pasion. Detecting unexploded ordnance with time domain electromagnetic induction. Master's thesis, University of British Columbia, 1999.

L. R. Pasion and D. W. Oldenburg. A discrimination algorithm for UXO using time domain electromagnetics. *Journal of Engineering and Environmental Geophysics*, 6(2):91–102, 2001a.

L. R. Pasion and D. W. Oldenburg. Locating and characterizing unexploded ordnance using time domain electromagnetic induction. Technical report, U.S. Army Research and Development Center, Vicksburg, MS, 2001b. ERDC/GSL TR-01-10.

L. R. Pasion, S. D. Billings, and D. W. Oldenburg. Guidelines on data quality requirements for advanced discrimination of uxo. Technical report, U.S. Army Research and Development Center, Vicksburg, MS, 2004. Project Number DACA42-03-P-0238.

L.R. Pasion, S.D. Billings, and D.W. Oldenburg. Joint and cooperative inversion of magnetic and time domain electromagnetic data for the characterization of uxo. In *Proceedings from SAGEEP 03*, 2003.

J. Putnam. Kaho'olawe program management and technology. In *Proc. 2001, UXO Forum*. New Orleans, LA, Apr 2001.

L.S. Riggs, J.E. Mooney, and D.E. Lawrence. Identification of metallic mine-like objects using low frequency magnetic fields. *IEEE Transactions on Geoscience and Remote Sensing*, 39(1), 2001.

M. Sambridge. Geophysical inversion with a neighbourhood algorithm – I. Searching a parameter space. *Geophysical Journal International*, 138:479–494, 1999a.

M. Sambridge. Geophysical inversion with a neighbourhood algorithm – II. Apprasing the ensemble. *Geophysical Journal International*, 138:727–746, 1999b.

I. Scollar, A. Tabbagh, A. Hesse, and I. Herzog. *Archaeological Prospecting and Remote Sensing*. Cambridge University Press, Cambridge, 1990.

I. Shamatava, F. Shubitidze, C. Chen, H. Youn, K. O'Neill, and K. Sun. Potential benefits of combining emi and gpr for enhanced UXO discrimination at highly contaminated sites. In *Proceedings of SPIE Detection and Remediation Technologies for Mines and Minelike Targets IX*, volume 5415, September 2004.

F. Shubitidze, K. O'Neill, S. A. Haider, K. Sun, and K. D. Paulsen. Application of the method of auxiliary sources for electromagnetic induction problem. *IEEE Trans. Geoscience & Remote Sensing*, 40:928–942, 2002a.

F. Shubitidze, K. O'Neill, S.A. Haider, K. Sun, and K.D. Paulsen. Application of the method of auxiliary sources to the wide-band electromagnetic induction problem. *IEEE transactions on geoscience and remote sensing*, 40(4):928–942, 4 2002b.

D. Sinex. Advancing the state of the art of UXO discrimination for total-field magnetic data. Master's thesis, Colorado School of Mines, 2006.

J.T. Smith, H. F. Morrison, and A. Becker. Parametric forms and the inductive response of a permeable conducting sphere. *Journal of Environmental And Engineering Geophysics*, 9:213–216, 2004.

D. D. Snyder, S. MacInnes, S. Urquhart, and K. L. Zonge. Possibilities for UXO classification using characteristic modes of the broad-band electromagnetic induction response. In *Proceedings of A New Technology Applications Conference on the Science and Technology of Unexploded Ordnance Removal and Site Remediation*, 1999.

A. Tarantola. *Inverse Problem Theory: Methods for Data Fitting and Model Parameter Estimation.* Elsevier, 1987.

T. J. Ulrych, M. D. Sacchi, and A. Woodbury. A Bayes tour of inversion: A tutorial. *Geophysics*, 66(1):55–69, 2001.

S. E. Walker, L. R. Pasion, D. W. Oldenburg, and S. D. Billings. Investigating the effect of data quality on time domain electromagnetic discrimination. *Journal of Applied Geophysics*, 61(3): 254–278, 2005a.

S.E. Walker, L.R. Pasion, S.D. Billings, D.W. Oldenburg, and Y. Li. Examples of the effect of magnetic soil environments on time domain electromagnetic data. In *Proceedings from SAGEEP 05*, 2005b.

S. H. Ward and G. W. Hohmann. *Electromagnetic Methods In Applied Geophysics: Theory*, volume 1, chapter Electromagnetic Theory for Geophysical Applications, pages 131–311. Society of Exploration Geophysicists, 1991.

G. H. Ware. EM-63 decay curve analysis for ordnance discrimination. In *Proceedings of Partners in Environmental Technology Techinical Symposium and Workshop*, 2001.

G.H. Ware. Geonics EM63 multichannel EM data processing algorithms for target location and ordnance discrimination. Technical report, Environmental Security Technology Certification Program, 2003. UX-0035.

P. B. Weichman. Surface Modes and Multipower-Law Structure in the Early-Time Electromagnetic Response of Magnetic Targets. *Physical Review Letters*, 93(2), July 2004. doi: 10.1103/PhysRevLett.93.023902.

I.J. Won, D. Keiswetter, D. R. Hanson, E. Novikova, and T.M. Hall. GEM-3: A monostatic broadband electromagnetic induction sensor. *Journal of Environmental and Engineering Geophysics*, 2 (1):53–56, March 1997.

D. Wright, D. Keiswetter, and W. SanFilipo. Advances in processing techniques for frequency domain electromagnetic induction data to improve detection of UXO-like material in adverse geologic conditions. In *Proceedings of UXO/Countermine Forum*, 2001.

Y. Zhang, L. Collins, H. Yu, C. E. Baum, and L. Carin. Sensing of unexploded ordnance with magnetometer and induction data: Theory and signal processing. *IEEE Transactions on Geoscience and Remote Sensing*, 41(5):1005–1015, May 2003.